NUREG/CR–
ANL–

Cladding Embrittlement during Postulated Loss-of-Coolant Accidents

Manuscript Completed:
Date Published: January 9, 2007 DRAFT

Prepared by
Michael Billone, Yong Yan, Tatiana Burtseva

Nuclear Engineering Division
Argonne National Laboratory
9700 South Cass Avenue
Argonne, IL 60439

H. Scott, NRC Project Manager

Prepared for
Division of Fuel, Engineering and Radiological Research
Office of Nuclear Regulatory Research
U. S. Nuclear Regulatory Commission
Washington, DC 20555
NRC JCN N6281

This page is intentionally left blank.

Abstract

The effect of fuel burnup on the embrittlement of various cladding alloys was examined with laboratory tests conducted under conditions relevant to loss-of-coolant accidents (LOCAs). The cladding materials tested were Zircaloy-4, Zircaloy-2, ZIRLO, M5 and E110. Tests were performed with specimens sectioned from as-fabricated cladding, from prehydrided (surrogate for high-burnup) cladding, and from high-burnup fuel rods, which had been irradiated in commercial reactors. The tests were designed to determine for each cladding alloy the ductile-to-brittle transition as a function of steam oxidation temperature, weight gain due to oxidation, hydrogen content, pre-transient cladding thickness, and pre-transient corrosion-layer thickness. For short, defueled cladding specimens oxidized at 1000-1200ºC, ring compression tests were used to determine post-quench ductility at ≤135ºC. For longer fueled-and-pressurized cladding segments subjected to LOCA-relevant heating and cooling rates, four-point-bend tests were used to determine post-quench ductility. The effect of breakaway oxidation on embrittlement was also examined for specimens oxidized at 800-1000ºC. The data generated in this study were used to develop empirical criteria that were found to be effective in identifying the onset of embrittlement. These criteria are performance-based and are expected to apply to other similar alloys of zirconium.

This page is intentionally left blank.

Foreword

Fuel rod cladding is the first barrier for retention of fission products, and the structural integrity of the cladding ensures coolable core geometry. In the early 1990s, new data from foreign research programs showed degraded cladding behavior for high-burnup fuel under certain postulated accident conditions. It thus became clear that extrapolation from a low-burnup data base needed to be reassessed for regulatory purposes.

One of NRC's central regulations used in plant licensing deals with postulated loss-of-coolant accidents (LOCAs); a portion of that regulation was based on data from unirradiated cladding material. The regulations in 10 CFR 50.46(b) specify criteria derived from tests with unirradiated Zircaloy cladding to limit the peak cladding temperature and the maximum cladding oxidation. These two limits are known as embrittlement criteria. Their purpose is to prevent cladding embrittlement during a LOCA, thus ensuring that the general core geometry will be maintained and be coolable.

In the mid-1990s, NRC sponsored a cooperative research program at Argonne National Laboratory to reassess these limits for the possible effects of fuel burnup. The program's industry partners included the Electric Power Research Institute, Framatome ANP (now AREVA), Westinghouse, and Global Nuclear Fuel; in general, the industry partners were responsible for providing precharacterized high-burnup fuel rods and unirradiated archive tubing for testing. NRC also maintained coordination through the program with the Department of Energy, the Institute for Radiological Protection and Nuclear Safety in France, the French Atomic Energy Commission, the Japan Atomic Energy Agency, the Halden Reactor Project in Norway, and the Russian Research Center's Kurchatov Institute.

Because 10 CFR 50.46 only applies to two of the earlier cladding alloys, case-by-case reviews and frequent license exemptions are required for two newer alloys. The research in this program has addressed these alloy-related issues, as well as burnup-related issues.

This report provides test results and related models and correlations that could be used to establish a technical basis for revision of 10 CFR 50.46(b). Other aspects of LOCA behavior, such as heat source redistribution and ballooning size, are also being investigated in this research program, but this report presents only those results that are relevant to cladding embrittlement.

Brian W. Sheron, Director
Office of Nuclear Regulatory Research
U.S. Nuclear Regulatory Commission

This page is intentionally left blank.

Contents

Figures

Tables

1 Introduction

By the mid 1990s, it was well known that significant cladding oxidation (corrosion) takes place during extended periods of normal operation and that some of the liberated hydrogen from the interaction with water is absorbed in the zirconium alloy cladding material. It thus seemed likely that an oxide layer on the surface and hydrogen in the metal would affect the cladding's behavior under conditions of a loss-of-coolant accident (LOCA). Because cladding behavior under those conditions is important in reactor safety analyses, research was begun in 1997 to investigate any such burnup-related effects.

Several aspects of cladding behavior under LOCA conditions are involved in safety analyses: ballooning strains, flow area reduction, rupture conditions, axial distribution of heat sources, and cladding embrittlement. All are being investigated in a broad research program at Argonne National Laboratory, but only cladding embrittlement will be addressed in this report. The conditions under which cladding on high-burnup fuel loses its ductility and becomes embrittled are needed to assess, and perhaps revise, the embrittlement criteria in 10 CFR 50.46(b) of the NRC's regulations. These criteria are given as limits on cladding temperature and on oxidation level calculated as a percentage of cladding oxidized (Equivalent Cladding Reacted [ECR]).

The current embrittlement criteria were based on tests with unirradiated Zircaloy cladding material and were adopted in 1973. The history of the development of these criteria is summarized in a paper by Hache and Chung [1]. The ductility tests themselves were of the ring-compression type, and the test results were evaluated at 135ºC, the saturation temperature during reflood. ECR was calculated for these tests using the Baker-Just oxidation kinetics equations.

Although significantly improved testing techniques and oxidation kinetics equations are employed in the present study, no change in the approach has been made to ensure that the basis for the criteria remains the same. Most importantly, the material tested in the current work includes cladding from high-burnup fuel rods, which were taken from commercial reactors, and a variety of unirradiated cladding alloys so that both burnup and alloy effects can be determined.

1.1 Cladding materials

Table 1 lists the nominal compositions of commercial cladding alloys that have been tested in this program. Zircaloy-2 cladding is used in BWRs. Zircaloy-4, ZIRLO, and M5 are used in PWRs. The Russian E110 cladding is used in VVERs and was included in the study because it has a similar composition to M5 yet behaves very differently under LOCA conditions [2]. Specific dimensions and alloy compositions for the materials tested in this program are described in Section 2.1.

The traditional zirconium-based alloys in the U.S. were variations of Zircaloy, which used tin as the major alloying element. In Russia, niobium was used as the major alloying element. Zirconium-niobium alloys tend to corrode less during normal operation than zirconium-tin alloys, so niobium has been added in recent years to alloys used in the U.S.

Niobium exhibits several differences compared with tin that affect the behavior of cladding under LOCA conditions. One is that the niobium solubility in zirconium is limited to about 0.5% at moderate temperatures such that about half of the niobium in the niobium-bearing alloys exists as precipitates or second-phase particles. This is in contrast to tin, which goes into complete solution with zirconium in Zircaloy. The niobium precipitates affect phase changes during a LOCA (see 1.2). These changes are observable in metallography and may account for some of the differences in the behavior of these alloys.

Table 1 Nominal Composition of Commercial Cladding Alloys

Element	Zircaloy-2[a]	Zircaloy-4[a]	ZIRLO[b,c]	M5[d]	E110[e]
Sn (wt%)	1.45	1.45	1.1	--	--
Nb (wt%)	--	--	1.1	1.0	1.0
Fe (wt%)	0.14	0.21	0.1	0.038	0.009
Cr (wt%)	0.10	0.10	--	--	--
Ni (wt%)	0.06	--	--	--	--
O (wt%)[f]	0.125	0.125	0.120	0.135	0.06
Zr	Balance	Balance	Balance	Balance	Balance

[a]ASTM B811 [3]

[b]R. Comstock et al. [4].

[c]W. Leech [5].

[d]J-P. Mardon et al. [6].

[e]P. V. Shebaldov et al [7].

[f]Oxygen is considered an alloying element in these alloys.

Another difference is that niobium, like zirconium, has a strong affinity for oxygen – unlike tin. This can be seen in Figure 1, which shows the free energy of formation of oxides of alloy constituents and some impurities [8,9]. Additionally, the prevalent form of niobium oxide is Nb_2O_5. That is, niobium has a valence of +5 in the oxide whereas zirconium has a valence of +4. Taken together, these characteristics lead to the inclusion of niobium in the oxide layer, and it is present there as an aliovalent impurity, which can affect the behavior of the oxide.

Because many of the results described below depend on cladding thickness and diameter, typical dimensions of commercial fuel rods are given in Table 2 [10,11].

1.2 Transient phase transformations

During a LOCA transient, much of the coolant inventory would be lost during the blowdown and the fuel cladding would begin to heat up. Around 800ºC on the temperature rise, the pressurized cladding would reach its ultimate tensile strength, and a local instability would produce a large ballooning strain and a rupture in fuel rods with sufficient pressure and temperature increase. A modest temperature reduction would accompany this deformation in the vicinity of the balloon because of enhanced cooling, but the temperature would then continue to rise. Eventually, the emergency cooling water would stop the temperature rise and begin to cool the cladding. When the temperature decreases to 400-800ºC, wetting of the cladding occurs and rapid cooling, or quenching, would take place. Such a temperature transient is shown schematically in Figure 2.

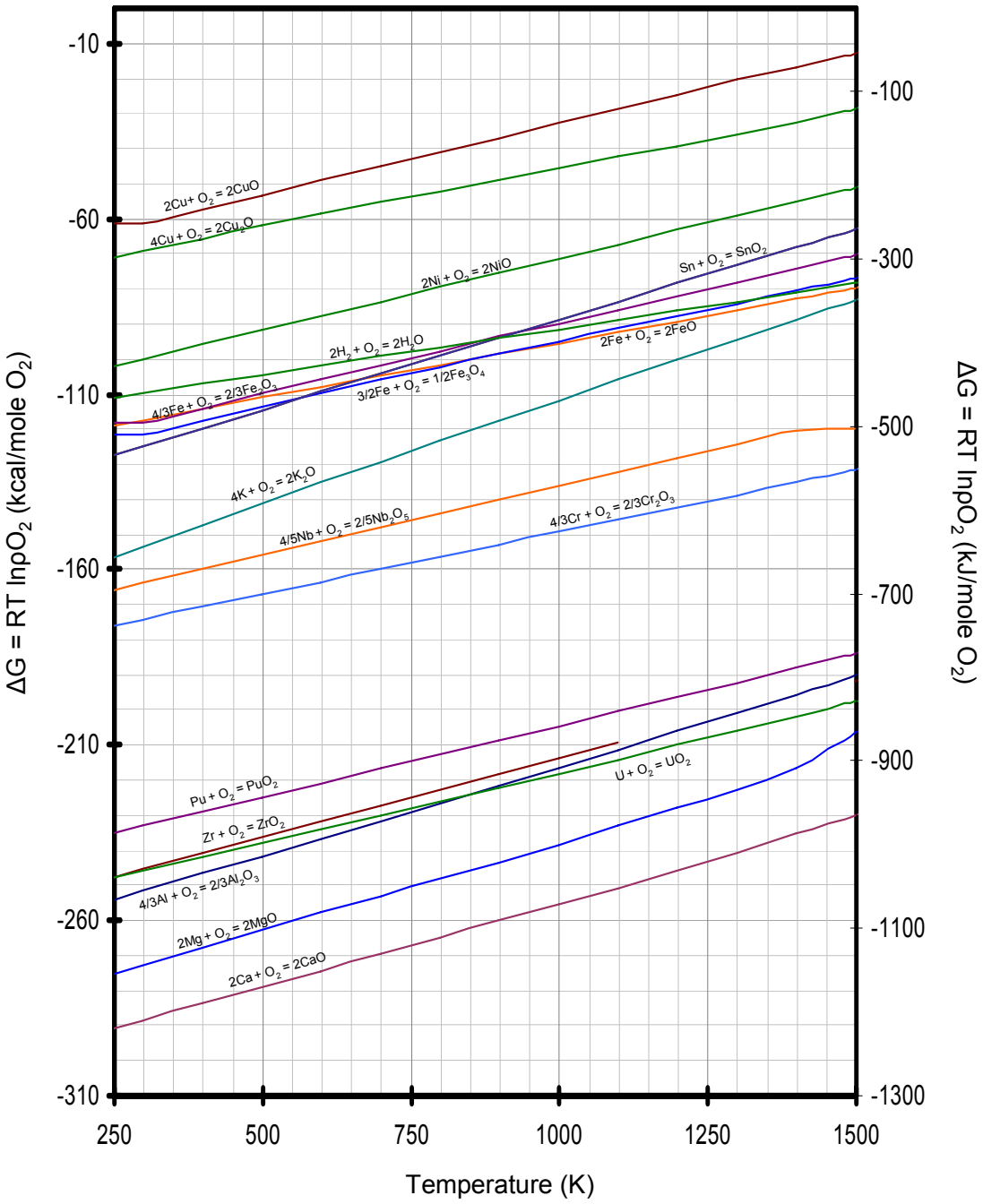

Figure 1. Free energy of formation of oxides of alloy constituents and some impurities [8,9].

Table 2 Typical Dimensions of Commercial Fuel Rods [10,11]

Cladding Type and Dimensions	BWR 8x8	BWR 9x9	BWR 10x10	PWR 14x14	PWR 15x15	PWR 16x16	PWR 17x17	VVER Hex.
Outside Diam. (mm)	12.3	10.8	10.0	11.2	10.7	9.7	9.4	9.1
Thickness (mm)	0.813	0.711	0.660	0.737	0.711	0.635	0.610	0.705

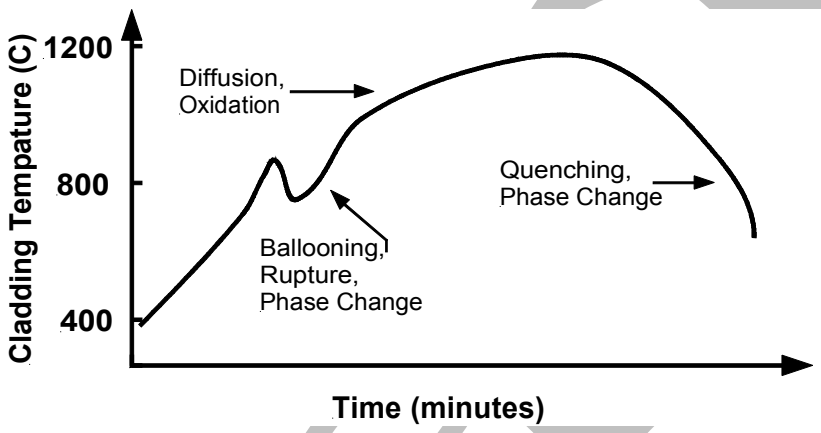

Figure 2. Schematic of cladding temperature during a LOCA.

From room temperature up to about 650-800ºC, the zirconium-based cladding alloys of interest have a hexagonal crystal structure, which is called the alpha phase. Above this temperature, which varies with alloy composition, there is a mixed-phase regime in which the crystal structure begins to change to a face-centered cubic geometry or beta phase. For Zry-4 with initial oxygen concentration of 0.11 wt. %, the alpha to the mixed alpha-beta phase change temperature is 810ºC and the alpha-beta to beta phase change temperature is about 980ºC. These values increase as the oxygen content increases and they decrease with increasing hydrogen. They also decrease with the substitution of Nb for Sn because Nb is a beta-stabilizer.

Oxygen diffusion in Zr metal and in ZrO_2 oxide becomes rapid enough above 800ºC that measurable changes occur during the time period of a LOCA transient. Diffusion controls the oxidation process and other processes involved in cladding embrittlement. Thus, after the zirconium alloy changes from the alpha to the alpha + beta to the beta phase, the temperature gets high enough that oxygen diffuses from the surface into the metal, quickly exceeding its solubility limit in the outer region of the cladding. Rather than precipitating some other phase or gas bubbles, this oxygen-rich metal transforms back to the alpha phase where the oxygen solubility limit is much higher than in the beta phase. Upon cooling, the beta phase also converts back to the alpha phase, but the prior-beta region and the oxygen-stabilized alpha layer are easily distinguished at room temperature in metallographic sections. Figure 3 is a qualitative diagram of this situation for an oxidation temperature greater than the alpha-plus-beta to beta phase temperature and for a location away from the balloon, where steam is not able to get inside the cladding.

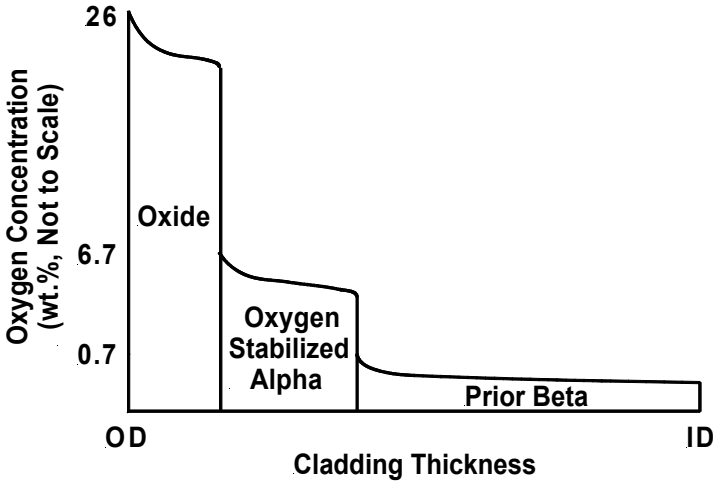

Figure 3. Qualitative diagram of oxygen concentration in Zircaloy cladding exposed at high temperature (>980ºC) to steam on the outside surface and cooled to room temperature. OD and ID are outer and inner diameters, respectively.

Figure 4 shows what these phases look like in a micrograph of an etched section of unirradiated Zircaloy-2 cladding after being oxidized (outside surface only) in steam for 600 seconds at 1200ºC.

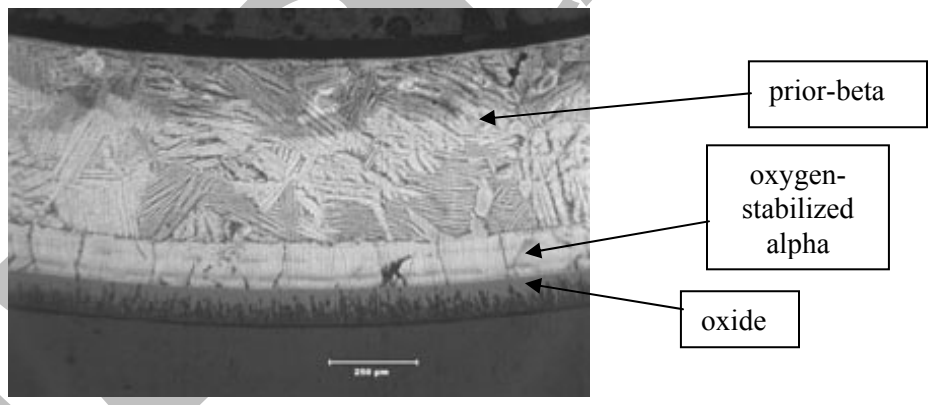

Figure 4. Unirradiated Zircaloy-2 after oxidation in steam at 1200ºC for 600 seconds.

The presence of niobium in zirconium alloys alters this picture somewhat, with a more uneven boundary between the alpha and prior-beta layers, but the principle is the same. Within a ruptured balloon, steam will also enter through the rupture and produce a similar oxygen profile on the inside surface of the cladding.

1.3 Oxidation equations

Although the Baker-Just equations [12] have been used in many LOCA analyses, the Cathcart-Pawel (CP) equations are more accurate and will be used throughout this report. In their report [13], Cathcart et al. gave four related rate equations, one for each of the following: (a) the oxide layer thickness, (b) the alpha layer thickness, (c) the sum of the oxide-plus-alpha layer thickness and (d) total oxygen consumed, which was given as weight gain in grams per square centimeter of surface area. All of these obeyed parabolic kinetics. The rate equation for weight gain, Wg (Cathcart et al. called it τ), is:

$$d(Wg)/dt = (k^2/2)/Wg, \quad (1)$$

where k is the temperature-dependent coefficient (Cathcart et al. labeled it δ_τ). Under isothermal oxidation conditions, the integration of Equation 1 is simply

$$(Wg)^2/2 = (k^2/2)\, t, \quad (2)$$

or

$$Wg = k\, t^{1/2} \quad (2a)$$

which is a parabola.

The coefficient, k, is an Arrhenius-type function:

$$k = a\ \exp(-Q/[RT]), \quad (3)$$

where R is the universal gas constant and the parameters a and Q are given by Cathcart et al. for each of the four rate equations. Using the Cathcart et al. (CP) values for "a" and "Q" for weight gain determined from metallographic results and the assumption of stoichiometric oxide, the isothermal CP equation becomes

$$Wg = 0.602\ \exp(-1.005\times10^4/T)\ t^{1/2}, \quad (4)$$

where Wg is given by Cathcart et al. in g/cm^2, T is temperature in K, and t is time in s. Thus, the weight gain increases as the square root of time at a given temperature, and the rate increases exponentially with temperature. Equation 4 should be multiplied by a factor of 10 to convert to the SI units of kg/m^2. For convenience in the current work, the measured weight gain is expressed as mg/cm^2. In comparing the measured weight gain per unit surface area to the CP-predicted weight gain, Equation 4 is multiplied by 10^3 to give units of mg/cm^2.

A related parameter that is often used is ECR, or equivalent cladding reacted. ECR is defined as the percentage of the cladding thickness that would be oxidized if all the oxygen pickup stayed in the oxide layer as ZrO_2. This is an artificial parameter because some of the oxygen diffuses into the metal, but it is useful and is directly related to weight gain by simple geometric factors, along with factors based on the density of Zr (6500 kg/m^3 = 6.5 g/cm^3), the atomic mass of Zr (91.2 kg/kg-mole) and the atomic mass of diatomic oxygen (32.0 kg/kg-mole). The conversion is given in Equation 5 for one-sided oxidation and Equation 6 for two-sided oxidation.

1-sided oxidation $\quad ECR = 43.9\ [(Wg/h)/(1 - h/Do)] \quad (5)$

2-sided oxidation $\quad ECR = 87.8\ Wg/h, \quad (6)$

where ECR is in %, Wg is in g/cm^2, h is cladding thickness in cm, and Do is cladding outside diameter in cm.

1.4 Embrittlement mechanisms

Six embrittlement mechanisms are described below. Three of them were known before this research was begun and three were not. Data relating to all of these mechanisms are presented in subsequent sections of this report.

1.4.1 Beta-layer embrittlement by oxygen

As temperature increases during a LOCA transient, the amount of oxygen that the beta phase can hold also increases. Above about 1200ºC, oxygen solubility in the beta phase becomes high enough in these cladding alloys that, after cooling, the prior-beta region will embrittle for relatively short oxidation times. This mechanism was understood in 1973, and the 1204ºC (2200ºF) temperature limit in NRC's regulation precluded such embrittlement in unirradiated Zircaloy [1].

1.4.2 Beta-layer thinning

With increasing time, diffusion of oxygen into the metal will convert more and more of the beta phase to the oxygen-stabilized alpha phase – the alpha layer grows and the beta region shrinks. For long times at temperature, the ductile prior-beta region becomes so thin that the macroscopic specimen exhibits brittle behavior. This mechanism was also understood in 1973 and is accommodated by the 17% ECR limit in NRC's regulation, provided oxidation is calculated with the Baker-Just correlation that was used in deriving the limit [1].

1.4.3 Localized hydrogen-induced embrittlement in the balloon region

Steam that enters through a rupture in a balloon causes oxidation inside the cladding. Hydrogen that is freed during this reaction is not swept away as it is on the outside of the cladding, but is absorbed in the metal, resulting in enhanced embrittlement in the balloon region or just beyond the necks of the balloon. This effect, which is neither burnup nor alloy dependent, was discovered earlier [1] and has been confirmed in the present research program.

1.4.4 Hydrogen-enhanced beta-layer embrittlement by oxygen

During normal operation, some hydrogen from the corrosion process is absorbed in the cladding metal. When that cladding is exposed to high-temperature LOCA conditions, the elevated hydrogen levels increase the solubility of oxygen in the beta phase. Thus, even for LOCA temperatures below 1204ºC, embrittlement can occur for times corresponding to less than 17% oxidation in corroded cladding.

1.4.5 General hydrogen-induced embrittlement from breakaway oxidation

Zirconium dioxide (ZrO_2) can exist in several crystallographic forms (allotropes). The normal tetragonal oxide that develops under LOCA conditions is dense, adherent and protective with respect to hydrogen pickup. There are, however, conditions that promote a transformation to the monoclinic phase – the phase that is grown during normal operation – that is neither fully dense nor protective. The tetragonal-to-monoclinic transformation is an instability that initiates at local regions of the metal-oxide interface and grows rapidly throughout the oxide layer. As this transformation results in an increase in oxidation rate, it is referred to as breakaway oxidation. Along with this increase in oxidation rate due to cracks in the monoclinic oxide, there is significant hydrogen pickup. Hydrogen that enters in this manner during a LOCA transient has the same effect on embrittlement as hydrogen from the normal burnup process. Although breakaway oxidation was known in 1973, a connection to embrittlement was not made at that time.

1.4.6 Oxygen pickup from the cladding inner surface

Figure 3 illustrates a situation where there is an oxygen source only on the cladding outer surface, and for unirradiated cladding this oxygen source is the zirconium dioxide that comes from high temperature oxidation in steam. As burnup increases, normal corrosion will contribute to the outer-surface oxide layer. There will also be an oxygen source on the inner surface of irradiated cladding due to gas-phase UO_3 transport and fuel-cladding-bond formation (UO_2 in solid-solution with ZrO_2). Under LOCA conditions, oxygen can thus enter the cladding from the inner surface even away from the balloon location. The situation is like a multilayer diffusion couple as illustrated in Figure 5. The actual thicknesses of the OD and ID oxygen sources may be relatively unimportant at high burnup because they contain much more oxygen than will diffuse into the metal (see related tests by Hofmann and Politis [14]). If the inner-surface oxide layer or the oxide-bond-fuel layer is well developed, the 2-sided ECR equation (Equation 6) would apply at all axial locations.

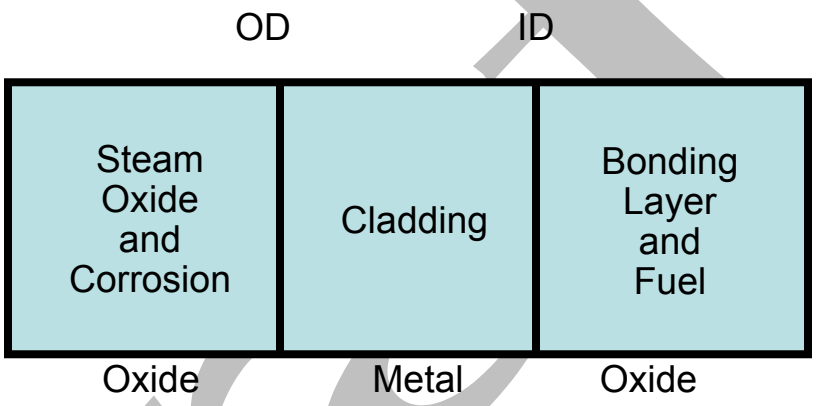

Figure 5. Diffusion couple character of oxygen sources and cladding metal.

2 Materials, Test Methods and Procedures

In order to properly interpret and use the data generated in this work, it is important to understand the cladding materials used for test samples, the test methods employed and the test procedures. These are described in this section.

2.1 Description of cladding alloys and high-burnup fuel segments

Unirradiated cladding alloys were provided by GNF (8×8, 9×9 and 10×10 Zry-2), Westinghouse (17×17 low-tin Zry-4 and ZIRLO), AREVA (1970s 15×15 Zry-4 tubing, 1990s 15×15 low-tin Zry-4, 15×15 low tin Zry-4, 15×15 M5, and 17×17 M5) and Fortum (E110 tubing and E110 cladding). Alloys, except for E110, that are listed without a decade are modern, belt-polished cladding alloys. The 8×8 Zry-2 was used for early thermal and metallurgical benchmark testing of the LOCA integral apparatus. The 9×9 Zry-2, although not archival cladding from the same lot, was fabricated by the same methods used to fabricate high-burnup Limerick fuel-rod cladding and has the same nominal composition and dimensions as the Limerick cladding. It has been used in this test program to generate baseline LOCA integral data and one-sided, high-temperature steam oxidation data. The 1970s 15×15 Zry-4 tubing is close to being archive material for the high-burnup H. B. Robinson (HBR) cladding tested in this program. However, this tubing has ≈0.05-mm larger outside diameter and ≈0.025-mm thicker wall than the HBR cladding. The final finishing step after fueling the HBR tubing to convert it to cladding was an outer-surface etch that removed ≈0.05-mm from the outer diameter. Because this tubing was not in final form, it was not used to generate baseline data for the high-burnup HBR cladding. Rather, the 1990s 15×15 low-tin Zry-4 cladding, which has similar dimensions, oxygen content and mechanical properties as the HBR cladding, is used in this work to determine baseline HBR oxidation and post-quench ductility properties.

Initial lengths of 15×15 and 17×17 M5 were provided by AREVA for benchmarking purposes but not for advanced-alloy data generation. This 17×17 M5 (0.57-mm wall) was characterized in terms of chemical composition and used to develop and benchmark the two-sided oxidation test train. At a later date, AREVA provided 17×17 M5 with 0.61-mm wall thickness for the purposes of data generation. The post-quench ductility of the 15×15 M5 and the 0.61-mm-wall 17×17 M5 was compared to confirm that post-quench ductility correlated with extent of oxidation (ECR) at a given temperature independent of cladding wall thickness and outer diameter.

For the advanced-alloy post-quench ductility program, the primary alloys of interest are 10×10 Zry-2, 17×17 low-tin Zry-4, 17×17 ZIRLO, and 17×17 M5 (0.61-mm wall). E110 was also added to the advanced-alloy testing program to try to determine why its steam-oxidation behavior is so poor as compared to M5, even though its alloy composition is similar. E110 tubing and cladding were provided by Fortum (Finland). The cladding was pickled (etched) and anodized to increase the outer-surface hardness. In addition to the supplied forms of E110, ANL-modified E110 had several variants, which included surface modification (polished, etched, etched-and-polished) and reduction in wall-thickness to ≈61-mm (inner-surface machined and polished). Valuable lessons were learned from the E110 study regarding the destabilizing effects of surface roughness, surface scratches, and surface chemistry (e.g., F from etching) on oxidation at 950-1100ºC. These experiences helped in planning the breakaway oxidation studies for all alloys.

For the breakaway-oxidation studies, it was planned to use the same alloys as for the post-quench-ductility studies. However, due to the very limited supply of 17×17 low-tin Zry-4, belt-polished 15×15 and HBR-type (rough surface) 15×15 low-tin Zry-4 were used instead. This allowed the effects of surface roughness to be included in these studies for Zry-4 samples with similar geometry, tin content and

oxygen content. The other three alloys (10×10 Zry-2, 17×17 ZIRLO, and 17×17 M5) used in the post-quench-ductility tests were also used in the breakaway oxidation tests.

For most of the cladding alloys received by ANL, measurements were performed to determine outer-diameter (OD), wall thickness, surface roughness, oxygen content and tin content. Some of the alloys were sent to an outside organization to determine chemical composition. For ZIRLO cladding, Westinghouse also performed chemical analysis on a sample of the cladding sent to ANL.

Table 3 summarizes the dimensions, surface conditions, and chemical composition of the Zr-lined Zry-2 used in the ANL test program. The Zr liner is on the cladding inner surface (≈10% of the wall thickness). Chemical composition data listed in Table 3 refer to the final cladding product (≈90% Zry-2 and ≈10% Zr liner). They should not be interpreted as the composition of standard Zry-2. The chemical composition listed in Table 1 for Zry-2 is closer to the composition of the Zry-2 alloys tested at ANL.

Table 3 Dimensions and Chemistry of Zr-lined Zry-2 used in the ANL Test Program; the "<" sign means below the detection limit

Parameter	8×8 Zry-2	9×9 Zry-2	10×10 Zry-2
OD, mm	12.27	11.18	10.29
Wall Thickness, mm	0.82	0.71	0.66
ID Liner Thickness, mm	≈0.08	≈0.07	≈0.07
OD Surface Roughness, μm	---	0.14	0.11
Sn, wt.%	---	1.18	---
Nb, wt.%	---	<0.01	---
O, wt.%	---	0.11	---
Fe, wt.%	---	0.20	---
Cr, wt.%	---	0.12	---
Ni, wppm	---	550	---
S, wppm	---	30	---
C, wppm	---	250	---
Hf, wppm	---	<100	---
Si, wppm	---	≤100	---
N, wppm	---	45	---
H, wppm	---	6	---

The dimensions and chemistry of the Zry-4 used in the ANL test program are listed in Table 4. Included in this table are the dimensions and chemistry for near-archive HBR tubing, even though this tubing was not used in the post-quench-ductility or breakaway-oxidation studies.

The dimensions and chemistry for 17×17 ZIRLO, 17×17 M5 (validation lot), 17×17 M5 (data lot), and 15×15 M5 (validation lot) used in the ANL test program are listed in Table 5.

Table 4 Dimensions and Chemistry of Zry-4 used in the ANL Test Program; the "<" sign means below the detection limit

Parameter	15×15 Zry-4 HBR Archive Tubing 1977[a]	15×15 Zry-4 HBR Baseline Cladding ≈1995[b]	15×15 Zry-4 Cladding Modern[c]	17×17 Zry-4 Cladding Modern[d]
OD, mm	10.84	10.77 (10.76)	10.91	9.50
Wall Thickness, mm	0.80	0.76 (0.77)	0.67	0.57
OD Surface Roughness, μm	0.36	0.32 (0.31)	0.10	0.14
Sn, wt.%	1.42	1.29	1.29±0.1	1.29±0.1
Nb, wt.%	---	---	---	---
O, wt.%	0.137	0.136	0.124	0.120
Fe, wt.%	0.21	---	---	---
Cr, wt.%	0.10	---	---	---
Ni, wppm	<35	---	---	---
S, wppm	---	---	---	---
C, wppm	140	---	---	---
Hf, wppm	<50	---	---	---
Si, wppm	92	---	---	---
N, wppm	54	---	---	---
H, wppm	12	22	26	5

[a]Sandvik Special Metals Corp Certificate of Quality; based on tubing (H, N, O) and ingot; 06-30-77.
[b]ANL data based on two AREVA lots received in April 2003 (0403) and November 2004 (1104).
[c]ANL data for AREVA cladding received in December 2004.
[d]ANL data for cladding provided by Westinghouse.

Fortum sent two types of E110 to ANL: tubing and cladding. The processing of tubing into cladding involves pickling (etching) and anodizing to grow a fine (<<1 μm) oxide layer on the outer surface of the tubing. The oxide layer enhances the surface hardness and protects the soft E110 cladding from scratching and abrading during handling and loading into fuel assemblies. ANL modified some of this tubing and cladding to study the effects of surface roughness and chemistry. The modifications are listed in Table 6 under the categories of "polished" and "machined-and-polished".

With regard to irradiated materials used in the ANL test program, EPRI provided ANL with several fueled TMI-1 PWR rods at 48-50 GWd/MTU for validating characterization and test methodologies, seven fueled Limerick BWR rods at 54-57 GWd/MTU for LOCA data generation, and seven fueled H. B. Robinson PWR rods at 64-67 GWd/MTU for LOCA data generation. Under a separate contract with

Table 5 Dimensions and Chemistry of ZIRLO and M5 used in the ANL Test Program; the "<" sign means below the detection limit

Parameter	17×17 ZIRLO[a]	17×17 M5[b] (Validation)	17×17 M5[c] (Data)	15×15 M5 [c] (Validation)
OD, mm	9.50	9.50	9.50	10.91
Wall Thickness, mm	0.57	0.57	0.61	0.64
OD Surface Roughness, μm	0.11	0.12	0.12	0.11
Sn, wt.%	0.99	0.02	---	---
Nb, wt.%	0.98	1.02	---	---
O, wt.%	0.12	0.145	0.145	---
Fe, wt.%	0.11	0.05	---	---
Cr, wt.%	<0.01	<0.01	---	---
Ni, wppm	<100	<100	---	---
S, wppm	---	25±5	---	---
C, wppm	135	110	---	---
Hf, wppm	40	<100	---	---
Si, wppm	53	<100	---	---
N, wppm	46	55	---	---
H, wppm	5	6	5	---

[a]Chemical data provided by Westinghouse and CONAM Materials Analysis Group; H and O content confirmed by ANL.
[b]Chemical data provided by CONAM Materials Analysis Group; H and O content confirmed by ANL.
[c]ANL data for AREVA M5 cladding.

INL, sponsored by EPRI and AREVA, four high-burnup fueled M5 rods at ≈71 GWd/MTU are scheduled to be shipped to ANL. Some segments of these M5 rods have been designated for LOCA integral tests. In addition, under agreements among NRC-Studsvik-AREVA and NRC-Studsvik-Westinghouse, high-burnup defueled M5 cladding from the European Ringhals PWR reactor and high-burnup defueled ZIRLO cladding from the North Anna PWR reactor, respectively, have been supplied to ANL for post-quench ductility testing. Relevant parameters for these irradiated materials are summarized in Table 7. Detailed characterization of the cladding materials are presented in sections relevant to the post-quench ductility and LOCA integral testing of these materials.

2.2 Oxidation and quench tests with short defueled cladding samples

The LOCA integral apparatus is designed to perform both LOCA integral tests using long (≈300 mm) fueled cladding samples and oxidation-quench tests using short (25 mm) defueled cladding samples. One unit is maintained out-of-cell for thermal-benchmarking purposes and for generating data for as-fabricated and prehydrided alloys. A second unit is maintained in-cell for testing fueled and defueled cladding. Both units use the same control and data acquisition systems. The main difference in LOCA-

Table 6 Dimensions and Chemistry of E110 Tubing and Cladding used in the ANL Test Program; the "<" sign means below the detection limit

Parameter	E110 Tubing[a]	E110[b] Cladding	E110[c] (Polished)	E110[d] (Machined-and-Polished)
OD, mm	9.17	9.13	9.14	9.14
Wall Thickness, mm	0.71	0.70	0.69	0.58-0.69
OD Surface Roughness, μm	0.35	0.19	0.14	0.14
Sn, wt.%	0.02	---	0.02	0.02
Nb, wt.%	1.03	---	1.03	1.03
O, wt.%	0.05	---	0.05	0.05
Fe, wt.%	0.055±0.015	---	0.055±0.015	0.055±0.015
Cr, wt.%	<0.01	---	<0.01	<0.01
Ni, wppm	<100	---	<100	<100
S, wppm	25±15	---	25±15	25±15
C, wppm	135	---	135	135
Hf, wppm	100	---	100	100
Si, wppm	100	---	100	100
N, wppm	46	---	46	46
H, wppm	5	---	5	5

[a]Chemical data provided by CONAM Materials Analysis Group; H and O content confirmed by ANL.
[b]Pickled and anodized to harden the outer-surface layer.
[c]Polishing done for about 2-minutes with 9-μm and 3-μm-grit Al_2O_3 paper.
[d]Machining of inner-surface and polishing of both outer- and inner-surfaces; a few test samples were prepared by machining 25-μm off the outer surface followed by polishing of both surfaces.

integral and oxidation-quench tests is the test train holding the sample in position within the quad-elliptical, radiant furnace and the connections required. The furnace has a 250-mm-high uniform heating zone with radiant heating from four vertical bulbs and a reflecting inner surface. The LOCA integral tests are conducted with long samples initially under high internal pressure (7-15 MPa), which requires a connection to the helium high-pressure line, along with top and bottom pressure transducers. The oxidation-quench tests do not require the high-pressure connection or the pressure transducers. Figure 6 shows the out-of-cell apparatus, with the essential components labeled. Figure 7 shows a schematic of the out-of-cell apparatus and the in-cell apparatus. The test chamber is first purged with high-purity argon gas to remove the air from the out-of-cell test chamber (quartz tube) or the nitrogen from the in-cell test chamber. Steam at near-atmospheric pressure flows up through the test chamber into a condenser. Following the oxidation and slow-cooling phases, the steam flow is turned off and quench water is introduce through bottom flooding to give very rapid cooling of the sample at the desired time and temperature during the transient.

Table 7 Characteristics of High-Burnup Fuel Rod Segments and Defueled High-Burnup Cladding for the ANL LOCA Test Program

Parameter	TMI-1	Limerick	H. B. Robinson	North Anna M5	North Anna ZIRLO	Ringhals M5
Reactor	PWR	BWR	PWR	PWR	PWR	PWR
Enrichment wt.%	4.00	3.95 (3.40-3.95)	2.90	4.20	≈4	≈4
Burnup GWd/MTU	48-50	54-57	63-67	≈71	75	63
Discharge Date	1997	1998	1995	2004	2001	2003
Fast Fluence 10^{25} n/m^2	9	11	14	Not Provided	Not Provided	Not Provided
Cladding	15×15 Low-Sn Zry-4	9×9 Zr-lined Zry-2	15×15 Zry-4	17×17 M5	17×17 ZIRLO	17×17 M5
Initial Wall Thickness mm	0.69	0.71	0.76	0.57	0.57	0.57
OD Oxide, μm	≤30	≈10 + ≈10 crud	≤100	<25	≈20-50	<25
Hydrogen Pickup wppm	≤300	70	≤800	<100	<600	<100
Fueled	Yes	Yes	Yes	Yes	No	No

The apparatus shown in the Figure 7 schematic was initially used for oxidation-kinetics tests of near-archive Limerick 9×9 Zry-2, high-burnup Limerick 9×9 Zry-2, and intermediate-burnup TMI-1 15×15 Zry-4 [15]. These one-sided oxidation tests, which were conducted in-cell, were performed without quench. Also, a slow-flowing argon purge was maintained inside the cladding and test train to minimize steam and hydrogen build-up. The test train used to conduct these in-cell tests is shown in Figure 8. Three Type S thermocouples are welded 120º apart onto the Inconel sample holder just above the sample. One of these thermocouples is used to control the furnace power to achieve the desired hold temperature. The other two are for monitoring circumferential temperature distribution. For these tests, a fourth thermocouple is suspended within the sample to determine the circumferentially averaged temperature. Prior to conducting these in-cell tests, thermal and metallurgical benchmark tests were conducted out-of-cell with thermocouples welded directly onto the sample outer surface. The thermal results showed excellent agreement in the long-time hold temperatures among the thermocouples welded onto the sample, the three thermocouples welded onto the Inconel holder above the sample, and the thermocouple suspended inside the sample. Although not important for these long-time tests, the temperature rise of the holder thermocouples lagged the temperature rise of the thermocouples welded onto the sample, and the temperature rise of the suspended thermocouple lagged the rise of the holder thermocouples.

Figure 6. Overview of the out-of-cell LOCA Integral Test Apparatus. The in-cell unit is located at Workstation 6 behind the hot-cell shield and seal windows.

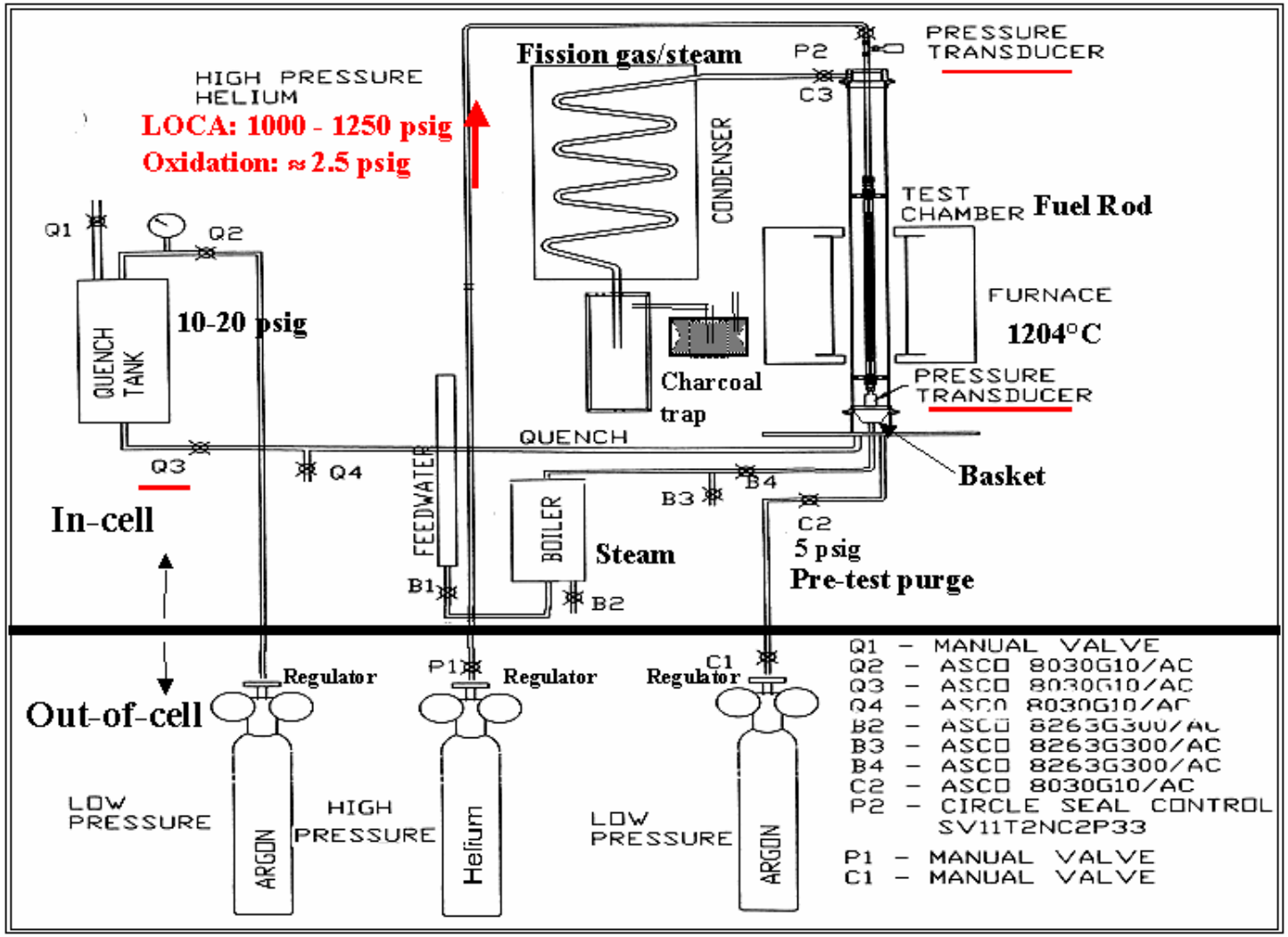

Figure 7. Schematic of Oxidation Kinetics and LOCA Integral Test Apparatus; test train shown is for LOCA Integral Testing.

The test train shown in Figure 8 was modified for the advanced-alloy post-quench ductility tests in order to conduct two-sided steam oxidation tests. The two-sided tests offered many advantages over the one-sided tests: better temperature control, uniform inner-surface oxidation, no change in sample hydrogen content due to inner-surface hydrogen pickup or hydrogen desorption to the purge gas, and a reliable and cost-effective way to determine weight gain by simply weighing the sample before and after the test. Figure 9 shows the test train used for oxidizing the post-quench ductility samples. Holes were drilled into the hollow Inconel holder below and above the sample to allow adequate steam flow inside the cladding sample. Other changes were made to the Inconel holder wall thickness and outer-diameter to reduce the thermal mass of the holder.

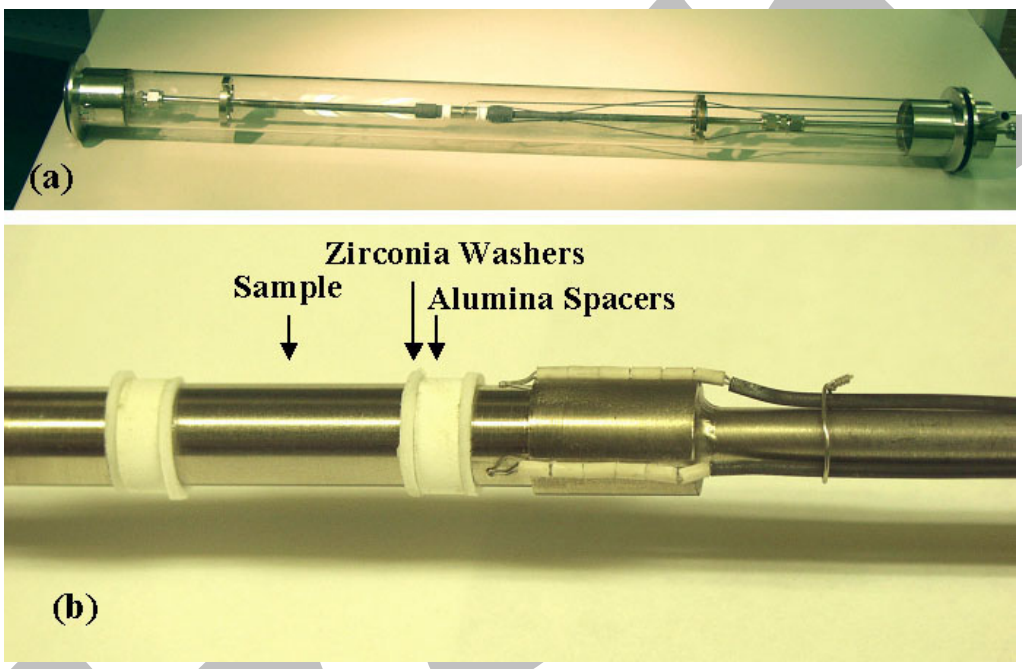

Figure 8. Test train for conducting one-sided steam-oxidation kinetics tests in-cell using ≈25-mm-long Zircaloy cladding samples: a) test train within quartz tube; b) enlarged view of sample region along the test train showing alumina spacers to inhibit Zircaloy-Inconel interaction and zirconia washers to minimize steam leakage to the sample inner surface.

Temperature control and monitoring is extremely important in conducting oxidation-quench tests, followed by post-quench ductility tests. As discussed in Section 1, the time-at-temperature for the transition between ductile and brittle behavior is a strong function of temperature. The furnace power and sample temperature are controlled by feedback from the thermocouple output through a proportional-integral-differential controller to the furnace power. Because the sample has such low thermal mass per unit length, it is important to ramp to the hold temperature as fast as possible for these tests without temperature overshoot due to the heat generated from oxidation during the ramp. In setting the controller parameters, the requirements are that the temperature overshoot during the ramp be <20ºC relative to the target hold temperature for a short period of time (seconds) and that the average hold temperature be within 10ºC of the target temperature. The 10ºC is reasonable given the uncertainty in the Type S thermocouples – a few degrees – at the maximum oxidation temperature (1204ºC). Temperature overshoot is not much of an issue for oxidation temperatures ≤1100ºC, but it can be a significant issue for higher oxidation temperatures. For tests conducted at 1200ºC, temperature overshoot was minimized by slowing down the heating rate for ramp temperatures within 50-100ºC of the target temperature.

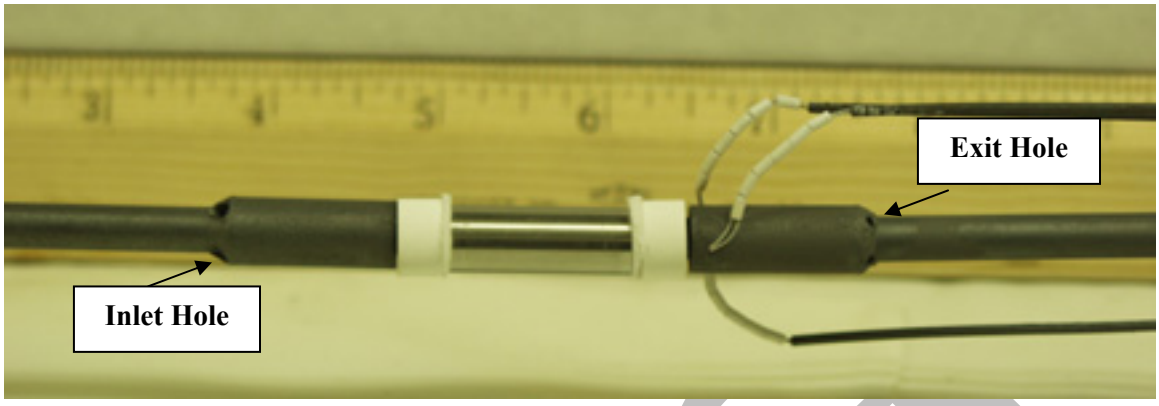

Figure 9. Test train design for two-sided oxidation tests with four holes drilled into the Inconel holder below the sample (left) for steam ingress and four holes drilled into the holder above the sample for steam egress. Also shown are the three TCs permanently welded to the Inconel holder just above the sample.

The following benchmarking procedure has been established for each test train:

a) weld two Type S TCs to sample at same orientation as holder control TC and another holder TC ±120º from the control TC;

b) use repeated testing with fresh samples and same orientation for TCs welded to sample to determine optimum controller parameters for desired temperature ramp and hold temperature;

c) for larger-diameter cladding, which exhibits higher circumferential temperature variation, repeat test with new sample, one TC welded on sample at the same orientation as the holder control TC, and one TC welded on sample at the same orientation as the third holder TC; this provides a good check of reproducibility of temperature results, as well as a better determination of circumferential variation;

d) perform metallographic examinations to determine outer-surface and inner surface oxide-layer thickness at eight circumferential locations; compare measured and predicted average values, as well as circumferential variation;

e) conduct oxidation test without TCs welded on the sample and compare the measured sample weight gain at a time corresponding to ≈10% ECR to the weight gain calculated with the Cathcart-Pawel (CP) correlation; also perform metallographic examination to determine the average inner- and outer-surface oxide layer thicknesses, as well as the variation;

f) if temperature requirements are satisfied, if measured weight gain is within 10% of predicted weight gain, if average oxide layer thickness on inner and outer surfaces is within 10% of the Cathcart-Pawel (CP) predicted thickness, and if the circumferential variation in oxide layer thickness is consistent with the circumferential temperature variation, then oxidation testing may begin with this test train; and

g) continue to run tests with the benchmarked test train and controller parameters for specific hold temperature until the measured weight gain and CP-predicted weight gain differ by ≥10%; repeated quench will cause some warping of the test train, which moves the sample away from the furnace

focal point; as all the data-generating tests are conducted without TCs welded onto the sample, this step is very important; generally, a test train will be good for ≈15 runs with quench and more without quench.

Figure 10 shows an example of the thermal benchmark results for as-fabricated HBR-type 15×15 Zry-4 cladding. In order not to obscure the results, the three holder temperatures for each of the two tests are not shown. For the controller parameters chosen, the hold temperature is 1204±10ºC, where the ±10ºC is the circumferential variation in temperature based on sample TC readings at 0º, 120º and 240º. On the average, there is no temperature overshoot. The highest reading of any one TC is 1220ºC for a brief period of time. For this particular set of controller parameters, the temperature ramp consists of a very fast ramp (≈75ºC/s) from 300ºC to ≈1100ºC and a slow ramp (≈1.3ºC/s) from 1100ºC to 1204ºC. At the end of the hold time, the furnace power is turned off and the sample cools in steam at ≈13ºC/s to the desired quench temperature of 800ºC. The actual cooling rate decreases exponentially with time, as would be expected for this zero-power phase of the transient. Part of the thermal benchmark testing is to determine the test time and temperature at which to stop the steam flow and initiate bottom-flooding quench-water flow to have rapid cooling occur at the desired quench or wetting temperature. The rapid cooling (≈150ºC/s) from the quench temperature to 100ºC is fast enough for these tests, but not as fast as in-reactor cooling rates following wetting. This is due to the limited quench water supply that can be used in-cell (<3 liters of steam-supply water plus quench water based on hot-cell criticality limitations). There is only enough quench water to fill the quartz tube chamber to an elevation just above the furnace.

As shown in Figure 10, the test is not isothermal. The significance of the weight-gain during the initial heating ramp depends on the hold temperature and the hold time. For the Figure-10 temperature history, the CP-predicted weight gain is determined numerically by integrating Equation 1 over the time-dependent temperature profile T(t):

$$(Wg)^2 = 0.362\int_0^t \exp(-20100/T)\, dt, \qquad (7)$$

where Wg is in g/cm^2, T is in K and t is in s. Because of the parabolic nature of the weight gain correlation, the small weight gain during the cooling ramp can generally be ignored. Also, the CP set of correlations were validated for T ≥ 1000ºC (1273 K). However, the weight gain correlation appears to give results consistent with ANL data for T ≥ 950ºC. For the ANL work, the integral in Eq. 7 is converted to an integral with respect to temperature and the integration for the high-temperature oxidation tests (e.g., Figure 10) is generally performed for T ≥ 1000ºC.

For oxidation and quench of samples used for post-quench ductility tests, the procedure is the same as the one used in the thermal and metallurgical benchmark tests:

a) stabilize the system at 300ºC in flowing saturated steam for 500 s;

b) initiate temperature ramp with feedback between the holder TC and the furnace power;

c) hold at temperature for a predetermined time to achieve the desired CP weight gain and ECR;

d) turn furnace power off while maintaining steam flow at the end of the hold time; and

e) valve off steam flow and initiate bottom-flooding quench at a test time that will give rapid cooling at the desired cladding temperature.

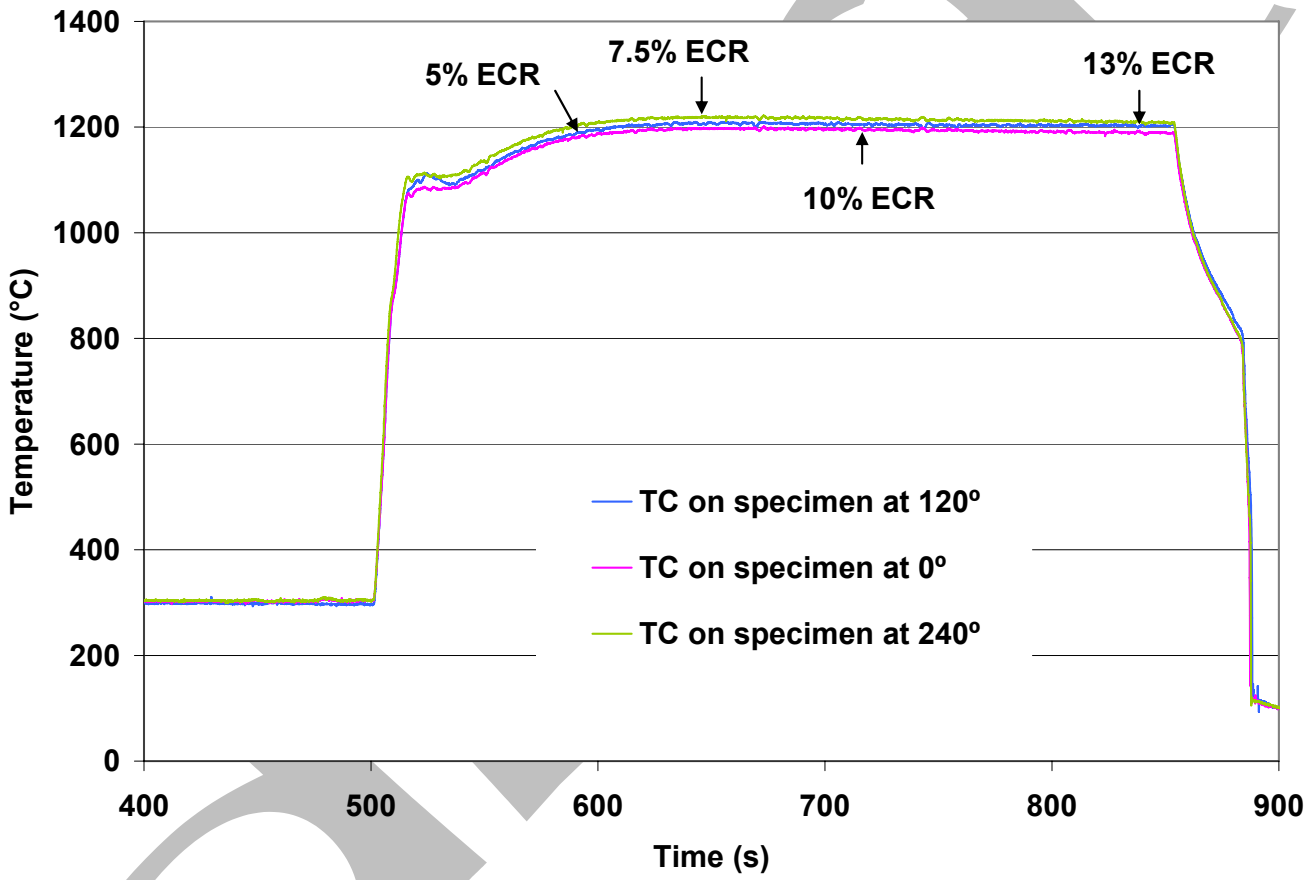

Figure 10. Thermal benchmark results from two tests, each with two TCs welded onto as-fabricated, HBR-type 15×15 Zry-4 cladding: test HBRU#20 had TCs welded onto the sample at 0º and 120º, while test HBRU#29 had TCs welded onto a new sample at 0º and 240º. The sample hold temperature is 1204±10ºC, where 1204ºC is the average of the three TC readings and ±10ºC is the standard deviation.

The procedure for conducting in-cell oxidation-quench tests with high-burnup cladding samples is similar to the one described above for out-of-cell tests with unirradiated cladding samples. However, the corroded, irradiated samples were not directly thermally benchmarked because ANL does not have the in-cell capability to locally remove the corrosion layer and spot-weld TCs to the cladding metal surface. With respect to the temperature history shown in Figure 10 for bare, unirradiated cladding, it is expected that pretest cladding corrosion would slow down the initial oxidation rate and the heating rate associated with the exothermic oxidation reaction. The presence of the corrosion layer would basically affect the heating ramp. This has been confirmed in out-of-cell tests using the following procedure to determine the temperature profile for high-burnup Zry-4 cladding with a 70-μm-thick corrosion layer and an 11±4-μm-thick fuel-cladding bond layer:

a) with TCs welded onto bare as-fabricated cladding, conduct the thermal benchmark test for a hold time selected to grow 40-μm-thick oxide layers on the inner- and outer- surfaces of the cladding;

b) cool to 300ºC and repeat thermal benchmark test using the same controller parameters as were used in (a); compare the two sets of results with emphasis on the maximum temperature at the end of the rapid temperature rise (first peak), the time to reach the hold temperature, and the hold temperature;

c) if necessary, increase the holder control temperature to achieve the desired hold temperature for cladding with pre-transient oxide layers;

d) install the calibrated test train in the in-cell furnace and conduct a metallurgical benchmark test with as-fabricated cladding without the TCs welded onto the cladding and with the hold time chosen to give a weight gain equivalent to 10% CP-ECR; if the out-of-cell and in-cell weight gains and converted ECRs are in good agreement, then the use of the test train in the in-cell furnace has been validated; and

e) use the results of the thermal benchmark in (b) and (c) – the one with oxide layers grown on the inner- and outer-surfaces prior to initiating the temperature ramp – to choose test times to give the desired CP-ECR values and to interpret the experimental results for high-burnup cladding.

The results of benchmark tests (a) and (b) indicated the following for HBR-type 15×15 Zry-4: the peak temperature at the end of the rapid heating rate was 40ºC less for pre-oxidized cladding as compared to bare cladding; the time to reach the hold temperature was about the same for both cases, and the hold temperature for the pre-oxidized cladding was ≈8ºC less than the hold temperature for the bare cladding. Knowing these effects helps to choose the optimum controller parameters for in-cell tests with high-burnup cladding samples. For example, higher heating rates and desired hold temperatures for high-burnup ZIRLO and M5 cladding can be achieved by selecting controller parameters to give rapid heating to the hold temperature for bare cladding and repeating the test with the appropriate steam-grown oxide layer thicknesses chosen to match the sum of the corrosion layer thickness and the fuel-cladding bond thickness. For high-burnup M5 with a 20-μm-thick corrosion layer and a 10-μm-thick fuel-cladding bond layer, the test time for the first benchmark would be chosen to grow 15-μm-thick oxide layers on the cladding inner- and outer-surfaces and the hold temperature would be chosen to be slightly higher (e.g., 1205-1210ºC) than the hold temperature targeted for the in-cell high-burnup cladding. Following cooling to 300ºC, the same controller parameters would be used to conduct the thermal benchmark for the in-cell tests. A bare-cladding thermal history, which is a good candidate for testing high-burnup ZIRLO and M5, is shown in Figure 11.

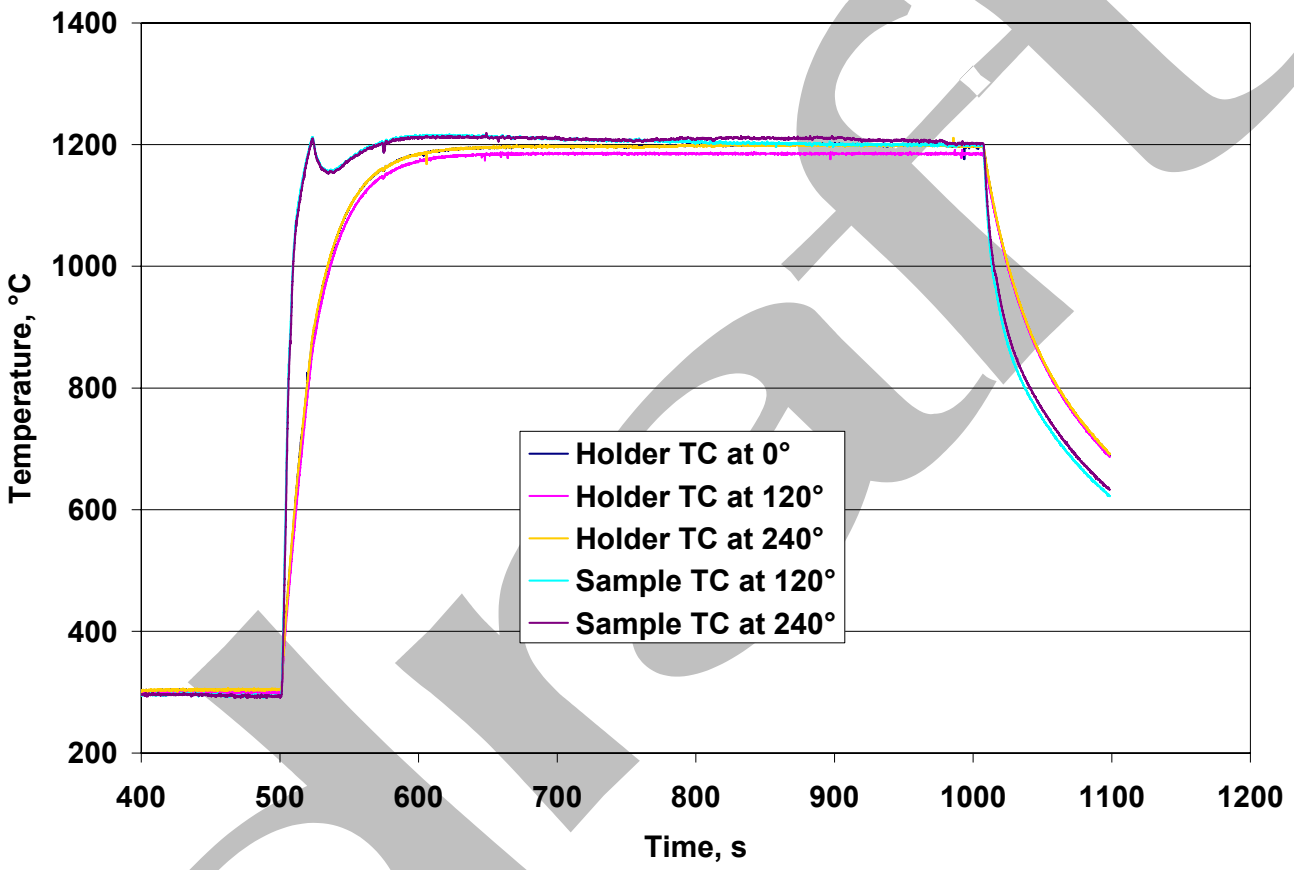

Figure 11. Thermal benchmark results with as-fabricated 17×17 ZIRLO sample; repeating this test following the growth of inner- and outer-surface oxide layers decreased the first peak during the heating ramp to <1200ºC and decreased the overshoot during the early part of the hold time to ≈1200ºC; the controller parameters used to generate this thermal history are used for in-cell tests with high-burnup ZIRLO and M5 cladding samples.

2.3 Ductility determination using ring-compression tests

Hobson [16] and Hobson and Rittenhouse [17] performed low- and high-strain-rate ring compression tests, respectively, using two-sided oxidized Zry-4 cladding samples over a wide range of temperatures. The results of the slow-strain-rate tests at ≈135ºC (275ºF) were used to formulate the 2200ºF peak cladding temperature and 17% maximum oxidation level (Baker-Just ECR). The ring-compression test is a good ductility screening test that is often used for near-brittle to brittle materials. However, the methods used by Hobson to determine oxidation temperatures and levels leading to brittle behavior were very crude. Rings were crushed to complete failure – often 4 cracks at the 0º (12 o'clock), 90º (3 o'clock), 180º (6 o'clock) and 270º (9 o'clock) positions relative to the loading platen. The pieces were reassembled. If the cracked pieces formed a circular shape vs. an oval shape, they were classified as brittle. Load-displacement curves for these tests were never published and apparently not used.

In the current work, 8-mm-long rings are compressed at a slow-displacement rate (0.0333 mm/s) in an Instron test machine. The load-displacement curves are analyzed in the standard way: linearize the initial loading curve, use the slope of the initial loading curve to mathematically unload the sample at the peak load before a significant load drop (≈30-50%) indicating a through-wall crack along the length of the sample, and determine the offset displacement (distance along the displacement axis between loading and unloading lines). This offset displacement is normalized to the pre-oxidation-test cladding outer diameter to determine a relative plastic strain. The methodology is illustrated in Figure 12 for 17x17 Zry-4 oxidized at 1100ºC to 20% CP-ECR (20.3% based on measured weight gain), quenched at 800ºC and ring-compressed at RT. The offset displacement for this sample is 0.455 mm. Normalizing this

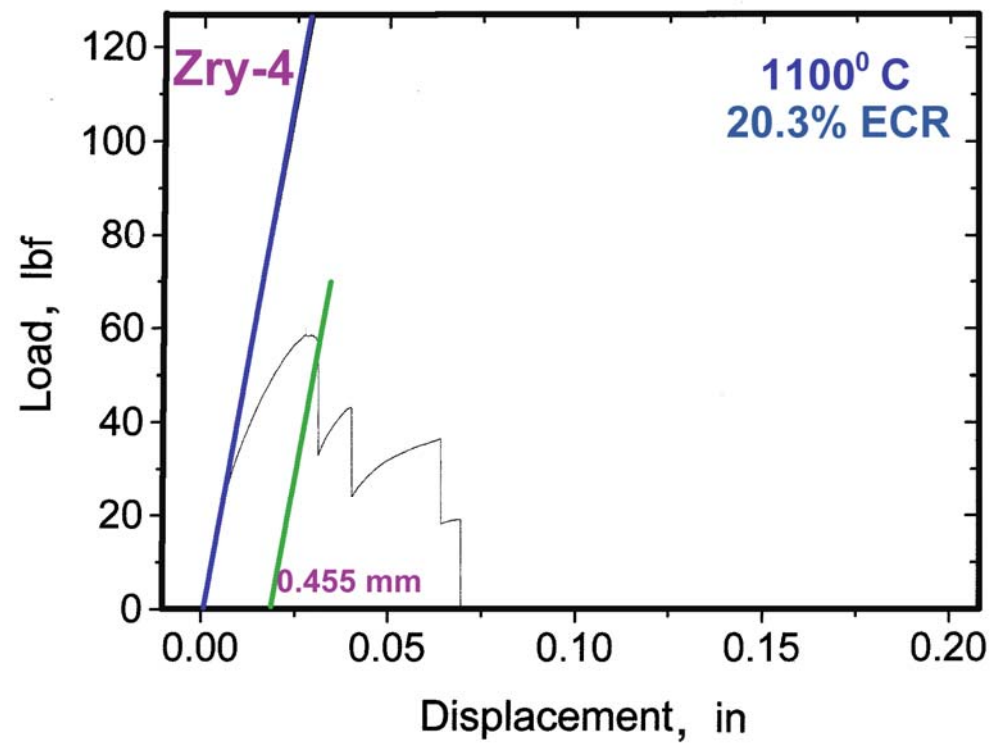

Figure 12. Ring-compression load-displacement data at RT for Zry-4 oxidized to 20% CP-ECR (20.3% ECR based on measured weight gain) at 1100˚C. The sample fractured into four pieces.

to the outer diameter of 9.50 mm for the pre-oxidation-test cladding gives an offset strain of 4.8%. Cladding alloys (Zry-4, ZIRLO, M5 and E110) oxidized at 1000ºC and 1100ºC were tested and analyzed with this procedure. However, a few questions arose during this work regarding the methodology: would the ring actually unload prior to failure at the initial loading slope; what is the uncertainty in determining offset strain; and, given this uncertainty, what minimum value of offset strain should be used as the criterion for nil-ductility?

To answer these questions, most of the cladding alloys listed in Tables 3-6 were compressed at RT and 0.0333 mm/s in the as-fabricated condition to a total displacement of 2 mm. The samples were unloaded and the post-test outer diameter for each ring was measured and compared to the pre-test outer diameter. The difference between these two diameters normalized to the initial diameter is a more direct measure of permanent strain and the ability of the material to deform plastically (i.e., exhibit ductility). It was found that the measured permanent displacement was ≤0.18 mm smaller than the offset displacement determined by the standard methodology shown in Figure 12. This converts to an over-prediction of ≤2% by using the offset-displacement method. The logical explanation for this difference is that the unloading slope must be less than the loading slope. When the sample is loaded, it starts out circular with zero internal stress and behaves like an elastic spring with spring constant k_s. For the 17×17, 15×15 and E110 samples tested, the calculated and measured spring constants were in good agreement, ranging from 0.9-2.0 kN/mm for 8-mm-long samples. The low value is for 17×17 Zry-4, ZIRLO and M5 with 0.57-mm wall thickness. The high value is for thick-wall/small-diameter E110. HBR-type 15×15 Zry-4 has an intermediate value of 1.4 kN/mm. When the sample is unloaded, it is somewhat oval, has residual bending stresses from non-uniform plastic deformation, and has a lower unloading slope. This was confirmed both experimentally and analytically. The experimental confirmation is presented in the following.

The 8511 servo-hydraulic Instron was programmed for a compression displacement of 2 mm at 0.0333 mm/s, followed by unloading at a controlled rate of 0.0333 mm/s. The sample used was HBR-type 15×15 Zry-4. The results are shown in Figure 13. Clearly, the unloading slope is not as steep as the loading slope. The offset displacement (1.32 mm) based on mathematical unloading of the sample at the loading slope is larger than the true offset displacement (1.19 mm) based on the unloading curve. The difference (0.13 mm) is equivalent to 1.2% for this cladding. The permanent displacement determined directly by measuring the pre-test and post-test diameter in the loading direction is in excellent agreement with the 1.19 mm determined from the full load-displacement curve including unloading.

For oxidized samples, it is not possible to perform controlled unloading just prior to failure because the displacement at which failure will occur is unknown. Therefore, the standard procedure shown Figure 12 is used to determine offset displacement and strain. To compensate for this over-estimation of offset strain, a limiting offset strain of 2% is set in the determination of ductile-to-brittle transition. In other words, there is confidence in labeling samples with ≥2% offset strain as ductile. For samples with offset strains <2%, it is not clear if they are ductile or brittle.

The 17×17 Zry-4, ZIRLO and M5 samples oxidized at 1000ºC and 1100ºC to 5-20% CP-ECR and quenched at 800ºC were initially compressed at RT and 0.0333 mm/s to complete failure (3-to-4 cracks) indicated by a load drop to zero. For samples that exhibited offset strains <2% (e.g., one M5 sample at 1.8%), the test was repeated with another 8-mm ring from the same oxidation-quench sample by stopping the test after the first significant load drop (30-50%). The sample was removed from the Instron and examined under a microscope to determine that a through-wall crack along the whole length of the sample had occurred. The post-test diameter was measured in the loading direction and compared to the pre-test diameter to determine permanent displacement and strain.

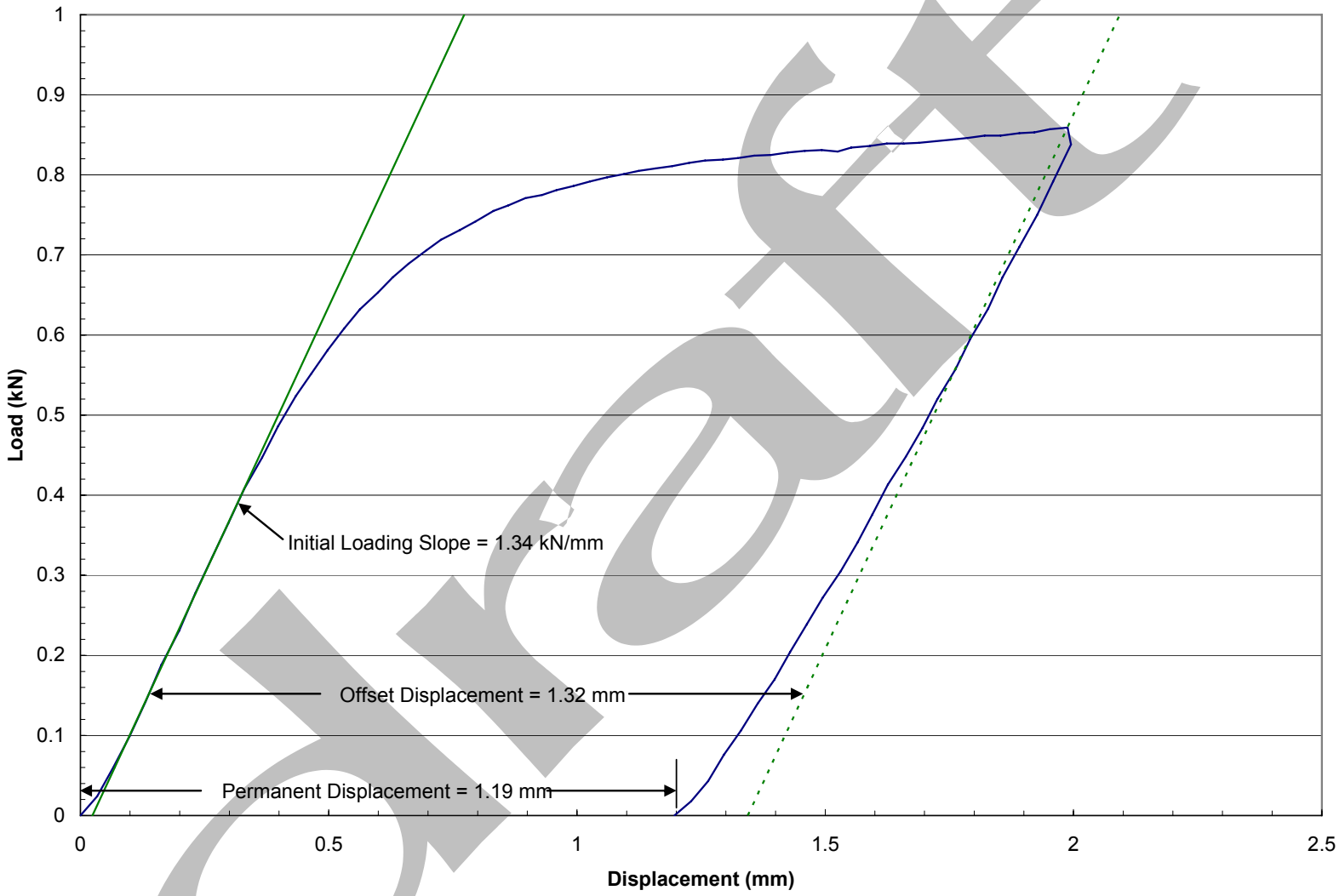

Figure 13. Load-displacement results from RT compression and unloading of an 8-mm-long ring of HBR-type 15×15 Zry-4 cladding.

If the measured permanent strain was ≥1%, the sample was classified as ductile. The 1% permanent strain criterion is based on uncertainties in measuring the post-test diameter of a cracked ring to infer the permanent strain for the sample if it had been unloaded just prior to cracking. Although it was not necessary for the samples oxidized at 1000ºC and 1100ºC, if the permanent strain were <1% based on the RT test, a new sample with the same oxidation conditions would have been compressed at 135ºC.

The procedure of interrupting the test following the first load drop worked so well, that it was adopted for all ring-compression tests of as-fabricated and prehydrided cladding oxidized at 1200ºC. The effects of hydrogen and high-temperature oxidation cause the cladding to embrittle at <17% CP-ECR for RT tests. As samples under these conditions had to be retested at 135ºC anyway, the RT tests were eventually eliminated for as-fabricated and prehydrided samples oxidized at 1200ºC.

The procedure for determining ductility and conditions (T, CP-ECR, H-content) under which ductile-to-brittle-transition occurs is summarized in the following:

a) section one or more 8-mm-long rings from the oxidation-quench sample; measure and record the precise length and outer-diameter of the oxidized sample; mark the circumferential location that will be contacted by the loading platen;

b) load ring into Instron (see Figure 14) with flat support and loading platens;

c) compress at RT (1000ºC- and 1100ºC-oxidized samples) or at 135ºC (1200ºC-oxidized samples) and 0.0333 mm/s;

d) Interrupt test following first significant load drop (>30%); this is relatively easy to do as concurrent with the load drop is a loud cracking noise; determine the offset strain from load-displacement data;

e) remove sample from Instron, allow sample to cool to RT, and examine it under microscope to determine if the sample failed with a single through-wall crack along the whole length of the sample or with multiple cracks; generally, load drops of 30-50% imply a single crack, while larger load drops (80-100%) imply two or three cracks;

f) if a single, tight, through-wall crack is found, measure the post-test diameter in the loading direction and determine the permanent displacement; normalize this displacement to the pre-oxidation-test outer diameter to determine the permanent strain; if permanent strain is <1%, classify sample as brittle; if multiple cracks are found, the post-test diameter measurement is meaningless and this step is eliminated;

g) if multiple cracks are found, use offset displacement and strain from load-displacement curve; for samples with <2% offset strain classify samples as brittle; and

h) record both offset and permanent strains, along with pre-oxidation-test characterization (as-fabricated, prehydriding H-content, irradiated with a measured H-content), oxidation temperature, CP-ECR, ECR determined from measured weight gain (i.e., measured ECR), quench temperature; ring compression test temperature; and number and location of cracks.

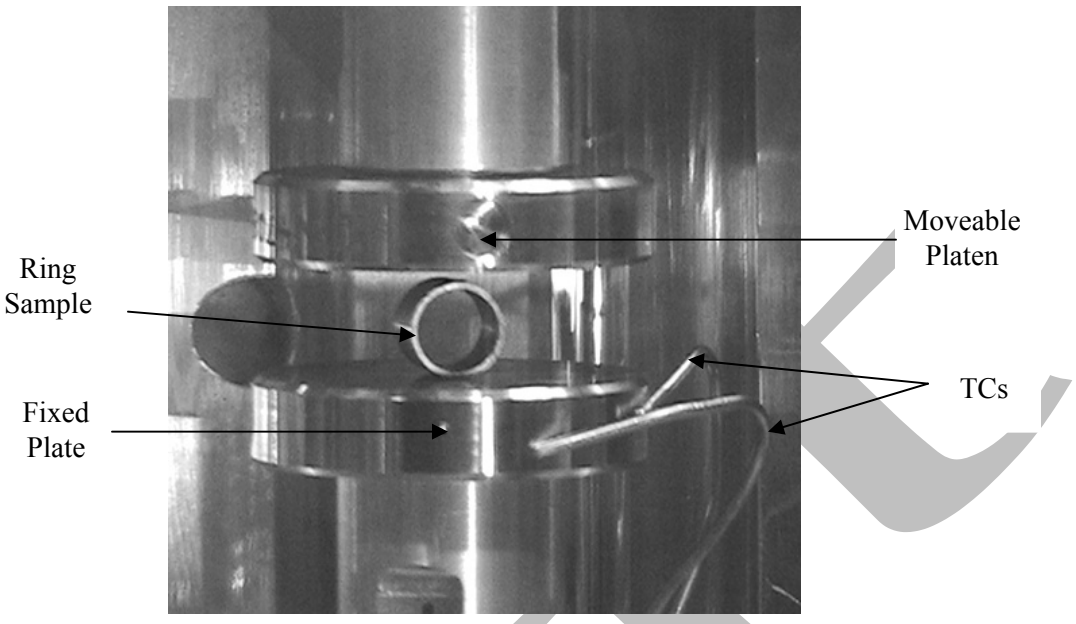

Figure 14. Photograph of ring compression sample supported by the fixed flat platen and loaded by the moveable, load-train platen for the Instron 8511.

2.4 LOCA integral tests with fueled-and-pressurized samples

Out-of-cell LOCA integral tests with as-fabricated cladding are relatively straightforward with regard to sample preparation and test conduct. Figure 15 shows the LOCA test train with as-fabricated cladding. For these tests the cladding sample is filled with ≈25-mm-long zirconia pellets to simulate the heat capacity of the fuel. There is a clearance of ≈13 mm between the top zirconia pellet and the top end fixture to prohibit contact during sample bending. The test train is supported at the top to minimize specimen bowing. The quartz tube encasing the test train provides an enclosed volume for steam flow and water quench, both of which are introduced through the bottom of the unit. The test train is centered within the quartz tube by means of two perforated spacer disks. Centering is very important as four vertical infrared lamps are focused within the furnace to heat the specimen. Swagelok fittings are used above the specimen to connect to the high-pressure gas line and top pressure gauge and below the specimen to connect to the lower pressure-gauge line. The total gas volume above the fuel column is 10 cm^3, most of which is outside the heated zone. Four Type S thermocouple lead wires are fed in through the top. Two of the thermocouples are spot-welded at the specimen midplane, 180° apart. The other two are spot welded 50-mm above and 50-mm below the midplane at the same angular orientation as one of the midplane thermocouples. These thermocouples are accurate to ±3°C at 1200°C. The signal from the top thermocouple is used to control the furnace power to achieve the desired temperature ramp, hold temperature and cooling rate prior to quench. Although the uniform heating zone of the furnace is 250-mm, the uniform temperature region of the undeformed sample is ≈125 mm, centered about the midplane of the sample. The system is designed to allow switching of the control thermocouple in case the top one fails. For the out-of-cell tests, hands-on assembly is used and bare-wire thermocouple beads are welded directly onto unirradiated tubing.

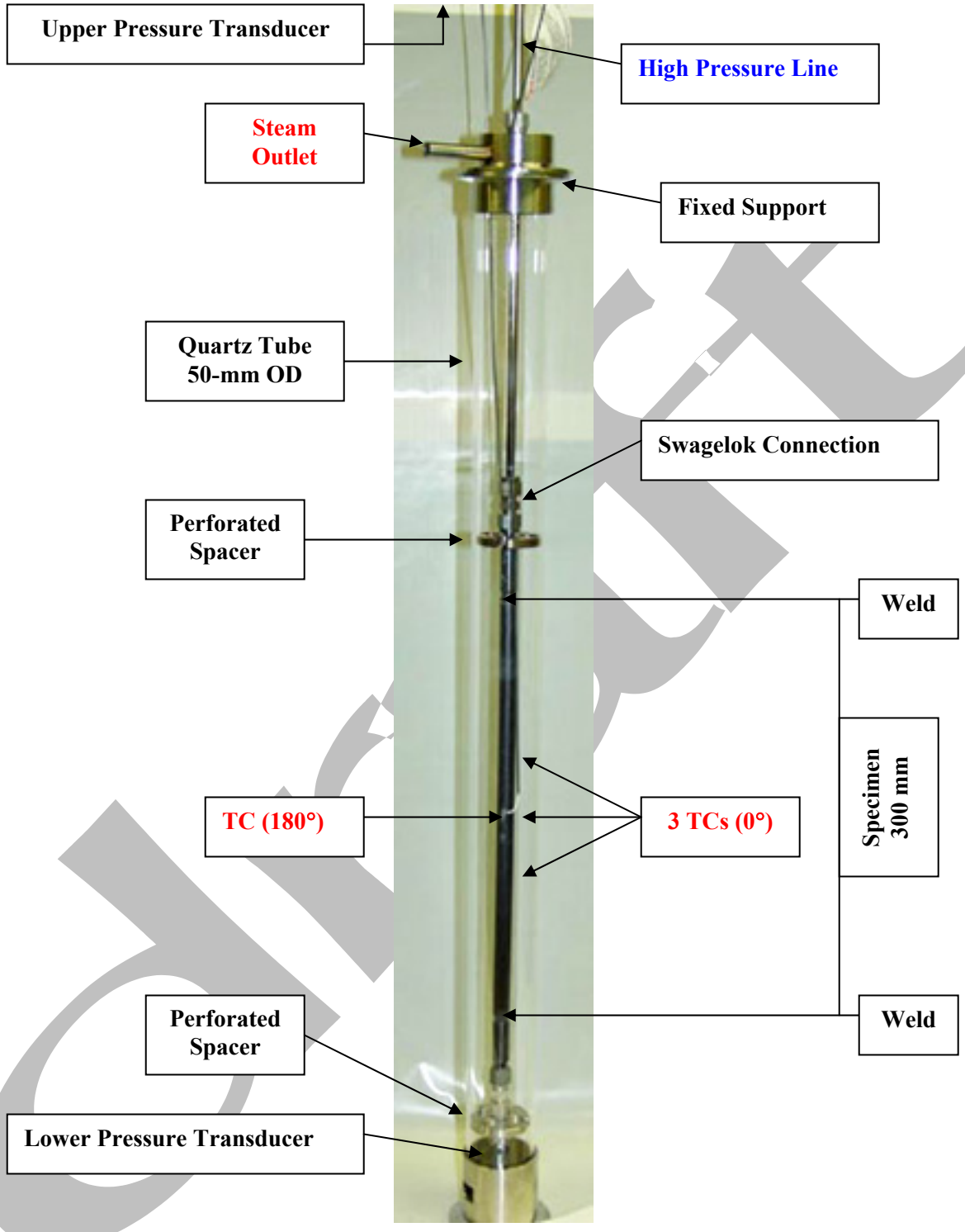

Figure 15. LOCA Integral Test Train Assembly and quartz tube.

Because of the high thermal mass of the sample, temperature control is much easier than for the short, defueled cladding oxidation samples. Figure 16 shows a schematic of the temperature history used for both out-of-cell and in-cell testing. Reference control parameters for BWR cladding are: 8.62-MPa (1250 psig) internal pressure with He at RT and 300ºC, 5°C/s heating rate, 1200°C hold temperature, variable hold time, 3°C/s cooling rate from the hold temperature to 800°C, rapid cooling from bottom-flooding quench at 800°C. As these parameters are controlled, they can be adjusted from test-to-test. The internal pressure of 8.62 MPa was chosen to ensure burst at ≈750°C, which is below the alpha-to-(alpha + beta) phase change temperature, for 9×9 Zry-2 cladding. This also results in large ballooning strains. Although many such tests were conducted during the development of the LOCA integral apparatus, the most important ones are those that provided a baseline for the in-cell tests: a) ramp-to-burst followed by slow cooling; b) ramp to 1200°C, hold for 300 s at 1200°C followed by slow cooling; and c) the full LOCA sequence including quench at 800°C.

For high-burnup test rod specimens, a drill with both rotary and cyclic horizontal motion is used to remove ≈13 mm of fuel from the bottom of the specimen (space for end-cap welding) and ≈20 mm of fuel from the top of the specimen (≈7 mm for end-cap welding and 13 mm for clearance). Following end-cap welding, the specimen is inserted into a holder for attaching the Swagelock fittings and for strapping two thermocouples 180° apart to the specimen ≈50-mm above the midplane. Although a test Train Assembly Device was designed and constructed to spot-weld TCs directly to the cladding metal following oxide removal, these operations were too challenging to perform remotely using manipulators. Comparisons between welded TCs and strapped TCs indicated less than a 10°C difference in readings. For the in-cell tests with high-burnup fueled cladding, axial gas flow rate is an important parameter. Prior to conducting the LOCA transient, the sample is pressurized rapidly at the top at RT and 300°C. The time response of the pressure transducer below the fuel column is used to evaluate the axial gas flow rate.

Online data of interest include the time response of the bottom pressure transducer at RT and 300°C, burst temperature and burst pressure. Following the test, the sample is photographed (low quality) in-situ in the vertical position and moved to other workstations for non-destructive characterization in the horizontal position: photography (high quality), profilometry, and gamma scanning. Destructive examinations are performed on some of the samples to determine: oxide and alpha layer thicknesses for inner- and outer-cladding surfaces (metallography), circumferential and axial distribution of oxygen (LECO) and circumferential and axial distribution of hydrogen (LECO). Prior to destructive examination, the sample is subjected to a four-point-bending test to determine failure bending moment and ductility. The four-point-bending fixture has been developed and tested in an Instron machine out-of-cell using nonirradiated cladding.

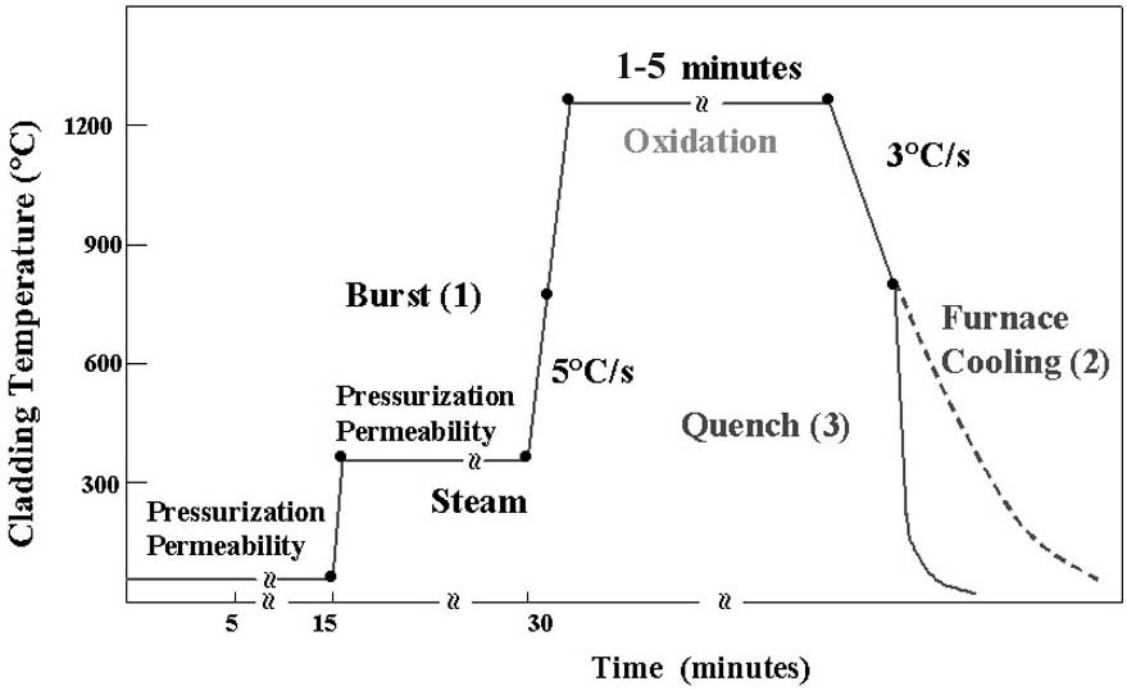

Figure 16. Schematic of the thermal history used for LOCA integral tests: zirconia-filled, as-fabricated cladding samples tested out-of-cell and fueled high-burnup cladding samples tested in-cell.

3 Results for As-fabricated Cladding Alloys

In this section, the performance of as-fabricated 17×17 ZIRLO and M5 is compared to the performance of modern 17×17 low-tin Zry-4. Modern Zr-lined 10×10 Zry-2 is also included in the test matrix. These materials are described in Tables 3-5. In parallel to these tests, considerable testing of HBR-type 15×15 Zry-4 (see Table 4) has been conducted to generate baseline data for the H. B. Robinson high-burnup cladding, as no high-burnup 17×17 low-tin Zry-4 was available to the program. Because the HBR-type 15×15 Zry-4 exhibited lower post-quench-ductility transition ECR than 17×17 Zry-4, the post-quench ductility of modern (belt-polished) 15×15 Zry-4 (see Table 4) oxidized at 1200ºC was studied. Oxidation kinetics studies were also conducted with as-fabricated 9×9 Zry-2 to generate baseline data for high-burnup Limerick Zry-2. In addition, breakaway oxidation studies at 800-1000ºC were conducted with HBR-type and belt-polished 15×15 Zry-4, 17×17 ZIRLO and 17×17 M5. E110 (see Table 6) was included in the breakaway oxidation studies to develop some fundamental understanding as to why this Zr-1Nb alloy exhibits such low breakaway-oxidation time as compared with another Zr-1Nb alloy, M5.

3.1 Zircaloy-4

3.1.1 Post-quench ductility of 17×17 Zry-4 oxidized at 1000ºC, 1100ºC and 1200ºC

This work was divided into two campaigns: characterization and RT-ring-compression testing of samples exposed to two-sided oxidization at 1000ºC and 1100ºC and quenched at 800ºC; and characterization and ring-compression testing (RT and 135ºC) of samples exposed to two-sided oxidization at 1200ºC and quenched at 800ºC. Characterization included weight gain, oxide- and alpha-layer thickness measurements (metallography), microhardness, and hydrogen pickup (LECO). All samples were oxidized in the same apparatus for test times corresponding to CP-predicted ECR values of 5, 10, 15, 17, and 20% for 0.57-mm-wall cladding. Additional tests were conducted at intermediate CP-ECR values for the 1200ºC-oxidized samples to better determine the ductile-to-brittle transition CP-ECR.

17×17 Zry-4 oxidized at 1000ºC and 1100ºC

Figures 17 and 18 show the thermal benchmark results for the 1000ºC- and 1100ºC- oxidation test trains, respectively. The ramp times to reach the hold temperature are short compared to the hold times at these temperatures. The average cooling rate to the 800˚C quench temperature is ≈10˚C/s (10˚C/s for 1100˚C and 11˚C/s for 1000˚C). The temperature-time curves were used to calculate the CP-predicted weight gain and ECR values. Table 8 lists the weight gain results for the oxidation tests at these temperatures. They are in very good agreement with the CP-predicted weight gains.

Table 9 gives the results of the RT post-quench ductility tests. It is clear from the results that 17×17 Zry-4 retains post-quench ductility up to 20% CP-ECR – the limit of the test matrix – at these oxidation temperatures. For the 1000ºC-oxidation tests, the offset strain levels off at ≈3%, while for the 1100ºC-oxidation tests the offset strain levels off at ≈5%. It appears from these results that Zry-4 will retain ductility at higher CP-ECR values and higher test times (e.g., >3400 s at 1000ºC until breakaway oxidation occurs). For 1100ºC-oxidized samples, breakaway oxidation does not occur and the beta layer does not appear to embrittle due to the low oxygen solubility (≈0.4 wt.%) in the beta phase at 1100ºC. At much higher ECR values, beta-layer thinning would cause brittle behavior of compressed rings. Photographs of the ring-compressed samples are shown in Figure 19. The 5% CP-ECR samples were intact at the maximum Instron displacement for these samples.

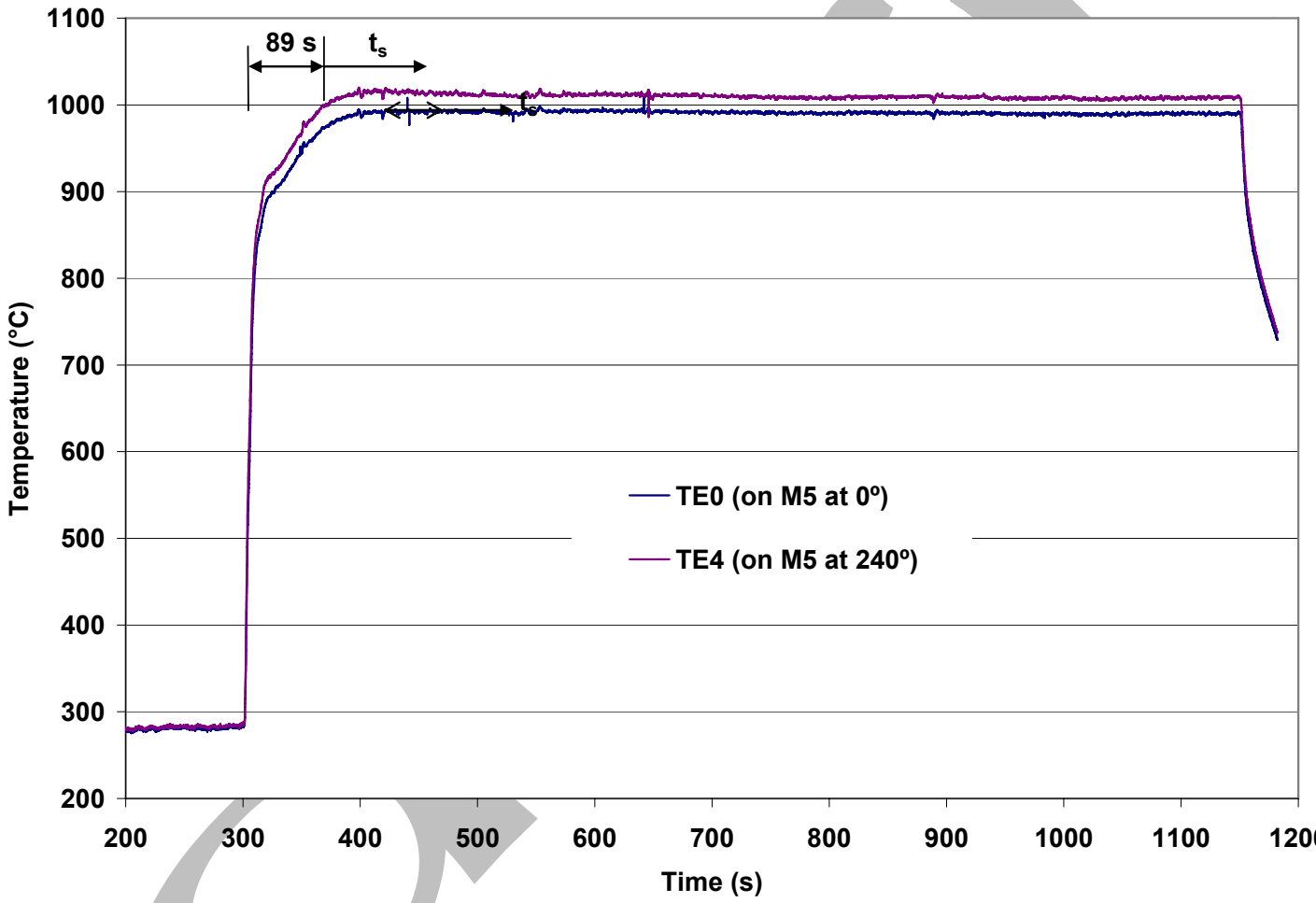

Figure 17. Thermal benchmark results for the 1000±10ºC oxidation tests. The sample used was from the 0.57-mm-wall validation lot of M5, which has the same inner and outer diameter as 17×17 Zry-4 and ZIRLO. Quench at 800ºC is not shown in this figure.

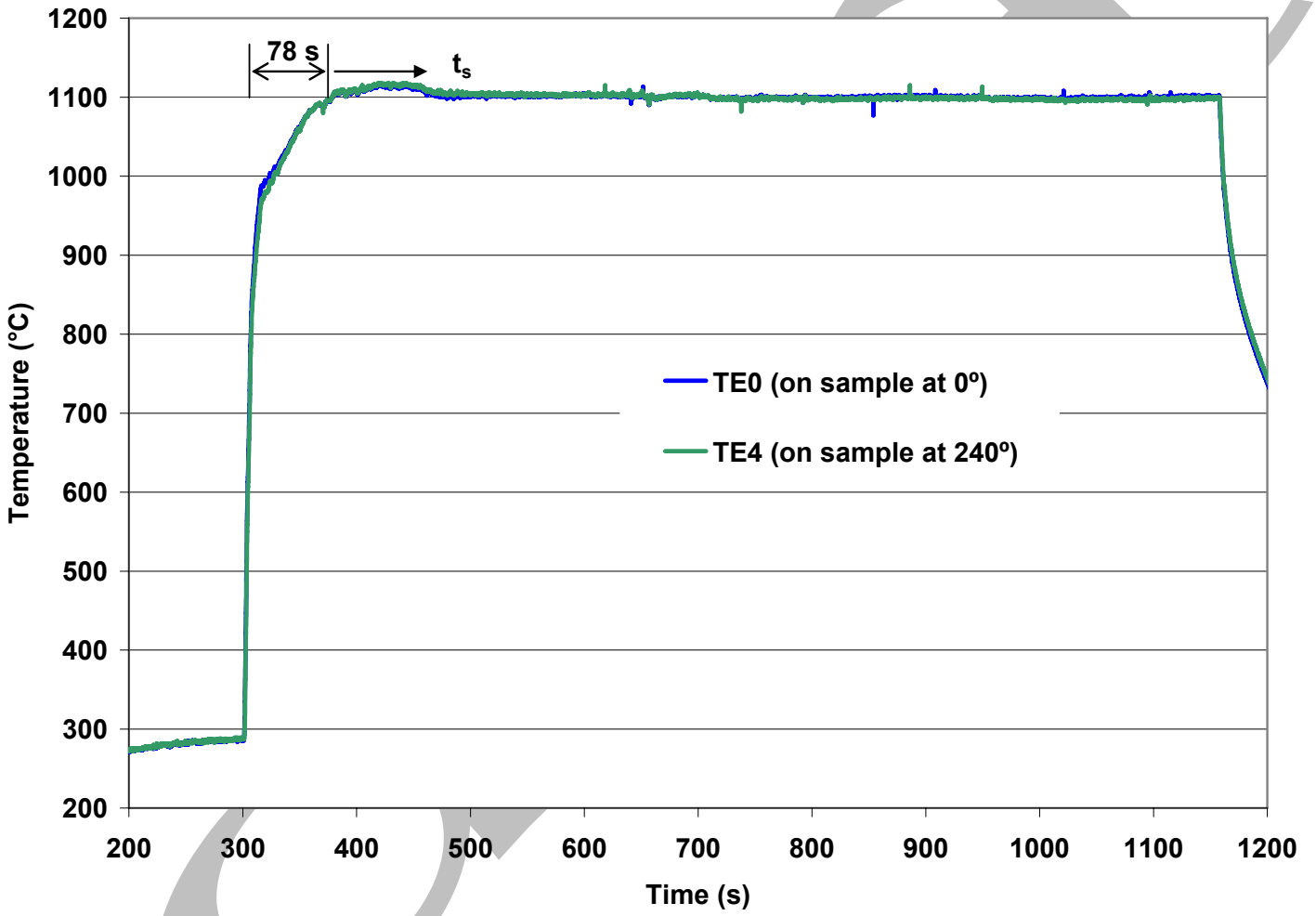

Figure 18. Thermal benchmark results for the 1100±2ºC oxidation tests. The sample used was from the 0.57-mm-wall validation lot of M5, which has the same inner and outer diameter as 17×17 Zry-4 and ZIRLO. Quench at 800ºC is not shown in this figure.

Table 8 Weight Gain (Wg in mg/cm^2) and Measured ECR (%) Values for 17×17 Zry-4 Oxidized in Steam at 1000˚C and 1100˚C. ECR = 1.538 Wg for 0.57-mm-wall cladding. Multiply weight gain results by a factor of 10 to convert to g/m^2. CP = Cathcart-Pawel.

Oxidation Temperature ºC	CP-Predicted ECR %	CP-Predicted Weight Gain mg/cm^2	Measured Weight Gain mg/cm^2	Measured ECR %
1000	5	3.25	3.9	6.1
1000	10	6.50	7.2	11.0
1000	15	9.75	11.0	16.9
1000	17	11.05	12.5	19.3
1000	20	13.00	14.6	22.4
1100	5	3.25	4.0	6.2
1100	10	6.50	7.1	10.9
1100	15	9.75	10.6	16.3
1100	17	11.05	11.7	18.0
1100	20	13.00	13.2	20.3

Table 10 summarizes the results of the metallography, microhardness and hydrogen pickup measurements. The hydrogen pickup is very low indicating that no breakaway oxidation occurred for these test times. The results in Table 10 are consistent with the post-quench ductility results. Metallographic images and graphical results for 17×17 Zry-4 are presented in the ZIRLO (3.3.1) and M5 (3.4.1) sections for purposes of comparison.

The post-quench ductility, as measured by offset strain, for Zry-4 oxidized at 1100˚C decreased with ECR up to ≈15% and remained essentially constant at ≈5% offset strain from 15 to 20% ECR (see Table 10). As the ductility of the prior-beta layer decreases with increasing oxygen content, the results suggest that the oxygen content in the beta layer reaches the solubility limit (0.38 wt.% [18]) at ≈15% CP-ECR, which corresponds to an equivalent isothermal time of ≈600 s. From 15% ECR (600 s) to 20% ECR (1065 s), the beta layer-thickness decreases to ≈300 μm (see Figure 48a), while the oxygen content and post-quench ductility of the prior-beta layer remained constant. Thus, neither oxygen- nor beta-layer-thinning-induced embrittlement was observed under these test conditions. As hydrogen pickup was negligible, hydrogen-induced embrittlement was also not observed.

Table 9 Ring Compression Test Results for 17×17 Zry-4 Samples Oxidized at 1000˚C and 1100˚C, Cooled at ≈10˚C/s to 800ºC and Quenched. ECR = 1.538 Wg for 0.57-mm-wall cladding. Tests were performed on 8-mm-long samples at RT and at 0.0333 mm/s displacement rate. Displacements in the loading direction were normalized to the as-fabricated outer diameter (9.50 mm) to calculate offset strain. A complete set of tests were performed using the Model 4505 Instron. A limited number of confirmation tests were performed with the Model 5566 Instron on rings cut from the same oxidation samples.

Oxidation Temperature ºC	Cathcart-Pawel ECR, %	Measured ECR %	Offset Displacement mm	Offset Strain %	Confirmation Tests Model 5566 Instron
1000	5	6.1	>4.4	>46	---
1000	10	11.0	2.74	29	Yes
1000	15	16.9	0.71	7.5	Yes
1000	17	19.3	0.48	5.1	---
1000	20	22.4	0.31	3.2	---
1100	5	6.2	>5.5	>58	---
1100	10	10.9	1.9	20	---
1100	15	16.3	0.52	5.4	---
1100	17	18.0	0.47	4.9	---
1100	20	20.3	0.46	4.8	---

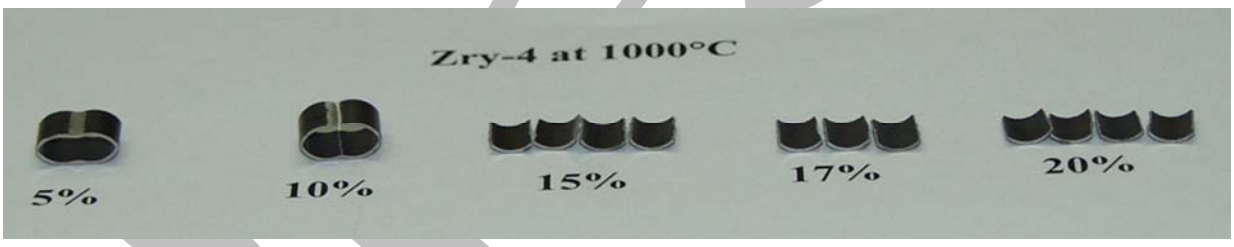

(a)

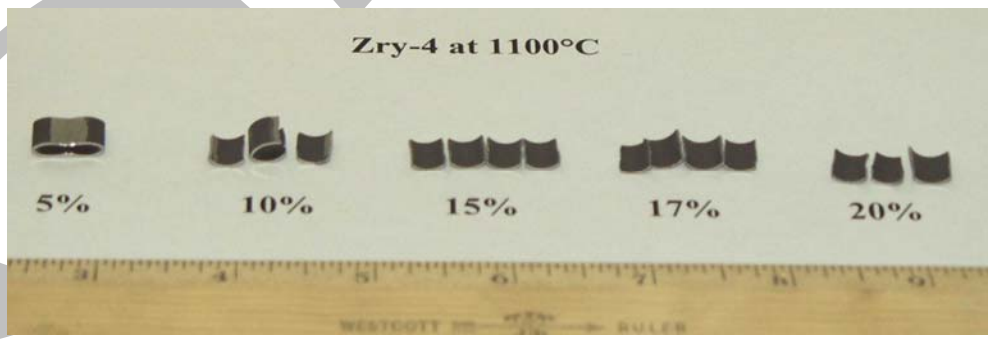

(b)

Figure 19. Post-test appearance of Zry-4 samples compressed at RT and 0.0333 mm/s: (a) samples oxidized at 1000˚C; and (b) samples oxidized at 1100˚C. ECR values below each sample are calculated using the Cathcart-Pawel weight gain correlation.

Table 10 Summary of Characterization Results for Highly Oxidized 17×17 Zry-4 Samples after Exposure to Steam at 1000˚C and 1100˚C, Cooling at ≈10˚C/s to 800˚C and Quench; CP-predicted ECR is 20%

Oxidation Temperature ˚C	Parameter	17×17 Zry-4
1000	Effective Oxidation Time, s	3364
	Weight Gain, mg/cm^2	14.6
	Measured ECR, %	22.4
	RT Offset Displacement, mm	0.31
	RT Offset Strain, %	3.2 **(ductile)**
	Hydrogen Content, wppm	19
	Hydrogen Pickup, wppm	15
	OD/ID Oxide Layer Thickness, μm	83/82
	Microhardness within Middle 0.2 mm of Prior-beta Layer, DPH	290-420
1100	Effective Oxidation Time, s	1065
	Weight Gain, mg/cm^2	13.2
	Measured ECR, %	20.3
	RT Offset Displacement, mm	0.46
	RT Offset Strain, %	4.8 **(ductile)**
	Hydrogen Content, wppm	22
	Hydrogen Pickup, wppm	19
	OD/ID Oxide Layer Thickness, μm	70/68
	Microhardness within Middle 0.2 mm of Prior-beta Layer, DPH	240-470

The variation of post-quench ductility with CP-ECR for 1000˚C-oxidized Zry-4 is similar to the variation for the 1100˚C oxidized samples. The primary difference is the slow decrease in ductility with ECR from 7.5% at 15% CP-ECR to 5.1% at 17% CP-ECR to 3.2% at 20% CP-ECR. The beta-layer oxygen-solubility at 1000˚C is less (0.24 wt.% [18]) than it is at 1100˚C, so higher ductility would be expected. However, 1000˚C is very close to the (alpha + beta) → beta phase transformation temperature. The oxidation temperature based on the thermal-benchmark history in Figure 17 is 1000±10˚C, which suggests that what is referred to as the beta layer may have contained a small fraction of alpha at the experimental oxidation temperature. Although it is not clear why 1000˚C-oxidized Zry-4 has lower post-quench ductility at 20% CP-ECR than 1100˚C-oxidized Zry-4 at 20% CP-ECR (3% vs. 5%), the differences are rather small and ductility is retained at both oxidation temperatures.

17×17 Zry-4 oxidized at 1200ºC

Many tests were conducted with 17×17 Zry-4 oxidized at 1200±5ºC to determine the ductile-to-brittle transition CP-ECR at RT and 135ºC. This required eight test trains and eight sets of thermal benchmark tests. Figures 20 and 21 show the thermal-benchmark results for the first test train and the most recent test train, respectively. Although the temperature ramps are different, these have little effect on the long-time tests used to determine the transition CP-ECR of ≈17% at 135ºC. Prior to quench, the sample cools at an average rate of ≈13˚C/s (1200˚C to 1000˚C in 6 s and 1000˚C to 800˚C in 23 s). Also, all ring-compression tests were stopped after the first significant load drop (>30%) to allow a measure of the permanent strain based on diameter change in the loading direction.

The weight gain results (expressed in terms of measured ECR) and the post-quench ductility (PQD) results are summarized in Table 11. The PQD results are plotted in Figure 22. It is clear that 17×17 Zry-4 embrittles at room temperature after oxidation to ≈9% CP-ECR and quench. This is confirmed by both the offset strain criterion (<2%) and the permanent-strain criterion (<1%) for embrittlement. The enhancement of ductility with the increase in ring-compression test temperature is quite pronounced. Based on the average of the permanent strain readings, the ductile-to-brittle transition CP-ECR is ≈18% at 135ºC. Based on the minimum values of permanent strain, 17% CP-ECR is a more conservative estimate. The variations of offset and permanent strains with CP-ECR are shown in Figures 22a and 22b, respectively, for the RT and 135ºC test conditions.

It is interesting to note that the oxygen solubility of the Zry-4 beta phase at 1200ºC is 0.57 wt.% [18]. The results in Table 11 suggest that oxygen saturation of the beta layer occurs at ≈17% CP-ECR for 1200ºC-oxidized Zry-4 and that an average oxygen content of ≈0.6 wt.% is enough to embrittle the Zry-4 prior-beta layer following quench. As is shown in Section 3.3.1 (Figure 52a), the physical picture is more complicated than this because the post-quench prior-beta layer consists of alpha incursions (>0.6 wt.% oxygen) in an oxygen-depleted (<0.6 wt.%) matrix due to precipitation of oxygen-stabilized alpha during cooling from 1200ºC to 800ºC.

Table 12 summarizes the characterization results for 17×17 Zry-4 oxidized at 1200ºC to 13% and 20% CP-ECR and quenched at 800ºC. As expected, the hydrogen pickup is very low. Also, there is excellent agreement between the inner-surface and outer-surface oxide layer thickness, indicating adequate steam flow at the inner surface. The microhardness results support the post-quench ductility results. Based on the room-temperature microhardness values, one would expect ductility at 13% CP-ECR and embrittlement at 20% CP-ECR at 135ºC. Metallographic images and additional graphical results are presented for comparison purposes in the sections on ZIRLO (3.3.1) and M5 (3.4.1).

Based on the hydrogen measurements and the metallographic results in Table 12, the embrittlement observed at 17% CP-ECR in Figure 22 is not due to hydrogen-induced embrittlement nor beta-layer thinning (>300-μm beta layer thickness at 17% CP-ECR). For as-fabricated Zry-4 oxidized at 1200ºC embrittlement appears to be caused by the elevated oxygen concentration in the beta layer due to higher oxygen solubility at 1200ºC, as compared to 1000-1100ºC.

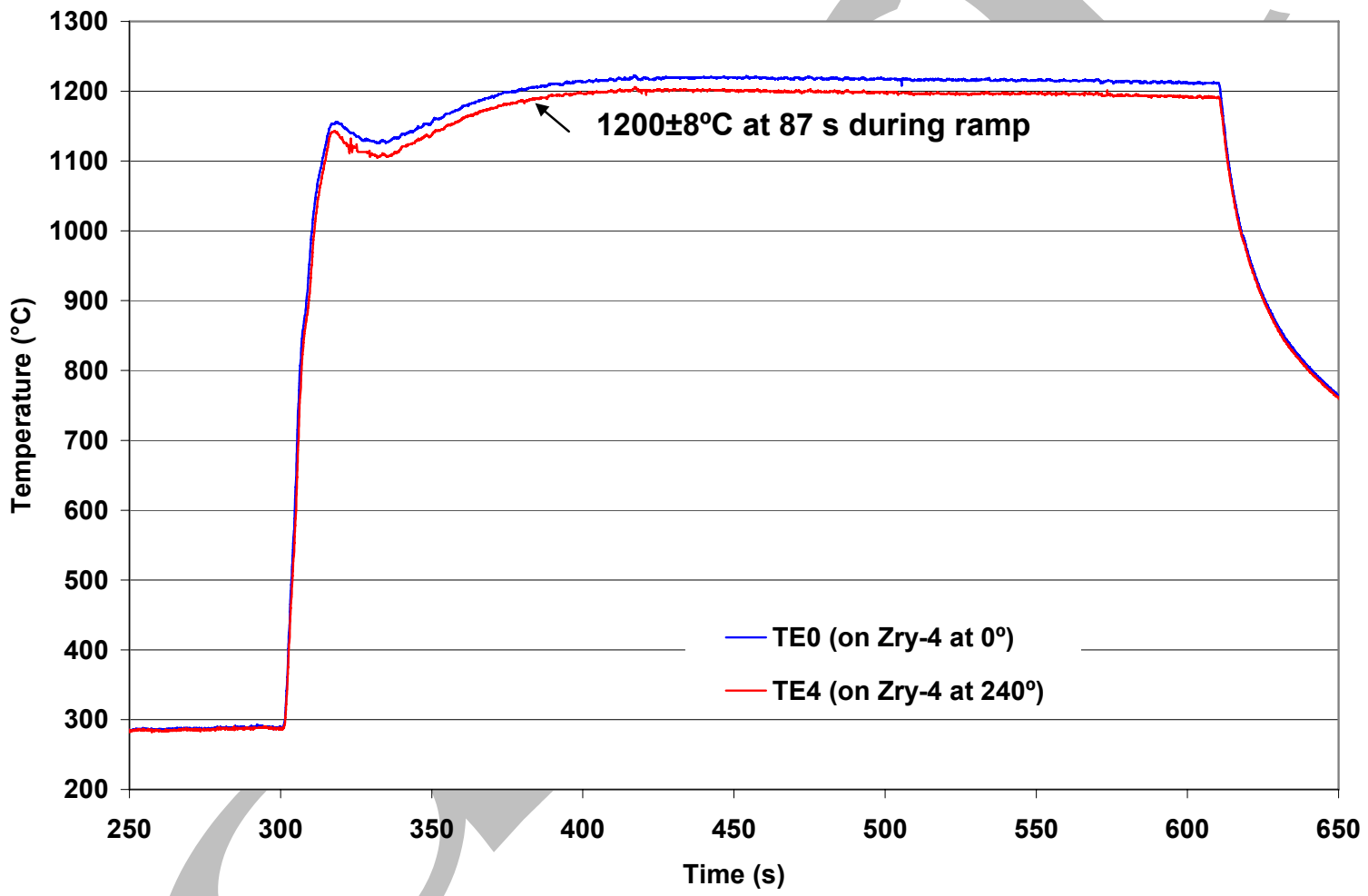

Figure 20. Thermal benchmark results (Test Train #1) for oxidation of 17×17 alloys at 1200±5ºC. The sample used for this benchmark was 17×17 Zry-4 with a wall thickness of 0.57 mm. Quench is not shown in this figure.

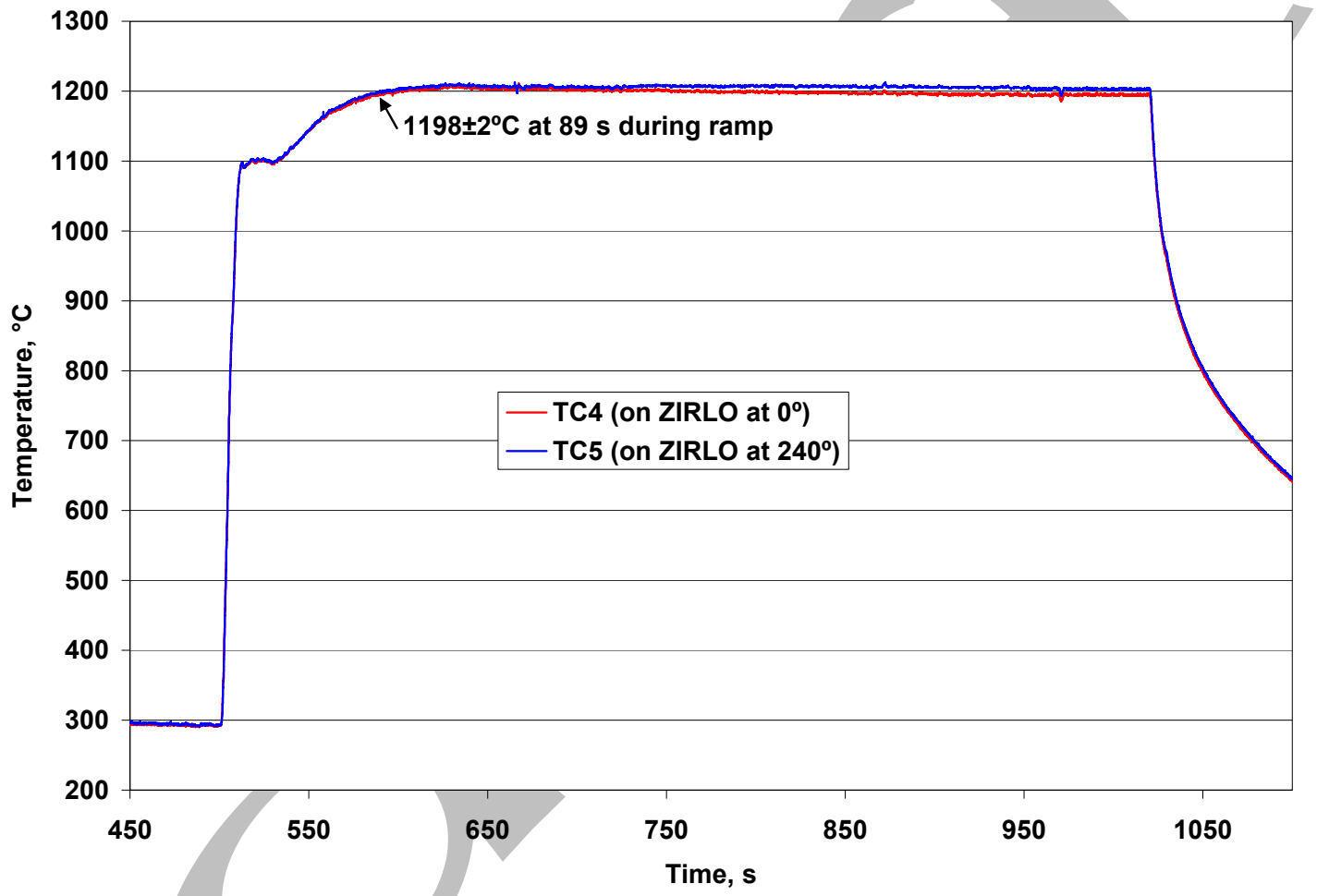

Figure 21. Thermal benchmark results (current test train) for oxidation of 17×17 alloys at 1200±5ºC. The sample used for this benchmark was 17×17 ZIRLO with a wall thickness of 0.57 mm. Quench is not shown in this figure.

Table 11 Ring Compression Test (RCT) Results for 17×17 Zry-4 Cladding Oxidized at 1200±5˚C, Cooled at ≈13˚C/s to 800˚C and Quenched. ECR = 1.538 Wg for 0.57-mm-wall cladding. Tests were performed on ≈8-mm-long samples at RT and 135ºC and at 0.0333 mm/s displacement rate. Displacements in the loading direction were normalized to the as-fabricated outer diameter (9.50 mm) to calculate offset and permanent strains.

Test Conditions		ECR %		Plastic Displacement, mm		Plastic Strain, %	
RCT T, ˚C	Ox. Test Time[a], s	CP	Meas.	Offset	Permanent	Offset	Permanent
RT	0	0	0	6.3	5.9	66	62
RT RT	60 60	4.9 4.9	5.5 5.5	>3.5 4.28	>3.23 ---	>37 45	>34 ---
RT	100	7.8	8.2	0.38	0.21	4.0	2.2
RT RT 135 135	136 151 151 151	10.0 10.8 10.8 10.8	10.9 11.9 11.9 11.9	0.10 0.08 2.14 >2.41	0.05 0.05 --- >1.92	1.0 0.8 23 >25	0.5 0.5 --- >20
RT RT 135	203 203 203	13.0 13.0 13.0	12.8 14.6 14.6	0.09 0.08 0.49	0.07 0.06 0.29	1.0 0.8 5.1	0.7 0.6 3.1
RT	258	15.7	17.1	0.04-0.12	---	≈0.8	---
RT RT 135 **135[b]** **135[b]**	310 310 310 **318** **318**	16.7 17.0 17.0 **17.0** **17.0**	18.0 18.1 18.1 **18.5** **18.5**	0.10 0.07 0.26 **0.26** **0.19**	0.06 0.05 0.14 **0.12** **0.07**	1.0 0.7 2.8 **2.8** **2.0**	0.6 0.5 1.4 **1.3** **0.7**
135[b] **135[b]**	**390** **390**	**19.0** **19.0**	**20.3** **20.3**	**0.29** **0.18**	**0.10** **0.08**	**3.1** **1.9**	**1.1** **0.8**
RT	428	20.0	20.7	0.05	0.04	0.5	0.4

[a]Includes ramp from 300ºC.

[b]Tests were conducted with current test train (see Figure 21 for thermal history).
Most other test results were conducted with the initial test train (see Figure 20 for thermal history).

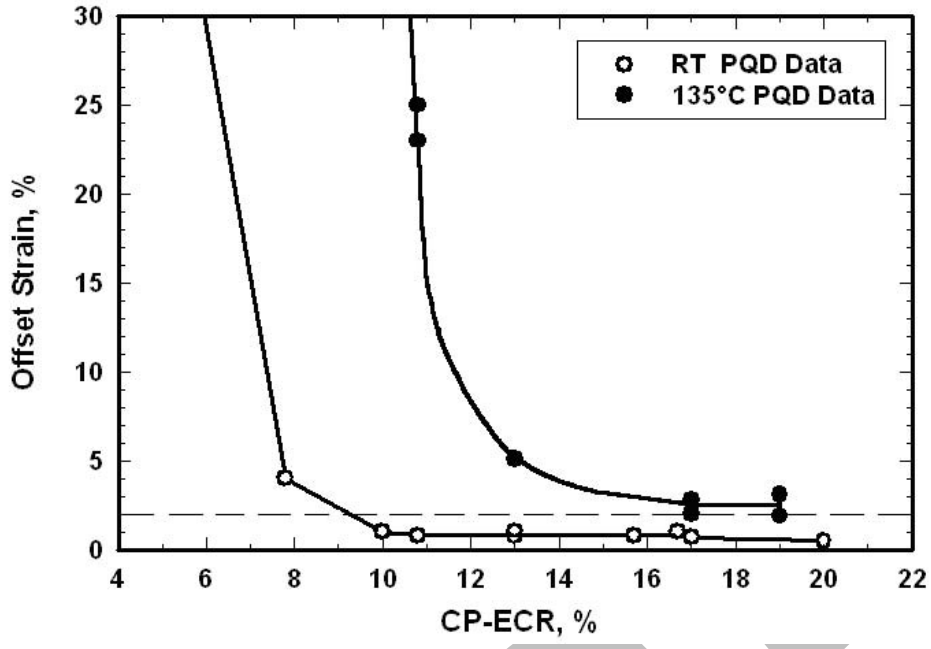

(a)

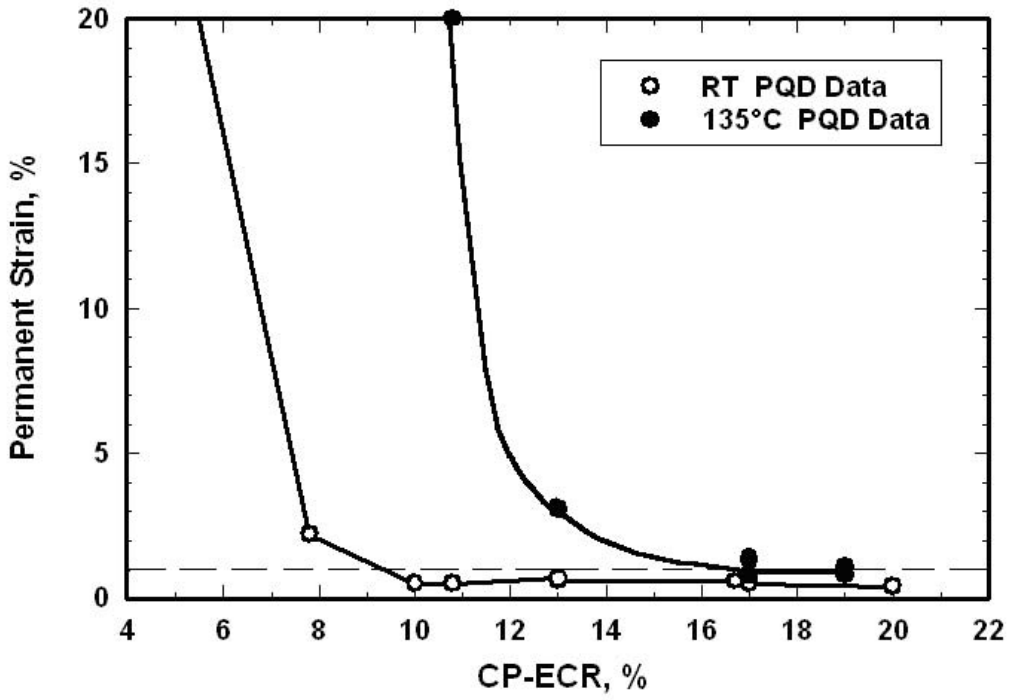

(b)

Figure 22. Offset (a) and permanent (b) strains vs. CP-ECR for 17×17 Zry-4 oxidized at 1200ºC, cooled at ≈13˚C/s to 800ºC, quenched and ring-compressed at RT and 135ºC.

Table 12 Summary of Characterization Results for 17×17 Zry-4 Samples after Exposure to Steam at 1200˚C to 13% and 20% CP-ECR, Cooling at ≈13˚C/s to 800˚C and Quench

Parameter	17×17 Zry-4	
	20% CP-ECR	13% CP-ECR
Effective Oxidation Time, s	400	166
CP-Predicted Weight Gain, mg/cm^2	13.5	8.35
Measured ECR, %	20.8	12.8
Offset Displacement, mm	0.049	0.090
RT Offset Strain, %	0.05	0.09
RT Measured Permanent Displacement, mm	0.04	0.07
RT Permanent Strain, %	0.4	0.7
RT Ductility, %	≤0.4 (brittle)	≤0.7 (brittle)
Hydrogen Content, wppm	17	low
Hydrogen Pickup, wppm	13	low
OD/ID Oxide Layer Thickness, μm	68/66	42/41
Prior-Beta-Layer Thickness, μm	266	419
Microhardness, DPH Oxide Layers Alpha Layers Prior-Beta Layer*	 570-960 530-730 280-600	 600-770 600-700 260-360

*Range includes microhardness values of oxygen-rich alpha incursions in this layer

3.1.2 Post-quench ductility of 15x15 Zry-4 oxidized at 1200ºC

Baseline data were generated for the post-quench ductility of HBR-type 15×15 low-tin Zry-4 oxidized at 1200ºC and quenched at 800ºC. A parallel study was conducted using belt-polished 15×15 low-tin Zry-4 to determine if modern Zry-4 has higher post-quench ductility than 1990s Zry-4. Data were also generated for both types of Zry-4 oxidized at 1000ºC as part of the breakaway oxidation study. The breakaway oxidation results are reported in the Section 3.1.3.

The first 1200ºC dataset was generated for a test train with the thermal benchmark shown in Figure 23. Based on two TCs welded to the sample 120º apart, the hold temperature was estimated to be 1200±17ºC. The oxidation and post-quench ductility results for HBR-type 15×15 low-tin Zry-4 exposed to the thermal history in Figure 23 are summarized in Table 13. For the samples compressed at RT, marginal ductility is indicated in the offset and permanent strains at 7.5% CP-ECR. The RT ductile-to-brittle transition is estimated to be 8% CP-ECR. At 135ºC, the samples are ductile at ≈10% CP-ECR and brittle at 13% CP-ECR. The ductile-to-brittle transition CP-ECR at 135ºC is ≈12%. Additional samples were oxidized at ≈1188ºC and ≈1176ºC to 12-13% CP-ECR. These samples remained brittle at RT even

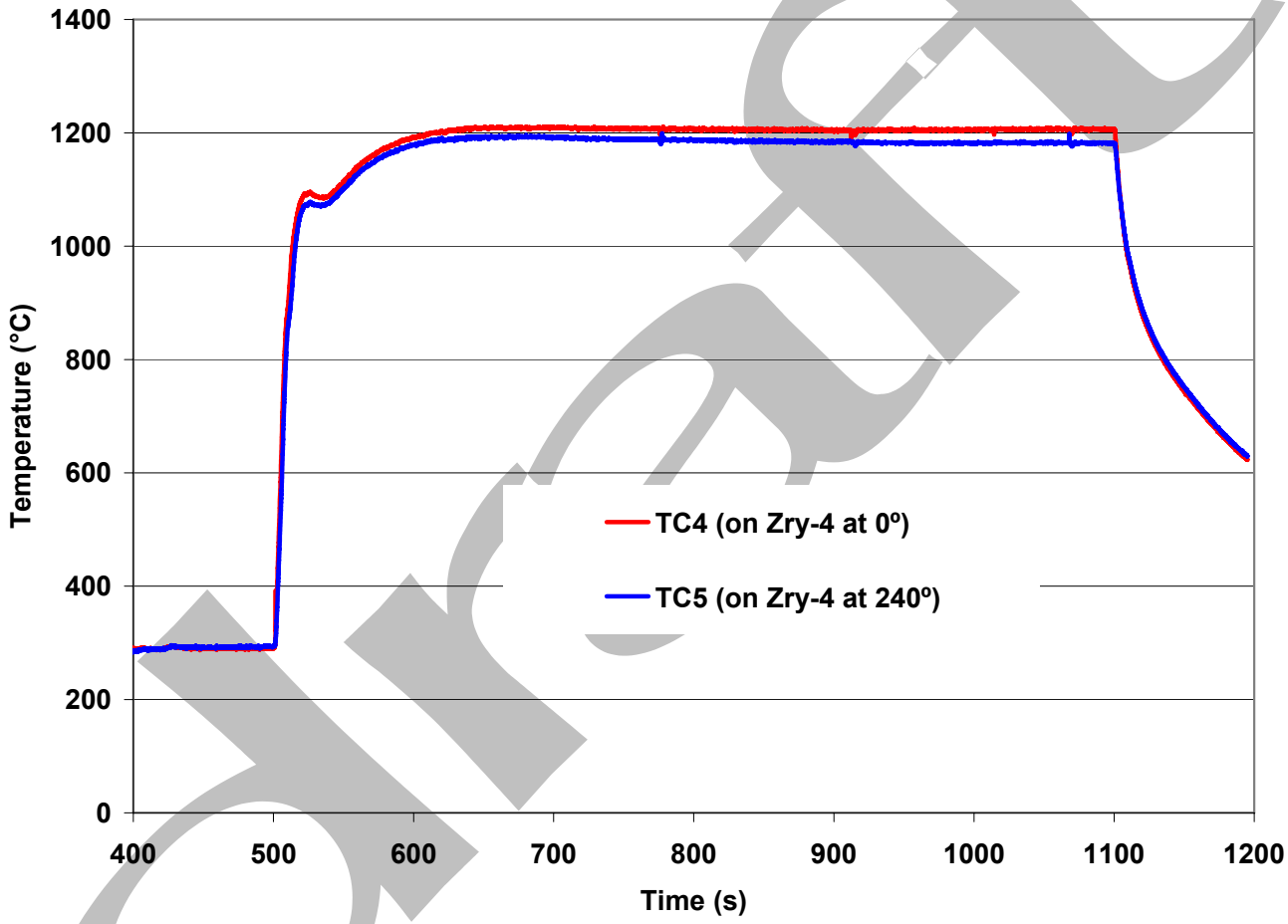

Figure 23. Thermal benchmark (HBRU#5A) results for first test train used to oxidize HBR-type 15×15 low-tin Zry-4. The hold temperature based on two sample-welded TCs is 1200±17°C.

with the reduction in oxidation temperature. Table 14 summarizes the results of the post-test characterization, while Figure 24 shows microhardness profiles across the prior-beta layer at 3 CP-ECR values. The microhardness values are consistent with the post-quench ductility results. The RT post-quench ductility results appear to be consistent with those shown in Figure 22a for 17×17 low-tin Zry-4, but the 135ºC data are not consistent as they indicated a ductile-to-brittle transition of only ≈12% CP-ECR, as compared to 17% CP-ECR for 17×17 low-tin Zry-4.

At the time the results were generated, it was not clear whether the HBR-type 15×15 low-tin Zry-4 was inferior to the modern 17×17 low-tin Zry-4 or whether the large circumferential temperature gradient leading to local temperatures ≥1217ºC was responsible for the low transition ECR. A new test train was built, and the thermal calibration was performed in two separate tests to give cladding temperatures at three circumferential locations: 0º, 120º, and 240º. During the calibration effort, the sample was rotated within the quartz tube to determine the sensitivity of temperature to angular orientation. Great care was exercised to center the larger-diameter cladding with respect to the test train, the quartz tube and the furnace. The thermal benchmark results for the improved test train are shown in Figure 10. The hold temperature for this test train was 1204±10ºC.

Extensive testing was performed using the thermal history in Figure 10 because of the higher degree of confidence in the average hold temperature and circumferential temperature variation: 1204±10ºC. Each oxidized sample was sectioned into three ≈8-mm-long rings, which were then compressed at RT, 100ºC and 135ºC. The 100ºC temperature is reasonable to assess long-term, post-LOCA core coolability. Table 15 summarizes the oxidation results and the post-quench ductility results. Although samples from two different lots were used in the testing, the agreement between these lots in terms of weight gain and post-quench ductility is excellent. Based on the data presented in Table 15 for permanent strains, the transition CP-ECR values are 7.5% at RT, 11.5% at 100ºC and 14% at 135ºC.

Figure 25 shows the comparison between the measured weight gain and the CP-predicted weight gain for HBR-type 15×15 Zry-4 oxidized at 1200ºC. The agreement is excellent. Figure 26 shows the decrease in post-quench ductility (offset strain) with increasing CP-ECR and decreasing ring-compression temperature. The lines in the figure represent trend curves rather than "best-fits" to the data.

Although the post-quench-ductility results with the new test train (Figure 10) are better than the ones with the old test train, the ductile-to-brittle transition CP-ECR (14%) is still lower for the rough-surface HBR-type 15×15 Zry-4 than for the belt-polished 17×17 low-tin Zry-4 (17%, Table 11). Several hypotheses were formulated and tested in an attempt to narrow down the reasons for these differences. The two alloys differ in surface roughness and possibly in surface chemistry, in OD and wall-thickness, in as-fabricated oxygen content, and in test time to reach a given ECR. Modern belt-polished (BP) 15×15 low-tin Zry-4 was provided by AREVA (see Table 4) to determine if this cladding had comparable post-quench ductility to modern 17×17 low-tin Zry-4. As can be seen in Table 4, the modern alloys have comparable surface roughness and oxygen content. A new test train was constructed and benchmarked for the oxidation phase of the testing. The thermal benchmark results for this test train with TCs welded to the modern 15×15 Zry-4 are shown in Figure 27. The post-quench ductility results at 135ºC are given in Table 16. The offset strains are compared in Figure 28 for the belt-polished 17×17 and 15×15 Zry-4, as well as the rough-surface HBR-type 15×15 Zry-4. The belt-polished 15×15 Zry-4 has a higher ductile-to-brittle transition CP-ECR (19%) than the belt-polished 17×17 Zry-4 (17%) and the rough-surface HBR-type 15×15 Zry-4 (14%). As the hydrogen pickup was insignificant for all three alloys and the as-fabricated oxygen content is comparable (see Table 4), there appears be alloy-to-alloy differences, which may result in different oxygen solubility levels or oxygen diffusion rates. The results suggest that the transition CP-ECR decreases as the cladding surface roughness increases. However, no mechanism

Table 13 Ring Compression Test (RCT) Results for HBR-type 15×15 Low-tin Zry-4 Samples Oxidized at 1200±17˚C, Cooled at ≈13˚C/s to 800˚C and Quenched. ECR = 1.1535 Wg for 0.76-mm-wall cladding. Tests were performed on ≈8-mm-long samples at RT and 135˚C and at 0.0333 mm/s displacement rate. Displacements in the loading direction were normalized to the as-fabricated outer diameter (10.77 mm) to calculate offset and permanent strains.

RCT Test Temperature ˚C	ECR, %		Displacement, mm		Offset Strain %	Permanent Strain %
	CP	Meas.	Offset	Permanent		
RT	0	0	7.0	6.8	65	63
RT RT ---[a]	4.9 4.9 4.9	6.1 6.1 5.8	1.77 1.33 ---	1.22 0.67 ---	16 12 ---	11 6 ---
RT RT	7.5 7.5	8.0 8.0	0.22 0.22	0.01 0.11	2.0 2.0	0.9 1.0
RT 135	9.8 9.8	10.6 10.6	0.06 0.31	0.05 0.19	0.6 2.9	0.5 1.8
RT 135	12.8 12.8	13.9 13.9	0.05 0.16	0.03 0.07	0.5 1.5	0.3 0.7
RT 135	16.7 16.7	17.8 17.8	0.06 0.14	0.05 0.05	0.6 1.3	0.5 0.5

[a]Additional test performed for metallographic and microhardness measurements

has been identified to explain the effects of surface roughness on post-quench ductility of Zry-4 alloys oxidized at 1200˚C.

It is interesting to note that the prior-beta layer thickness of HBR-type 15×15 Zry-4 is ≈420 μm at the embrittlement CP-ECR of 14%, while the prior-beta layer thickness of modern 17×17 Zry-4 is ≈320 μm at the embrittlement CP-ECR of 17%. It appears that the ductile-to-brittle transition is controlled by the average oxygen content in the beta layer and is relatively insensitive to beta-layer thickness for thicknesses > 300 μm.

Table 14 Oxide, Alpha, and Prior-Beta Layer Thicknesses at Four CP-ECR Values for HBR-type 15×15 Low-tin Zry-4 Oxidized at 1200±17˚C, Cooled at ≈13˚C/s to 800˚C and Quenched

Parameter	CP-ECR, %			
	≈5	7.5	9.8	12.8
Outer Oxide Layer Thickness, μm	26	35	61	80
Outer Alpha Layer Thickness, μm	24	41	113	102
Prior-Beta Layer Thickness, μm	690	636	513	453
Inner Alpha Layer Thickness, μm	23	40	113	108
Inner Oxide Layer Thickness, μm	24	36	62	79
Measured Weight gain, mg/cm^2	5.0	7.0	9.2	12.1
Measured ECR, %	5.8	8.0	10.6	13.9
RT Offset Strain, %	≈10%	≈1.0	0.3	0.5
135˚C Offset Strain, %	---	---	2.9	1.5

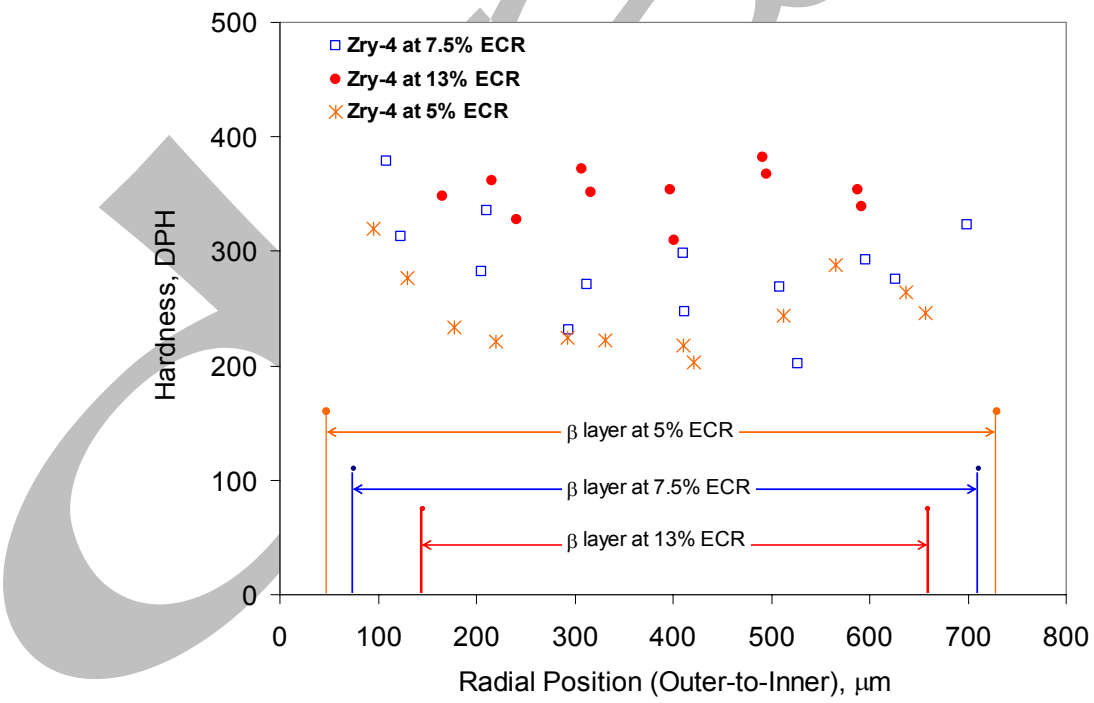

Figure 24. RT microhardness across prior-beta layer for 1200ºC-oxidized HBR-type 15×15 Zry-4.

Table 15 Ring Compression Test Results for HBR-type 15×15 Low-tin Zry-4 Cladding Oxidized at 1204±10˚C, Cooled at ≈13˚C/s to 800˚C and Quenched. ECR = 1.1535 Wg for 0.76-mm-wall cladding. Tests were performed on ≈8-mm-long samples at RT, 100˚C and 135ºC and at 0.0333 mm/s displacement rate. Samples from two different lots were used to generate these data: 10.77-mm OD and 0.76-mm wall; and 10.76-mm OD and 0.77-mm wall. Displacements in the loading direction were normalized to the as-fabricated outer diameter to calculate offset and permanent strains.

Test Conditions		ECR %		Plastic Displacement, mm		Plastic Strain, %	
T, ˚C	Test Time[a], s	CP	Meas.	Offset	Permanent	Offset	Permanent
RT	0	0	0	7.0	6.8	65	63
RT	96	5.0	5.5	1.98	---	18	---
RT	93	5.0	5.1	2.34	---	20	---
RT	96	5.0	5.5	>5.5	>4.9	>51	>45
100	93	5.0	5.1	>5.6	>5.0	>52	>46
100	96	5.0	5.5	>5.6	>5.1	>52	>47
135	93	5.0	5.1	>6.0	>5.5	>56	>51
RT	154	7.5	8.1	0.25	0.11	2.3	1.0
RT	145	7.4	7.6	0.23	0.14	2.1	1.3
100	154	7.5	8.1	>3.9	>3.4	>36	>32
100	145	7.4	7.6	>2.2	>2.0	>20	>18
135	154	7.5	8.1	>4.7	>4.3	>43	>40
135	145	7.4	7.6	5.53	---	51	---
RT	230	10.0	10.4	0.08	0.04	0.7	0.4
RT	230	10.3	10.7	0.06	0.05	0.6	0.5
100	230	10.0	10.4	0.34	0.21	3.2	1.9
100	230	10.3	10.7	0.26	0.16	2.4	1.5
135	230	10.0	10.4	1.60	1.32	14.9	12.3
135	230	10.3	10.7	1.45	1.10	13.5	10.2
100	278	11.7	11.8	0.16	0.09	1.4	0.9
135	278	11.7	11.8	0.31	0.19	2.9	1.7
RT	353	13.0	13.2	0.04	0.03	0.4	0.3
RT	353	12.8	13.2	0.07	0.05	0.6	0.5
100	353	13.0	13.2	0.12	0.07	1.1	0.6
100	353	12.8	13.2	0.10	0.05	0.9	0.5
135	353	13.0	13.2	0.37	0.16	3.4	1.5
135	353	12.8	13.2	0.22	0.13	3.1	1.2
135	432	15.0	14.8	0.17	0.09	1.6	0.8

[a]Includes time for ramp from 300ºC and hold time.

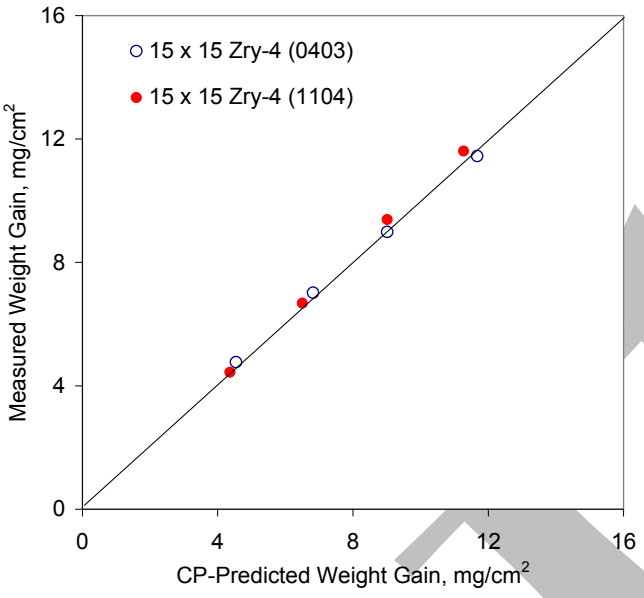

Figure 25. Measured vs. predicted weight gain for two lots of HBR-type 15×15 low-tin Zry-4 oxidized at 1204±10ºC and quenched at 800ºC.

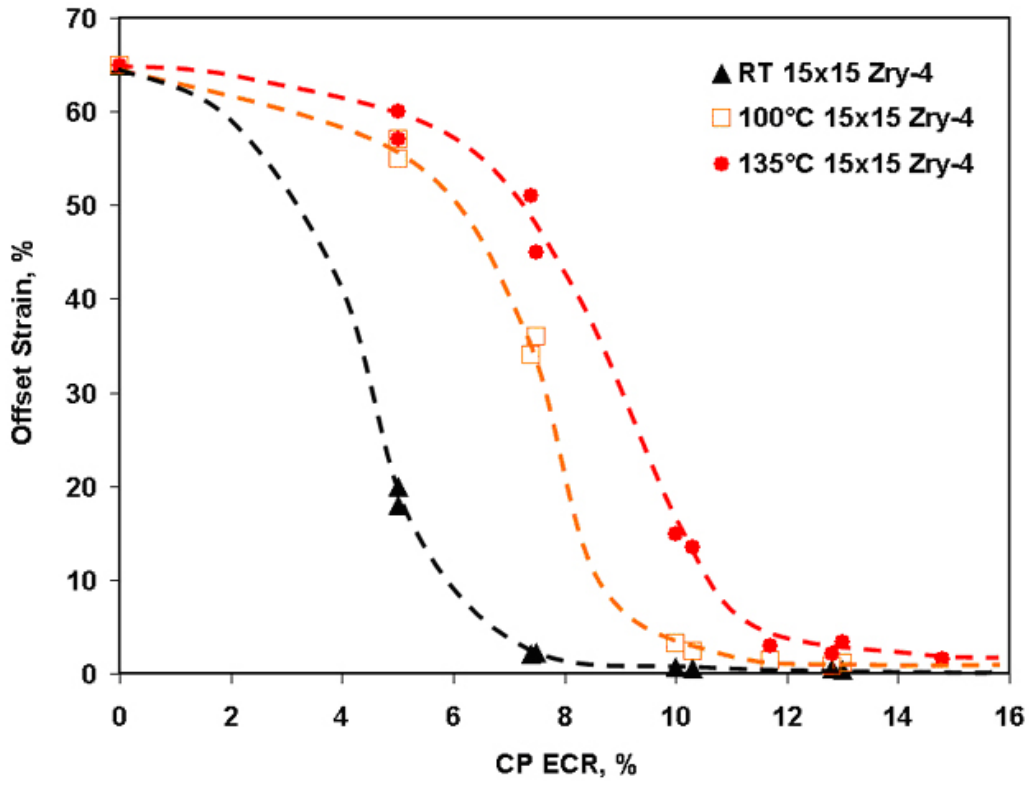

Figure 26. Offset strain vs. CP-ECR and ring-compression test temperature for two lots of HBR-type 15×15 low-tin Zry-4 oxidized at 1204±10ºC, cooled at ≈13˚C/s to 800ºC and quenched.

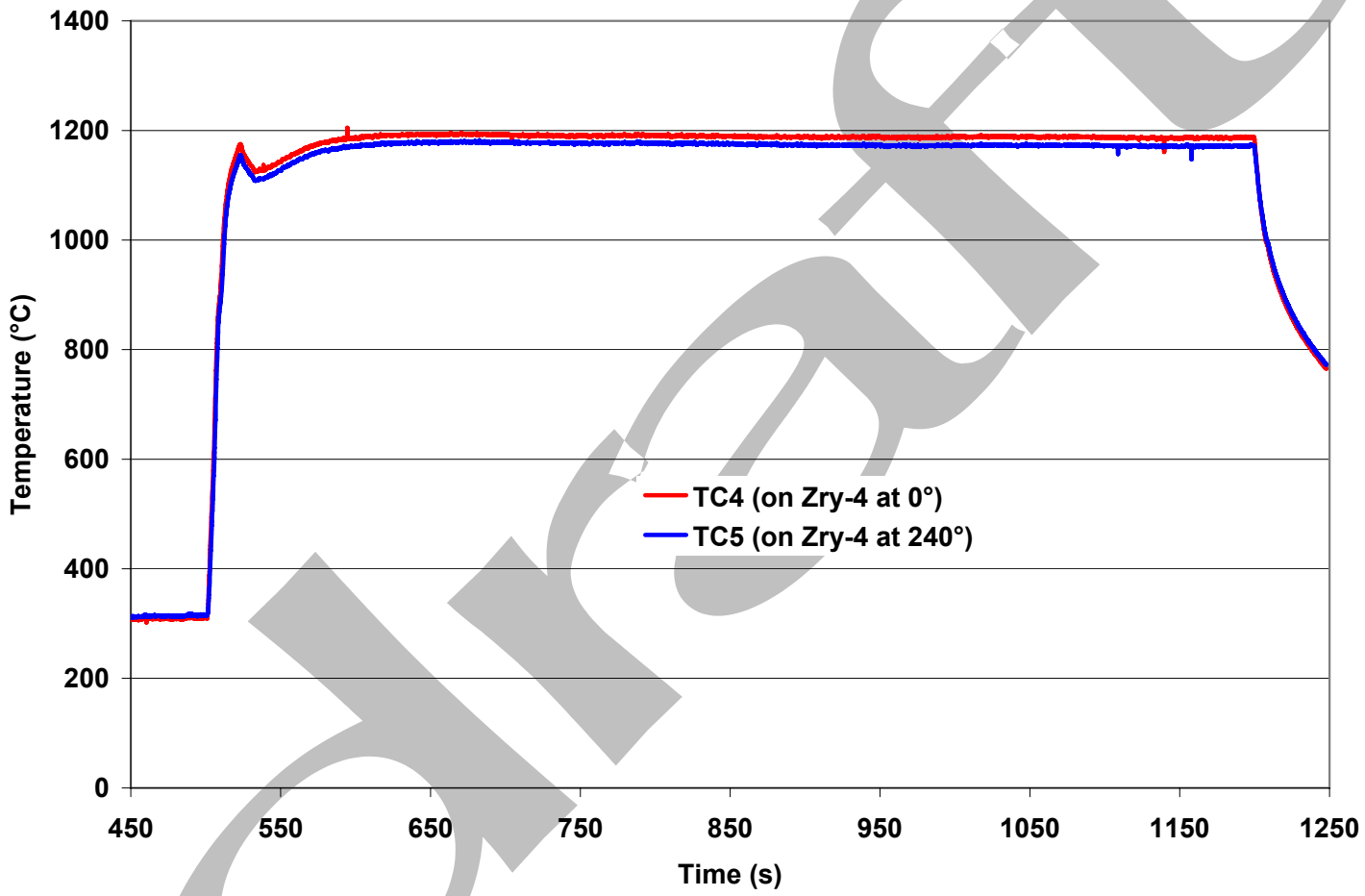

Figure 27. Thermal benchmark results for belt-polished 15×15 low-tin Zry-4 with a hold temperature of ≈1190ºC. Data-generating tests were conducted by increasing the holder control TC setting by 10ºC to give a hold temperature of 1200ºC.

Table 16 Ring Compression Test (RCT) Results for Belt-polished 15×15 Zry-4 Cladding Oxidized at 1200˚C, Cooled at ≈13˚C/s to 800˚C and Quenched. ECR = 1.308 Wg for 0.67-mm wall cladding. RCTs were performed on ≈8-mm-long samples at 135ºC and 0.0333 mm/s displacement rate.

Test Conditions		ECR %		Plastic Displacement, mm		Plastic Strain, %	
RCT T, ˚C	Ox. Test Time[a], s	CP	Meas.	Offset	Permanent	Offset	Permanent
135	210	11.0	11.5	>3.6	>3.2	>33	>29
135	210	11.0	11.5	>3.5	>3.1	>32	>28
135	280	13.0	12.7	4.15	3.58	38	33
135	280	13.0	12.7	2.60	2.35	24	22
135	360	15.0	15.0	0.50	0.24	4.6	2.2
135	360	15.0	15.0	0.35	0.17	3.2	1.6
135	495	17.0	17.2	0.42	0.22	3.8	2.0
135	495	17.0	17.2	0.30	0.16	2.7	1.5
135	620	20.0	19.8	0.28	0.15	2.6	1.4
135	620	20.0	19.8	0.23	0.09	2.1	0.8

[a]Includes ramp from 300ºC.

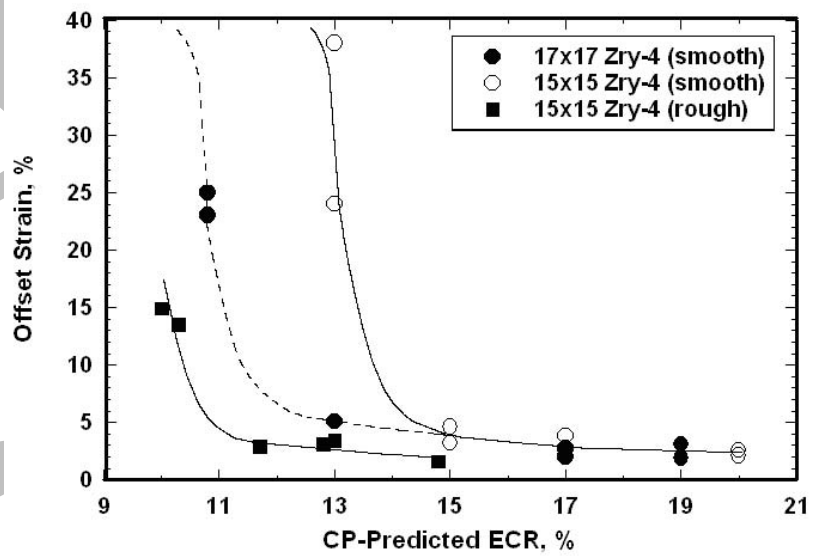

Figure 28. Comparison of offset strain vs. CP-ECR for 15×15 and 17×17 Zry-4 samples oxidized at 1200ºC, cooled at ≈13˚C/s to 800ºC and quenched. Ring compression tests were conducted at 135ºC and 0.0333 mm/s displacement rate. Nominal offset strain for ductile-to-brittle transition ECR is 2%.

3.1.3 Breakaway oxidation time for 15×15 Zry-4 samples oxidized at 800-1000ºC

Breakaway oxidation at T ≤ 1000ºC has been studied by Leistikow and Schanz [19,20] for Zry-4 and Mardon et al. [21] for Zry-4 and M5. Although the breakaway oxidation time is generally defined as the time corresponding to an increase in oxidation rate (i.e., weight gain rate), it is the associated hydrogen pickup that causes embrittlement. Leistikow and Schanz presented trend curves (see Figure 6 in Ref. 20) for weight gain vs. time at temperature and a data plot (see Figure 8 in Ref. 20) for hydrogen content vs. time at temperature for 650-1000ºC. They used an older vintage of standard Zry-4 with 1.6 wt.% Sn, 0.12 wt.% O, and 0.725-mm wall thickness. Typically the Zry-4 cladding of that vintage had ≈0.3-μm surface roughness. Sample preparation included degreasing, pickling in a nitric-fluoric acid mixture and cleaning in boiling water. Such treatment may leave a fine surface layer containing fluorine impurities. Both surface roughness and surface fluorine impurities can destabilize the oxide layer growth through early transformation from the tight tetragonal phase to the weaker monoclinic phase. Two-sided oxidation tests were performed in their study. Thus, the condition of the cladding inner surface may influence the breakaway oxidation times reported by Leistikow and Schanz.

Mardon et al. [21] presented hydrogen-concentration results vs. time at 1000ºC for belt-polished 17×17 low-tin Zry-4 (1.29 wt.% Sn, 0.12 wt.% O and ≈0.1-μm surface roughness). The oxidation was one-sided – outer-surface only. Thus, the condition of the cladding ID surface had no influence on their results.

The results of these two studies are compared in Table 17 in terms of breakaway time for weight-gain rate increase and hydrogen content increase to 200 wppm. It is clear that the belt-polished Zry-4 has a longer breakaway time at 1000ºC than the pickled-and-cleaned rough-surfaced Zry-4.

Table 17 Breakaway Oxidation Time vs. Temperature for Zry-4 in Terms of Increase in Weight Gain Rate and Hydrogen-content Increase (200 wppm); references are: L-S = Leistikow and Schanz [19,20] and M = Mardon et al. [21]

T ºC	Outer-Surface Treatment	Oxidation	Breakaway Time, s		Ref
			Weight Gain Rate Increase*	200-wppm H Content	
1050	Pickled/Cleaned	2-sided	≈5700	---	L-S
1000	Pickled/Cleaned	2-sided	≈1560	1800	L-S
	Belt Polished	1-sided	---	5400	M
950	Pickled/Cleaned	2-sided	≈3500	---	L-S
900	Pickled/Cleaned	2-sided	≈21,600	50,400	L-S
850	Pickled/Cleaned	2-sided	≈6300	---	L-S
800	Pickled/Cleaned	2-sided	≈1980	3600	L-S
750	Pickled/Cleaned	2-sided	≈2100	---	L-S
700	Pickled/Cleaned	2-sided	≈2640	---	L-S
650	Pickled/Cleaned	2-sided	≈11,400	50,000	L-S

*For the L-S results, the hydrogen vs. time curve was used as a guide in determining breakaway oxidation time based on weight-gain-rate increase for curves with very gradual increase in slope.

Based on the results in Table 17, it is clear that breakaway oxidation time is not a monotonic function of decreasing or increasing oxidation temperature. To illustrate this point, a trend curve is plotted in Figure 29 based on the Leistikow and Schanz breakaway-oxidation weight-gain results. It is also clear in comparing results for older cladding (pickled-and-cleaned, high surface roughness) to modern cladding (belt polished) that there can be significant differences in breakaway oxidation time for Zry-4 at the same oxidation temperature. There may also be a difference in results for one-sided (OD surface) vs. two-sided oxidation tests because the inner surface may have different surface conditions than the outer surface.

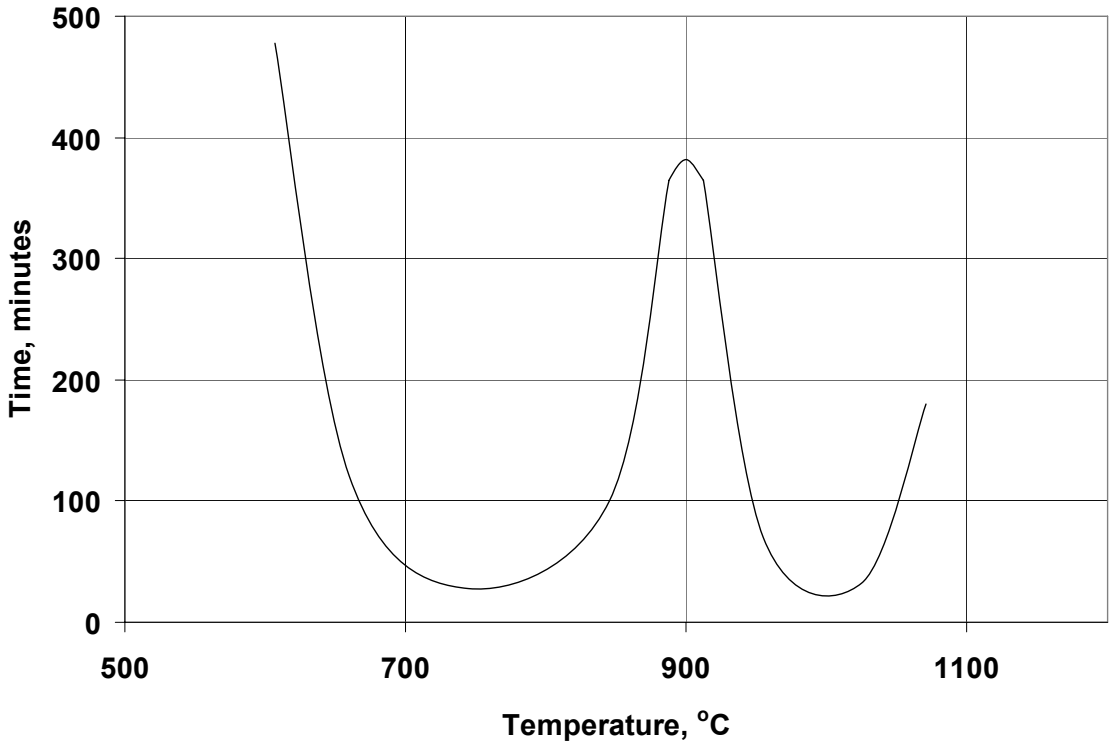

Figure 29. Breakaway-oxidation time vs. oxidation temperature determined from the trend curves presented by Leistikow and Schanz [19,20] for Zry-4 weight-gain vs. time.

From the Leistkow and Schanz work, it appears that minimum times for breakaway oxidation in Zry-4 occur at oxidation temperatures of 800ºC and 1000ºC. In terms of hydrogen pickup, 1000ºC-oxidation gives the minimum breakaway time. However, no studies were found that explored the sensitivity of breakaway-oxidation time to temperatures within the range of 975-1025ºC. In the ANL tests, breakaway oxidation time was determined within this temperature range by targeting average temperatures of 985ºC, 1000ºC and 1015ºC for the two-sided oxidation tests performed. With anticipated circumferential temperature variation of 10-15ºC for large-diameter 15×15 cladding, these average temperatures include local temperatures of ≈975-1025ºC. As the alpha + beta → beta phase transition temperature for Zry-4 is within this range, the results may shed some light on the effects of this transition temperature on breakaway oxidation. The alpha → alpha + beta phase transition temperature is ≈810ºC for as-fabricated Zry-4. Breakaway oxidation tests were also conducted at 800ºC oxidation temperature.

The ANL criterion for breakaway-oxidation time is a hydrogen pickup of 200 wppm. RT post-quench ductility results for ZIRLO oxidized at 1000ºC showed ductility after a CP-equivalent oxidation time of ≈3360 s at 1000ºC with a hydrogen pickup of ≈100 wppm (see 3.3.1). RT post-quench ductility results for E110 after an oxidation time of ≈300 s at 1000ºC showed ductility with a hydrogen pickup of ≈150 wppm (see 3.5.2). Ductility tests at 135ºC were conducted on Zry-4 samples with ≈200 wppm hydrogen to confirm that ductility is retained with ≤200-wppm H.

The classical view of the progression leading to breakaway oxidation is given by Leistikow and Schanz:

a) breakaway-oxidation instability initiates at the metal oxide interface with local formation of monoclinic oxide;

b) the precursor to breakaway oxidation is the transition from a "flat" oxide-metal interface to a wavy interface (i.e., this is referred to as rugosity);

c) the wavy surface creates alternating regions of tensile and compressive stresses in the near-surface oxide;

d) local regions under tensile stress transform first from tetragonal to monoclinic oxide;

e) the tetragonal-to-monoclinic oxide transition spreads from inner-surface to outer-surface; and

f) cracking of the weak monoclinic oxide results in increase in weight-gain rate and in hydrogen pickup.

In applying this conceptual model to experimental procedures, it is clear that by the time the outer-surface is observed to turn from black (tetragonal) to gray (monoclinic), the weight-gain rate and hydrogen-pickup rate are such that the oxide is well into the breakaway regime and the breakaway-oxidation time is exceeded. As the furnace used for the ANL tests has a window for viewing a portion of the outer-surface of the sample, it is relatively straightforward to turn off the furnace power and cool the sample at the oxidation time at which gray spots are observed on the outer surface of the cladding.

The thermal benchmark results for HBR and belt-polished 15×15 Zry-4 are shown in Figures 30 and 31, respectively, for a target hold temperature of 985ºC. These tests were conducted for a total test time of 1500 s including the ramp time from 300ºC to ≈1000ºC through the end of the hold time. Samples were cooled without quench, which is the standard test protocol for determining breakaway-oxidation time. Excellent agreement was achieved between the CP-calculated and measured weight gain under these test conditions. For HBR-type Zry-4, the cladding temperature was 992±9ºC at 78 s from temperature-ramp initiation and coasted down to a long-time temperature of 984±10ºC. Based on the flatness of the temperature profile, the cladding temperature is assumed to be 984±10ºC for test times beyond 1500 s. The breakaway-oxidation times reported in this work are referenced to zero time at the initiation of the ramp from 300ºC. As the ramp time is short (78 s) relative to the breakaway-oxidation time and shorter than the expected data scatter in this time, the ramp time has no significant effect on the breakaway time.

For the belt-polished Zry-4 thermal history shown in Figure 31, the cladding temperature at 95 s was 1000±12ºC and the long-time temperature was 986±10ºC. Thus, within experimental uncertainty, the long-time oxidation temperature for BP Zry-4 was essentially the same as the temperature for HBR-type Zry-4. Because of the large data scatter found for BP Zry-4 hydrogen pickup – due partly to

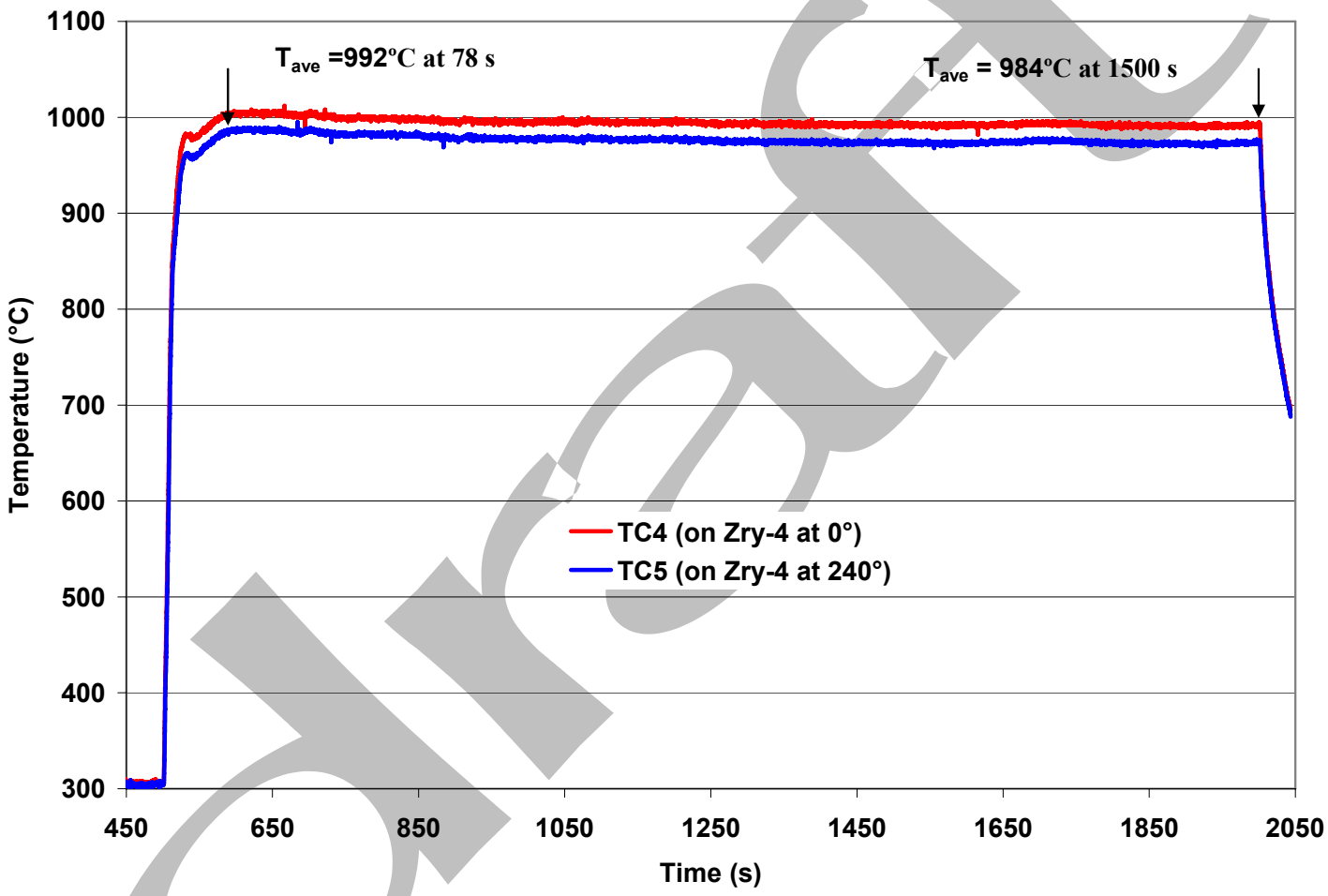

Figure 30. Results of thermal benchmark test with HBR-type 15×15 low-tin Zry-4. Measured weight gain is within 1% of the CP-predicted weight gain. Hold temperature is 992±9ºC at 78 s and 984±10ºC at 1500 s, beyond the temperature-ramp initiation.

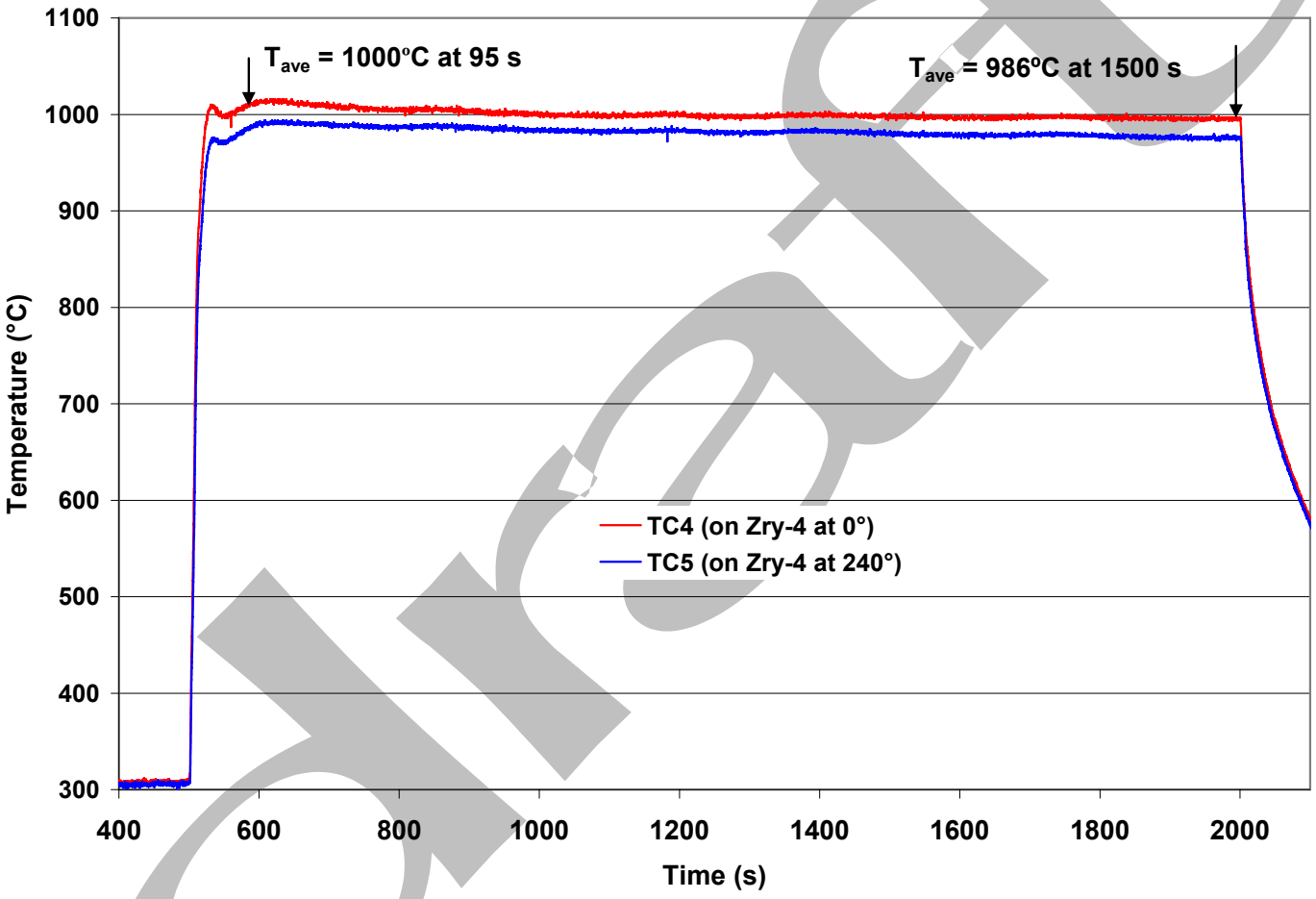

Figure 31. Results of 1st thermal benchmark test with belt-polished 15x15 low-tin Zry-4. Measured weight gain is within 6% of the CP-predicted weight gain. Hold temperature is 1000±12ºC at 95 s and 986±10ºC at 1500 s, beyond the temperature-ramp initiation.

scratches introduced during sample sectioning – the BP thermal benchmark was rerun for a longer time and with a controller setting designed to minimize overshoot (Figure 32). In addition, the test train length was decreased to adapt it to in-cell testing. The long-time temperature for this benchmark was 986±12ºC. Tests were conducted at 1000±12ºC and 1014±12ºC long-time temperatures. Because the ±12ºC was determined from 3 TC readings, it is also used for tests conducted with temperatures shown in Figure 31.

Table 18 lists the breakaway-oxidation results at 984±10ºC for HBR-type, low-tin 15×15 Zry-4. Based on two tests at 3800 s, the hydrogen pickup is <200 wppm and the breakaway time is >3800 s. Based on the 4000-s test result (1810-wppm H-pickup), it was expected that a test time of 3900 s would give ≈200-400 wppm H pickup. However, the H-pickup after 3900 s was 1320 wppm. Given that considerable data scatter is expected for breakaway-oxidation time, no further testing was conducted for test times within 3800-3900 s, and 3800 s is identified as the breakaway-oxidation time. One sample (HBRU#96) had pretest surface scratches introduced during sectioning. The sample was subjected to post-oxidation ductility testing because of the hydrogen pickup (170±80 wppm). The offset and permanent strains for this sample at 135ºC were 5.2% and 2.5%, respectively, indicating Zry-4 is ductile with ≈200-wppm H-pickup. However, because the sample was scratched prior to testing, the hydrogen-pickup results were not used to determine breakaway oxidation time (see 3.5.1).

Metallography was performed for HBR-type Zry-4 samples oxidized for 159 s, 3600 s, and 5400 s. Results for these times are shown in Figures 33-35 at two different magnifications. The results support the Leistikow and Schanz description of breakaway oxidation evolution. In Figure 33, the oxide layers are clearly tetragonal with black outer surface and smooth interface between the oxide layers and the metal. In Figure 34 – taken from the black non-scratched area of the HBRU#96 test sample – the inner-surface and outer-surface oxide layers exhibit a wavy boundary at the oxide-metal interface. This is the precursor to breakaway oxidation. Both inner- and outer-oxides exhibit the same transition morphology, which suggests that there is no preference for the inner-surface to experience breakaway prior to the outer surface. In Figure 35, the oxide layers are well beyond the breakaway transition. The outer and inner surfaces are gray and significant cracking is observed on and within the oxide layers.

The results for belt-polished Zry-4 oxidized at 986±12ºC (see Figure 31) are summarized in Table 19, followed by metallographic results in Figures 36-37. As expected, the breakaway oxidation time (≈5000 s) is longer for belt-polished Zry-4 as compared to the rough-surface Zry-4 (≈3800 s). The BPZ4#18 test sample, which was oxidized for 5000 s, had a hydrogen pickup of 280±160 wppm. Although this is higher than the ANL 200-wppm-H criterion, the sample did retain ductility (≈6% offset and permanent strains) at 135ºC. The ductility results support the use of the ANL 200-wppm-H-pickup criterion for Zry-4 breakaway-oxidation time. Test sample BPZ4#18 is particularly interesting because it experienced very local breakaway at the outer surface. Figure 38a shows the sample discoloration along an axial strip and Figure 38b shows the corresponding outer-surface oxide layer in this region. Tetragonal-to-monoclinic transition was observed only in this region. Also, the hydrogen concentration (224, 123, 467, and 352 wppm) at this axial location was highly non-uniform in the circumferential direction, indicating little time for hydrogen diffusion following local breakaway.

Because the test train used to generate the Table 18-19 results was at the end of its useful life, a new test train was built and benchmarked (see Figure 32). This shorter test train was used to examine the sensitivity of breakaway time to oxidation temperatures of 986-1014ºC and to mild surface scratches (see 3.5.1). No breakaway oxidation was observed (Table 20) at 5400 s for 986ºC, 1000ºC, and 1014ºC. Although the second test train gives longer breakaway oxidation times (>5400 s), such variation is not surprising because breakaway oxidation is an instability phenomenon, which is sensitive to local surface conditions and temperature gradients, as well as other subtle differences in test conditions. Nevertheless,

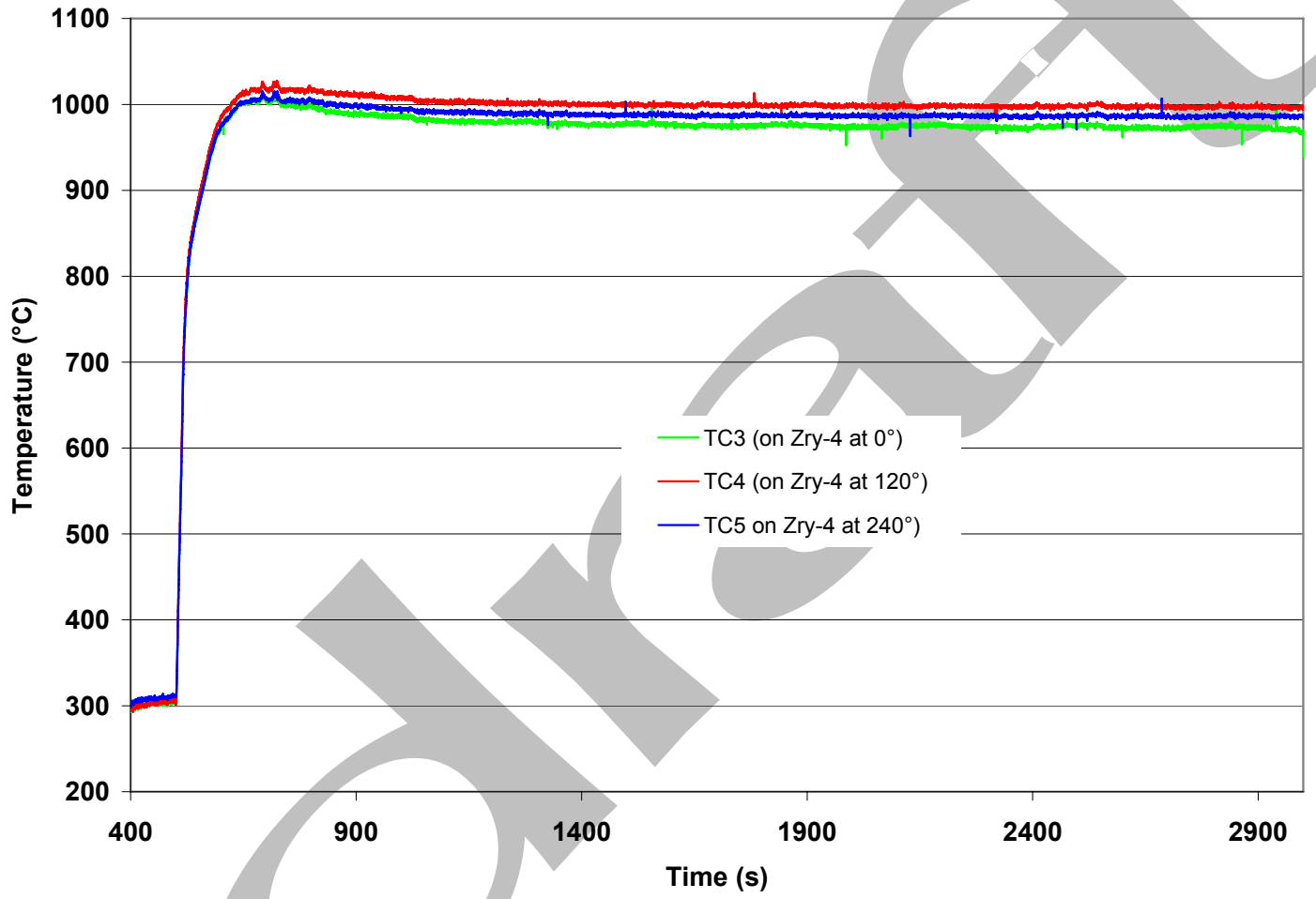

Figure 32. Results of 2nd thermal benchmark test with belt-polished 15×15 low-tin Zry-4. Initial overshoot temperature is 1012±7ºC and long-time hold-temperature is 986±12ºC. Results are based on the readings of three TCs welded to the sample 120º apart.

Table 18 Results of Breakaway Oxidation Tests at 984±10ºC for HBR-type 15×15 low-tin Zry-4. The hydrogen content (C_{Hi}) of the as-fabricated cladding is 22 wppm. The hydrogen content of the oxidized sample (L_H) was measured with the LECO Hydrogen Determinator. Breakaway-oxidation time based on 200-wppm hydrogen pickup is ≈3800 s.

Test ID	Test Time, s	Weight Gain, mg/cm^2		H-Content wppm	H-pickup[a] wppm	Offset Stain at 135ºC, %
		CP	Measured			
HBRU#93	159	2.45	2.82	Low	Low	---
HBRU#90	1500	7.89	7.85	Low	Low	---
HBRU#84	3600	12.2	10.7	57	40	---
HBRU#96[b]	**3600**	**12.2**	**12.6**	**186**	**170**	**5.2**
HBRU#95	3800	12.5	10.6	61	40	---
HBRU#88	3800	12.5	10.7	42	20	---
HBRU#92	3900	12.7	16.4	1260	1320	---
HBRU#91	4000	12.9	16.2	1723	1810	---
HBRU#87	4500	13.6	16.4	1581	1650	---
HBRU#81	5400	14.9	22.2	2111	2300	---
HBRU#82	7200	17.4	28.8	2769	3170	---

[a]The hydrogen pickup (ΔC_H) is referenced to the as-fabricated weight of the sample and is calculated from $\Delta C_H = (1 + 4\times10^{-3}\ Wg)\ L_H - C_{Hi}$, where Wg is the measured weight gain in mg/cm^2.

[b]Sample was scratched during pretest sectioning; see 3.5.1 for details.

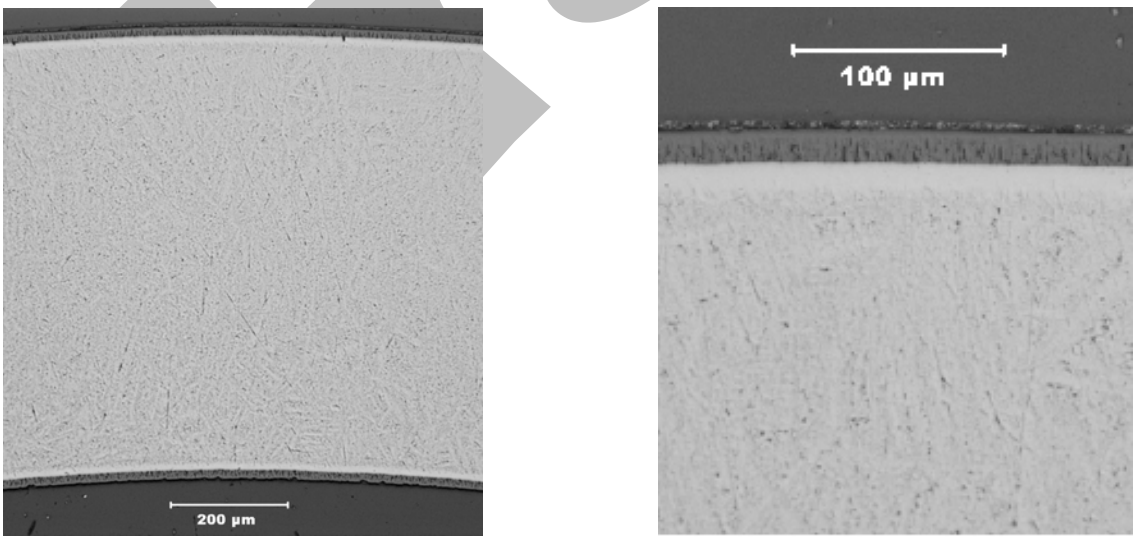

Figure 33. Low-magnification (left) of inner- and outer-surface oxide layers for HBR-type 15×15 low-tin Zry-4 oxidized at ≈1000ºC for 159 s; higher-magnification (right) of the outer-surface oxide layer shows the smooth boundary between oxide and metal.

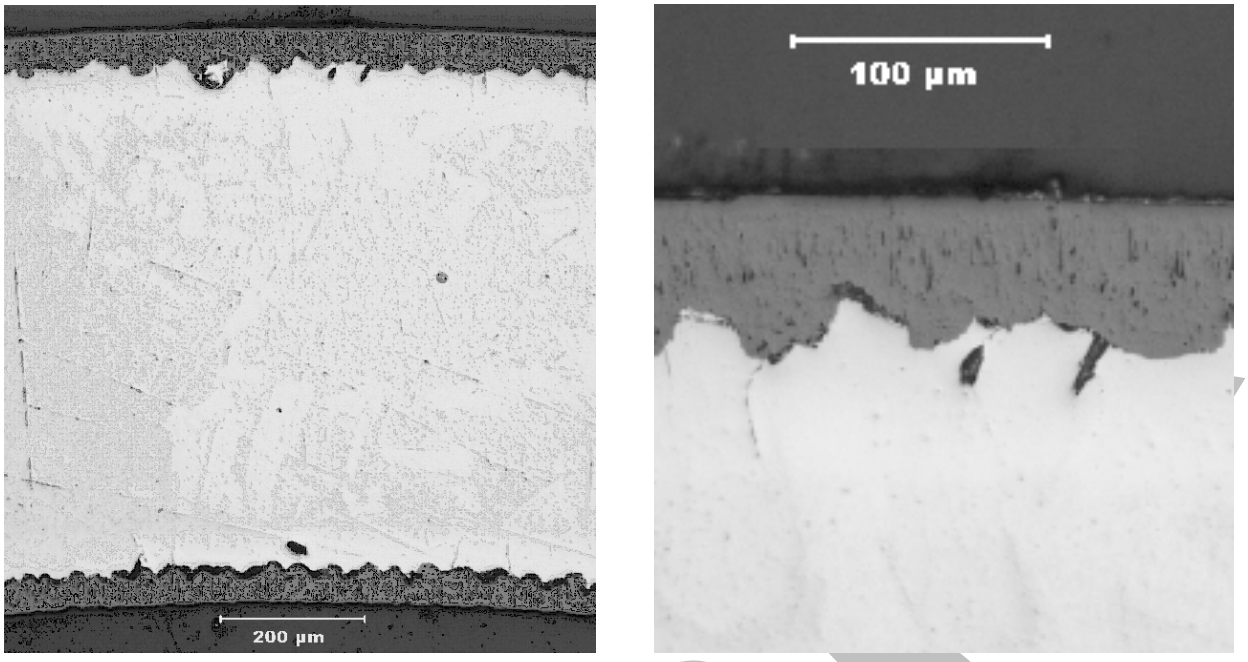

Figure 34. Low-magnification (left) of inner- and outer-surface oxide layers for HBR-type 15×15 low-tin Zry-4 oxidized at 984±10ºC for 3600 s; higher-magnification (right) of the outer-surface oxide layer shows the wavy boundary between oxide and metal, which is a precursor to breakaway.

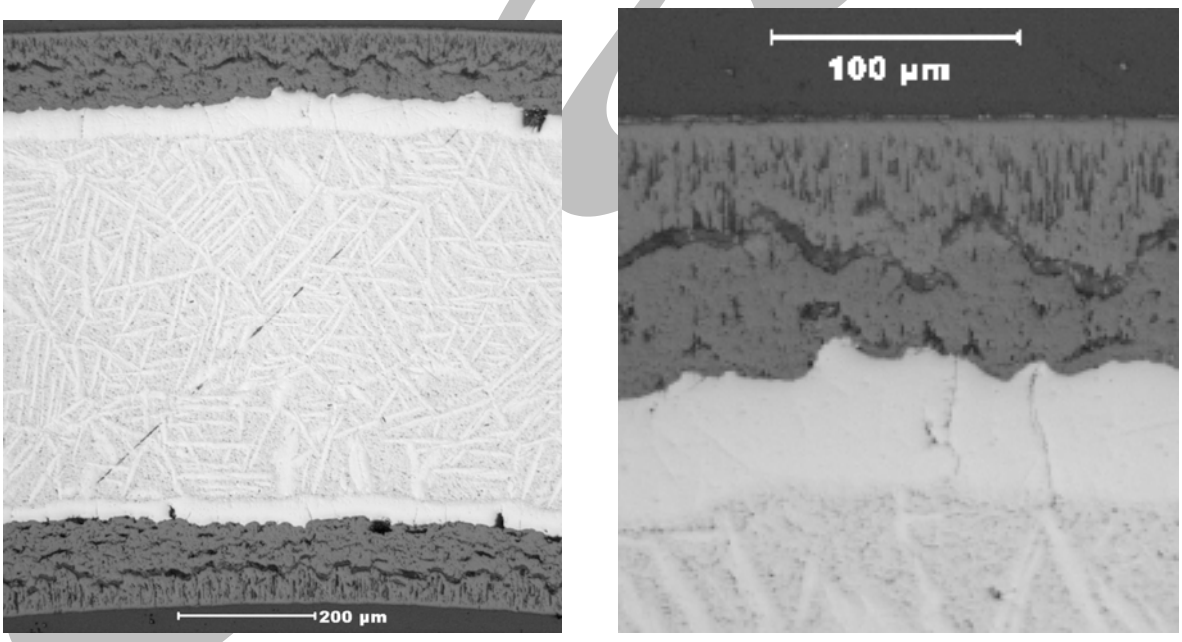

Figure 35. Low-magnification (left) of inner- and outer-surface oxide layers for HBR-type 15×15 low-tin Zry-4 oxidized at 984±10ºC for 5400 s; higher-magnification (right) of outer-surface oxide layer shows cracks in monoclinic oxide layer formed during the transition to breakaway oxidation.

Table 19 First Set of Results for Breakaway Oxidation at 986±12ºC (Figure 31) for Belt-polished 15×15 low-tin Zry-4. The hydrogen content (C_{Hi}) of the as-fabricated cladding is 26 wppm. The hydrogen content of the oxidized sample (L_H) was measured with the LECO Hydrogen Determinator. Breakaway-oxidation time based on 200-wppm hydrogen pickup is ≈5000 s.

Test ID	Test Time, s	Weight Gain, mg/cm^2		H-Content wppm	H-pickup[a] wppm	Offset Stain at 135ºC, %
		CP	Measured			
BPZ4#16	135	2.45	2.85	Low	Low	---
BPZ4#15	1500	8.58	8.07	Low	Low	---
BPZ4#10	3600	12.7	10.8	20	0	---
BPZ4#18	5000	14.9	12.6	286	280	6.0
BPZ4#13	5400	15.5	12.1	411	410	---
BPZ4#12	7200	17.7	18.7	1798	1930	---

[a]The hydrogen pickup (ΔC_H) is referenced to the as-fabricated weight of the sample and is calculated from $\Delta C_H = (1 + 4.6\times10^{-3}\ Wg)\ L_H - C_{Hi}$, where Wg is the measured weight gain.

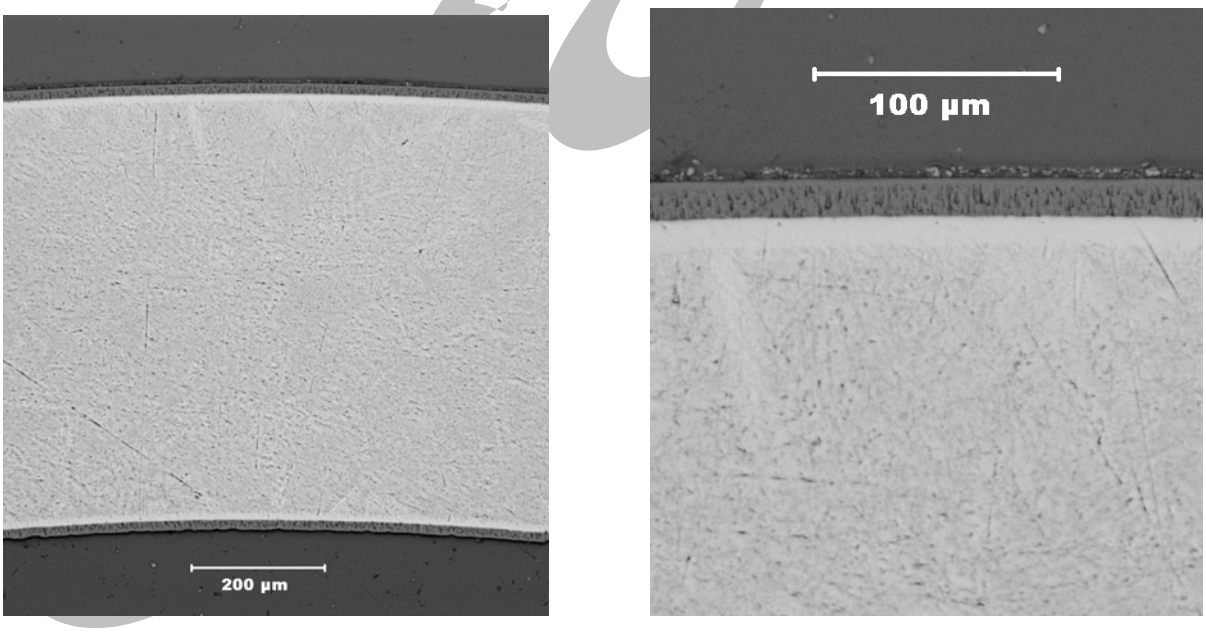

Figure 36. Low-magnification (left) of inner- and outer-surface oxide layers for belt-polished 15×15 low-tin Zry-4 oxidized at ≈1000ºC for 135 s; higher-magnification (right) of outer-surface oxide layer shows the smooth boundary between oxide and metal.

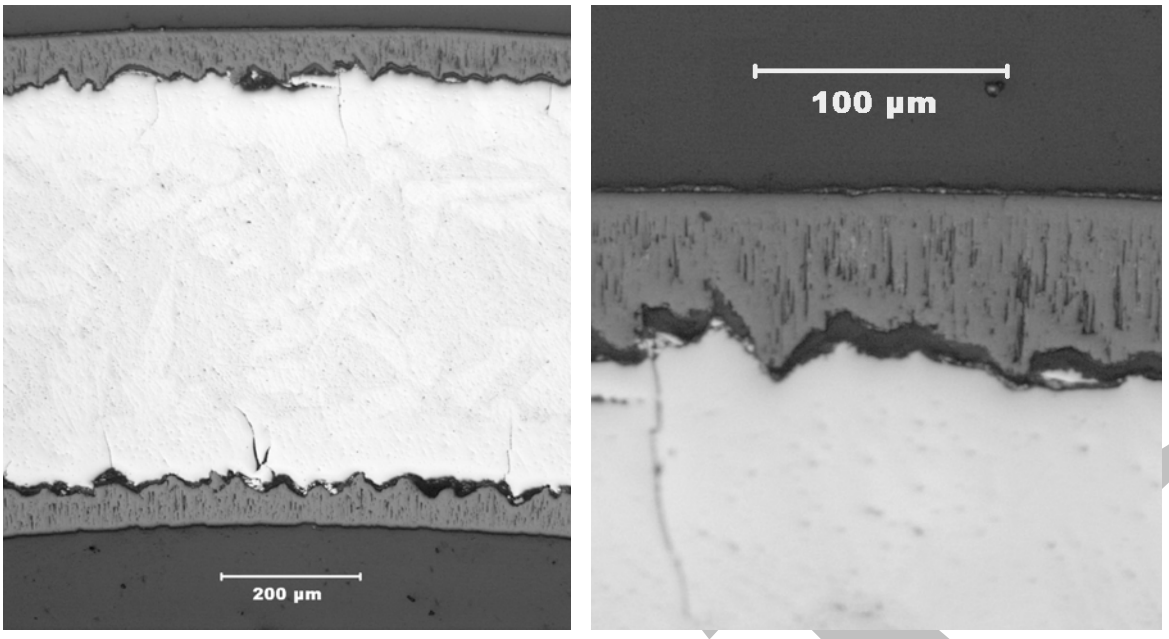

Figure 37. Low-magnification (left) of inner- and outer-surface oxide layers for belt-polished 15×15 low-tin Zry-4 oxidized at 986±12ºC for 5400 s (BPZ4#13); higher-magnification (right) of outer-surface oxide layer shows wavy metal-oxide interface and initiation of breakaway oxidation.

Table 20 Second Set of Results for Breakaway Oxidation of Belt-polished 15×15 Low-tin Zry-4 at Long-time Test Temperatures of 986ºC (see Figure 32), 1000ºC and 1014ºC; hydrogen content (C_{Hi}) of as-fabricated cladding is 26 wppm; hydrogen content of the oxidized sample (L_H) was measured with the LECO Hydrogen Determinator; breakaway-oxidation time based on 200-wppm hydrogen pickup is >5400 s

Test ID	Test T, ºC	Test Time, s	Weight Gain, mg/cm^2		H-Content wppm	H-pickup[a] wppm
			CP	Measured		
BPZ4#30	986±12	4000	13.1	11.6	18	0
BPZ4#31	986±12	4500	13.9	12.8	18	0
BPZ4#33	986±12	5000	14.7	12.2	18	0
BPZ4#34	986±12	5400	15.2	11.7	19	0
BPZ4#38	1000±12	5400	16.6	14.6	18	0
BPZ4#41	1014±12	5400	18.1	15.3	19	0

[a]The hydrogen pickup (ΔC_H) is referenced to the as-fabricated weight of the sample and is calculated from $\Delta C_H = (1 + 4.6\times10^{-3}\ Wg)\ L_H - C_{Hi}$, where Wg is the measured weight gain.

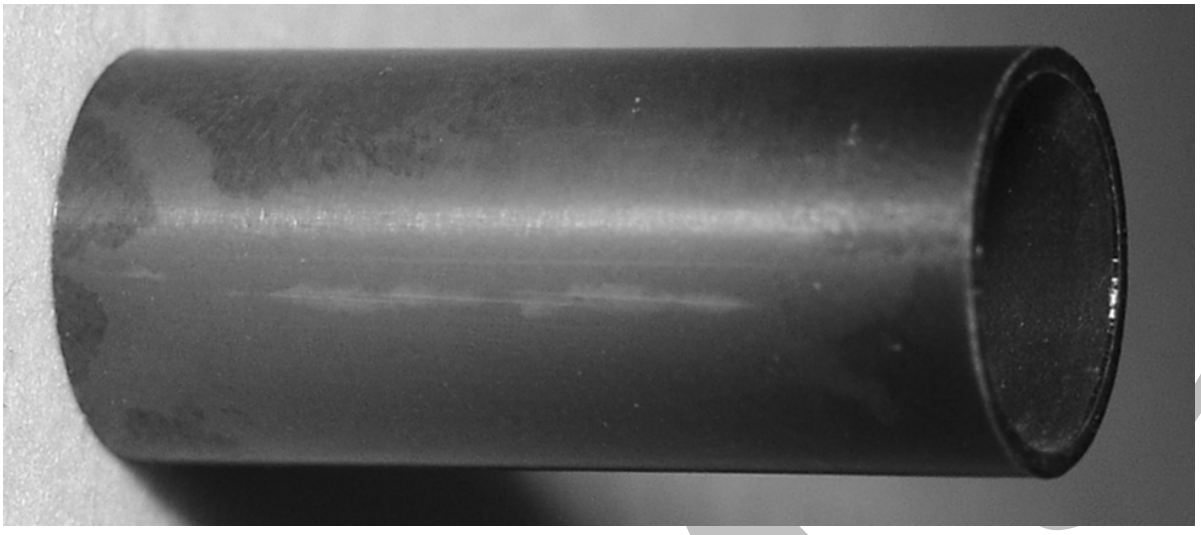

(a)

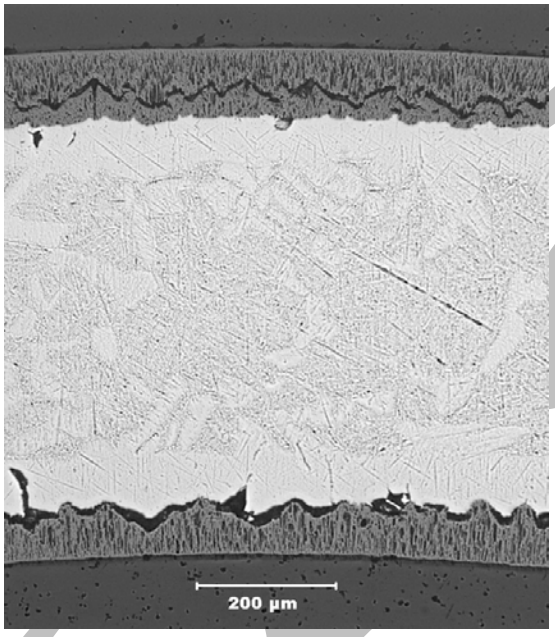

(b)

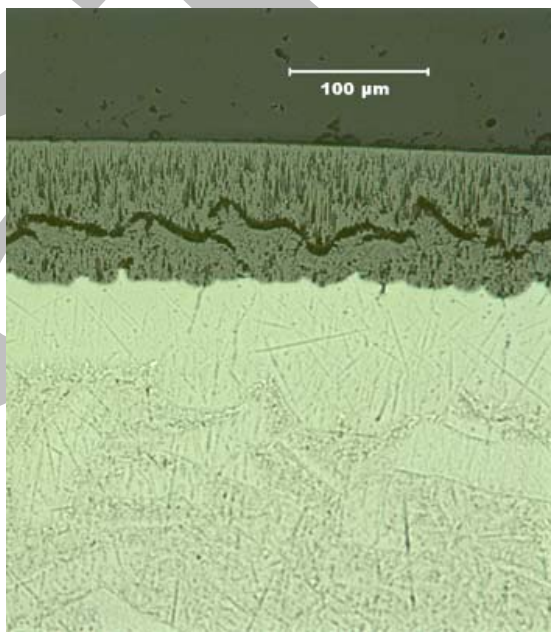

(c)

Figure 38. Images of belt-polished 15×15 sample BPZ4#18: (a) appearance of outer surface of sample showing local breakaway along a longitudinal strip; (b) inner and outer oxide layers showing pre-breakaway morphology of inner-surface oxide layer and post-breakaway morphology of outer-surface oxide layer; and (c) high magnification of outer-surface oxide layer.

for LOCA-criteria purposes it does not really matter whether the breakaway time for unscratched BP Zry-4 is 5000 s or >5400 s, as both times are very long.

The hydrogen pickup vs. oxidation time results for rough-surface and belt-polished 15×15 Zry-4 are plotted in Figure 39 based on the data in Tables 18 and 19. Both sets of results were generated using

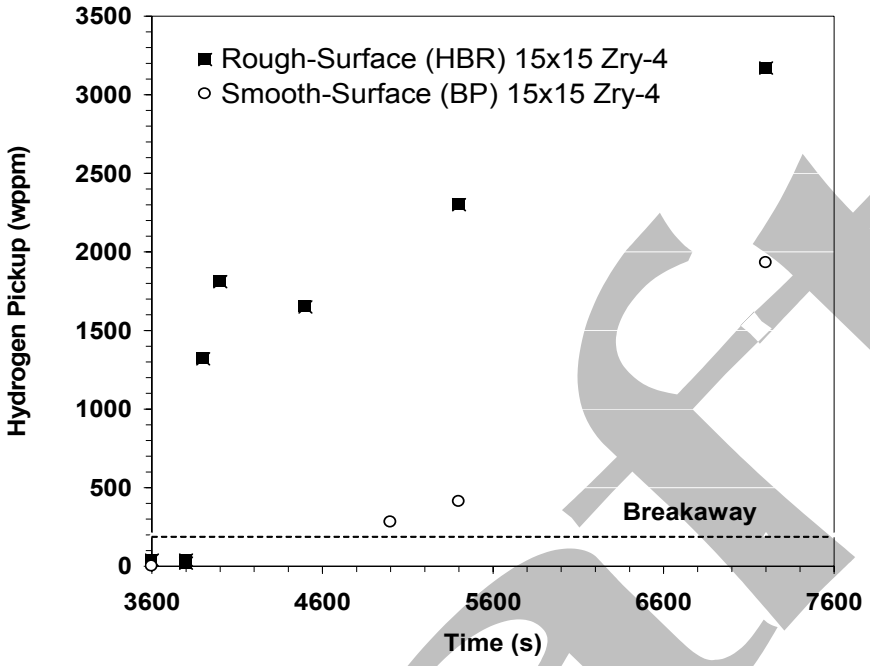

Figure 39. Comparison of breakaway-oxidation data for HBR-type (0.3-μm surface roughness) and belt-polished (0.1-μm surface roughness) 15×15 Zry-4 oxidized in the same apparatus at 985±12ºC. Based on the ANL 200-wppm-hydrogen-pickup criterion, breakaway oxidation time is ≈3800 s for HBR-type 15×15 Zry-4 and ≈5000 s for belt-polished (BP) 15×15 Zry-4.

the same oxidation test train. The lower breakaway-oxidation time for the rough-surface HBR-type Zry-4 appears to be due to its higher surface roughness. However, the surface and near-surface chemistry (i.e., impurities) and microstructure may be different for this cladding. Belt-polishing removes surface impurities in the range of 0.1-0.3 μm and may result in some additional cold-working of the near-surface metal. In terms of hydrogen content or hydrogen pickup, the HBR-type Zry-4 (1990s) has a much higher breakaway-oxidation time (≈3800 s) than the time (≈1800 s) determined by Leistikow and Schanz [19,20] for 1970's Zry-4. The breakaway-oxidation time (≈5000 s) for modern AREVA 15×15 Zry-4 tested by ANL is comparable to the breakaway-oxidation time (≈5400 s) determined by Mardon et al. [21] for modern AREVA 17×17 Zry-4. Even though the Mardon et al. tests were one-sided with only outer-surface breakaway, the ANL two-sided oxidation test results are comparable because the outer-surface oxide layer experienced breakaway oxidation earlier than the inner surface.

3.2 Zircaloy-2

One-sided oxidation tests were conducted with as-fabricated and high-burnup 9×9 Zry-2 (see Tables 3 and 7 for material parameters) to determine the oxidation kinetics [15]. Tests were conducted at 1000ºC (1200-6000 s), 1100ºC (600-3000 s), and 1204ºC (300-1200 s). Measured weight gain based on the increase in sample weight tended to be higher than CP-predictions due to some steam leakage causing inner-surface oxidation near the sample ends for all three oxidation temperatures. The weight-gain results based on metallographic images and analysis were in excellent agreement with the CP-predicted weight

gains for the 1204ºC-oxidized samples. The measured oxide layer thicknesses were also in excellent agreement with the CP-predicted oxide layer thicknesses (see page 74 of Ref. 13). However, the measured oxygen-stabilized-alpha layer thicknesses were as much as 40% higher than the CP-predicted values. This is important in evaluating the use of the CP-correlations in deducing beta-layer thickness vs. time at temperature. In the ANL tests, the argon purge flowing through the inside of the samples minimized hydrogen pickup (<50 wppm) from inner-surface oxidation and allowed desorption of hydrogen from the beta layer to the purge. According to Cathcart et al. (Appendix B, Table B1, page 166), samples oxidized (one-sided) at 1203ºC for only 236 s picked up 250-450 wppm hydrogen. Samples oxidized at lower temperatures for longer times picked up as much as 750-wppm hydrogen. Hydrogen is a beta-stabilizer, which results in a decrease in alpha layer thickness and an increase in beta-layer thickness. Figure 40 [22] shows the comparison of the ANL measured (alpha + oxide)-layer thickness and the CP-predicted (alpha + oxide)-layer thickness. The higher measured values are due to the higher measured values for the alpha-layer thickness.

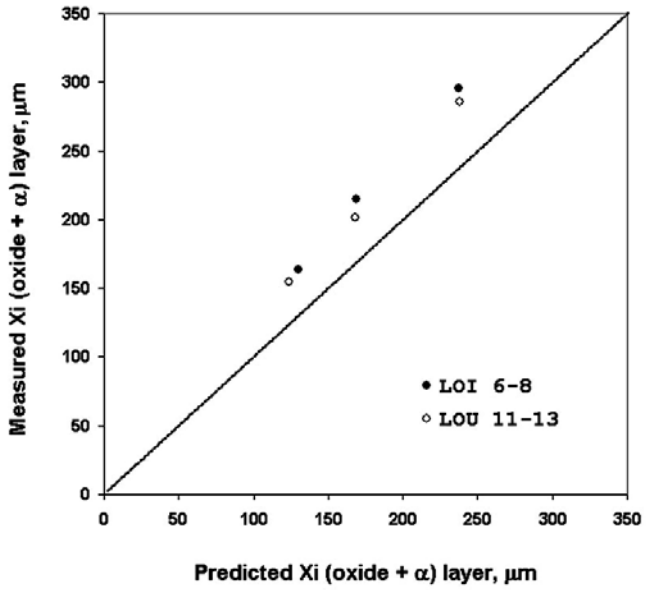

Figure 40. Measured vs. CP-model-predicted Xi (oxide + alpha) layers after steam-oxidation tests (300, 600 and 1200 s at ≈1204°C) with irradiated (LOI 6-8) and unirradiated (LOU 11-13) Zry-2.

3.2.1 Post-quench ductility of 10×10 Zry-2 oxidized at 1000ºC and 1200ºC

10×10 Zry-2 was oxidized (two-sided) at 1200˚C and 1000˚C to 10%, 13% and 17% CP-ECR. Following oxidation, the samples were cooled from 1200˚C to 800˚C at ≈13˚C/s and from 1000˚C to 800˚C at ≈10˚C/s. The samples were quenched at 800˚C and ring-compressed at 135˚C and 0.0333 mm/s. For the 1200˚C-oxidized samples, the offset and permanent strains, respectively, were: 24-25% and 21-22% at 10% CP-ECR; 11-14% and 13% at 13% CP-ECR; and 5.4-7.3% and 2.8% at 17% CP-ECR. Based on extrapolation, the ductile-to-brittle transition CP-ECR is estimated to be ≈20%. By comparing the offset strains for Zry-2 to those of Zry-4 shown in Figure 28, it is clear that the belt-polished Zry-2 results are consistent with the results for belt-polished Zry-4. However, metallographic images and crack-initiation location indicate significant difference in the behavior of Zry-2 with a Zr inner liner (≈10% of wall thickness). For the thermal benchmark test at 1200˚C after 400 s, the inner-surface oxide was 23% thinner than the outer-surface oxide. At 10% and 13% CP-ECR through-wall cracks were observed at

locations perpendicular to the loading direction where the bending stress is tensile at the outer surface. Both metallography and ring-compression failure locations indicate that oxygen diffuses faster into the beta layer through Zry-2 as compared to the Zr inner liner. For the oxidation tests at 1000˚C, the inner-surface oxide layer was 43% thinner than the outer-surface layer. {1000˚C results to be inserted here}

3.2.2 Breakaway oxidation time for 10×10 Zry-2 samples oxidized at 800-1000ºC

The breakaway oxidation time for 10×10 Zry-2 is expected to be about the same as the breakaway oxidation time for 9×9 Zry-2. One-sided oxidation tests using as-fabricated and high-burnup 9×9 Zry-2 were conducted at 1000°C for hold-times of 1200 s, 3600 s and 6000 s. Although metallographic analysis of these samples has not yet been conducted, sample weight gains were measured for the high-burnup samples. The results from Yan et al. [22] are presented in Figure 41. Even with the artifact of some inner-surface oxidation contributing to measured weight gain, the 3600-s sample shows no evidence of breakaway oxidation. The 6000-s sample had a weight gain 25% higher than the CP-predicted weight gain. At least 10% of this can be attributed to inner-surface oxidation near the ends of the sample. The remaining 15% may be a combination of breakaway oxidation and/or additional inner-surface oxidation for such a long test time. Based on the belt-polished Zry-4 results, the expected breakaway-oxidation time is ≈5400 s for the belt-polished 10×10 Zry-2 and 9×9 Zry-2. {A few confirmation tests are planned for the 10×10 Zry-2 oxidized at 1000°C and 800°C for 5000-6000 s. Results to be inserted here}

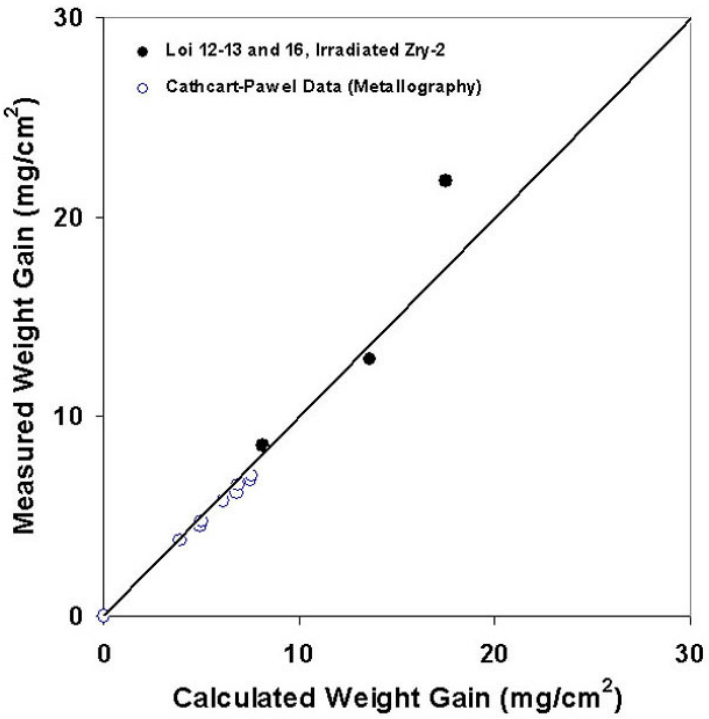

Figure 41. Comparison of Cathcart-Pawel model predictions to ANL sample weight gain data for irradiated (Limerick) Zry-2 after steam oxidation at ≈1000˚C for test times of 1200 s, 3600 s and 6000 s.

3.3 ZIRLO

3.3.1 Post-quench ductility of 17×17 ZIRLO oxidized at 1000ºC, 1100ºC and 1200ºC

This work was performed in sequence with the 17×17 Zry-4 testing and characterization. The same test trains, thermal-benchmark temperature histories (Figures 17, 18, 20 and 21), test times, and CP-ECR values were used, as the ZIRLO cladding has the same dimensions as the Zry-4 cladding. Results are also presented with the same subdivision as for Zry-4: characterization and RT-ring-compression testing of samples two-sided oxidized at 1000ºC and 1100ºC and quenched at 800ºC; and characterization and ring-compression testing (RT and 135ºC) of samples exposed to two-sided oxidization at 1200ºC and quenched at 800ºC. Characterization included weight gain, oxide- and alpha-layer thickness measurements (metallography), microhardness and hydrogen pickup (LECO). All samples were oxidized to CP-predicted ECR values of 5, 10, 15, 17, and 20%. Additional tests were conducted at intermediate CP-ECR values for the 1200ºC-oxidized samples to better determine the ductile-to-brittle transition CP-ECR value for this oxidation temperature.

17×17 ZIRLO oxidized at 1000ºC and 1100ºC

Table 21 shows the weight gain results for the ZIRLO oxidized at 1000ºC and 1100ºC. They are in very good agreement with the CP-predicted weight gain at these oxidation temperatures, except for the lower measured values for the 1000ºC oxidation samples at ≥15% CP-ECR. Figures 42a and 42b show the measured weight gains for ZIRLO and Zry-4 oxidized at 1000ºC and 1100ºC, respectively, as compared to the CP-predicted weight gains.

Table 22 lists the results of the RT post-quench ductility tests for the 1000ºC- and 1100ºC-oxidation samples. It is clear from the results that 17×17 ZIRLO retains post-quench ductility up to 20% CP-ECR – the limit of the test conditions – for these oxidation temperatures. The results are shown graphically in Figures 43 and 44 for 1000ºC- and 1100ºC-oxidized samples, respectively. Because of the differences in weight gain between ZIRLO and Zry-4 oxidized at 1000ºC, offset strains are displayed as functions of measured ECR (43a) and CP-ECR (43b). For oxidation at 1100ºC, both alloys exhibit essentially the same weight gain for the same test time, so post-quench ductility results are plotted in Figure 44 as a function of CP-ECR only. For the 1000ºC- and 1100ºC-oxidation tests, the offset strain leveled out at ≈3%. It appears from these results that ZIRLO will retain ductility at higher CP-ECR values and higher test times (>3400 s at 1000ºC) until breakaway oxidation or beta-layer thinning occurs. For 1100ºC-oxidation, breakaway oxidation should not occur, and the beta-layer does not appear to embrittle due to the low saturation-level oxygen content. At much higher ECR values, the beta layer would thin enough to make the ring structure behave in a brittle manner. Photographs of the ring-compressed samples are shown in Figure 45a (1000ºC) and b (1100ºC). The 5% and 10% CP-ECR samples oxidized at 1000ºC were intact at the maximum Instron displacement. The 5% CP-ECR sample oxidized at 1100ºC was also intact.

Table 23 summarizes the results of the metallography, microhardness and hydrogen pickup measurements for ZIRLO as compared to Zry-4. The hydrogen pickup is very low for 1100ºC-oxidized ZIRLO samples. However, hydrogen pickup is ≈100 wppm for ZIRLO oxidized at 1000ºC for 3364 s (20% CP-ECR). Metallographic images indicate that the inner-surface oxide is undergoing breakaway oxidation. Breakaway oxidation for ZIRLO oxidized at 800-1000ºC is discussed in section 3.3.2. The microhardness results in Table 22 are consistent with the post-quench ductility results.

Figure 46 shows metallographic images of ZIRLO and Zry-4 oxide layers following 1000ºC oxidation to 20% CP-ECR. From these images, it is clear that the higher weight gain for Zry-4 oxidized

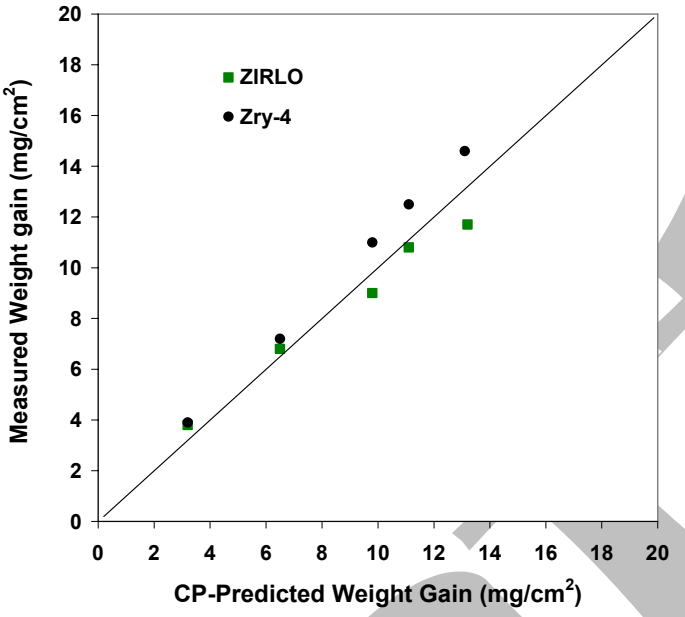

(a)

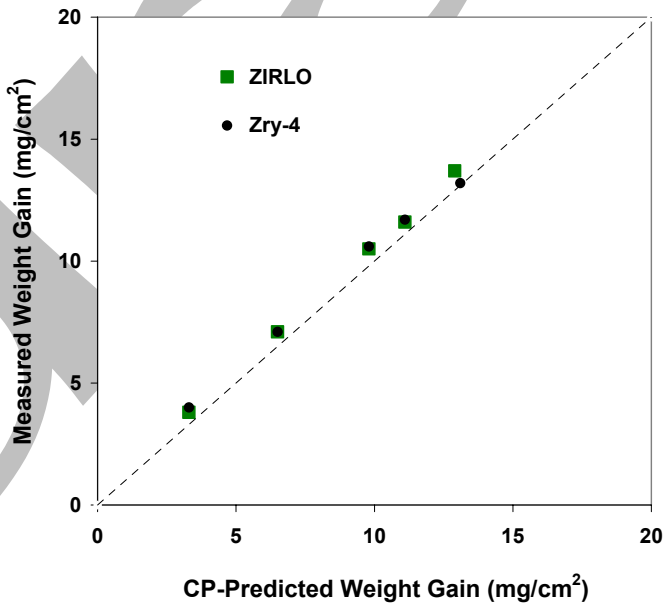

(b)

Figure 42. Comparison between weight gain data for ZIRLO and Zry-4 and weight gain predicted by the Cathcart-Pawel (CP) correlation for samples oxidized (two-sided) in steam at 1000˚C (a) and 1100˚C (b). Data correspond to CP-ECR values of 5, 10, 15, 17, and 20%.

Table 21 Weight Gain (Wg in mg/cm^2) and Measured ECR (%) Values for 17×17 ZIRLO Oxidized in Steam at 1000˚C and 1100˚C and Quenched at 800˚C. ECR = 1.538 Wg for the 0.57-mm-wall thickness. Multiply weight gain results by a factor of 10 to convert to g/m^2.

Oxidation Temperature, ºC	Cathcart-Pawel ECR, %	Measured Weight Gain (Wg), mg/cm^2	Measured ECR, %
1000	5	3.8	5.9
1000	10	6.8	10.5
1000	15	9.0	13.8
1000	17	10.8	16.6
1000	20	11.7	18.0
1100	5	3.8	5.9
1100	10	7.1	10.9
1100	15	10.5	16.1
1100	17	11.6	17.9
1100	20	13.7	21.1

at this temperature is due to the thicker oxide layers grown on the Zry-4 surfaces. This is an alloy effect. Also, as is discussed in Section 3.3.2, the waviness of the ZIRLO oxide layers, particularly the inner-surface oxide layer, is a precursor to breakaway oxidation and hydrogen pickup. Table 23 lists the inner-surface oxide layer on ZIRLO as 9-µm thicker than the outer-surface oxide. These results suggest that the inner-surface is transforming from stable tetragonal growth to unstable monoclinic growth. Figure 47 shows higher magnification and better contrast for the outer- and inner-surface oxide layers grown on this ZIRLO sample. It is clear from Figure 47b that the inner-surface oxide layer is in transition from the tight tetragonal (dark) oxide phase to the cracked monoclinic (light) oxide phase. This supports the view that the ZIRLO hydrogen pickup is through the inner-surface oxide layer. Visual examination confirmed that the inner-surface oxide was gray, as compared to the black surface observed inside the Zry-4 sample oxidized under the same conditions.

Figure 48 shows the comparison between the metallographic images for ZIRLO and Zry-4 oxidized to 20% CP-ECR at 1100ºC. The Zry-4 prior-beta layer exhibits incursions of higher-oxygen alpha-phase material, which precipitated during cooling from 1100ºC to 800ºC prior to quench. The ZIRLO alpha and prior-beta layers are quite different in appearance from those of Zry-4. While oxygen is an alpha-stabilizer, Nb is a beta-stabilizer. The oxygen-stabilized alpha "layer" formed at high temperature in ZIRLO is not as uniform as the one formed in Zry-4 because Nb causes local regions of beta-stabilization even at higher oxygen contents. Precipitation of oxygen-stabilized alpha regions during cooling is also different in the ZIRLO prior-beta layer because of the presence of Nb. Yet, even with these differences in microstructure and phase distribution, the post-quench ductility of the two alloys oxidized at 1000ºC and 1100ºC is remarkably similar.

The comparison between ZIRLO and Zry-4 oxidized at 1000ºC for up to ≈3360 s (20% CP-ECR) indicates that: the weight gain for ZIRLO is ≈10% lower than predicted by the CP correlation, while the weight gain for Zry-4 is ≈10% higher than the CP-predicted correlation; the 20% difference in weight gain has no influence on post-quench ductility, as it merely reflects the differences in oxide-layer thickness rather than the oxygen content in the prior-beta layer; both alloys have adequate post-quench

Table 22 Ring Compression Test Results for 17×17 ZIRLO Samples Oxidized at 1000˚C and 1100˚C, Cooled at ≈10˚C/s to 800˚C and Quenched. ECR = 1.538 Wg for 0.57-mm-wall cladding. Tests were performed on 8-mm-long samples at RT and 0.0333 mm/s displacement rate. Displacements in the loading direction were normalized to the as-fabricated outer diameter (9.50 mm) to calculate offset strain. A complete set of tests were performed using the Model 4505 Instron. A limited number of confirmation tests were performed with the Model 5566 Instron on rings cut from the same oxidation samples.

Oxidation Temperature ºC	Cathcart-Pawel ECR, %	Measured ECR %	Offset Displacement mm	Offset Strain %	Confirmation Tests Model 5566 Instron
1000	5	5.9	>4.9	>52	---
1000	10	10.5	>2.35	>25	Yes
1000	15	13.8	1.92	20	Yes
1000	17	16.6	0.45	4.7	---
1000	20	18.0	0.27	2.9	---
1100	5	5.9	>5.0	>52	---
1100	10	10.9	2.1	22	---
1100	15	16.1	0.48	5.1	Yes
1100	17	17.9	0.33	3.5	---
1100	20	21.1	0.32	3.3	---

ductility at 20% CP-ECR; and the ZIRLO inner-surface oxide layer is in breakaway-oxidation transition at 3360 s based on hydrogen pickup and metallographic imaging. The differences in weight gain are attributable to alloy effects, particularly the Nb in ZIRLO. Better agreement for the offset strains of these two alloys is observed at high oxidation times in Figure 43b where the offset strain is plotted as a function of CP-ECR. The results in Figure 43b clearly show that Zry-4 and ZIRLO have essentially the same post-quench ductility for equivalent isothermal oxidation times of 2430-3365 s at 1000ºC. The comparison between ZIRLO and Zry-4 oxidized at 1100ºC for up to ≈1070 s (20% CP-ECR) indicates differences in microstructure and phase distribution but no significant differences in weight-gain kinetics and post-quench ductility.

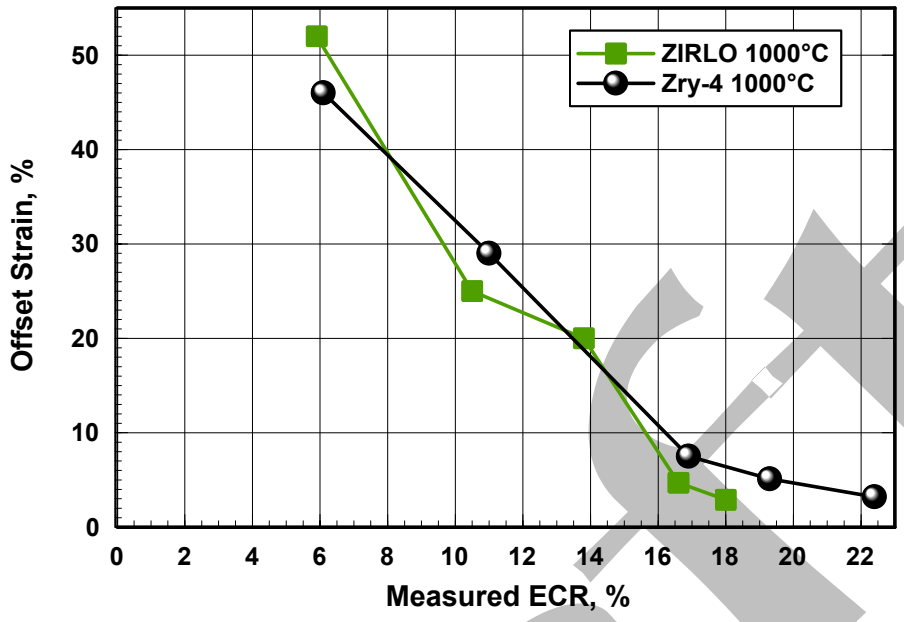

(a)

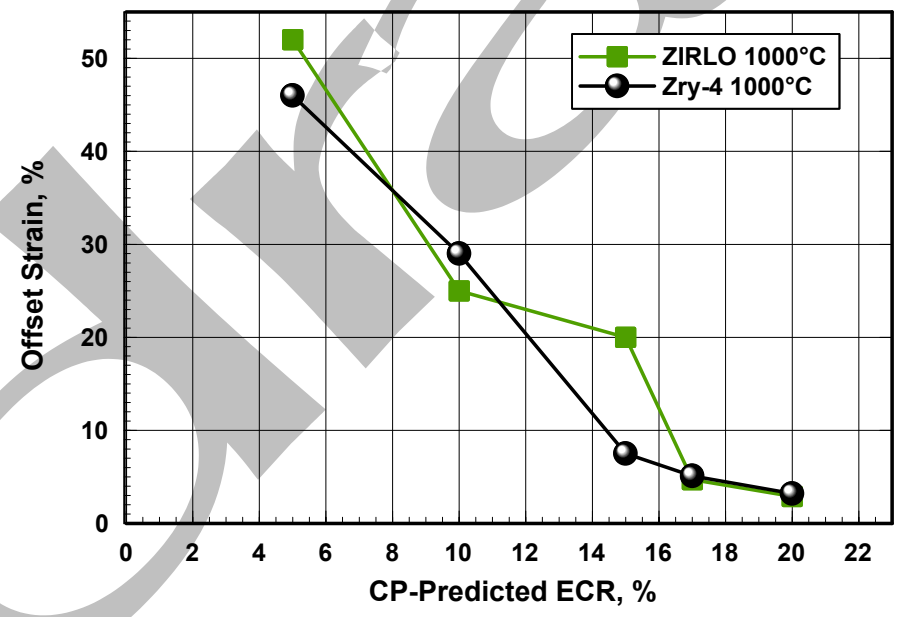

(b)

Figure 43. Post-quench ductility vs. measured (a) and CP-predicted (b) ECR for ZIRLO and Zry-4 oxidized at 1000˚C, cooled at ≈10˚C/s to 800ºC and quenched. Ductility is based on offset strain determined from ring-compression data for tests conducted at RT and 0.0333 mm/s displacement rate.

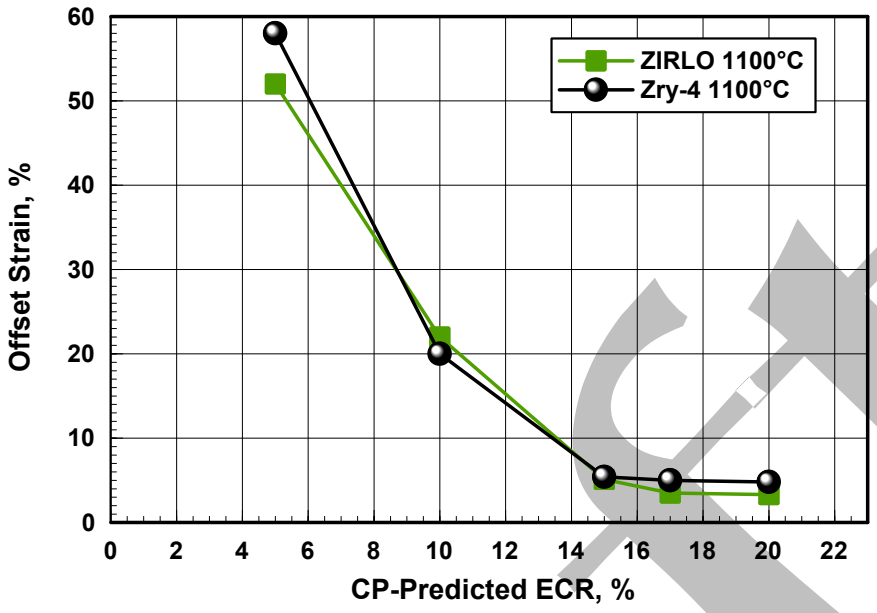

Figure 44. Post-quench ductility vs. CP-predicted ECR for ZIRLO and Zry-4 oxidized at 1100˚C, cooled at ≈10˚C/s to 800ºC and quenched. Ductility is based on offset strain determined from ring-compression data for tests conducted at RT and 0.0333 mm/s displacement rate.

(a)

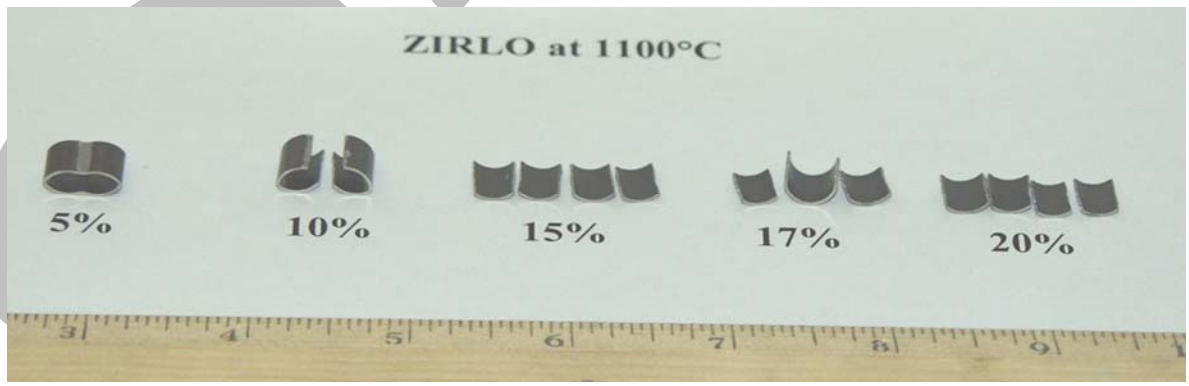

(b)

Figure 45. Post-test appearance of ZIRLO ring-compression samples tested at room temperature and 0.0333 mm/s: (a) samples oxidized at 1000˚C; and (b) samples oxidized at 1100˚C. ECR values are calculated using the Cathcart-Pawel weight gain correlation.

Table 23 Summary of Characterization of Highly Oxidized (20% CP-ECR) 17×17 Zry-4 and ZIRLO Samples after Exposure to Steam at 1000˚C and 1100˚C, Cooling at ≈10˚C/s to 800˚C and Quench

Oxidation Temperature ˚C	Parameter	Zry-4	ZIRLO
1000	Effective Oxidation Time, s	3364	3364
	Weight Gain, mg/cm^2	14.6	11.7
	Measured ECR, %	22.4	18.0
	RT Offset Displacement, mm	0.31	0.27
	RT Offset Strain, %	3.2 (ductile)	2.9 (ductile)
	Hydrogen Content, wppm	19	102
	Hydrogen Pickup, wppm	15	103
	OD/ID Oxide Layer Thickness, μm	83/82	57/66
	Microhardness within Middle 0.2 mm, DPH	290-420	290-400
1100	Effective Oxidation Time, s	1065	1065
	Weight Gain, mg/cm^2	13.2	13.7
	Measured ECR, %	20.3	21.1
	RT Offset Displacement, mm	0.46	0.32
	RT Offset Strain, %	4.8 (ductile)	3.3 (ductile)
	Hydrogen Content, wppm	22	22
	Hydrogen Pickup, wppm	19	18
	OD/ID Oxide Layer Thickness, μm	70/68	72/69
	Microhardness within Middle 0.2 mm, DPH*	240-470	330-460

*Includes oxygen-stabilized alpha needles (ZIRLO) and alpha incursions (Zry-4) in prior-beta layer.

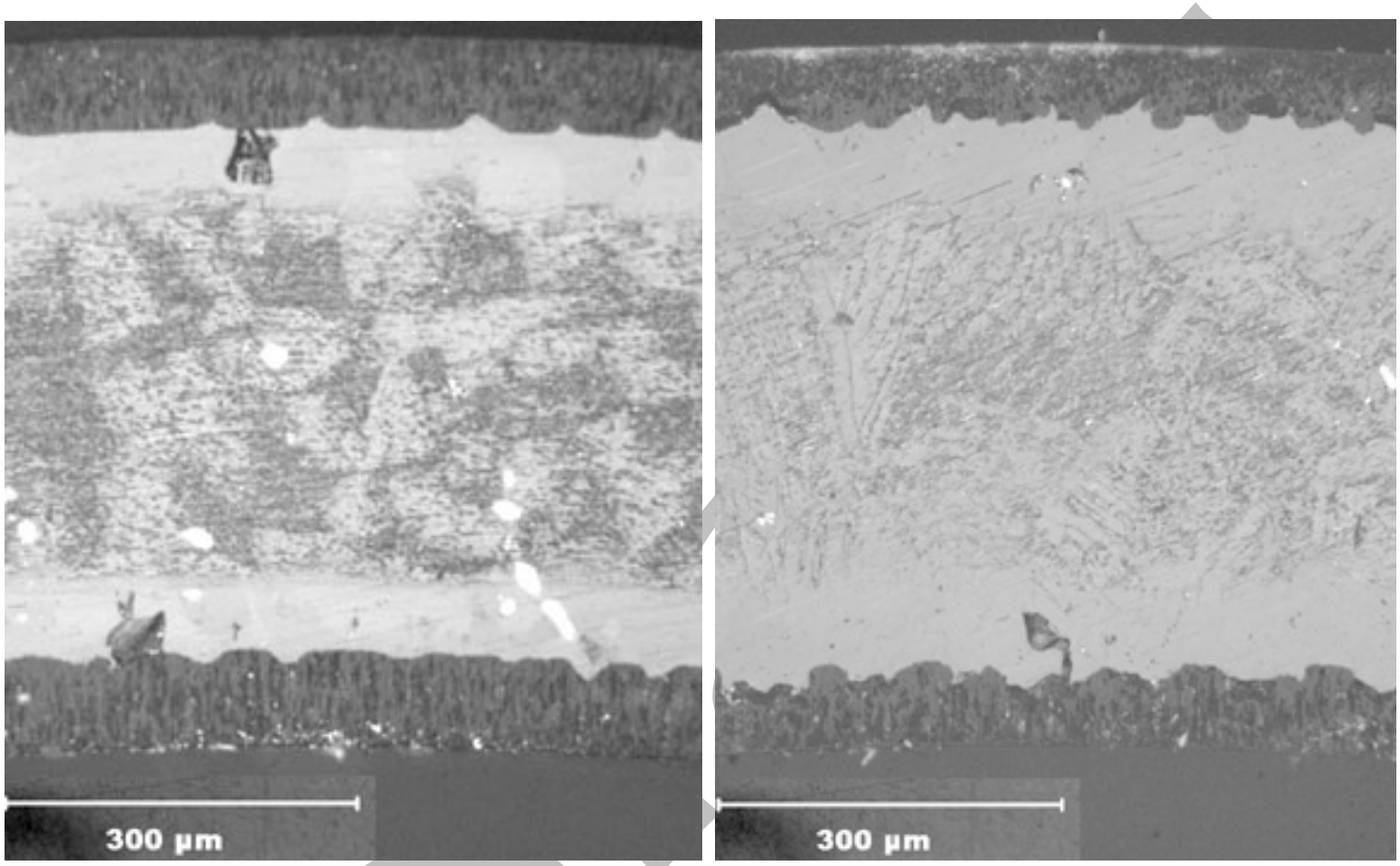

(a) Zry-4 (b) ZIRLO

Figure 46. Metallography of as-polished Zry-4 (a) and ZIRLO (b) oxidized in steam at 1000˚C for ≈3360 s, cooled at ≈10˚C/s to 800˚C and water quenched. Measured ECR values are 22.4% for Zry-4 and 18.0% for ZIRLO.

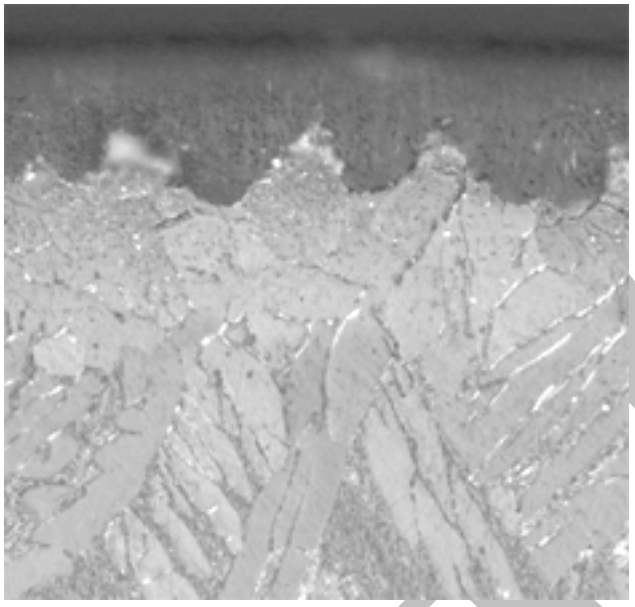

(a)

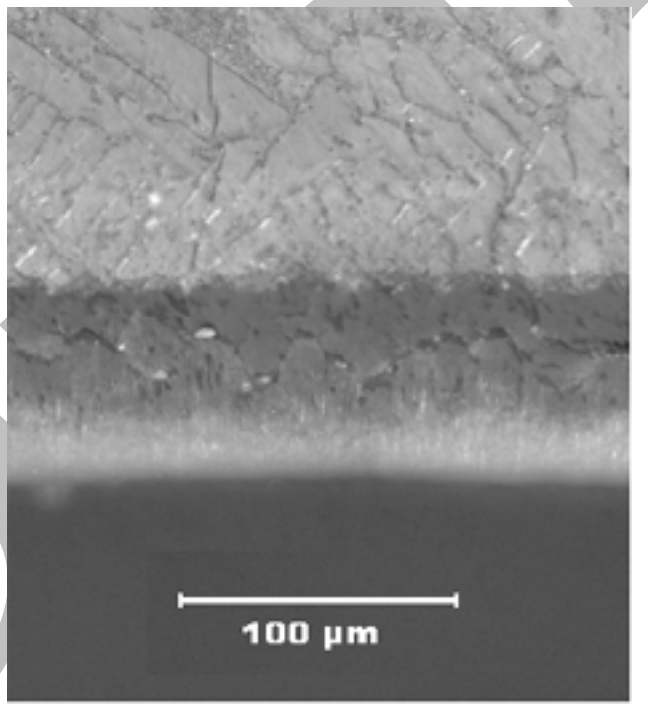

(b)

Figure 47. High-magnification images of etched ZIRLO sample following oxidation at 1000ºC for 3360 s to 20% CP-ECR. The outer-surface oxide layer (a) is tetragonal, but the wavy oxide-metal interface indicates a precursor to breakaway oxidation. The inner-surface oxide layer (b) is thicker, has lateral cracks, appears to be monoclinic and is in breakaway oxidation. The hydrogen pickup through the inner-surface is ≈100 wppm.

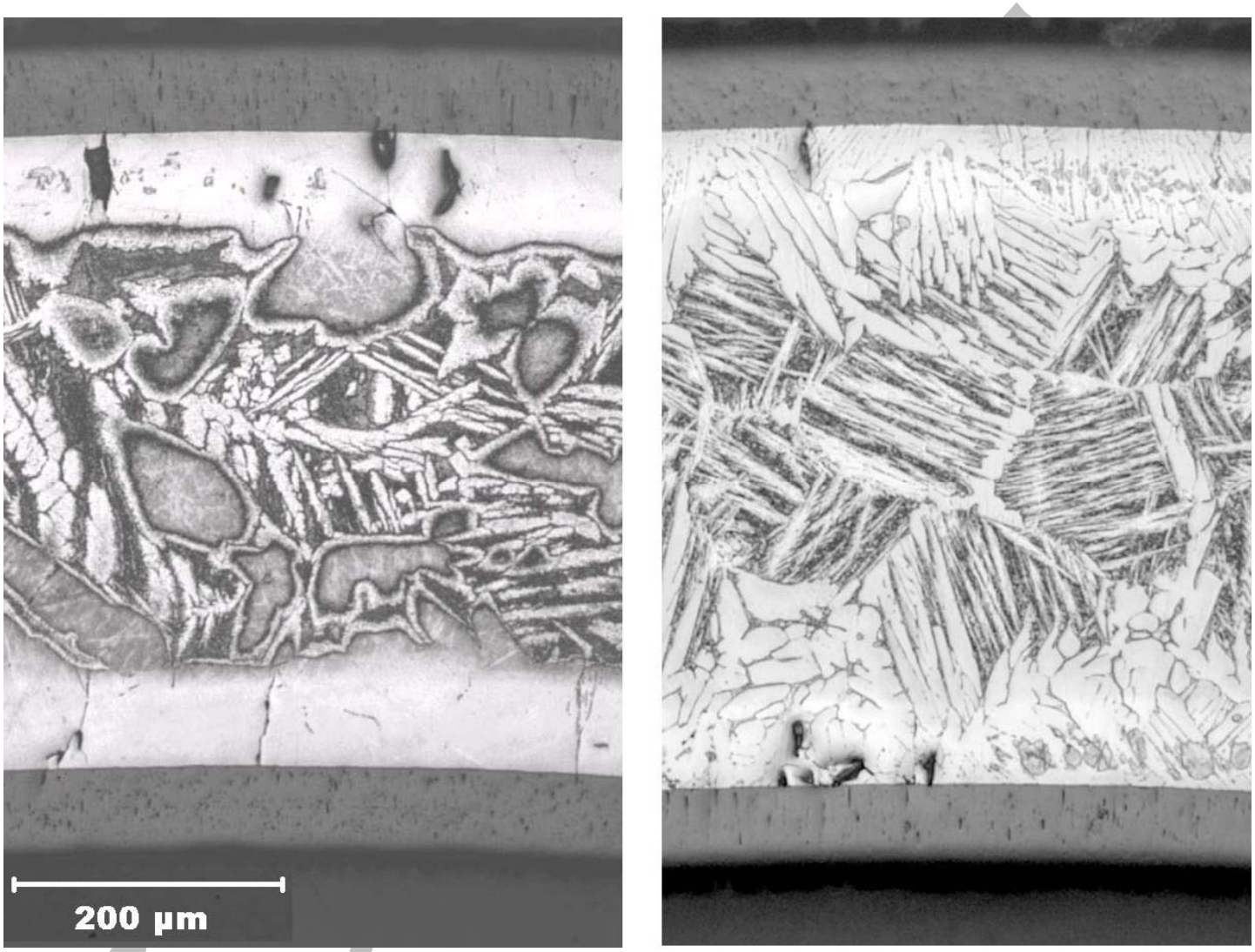

(a) Zry-4 (b) ZIRLO

Figure 48. Metallography of etched Zry-4 (a) and ZIRLO (b) oxidized in steam at 1100˚C for ≈1070 s to 20% CP-ECR, cooled at ≈10˚C/s to 800˚C, and water quenched. Measured ECR values are 20.3% for Zry-4 and 21.1% for ZIRLO.

17×17 ZIRLO oxidized at 1200ºC

In parallel with the testing of Zry-4, numerous tests were conducted with 17×17 ZIRLO oxidized at 1200±5ºC to determine the ductile-to-brittle transition CP-ECR at RT and 135ºC. Figures 20 and 21 show the thermal-benchmark results for the first and most recent test trains Although the temperature ramps are different, these have little effect on the long-time tests used to determine the high-transition CP-ECR at 135ºC. Also, all tests were stopped after the first significant load drop to allow a measure of the permanent strain based on diameter change in the loading direction.

The weight gain (expressed in terms of measured ECR) and the post-quench ductility results are summarized in Table 24. Figure 49 shows the ZIRLO and Zry-4 measured weight gains, as compared to the CP-predicted weight gains. The experimental results for both alloys are in excellent agreement with each other and with the predicted values.

ZIRLO appears to embrittle at room temperature after oxidation to ≈11% CP-ECR and quench. This is confirmed by both the offset (<2%) and the permanent-strain (<1%) criteria for embrittlement. The enhancement of ductility with the increase in test temperature is quite pronounced. Based on the offset and permanent strain data, the ductile-to-brittle transition CP-ECR is ≈19% at 135ºC. The variations of offset strain and permanent strain with CP-ECR are shown in Figures 50a and 50b, respectively, for the RT and 135ºC test conditions. Figure 51 is a comparison between the post-quench ductility (offset strain) at 135ºC of ZIRLO and Zry-4 vs. CP-ECR following oxidation at 1200ºC and quench at 800ºC. At CP-ECR values <17%, ZIRLO has significantly higher post-quench ductility than Zry-4. However, both alloys show low ductility at ≥17% CP-ECR for ring-compression at 135ºC.

The higher ductile-to-brittle transition ECR for 17×17 ZIRLO (19%) as compared to 17×17 Zry-4 (17%) does not appear to be an alloy effect. Based on Figure 28, modern 15×15 Zry-4 has the same ductile-to-brittle transition ECR (19%) as modern 17×17 ZIRLO. It appears that fabrication differences from lot-to-lot of Zry-4 have more of an effect on the embrittlement threshold for 1200ºC-oxidized samples than alloy differences.

Table 24 Ring Compression Test (RCT) Results for 17×17 ZIRLO Cladding Oxidized at 1200˚C, Cooled at ≈13˚C/s to 800˚C, and Quenched. ECR = 1.538 Wg for 0.57-mm-wall thickness. Tests were performed on ≈8-mm-long samples at RT and 135ºC and at 0.0333 mm/s displacement rate. Displacements in the loading direction were normalized to the as-fabricated outer diameter (9.50 mm) to calculate offset and permanent strains.

Test Conditions		ECR %		Plastic Displacement, mm		Plastic Strain, %	
RCT T, ˚C	Test Time[a], s	CP	Meas.	Offset	Permanent	Offset	Permanent
RT	60	4.9	4.8	>5.55	>5.24	>58	>53
RT	136	10.0	10.3	0.26	0.13	2.7	1.4
135	136	10.0	10.3	>4.8	>4.8	>51	>51
RT	203	13.0	13.4	0.11	0.07	1.2	0.7
135[b]	**203**	**13.0**	**14.3**	**1.96**	**1.47**	**20.7**	**15.5**
135[b]	**203**	**13.0**	**14.3**	**3.12**	**>2.46**	**33**	**>26**
RT	248	15.1	15.4	0.18	0.11	1.8	1.2
135	248	15.1	15.4	1.73	1.28	18.2	13.4
RT	310	17.1	17.8	0.16	0.06	1.0	0.6
135	310	17.1	17.8	0.66	---	7.0	---
135[b]	**318**	**17.0**	**18.4**	**0.59**	**0.27**	**6.2**	**2.8**
135[b]	**318**	**17.0**	**18.4**	**0.36**	**0.17**	**3.8**	**1.8**
135[b]	**390**	**19.0**	**21.2**	**0.29**	**0.11**	**3.1**	**1.2**
135[b]	**390**	**19.0**	**21.2**	**0.19**	**0.11**	**2.0**	**0.9**
RT[c]	428	21.2	22.3	0.11	0.06	1.1	0.6
135[c]	448	21.7	23.4	0.20	0.11	2.1	1.2
135[c]	448	21.7	23.4	0.20	---	2.1	---

[a]Includes time for ramp from 300ºC and hold time.

[b]**Tests were conducted with current test train (see Figure 21 for thermal history).** Most other test results were generated with the initial test train (see Figure 20 for thermal history).

[c]Control TC switched prior to runs; estimated cladding temperature is ≈1215˚C.

Table 25 summarizes the characterization results for 17×17 Zry-4 and ZIRLO oxidized at 1200ºC to 13% and 20% ECR and quenched at 800ºC. As expected, hydrogen pickup is very low. Also, there is excellent agreement between the inner-surface and outer-surface oxide layer thickness, indicating adequate steam flow at the inner surface. The microhardness results support the post-quench ductility results. Based on the room-temperature microhardness values, one would expect ductility at 13% CP-ECR and embrittlement at 20% CP-ECR at the 135ºC test temperature. The microstructures across the cladding wall are shown in Figures 52a for Zry-4 and 52b for ZIRLO oxidized at 1200ºC to ≈20% CP-ECR. As with the lower oxidation temperatures, Zry-4 has well defined oxygen-stabilized alpha layers grown at 1200ºC, while the presence of Nb in ZIRLO results in a less clear distinction of this layer. The microhardness indents for Zry-4 and ZIRLO oxidized to ≈13% CP-ECR are shown in Figures 53a and 53b, respectively.

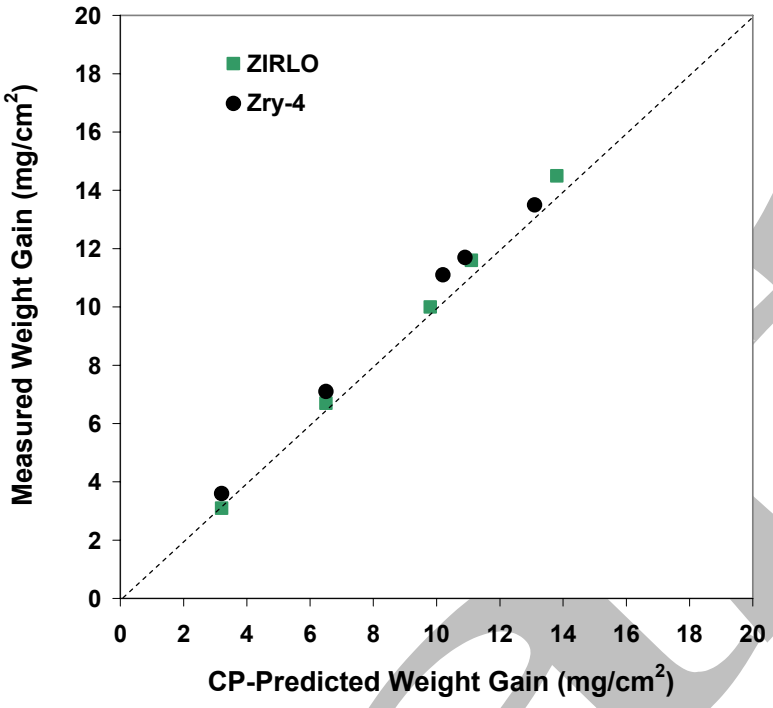

Figure 49. Comparison between weight gain data for ZIRLO and Zry-4 and CP-predicted weight gain for samples oxidized (two-sided) in steam at 1200˚C and quenched at 800˚C.

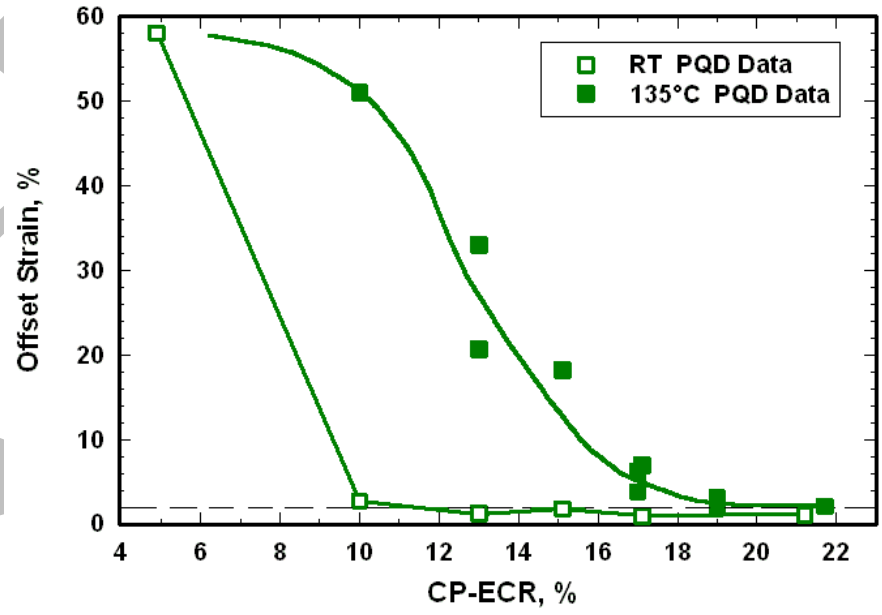

Figure 50a. Offset strain vs. CP-ECR for 17×17 ZIRLO oxidized at 1200ºC, cooled at ≈13˚C/s to 800˚C, quenched, and ring-compressed at RT and 135ºC.

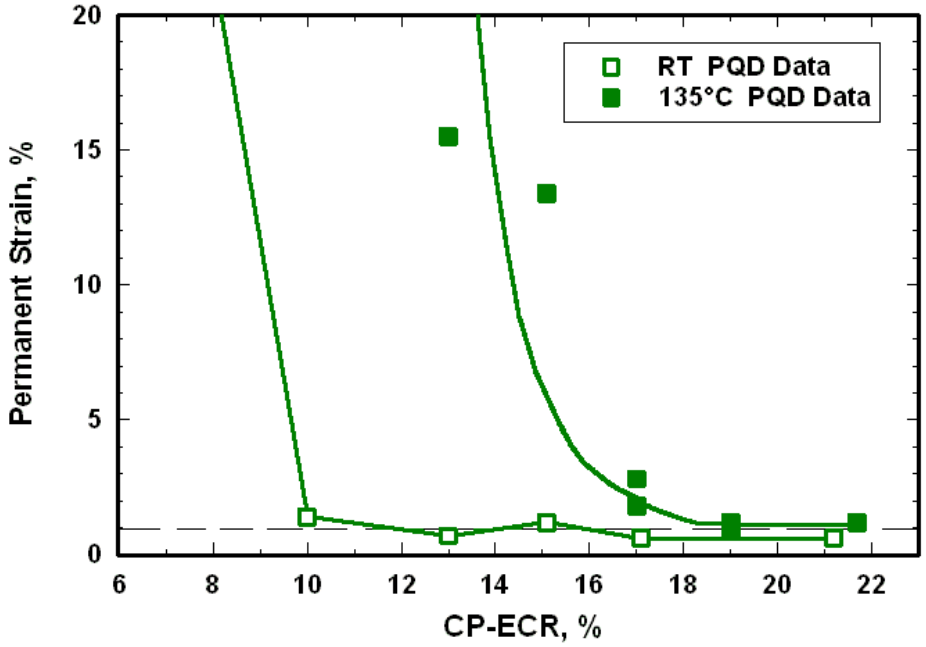

Figure 50b. Permanent strain vs. CP-ECR for 17×17 ZIRLO oxidized at 1200˚C, cooled at ≈13˚C/s to 800˚C, quenched, and ring-compressed at RT and 135ºC.

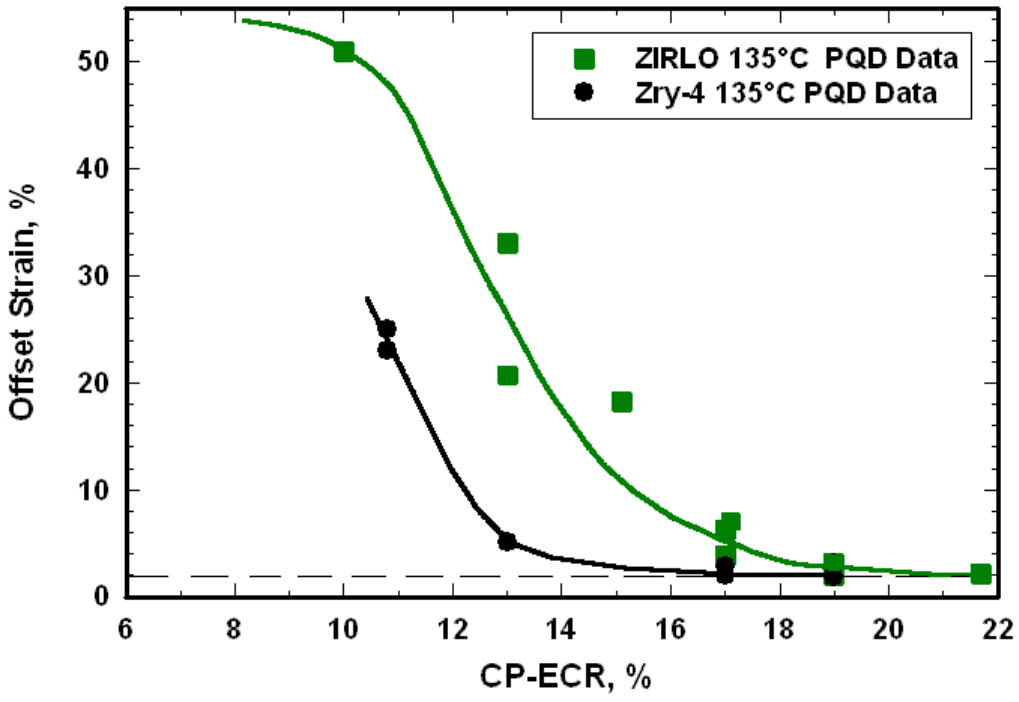

Figure 51. Offset strain vs. CP-ECR for 17×17 ZIRLO and Zry-4 oxidized at 1200ºC, cooled at ≈13˚C/s to 800˚C, quenched, and ring-compressed at 135ºC.

Table 25 Summary of Characterization of 17×17 Zry-4 and ZIRLO Samples after Exposure to Steam at 1200˚C to 13% and 20% CP-ECR, Cooling at ≈13˚C/s to 800˚C and Quenching

Parameter	Zry-4		ZIRLO	
	20% ECR	13% ECR	20% ECR	13% ECR
Effective Time, s	400	166	444	166
Weight Gain, mg/cm^2	13.5	8.35	14.5	8.70
Measured ECR, %	20.8	12.8	22.3	13.4
RT Offset Displacement, mm	0.05	0.09	0.11	0.11
RT Offset Strain, %	0.5	0.9	1.2	1.2
RT Measured Permanent Displacement, mm	0.04	0.07	0.06	0.07
RT Permanent Strain, %	0.4	0.7	0.6	0.7
RT Ductility, %	≤0.4 (brittle)	≤0.7 (brittle)	≤0.6 (brittle)	≤0.7 (brittle)
Hydrogen Content, wppm	17	low	17	low
Hydrogen Pickup, wppm	13	low	14	low
OD/ID Oxide Thickness, μm	68/66	42/41	74/71	44/43
Prior-Beta-Layer Thickness, μm	266	419	≈150	≈370
Microhardness, DPH Oxide Layers Alpha Layers Prior-Beta Layer*	 570-960 530-730 280-600	 600-770 600-700 260-360	 560-1160 600-800 350-530	 610-770 650-860 350-450

*Range includes microhardness values of oxygen-rich alpha needles (ZIRLO) and alpha incursions (Zry-4) in this layer.

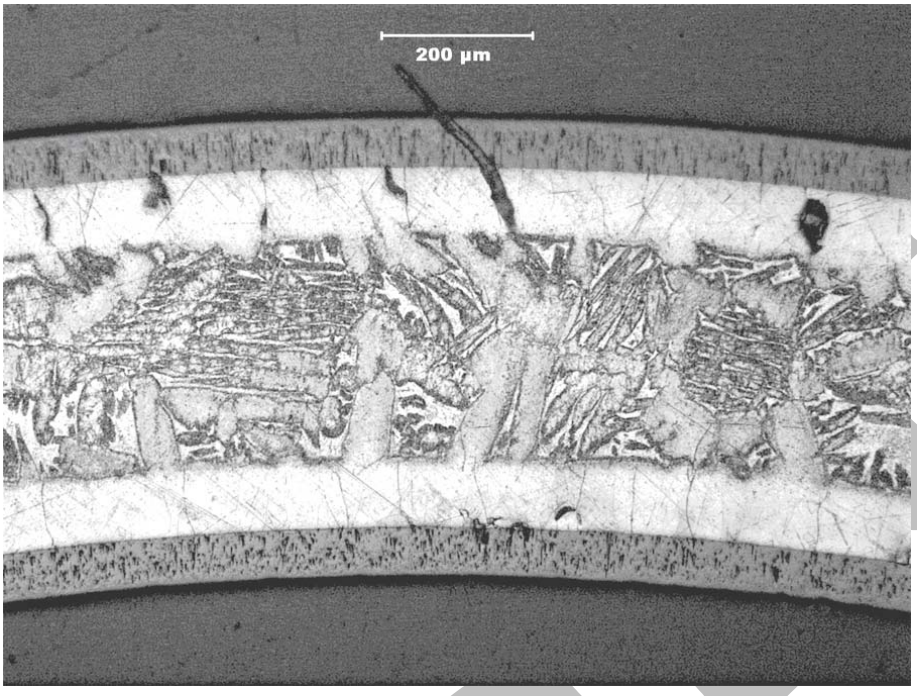

(a) Zry-4

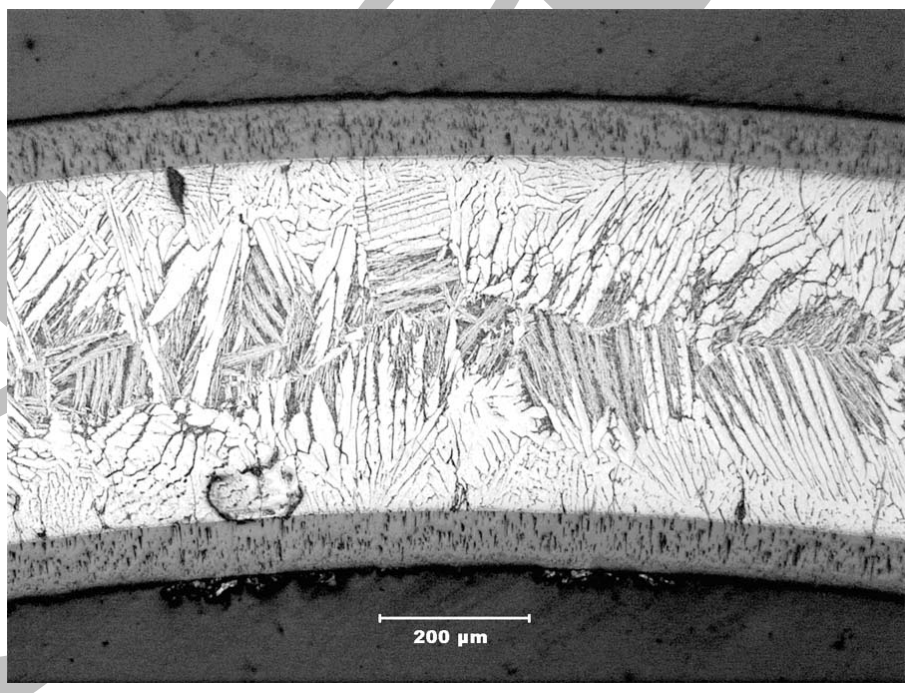

(b) ZIRLO

Figure 52. Metallography of etched Zry-4 (a) and ZIRLO (b) oxidized in steam at 1200˚C for ≈400 s and ≈440 s, respectively, cooled at ≈13ºC/s to 800˚C and quenched. Measured ECR values are 20.8% for Zry-4 and 22.3% for ZIRLO.

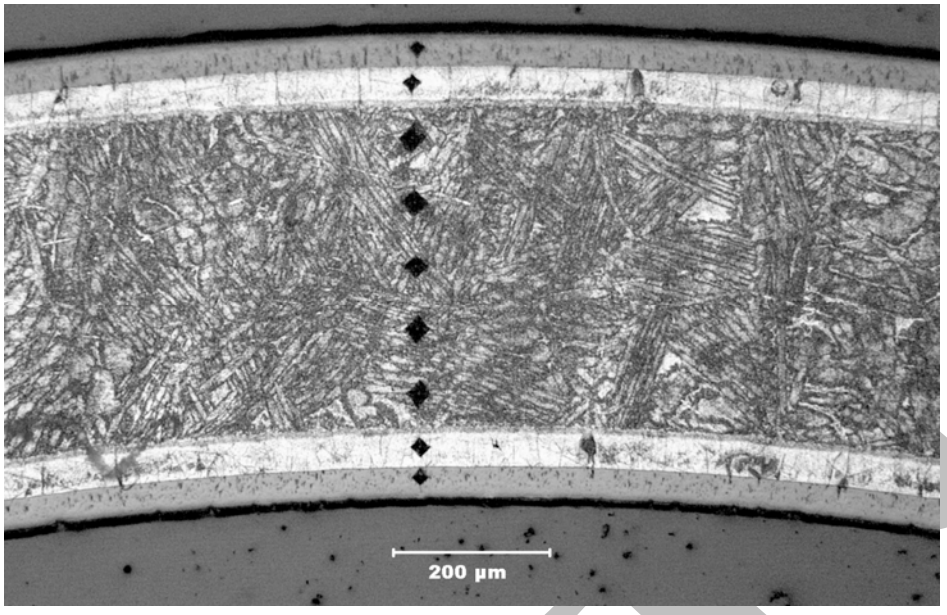

(a) Zry-4

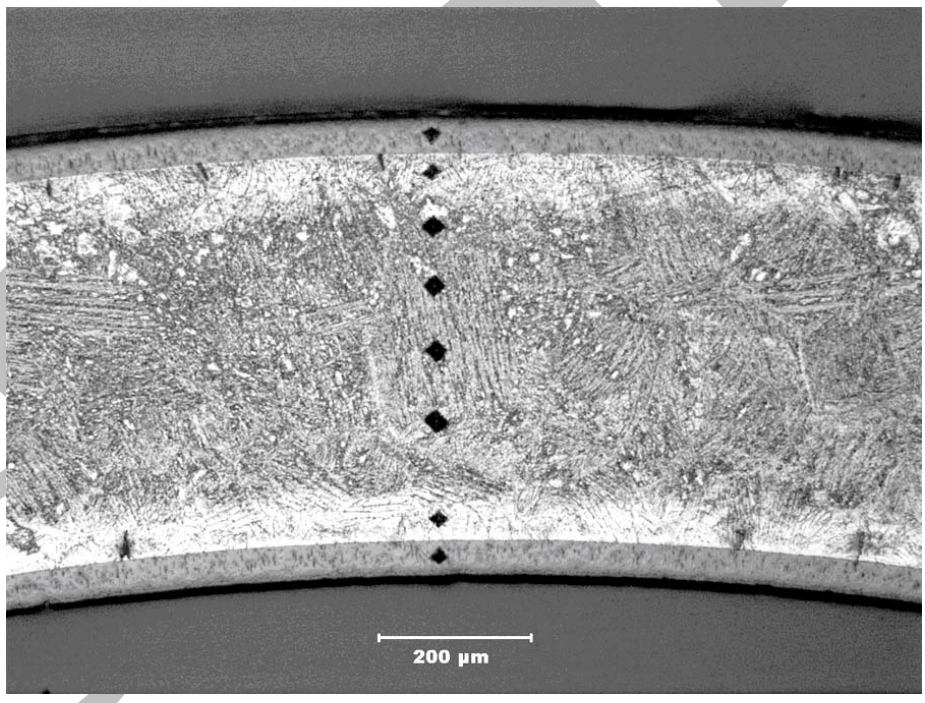

(b) ZIRLO

Figure 53. Metallography and microhardness indents across the radius of 17×17 Zry-4 (a) and ZIRLO (b) oxidized at 1200˚C to 13% ECR, cooled at ≈13˚C/s to 800˚C and quenched. The measured ECR values are 12.6% for Zry-4 and 13.4% for ZIRLO.

3.3.2 Breakaway oxidation time for 17×17 ZIRLO samples oxidized at 800-1015ºC

Unlike Zry-4, there are no published data on the breakaway oxidation time vs. temperature for ZIRLO. Thus, the approach adopted in this work was to explore breakaway oxidation times in the range of 950-1015ºC to determine the minimum breakaway time. A test was also run at 800ºC at a time greater than the minimum time for 950-1015ºC to demonstrate that breakaway did not occur at earlier times at 800ºC. Based on the results shown in Figure 47b for ZIRLO received and tested in 2003 (ZIRLO-2003), the inner-surface oxide layer is already in breakaway following oxidation at 1000ºC for ≈3400 s. However, breakaway oxidation time is most relevant to the cladding outer-surface away from the balloon region. Given that ZIRLO may pick up hydrogen from the inner surface before the outer surface experiences breakaway oxidation, it was necessary to determine by visual inspection and metallography if the outer surface was in breakaway oxidation at the time corresponding to ≈200-wppm hydrogen pickup. Outer-surface appearance and metallography are shown in Figure 54 for a sample oxidized for 3600 s at 985ºC, which is beyond the breakaway transition with 270±165 wppm hydrogen pickup.

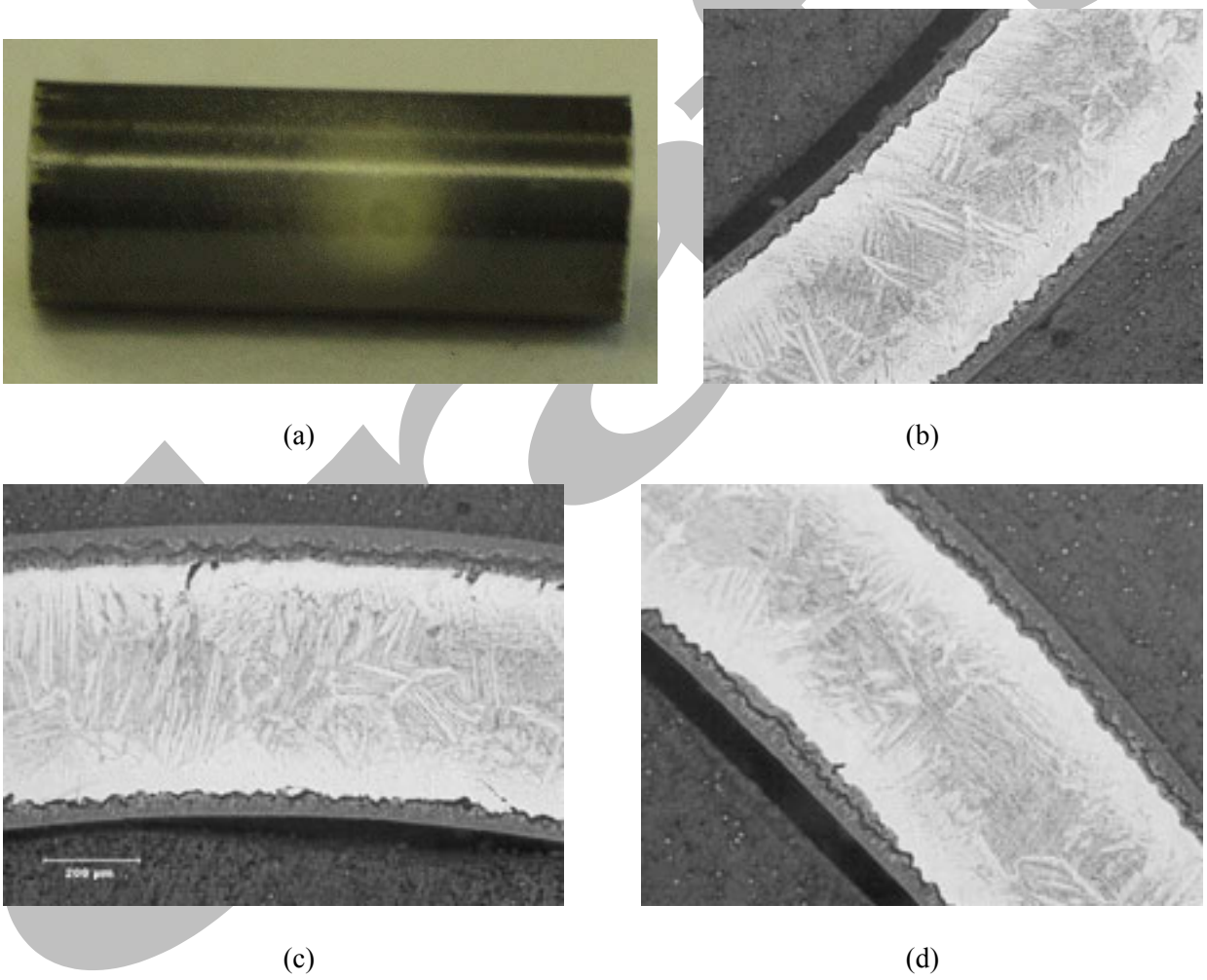

Figure 54. Surface appearance and oxide layers of ZIRLO oxidized at 985˚C for 3600 s with 270±165 wppm hydrogen pickup in a ring including the yellow area: (a) outer surface with yellow area (440 wppm H under this layer) in black matrix; (b) outer- and inner-surface oxide layers (no breakaway) under black area; (c) outer-surface (breakaway) and inner-surface (no breakaway) oxide layers under yellow area; and (d) outer- and inner-surface oxide layers under yellow, both in breakaway.

ZIRLO tubing from a different lot was supplied to ANL by Westinghouse in 2006 for breakaway oxidation studies. Dimensions (9.49-mm OD, 0.57-mm wall), oxygen content (1164 wppm) and hydrogen content (11 wppm) are comparable to those for ZIRLO-2003. The surface roughness of "ZIRLO-2006" is a little higher (0.17±0.03 μm) than the roughness of "ZIRLO-2003" (0.11±0.01 μm). Table 26 summarizes the ZIRLO breakaway oxidation results. Based on the 200-wppm hydrogen pickup criterion, the minimum breakaway time is ≈3000 s and it occurs at 970°C. The breakaway oxidation times for higher (985-1015°C) and lower (800°C and 950°C) oxidation temperatures were >3000 s. The post-oxidation ductility at 135°C for samples with significant hydrogen pickup was ≥1.7% for 215±125 wppm H pickup (may be brittle) and 5.1% for 175±145 wppm H pickup (ductile). The ring with 215±125 wppm hydrogen had hydrogen concentration of 270 wppm at one end. These results support the 200-wppm-H breakaway-oxidation criterion.

Table 26 Data Summary for ZIRLO Breakaway Oxidation Tests at 950-1015°C and 800ºC; ZIRLO-2003 samples were quenched at 800ºC; ZIRLO-2006 samples were slow cooled from the hold temperature to RT

ZIRLO Lot	T °C	Test Time[a] s	CP Wg mg/cm^2	Measured Wg, mg/cm^2	Hydrogen Content (L_h) wppm	Hydrogen Pickup (ΔC_H)[b] wppm
2006	1015	4000	15.6	15.1	30	21
2006	1000	1500	8.63	8.68	15	0
2003	1000	2440	11.1	10.8	36	33
2003	1000	3480	13.0	11.7	102	103
2006	1000	3600	13.5	11.4	68	60
2006	1000	4000	14.2	12.6	131±12	130
2006	1000	4200	14.5	14.3	608±366	630
2006	1000	5000	15.9	16.9	1246±83	1350
2006	985	3400	11.9	9.6	46	37
2006[c]	**985**	**3400**	**11.9**	**9.9**	**174±140**	**175±145**
2006	985	3600	12.3	10.0	267±158	270
2006	985	4000	12.9	11.8	847±143	890
2006[c]	**970**	**2600**	**9.5**	**7.8**	**53**	**44**
2006	970	3000	10.2	8.1	199±150	200
2006	970	3400	10.8	8.6	565±85	580
2006	950	3000	8.9	6.8	31	20
2006	800	4000	---	2.62	14	3

[a]Includes time from beginning of ramp at 300ºC to end of hold time at oxidation temperature.

[b]Hydrogen pickup (ΔC_H) is referenced to the as-fabricated sample weight:
$\Delta C_H = (1 + 5.4\times10^{-3}\ Wg)\ L_H - C_{Hi}$, where C_{Hi} is as-fabricated hydrogen content.

[c]Samples with machined scratch, ≈20-μm deep into the outer surface (see Section 3.5.2 for details).

3.4 M5

3.4.1 Post-quench ductility of 17×17 M5 oxidized at 1000ºC, 1100ºC and 1200ºC

This work was performed in parallel with the 17×17 Zry-4 and ZIRLO testing and characterization. Although the same test times were used for M5 as for Zry-4 and ZIRLO, the thicker M5 wall (0.61-mm) required new thermal benchmarks for each oxidation temperature. Also, the CP-ECR was reduced by a factor of 0.57/0.61 = 0.934 for the M5 relative to Zry-4: ECR = 1.437 Wg. M5 results are presented with the same subdivision as used for Zry-4: characterization and RT-ring-compression testing of samples two-sided oxidized at 1000ºC and 1100ºC and quenched at 800ºC; and characterization and ring-compression testing (RT and 135ºC) of samples exposed to two-sided oxidization at 1200ºC and quenched at 800ºC. Characterization included weight gain, oxide- and alpha-layer thickness measurements (metallography), microhardness and hydrogen pickup (LECO). M5 samples were oxidized to CP-predicted ECR values of 4.7, 9.3, 14.1, 16.0, and 18.8%. Additional M5 oxidation tests were conducted at 1000ºC and 1100ºC to 20-21% CP-ECR to allow a direct comparison with the Zry-4 results in terms of CP-ECR. As with the Zry-4 tests, additional M5 tests were conducted at intermediate CP-ECR values for the 1200ºC-oxidized samples to better determine the ductile-to-brittle transition ECR value for this oxidation temperature.

17×17 M5 oxidized at 1000ºC and 1100ºC

The thermal benchmarks used for the thicker M5 cladding are shown in Figure 55 for 1000ºC tests and Figure 56 for 1100ºC tests. Table 27 lists the weight gain results for M5 at 1000ºC and 1100ºC oxidation temperatures. The results at 1100ºC are in very good agreement with both the Zry-4 results and the CP-predicted weight gain. For 1000ºC oxidation, M5 exhibits significantly lower weight gain than Zry-4 and the CP-predicted weight gain for the same oxidation time. The M5 and Zry-4 weight gains are plotted in Figure 57: 1000ºC results in Figure 57a and 1100ºC results in Figure 57b.

Table 28 lists the results of the RT post-quench ductility tests. It is clear that 17×17 M5 retains post-quench ductility up to 20% CP-ECR – the limit of the test conditions – at these oxidation temperatures. The results are shown graphically in Figures 58 and 59 for 1000ºC and 1100ºC oxidation temperatures, respectively. Because of differences in weight gain between M5 and Zry-4 oxidized at 1000ºC, offset strains are plotted as functions of measured ECR (Figure 58a) and CP-ECR (Figure 58b). For oxidation at 1100ºC, both alloys exhibit essentially the same weight gain for the same test time. Thus, post-quench ductility results are plotted in Figure 59 as a function of CP-ECR only. For the 1000ºC- and 1100ºC-oxidation tests, the M5 offset strain levels out at ≈3%. It appears that M5 will retain ductility at higher CP-ECR values and higher test times until breakaway oxidation (>4100 s at 1000ºC) or significant beta-layer thinning (>20% CP-ECR at 1100ºC) occurs. For 1100ºC-oxidation, breakaway oxidation should not occur, and the beta layer does not appear to embrittle due to the low

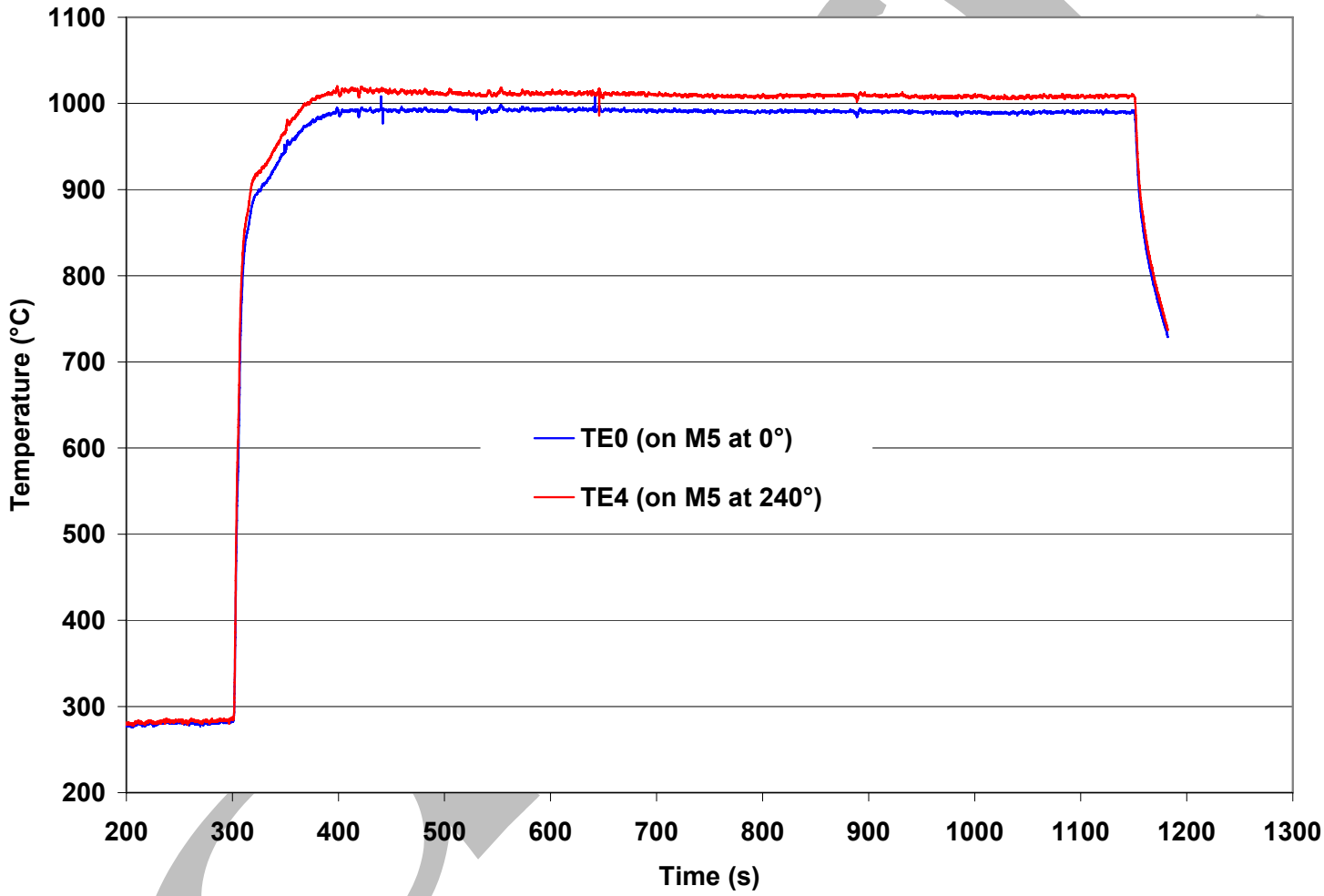

Figure 55. Thermal benchmark results for 17×17 M5 oxidation tests at 1000ºC. The cladding OD is 9.50 mm and the wall thickness is 0.61 mm. Quench at 800ºC is not shown in this figure.

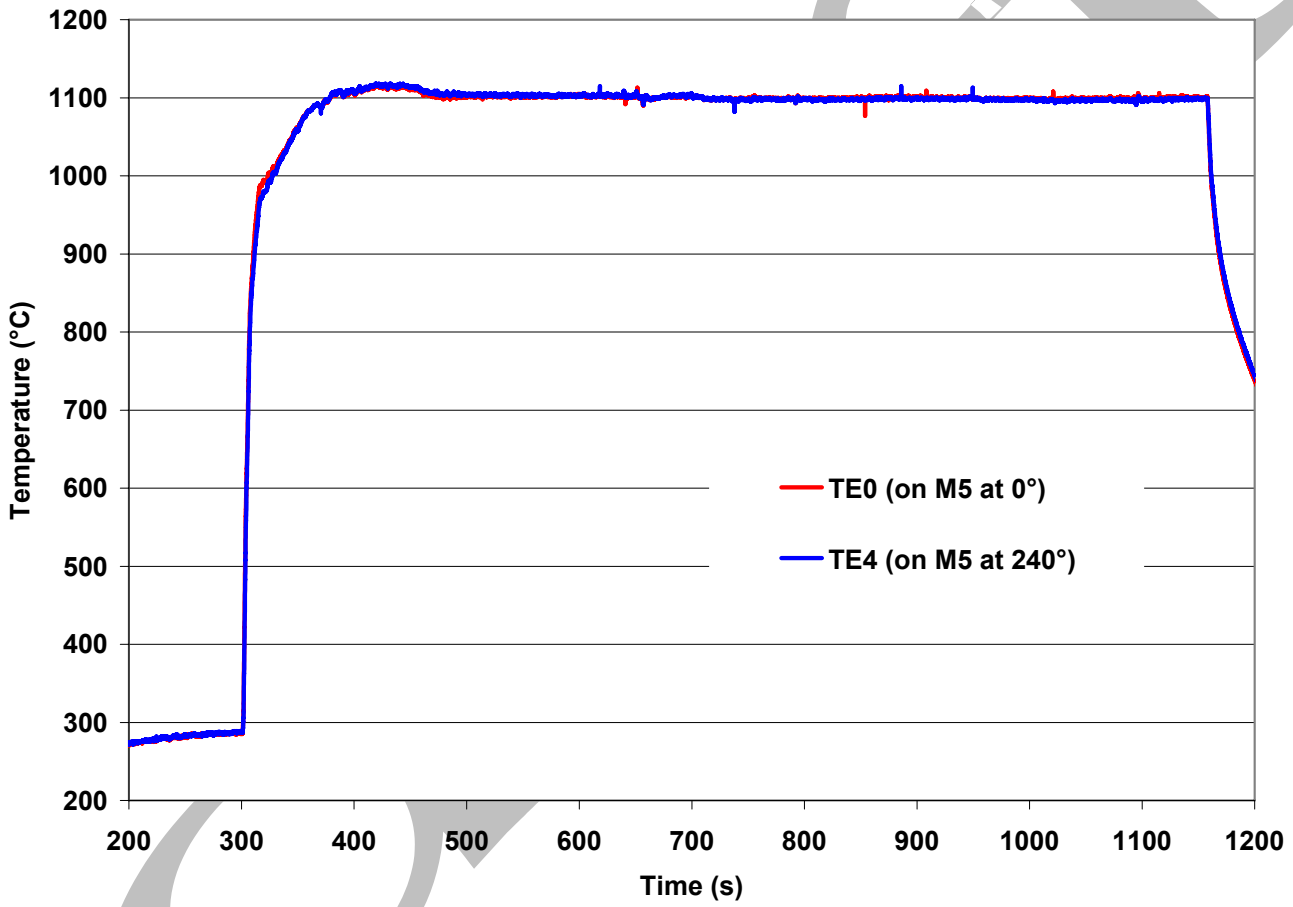

Figure 56. Thermal benchmark results for 17×17 M5 oxidation tests at 1100ºC. The cladding OD is 9.50 mm and the wall thickness is 0.61 mm. Quench at 800ºC is not shown in this figure.

Table 27 Weight Gain (Wg in mg/cm^2) and Measured ECR (%) Values for 17×17 M5 Oxidized in Steam at 1000˚C and 1100˚C and quenched at 800˚C; ECR = 1.437 Wg for the 0.61-mm-wall thickness; multiply weight gain results by a factor of 10 to convert to g/m^2.

Oxidation Temperature, ºC	Cathcart-Pawel ECR, %	Measured Weight Gain mg/cm^2	Measured ECR, %
1000	4.7	3.0	4.3
1000	9.3	5.3	7.6
1000	14.1	7.4	10.7
1000	16.0	8.0	11.6
1000	18.8	9.2	13.3
1000	20.7	8.6	12.4
1100	4.7	3.2	4.6
1100	9.3	6.4	9.2
1100	14.1	9.6	13.8
1100	16.0	11.3	16.2
1100	18.8	13.3	19.1
1100	20.4	14.3	20.6

saturation-level oxygen content. Photographs of the ring-compressed samples are shown in Figure 60a for 1000ºC-oxidized samples and 60b for 1100ºC-oxidized samples. The 5% (actually 4.3%) and 10% (actually 9.3%) CP-ECR samples oxidized at 1000ºC were intact at the maximum test displacement. The 10% (actually 9.3%) CP-ECR sample oxidized at 1100ºC was also intact.

Table 29 summarizes the results of the metallography, microhardness and hydrogen pickup measurements for M5 as compared to Zry-4. The hydrogen pickup is very low for the 1000ºC- and 1100ºC-oxidized samples. The results in Table 28 are consistent with the post-quench ductility results.

Figure 61 shows metallographic images of Zry-4 and M5 oxide layers following 1000ºC oxidation for 3364 s. From these images, it is clear that the higher weight gain for Zry-4 oxidized at this temperature is due to the thicker oxide layers grown on the Zry-4 surfaces. This is clearly an alloy effect. Also, as will be discussed in Section 3.4.2, the mild waviness of the M5 oxide layers is an early precursor to breakaway oxidation and hydrogen pickup. Table 29 shows that the outer-surface oxide layer is only 4-μm thicker than the inner-surface oxide. These results, along with the results for the sample oxidized for 4100 s, suggest that the breakaway oxidation time for M5 oxidized at 1000ºC may be significantly > 4100 s. Figure 62 shows higher magnification and better contrast for the outer-surface oxide layer grown on the M5 sample oxidized for ≈3400 s.

Figure 63 shows the comparison of metallographic results for M5 and Zry-4 oxidized at 1100ºC for 1065 s. The Zry-4 prior-beta layer includes regions of higher-oxygen alpha-phase material – alpha incursions – which precipitated during cooling from 1100ºC to 800ºC prior to quench. The M5 alpha and prior-beta layers are quite different in appearance from those of Zry-4. While oxygen is an alpha-

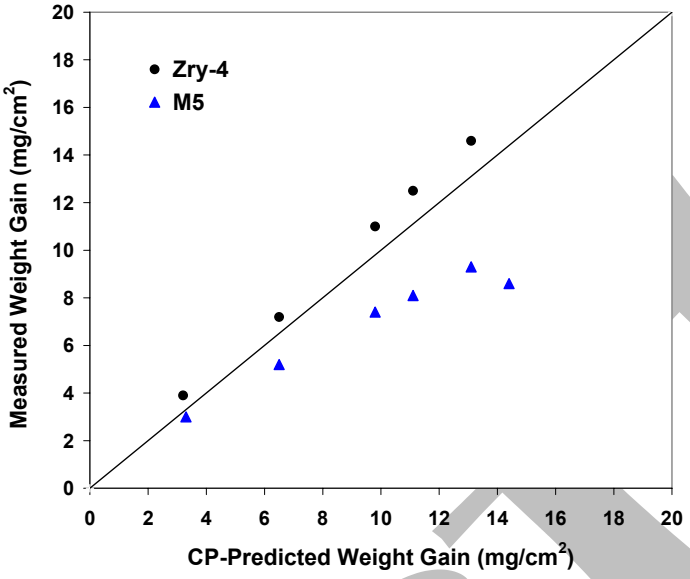

(a)

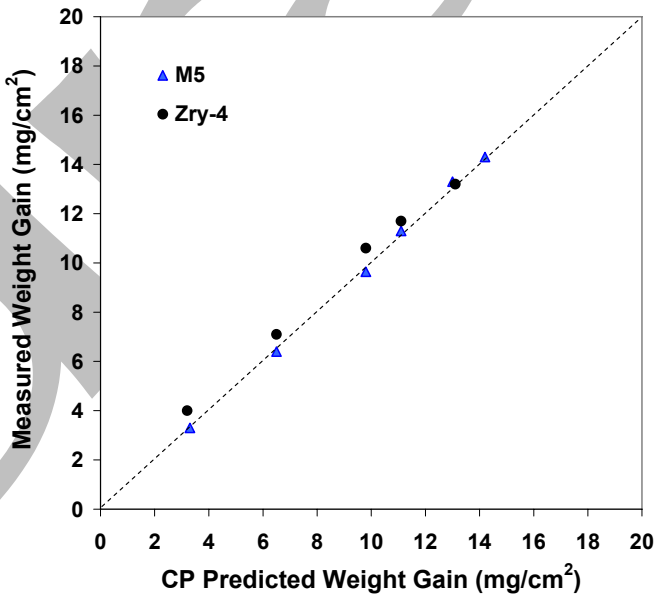

(b)

Figure 57. Comparison between weight gain data for M5 and Zry-4 and weight gain predicted by the Cathcart-Pawel (CP) correlation for samples oxidized (two-sided) in steam at 1000˚C (a) and 1100˚C (b). Test times correspond to CP-ECR values of ≈5-20%.

Table 28 Ring Compression Test Results for 17×17 M5 Samples Oxidized at 1000˚C and 1100˚C, Cooled at ≈10˚C/s to 800˚C and Quenched. ECR = 1.437 Wg for 0.61-mm-wall cladding. Displacements in the loading direction were normalized to the as-fabricated outer diameter (9.50 mm) to calculate offset strain. Tests were performed on 8-mm-long samples at RT and 0.0333 mm/s displacement rate in the Model 4505 Instron. Some confirmation tests were conducted in the new Model 5566 Instron on rings from the same oxidation samples.

Oxidation Temperature ºC	Cathcart-Pawel ECR, %	Measured ECR %	Offset Displacement mm	Offset Strain %	Confirmation Tests Model 5566 Instron
1000	4.7	4.3	>4.6	>48	---
1000	9.3	7.6	>4.9	>51	Yes
1000	14.1	10.7	3.76	40	Yes
1000	16.0	11.6	≤1.82	≤19	---
1000	18.8	13.3	0.302	3.2	---
1000	20.7	12.4	0.238	2.5	---
1100	4.7	4.6	5.4	57	---
1100	9.3	9.2	>3.7	>39	---
1100	14.1	13.8	0.71	7.5	Yes
1100	16.0	16.2	0.38	4.0	---
1100	18.7	19.1	0.17	1.8	---
1100	20.4	20.6	0.31	3.2	---

stabilizer, Nb is a beta-stabilizer. The oxygen-stabilized alpha "layer" formed at high temperature in M5 is not as uniform as the one formed in Zry-4 because Nb causes local regions of beta-stabilization even at higher oxygen contents. Precipitation of oxygen-stabilized alpha regions during cooling is also different in the M5 prior-beta layer because of the presence of Nb. Yet, even with these differences in microstructure and phase distribution, the post-quench ductility of the two alloys oxidized at 1000ºC and 1100ºC for the same duration is remarkably similar.

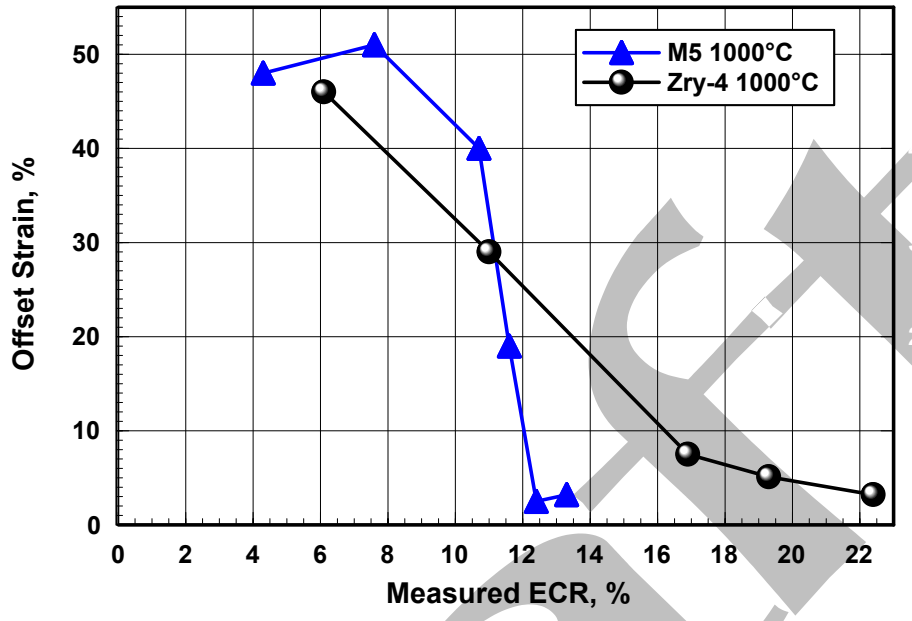

(a)

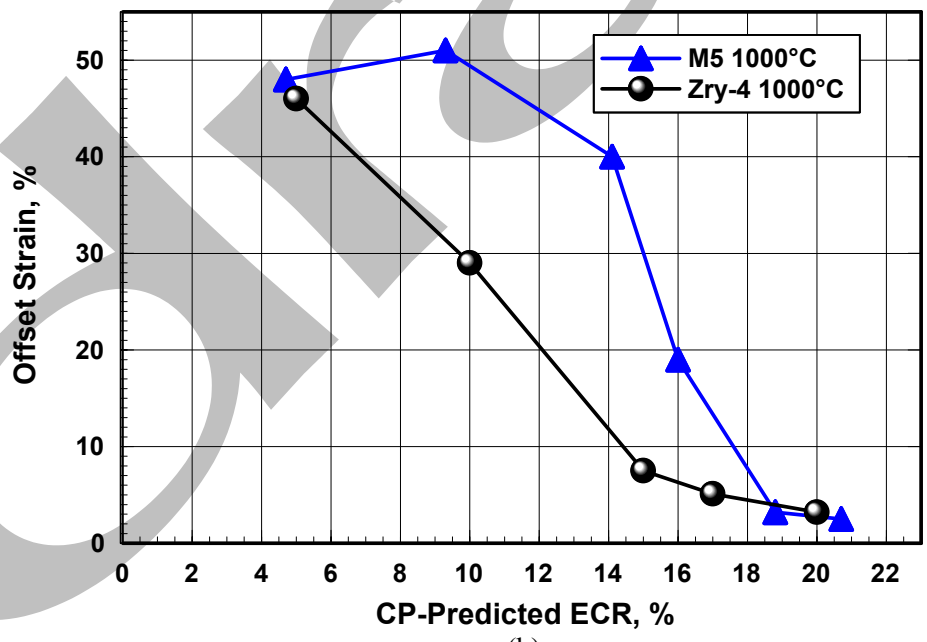

(b)

Figure 58. Post-quench ductility vs. measured (a) and CP-predicted (b) ECR for 17×17 M5 and Zry-4 oxidized in steam at 1000˚C, cooled at ≈10˚C/s to 800˚C and quenched. Offset strain was determined from results of ring-compression tests conducted at RT and 0.0333 mm/s displacement rate.

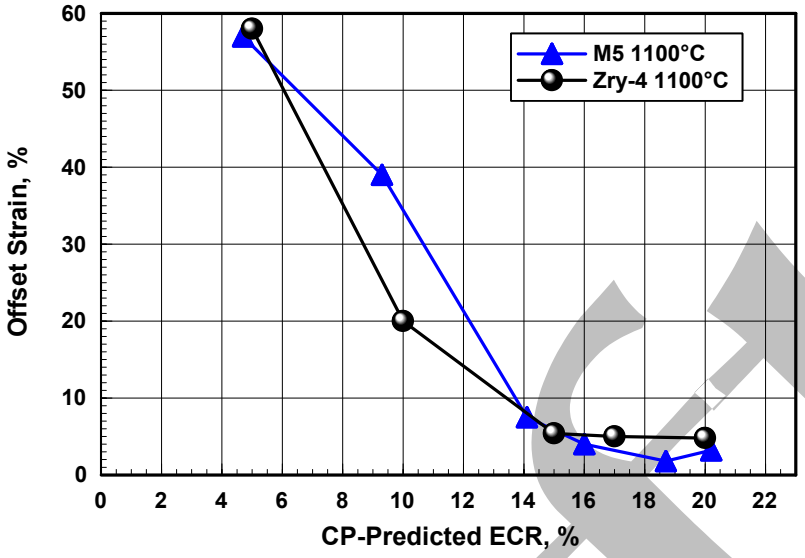

Figure 59. Post-quench ductility vs. CP-predicted ECR for 17×17 M5 and Zry-4 oxidized in steam at 1100˚C, cooled at ≈10˚C/s to 800˚C and quenched. Offset strain was determined from results of ring-compression tests conducted at RT and 0.0333 mm/s displacement rate.

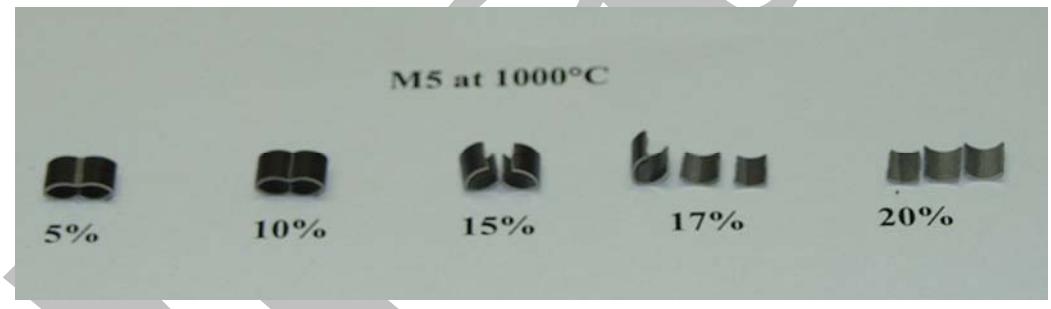

(a)

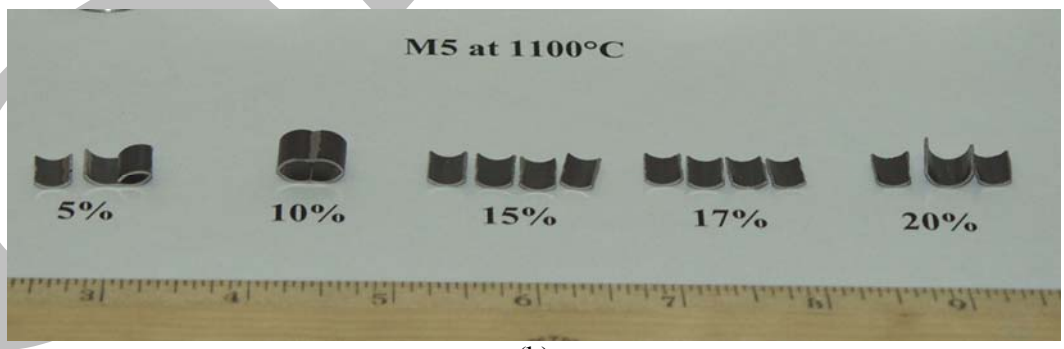

(b)

Figure 60. Post-test appearance of M5 ring-compression samples tested at room temperature and 0.0333 mm/s: (a) samples oxidized at 1000˚C; and (b) samples oxidized at 1100˚C. ECR values are calculated using the Cathcart-Pawel weight gain correlation and 0.57-mm wall. For 0.61-mm-wall M5 they should be reduced to 4.7%, 9.3%, 14.1%, 16.0% and 18.8%.

M5 exhibits very slow oxide-layer-growth and weight-gain-increase rates at 1000ºC as compared to Zry-4. Also, above ≈10% CP-ECR (≈960 s equivalent isothermal time), weight gain does not increase in a consistent manner with oxidation time or the square-root of time. For example, the ECR based on weight gain was determined to be 10.7% at 1890 s, 11.6% at 2430 s, 13.3% at 3365 s and 12.2% at 4065 s. The offset strain decreases very steeply (40% to 3%) with a small increase in measured ECR (10.7% to 13.3%) corresponding to a large increase in oxidation time (1890 s to 4065 s). Based on fundamental considerations regarding oxygen increase in the beta layer, it appears more meaningful to express M5 post-quench ductility (offset strain) as a function of CP-ECR.

Table 29 Summary of Characterization of Highly Oxidized 17×17 Zry-4 and M5 Samples after Exposure to Steam at 1000˚C and 1100˚C, Cooling at ≈10˚C/s to 800˚C and Water Quench

Oxidation Temperature ˚C	Parameter	Zry-4 20% CP-ECR	M5 18.8% CP-ECR
1000	Effective Oxidation Time, s	3364	3364
	Weight Gain, mg/cm^2	14.6	9.2
	Measured ECR, %	22.4	13.3
	RT Offset Displacement, mm	0.31	0.31
	RT Offset Strain, %	3.2 (ductile)	3.2 (ductile)
	Hydrogen Content, wppm	19	26
	Hydrogen Pickup, wppm	15	22
	OD/ID Oxide Thickness, μm	83/82	36/32
	Microhardness within Middle 0.2 mm, DPH	290-420	300-430
1100	Effective Oxidation Time, s	1065	1065
	Weight Gain, mg/cm^2	13.2	13.3
	Measured ECR, %	20.3	19.1
	Offset Displacement, mm	0.46	0.17
	RT Offset Strain, %	4.8 (ductile)	1.8 (borderline*)
	Hydrogen Content, wppm	22	17
	Hydrogen Pickup, wppm	19	12
	OD/ID Oxide Layer Thickness, μm	70/68	72/62
	Microhardness within Middle 0.2 mm, DPH**	240-470	260-400

*New sample oxidized to higher EP-ECR (20.4%) was ductile (3.2% offset strain).

**Includes oxygen-stabilized alpha needles (M5) and alpha incursions (Zry-4) in prior-beta layer.

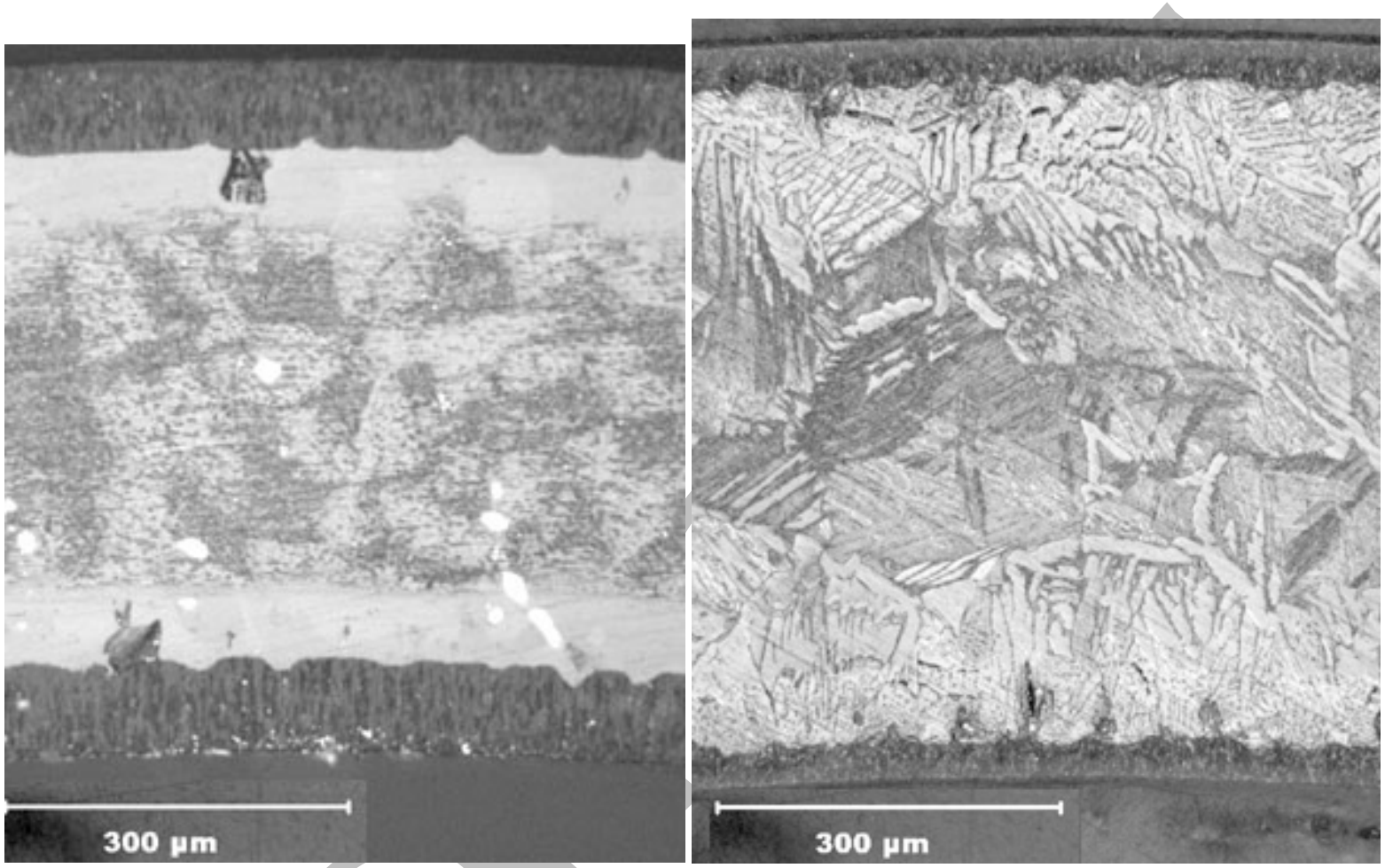

(a) Zry-4 (b) M5

Figure 61. Metallography of as-polished Zry-4 (a) and M5 (b) oxidized in steam at 1000˚C for ≈3360 s, cooled at ≈10ºC/s to 800˚C and water quenched. Measured ECR values are 22.4% for Zry-4 and 13.3% for M5.

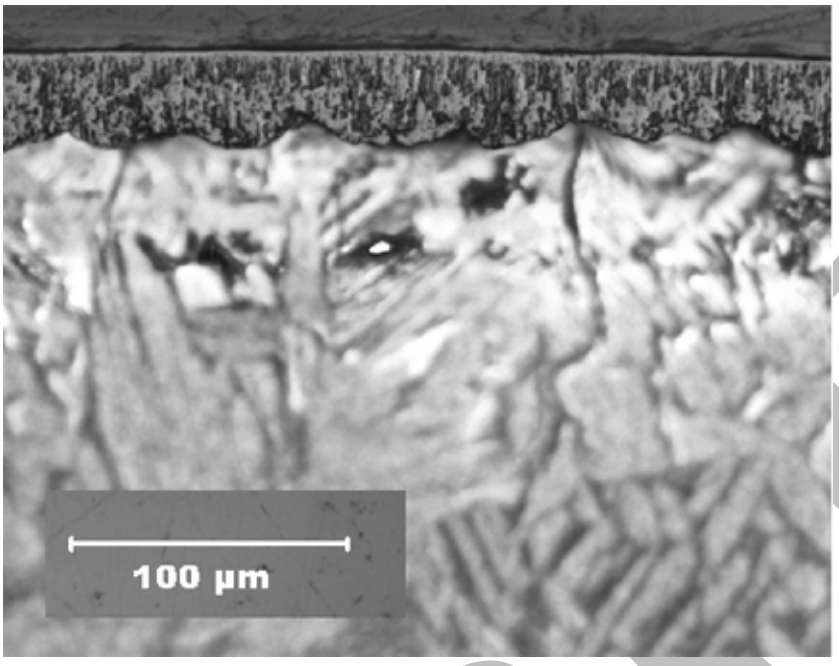

Figure 62. High-magnification image of etched M5 outer-surface oxide and alpha layers following oxidation at 1000ºC for 3360 s. The outer-surface oxide layer is tetragonal, but the wavy oxide-metal interface is a precursor to breakaway oxidation.

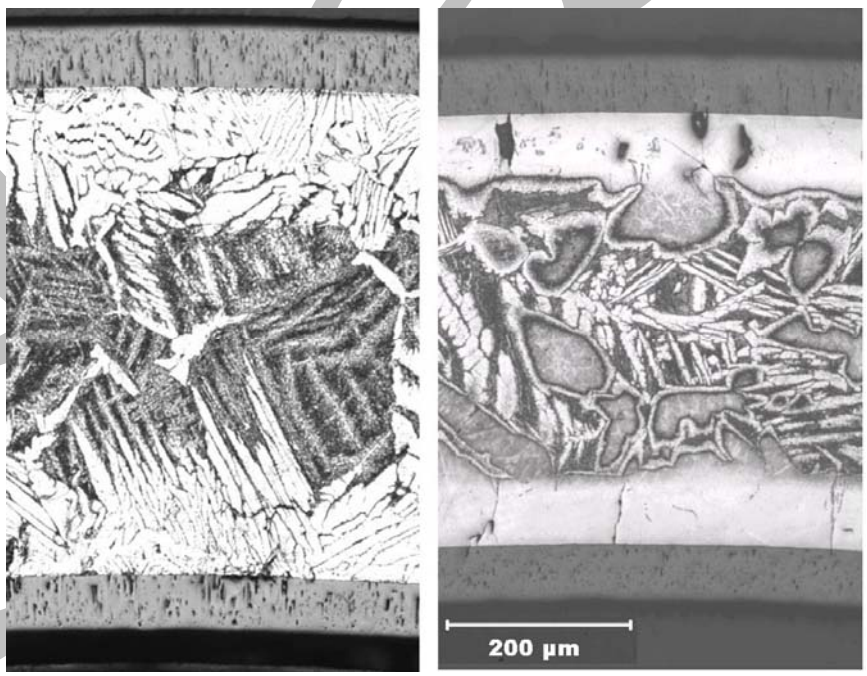

(a) M5 (b) Zry-4

Figure 63. Metallography of etched M5 (a) and Zry-4 (b) oxidized in steam at 1100˚C for ≈1070 s, cooled at ≈10˚C/s to 800˚C, and water quenched. Measured ECR values are 19.1% for M5 and 20.3% for Zry-4.

17×17 M5 oxidized at 1200ºC

In parallel with the testing of Zry-4, numerous tests were conducted with 17×17 M5 oxidized at 1200±5ºC to determine the ductile-to-brittle transition CP-ECR at RT and 135ºC. Figure 64 shows the thermal-benchmark results for the first test train. Because the differences in ramp rates are small for the 0.61-mm M5 vs. the 0.57-mm Zry-4 and ZIRLO, the thermal benchmark results shown in Figure 21 were used for more recent tests with M5. Although the temperature ramps are different, these have little effect on the long-time tests used to determine the high transition CP-ECR at 135ºC. Also, all tests were stopped after the first significant load drop to allow a measure of the permanent strain based on diameter change in the loading direction.

The weight gain results (expressed in terms of measured ECR) and the post-quench ductility results are summarized in Table 30. Figure 65 shows the measured M5 and Zry-4 weight gains, as compared to the CP-predicted weight gains. The experimental results for both alloys are in excellent agreement with each other and with the predicted values

M5 appears to embrittle at room temperature after oxidation at 1200ºC to ≈12% CP-ECR and quench. This is confirmed by both the offset strain-criterion (<2%) and the permanent-strain criterion (<1%) for embrittlement. The enhancement of ductility with the increase in test temperature is quite pronounced. Based on the offset and permanent strain data, the ductile-to-brittle transition CP-ECR is ≈20% at 135ºC. The variations of offset and permanent strains with CP-ECR are shown in Figures 66a and 66b, respectively, for the RT and 135ºC test conditions. Figure 67 is a comparison between the post-quench ductility (offset strain) at 135ºC for M5 and Zry-4 vs. CP-ECR following oxidation at 1200ºC and quench at 800ºC. At CP-ECR values <17%, M5 has significantly higher post-quench ductility than Zry-4.

Table 30 summarizes the characterization results for 17×17 Zry-4 and M5 oxidized at 1200ºC for times equivalent to 13% and 20% CP-ECR (based on 0.57-mm-wall cladding) and quenched at 800ºC. As expected, the hydrogen pickup is very low. Also, there is excellent agreement between the inner-surface and outer-surface oxide layer thickness, indicating adequate steam flow at the inner surface. The microhardness results support the post-quench ductility results. Based on the room-temperature microhardness values, one would expect M5 to retain post-quench ductility at ≤20% CP-ECR at the elevated test temperature of 135ºC. The microstructures across the cladding wall are shown in Figure 68 for Zry-4 and M5 oxidized at 1200ºC to ≈20% CP-ECR. As with the lower oxidation temperatures, Zry-4 has well defined oxygen-stabilized alpha layers grown at 1200ºC, while the presence of Nb in M5 results in a less clear distinction of this layer. The microhardness indents for Zry-4 and M5 oxidized to ≈13% CP-ECR are shown in Figures 69a and 69b, respectively.

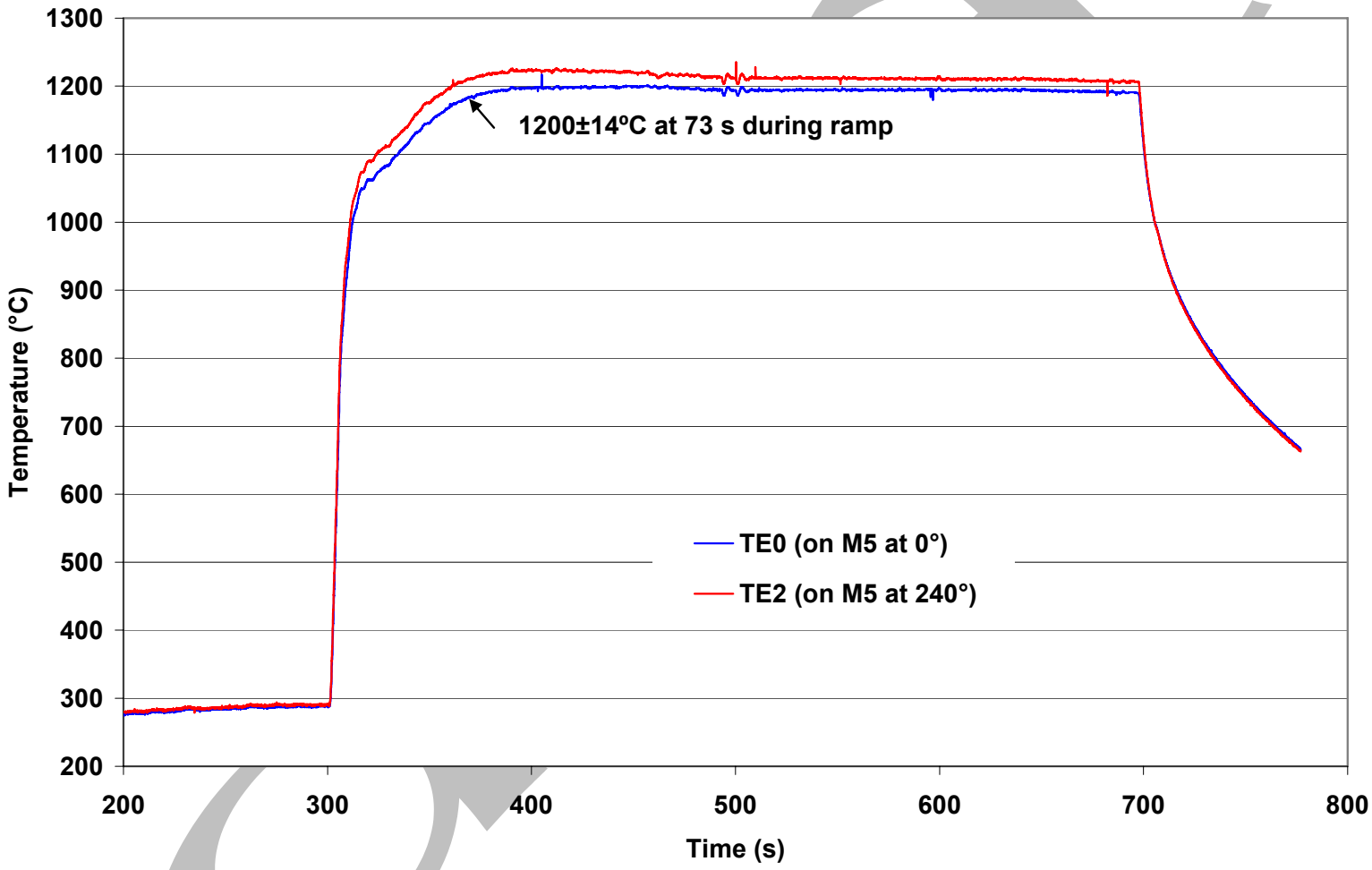

Figure 64. Thermal benchmark results for 1st test train for 17×17 M5 oxidation tests at 1203±8ºC. The cladding OD is 9.50 mm and the wall thickness is 0.61 mm. Quench at 800ºC is not shown in this figure.

Table 30 Ring Compression Test (RCT) Results for 17×17 M5 Cladding Oxidized at 1200˚C, Cooled at ≈13˚C/s to 800ºC, and Quenched. ECR = 1.437 Wg for 0.61-mm-wall thickness. Tests were performed on ≈8-mm-long samples at RT and 135˚C and at 0.0333 mm/s displacement rate. Displacements in the loading direction were normalized to the as-fabricated outer diameter (9.50 mm) to calculate offset and permanent strains.

Test Conditions		ECR %		Plastic Displacement, mm		Plastic Strain, %	
RCT T, ˚C	Test Time[a], s	CP	Meas.	Offset	Permanent	Offset	Permanent
RT	58	4.5	4.0	>5.35	>5.0	>56	>53
RT 135	132 132	9.1 9.1	9.1 9.1	0.32 >4.8	0.13 >4.8	3.4 >51	1.6 >51
RT	203	12.1	13.1	0.17	0.09	1.8	0.9
135[b] **135[b]**	**226** **226**	**13.0** **13.0**	**13.6** **13.6**	**1.43** **1.20**	**1.13** **0.84**	**15.0** **12.6**	**11.9** **8.8**
RT 135	248 248	14.1 14.1	13.8 13.8	0.16 1.73	0.07 1.25	1.7 18.2	0.7 13
RT 135 **135[b]** **135[b]**	308 308 **318** **318**	16.0 16.0 **16.0** **16.0**	15.7 15.7 **17.4** **17.4**	0.13 1.02 **0.52** **0.52**	0.06 --- **0.27** **---**	1.4 10.7 **5.4** **5.4**	0.6 --- **2.8** **---**
RT	428	18.7	18.8	0.195	0.06	2.0	0.6
135[b] **135[b]**	**480** **480**	**19.9** **19.9**	**21.4** **21.4**	**0.36** **0.29**	**0.10** **0.10**	**3.8** **3.1**	**1.0** **1.0**

[a]Includes time for ramp from 300ºC and hold time.

[b]**Tests were conducted with current test train (see Figure 21 for thermal history).** Most other test results were generated with the initial test train (see Figure 64 for thermal history).

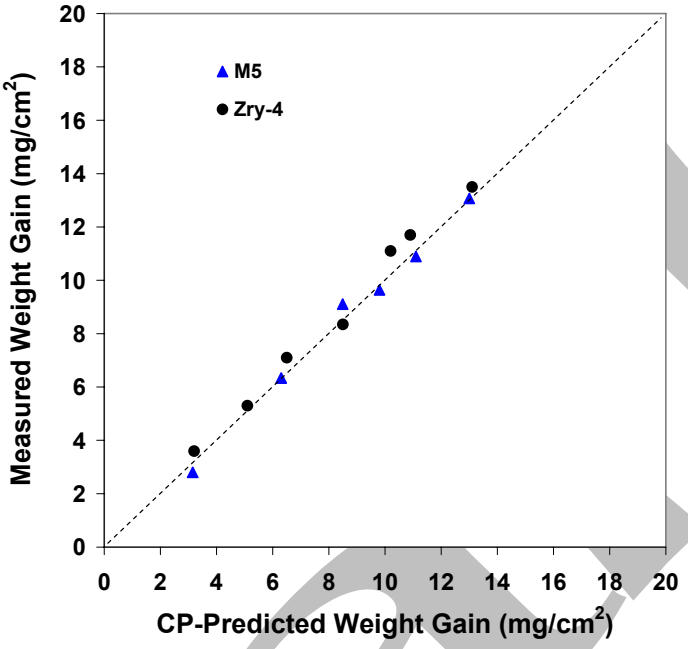

Figure 65. Comparison between weight gain data for M5 and Zry-4 and CP-predicted weight gain for samples oxidized (two-sided) in steam at 1200˚C and quenched at 800˚C.

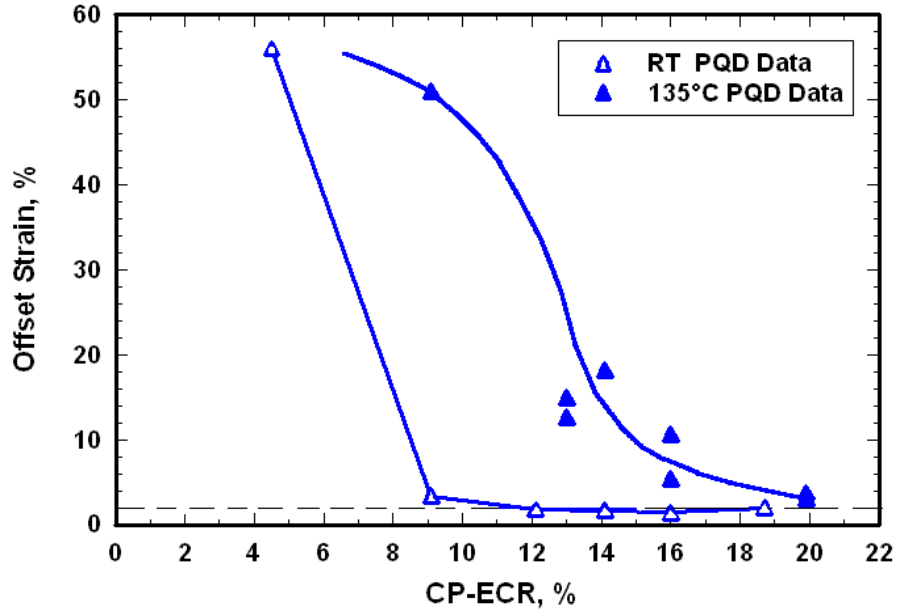

Figure 66a. Offset strain vs. CP-ECR for 17×17 M5 oxidized at 1200ºC, cooled at ≈13˚C/s to 800ºC, quenched and ring-compressed at 135ºC.

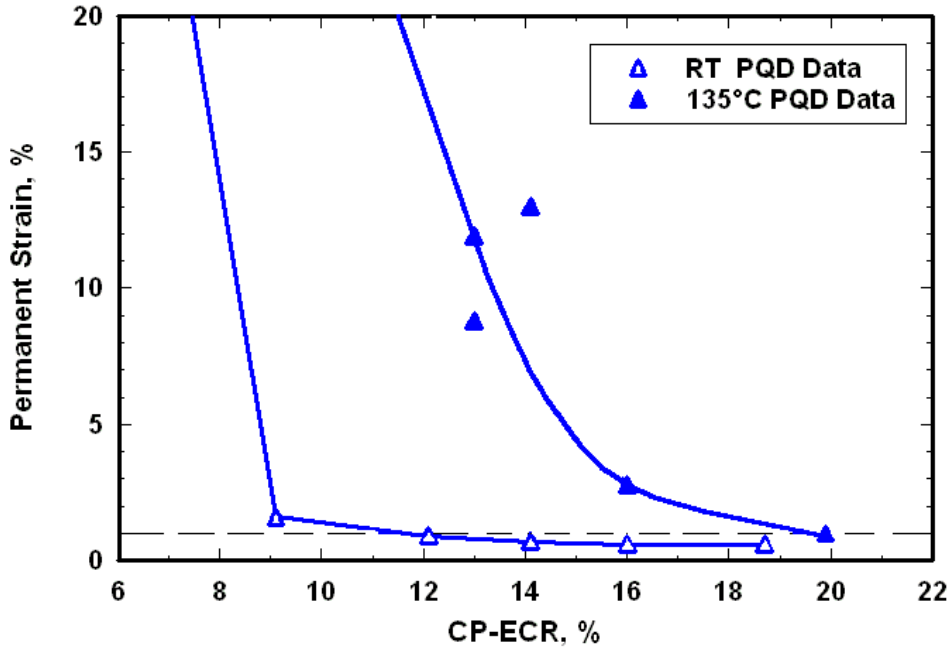

Figure 66b. Permanent strain vs. CP-ECR for 17×17 M5 oxidized at 1200ºC, cooled at ≈13˚C/s to 800ºC, quenched and ring-compressed at 135ºC.

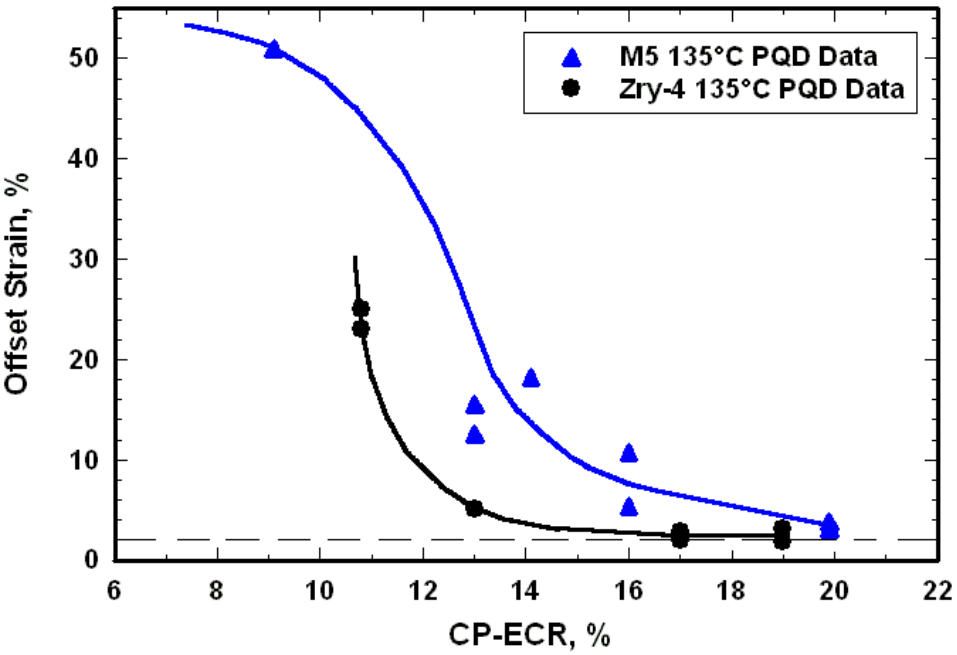

Figure 67. Offset strain vs. CP-ECR for 17×17 M5 and Zry-4 oxidized at 1200ºC, cooled at ≈13˚C/s to 800ºC, quenched and ring-compressed at 135ºC.

Table 31 Summary of Characterization of 17×17 Zry-4 and M5 Samples after Exposure to Steam at 1200˚C for Durations of 166 and 400 s, Cooling at ≈13˚C/s to 800˚C and Water Quench

Parameter	Zry-4		M5	
	20% ECR	13% ECR	18.7% ECR	12.1% ECR
Effective Time, s	400	166	400	166
Weight Gain, mg/cm^2	13.5	8.35	13.1	9.11
Measured ECR, %	20.8	12.8	18.8	13.1
RT Offset Displacement, mm	0.05	0.09	0.20	0.11
RT Measured Permanent Displacement, mm	0.04	0.07	0.06	0.09
RT Permanent Strain, %	0.4	0.7	0.6	0.9
RT Ductility	≤0.4 (brittle)	≤0.7 (brittle)	≤0.6 (brittle)	≤0.9 (brittle)
Hydrogen Content, wppm	17	low	19	low
Hydrogen Pickup, wppm	13	low	14	low
OD/ID Oxide Thickness, μm	68/66	42/41	68/61	46/40
Prior-Beta-Layer Thickness, μm	266	419	≤360	≈442
Microhardness, DPH Oxide Layers Alpha Layers Prior-Beta Layer*	 570-960 530-730 280-600	 600-770 600-700 260-360	 650-780 580-850 280-450	 580-680 680-880 300-410

*Range includes microhardness values of oxygen-rich alpha needles (M5) and alpha incursions (Zry-4) in this layer.

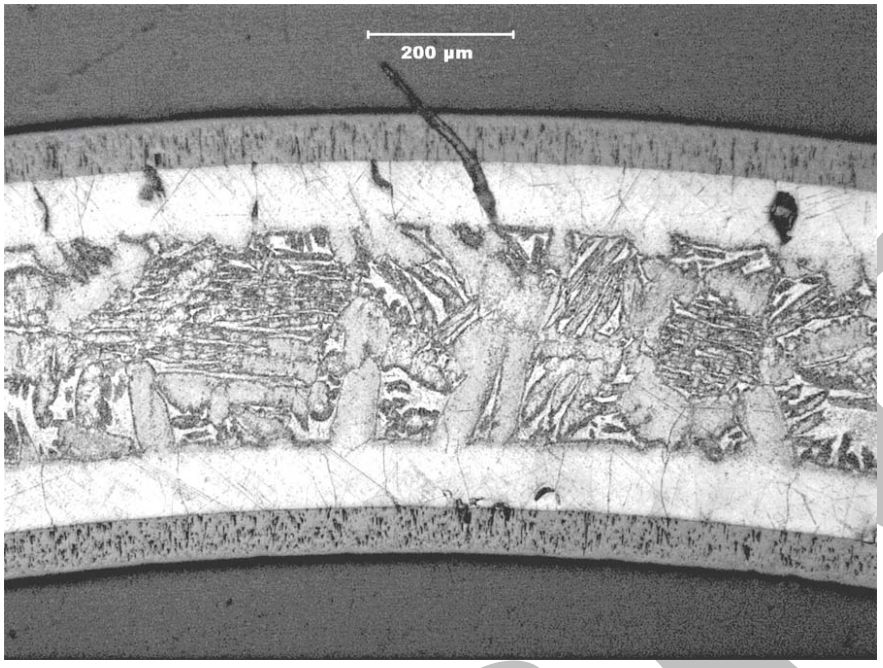

(a) Zry-4

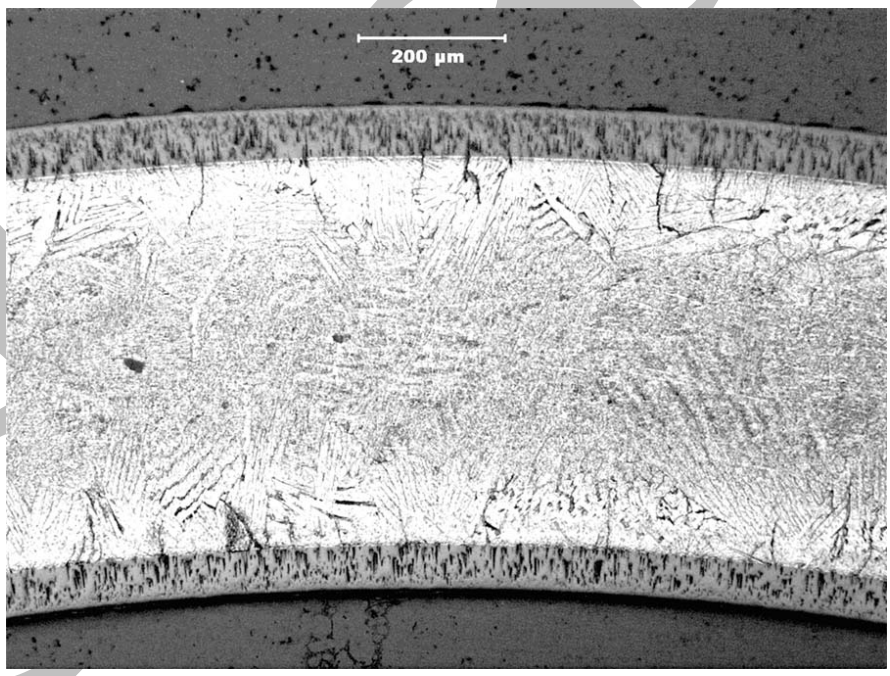

(b) M5

Figure 68. Metallography of etched Zry-4 (a) and M5 (b) oxidized in steam at 1200˚C for ≈400 s, cooled at ≈13˚C/s to 800˚C and water quenched. Measured ECR values are 20.8% for Zry-4 and 18.8% for M5.

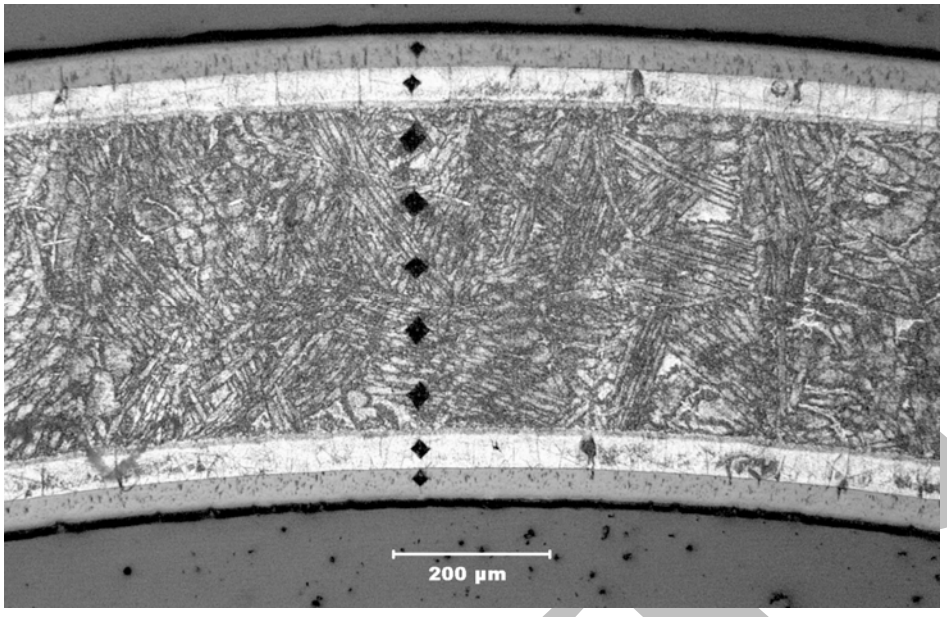

(a) Zry-4

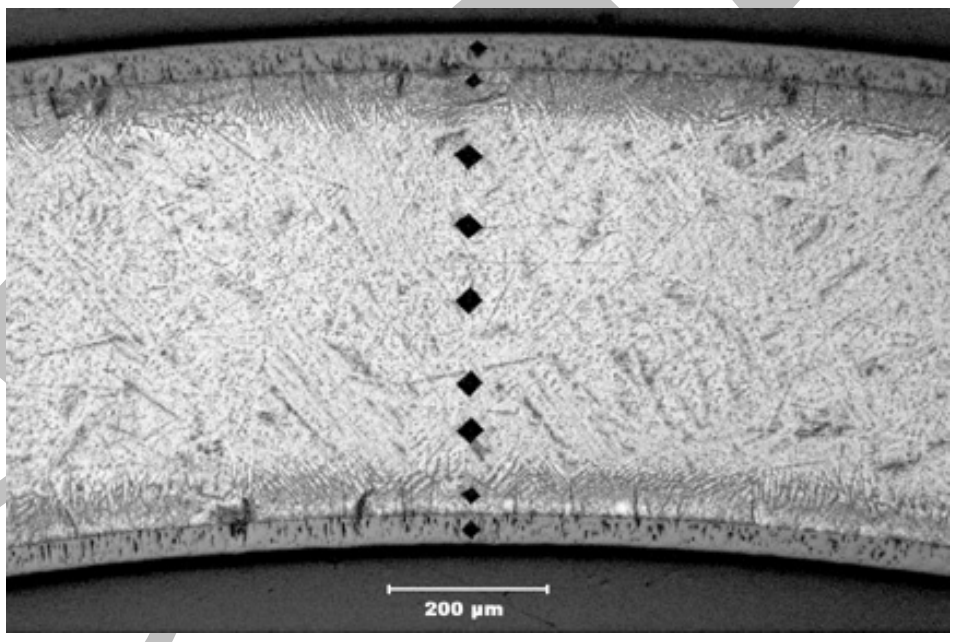

(b) M5

Figure 69. Metallography and microhardness indents across the radius of 17×17 Zry-4 (a) and M5 (b) oxidized at 1200˚C to 12-13% CP-ECR. The measured ECR values are 12.6% for Zry-4 and 13.1% for M5. Samples were quenched at 800˚C following cooling at ≈13˚C/s.

3.4.2 Breakaway oxidation time for 17×17 M5 samples oxidized at 800-1000ºC

Based on the work of Mardon et al. [21] the breakaway oxidation time for M5 corresponding to ≈200-wppm H pickup is ≈6400 s. However, M5 exhibits very slow growth rate of inner- and outer-surface oxide layers at 1000ºC, which may prolong breakaway oxidation. Also, breakaway-oxidation times at 975-1025ºC or at lower temperatures have not been reported in the open literature. {The ANL tests on M5 breakaway oxidation parallel those for Zry-4 and ZIRLO with regard to oxidation temperatures of 1000±15ºC and 800ºC. Text to be inserted here and results to be inserted In Table 32.}

Table 32 Data Summary for M5 Breakaway Oxidation Tests at 1000±15°C and 800ºC; test times are from beginning of ramp at 300°C to the end of the hold time

Cooling	T °C	Test Time s	CP Wg mg/cm^2	Measured Wg, mg/cm2	Hydrogen Content (L_h) wppm	Hydrogen Pickup (ΔC_H)[a] wppm
Q at 800°C	1000	3450	13.1	9.2	26	22
Q at 800°C	1000	4100	11.1	10.8	13	8
SC	1000	6000				
SC	985	6000				
SC	1015	6000				
SC	800	6000				

[a]Hydrogen pickup (ΔC_H) is referenced to the as-fabricated sample weight:
$\Delta C_H = (1 + 5.4\times10^{-3}\ Wg)\ L_H - C_{Hi}$, where C_{Hi} is as-fabricated hydrogen content.

3.5 Effects of surface conditions on cladding performance

Breakaway oxidation is an instability phenomenon that leads to transformation from the tight-tetragonal-oxide phase (black) to the cracked-monoclinic-oxide phase (gray). The time-at-temperature and temperature at which the breakaway occurs may be dependent on cladding surface conditions (roughness, scratches, and chemistry) and near-surface chemistry. The tetragonal oxide phase of ZrO_2 is not thermodynamically stable at temperatures below ≈1150ºC. However, this black oxide phase is observed on cladding surfaces following steam oxidation at temperatures much less than 1150ºC. It is even observed as part of the tight sub-micron corrosion layer adherent to the cladding surface grown at normal reactor operating temperatures. Compressive stress and hypostoichiometry [$ZrO_{(2-x)}$] appear to stabilize the tetragonal phase at temperatures much lower than the phase-transition temperature. As the density of the oxide is lower than the cladding metal, the volume expansion during oxide formation leads to compressive stress in the oxide. Also, as oxidation progresses in steam at high temperature, oxygen continues to diffuse from the oxide to the oxygen-stabilized alpha layer, leaving an oxygen gradient in the oxide and hypostoichiometric oxide at the Zr-alloy surface. Conversely, irregularities in surface geometry can result in alternating regions of compressive and tensile stresses. According to Leistikow and Schanz [19,20], such irregularities along the metal-oxide surface are a precursor to tetragonal-to-monoclinic transformation and breakaway oxidation.

Surface and near-surface chemistry can play a significant role in the breakaway oxidation phenomenon. Cladding impurities and/or alloy constituents can induce early monoclinic-oxide formation. They can also delay the transformation. In general, impurities and alloy constituents in the oxide layer with valences less than +4 (e.g., Al^{+3}, Cr^{+3}, Ca^{+2}, Mg^{+2}) help preserve hypostoichiometry, while elements with valences greater than +4 (e.g., Nb^{+5}) tend to drive the oxide toward ZrO_2 and the monoclinic phase. Also, fluorine surface impurities from the pickling (i.e., etching) process are known to induce monoclinic

oxide formation. Extensive studies have been performed by Cheng and Adamson [23] and Cheng et al. [24] on the effects of fluorine-impurities on nodular corrosion in BWR cladding and early breakaway oxidation time.

In this section, the effects on breakaway oxidation of surface roughness, surface scratches, and surface chemistry are examined. HBR-type Zry-4 and modern Western cladding alloys are discussed in 3.5.1, while E110 is discussed in 3.5.2.

3.5.1 Effects of surface conditions on HBR-type Zry-4 and modern cladding alloys

Surface roughness

The HBR-type 15×15 Zry-4 (1990s vintage) exhibits breakaway oxidation at ≈3800 s, while the belt-polished 15×15 Zry-4 has a breakaway oxidation time of ≈5000 s at ≈1000ºC oxidation temperature. Based on ANL measurements and observations, the only significant difference between these Zry-4 claddings is the surface roughness (0.3 μm for HBR and 0.1 μm for BP). Although it is certainly possible that surface chemistry may differ, it appears that high surface roughness has a significant effect on reducing breakaway oxidation time at ≈1000ºC.

Surface scratches and abrasions

In the process of handling cladding during fueling, end-cap welding, insertion into the fuel assembly, and core loading, scratches and abrasions will occur on the cladding outer surface. Such scratches could reduce the breakaway-oxidation time for fresh cladding in the reactor core. Vendors have a "design-basis" scratch depth, which is based on a stress criterion given that the scratch will locally thin the cladding wall and increase the hoop stress for a given pressure loading. For Western cladding alloys, the depth of the design-basis scratch is <10% of the wall thickness, which is <57 μm. Generally, vendors use ≈2 mils (≈50 μm) as the design-basis scratch depth.

The as-fabricated cladding segments received by ANL did not have "normal" or "design-basis" scratches although they did have mild abrasions. Figure 70 shows images of the belt-polished 15×15 Zry-4 outer surface: (a) smooth; and (b) local abrasions. This smooth exterior is characteristic of most of the belt-polished 15×15 Zry-4 cladding segments received by ANL, as well as the belt-polished 17×17 PWR and 10×10 BWR alloys.

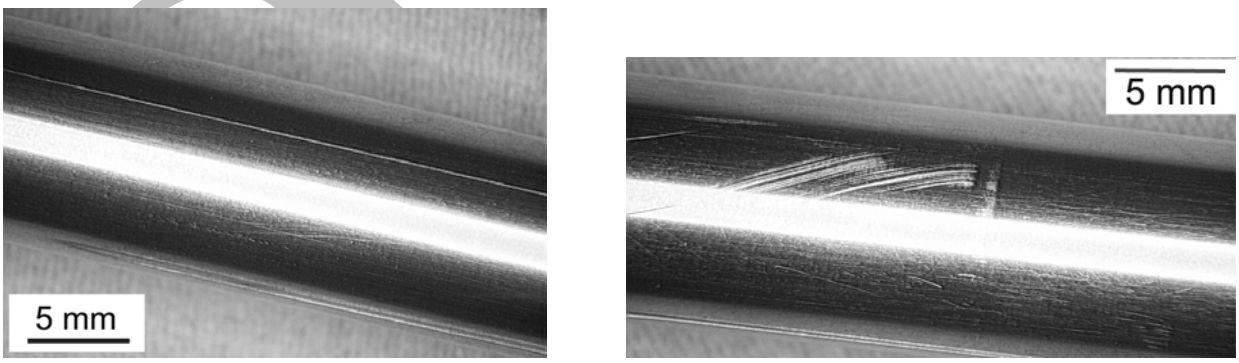

(a) (b)

Figure 70. Outer surface of belt-polished 15×15 Zry-4: (a) smooth exterior; and (b) local region of surface abrasions.

A sample was sectioned from the mildly abraded region and oxidized for 5000 s at 986±12ºC. The outer surface was lustrous black and the hydrogen pickup was negligible, indicating that mild abrasions do not have a significant effect on breakaway-oxidation time of Zry-4 within the range of times tested.

The HBR sample (HBRU#96) had visible outer-surface scratches prior to testing. Following oxidation at 985ºC for 3600 s, the measured weight gain was only 3% higher than the CP-predicted weight gain and the outer-surface was black. However, the hydrogen content and pickup were 186±75 wppm and 174±80 wppm, respectively. The oxidized sample was sectioned in the region of longitudinal scratches and examined by optical microscopy. The results at four circumferential locations of the cross-section are shown in Figure 71. The 0º (top) and 180º (bottom) sectors are in breakaway oxidation, while the 90º and 270º are not. Based on the appearance of the outer surface and on the metallographic results, it is clear that local breakaway oxidation and hydrogen pickup occurred in the scratched region. The results suggest that the breakaway oxidation time could be ≈200 s less at ≈1000ºC for fuel rods clad in scratched HBR-type Zry-4 at the beginning of reactor operation.

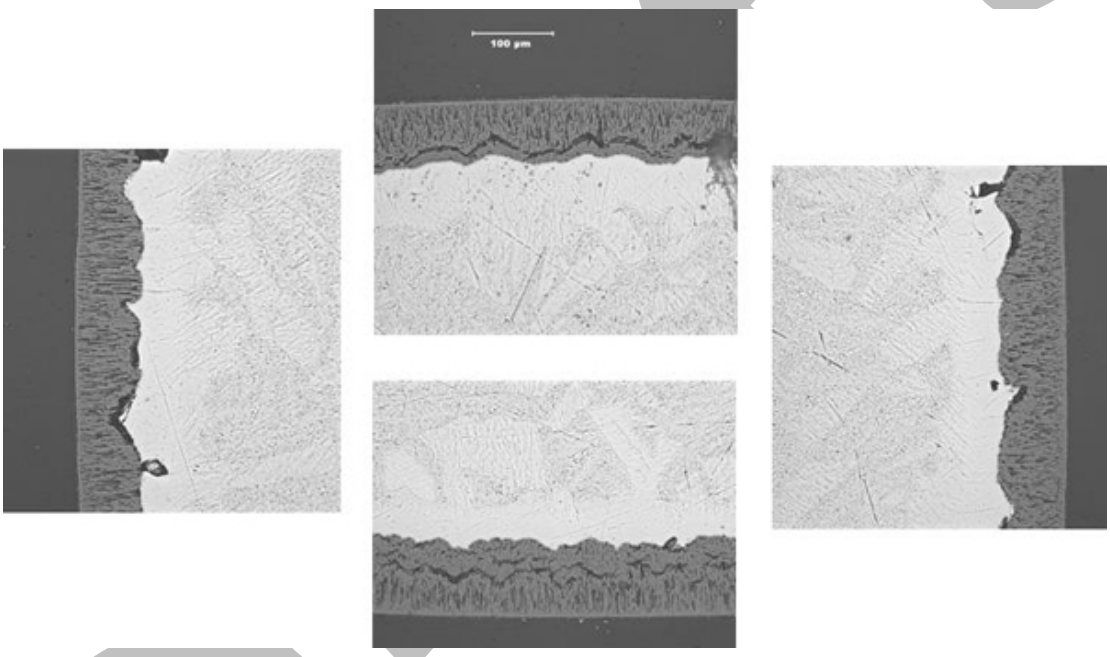

Figure 71. Metallographic images in the scratched region of an HBR-type 15×15 Zry-4 sample (HBRU#96) following oxidation at 985±12ºC for 3600 s. The top and bottom sectors are in breakaway oxidation, while the left and right sectors are not. The sample was prepared from a region of the cladding with scratches observed during pre-test and post-test characterization.

A scratch depth of ≈20 µm was machined into the outer surface of belt-polished 17×17 ZIRLO along a length of about 2 inches. The scratch geometry is shown in Figure 72 cladding cross section. The scratched samples were oxidized for 985ºC for 3400 s and at 970ºCfor 2600 s (see Table 26 for results). Breakaway oxidation did initiate along the scratched regions as shown in Figures 73 and 74. For the scratched sample oxidized at 985ºC for 3400 s, the midplane hydrogen pickup was 175±145 wppm, as compared to only 37 wppm for the smooth sample oxidized under the same conditions. Underneath the yellow oxide shown in Figure 74a, the hydrogen content was as high as 400 wppm. Given that the

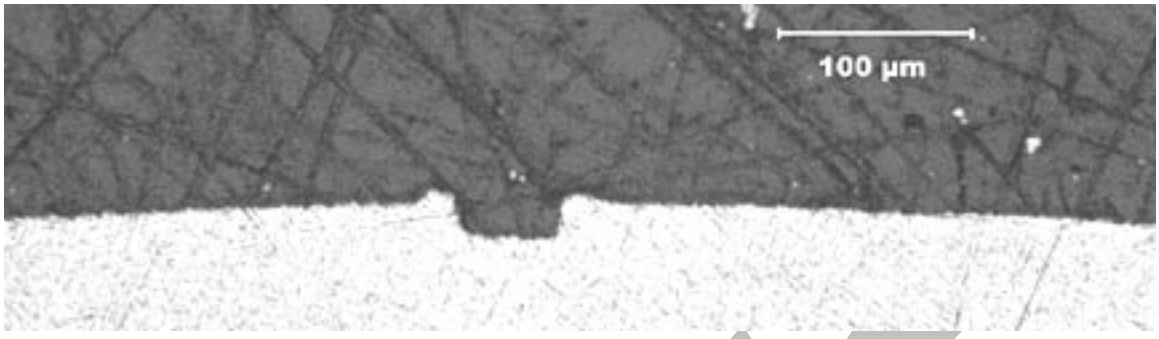

Figure 72. Cross section of ZIRLO cladding with machined scratch ≈20-µm deep into outer-surface.

Figure 73. Outer surface of scratched ZIRLO sample following oxidation at 985ºC for 3400 s. The local hydrogen pickup under the yellow surface is 440 wppm.

Figure 74. Outer surface of scratched ZIRLO sample following oxidation at 970ºC for 2600 s. The local hydrogen pickup under the yellow surface is 120 wppm.

breakaway oxidation time is estimated to be 3500±100 s for smooth ZIRLO oxidized at 985ºC, the 20-μm-deep scratch in the ZIRLO outer surface appears to reduce that time by only 100-200 s. For the scratched ZIRLO sample oxidized at 970ºC for 2600 s, the average hydrogen pickup at the midplane was only 44 wppm, with a local hydrogen pickup under the yellow oxide of 120 wppm. Again it appears that the scratch reduced the breakaway-oxidation time by ≈200 s relative to smooth cladding.

3.5.2 Effects of surface conditions on E110 tubing and cladding

Although Russian E110 cladding is not used in the U.S., it was added to the ANL test program for the purposes of gaining some understanding as to why this particular Zr-1Nb alloy experiences such early breakaway oxidation time and ductility loss for 1000-1100ºC steam-oxidation temperatures. Breakaway oxidation times reported in the literature for E110 are as low as 500 s based on ductility loss, >200-wppm hydrogen pickup, weight-gain-rate increase or visual appearance with correspondingly low CP-ECR values. However, in reviewing the literature for E110, it was very difficult to compare data sets because oxidation test methods varied considerably (e.g., heating and cooling rates) and E110 chemistry, thermomechanical treatment, and surface finish varied considerably.

Concurrent with the ANL E110 study, an extensive study of E110 was being conducted at the Russian Research Center "Kurchatov Institute" (RRC-KI) and the Research Institute of Atomic Reactors (RIAR). The RRC-KI/RIAR study was sponsored by NRC, ISRN and TVEL (E110 vendor). Close collaboration was maintained between the ANL program and the Russian program, particularly with regard to test-sample oxidation and post-oxidation ductility-determination methodologies. The Russian program results are well documented in NUREG/IA-0211 [2]. In some cases, efforts were duplicated to confirm results. For most of the research, ANL concentrated on the evolution of E110 breakaway oxidation at 1000ºC – particularly the effects of surface roughness, surface scratches, and surface chemistry – while the Russian program, which had access to numerous heats of E110, concentrated on the effects of alloying elements and impurities in the bulk. In the Russian program, the following differences between Russian E110 and Western cladding alloys were considered and investigated: impurities in Zircon ore, electrolytic refinement vs. Kroll process for reducing the ore to produce Zr ingots, variations in alloying elements (e.g., oxygen), and fabrication processes for making tubing from the ingot. The most substantial improvement in E110 behavior came from fabricating E110 cladding from a Western Zr ingot. These results suggest that electrolytic refinement removes impurities that may help stabilize the oxide layer grown on the surface.

ANL had access to only one heat of E110 – the tubing and cladding provided by Fortum in Finland. Because the ANL study was restricted to this one heat, the focus of the ANL program was on the effects of surface finish, which could be modified by machining, polishing and etching.

Characterization of E110 tubing and cladding

Dimensional, chemical, and microstructural analyses of E110 tubing were performed by ANL to verify that the E110 received from Fortum was within specifications and to try to ascertain any differences that would explain the poor LOCA performance of E110 and the excellent performance of M5. The dimensional and chemical characterization results are listed in Table 6 for E110 and Table 5 for M5. For the alloying and impurity elements measured, the materials used in the ANL test program are within specifications for E110 [7] and M5 [6]. Three noticeable differences in materials are: thicker wall for E110 (0.71 mm vs. 0.57-0.61 mm for M5), higher surface roughness for E110 tubing (0.34 μm vs. 0.12 μm for M5), and lower oxygen content for E110 (0.05 wt.% vs. 0.145 wt.% for M5). As Zry-4 cladding with thicker walls (0.67-0.77 mm) showed no adverse effects due to wall thickness, it appeared

highly unlikely that wall thickness alone would contribute to the poor LOCA performance of E110. The higher surface roughness could contribute directly or indirectly to early breakaway oxidation. However, the breakaway oxidation time (≈3800 s at 1000ºC) determined by ANL for 0.32-μm-rough HBR-type Zry-4 was significantly higher than what is reported for E110 in the Russian program [2] for 1000ºC oxidation temperature. Also, E110 cladding (etched and anodized) had a lower surface roughness (0.19 μm) than the tubing, but the cladding exhibited early breakaway oxidation times comparable to the tubing in ANL tests for samples oxidized at 1100ºC (one-sided). It seemed more likely that high surface roughness could result in earlier initiation of breakaway oxidation for an alloy that is inherently unstable. It is also likely that negative effects of surface impurities would be exaggerated for materials with higher surface roughness and higher local surface areas, which provide more sites for initiation of instability.

With regard to the lower oxygen content of E110, as compared to M5, it was shown in the Russian program that E110 heats with oxygen content as high as 0.11 wt.% exhibited early breakaway oxidation. In a study performed by Bochvar Institute and TVEL [25], E110 heats with as much as 0.13 wt.% oxygen showed early breakaway oxidation and hydrogen pickup at oxidation temperatures as high as 1100ºC.

ANL performed SEM and TEM studies with E110 and M5 samples to determine if there were significant differences in grain size, in Zr(Nb, Fe, Cr) precipitate size and distribution, and in Zr-Nb precipitate size and distribution. The E110 grain size was determined by SEM to be 4.7 μm, which is within the acceptable range for M5 (3-5 μm). The E110 Nb-Fe-rich precipitates were found to be >100 nm, which is consistent with the 100-200 nm reported by Mardon et al. [6] for M5 and measured by ANL. The E110 Nb-rich precipitates were determined to be ≈40 nm, which is consistent with the 50 nm reported by Mardon et al. [6] for M5 and measured by ANL. A non-uniform cluster of precipitates was found in one location of an E110 TEM sample, while Mardon et al. [6] reported uniform distribution of such precipitates. However, given the very small size of the TEM sample area examined, it is not clear that such non-uniform clusters are characteristic of the bulk of E110 tubing and cladding.

Within the limits of what ANL did measure for E110 and M5 alloys, no differences could be found in the characterization to explain the differences in LOCA performance. However, because the early breakaway oxidation could be due to surface, as well as bulk effects, ANL tested several surface-modified types of E110: as-received tubing, polished tubing, machined-and-polished tubing, tubing etched in an acid bath containing HF, and cladding that was etched and anodized. The outer surfaces of the as-received (a), polished (b) and etched (c) tubing samples are shown in Figure 75 at low magnification (50X). Figure 75a shows the rough surface of as-received tubing. The tubing exhibited longitudinal and circumferential scratches, as well as high surface roughness. Figure 75b shows the outer surface of polished and machined-and-polished E110 tubing with a reduced roughness of 0.14 μm. Polishing also removed some of the surfaces scratches. Figure 75c shows the outer surface of a sample etched in an HF-containing solution (13.5% HF + 13.5% HNO_3 +40% $C_3H_6O_3$ + 33% H_2O for 30-s). The surface roughness appears to have decreased, but the longitudinal and axial scratches are more readily observed. Preferential etching may have widened and deepened these scratches.

As-fabricated E110 tubing and cladding oxidized at 1000ºC

Because the results of the Russian program indicated very early breakaway at 1000ºC oxidation temperature, testing at ANL focused on this temperature. The thermal benchmark for the 1000ºC tests is shown in Figure 76. The ramp time from 300ºC to 1000ºC is 75 s. Hold times of 5 s to 1350 s were investigated. The reference hold time for most tests was 290 s. Table 33 summarizes the test conditions and observations for the more interesting tests conducted with as-received E110 tubing.

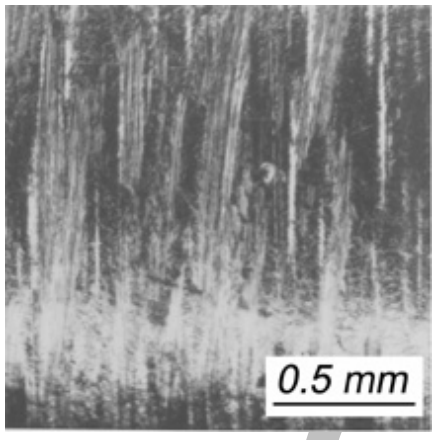

Figure 75a. Outer surface of E110 tubing in the as-received condition (0.35-μm surface roughness). Axial direction is left-to-right.

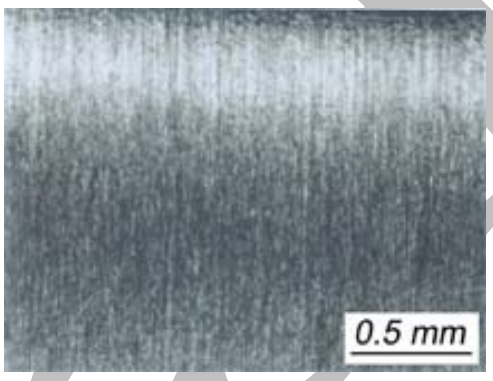

Figure 75b. Outer surface of E110 tubing in the polished condition (0.14-μm outer-surface roughness). Axial direction is left-to-right.

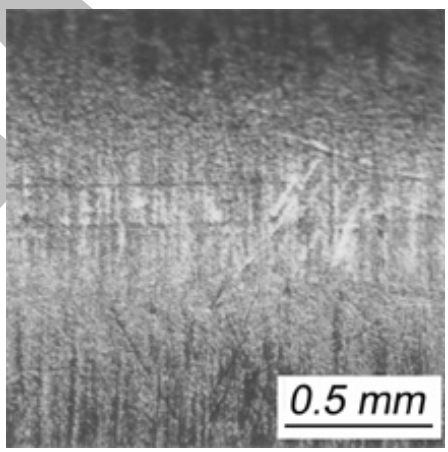

Figure 75c. Outer surface of E110 tubing following etching in HF-containing pickling solution. Axial direction is left-to-right.

Test EU#10 was conducted to observe the behavior of the outer-surface oxide layer following the ramp to 1000ºC. The hold time at 1000ºC was only 5 s. Although the outer-surface oxide layer appeared to be lustrous black (see Figure 77a), higher magnification images revealed the presence of white or "gray" spots (≤50-μm diameter) and streaks within the lustrous black matrix (see Figure 77b). It is assumed that these spots and streaks represent monoclinic oxide in a tetragonal matrix. Such behavior was not observed for any other cladding alloy tested. The white spots are not observed until much later times for polished E110 samples.

Test EU#9 was the thermal benchmark test with thermocouples (TCs) welded directly onto the E110 tubing. The TCs resulted in an abrupt change in geometry – much like the change at the ends of the sample – at the cladding surface, which can alter the stress state and induce early breakaway oxidation. This sample had a larger area of gray monoclinic oxide on the outer surface (see Figure 78) than the EU#12 sample (see Figure 79a), which had no welded TCs on the sample. Metallography of the cross-section (see Figure 79b) shows that some of the oxide layer has already experienced delamination after only 290-s hold time for the companion EU#13 sample. Breakaway oxidation is both local and extensive. It appears that hydrogen is absorbed locally into E110 at breakaway locations, but the hydrogen does not have time to diffuse and homogenize during the short hold time at temperature. Sample EU#11 was oxidized at 950ºC for 290-s hold-time. Breakaway oxidation is evident in Figure 80.

Sample EU#36 had a hold time of 395 s at 1000ºC. However, breakaway was less extensive than for the 290-s hold-time sample. Thus, the hydrogen pickup was low at the sample midplane and <50 wppm in the regions between the midplane and the ends of the sample. These results confirm that breakaway oxidation is an instability phenomenon with variation in the extent of breakaway vs. hold-time at temperature. At the longer hold time of 625 s, sample EU#38 picked up a significant amount of hydrogen. The midplane of the sample had local hydrogen readings ranging from very low values to ≈180 wppm, with the low values occurring under black oxide and the higher values occurring under regions of gray oxide. At the off-center locations, the hydrogen pickup was much higher (420±160 wppm). Even for a longer hold time (625 s), hydrogen does not diffuse enough to homogenize the concentration. Figure 81 shows the axial variation of hydrogen content for the EU#38 test sample.

Samples with hold times of 825 to 1350 s experienced significant oxide delamination and spallation, as well as significant hydrogen pickup. The hydrogen concentration was still highly non-uniform after 825 s, but it was both high and homogeneous after a 1350-s hold time at 1000ºC. The 1350-s sample (EU#8) is shown in Figure 82.

Some of the 1000ºC-oxidized samples were sectioned into 8-mm-long rings and ring-compressed at RT. The results are summarized in Table 34. The ductile-to-brittle transition CP-ECR was in the range of 6-7% (see Figure 83). The corresponding embrittlement hold-time at 1000ºC is 500±100 s, with total test times including the ramp from 300ºC of 575±100 s. For E110 oxidized under these conditions, embrittlement occurs with hydrogen contents >200 wppm. However, there was significant circumferential and axial variation in hydrogen content (25-560 wppm) for the embrittled sample at ≈7% CP-ECR. Thus, a precise determination between H-content and embrittlement could not be made for these samples.

Effects of etching E110 tubing prior to oxidizing at 1000ºC

The results in Figure 77 suggest that surface and substrate impurities may serve as initiation sites for E110 breakaway oxidation. E110 tubing is pickled and anodized to produce cladding with an increased surface hardness to make it more scratch resistant. The specific acid mixture and pickling time

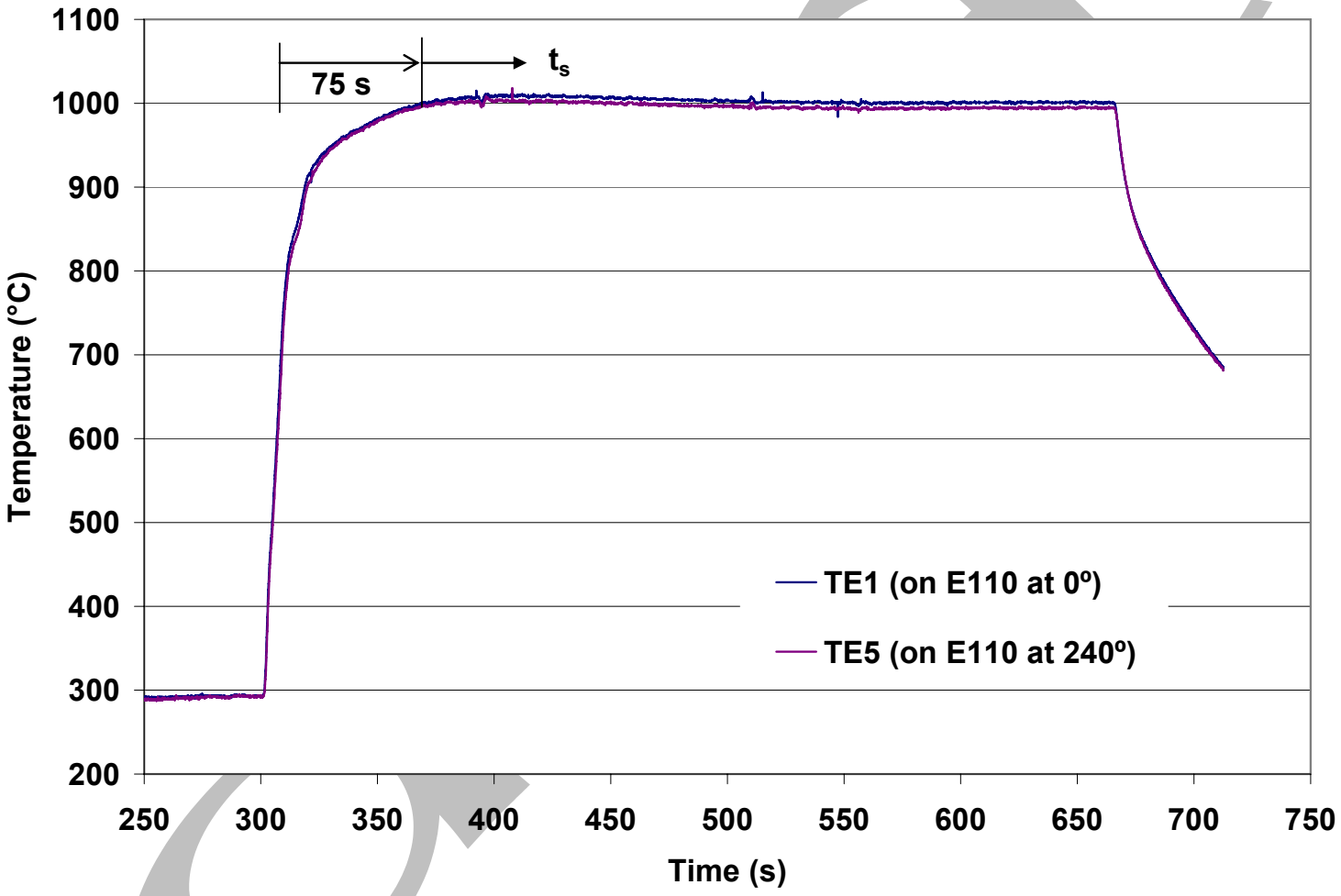

Figure 76. Thermal benchmark results for as-received E110 tubing and cladding oxidized in steam at 1000ºC. Ramp time is 75 s.

Table 33 Two-Sided Steam Oxidation Tests Conducted at 1000°C with As-Received E110 Tubing; 9.17-mm OD; 0.71-mm wall thickness; CP-ECR = 1.235 CP-Wg; 0.35-μm outer-surface roughness; ≈25-mm sample length; hydrogen samples were cut from center (C) and off-center (OC) sample locations; note that Test EU#11 was conducted at 950°C

Test ID#	Hold Time s	Total Time s	CP-ECR %	H Content wppm	Sample Condition Observations
EU#10	5	80	1.8	---	Black oxide layer (Fig. 77a); white spots ≤50 μm (Fig. 77b)
EU#9	290	365	5.0	---	Extensive monoclinic oxide around welded TCs (Fig. 78)
EU#12	290	365	5.0	120±45 (C)	Nonuniform oxide (Fig. 79a)
EU#13	290	365	5.0	---	Half the sample was as-fabricated; oxide delamination (Fig. 79b)
EU#11	290 at 950°C	365	<5	---	Oxide surface (Fig. 80) may be worse than EU#12 sample
EU#36	395	470	5.8	7±3 (C) 44±7 (OC)	Nonuniform oxide layer
EU#38	625	700	7.1	80±40 (C) 90±90 (C) 420±160 (OC)	Significant axial distribution of hydrogen content (Fig. 81)
EU#40	825	900	8.1	540±80 (C) 1430±110 (OC)	Delamination-spallation from half the sample
EU#8	1350	1425	10.4	4230±250 (C)	Extensive delamination-spallation (see Fig. 82)

used by TVEL is proprietary. However, based on the Russian program tests and one test conducted by ANL with E110 cladding oxidized at 1100ºC for ≈500 s, the extent of outer-surface breakaway oxidation was comparable for the cladding and the tubing.

In an effort to determine the effects of pickling (etching) on breakaway oxidation, E110 tubing was exposed to two types of acid-bath mixtures prior to cleaning and oxidation: (a) a solution used by ANL to clean steel and vanadium surfaces (30-s exposure to 13.5% HF + 13.5% HNO_3 + 40% $C_3H_6O_3$ + 33% H_2O); and (b) a solution used to etch Zry-2 cladding in the 1980s (180-s exposure to 3.5% HF + 45% HNO_3 + 51.5% H_2O). Samples were then cleaned and oxidized at 1000ºC for a hold time of 290 s. Both (a) and (b) resulted in extensive monoclinic oxide formation and breakaway oxidation of the E110 outer-surface oxide. The results suggest that E110 oxidation behavior is very sensitive to sub-micron-deep F impurities. Figure 84a shows the silver-gray appearance of the outer surface following etching with solution (b) and oxidation. Figure 84b shows the partial, but extensive breakaway oxidation of polished-and-etched (b) E110. Figure 84c shows the lustrous black appearance of an E110-tubing sample that was

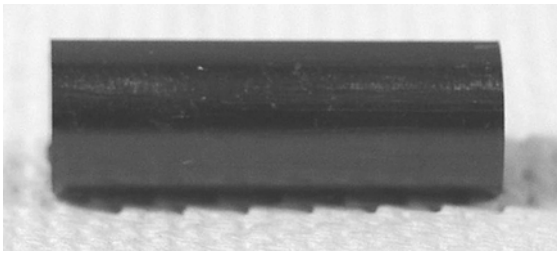

(a)

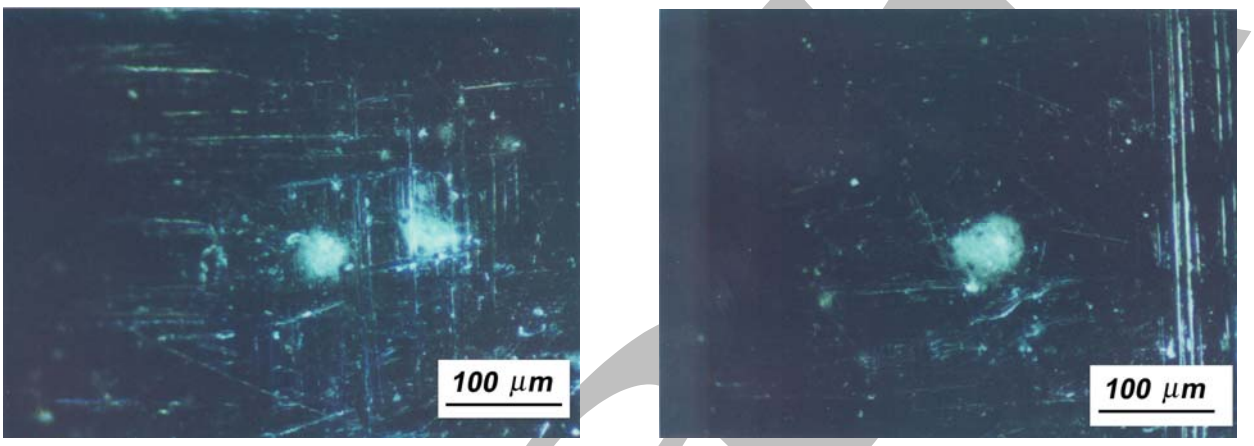

(b)

Figure 77. As-fabricated E110 tubing oxidized in steam for a 75-s ramp from 300ºC to 1000ºC, followed by a 5-s hold at 1000ºC and slow cooling: (a) low magnification of lustrous black outer surface oxide; and (b) higher magnification of outer-surface oxide showing white spots and streaks believed to be monoclinic oxide and oxide-instability initiation sites.

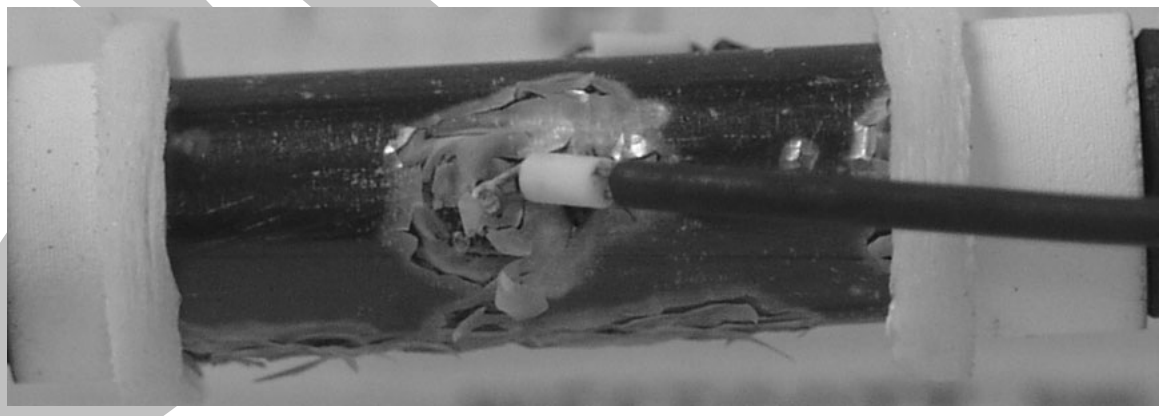

Figure 78. As-fabricated E110 thermal-benchmark (EU#9) sample showing excessive monoclinic oxide formation around the welded thermocouple after 290-s hold time at 1000ºC.

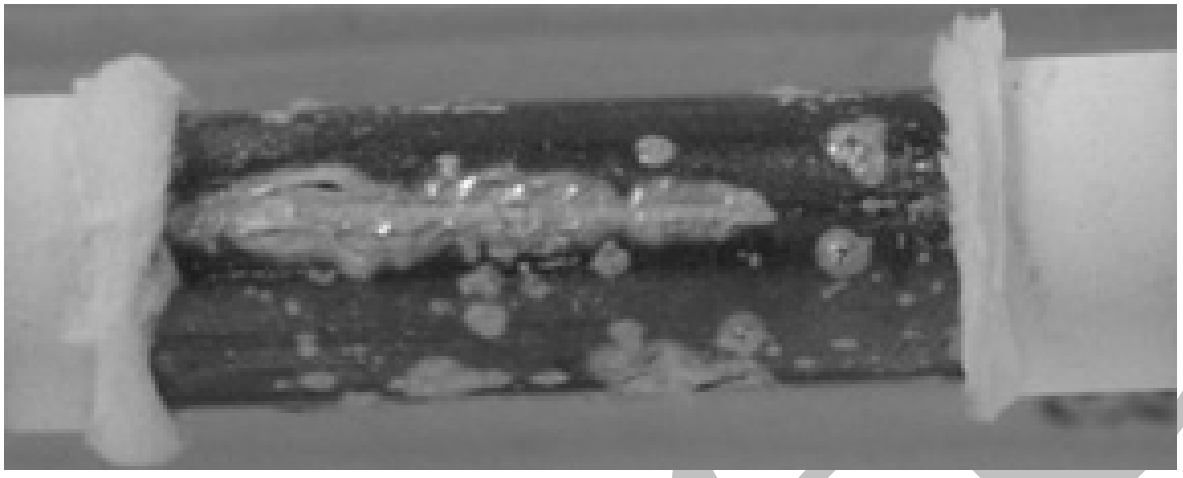

(a)

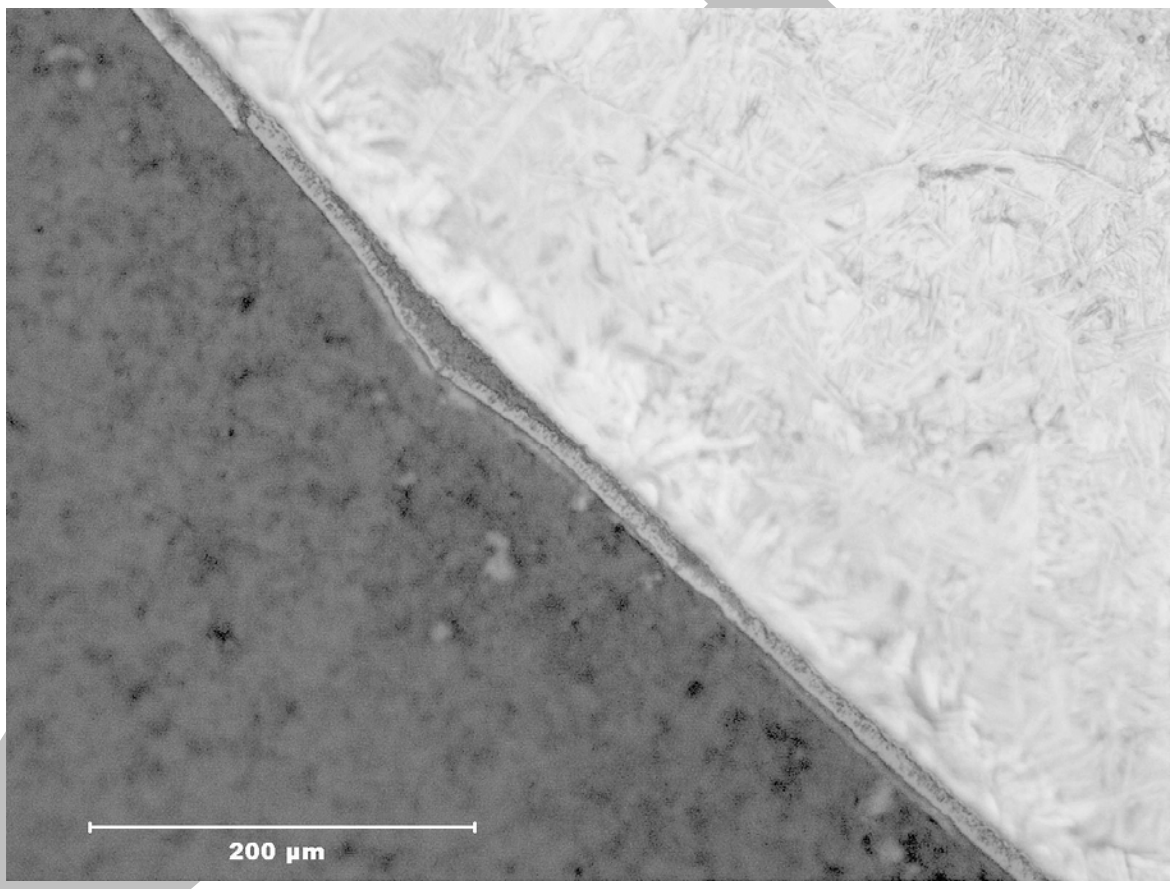

(b)

Figure 79. As-fabricated E110 sample oxidized in steam for a hold time of 290 s at 1000ºC: (a) low magnification image of breakaway oxidation on the outer surface oxide of EU#12 sample; and (b) higher magnification image of delaminated outer-surface oxide layer on EU#13 sample.

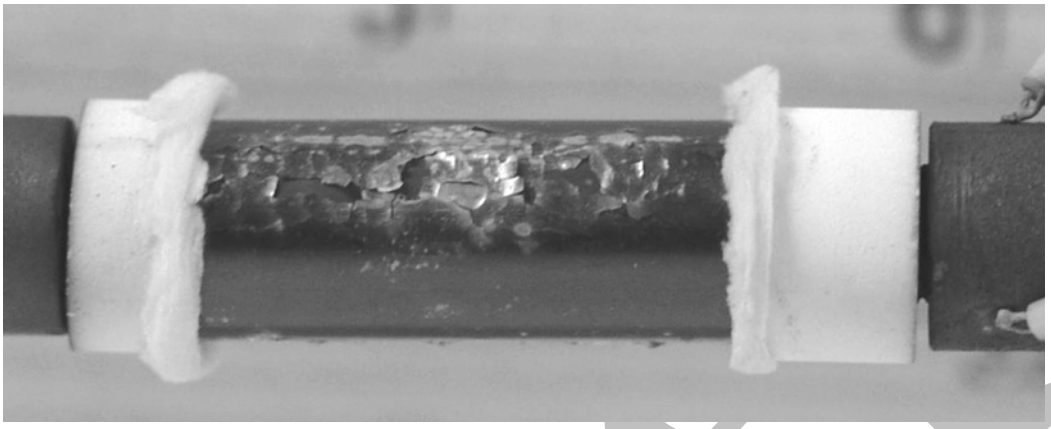

Figure 80. EU#11 sample oxidized for a hold time of 290 s at 950ºC. Breakaway oxidation is as extensive as for the EU#12 sample oxidized for the same hold time at 1000ºC.

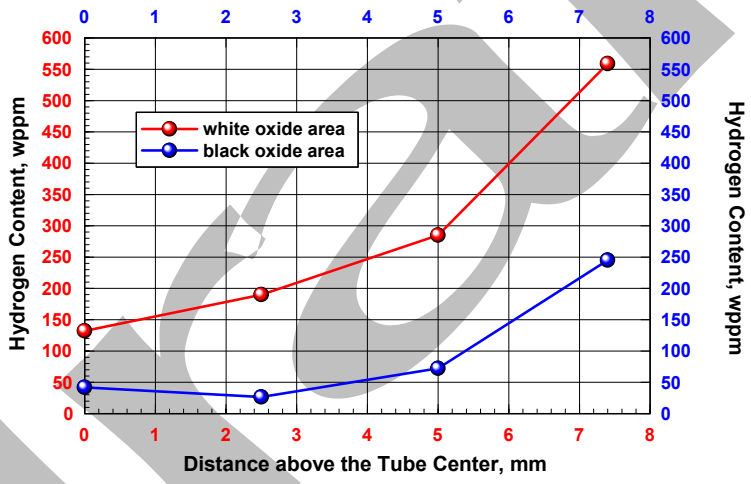

Figure 81. Hydrogen content distribution in E110 after oxidation Test EU#38 with as-fabricated E110 exposed to steam at 1000°C for a hold time of 625 s (≈7% CP-ECR).

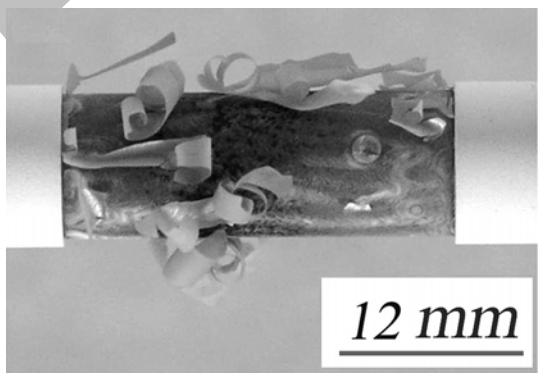

Figure 82. EU#8 sample oxidized for a hold time of 1350 s at 1000ºC. Breakaway oxidation, delamination and spallation are evident. The hydrogen pickup was ≈4200 wppm.

Table 34 Ring Compression Test Results for E110 Samples Oxidized at 1000˚C and Slow Cooled. Tests were performed on 8-mm-long samples at RT and 0.0333 mm/s displacement rate.

Test ID	Hold Time s	Total Time s	ECR, % CP-Model	H Content (Variation) wppm	RT Offset Displacement mm	RT Offset Strain %
E110	0	0	0	3	6	66
EU#10	5	80	1.8	---	6.05	66
EU#9	290	365	5.0	---	---	---
EU#12	290	365	5.0	120 (70-170)	5.44	59
EU#36	395	470	5.8	32 (4-84)	5.82	63
EU#38	625	700	7.1	275 (25-560)	0.13	1.4 (brittle)
EU#40	825	900	8.1	925 (440-1500)	0.04	0.4 (brittle)

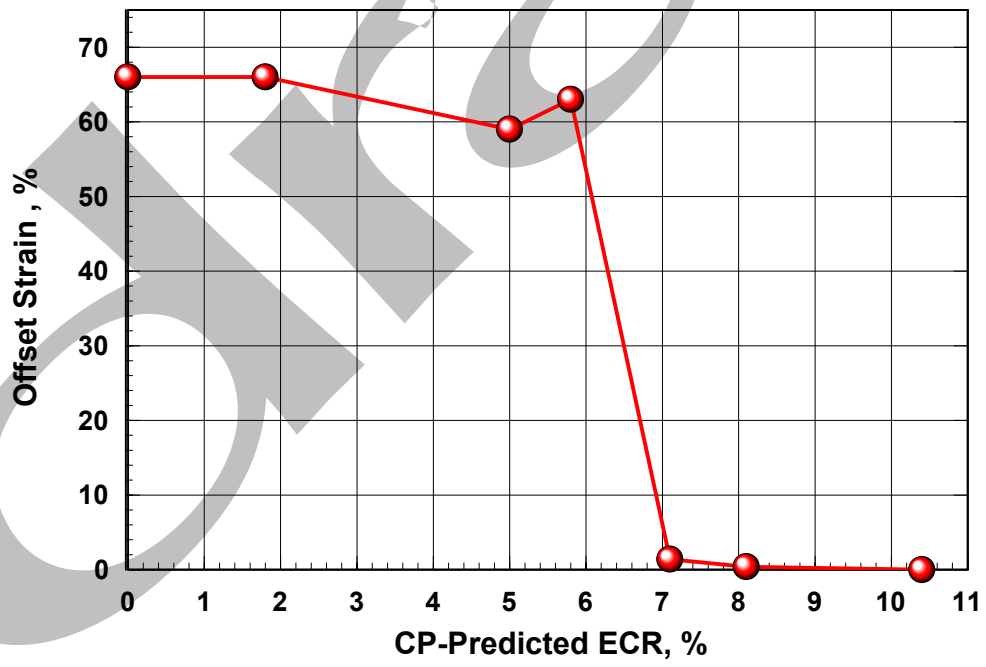

Figure 83. RT offset strain vs. CP-ECR of as-fabricated E110 tubing oxidized (two-sided) in steam at 1000˚C for hold times of 0-825 s. Sample length is 8 mm and displacement rate is 0.0333 mm/s. Embrittlement is due to excessive hydrogen pickup (>200 wppm).

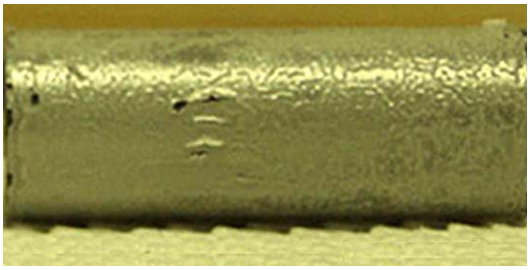

(a)

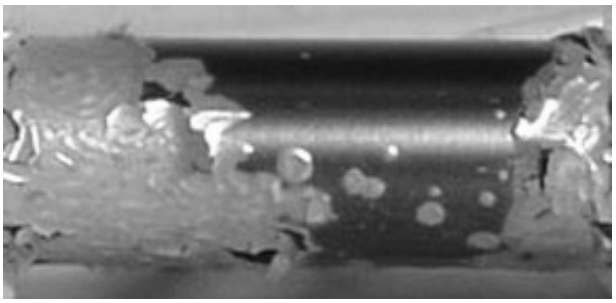

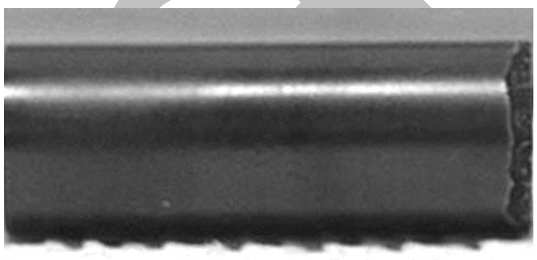

(b) (c)

Figure 84. The effects of pickling (etching) E110 tubing prior to oxidation at 1000ºC for 290 s: (a) etched (180-s exposure to 3.5% HF + 45% HNO_3 + 51.5% H_2O) tubing sample; (b) polished-and-etched E110 sample; and (c) etched-and-polished E110 sample.

etched with (b) and then polished. The results of this limited study suggest that pickling (etching) E110 with an acid solution containing HF can promote earlier and more extensive breakaway oxidation, while polishing the sample following etching appears to remove the sub-micron-deep layer containing F impurities.

Effects of polishing and machining-and-polishing E110 tubing prior to oxidizing at 1000ºC

In Test EU#13, half of the sample was in the as-fabricated condition and half the sample was machined on the outer surface (38 μm removed) and polished. The hybrid sample was oxidized at 1000ºC for 290-s hold time. Based on visual inspection, the oxide on the machined-polished segment is lustrous black, while the non-treated segment shows the mix of grayish-white (monoclinic oxide) regions in a matrix of black (tetragonal) oxide observed in all other tests with as-received E110 (see Figure 85).

Test EU#14 was conducted to determine the relative benefits of polishing vs. machining-and-polishing on E110 steam-oxidation performance. The hybrid sample consisted of three axial regions: a) one-half-segment prepared by machining (25 μm removed) and polishing; b) one-quarter-segment prepared by polishing only; and c) one-quarter-segment of as-fabricated E110 tubing. This hybrid sample was also oxidized at 1000ºC for 290-s hold time. As shown in Figure 86, both the polished-only and the machined-and-polished regions of the sample exhibited lustrous black outer-surface oxides, while the as-fabricated region exhibited breakaway oxidation. From Figure 86, it appears that polishing alone is sufficient to improve the behavior of E110. Polishing smoothes out the surface roughness by removing <5 μm of material and chemical impurities at the surface and in the substrate.

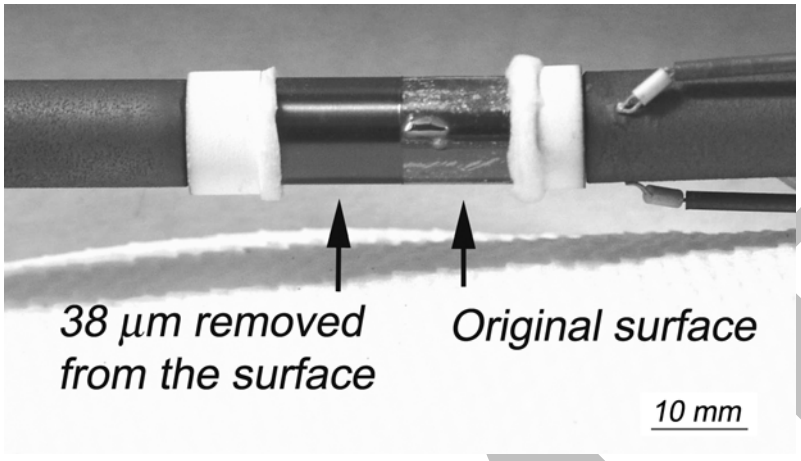

Figure 85. Hybrid E110 sample (EU#13) following oxidation at 1000ºC for 290-s. Machined-and-polished section is lustrous black, while as-fabricated E110 section is in breakaway oxidation.

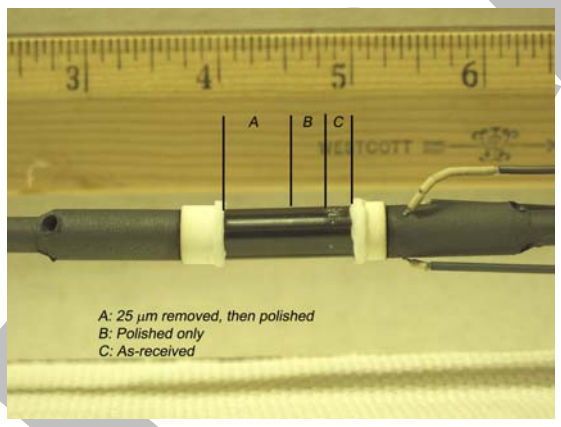

Figure 86. Effects of polishing vs. machining-and-polishing on E110 oxidation at 1000ºC for 290 s.

To further investigate the effects of polishing and machining-polishing, higher (200X) magnification photographs were taken of the surfaces of the three regions of the EU#14 sample. Figure 87a shows the outer surface of the as-fabricated material after oxidation with large regions of monoclinic (light-colored) oxide. Figure 87b shows the same magnification of the machnined-and-polished outer surface after oxidation with very small, isolated spots of monoclinic oxide. The largest spot diameter in the image is ≈25 µm. Figure 87c shows the same magnification of the polished outer surface after oxidation with small – compared to the as-received material – spots of monoclinic oxide. The largest spot diameter in Figure 86c is ≈75 µm.

It is clear that the quality of the oxide layer on the polished surface is much better than the as-fabricated tubing surface. This suggests that the oxidation behavior of the E110 alloy is sensitive to some combination of surface roughness and surface chemistry. Further improvement may be made by removing some of the near-surface layer, as well as the surface itself. It is also worth noting that the untreated inner surface of the whole sample had large regions of monoclinic oxide visible by eye.

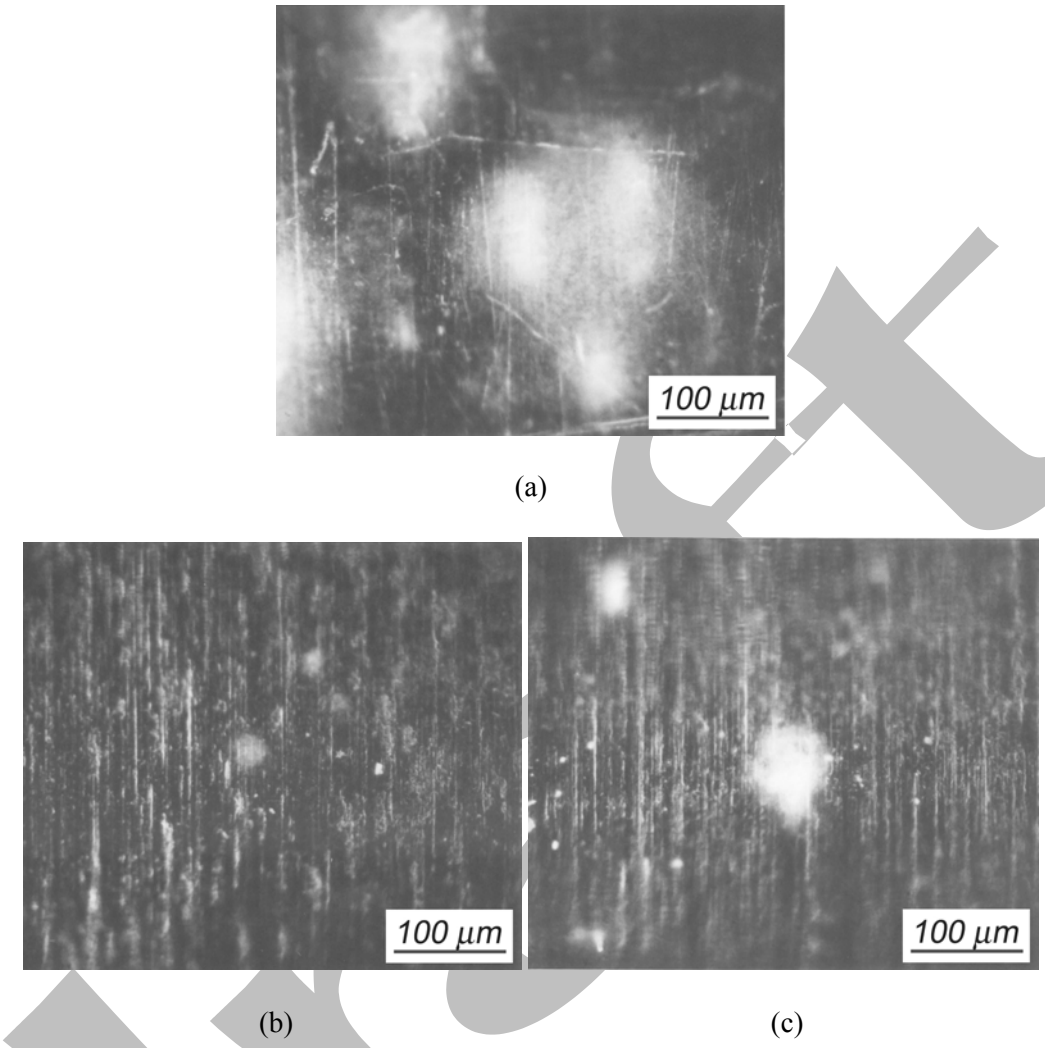

Figure 87. High magnification (200X) image of outer surface oxide layers following oxidation at 1000ºC for 290 s: (a) as-fabricated E110; (b) machined-and-polished E110; and (c) polished E110.

In order to better compare E110 oxidation performance to the performance of Western alloys, E110 samples were modified to give the same wall-thickness (≈0.6 mm) and comparable outer-surface roughness as M5 (see Table 5). The ANL-modified E110 was fabricated by machining about 100 µm from the inner-surface wall, polishing the inner surface and polishing the outer surface to a roughness level of 0.14-µm. Oxidation tests of these samples were designed to determine breakaway oxidation time in terms of outer-surface oxide appearance and hydrogen pickup. The thermal benchmark results for the M5 oxidation tests were used to plan and interpret the E110 tests (see Figure 55). The E110 results are summarized in Table 35. Not included in Table 35 are tests conducted for 0 to 190-s hold times for which the samples were lustrous black with no hydrogen pickup.

For the machined-and-polished samples, breakaway oxidation initiated at the ends of the sample and progressed towards the middle of the sample. It is certainly possible that longer breakaway oxidation times could have been achieved with longer, more continuous samples without abrupt changes in geometry (e.g., ends of 25-mm-long ANL samples). However, polishing of the E110 surfaces did

Table 35 Two-Sided Oxidation Tests Conducted on Modified E110 Cladding at 1000°C; polished cladding outer diameter (9.17 mm); machined and polished inner diameter (7.98 mm); and 0.6-mm wall thickness

Test ID#	Hold Time s	Total Time s	H Content wppm	Outer-Surface Oxide
EU#22	292	382	---	Lustrous Black
EU#24	413	503	11±5	Lustrous Black with white ends
EU#37	815	905	6±1	---
EU#16	1025	1115	150 (32-342)	See Figure 88 for variation in outer surface oxide layer
EU#41	2025	2115	1280±100	---

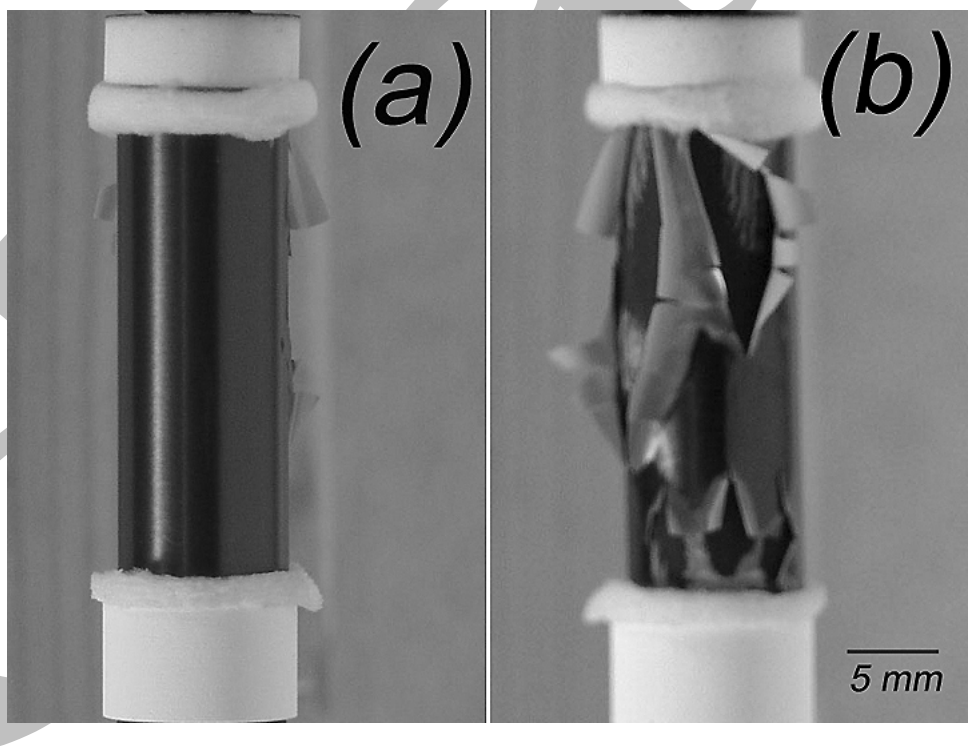

(a) (b)

Figure 88. Machined-and-polished E110 sample (EU#16) after 1025-s hold time in steam at 1000°C: (a) lustrous black oxide surface on the other side of the sample; and (b) extensive monoclinic oxide formation, delamination and spallation evident on one side of the sample.

significantly delay breakaway oxidation time in terms of hydrogen pickup. Figure 89 shows the hydrogen pickup vs. time for as-fabricated E110 samples vs. ANL-modified (OD polishing, ID machining-and-polishing) E110 samples. Breakaway oxidation time was essentially double for the polished E110 as compared to the as-fabricated E110 tubing.

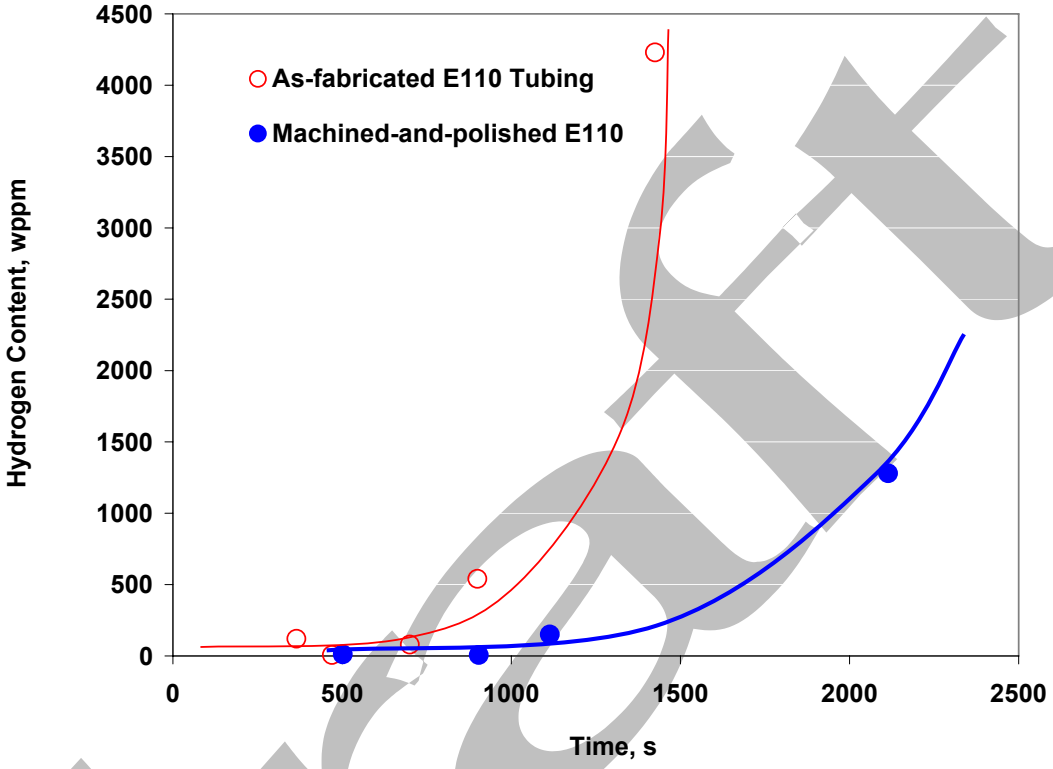

Figure 89. Hydrogen pickup vs. total test time for as-fabricated E110 tubing and ANL-modified machined-and-polished E110. The ramp time from 300ºC to 1000ºC is 75 s for the as-fabricated tubing (0.70-mm wall) and 90 s for the machined-and-polished samples (0.6-mm wall).

Effects of machining-and-polishing E110 tubing prior to oxidizing at 1100ºC

A series of tests were conducted with ANL machined-and-polished E110 samples oxidized at 1100°C to determine post-oxidation ductility vs. CP-ECR. The M5 thermal benchmark results for 1100°C tests were used to plan these tests and interpret the results (see Figure 56). All samples exhibited a lustrous black oxide layer up to the highest hold (1011 s) at 1100˚C. At this hold time, small white spots were observed on the outer surface oxide layer.

The investigation of ANL-modified post-oxidation ductility was motivated by the results of Bochvar-Institute/TVEL work [25] for the RT ring-compression ductility of 7 lots of E110, with varying concentrations of Hf, Fe, and O (all within material specification ranges), as well as varying combined impurity levels (Ni, Al, Si, Ca, K, F, Cl, Na, Mg). The E110 tubing used in the Bochvar/TVEL study had an outer-diameter of 9.13 mm after "pickling". Although not specified, it is assumed that the tubing wall thickness was 0.71 mm. It is not clear whether or not the tubing was anodized – standard procedure to convert tubing into cladding – following pickling. 30-mm-long tubing segments were exposed to two-sided steam oxidation for 600 s. Both heating (300˚C to 1100˚C in ≈2 s) and cooling (1100˚C to 300˚C in

15-20 s) rates were relatively fast. The corresponding CP-ECR is 12% for 0.71-mm-wall cladding oxidized (two-sided) to 1100˚C for 600 s.

Four of the Bochvar-TVEL lots with a combined impurity level of 110-135 wppm exhibited outer-surface breakaway oxidation, high hydrogen pickup (200-600 wppm), and low RT ring-compression ductility (<5%). Three of the lots with combined impurity levels of 25-45 wppm exhibited stable oxide growth (observed at low-magnification), lower hydrogen pickup (60-200 wppm) and higher RT ring-compression offset strain (5-10%). Based on ANL experience with the effects of surface finish (polishing vs. pickling), it was hypothesized that the Bochvar-TVEL samples would have exhibited longer-time stable oxide growth, lower hydrogen pickup and higher ductility if the surfaces had been polished, rather than pickled. In order to test this hypothesis, ANL machined-and-polished (M-P) samples were subjected to RT ring-compression tests. The results of these tests are compared to the best of the Bochvar-TVEL results (Lots 2-4) in Table 36 and Figure 90.

Table 36 Comparison of E110 Post-Oxidation RT Ductility between ANL Machined-and-Polished (M-P) Cladding Samples and Bochvar-TVEL (BT) Lots 2-4 Pickled Cladding Samples [25] Following Two-Sided Steam Oxidation at 1100˚C

E110 Material	Wall Thickness mm	CP ECR %	Meas. ECR %	Offset Displacement mm	Offset Strain %
ANL M-P	0.61	7.5	7.0	5.47	60
ANL M-P	0.69	10.5	9.2	2.86	31
BT Lot 2	0.71	12	≈10	---	10
BT Lot 3	0.71	12	≈10	---	6.6
BT Lot 4	0.71	12	≈10	---	4.4
ANL M-P	0.58	14.4	12.7	1.94	21
ANL M-P	0.58	19.4	16.0	0.58	6.3

Significantly higher post-oxidation ductility was achieved by machining the inner-surface to give a wall thickness comparable to M5 and by polishing both inner and outer surfaces. The Bochvar-TVEL samples, which were pickled rather than polished, may have exhibited higher post-oxidation ductility if the surfaces had been polished following pickling or if the surfaces had not been pickled at all. Also, the machined-and-polished E110 post-oxidation ductility results for 1100ºC-oxidized samples are comparable to the results obtained for the modern 17×17 alloys (Zry-4, ZIRLO, and M5) used in U.S. reactors.

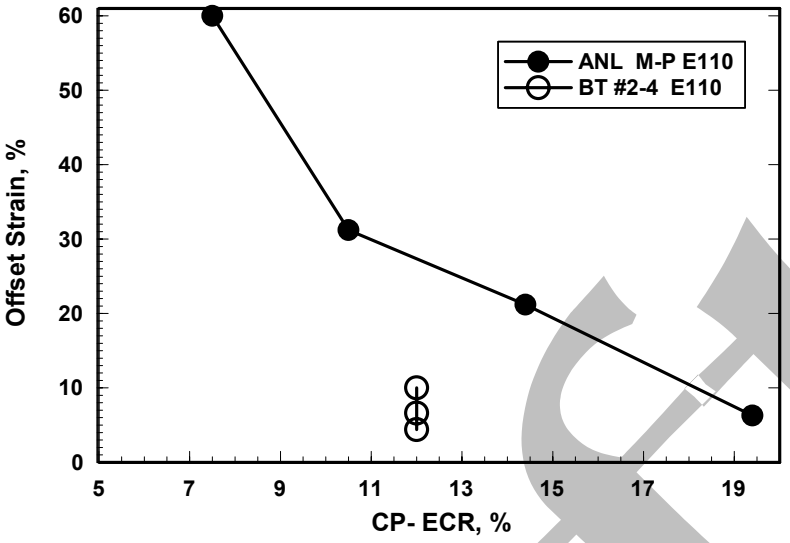

Figure 90. Post-oxidation RT ductility vs. CP-ECR for ANL machined-and-polished (M-P) E110 samples and Bochvar-TVEL (BT) pickled E110 cladding following two-sided steam oxidation at 1100˚C.

Effects of machining-and-polishing E110 tubing prior to oxidizing at 1200ºC

Machined-and-polished E110 samples were oxidized at 1200ºC, slow-cooled and ring-compressed at 135ºC. Because the ductility of the ANL-modified E110 was so good following 1100ºC, the 1200ºC-oxidized samples were tested to see how they compared to the U.S. alloys. The 1200ºC thermal benchmark results for M5 (see Figure 64) were used to plan the tests and interpret the results. Table 37 summarizes the results for the oxidation levels and ring compression offset strains for these E110 tests.

Table 37 Post-oxidation Ductility at 135ºC for ANL Machined-and-Polished E110 Samples following Oxidation at 1200˚C and Slow Cooling; samples were fabricated from E110 cladding (etched and anodized): polished outer diameter (9.07 mm), machined-and-polished inner surface, and 0.6-mm wall thickness

E110 Test #	Wall Thickness mm	CP ECR %	Meas. ECR %	Offset Displacement mm	Offset Strain %
EU#53	0.60	7.5	8.6	>5	>55
EU#51	0.60	10.0	10.4	>5	>55
EU#52	0.61	13.0	13.8	1.47	16
	0.61	13.0	13.8	0.66	7

The ductility of ANL-modified E110 oxidized at 1200ºC is higher than the ductility of HBR-type 15×15 Zry-4 and modern 17×17 Zry-4 cladding for ≤13% CP-ECR. The post-oxidation ductility of ANL-modified E110 is comparable (12% for E110 and 14% for M5) to that of 17×17 M5 at 13% CP-ECR. The ductile-to-brittle transition CP-ECR for ANL-modified E110 was not determined in this program.

3.6 Effects of cooling rate and quench temperature on post-quench ductility

The protocol for preparing samples for post-quench ductility was the same for 17×17 Zry-4, ZIRLO and M5: cooling in steam at ≈10-13ºC/s from the oxidation temperature to 800ºC; and rapid-cooling (quench) from 800ºC to 100ºC. As 800ºC is below the (alpha + beta) → alpha phase-transformation temperature for as-fabricated Zry-4, the quench temperature is low enough to allow the phase transformation to occur prior to "freezing" in the microstructure at 800ºC. While a slower cooling rate from the oxidation temperature to the quench temperature could result in more redistribution of oxygen between oxygen-rich alpha incursions and low-oxygen beta, there is no clear evidence that this would affect post-quench ductility. However, for as-fabricated M5 the (alpha + beta) → alpha phase-transformation temperature is ≈650ºC. For as-fabricated ZIRLO, this phase transformation temperature is expected to be between 650ºC and 800ºC. Thus, the phase transformation for M5 and ZIRLO is not complete at the time of the 800ºC quench (Q) used in the ANL test program. Additional tests were conducted with samples oxidized at 1200ºC. Following cooling at ≈13ºC/s to 800ºC, samples were further slow cooled (SC) to RT and ring-compressed at 135ºC.

3.6.1 Effects of quench temperature on post-quench ductility of 17×17 Zry-4

The post-oxidation ductility results for Zry-4 subjected to slow-cooling are presented in Table 38. The slow-cooled samples were oxidized in a separate test train with the thermal history shown in Figure 91. The complete data set presented in Table 11 (Q) is combined with the data set in Table 38 (SC) to generate the graphical results shown in Figure 92 for offset strain vs. CP-ECR.

Table 38 Ring Compression Test Results at 135˚C and 0.0333 mm/s for 17×17 Zry-4 Cladding Oxidized at 1200˚C and Slow Cooled (SC); ECR = 1.538 Wg for 0.57-mm-wall cladding

Test Conditions		ECR %		Plastic Displacement, mm		Plastic Strain, %	
Ox. Test Time[a], s	Cooling	CP	Meas.	Offset	Permanent	Offset	Permanent
187	SC	13.0	13.2	1.03	---	11	---
187	SC	13.0	13.2	0.61	---	6.5	---
288	SC	17.0	18.5	0.30	0.16	3.2	1.7
288	SC	17.0	18.5	0.12	0.05	1.3	0.5

[a]Includes time for ramp from 300ºC and hold time.

At 13% CP-ECR, the slow-cooled Zry-4 samples have an average offset strain of 9% (6.5-11%) as compared to 5.1% for quenched Zry-4. Although there is an apparent enhancement in ductility with slow-cooling at 13% CP-ECR, this may be due to data scatter as there is an abrupt decrease in ductility of Zry-4 in the range of 11-15% CP-ECR. At 17% CP-ECR, the ductility strains of the slow-cooled and quenched Zry-4 samples are essentially the same : 2.3% (1.3-3.2%) average offset strain and 1.1% (0.5-1.7%) average permanent strain for slow-cooled Zry-4 samples; and 2.5% (2.0-2.8%) average offset strain and 1.1% (0.7-1.4%) permanent strain for quenched Zry-4. Thus, it can be concluded that the ductile-to-brittle transition CP-ECR for 1200˚C-oxidized Zry-4 is insensitive to quench at ≤800˚C.

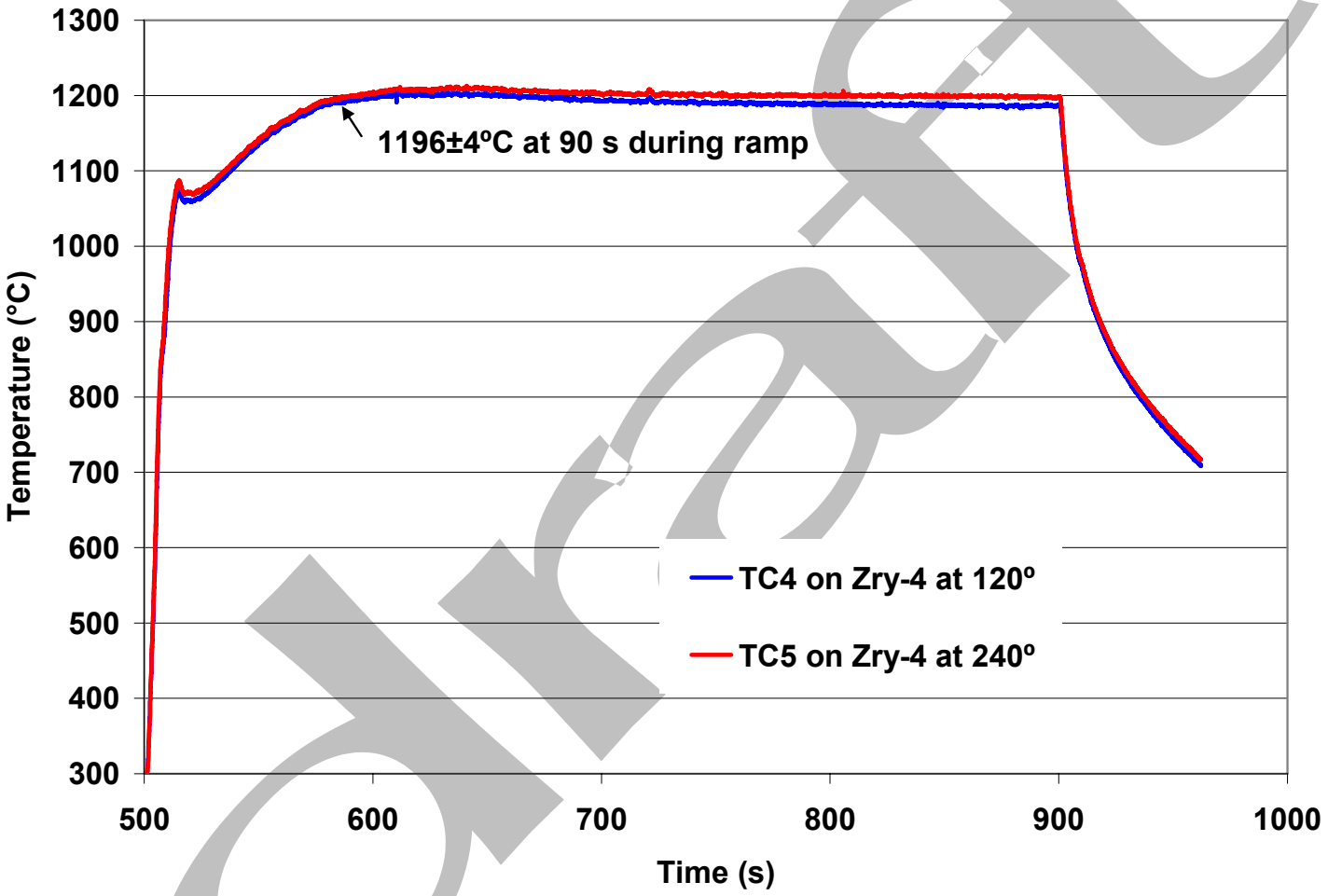

Figure 91. Thermal benchmark test results for slow-cooled 17×17 Zry-4, ZIRLO and M5 samples oxidized at 1200ºC.

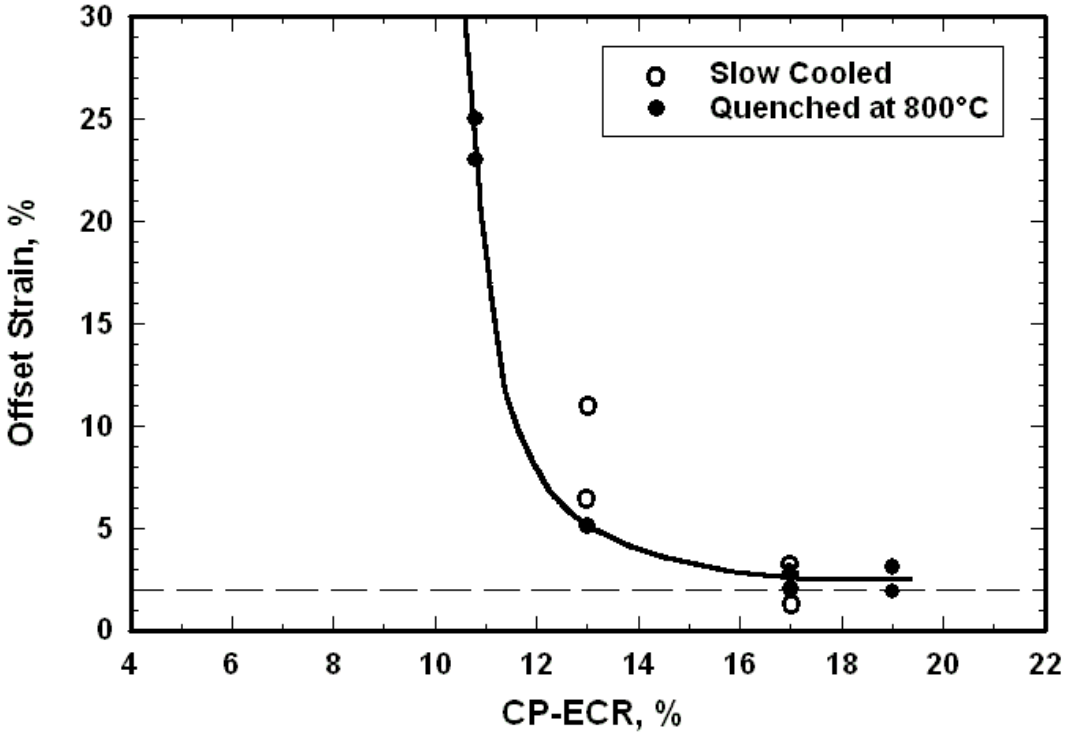

Figure 92. Effects of quench vs. slow cooling on the post-oxidation ductility of 17×17 Zry-4 (0.57-mm wall) oxidized at 1200ºC, cooled at ≈13ºC/s to 800ºC and either quenched at 800ºC or slow cooled from 800ºC to RT. Ring-compression tests were performed at 135ºC and 0.0333 mm/s displacement rate.

3.6.2 Effects of quench temperature on post-quench ductility of 17×17 ZIRLO

The post-oxidation ductility results for ZIRLO subjected to slow cooling are given in Table 39. The slow-cooled samples were oxidized in a separate test train with the thermal history shown in Figure 91. The complete data set presented in Table 24 (Q) is combined with the data set in Table 39 (SC) to generate the graphical results shown in Figure 93 for offset strain vs. CP-ECR.

At 13% CP-ECR, the slow-cooled ZIRLO samples have an average offset strain of 9% (8.1-9.3%) as compared to 27% (21-33%) for quenched ZIRLO. This factor of 3 reduction in ductility for slow-cooled samples appears to be significant. However, at 17% CP-ECR, the ductility strains of slow-cooled and quenched ZIRLO are within data scatter: 3.6% (2.0-5.5%) average offset strain and 1.5% (1.2-1.8%) average permanent strain for slow-cooled ZIRLO samples; and 5.7% (3.8-7.0%) average offset strain and 2.3% (1.8-2.8%) permanent strain for quenched ZIRLO. Thus, it can be concluded that the ductile-to-brittle transition CP-ECR for 1200˚C-oxidized ZIRLO is relatively insensitive to quench at ≤800˚C. For <17% CP-ECR, slow-cooled ZIRLO samples may have less ductility than quenched samples at the same CP-ECR (e.g., 13%). However, considerably more data would need to be generated to establish such a trend.

Table 39 Ring Compression Test Results at 135˚C and 0.0333 mm/s for 17×17 ZIRLO Cladding Oxidized at 1200˚C and Slow-cooled (SC); ECR = 1.538 Wg for 0.57-mm-wall cladding

Test Conditions		ECR %		Plastic Displacement, mm		Plastic Strain, %	
Ox. Test Time[a], s	Cooling	CP	Meas.	Offset	Permanent	Offset	Permanent
187	SC	13.0	13.5	0.77	---	8.1	---
187	SC	13.0	13.5	0.89	---	9.3	---
288	SC	17.0	17.3	0.32	0.17	3.4	1.8
288	SC	17.0	17.3	0.32	0.14	3.4	1.5
288	SC	17.0	17.3	0.52	---	5.5	---
288	SC	17.0	17.3	0.20	0.11	2.0	1.2

[a]Includes time for ramp from 300ºC and hold time.

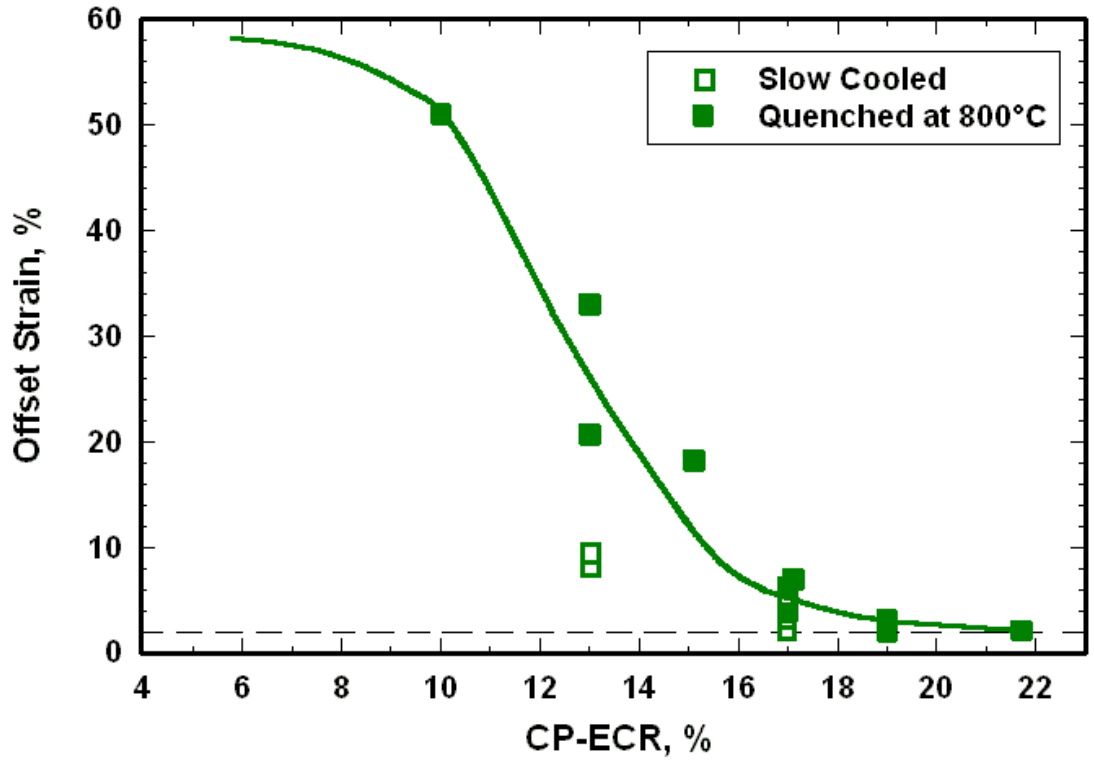

Figure 93. Effects of quench vs. slow cooling on the post-oxidation ductility of 17×17 ZIRLO (0.57-mm wall) oxidized at 1200ºC, cooled at ≈13ºC/s to 800ºC and either quenched at 800ºC or slow cooled from 800ºC to RT. Ring-compression tests were performed at 135ºC and 0.0333 mm/s displacement rate.

3.6.3 Effects of quench temperature on post-quench ductility of 17×17 M5

The post-oxidation ductility results for M5 subjected to slow cooling are given in Table 40. The slow-cooled samples were oxidized in a separate test train with the thermal history shown in Figure 91. The complete data set presented in Table 29 (Q) is combined with the data set in Table 40 (SC) to generate the graphical results shown in Figure 94 for offset strain vs. CP-ECR. The post-oxidation ductility of M5 appears to be insensitive to quench temperatures ≤800ºC. The strain data for the slow-cooled samples are within the scatter of the strain data for the samples quenched at 800ºC.

Table 40 Ring Compression Test Results at 135˚C and 0.0333 mm/s for 17×17 M5 Cladding Oxidized at 1200˚C and Slow-cooled (SC); ECR = 1.437 Wg for 0.61-mm-wall cladding

Test Conditions		ECR %		Plastic Displacement, mm		Plastic Strain, %	
Ox. Test Time[a], s	Cooling	CP	Meas.	Offset	Permanent	Offset	Permanent
208 208	SC SC	13.0 13.0	13.3 13.3	1.54 1.18	--- ---	16 13	--- ---
288 288	SC SC	16.0 16.0	17.3 17.3	0.32 0.32	0.17 0.14	3.4 3.4	1.8 1.5

[a]Includes time for ramp from 300ºC and hold time.

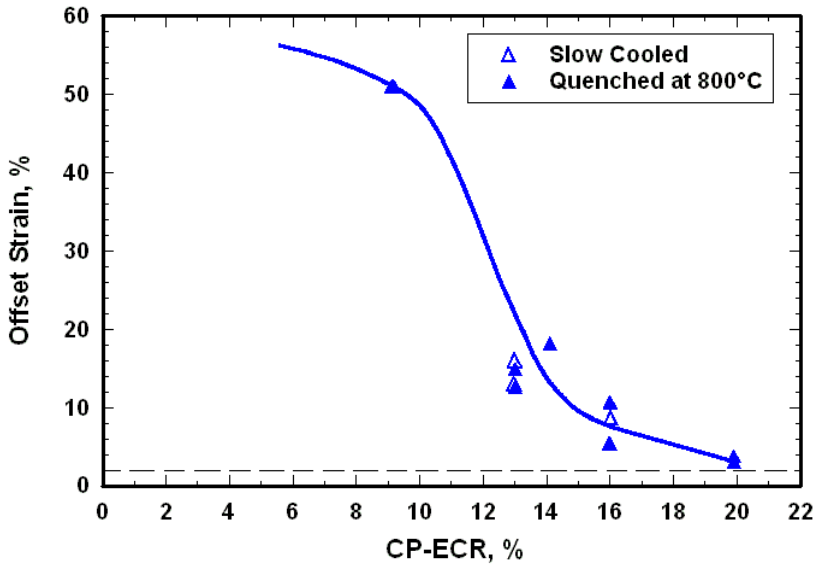

Figure 94. Effects of quench vs. slow cooling on the post-oxidation ductility of 17×17 M5 (0.61-mm wall) oxidized at 1200ºC, cooled at ≈13ºC/s to 800ºC and either quenched at 800ºC or slow cooled from 800ºC to RT. Ring-compression tests were performed at 135ºC and 0.0333 mm/s displacement rate.

3.7 Summary of results for as-fabricated cladding

Modern PWR and BWR cladding alloys are belt-polished on the cladding outer surface to reduce surface roughness to ≈0.1 μm. In addition to resulting in a smoother outer surface, the belt-polishing mechanically removes surface and substrate (<0.3 μm) impurities. The cladding inner-surface roughness is also reduced through a variety of techniques, including sand-blasting. Pickling (etching) with an acid mixture containing HF, which was used in the 1970s-1980s to remove surface impurities, is no longer used as a finishing step to convert tubing into cladding. This fabrication change has made the modern alloys more resistant to breakaway oxidation in the temperature range of 800-1000ºC. The modern alloys also retained post-quench ductility to higher CP-ECR (≥17%) values for oxidation temperatures in the range of 1000-1200ºC.

For steam-oxidation temperatures of 1000ºC and 1100ºC, modern PWR 17×17 alloys (Zry-4, ZIRLO and M5) retained RT post-quench ductility following two-sided oxidation to 20% CP-ECR, which is the highest oxidation level investigated in the ANL program, and quench at 800ºC. Hydrogen pickup for Zry-4 and M5 was very low (<25 wppm) for samples oxidized to 20% CP-ECR, so hydrogen did not induce embrittlement in these samples. For ZIRLO, hydrogen pickup was low (<20 wppm) for 1100ºC-oxidized samples and ≈100 wppm for the 1000ºC-oxidized sample at 20% CP-ECR (≈3400 s). Alloy differences in weight gain vs. time at 1000ºC were observed for ZIRLO and M5 as compared to Zry-4. The weight gain for each alloy correlated with the total (OD+ID) oxide layer thickness. However, the post-quench ductility of the three alloys was essentially the same after long-time oxidation at these temperatures and quench. In particular, the low weight gain and ECR (13%) measured for M5 after long-time oxidation at 1000ºC did not result in an enhancement in post-quench ductility relative to Zry-4, which exhibited higher weight gain and measured ECR (22%).

For Zry-4, ZIRLO and M5 oxidized at 1200ºC and quenched at 800ºC, RT embrittlement was observed at CP-ECR values significantly below 17%. However, when these samples were ring-compressed at 135ºC, the ductile-to-brittle transition CP-ECR increased to ≥17% (17% for Zry-4, 19% for ZIRLO and 20% for M5). Modern 15×15 Zry-4, which was also tested under these conditions, had a ductile-to-brittle transition CP-ECR of 19%. The 17×17 alloys were also tested after slow cooling from 1200ºC with no quench. The slow cooling had no effect on the ductile-to-brittle transition CP-ECR, indicating that lower quench temperatures would not result in an enhancement in ductility. Hydrogen pickup was very low for all three alloys and the prior-beta layer was thick enough (>0.25 mm) to preclude hydrogen-induced and beta-layer-thinning-induced embrittlement. Although the details of prior-beta-layer microstructure were observed to be quite different for ZIRLO and M5, the post-quench ductility results were comparable and correlated quite well with CP-ECR.

Although two-sided oxidized cladding samples maintain ductility up to 20% CP-ECR following oxidation at 1000ºC, the test times are short (3400 s for Zry-4 and ZIRLO, 4100 s for M5) relative to the test times needed to achieve these high CP-ECR levels for one-sided-oxidized cladding. Breakaway oxidation, hydrogen pickup and embrittlement occur for all Zr-based cladding alloys. However, there is considerable variability in time-at-temperature to initiate this instability and to pick up enough hydrogen to embrittle the cladding. Previous studies have shown early breakaway oxidation times for Zry-4 oxidized at 800ºC and 1000ºC. With respect to hydrogen pickup, these studies have also shown that oxidation at 1000ºC results in the shortest time to pickup 200-wppm hydrogen relative to other temperatures within the range of 800-1000ºC. In the ANL test program, two types of Zry-4 cladding alloys were subjected to numerous two-sided-oxidation tests at 985-1015ºC to determine breakaway oxidation time: HBR-type 15×15 low-tin Zry-4 and modern belt-polished (BP) 15×15 low-tin Zry-4. The only observable difference in the as-fabricated materials was the outer-surface roughness (0.32 μm

for HBR-type Zry-4 and 0.10 μm for BP Zry-4). However, when oxidized in the same test apparatus, the breakaway oxidation time – time to pick up 200 wppm H – for the rougher cladding was ≈3800 s, while the breakaway time for the smoother cladding was ≈5000 s. The effects of surface scratches, inadvertently induced during sample sectioning of HBR-type Zry-4, resulted in initiation of breakaway in the scratched region, hydrogen pickup and ≈200-s reduction in the breakaway time (3600 s vs. 3800 s). For BP 17×17 ZIRLO, the breakaway oxidation tests were conducted at 800ºC and 950-1015ºC. The minimum breakaway oxidation time was found to occur at 970ºC: 3000 s for smooth ZIRLO and 2700-2800 s for ZIRLO with a 20-μm-deep axial scratch machined into the outer surface. Thus, it appears that "normal" surface scratches that may be formed during handling and loading of rods into the assembly have a small influence on breakaway oxidation time.

The Russian Zr-1Nb cladding (E110) was added to the ANL test program to determine why this cladding exhibited such short breakaway oxidation times (600±100 s at 1000ºC) as compared to the breakaway oxidation times (>6000 s at 1000ºC) for the Zr-1Nb cladding (M5) used in the U.S. The ANL study focused primarily on E110 tubing (0.35-μm surface roughness), although some tests were conducted with pickled-and-anodized E110 cladding (0.19-μm surface roughness). Within the limitations of what ANL could measure and vary, no significant differences were found in chemical composition or microstructure between E110 and M5. Differences in surface roughness, along with possible differences in surface impurities, were considered as plausible reasons for behavior differences. ANL tests confirmed the poor performance of E110 at 1000ºC in terms of early hydrogen pickup and embrittlement and identified instability initiation sites (≤50 μm) on the E110 outer-surface oxide as early as 5 s at 1000ºC following a 75-s ramp from 300ºC to 1000ºC. ANL modified the E110 cladding to be more similar to M5 by polishing the outer surface to 0.14-μm surface roughness and by machining-and-polishing the inner surface to give the same wall thickness (0.6 mm) as M5. The outer-surface polishing increased the breakaway time from ≈600 s to ≈1200 s for the 1000ºC tests. For 1100ºC and 1200ºC oxidation temperatures, breakaway oxidation was not observed and post-oxidation ductility of the ANL-modified E110 was as good as Zry-4 and M5. Etching the E110 tubing surface with HF-containing acid baths tended to exacerbate breakaway oxidation for pre-etched samples oxidized at 1000ºC for a 290-s hold time. In a parallel study, pre-etched modern Zry-4, M5 and ZIRLO were oxidized at 1000ºC for 2400 s. Outer-surface oxidation of these alloys was much less sensitive than E110 to pre-etching with acid mixtures containing HF. However, the inner surface of the alloys, which is rougher than the belt-polished outer-surface, exhibited a superficial layer of gray monoclinic oxide following 2400 s at 1000ºC. The results support the contention that the combination of higher-surface roughness and etching with HF-containing acid mixtures promotes monoclinic-oxide formation, which can reduce breakaway oxidation time. The less stable the alloy, the more significant the reduction in breakaway-oxidation time.

Although the bulk properties of E110 may certainly make the alloy unstable, the instability is initiated earlier in time by high surface roughness, by deep surface scratches, by abrupt changes in geometry, and by surface-layer impurities (e.g., F). Based on the combined work of the Russian and ANL test programs, it appears that E110 can be fabricated to behave more like Western cladding under LOCA conditions if the Kroll process is used to refine the Zircon ore (rather than electrolytic refining), if pickling is not used to clean the inner surface, and if the outer-surface is belt-polished rather than pickled-and-anodized. Pickling can be used in intermediate fabrication steps if polishing or sand-blasting is used as a final finishing step to mechanically remove the sub-micron layer of F impurity resulting from pickling.

4 Results for Prehydrided Cladding Alloys

High-burnup operation results in cladding outer-surface corrosion (oxidation) and hydrogen pickup. Hydrogen can reduce significantly the ductile-to-brittle transition ECR, especially at high oxidation temperatures. Baseline data are needed on the effects of hydrogen on embrittlement. Such data are generated with non-irradiated cladding, which has been prehydrided prior to testing. As tests with non-irradiated cladding are much easier to conduct, a relatively large number of tests can be conducted to map out embrittlement as a function of hydrogen content, oxidation temperature, oxidation level (e.g., CP-ECR) and quench temperature. The data generated using prehydrided cladding samples help in both planning and interpreting the results of tests conducted with high-burnup cladding.

In this section, post-quench ductility data are presented for prehydrided Zry-4 cladding oxidized at 1200ºC and either slow cooled to RT or quenched at 800ºC, 700ºC, or 600ºC. The reference test conditions are the same as those for the as-fabricated alloys: oxidize 25-mm-long samples at 1200ºC to the desired CP-ECR level, cool at ≈13ºC/s from 1200ºC to 800ºC, and rapidly cool (by means of bottom-flooding quench water flow) from 800ºC to 100ºC, slow cool from 100ºC to RT, and ring-compress at 135ºC 8-mm-long rings sectioned from the oxidation sample.

4.1 Prehydrided Zircaloy-4 oxidized at 1200ºC and quenched at 800ºC

Two methods have been used to introduce hydrogen into Zry-4 segments. During the period of June – October 2004, prehydriding was performed at 400ºC in a closed, quartz chamber (1.5-liter volume) with a gas mixture of 4% H_2 in argon at near ambient pressure. The 100-mm-long segments were wrapped in aluminum foil to prevent oxide film buildup while allowing hydrogen atoms to permeate to the surface of the Zry-4 sample. The exposure times used to introduce 200-600 wppm of hydrogen into the segment were 1500 to 4500 s. This simple procedure resulted in circumferential hydrides uniformly distributed through the wall of the Zry-4 segments (see Figure 95).

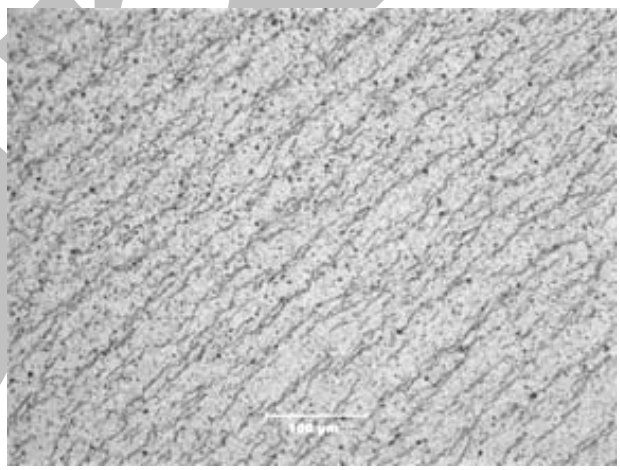

Figure 95. Uniform distribution of circumferential hydrides across the wall of HBR-type 15×15 Zry-4 prehydrided to 400 wppm H.

However, due to furnace temperature gradients and non-uniform cladding surface conditions, the hydrogen-concentration gradients in the axial and circumferential directions were significant. For a segment with a target hydrogen content of 500 wppm, the axial gradient was ≈4 wppm/mm and the circumferential gradient varied from ≈0.6-to-6 wppm/mm for a 25-mm-long sample. The procedure for

homogenization of the hydrogen calls for heating the sample to 400ºC for 72 hours in an inert atmosphere. However, even high-purity argon contains trace impurities of oxygen, moisture and nitrogen, which would result in the growth of surface oxide layers and possible nitrogen-contamination of these layers. As it was desirable to avoid surface modification during sample preparation for steam-oxidation tests, this homogenization step was not used for LOCA test samples. In planning the oxidation tests for prehydrided cladding alloys, it was assumed that homogenization of hydrogen would occur during the oxidation heating ramp.

Early test results indicated that the circumferential and axial gradients in hydrogen content remained after oxidation tests conducted at 1200ºC. Redistribution of hydrogen across the wall of the cladding should be very rapid as the wall is thin (0.57-0.77 mm) and the beta layer has a very high affinity for hydrogen. However, it was surprising to discover that no significant redistribution of hydrogen occurred in the longer axial direction (25 mm) or the circumferential direction (≈30 mm). Figure 96 shows the hydrogen distribution for a prehydrided HBR-type Zry-4 oxidation sample before and after testing. Prior to oxidation, hydrogen levels were measured for 2-mm-long rings cut from both sides of a 30-mm-long sample. Following oxidation of the remaining 25-mm-long sample to 5% CP-ECR (92-s from beginning of ramp to the end of the 1200ºC hold time), hydrogen readings were obtained from the center of the oxidized sample and from the 8-mm-long rings used in the ring compression tests. These post-oxidation hydrogen measurements were corrected for weight gain for comparison to pretest values.

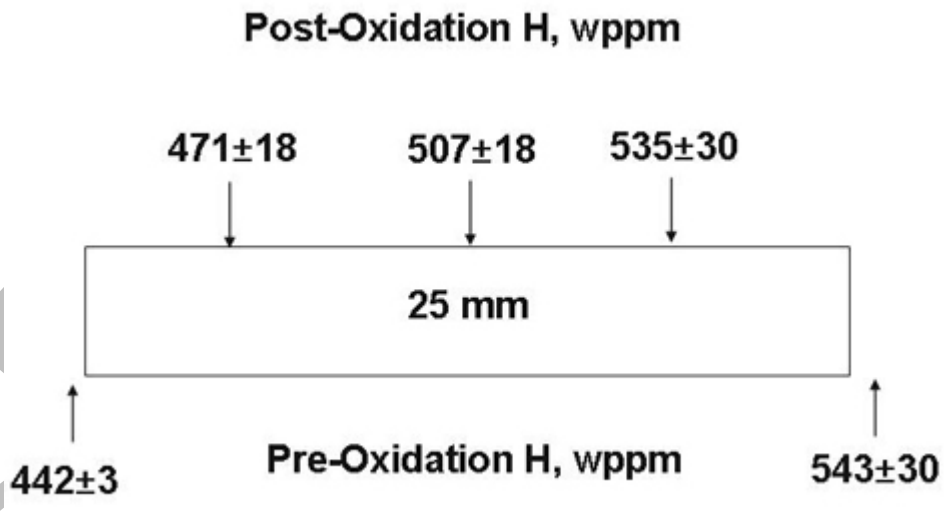

Figure 96. Hydrogen concentration in a prehydrided HBR-type 15×15 Zry-4 sample before and after oxidation at 1200ºC to 5% CP-ECR. Hydrogen contents after oxidation were corrected for sample weight gain to allow direct comparison with pre-test hydrogen contents.

The gradients following high-temperature oxidation were comparable to the pretest gradients, indicating that hydrogen did not homogenize under these test conditions. Although gradients in hydrogen concentration are not desirable for controlled studies, the relative immobility of the hydrogen allowed ANL to study the local effects of hydrogen concentration on post-quench ductility for samples oxidized to the same CP-ECR levels. The approach is reasonable even for samples with more uniform distribution of hydrogen. As prehydriding Zry-4 is more of an art than a science, prehydrided Zry-4 used in other LOCA-relevant studies (e.g., CEA, JAEA) does have axial gradients that lead to sample-to-sample variation in hydrogen for samples cut from the same prehydrided segment.

Modern 17×17 Zry-4 and HBR-type 15×15 Zry-4 segments were prehydrided by the closed-system method. Due to material available, more 15×15 Zry-4 segments were prehydrided for oxidation tests. The baseline data generated for HBR-type 15×15 Zry-4 were used to plan the in-cell oxidation tests with high-burnup HBR cladding (see 5.1).

The improved and more recent method used for prehydriding cladding alloys utilizes a three-stage furnace for temperature control and flowing gas containing either a 4% H_2 - 96% Ar mixture or 100% H_2. Prehydriding has been conducted at 350ºC with this system. Segments were 50-to-100-mm-long HBR-type 15×15 Zry-4 prehydrided to 180-880 wppm. Because of the temperature uniformity in the new system, better homogenization of hydrogen was achieved in the axial and circumferential direction with this system. It was difficult to control the final hydrogen content for segments prehydrided with 100% H_2, which was both flowing and at a slightly elevated pressure (0.1113 MPa absolute). Hydrogen uptake progressed very slowly for the first 4.5 hours of exposure with hydrogen contents ranging from ≈70 wppm at 2-hours exposure to ≈180 wppm at 4.75-hours exposure. Within the range of 5 to 8 hours, hydrogen uptake increased dramatically from 200 wppm to 900 wppm, but duplicate tests conducted for the same time-temperature history did not result in the same hydrogen contents (e.g., for a 7-hour hold time at 350 ºC, one sample picked up 140 wppm while another sample picked up 730 wppm). Also, for >200-wppm-H pickup, a dense hydride rim formed on or near the inner-surface of the cladding, even though hydrogen flowed along both the inside and outside of the segment. Several oxidation samples were prepared by this technique. The dense hydride rim near the inner-cladding surface was not considered to be an issue for oxidation tests because hydrogen redistribution across the wall of the cladding is rapid in the beta phase and this phase has a high affinity for hydrogen.

Better control was achieved using the 4% H_2 - 96% Ar gas mixture at the same ambient temperature (350ºC) and absolute pressure (0.1113 MPa). However, it was necessary to pre-wrap the segments in aluminum foil to reduce test time and to inhibit oxide buildup on the cladding segment surfaces. This process was used to generate HBR-type Zry-4 samples for post-quench ductility studies.

4.1.1 Post-quench ductility of prehydrided 17×17 Zry-4 oxidized at 1200ºC

The ANL tests with prehydrided 17×17 Zry-4 samples were conducted during June-October 2004 with samples prepared by the old prehydriding method. Because of ANL's limited supply of 17×17 Zry-4 and the old oxidation test train used, the results should be used more for scoping purposes to determine ranges of hydrogen contents and CP-ECR levels for which post-quench ductility was retained. There were indications from foreign partners that hydrogen contents of 300-600 wppm were enough to completely embrittle Zry-4 after exposures to 1200ºC for test times <60 s and CP-ECR levels <5%. These test results were later published by Mardon et al. [21]. The results were generated using very rapid heating to 1200ºC, oxidation at 1200ºC for various hold times, and direct quench at 1200ºC. Thus, it was important to conduct companion tests with the ANL test protocol (slow ramp from about 1150ºC to 1200ºC, hold at 1200ºC for various test times, cool at ≈13ºC/s, quench at 800ºC, slow cool from 100ºC to RT, and ring-compress at 135ºC). Because of the axial gradients in the ANL prehydrided samples, the approach used was to study the effects of hydrogen on embrittlement at two target CP-ECR values: 7.5% and 10%. The thermal history for the test train used for oxidation is given in Figure 20. However, because so many tests had been conducted with this test train, it was re-benchmarked during the testing of the prehydrided 17×17 Zry-4 samples.

Table 41 summarizes the post-quench ductility results for prehydrided 17×17 Zry-4 oxidized at 1200ºC to target CP-ECR levels of 7.5% and 10%. Test times were selected based on the thermal history

in Figure 20. Calculated CP-ECR levels were later corrected based on the thermal re-benchmarking for the old test train. The hydrogen contents listed in Table 41 were determined from 2-mm-long rings cut

Table 41 Ring Compression Test Results for Prehydrided 17×17 Zry-4 Cladding Oxidized at 1200˚C, Cooled at ≈13ºC/s to 800˚C and Quenched. ECR = 1.538 Wg for 0.57-mm-wall cladding. Tests were performed on ≈8-mm-long samples at 135ºC and 0.0333 mm/s displacement rate.

Test Conditions		ECR %		Plastic Displacement, mm		Plastic Strain, %	
H Content wppm	Ox. Test Time[a], s	CP	Meas.	Offset	Permanent	Offset	Permanent
5	100	7.8	8.2	5.48	4.82	58	51
247	95	7.6	8.5	3.30	3.02	35	32
278	95	7.6	8.5	1.13	---	12	---
314	95	7.6	8.5	1.95	---	21	---
412	100	7.5	8.8	0.05	0.07	0.5	0.7
438	100	7.5	8.8	0.06	0.08	0.6	0.8
524	100	7.5	8.8	0.06	---	0.6	---
5	151	10.8	11.9	2.14	---	23	---
5	151	10.8	11.9	>2.41	>1.92	>25	>20
154	136	9.4	9.9	2.87	2.58	30	27
209	136	9.4	9.9	0.52	0.31	5.5	3.3
274	136	9.4	9.9	0.27	---	2.8	---
335	141	10.1	12.8	0.06	0.04	0.6	0.4
462	141	10.1	11.2	0.04	0.08	0.4	---
499	141	10.1	11.2	0.05	0.04	0.5	0.4

[a]Includes time for ramp from 300ºC and hold time.

from prehydrided segments prior to oxidation and post-oxidation samples cut before and after ring-compression testing. For the post-oxidation hydrogen readings, the hydrogen concentration was corrected for weight gain to reference the hydrogen content to the pre-oxidized sample weight. The nominal CP-ECR values used for plotting trend curves are 7.5% and 10%. The lower CP-ECR values for the prehydrided samples are 7.5-7.6%. The 7.8% CP-ECR for the as-fabricated sample (no prehydriding) is not significantly different from 7.5% because the ductility is so high. The higher CP-ECR values for the prehydrided samples are 9.4-10.1% and 10.8% for the as-fabricated sample (no prehydriding). Given the sparse data set, the variable hydrogen content along the samples, and the condition of the test train used, the CP-ECR groupings are reasonable.

The offset strain data and the trend curves are plotted in Figure 97. At 7.5% CP-ECR, the ductile-to-brittle transition occurs between 314 wppm and 412 wppm hydrogen. The ductile-to-brittle transition is interpolated to occur at 375±25 wppm for 7.5% CP-ECR oxidation level. At 10% CP-ECR, Zry-4 is ductile at 274-wppm H and brittle at 335-wppm H. The ductile-to-brittle transition is interpolated to

occur at 300±25 wppm H for 10% CP-ECR oxidation level. These results are not inconsistent with the results presented by Mardon et al. [21]. The hydrogen content for their samples was 600-wppm (most likely 600±50 wppm) in 17×17 Zry-4 with 0.57-mm-wall thickness; the samples were one-sided oxidized at 1200ºC under isothermal conditions; and the samples were quenched at 1200ºC.

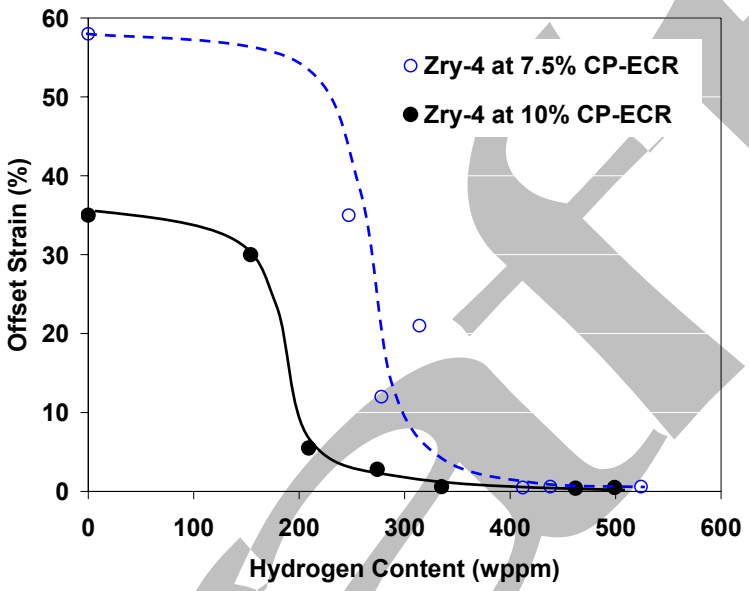

Figure 97. Variation of post-quench ductility with pre-test hydrogen content for modern 17×17 Zry-4 oxidized at 1200ºC to 7.5% and 10% CP-ECR (see Figure 20 for temperature history), cooled at ≈13ºC/s, quenched at 800ºC and ring-compressed at 135ºC and 0.0333 mm/s.

More data would be needed for modern 17×17 Zry-4 to map out combinations of hydrogen content, oxidation temperature and CP-ECR leading to embrittlement; to determine the influence of heating rate on post-quench ductility; and to determine the influence of cooling rate and quench temperature on post-quench ductility. The database for HBR-type 15×15 Zry-4 oxidized at 1200ºC is more extensive and is presented in 4.1.2 for quench at 800ºC and in 4.2 for quench at 700ºC and 600ºC vs. slow-cooling to RT.

4.1.2 Post-quench ductility of prehydrided HBR-type 15×15 Zry-4 oxidized at 1200ºC

The tests with prehydrided 15×15 Zry-4 samples were conducted with well-benchmarked test trains. Tests conducted during June-December 2004 used the test train with the temperature history shown in Figure 10. Tests conducted from January-June 2006 have a thermal history presented in Figure 98, which is very similar to the one in Figure 10. Tests conducted after June 2006 are characterized by the thermal history shown in Figure 99, which has a faster ramp to 1200ºC and a temperature overshoot of 16ºC early in the transient. The same test protocol used for oxidizing prehydrided 17×17 Zry-4 was used for the HBR-type Zry-4. However, as this material in the as-fabricated condition exhibited a relatively low ductile-to-brittle-transition CP-ECR (14%), the target CP-ECR values were reduced to 5% and 7.5%. The 7.5% CP-ECR oxidation level allowed a direct comparison of the two data bases. In evaluating the ANL data, it is important to note that 5% CP-ECR was reached for most samples during the slow part of

the heating ramp with a peak temperature of 1190ºC (Figure 10) or 1180ºC (Figure 98) prior to cooling. The oxidation level of 7.5% was achieved for most samples at the end of a 55-s hold time at 1204ºC. Tables 42 and 43 summarize the post-quench ductility results for prehydrided 15×15 Zry-4 oxidized to target CP- ECR levels of 5% and 7.5%, respectively. The footnotes to Tables 42 and 43 identify the thermal history for the tests conducted in 2006.

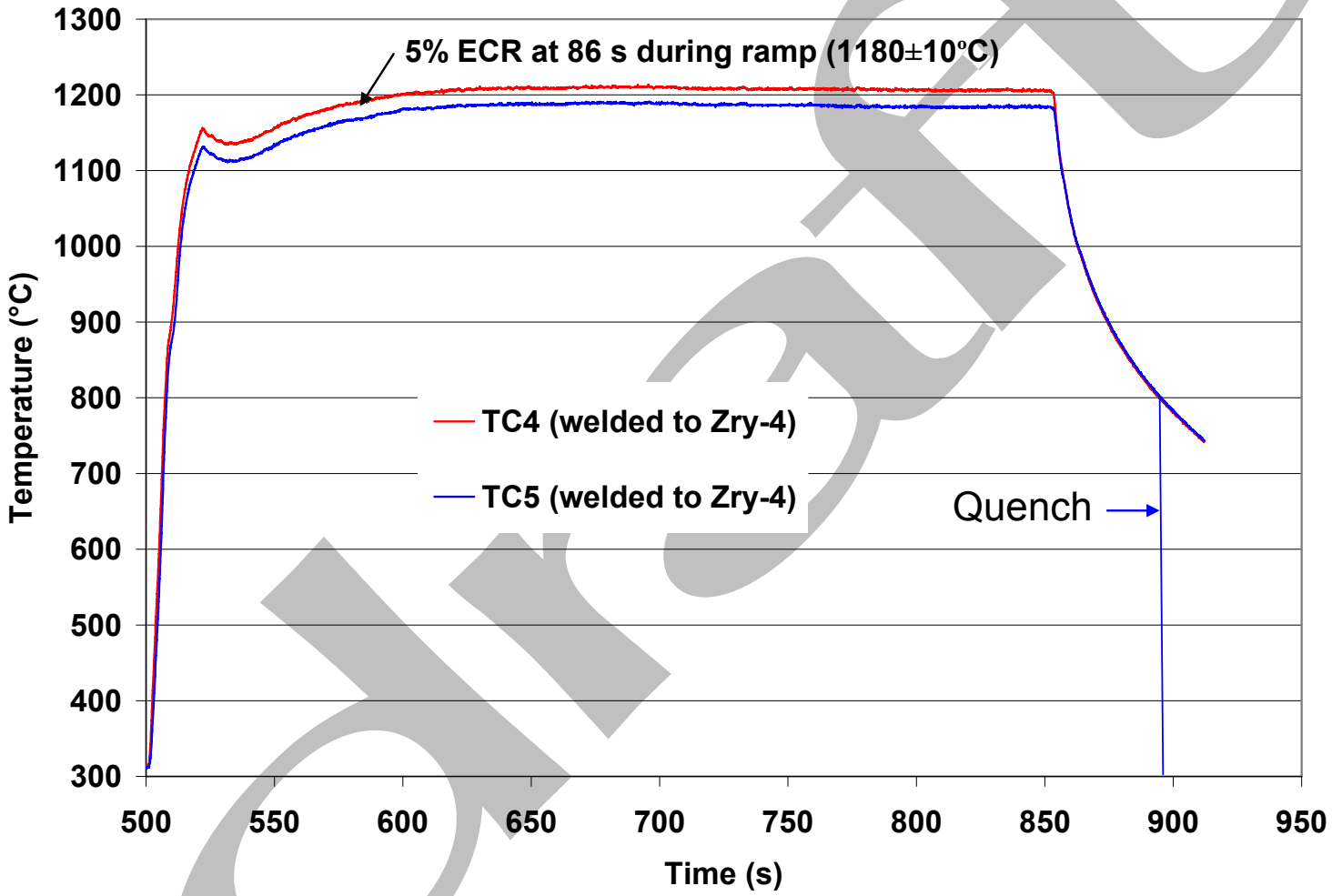

Figure 98. March 2006 thermal benchmark results for HBR-type 15×15 Zry-4 with a target oxidation temperature of 1200ºC.

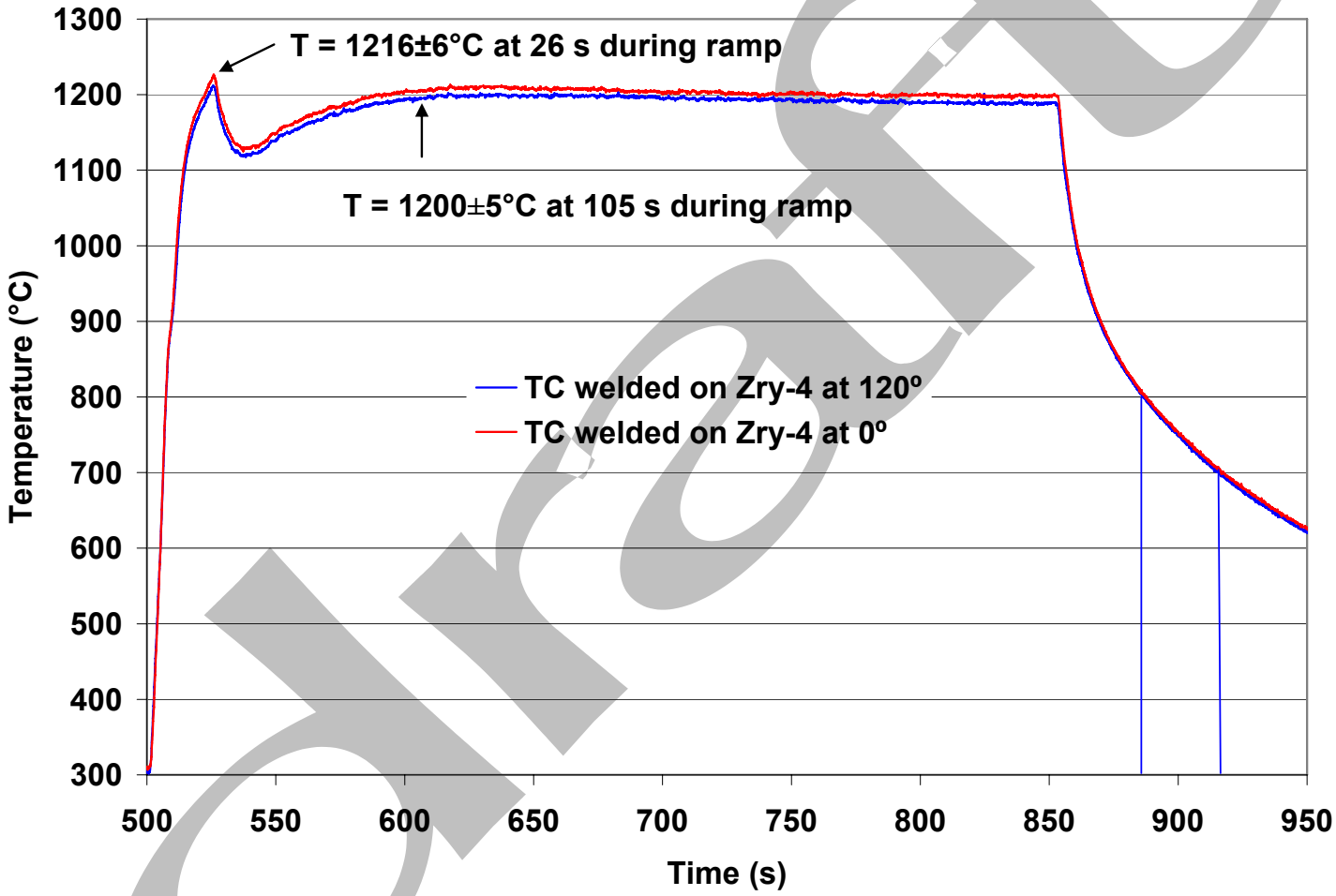

Figure 99. June 2006 thermal benchmark results for HBR-type 15×15 Zry-4 with a target oxidation temperature of 1200ºC.

Data and trend curves for offset strain vs. pre-oxidation hydrogen content are given in Figures 100 and 101 for the 5% and 7.5% CP-ECR oxidation levels, respectively. For 5%-CP-ECR test conditions, Zry-4 exhibits post-quench ductility up to ≈550-wppm hydrogen and is definitely brittle at ≈640-wppm hydrogen. Although the ductile-to-brittle-transition hydrogen content at 5% CP-ECR is not precisely determined, 600-wppm hydrogen appears to be a reasonable value based on interpolation. The transition CP-ECR and/or the hydrogen content would decrease for tests with faster heating ramps and longer hold-times at ≈1200ºC.

For the 7.5% CP-ECR oxidation level, one Zry-4 sampled exhibited ductility at 400-wppm hydrogen. However, embrittlement is observed for other test samples with hydrogen contents as low as 335 wppm. For the slower heating-rate cases (Figure 10 and Figure 98), the ductile-to-brittle transition hydrogen level can be characterized as 375±25 wppm. These results are consistent with the results for 17×17 Zry-4 oxidized at 1200ºC to 7.5% CP-ECR. Thus, within the data scatter, it does not appear that the higher transition CP-ECR for as-fabricated 17×17 Zry-4 leads to higher transition values for prehydrided 17×17 Zry-4, as compared to HBR-type 15×15 Zry-4. For the heating rate shown in Figure 99 Zry-4 embrittlement can occur at hydrogen levels as low as 335 wppm at 7.5% CP-ECR.

Table 42 Post-quench Ductility of Prehydrided HBR-type 15×15 Zry-4 Cladding Oxidized to 5% CP-ECR with T = 1180-1190ºC at End of Heating Ramp, Cooled at ≈13ºC/s to 800˚C and Quenched (Q); ring-compression tests were performed on ≈8-mm-long samples at 135ºC and 0.0333 mm/s displacement rate; ECR = 1.1535 Wg for 0.76-mm wall and 1.1385 Wg for 0.77-mm wall; displacements were normalized to 10.77-mm OD for 0.76-mm-wall and 10.76-mm OD for 0.77-mm-wall cladding

Sample and Test Conditions			ECR %		Plastic Displacement, mm		Plastic Strain, %	
Q-T ºC	Test Time[a], s	H wppm	CP	Meas.	Offset	Permanent	Offset	Permanent
800	93	22	5.0	5.1	>6.0	>5.5	>56	>51
800	92	320	5.0	5.4	5.49	---	51	---
800	92	375	5.0	5.4	3.38	3.36	31	30
800	92	400	5.0	5.4	3.91	3.56	36	33
800	92	400	5.0	5.4	2.98	3.02	28	28
800	92	480	5.0	5.4	0.68	---	6.3	---
800	92	517	5.0	5.4	0.57	---	5.4	---
800	92	545	5.0	5.4	1.45	---	13.5	---
800	92	636	5.0	5.6	0.06	0.04	0.5	0.4
800[b]	**96**	**710**	**5.0**	**5.7**	**0.06**	**0.07**	**0.5**	**0.6**
800[b]	**96**	**730**	**5.0**	**5.7**	**0.05**	**---**	**0.5**	**---**
800[b]	**96**	**760**	**5.0**	**5.7**	**0.03**	**---**	**0.3**	**---**
800	92	800	5.0	5.4	0.03	---	0.3	---

[a]From beginning of ramp at 300ºC to end of hold time at 1204ºC (see Figure 10 for thermal history).

[b]See Figure 98 for thermal history of these tests conducted in 2006; ECR = 1.1385 Wg.

Table 43 Post-quench Ductility of Prehydrided HBR-type 15×15 Zry-4 Cladding Oxidized at 1200˚C to 7.5% CP-ECR, Cooled at ≈13ºC/s to 800˚C and Quenched (Q); ring-compression tests were performed on ≈8-mm-long samples at 135ºC and 0.0333 mm/s displacement rate; ECR = 1.1535 Wg for 0.76-mm wall and 1.1385 Wg for 0.77-mm wall; displacements were normalized to 10.77-mm OD for 0.76-mm-wall and 10.76-mm OD for 0.77-mm-wall cladding

Sample and Test Conditions			ECR %		Plastic Displacement, mm		Plastic Strain, %	
Q-T ºC	Test Time[a] s	H wppm	CP	Meas.	Offset	Permanent	Offset	Permanent
800 800	154 145	22 22	7.5 7.5	8.1 7.6	>4.7 5.53	>4.3 ---	>43 51	>40 ---
800[b]	**144**	**185**	**7.4**	**8.1**	**1.41**	**1.2**	**13**	**11**
800[c] **800[c]**	**132** **132**	**335** **335**	**7.4** **7.4**	**7.7** **7.7**	**0.08** **0.12**	**---** **0.08**	**0.7** **1.1**	**---** **0.7**
800	145	360	7.5	7.6	0.54	---	5.0	---
800	145	386	7.5	7.7	0.20	---	1.9	---
800	145	386	7.5	7.7	0.11	0.07	1.0	0.6
800	145	386	7.5	7.7	0.06	0.04	0.6	0.4
800	145	390	7.5	7.6	0.09	---	0.8	---
800	145	400	7.5	7.6	0.23	0.11	2.1	1.0
800[b]	**144**	**435**	**7.4**	**8.0**	**0.05**	**0.03**	**0.5**	**0.3**
800[b]	**144**	**435**	**7.4**	**8.0**	**0.05**	**0.03**	**0.5**	**0.3**
800	145	533	7.5	8.1	0.05	---	0.5	---
800	145	600	7.5	8.1	0.04	---	0.4	---

[a]From beginning of ramp at 300ºC to end of hold time at 1204ºC (see Figure 10 for thermal history).

[b]Tests conducted with thermal history shown in Figure 98; ECR = 1.1385 Wg.

[c]Tests conducted with thermal history shown in Figure 99; ECR = 1.1385 Wg.

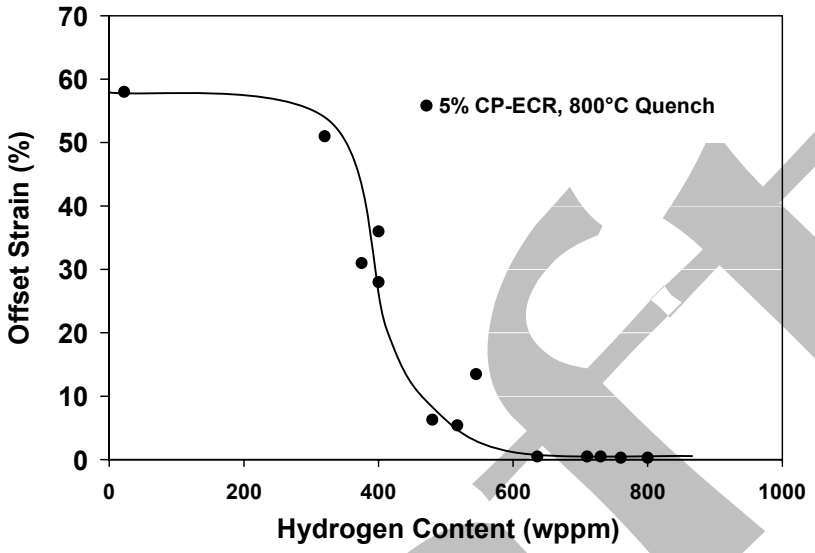

Figure 100. Variation of post-quench ductility with pre-test hydrogen content for HBR-type 15×15 Zry-4 oxidized to 5% CP-ECR with an end-of-heating temperature of 1180-1190ºC (see Figures 10 and 98), cooled at ≈13ºC/s, quenched at 800ºC and ring-compressed at 135ºC.

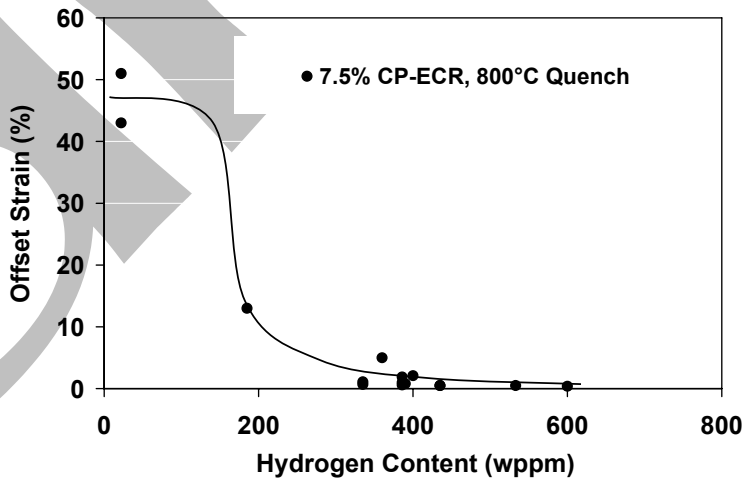

Figure 101. Variation of post-quench ductility with pre-test hydrogen content for HBR-type 15×15 Zry-4 oxidized at 1204ºC to 7.5% CP-ECR (see Figures 10, 98 and 99), cooled at ≈13ºC/s, quenched at 800ºC and ring-compressed at 135ºC.

In order to better understand the significant decrease in post-quench ductility with increasing hydrogen content, metallography and microhardness were performed on as-received HBR-type Zry-4 and prehydrided (600 wppm) HBR-type Zry-4 both oxidized at ≈1200ºC to 7.5% CP-ECR. Figure 102 shows typical cross sections (one out of eight circumferential locations) of the as-received (102a) and prehydrided (102b) samples following oxidation and quench at 800ºC. Although both samples show evidence of alpha incursions precipitated during cooling in the prior-beta layer, they appear to be larger and more pronounced in the as-received Zry-4. The layer thicknesses are comparable and do not reveal any indication that would suggest one sample was highly ductile and the other sample was highly brittle. Table 44 summarizes measured sample weight gain, layer thicknesses determined from metallographic images, weight gain determined from the layer thicknesses, and post-quench ductility. The presence of 600-wppm hydrogen resulted in embrittlement (nil-ductility) of Zry-4 oxidized to 7.5% CP-ECR, whereas the as-received Zry-4 sample exhibited a very high offset strain of >43% (limit of this particular test) at 135ºC RCT temperature. The prior-beta-layer microhardness profiles shown in Figure 103 also reveal significant differences between the two samples. The local and average microhardness values in the prior-beta layer for the prehydrided sample are significantly higher than the ones for the as-received sample. These results are consistent with the post-quench ductility results.

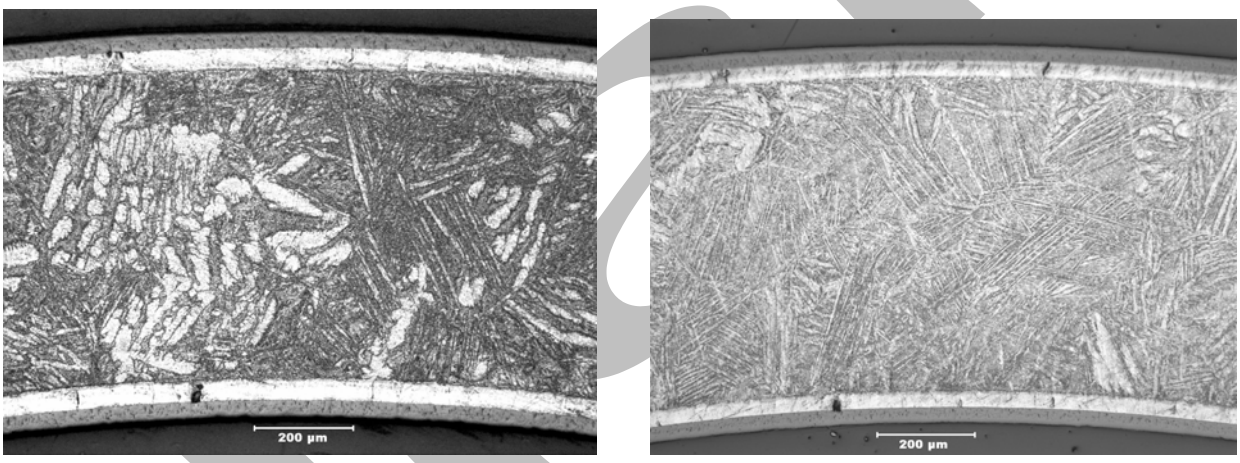

(a) As-received (b) 600-wppm hydrogen

Figure 102. Metallographic images of HBR-type 15×15 Zry-4 following oxidation at ≈1200ºC to 7.5% CP-ECR, cooling at ≈13ºC/s to 800ºC, and quench at 800ºC: (a) as-received; and (b) 600-wppm hydrogen.

Table 44 Comparison of Results for As-received and 600-wppm-prehydrided HBR-type 15×15 Zry-4 Samples after Exposure to Steam at ≈1200˚C to 7.5% CP-ECR, Cooling at ≈13ºC/s to 800˚C and Quench at 800˚C

Parameter	HBR-Type 15x15 Zry-4	
	As-received	**Prehydrided**
Hydrogen Content, wppm	≈10	600
Hold Temperature, ˚C	1200±17	1204±10
CP-ECR, %	7.5	7.5
CP Weight Gain, mg/cm^2	6.5	6.5
Measured Weight Gain based on Change in Sample Weight, mg/cm^2	6.94	6.75
Measured ECR, %	8.0	7.8
Outer-surface Oxide Layer, µm	35	33
Outer-surface Alpha Layer, µm	41	38
Prior-beta Layer, µm	636	640
Inner-surface Alpha Layer, µm	40	39
Inner-surface Oxide Layer, µm	36	34
Weight Gain Determined from Metallography, mg/cm^2	---	6.7
Post-Quench Ductility, % (Offset Strain)	>43	0.4

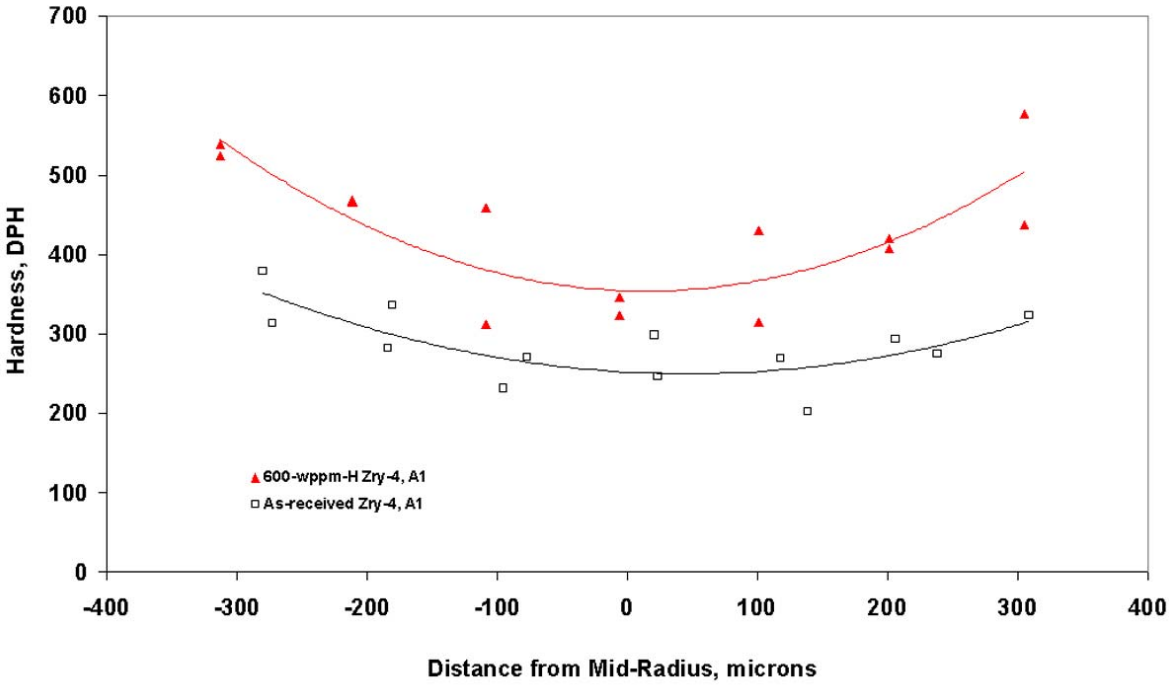

Figure 103. RT microhardness profiles across the prior-beta layer of two samples oxidized at ≈1200˚C to 7.5% CP-ECR, cooled at ≈13ºC/s to 800˚C and quenched at 800˚C: as-received and 600-wppm-hydrogen HBR-type 15×15 Zry-4.

The elevated RT microhardness for the prehydrided sample suggests that hydrogen increases the rate of oxygen diffusion into the beta layer during oxidation at elevated temperature and/or that hydrogen has a direct effect on increasing hardness and embrittlement. Based on the results of Mardon et al. [21, Figure 16], 600-wppm of hydrogen causes the solubility limit of oxygen in the prior-beta layer to increase by 0.4±0.1 wppm relative to as-received material oxidized at 1200ºC. If the Chung and Kassner [18] solubility limit of 0.57-wt.% oxygen at 1200˚C is used for as-received Zry-4, then the oxygen solubility limit for 600-wppm-H Zry-4 would be 1.0±0.1 wt.%. The oxygen concentration in the beta layer at the alpha-beta boundary would increase from ≈0.6 wt.% to ≈1.0 wt.%. Using the oxygen diffusivity determined by Pawel et al. [26], the solubility limit for the oxygen concentration at the alpha-beta boundary, the as-received oxygen concentration for the "zero-time" oxygen concentration across the beta layer, and end-of-oxidation beta-layer thickness (approximation to bypass more complicated moving-boundary problem), the oxygen profiles were calculated and compared to the microhardness profiles across the beta layer for as-received and 600-wppm-prehydrided Zry-4. The results are given in Figure 104 for as-received (a) and prehydrided (b) Zry-4 oxidized at ≈1200˚C to 7.5% CP-ECR. These calculated oxygen concentrations do not agree very well with the microhardness vs. oxygen-content results of Mardon et al. [21, Figure 16]. The results of Mardon et al. show a linear relationship between microhardness and oxygen concentration for samples oxidized long enough at 1000-1200ºC to approach the solubility limit. The non-linear relationships shown in Figures 104a and 104b suggest that the model and oxygen diffusivity used to calculate the oxygen profiles may need some improvement.

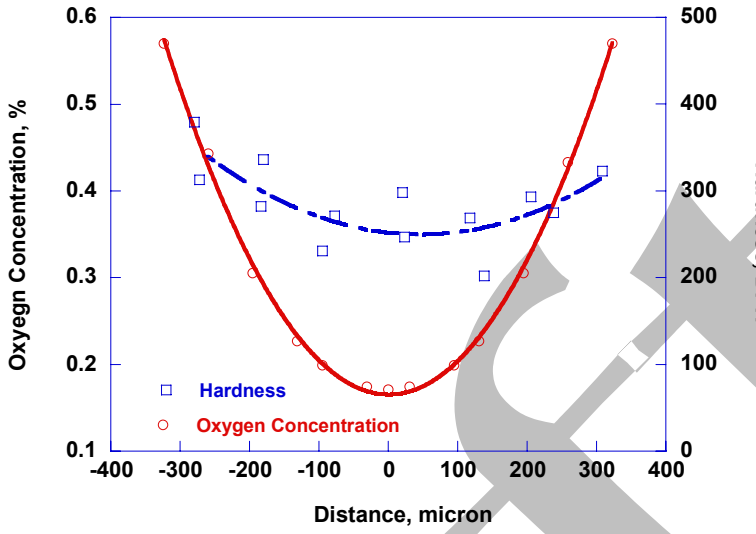

(a)

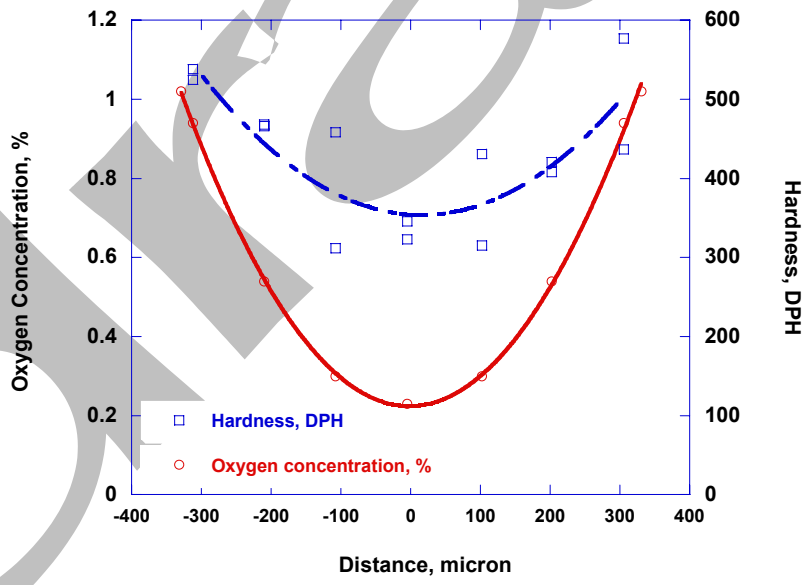

(b)

Figure 104. RT microhardness and oxygen-concentration profiles across the beta layers of HBR-type 15×15 Zry-4 oxidized at ≈1200˚C to 7.5% CP-ECR, cooled at ≈13ºC/s to 800˚C and quenched at 800˚C: (a) as-received; and (b) 600-wppm hydrogen.

4.2 Effects of cooling rate and quench temperature on post-quench ductility

The effects of heating rate on post-quench ductility and ductile-to-brittle transition CP-ECR are reasonably well understood. At a fixed CP-ECR, cladding oxidized at a slow heating rate to 1200ºC will exhibit higher post-quench ductility than cladding oxidized at a very rapid heating rate to 1200ºC. The rapidly heated sample would experience more time at 1200ºC and would pick up more oxygen in the beta layer due to higher diffusivity and solubility at 1200ºC as compared to lower oxidation temperatures. However, the effects of cooling rate and quench temperature on post-quench ductility are not well understood. In section 3.6, it was shown that as-fabricated Zry-4, ZIRLO and M5 samples quenched at 800ºC after oxidation at 1200ºC exhibited the same ductile-to-brittle-transition CP-ECR as samples slow cooled from 1200ºC to RT. These transitions occurred at 17-20% CP-ECR and correspond to relatively long test times. For the oxygen-induced embrittlement of as-fabricated cladding alloys, the cooling rate from 800ºC to RT appears to be insignificant. However, tests needed to be conducted with prehydrided and high-burnup samples before conclusions could be drawn with regard to the effects of cooling rate and quench temperature on post-quench ductility.

In order to address these issues for prehydrided samples, tests were conducted with prehydrided HBR-type 15×15 Zry-4 to determine the effects of quench temperature on post-quench ductility for samples oxidized at 1200ºC. Prehydrided samples were oxidized to the same CP-ECR level and: cooled at an average rate of 13ºC/s to 800ºC and quenched (Q); or cooled at an average rate of 7.3ºC/s to 700ºC and quenched, or slow cooled (SC) from 1200ºC to RT. The relevant temperature histories for these tests are shown in Figures 98 and 99. Because of the significant database presented in 4.1 for HBR-type 15x15 Zry-4 at 5% and 7.5% CP-ECR, the same oxidation levels were used in this study. The results for Zry-4 oxidized to 5% CP-ECR are listed in Table 45 and shown in Figure 105, along with the data in Table 42. The 7.5% CP-ECR results are listed in Table 46 and shown in Figure 106, along with the data in Table 43.

The prehydrided (710-760 wppm) samples quenched at 800ºC were brittle after oxidation to 5% CP-ECR. Slow-cooled samples with the same hydrogen content and oxidized to the same CP-ECR had marginally higher offset and permanent strains. Nevertheless, the difference is significant as all 6 samples exhibited low ductility (offset strain ≥ 2.0%, permanent strain ≥ 1.4%). Quenching at 800ºC essentially "freezes" in the distribution of oxygen within the high-oxygen-containing alpha incursions precipitated during very rapid cooling from 800ºC to 100ºC and the low-oxygen-containing prior beta matrix. For the slow-cooled samples, oxygen diffusion is very slow below 800ºC and is not predicted to occur. However, most of the hydrogen is expected to be in solution in the low-oxygen-containing part of the prior-beta layer. Hydrogen has more mobility than oxygen at <800ºC. It can move to the interfaces of these two regions and form small precipitates. If the oxygen concentration remains the same in the low-oxygen containing prior-beta and the hydrogen concentration decreases with slow cooling, the ductility results suggest that hydrogen causes a small amount of embrittlement beyond what is expected due to its enhancement of oxygen solubility in the prior-beta layer. If the hydrogen is given time to migrate out of the low-oxygen prior-beta regions, then ductility of these regions appears to be enhanced.

The results following oxidation to 7.5% CP-ECR are equally interesting. These prehydrided samples were at a hold temperature of ≈1200ºC for ≈60 s. Depending on the heating rate (Figure 10, 98 or 99), embrittlement for 800ºC-quenched Zry-4 samples occurred in the range of 335-wppm (Figure 99 heating rate) to 400-wppm H (one sample with Figure 10 heating rate). However, slow-cooled samples exhibited low ductility for hydrogen contents up to ≈550 wppm, with one sample marginally brittle at 530 wppm H and another one ductile at 570 wppm. As with the prehydrided 5% CP-ECR samples, the enhancement in offset and permanents strains is small but significant. For the aggressive heating rate in

Figure 99, samples with ≈330 wppm H were brittle following quenching at 800ºC, brittle (2 out of 3 samples) following quenching at 700ºC, and marginally ductile following slow-cooling to RT.

Table 45 Post-quench Ductility of Prehydrided HBR-type 15×15 Zry-4 Cladding Oxidized to 5% CP-ECR with T = 1180ºC at End of Heating Ramp, Cooled at 13ºC/s to 800˚C, and either Quenched (Q) at 800ºC or Slow Cooled to RT; ECR = 1.1385 Wg; ring-compression tests performed on ≈8-mm-long samples at 135ºC and 0.0333 mm/s displacement rate

Sample and Test Conditions			ECR %		Plastic Displacement, mm		Plastic Strain, %	
Q-T, ºC or SC	Test Time[a], s	H wppm	CP	Meas.	Offset	Permanent	Offset	Permanent
800	96	710	5.0	5.7	0.06	0.07	0.5	0.6
SC	96	720	5.0	5.7	0.37	0.29	3.4	2.7
SC	96	720	5.0	5.6	0.18	0.14	2.3	1.4
SC	96	720	5.0	5.6	0.22	0.19	2.1	1.8
SC	96	720	5.0	5.6	0.21	0.17	2.0	1.6
800	96	730	5.0	5.7	0.05	---	0.5	---
SC	96	740	5.0	5.7	0.30	0.25	2.8	2.3
800	96	760	5.0	5.7	0.03	---	0.3	---
SC	96	760	5.0	5.7	0.32	0.17	3.0	1.6

[a]From beginning of heating ramp at 300ºC to time at 1180ºC (see Figure 98 for thermal history).

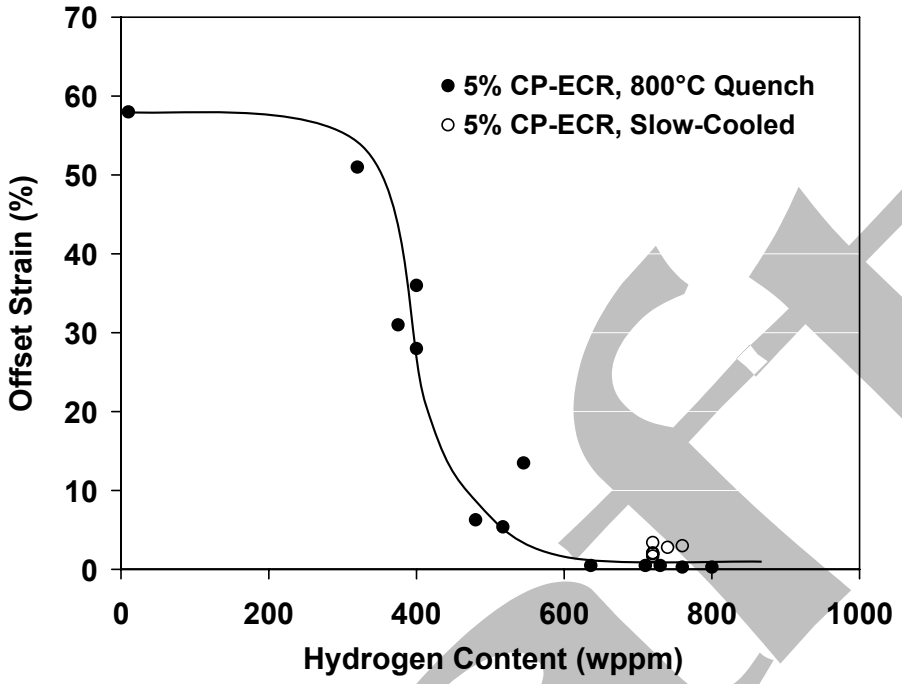

Figure 105. Effects of slow cooling vs. quench at 800ºC on the post-test ductility at 135ºC for HBR-type 15x15 Zry-4 oxidized to 5% CP-ECR at a peak temperature of 1180-1190ºC prior to cooling. Plot includes data shown in Figure 100.

The CP-ECR values reported throughout Sections 3-4 are based on the integrated value up through the end of the heating phase. For the rapid cooling rate in the ANL experiments, oxygen diffusion into the beta layer is negligible during cooling. However, the calculated weight gain for the cooling phase does add a little to the CP-ECR value. The CP weight gain for the cooling phase from 1200ºC to 800ºC is 1.52 mg/cm^2. Because of the parabolic nature of diffusion and weight gain, the contribution of the cooling weight gain is not linear. Let $(Wg)_t$ be the total weight gain prior to quench at 800ºC, $(Wg)_h$ be the weight gain at the end of the heating phase, and $(Wg)_c$ be the weight gain calculated from the cooling curve by ignoring the heating phase. Then $(Wg)_t = [(Wg)_h^2 + (Wg)_c^2]^{0.5} = [(Wg)_h^2 + 2.3]^{0.5}$. Using the conversion factors for weight gain to ECR and the same notation for total, heating and cooling, we can write $ECR_t = [(ECR_h)^2 + (ECR_c)^2]^{0.5}$. For 17×17 Zry-4 results in Table 41, the 7.5% heating-phase CP-ECR would convert to a total CP-ECR of 7.9% and the 10% heating-phase CP-ECR would convert to a total CP-ECR of 10.3%. For the HBR-type 15×15 Zry-4 results in Tables 42-47, the heating-phase CP-ECR values of 5%, 6% and 7.5% would convert to total CP-ECR values of 5.3%, 6.2% and 7.7%.

Table 46 Post-quench Ductility of Prehydrided HBR-type 15×15 Zry-4 Cladding Oxidized to 7.5% CP-ECR at 1204ºC, Cooled at 13ºC/s to 800˚C, and either Quenched (Q) at 800ºC, Quenched at 700ºC or Slow Cooled to RT; ECR = 1.1385 Wg; ring-compression tests performed on ≈8-mm-long samples at 135ºC and 0.0333 mm/s displacement rate

Sample and Test Conditions			ECR %		Plastic Displacement, mm		Plastic Strain, %	
Q-T, ºC or SC	Test Time[a] s	H wppm	CP	Meas.	Offset	Permanent	Offset	Permanent
800[b]	144	185	7.4	8.0	1.41	1.2	13	11
SC[b]	144	180	7.4	8.1	1.40	1.2	13	11
SC[b]	144	185	7.4	8.1	2.04	1.8	19	17
800[c]	132	335	7.4	7.7	0.12	0.08	1.1	0.7
800[c]	132	335	7.4	7.7	0.08	---	0.7	---
700[c]	132	335	7.4	7.6	0.24	0.11	2.2	1.0
700[c]	132	335	7.4	7.6	0.11	0.08	1.0	0.7
700[c]	132	335	7.4	7.6	0.15	0.09	1.3	0.8
SC[c]	132	327	7.4	7.6	0.45	0.27	4.2	2.5
SC[c]	132	327	7.4	7.6	0.31	0.23	2.8	2.1
800[b]	144	435	7.4	8.0	0.05	0.03	0.5	0.3
800[b]	144	435	7.4	8.0	0.05	0.03	0.5	0.3
SC[b]	144	490	7.4	8.0	0.36	0.26	3.3	2.4
SC[b]	144	530	7.4	8.0	0.15	0.10	1.4	0.9
SC[b]	144	570	7.4	8.0	0.19	0.14	1.8	1.3

[a]From beginning of ramp at 300ºC to end of hold time at ≈1200ºC.

[b]Tests conducted with thermal history shown in Figure 98.

[c]Tests conducted with thermal history shown in Figure 99.

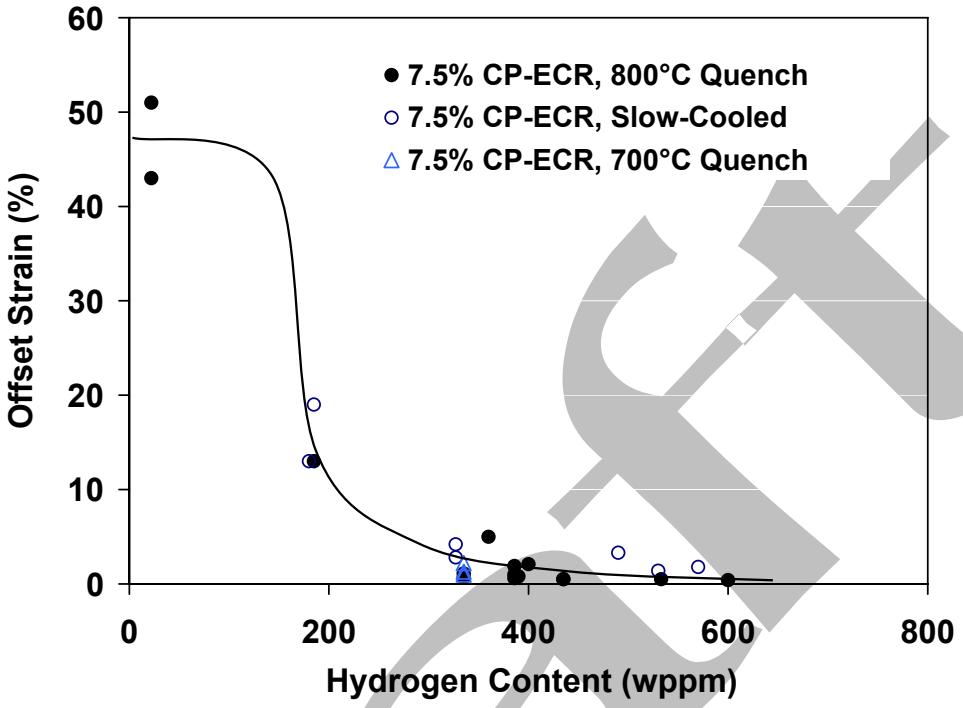

Figure 106. Effects of slow cooling vs. quench at 700ºC and 800ºC on ductility at 135ºC for HBR-type 15×15 Zry-4 oxidized to 7.5% CP-ECR at 1204ºC prior to cooling. Plot includes data shown in Figure 101.

In order to better understand the effects of quench temperature on post-quench ductility, an additional set of tests was conducted with a heating rate comparable to the ones shown in Figures 10 and 98, which were used to oxidize most of the prehydrided samples prior to conducting post-quench ductility tests. Figure 107 shows the thermal history for these additional tests. The slower heating rate to 1200ºC is comparable to the heating rates shown in Figures 10 and 98, as well as the ones used to oxidize high-burnup Zry-4 samples (see Section 5).

Previous data for prehydrided HBR cladding were generated for samples oxidized to 5% and 7.5% CP-ECR. Additional tests were conducted with 450-470 wppm hydrogen Zry-4 oxidized to 6% CP-ECR. During the oxidation phase, the samples were at 1200-1204ºC for 17 s and >1180ºC for 86 s. The uniformity of hydrogen content from sample to sample allowed for a good comparison of ductility for Zry-4 quenched at 800ºC (450±20 wppm H), 700ºC (450±20 wppm H), and 600ºC (460±30 wppm H), as well as the sample that was slow-cooled to RT (470±30 wppm H). The post-test ductility results are given in Table 47. The samples quenched at 600-800˚C were all brittle by both the offset and permanent strain criteria. The slow-cooled samples were ductile with 3.5±1.4% offset strain and 2.7±1.0% permanent strain. Although the average cooling rates decreased from 13˚C/s (1200˚C to 800˚C) to 3˚C/s (800˚C to 700˚C) to 2˚C/s (700˚C to 600˚C), it is only the very slow cooling at <<2˚C/s from 600˚C to RT that results in ductility enhancement. Oxygen redistribution at 600˚C to RT is highly unlikely due to the slow diffusivity of oxygen. The phase change from (beta + alpha) → alpha is complete by about 750˚C,

so no further phase change is expected from 600˚C to RT. However, hydrogen diffusivity is much faster than oxygen diffusivity. Thus, hydrogen can come out of solid solution and precipitate as

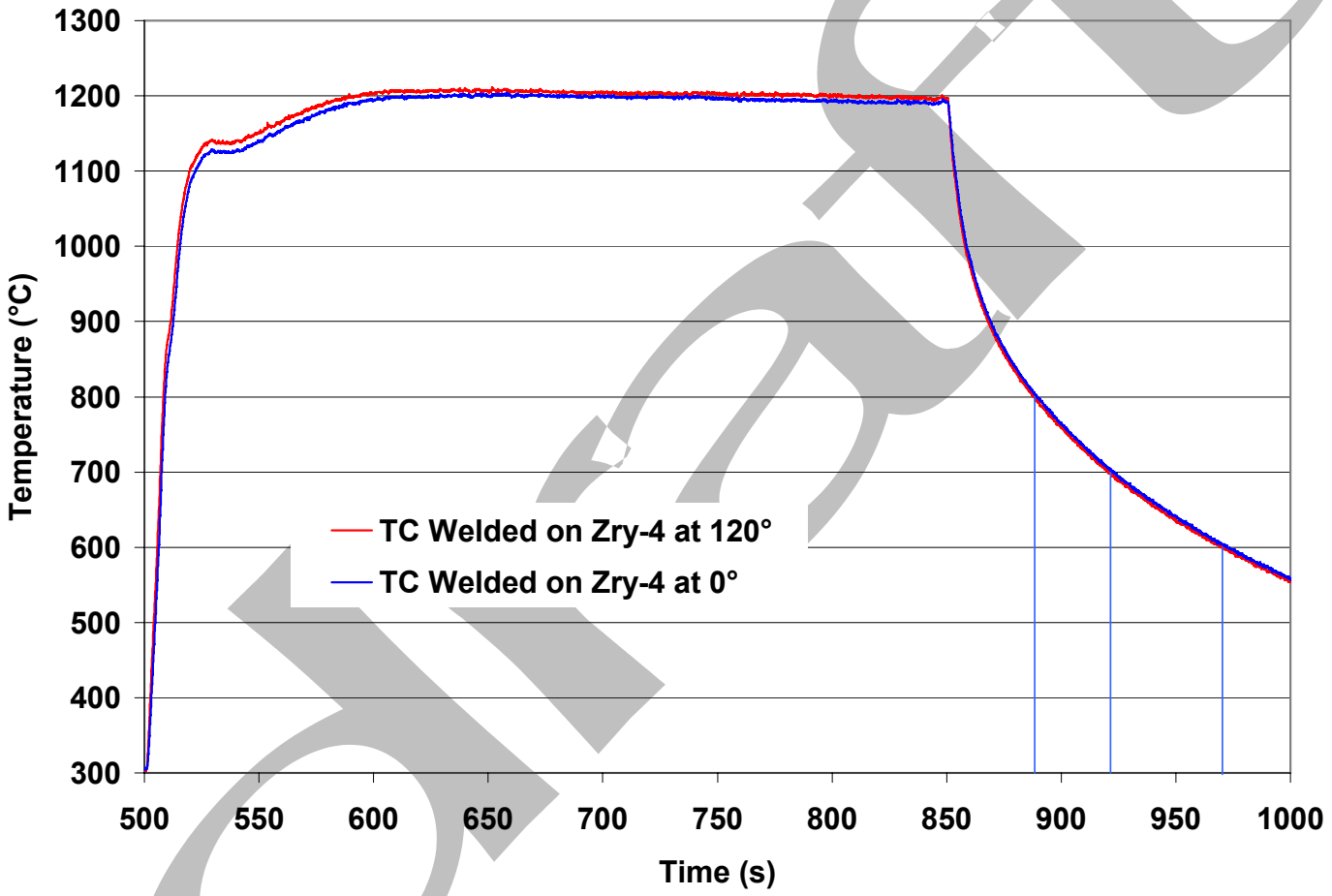

Figure 107. November 2006 thermal benchmark results for HBR-type 15×15 Zry-4 with a sample oxidation temperature of 1201±3ºC. Vertical blue lines indicate different quench temperatures for tests with prehydrided Zry-4 samples.

Table 47 Post-quench Ductility of Prehydrided HBR-type 15×15 Zry-4 Cladding Oxidized to 6% CP-ECR at 1200ºC, Cooled at 13ºC/s to 800˚C and Quenched (Q) at 800˚C, Cooled from 800˚C to 700˚C at 3˚C/s and Quenched at 700˚C, Cooled from 700˚C to 600˚C at 2˚C/s and Quenched at 600˚C or Slow Cooled from 600˚C to RT at <2˚C/s; thermal history is shown in Figure 107; CP-ECR is calculated from beginning of ramp to end of hold time; ring-compression tests performed on ≈8-mm-long samples at 135ºC and 0.0333 mm/s displacement rate

Sample and Test Conditions			ECR[b] %		Plastic Displacement, mm		Plastic Strain, %	
Q-T, ºC or SC	Test Time[a] s	H wppm	CP	Meas.	Offset	Permanent	Offset	Permanent
800	106	450	6.0	6.5	0.10	0.08	0.9	0.7
800	106	450	6.0	6.5	0.09	0.07	0.8	0.7
700	106	450	6.0	6.6	0.07	0.05	0.6	0.5
700	106	450	6.0	6.6	0.10	0.05	0.9	0.5
600	106	460	6.0	6.5	0.08	0.05	0.7	0.5
600	106	460	6.0	6.5	0.13	0.08	1.2	0.7
SC	106	470	6.0	6.4	0.22	0.18	2.1	1.7
SC	106	470	6.0	6.4	0.53	0.39	4.9	3.6

[a]From beginning of ramp at 300ºC to end of hold time at ≈1200ºC.
[b]Total CP-ECR, including cooling phase is 6.2%.

very small hydrides during very slow cooling from 600˚C to RT. The ductility enhancement with slow-cooling to RT is important to incorporate in data interpretation (see Section 5), but it may not be relevant to LOCA post-quench ductility for quench temperatures ≥600˚C.

There are two purposes for generating data with prehydrided samples in the ANL program: a) to help plan test times for high-burnup cladding in order to bracket the ductile-to-brittle transition CP-ECR; and b) to determine if prehydrided cladding is a good surrogate for high-burnup cladding. Based on the test data presented in this section, ductile-to-brittle transitions for HBR-type Zry-4 quenched at 600-800˚C are expected to be ≈5% CP-ECR for 600 wppm H (Table 42), >5% but <6% CP-ECR for 450 wppm H (Table 47), and ≈7.5% CP-ECR for ≈370 wppm H (Table 43). These conditions for embrittlement are for the heating rates used in this study, which are much higher than LOCA heating rates from about 300˚C to 1125˚C and more prototypic of predicted LOCA heating rates from 1125˚C to 1200˚C. From a mechanistic point of view, high experimental heating rates to 1200ºC are conservative and would result in lower transition CP-ECR values for a given hydrogen content because longer time would be spent at 1200ºC for the same CP-ECR.

The test results also show that slow-cooling, particularly from 600ºC to RT, gives a small enhancement in ductility that increases the ductile-to-brittle transition CP-ECR for a given hydrogen content. At 7.5% CP-ECR, the hydrogen content needed to embrittle the cladding appears to increase from ≈370 wppm to ≈550 wppm.

4.3 Summary of post-quench ductility results for prehydrided Zry-4

Hydrogen has a significant effect on reducing post-quench ductility. For HBR-type 15×15 Zry-4 oxidized to 5% CP-ECR at ≈1190ºC maximum oxidation temperature and quenched at 800ºC, the ductile-to-brittle transition hydrogen content was determined to be ≈600 wppm. For both 17×17 Zry-4 and HBR-type 15×15 Zry-4 oxidized to 7.5% CP-ECR at slow-heating rates from ≈1150ºC to ≈1200ºC and no temperature overshoot, the ductile-to-brittle-transition hydrogen content was determined to be ≈370 wppm. However, for a more aggressive heating rate with an early temperature peak of 1216ºC, embrittlement at 7.5% CP-ECR occurred in HBR-type Zry-4 with a hydrogen content of ≈340 wppm. For 17×17 Zry-4 oxidized at 1200ºC to ≈10% CP-ECR, the embrittlement hydrogen concentration was determined to be ≈300 wppm.

As-received HBR-type 15×15 Zry-4 has a very high post-quench ductility at 7.5% CP-ECR following oxidation at ≈1200ºC and quench at 800ºC, while the same material prehydrided to 600-wppm hydrogen has essentially no post-quench ductility. The as-received and prehydrided samples were characterized and compared following oxidation and quench. The RT microhardness profile was significantly higher for the prehydrided Zry-4 sample as compared to the as-received sample. In particular, the 600-wppm-H Zry-4 has higher microhardness values in the prior-beta layer at the boundary of the alpha and beta layers. The ANL results are consistent with the results presented by Mardon et al. [21] demonstrating that hydrogen increases the hardness and oxygen-solubility limit in the Zry-4 prior-beta phase. This also results in higher oxygen concentration gradients and higher early-time diffusion rates of oxygen into the beta layer.

Although the embrittlement CP-ECR of as-fabricated alloys oxidized at 1200ºC was relatively insensitive to quench at 800ºC vs. slow-cooling to RT, the same was not true for prehydrided HBR-type 15×15 Zry-4. Slow-cooling to RT resulted in a small, but significant, increase in ductility. At 5% CP-ECR, slow-cooling increased the hydrogen embrittlement threshold from ≈600 wppm to ≈750 wppm. At 7.5% CP-ECR, slow cooling increased the embrittlement hydrogen threshold from ≈370 wppm to ≈550 wppm.

Based on two series of tests conducted with prehydrided Zry-4 oxidized to 6% and 7.5% CP-ECR at ≈1200ºC, lowering the quench temperature from 800ºC to 700ºC to 600ºC had no effect on post-quench ductility for hydrogen contents of 450 wppm and 340 wppm, respectively. All quenched samples were brittle under these conditions, while the samples that were slow-cooled from 1200ºC to RT retained a small level of ductility. These results indicate that the ductility enhancement arises from slow cooling at <<2ºC/s from 600ºC to RT. During this interval, hydrogen would have time to diffuse short distances out of the matrix of prior-beta grains and precipitate as fine hydrides. If this were the case, then the results suggest that there is intrinsic hydrogen embrittlement for hydrogen dissolved in the prior-beta matrices, as well as enhancement in oxygen-induced embrittlement caused by increased solubility of oxygen in beta layers with dissolved hydrogen.

5 Results for High-Burnup Zry-4, ZIRLO and M5

Two-sided oxidation tests were conducted at a target temperature of 1200ºC with defueled cladding samples sectioned from a high-burnup H. B. Robinson (HBR) rod with a rod-averaged burnup of 64 GWd/MTU. Characterization of the samples is presented in 5.1.1. The characterization of the as-irradiated samples includes gamma scanning, corrosion-layer-thickness measurements (metallography), hydrogen-content measurements (LECO) and oxygen-content measurements (LECO). Five oxidation tests were conducted at 1200ºC to ≈3-9% CP-ECR followed by slow cooling to room temperature (RT) and ring-compression testing at 135ºC. In the as-irradiated condition, these samples had a corrosion layer thickness in the range of 70-75 μm and a hydrogen content of 550 wppm. The samples were slow-cooled to ensure that the three thermocouples welded to the test-train holder would remain intact. A sixth test was conducted with oxidation at 1200ºC to 7.5% CP-ECR and quench at 800ºC. This sample had a corrosion-layer thickness of 95 μm and a hydrogen content of 740 wppm. Post-oxidation characterization and ring-compression results are presented in 5.1.2 for the two-sided oxidation tests.

One-sided oxidation tests were conducted at 1200ºC with defueled cladding samples sectioned from another HBR rod, which had a similar location within the HBR assembly and the same burnup as the rod used to section the two-sided oxidation test samples. The purpose of these tests was to determine steam-oxidation layer growth and post-oxidation ductility of high-burnup cladding away from the balloon region. Four oxidation tests were conducted at 1200ºC to 5-9% CP-ECR (one-sided) with samples characterized by 70-μm corrosion-layer thickness and 550-wppm hydrogen. Two tests were conducted were samples from lower grid span locations and ≈42-μm corrosion layers. The six samples were slow-cooled following oxidation. Characterization of the as-irradiated Zry-4 cladding is given in 5.1.1 and the post-oxidation results are given in 5.1.3.

{Two-sided oxidation tests were conducted at 1200ºC with high-burnup ZIRLO (5.2) and M5 (5.3). Because of the lower hydrogen content of the ZIRLO and M5 cladding samples and the higher ductile-to-brittle transition CP-ECR values (19-20% vs. 14% for HBR-type Zry-4) for as-fabricated alloys, these samples were oxidized to higher CP-ECR values (7.5-13%) than the high-burnup Zry-4 samples (3-9%). Three samples were slow-cooled to determine an upper bound on post-quench ductility. The fourth sample, which was oxidized to an intermediate CP-ECR, was quenched at 800ºC.}

5.1 Results for high-burnup H. B. Robinson 15×15 Zry-4

5.1.1 Characterization of high-burnup H. B. Robinson 15×15 Zry-4

Seven high-burnup HBR rods (64-67 GWd/MTU) were received by ANL in May 2001 for LOCA-related testing. Ruzaukas and Fardell [27] and Van Swam et al. [28] give a detailed description of the as-fabricated cladding, the irradiation history, the nondestructive testing results (eddy-current, profilometry, fission-gas release, etc.), and the fuel isotopic content for these rods. EPRI, in cooperation with Framatome ANP Richland (now AREVA ANP), arranged for the shipment of the rods from the Robinson plant to GE Vallecitos Nuclear Center (VNC) to ANL. The seven rods, along with 5 other HBR rods, were sectioned into ≈0.9-m (≈35-inch) lengths by GE-VNC and shipped to ANL in DOE T-2 casks.

Characterization was performed on HBR rod A02 (67 GWd/MTU) as part of the NRC spent-nuclear-fuel program [29]. This rod was irradiated in an edge-next-to-corner position within the assembly. HBR rod R01 (67 GWd/MTU), also an edge-next-to-corner rod, was characterized for a spent-nuclear fuel program conducted by Sandia National Laboratory and sponsored by DOE, NRC and

international partners. Fuel ceramography, cladding metallography, and hydrogen concentration measurements for A02 and R01 indicated significant circumferential temperature variation in the fuel and cladding. The circumferential variation in hydrogen content at 0.5-0.9 m above the core midplane was ±100 wppm based on 4 quadrant measurements. Metallography of circumferential sections, which showed regions of very dense hydrides across the cladding wall, suggested that the circumferential variation of hydrogen was >200 wppm. This was a concern for LOCA oxidation tests because experience with prehydrided HBR-type Zry-4 (see Figure 96) indicated that hydrogen did not homogenize in the circumferential direction during oxidation to 1200ºC for short test times corresponding to 5-7.5% CP-ECR. Large circumferential variation in hydrogen content would make interpretation of test data difficult.

Interior rods F07 and G10 were selected for two-sided and one-sided oxidation tests, respectively. These rods were not near the assembly edge nor were they next to guide tubes. The expectation was that these rods would have smaller circumferential temperature variation and more uniform hydrogen concentration and hydride morphology. Based on data for rods A02 and R01, cladding at the fuel midplane was expected to have a corrosion layer thickness of ≈70 μm and a hydrogen content of ≈550 wppm. Based on the results for prehydrided HBR-type Zry-4 (see Figures 100 and 101), embrittlement was anticipated for samples with >600-wppm hydrogen oxidized at 1200ºC to 5-7.5% CP-ECR. These were important factors in the decision to section oxidation samples primarily from near the core midplane.

The fuel midplane is located near the top of grid span #3 and close to one end of the middle fuel-rod segment. It is labeled in the gamma scanning profile for the middle segments of rods F07 (Figure 108) and G10 (Figure 109); the locations of grid spacer #4 and grid span #4 are also labeled. The gamma-scan results were used to select samples from uniform burnup regions, away from the cut ends and away from regions under grid spacers.

The sectioning diagram for characterization samples and test samples for two-sided oxidation tests is show in Figure 110. The same basic sectioning diagram was used for the one-sided tests except that the test samples were longer (Figure 111). The characterization results for rods F07 and rod G10, along with the A02 and R01 results, are summarized in Table 48. For short (1.5-mm-long) F07 cladding samples, the circumferential variation in hydrogen content was in the range of ±70 to ±90 wppm (standard deviation of 4 data points per location). Taking the average of the eight sets of hydrogen readings, a reasonable hydrogen content to use for the near-midplane samples is 550±100 wppm (includes circumferential and axial variations in hydrogen concentration) for oxidation test samples sectioned from a span of 140 mm from near the fuel midplane. This hydrogen level is consistent with the hydrogen measurement for the G10 near-midplane sample (550±90 wppm) and the A02 near-midplane sample (580±65 wppm). These hydrogen concentrations are referenced to the weight of the corroded cladding. Converting to hydrogen concentration for the weight of the cladding metal alone would result in a small increase in hydrogen concentration. However, this correction was not made because of the uncertain amount of corrosion layer lost during cutting and snipping used to prepare small samples for LECO hydrogen determination.

The F07 hydrogen measurement (545±90 wppm) taken at 320 mm above the fuel midplane is consistent with the R01 measurement (550±80 wppm) taken at 360 mm. The F07 measurement (800±110 wppm after high-temperature oxidation) taken at 650 mm above the fuel midplane is higher than the A02 and R01 measured values with comparable corrosion-layer-thickness values. Based on the corrosion layer thickness (95 μm) for the F07 sample at this elevation, a hydrogen content of 730-750 wppm was expected. However, when corrected for the sample weight loss due to spallation of the corrosion layer

during the oxidation test, the hydrogen content would be reduced from 800 wppm to ≈715 wppm. Given the uncertainty in this measurement, a value of 740±110 wppm is used based on scaling the A02 and R01 results.

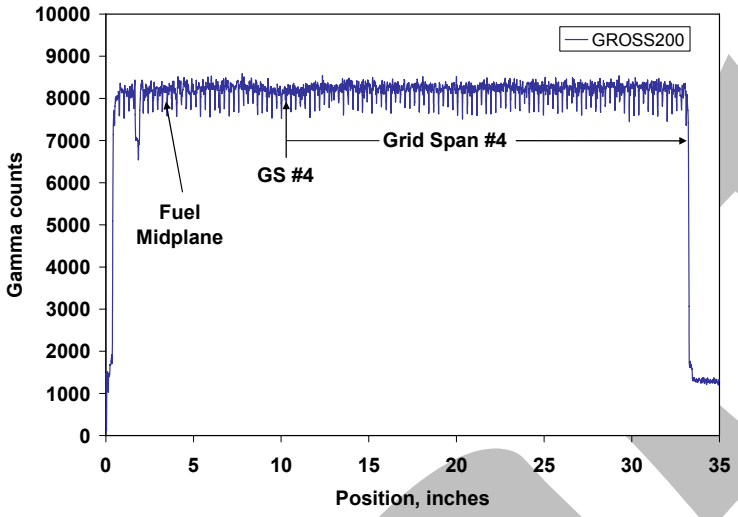

Figure 108. Gamma scan profile for HBR rod F07, from which samples were sectioned for hydrogen-content analysis, oxygen-content analysis, metallography and two-sided oxidation tests.

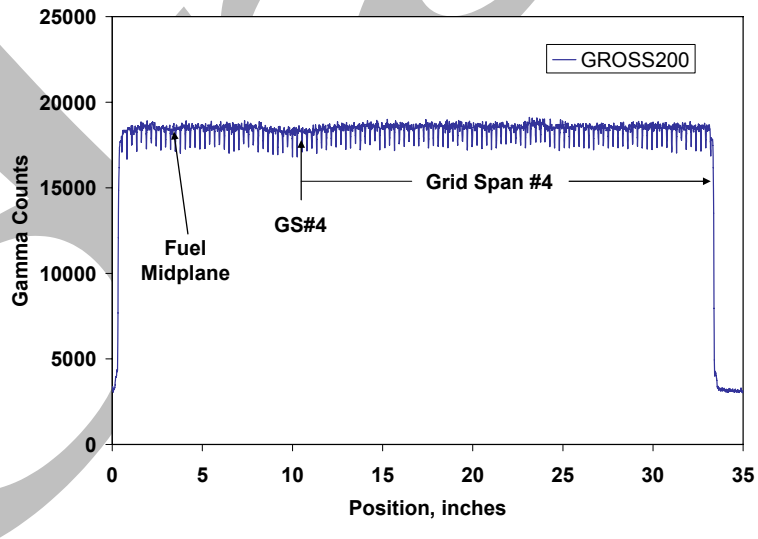

Figure 109. Gamma scan profile for HBR rod G10, from which samples were sectioned for hydrogen-content analysis, oxygen-content analysis, metallography and one-sided oxidation tests.

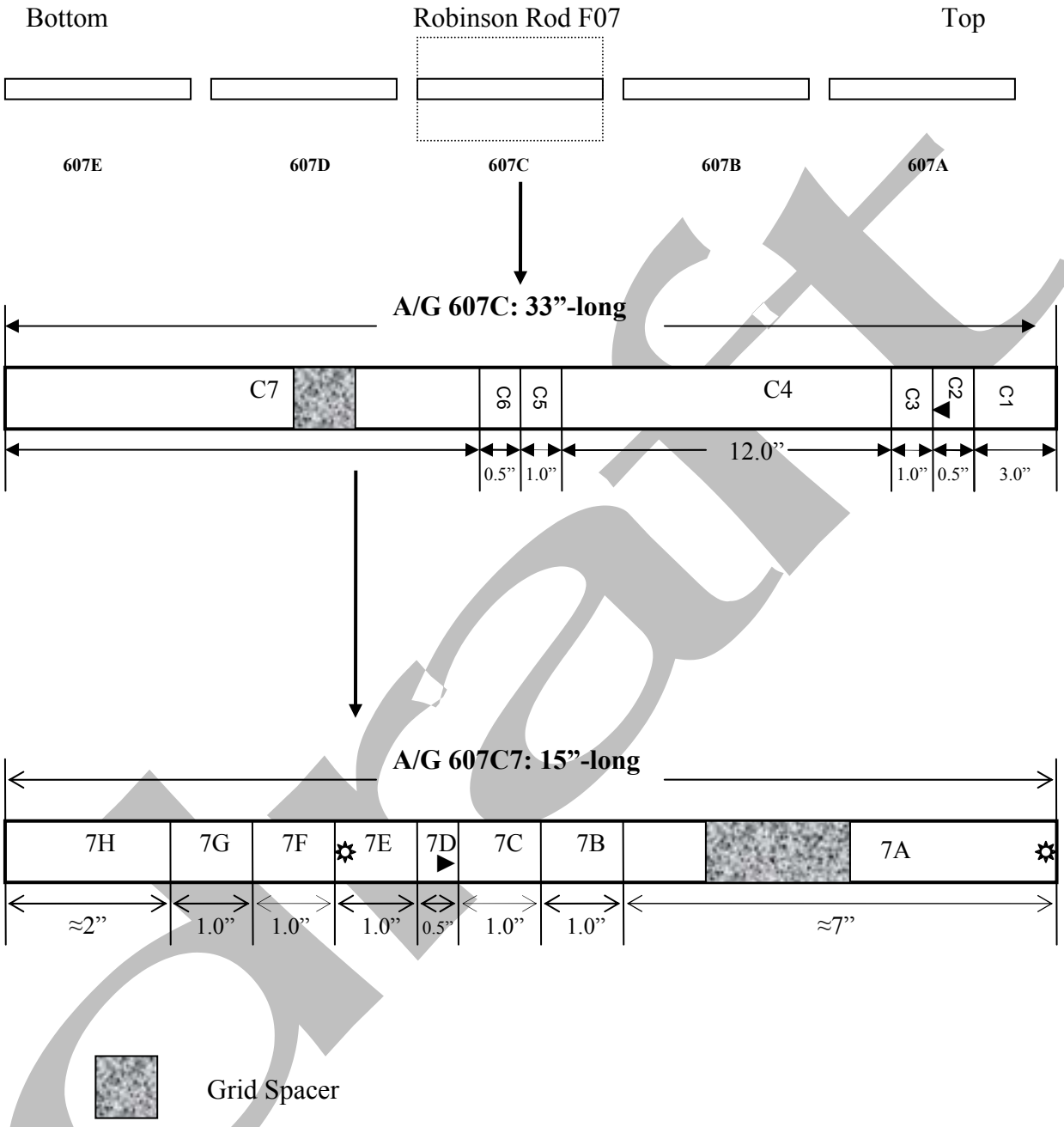

Figure 110. Sectioning diagram for characterization samples and two-sided-oxidation test samples. Eight 1.5-mm-long hydrogen-content samples were cut from 7H. One 13-mm-long sample (7D) was prepared for metallography, one 25-mm-long sample was cut for hydrogen and oxygen analyses (7E), and four 25-mm-long samples (7B, 7C, 7F and 7G) were sectioned from near the core midplane for oxidation tests. C2 and C6 were used as metallography samples and C3 and C5 were used as oxidation test samples.

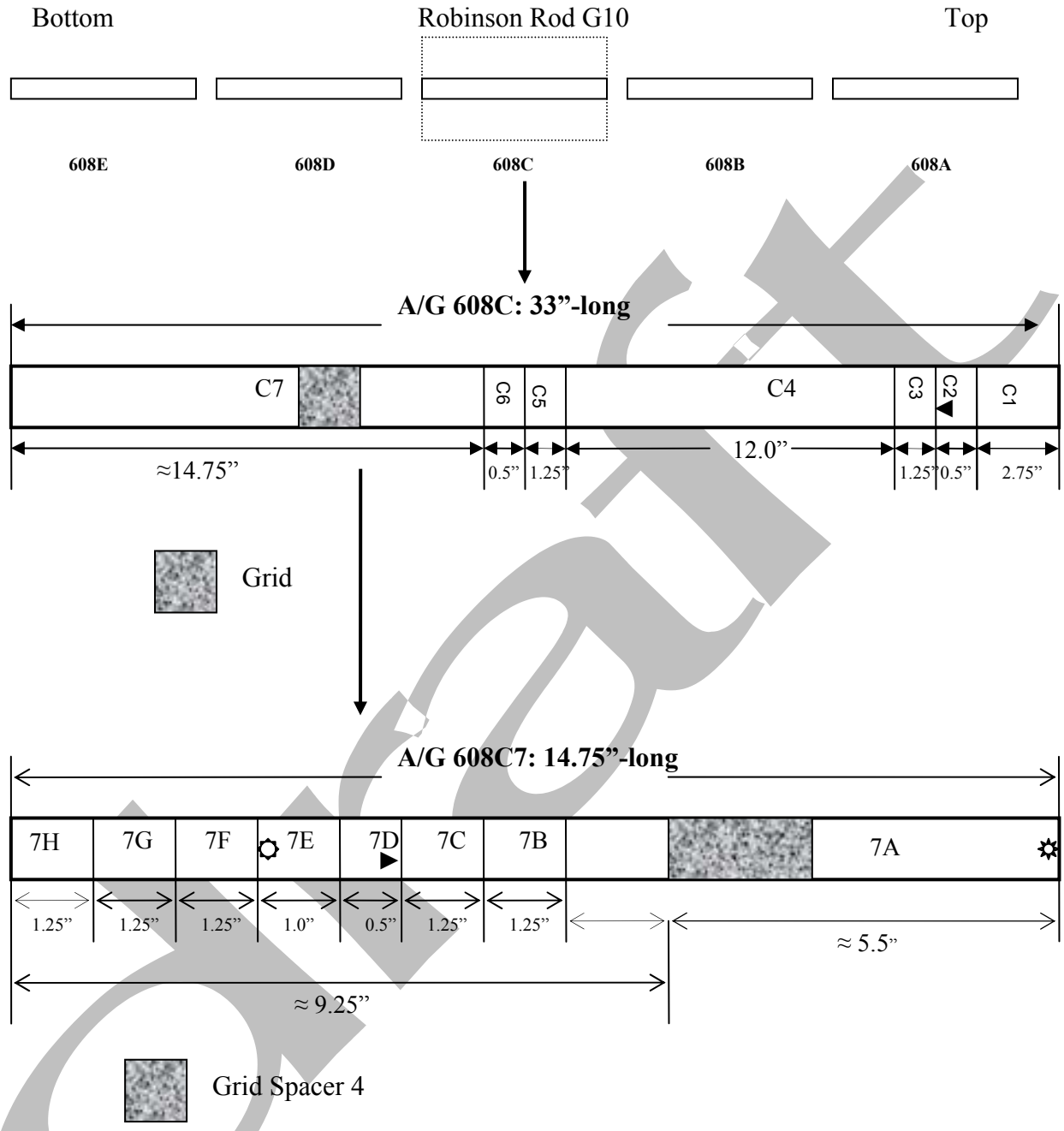

Figure 111. Sectioning diagram for characterization samples and one-sided-oxidation test samples. Sample 7E was used for hydrogen and oxygen analysis. Sample 7D was used for metallographic analysis. Four 32-mm-long samples (7B, 7C, 7F and 7G) were sectioned from near the core midplane for oxidation tests.

Table 48 Corrosion Layer Thickness and Hydrogen Content Results for H. B. Robinson Rods F07 and G10, Used for Oxidation Tests, and for Rods A02 and R01; axial locations are relative to the midplane of the 3658-mm-long fuel column

Axial Location Relative to Fuel Midplane mm	Rod F07 H-Content (Corrosion Layer)	Rod G10 H-Content (Corrosion Layer)	Rod A02 H-Content (Corrosion Layer)	Rod R01 H-content (Corrosion Layer)
-920		≈360[a] (≈40[a])		
-580		≈400[a] (44±2)		
±50	545±85 wppm 530±80 wppm 530±90 wppm 535±85 wppm 555±85 wppm 575±80 wppm 535±80 wppm 565±70 wppm 550±100 wppm (71±5 μm)	550±90 wppm (68±2 μm)	580±65 wppm (70 μm)	
+320	545±80 wppm (74±5 μm)			
+360				550±180 wppm (77 μm)
+510				650±150 wppm (89 μm)
+650	740±110 wppm[a] (95±4 μm)			
700			750±90 wppm (98 μm)	
740				770±125 wppm (98 μm)

[a]Estimated by interpolation/extrapolation and scaling. Hydrogen measurements following oxidation and ring-compression tests were higher for rod F07 at +650 mm (800±110 wppm) due to weight loss from corrosion-layer spalling and higher for rod G10 at -920 mm (550±70 wppm) and at -580 mm (570±70 wppm) due to inner-surface hydrogen pickup during one-sided oxidation tests.

The corrosion layer thicknesses measured for rods F07 and G10 are in good agreement with those measured for rods A02 and R01 at the axial locations examined. For the F07 and G10 samples oxidized and slow cooled, the corrosion layer thickness is ≈70 μm (68-74 μm). The two-sided oxidation sample that was quenched had a corrosion layer thickness of 95 μm.

Half of sample 7E in Figure 110 was sectioned for LECO oxygen determination. The measured oxygen concentration (2.08±0.19 wt.%) is in good agreement with the ≈70-μm corrosion layer thickness if the Pilling-Bedworth ratio (1.75) recommended by Van Swam et al. [30] is used for the HBR corrosion layer. The 1.75 ratio is consistent with ≈10% porosity in the HBR corrosion layer.

Detailed characterization was performed for the midplane region of the F07 rod to determine the fuel, fuel-cladding bond, corrosion layer and hydride morphology. Figure 112 shows a low magnification image of the fuel morphology. The central darkened region is not symmetric with respect to the center of the pellet, which indicates asymmetric power distribution and fuel temperature, as well as circumferential variation in cladding temperature.

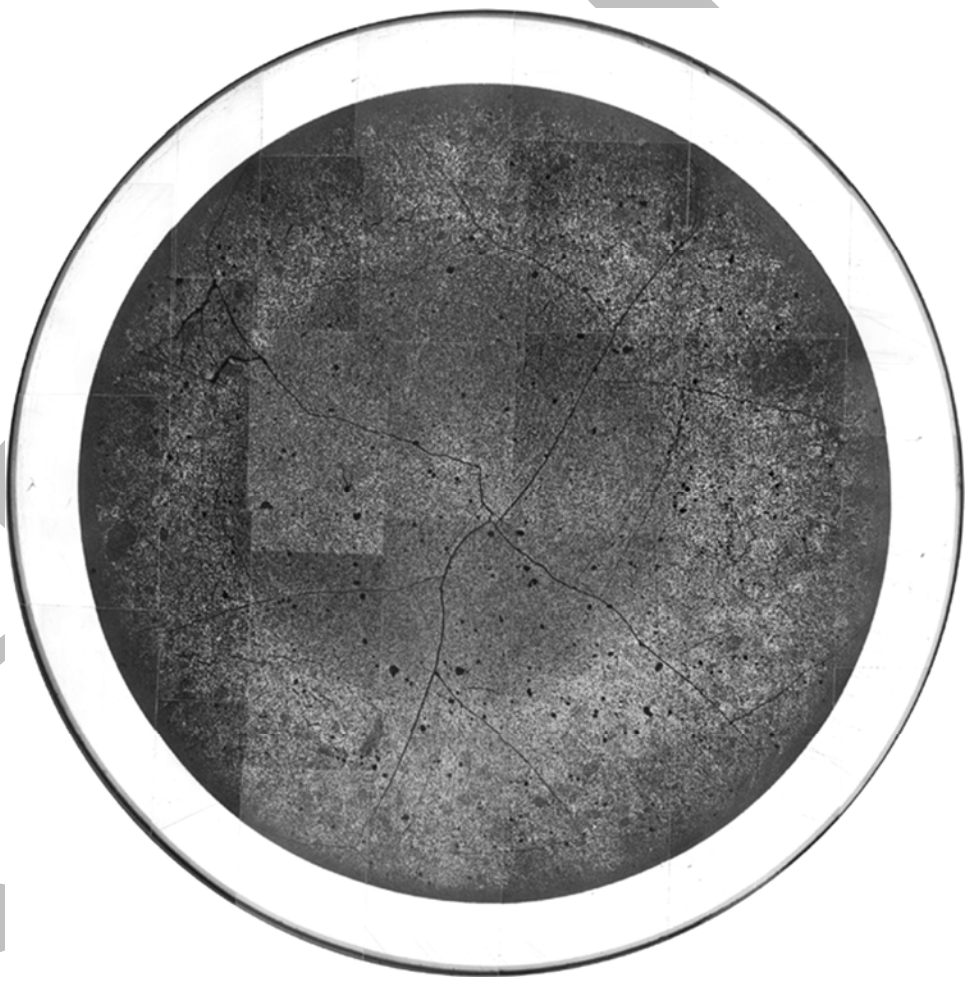

Figure 112. High-burnup HBR fuel morphology for the fuel midplane cross section of rod F07 showing indications of asymmetric power and temperature distributions relative to the center of the pellet.

The fuel-cladding bond appears to be well developed at the F07 rod midplane. This is consistent with characterization results for the A02 and R01 HBR rods. Figure 113 shows the fuel-cladding bond within one circumferential sector of the fuel shown in Figure 112. The bond thickness is 11±4 μm. A higher magnification image is shown in Figure 114 for rod A02 fuel-cladding bond. The fuel-cladding bond layer remains intact and adherent to the cladding inner-surface after nitric-acid defueling. This has been demonstrated for high-burnup Limerick BWR cladding (see Figure 115). It is an additional source of oxygen, beyond the oxygen from steam, during two-sided oxidation tests. For one-sided (outer-surface) oxidation tests, it is the primary source of oxygen on the inner-surface of defueled cladding. According to Une et al. [30], the bond layer is primarily ZrO_2 with some UO_2 in solid solution. It is not clear if all of the UO_2 in the bond remains following nitric-acid defueling.

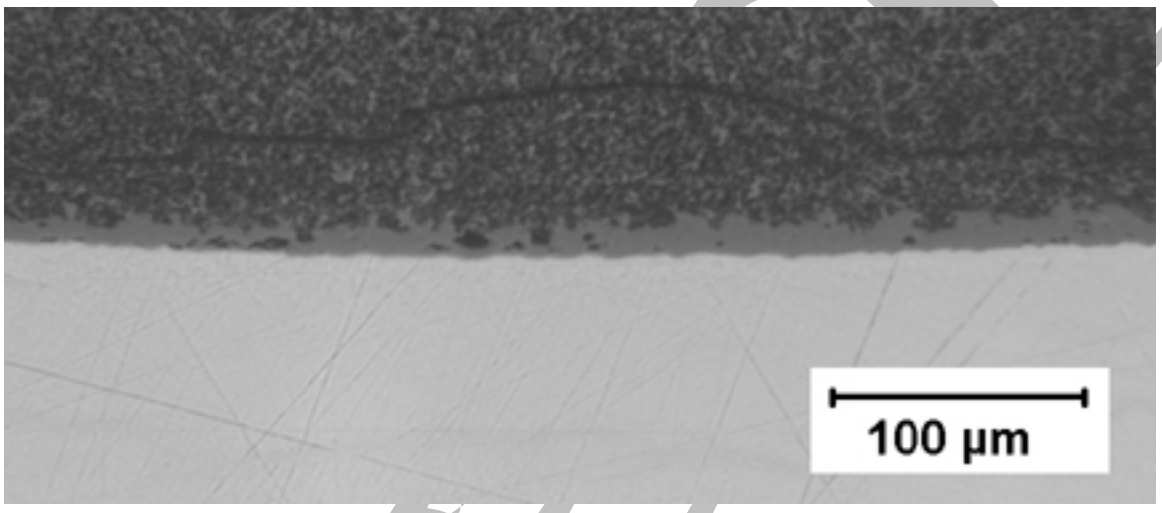

Figure 113. Fuel (dark region), cladding (light region) and fuel-cladding bond layer (gray) at the midplane of HBR rod F07. The image is a magnification of a small region from the fuel cross-section shown in Figure 112.

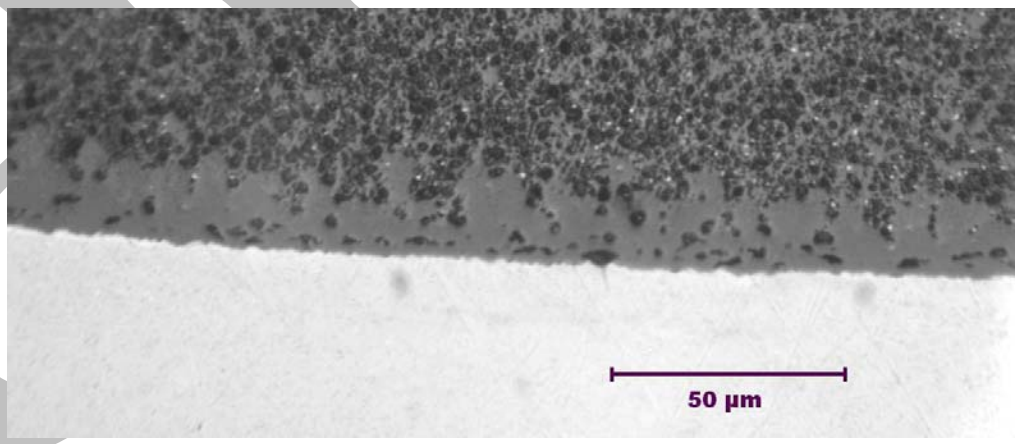

Figure 114. High magnification image of fuel-cladding bond layer at the fuel midplane of HBR rod A02.

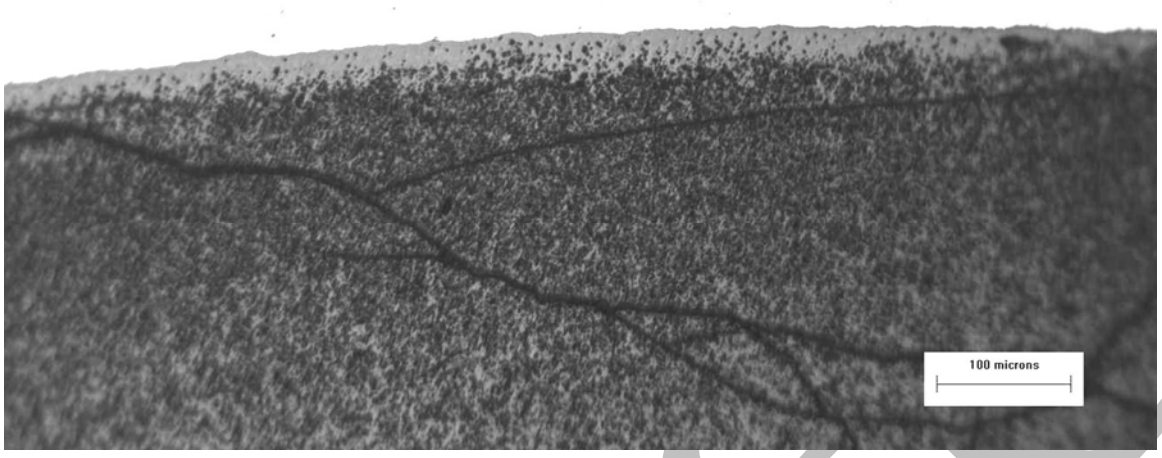

(a)

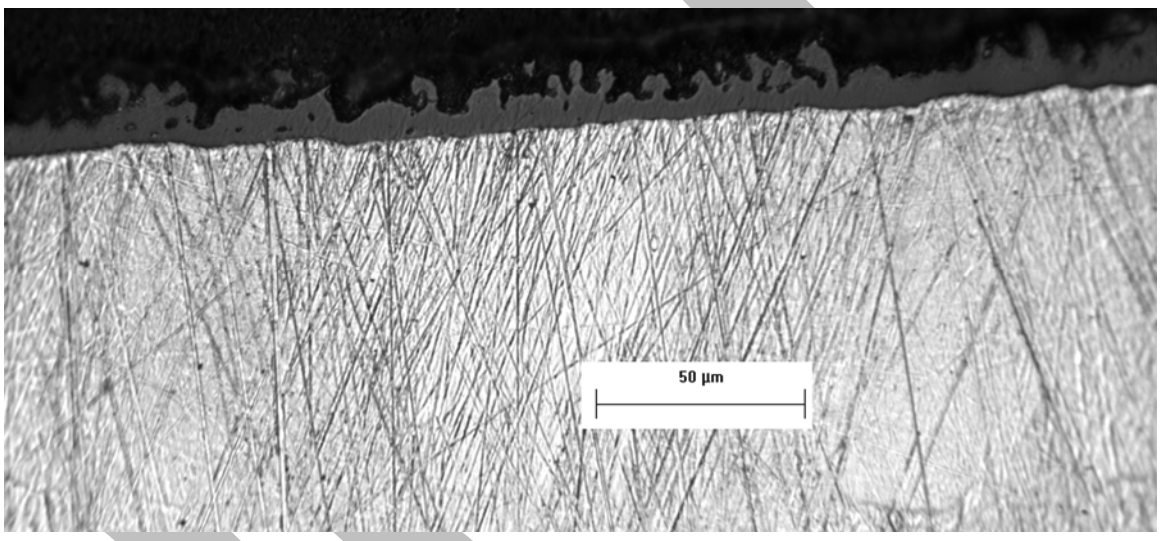

(b)

Figure 115. Images of high-burnup Limerick BWR fuel-cladding bond at a fuel-midplane location: (a) prior to defueling in nitric acid; and (b) after defueling in nitric acid.

High-magnification images were taken from three axial locations of the HBR rod F07 to determine the corrosion layer thickness, the cladding metal thickness and the hydride distribution and morphology. At each axial location, eight circumferential regions were magnified to obtain the data. The corrosion layer thickness was measured to be: 71±5 µm at the midplane (in grid span #3); 74±5 µm at 320 mm above the midplane (in grid span #4); and 95±4 µm at 650 mm above the midplane (in grid span #4). From the metallography, it was determined that the average cladding wall thickness at the midplane was 0.712 mm for rod F07 and 0.720 mm for rod G10. These wall thicknesses were used in the determination of test times and CP-ECR values. Samples of metallographic images of the corrosion layer at three relevant axial locations along rod F07 are shown in Figure 116.

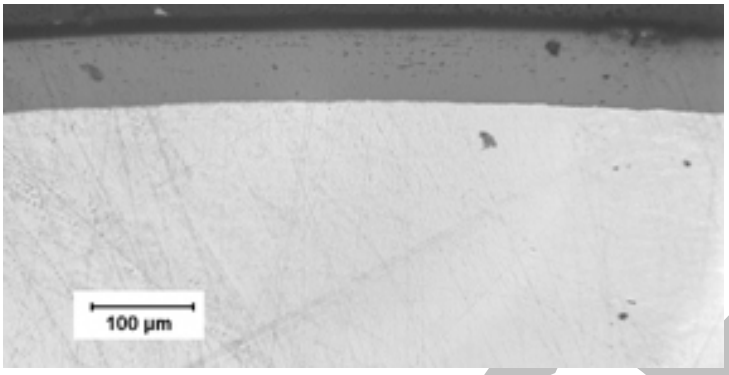

(a) Midplane

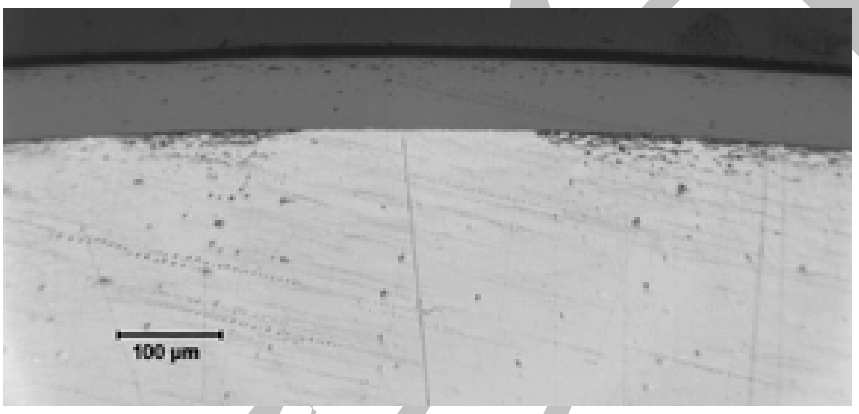

(b) 320 mm above midplane

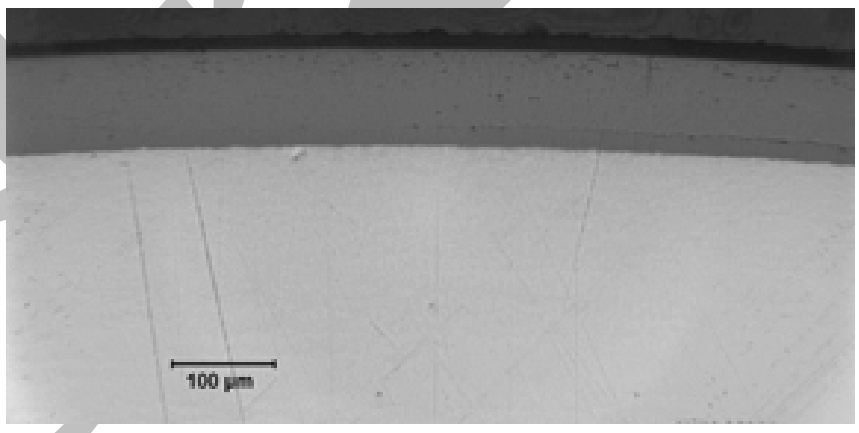

(c) 650 mm above midplane

Figure 116. Outer-surface corrosion layer for two-sided-oxidation test samples from HBR rod F07: (a) fuel midplane (71 µm); (b) 320 mm above midplane (74 µm); and (c) 650 mm above midplane (95 µm).

Hydride distribution and morphology are important parameters for oxidation and post-oxidation ductility tests. Images of etched samples are shown in Figure 117 for the three axial locations of interest for HBR rod F07. Of the eight images taken at each axial location, no unusual hydride morphology was observed.

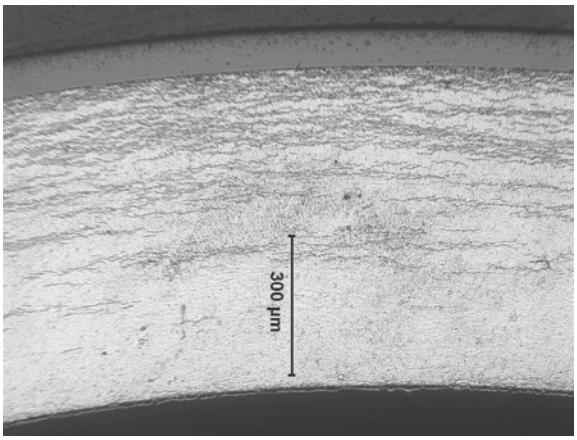

(a) Midplane

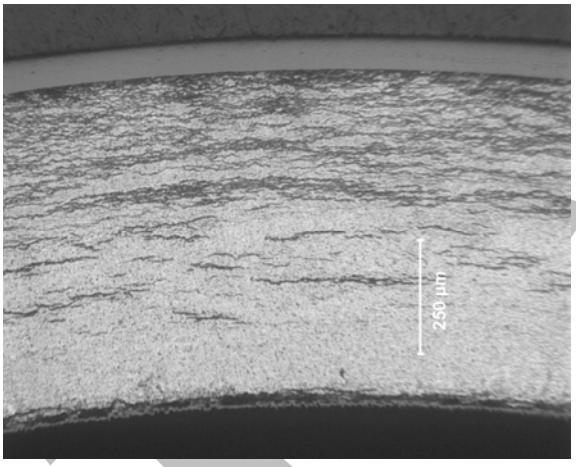

(b) 320 mm above midplane

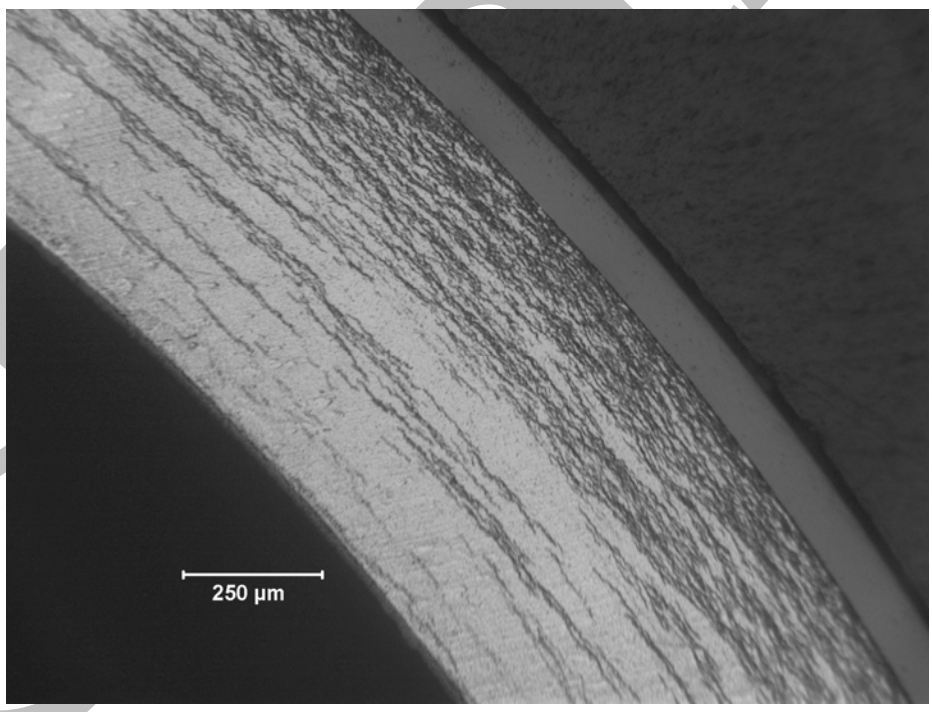

(c) 650 mm above midplane

Figure 117. Hydride distribution and morphology in HBR rod F07 cladding near locations used to section two-sided-oxidation test samples: a) fuel midplane (550-wppm H); b) 320 mm above midplane (550-wppm H); and c) 650 mm above midplane (740-wppm H).

For HBR Rod G10, from which one-sided oxidation samples were sectioned, metallographic images from etched cladding areas at the fuel midplane location revealed areas of typical (Figure 118a) and atypical (Figure 118b) hydride distribution and morphology. The hydrides in Figure 118b appear to be much denser across the cladding wall and appear to have more hydrogen than the region shown in Figure 118a. This was confirmed for rod R01, which had circumferential variations of 450-770 wppm hydrogen with atypical hydride morphology within about 50% of the cross section.

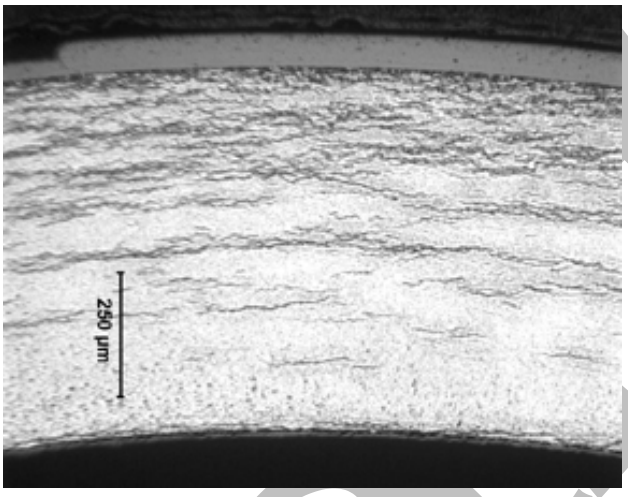

(a) Typical hydride morphology

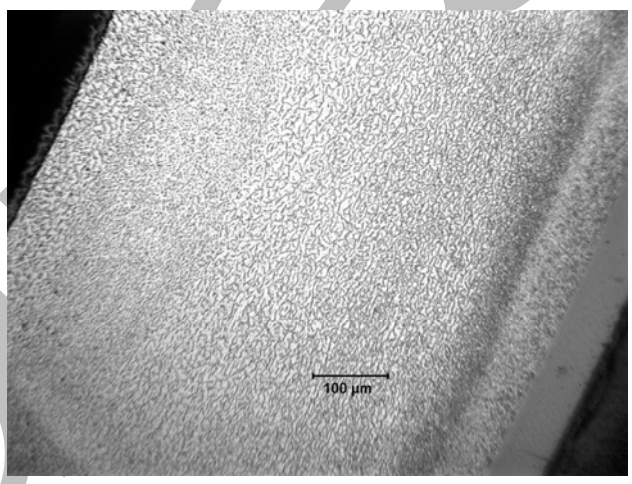

(b) Atypical hydride morphology

Figure 118. Hydride distribution and morphology in HBR rod G10 cladding at the core midplane: (a) typical hydride distribution across cladding wall; and (b) atypical hydride distribution with a very dense hydride band near the outer surface and smaller dense hydrides across the wall.

Table 49 summarizes the data used to plan and interpret the test results for two-sided and one-sided oxidation tests.

Table 49 Summary of Cladding Characterization for HBR Fuel Rod Segments used for Pre- and Post-test Analysis of Two-sided and One-sided Oxidation Tests

Test Type	Sample ID	Corrosion Thickness μm	Corrosion ECR %	Hydrogen Content wppm	Cladding Thickness mm	Cladding OD[a] mm
Two-sided	Rod F07 C7B, C7C C7F, C7G	71	5.3	550±100	0.712	10.58
Two-sided	Rod F07 C5	74	5.6	550±100	0.714	10.58
Two-sided	Rod F07 C3	95	7.1	740±110	0.702	10.54
One-sided	G10 C7B, C7C C7F, C7G	68	5.1	550±100	0.720	10.60
One-sided	D3 D5	44 ≈40	3.3 ≈3.0	≈400 ≈360	0.740 0.742	10.65 10.65

[a]Deduced from interpolation of outer diameters reported in Ref. 27 minus two times the corrosion layer thickness measured by ANL. A reasonable value to use for all these samples is 10.6 mm for normalizing the offset and permanent displacements to determine strains.

5.1.2 Results of two-sided oxidation tests for high-burnup HBR 15×15 Zry-4

Six two-sided oxidation tests were conducted during January-February 2005 in the in-cell LOCA oxidation-quench apparatus. Because of the limited availability of the Alpha-Gamma Hot Cell (AGHC), the tests had to be planned carefully and conducted quickly. If time had permitted, these tests would have been conducted sequentially with a full post-test data set (metallography and post-oxidation or post-quench ductility) from the previous test used to plan the next test. A new test train was constructed, benchmarked out-of-cell with non-irradiated cladding samples to determine the temperature history and verify that the weight gain and oxide layer thickness data were within 10% of the CP predicted values, and benchmarked in-cell with a nonirradiated cladding sample to demonstrate that the same weight gain results were obtained using the in-cell furnace. The weight gains measured following out-of-cell and in-cell tests were in excellent agreement with the CP-predicted values. The thermal history for this test train is shown in Figure 119, along with times corresponding to CP-ECR values of 3-10% for the 0.77-mm wall as-fabricated cladding. In planning and conducting the in-cell tests, the test times corresponding to the target CP-ECR values were adjusted for the difference in cladding wall thickness (0.71 mm vs. 0.77 mm).

As described below, the corrosion layer was found to be partially protective with regard to high-temperature oxidation layer growth with time. Thus, the rate of oxidation of the corroded high-burnup cladding is somewhat lower than that of the as-fabricated cladding used to generate the temperature history in Figure 119. The lower oxidation rate corresponds to lower heat-generation rate and lower cladding temperatures during the ramp from 300ºC to 1200ºC. Consequently, additional thermal benchmark tests were conducted after the in-cell tests were completed to better determine the temperatures to use for interpretation of the high-burnup results.

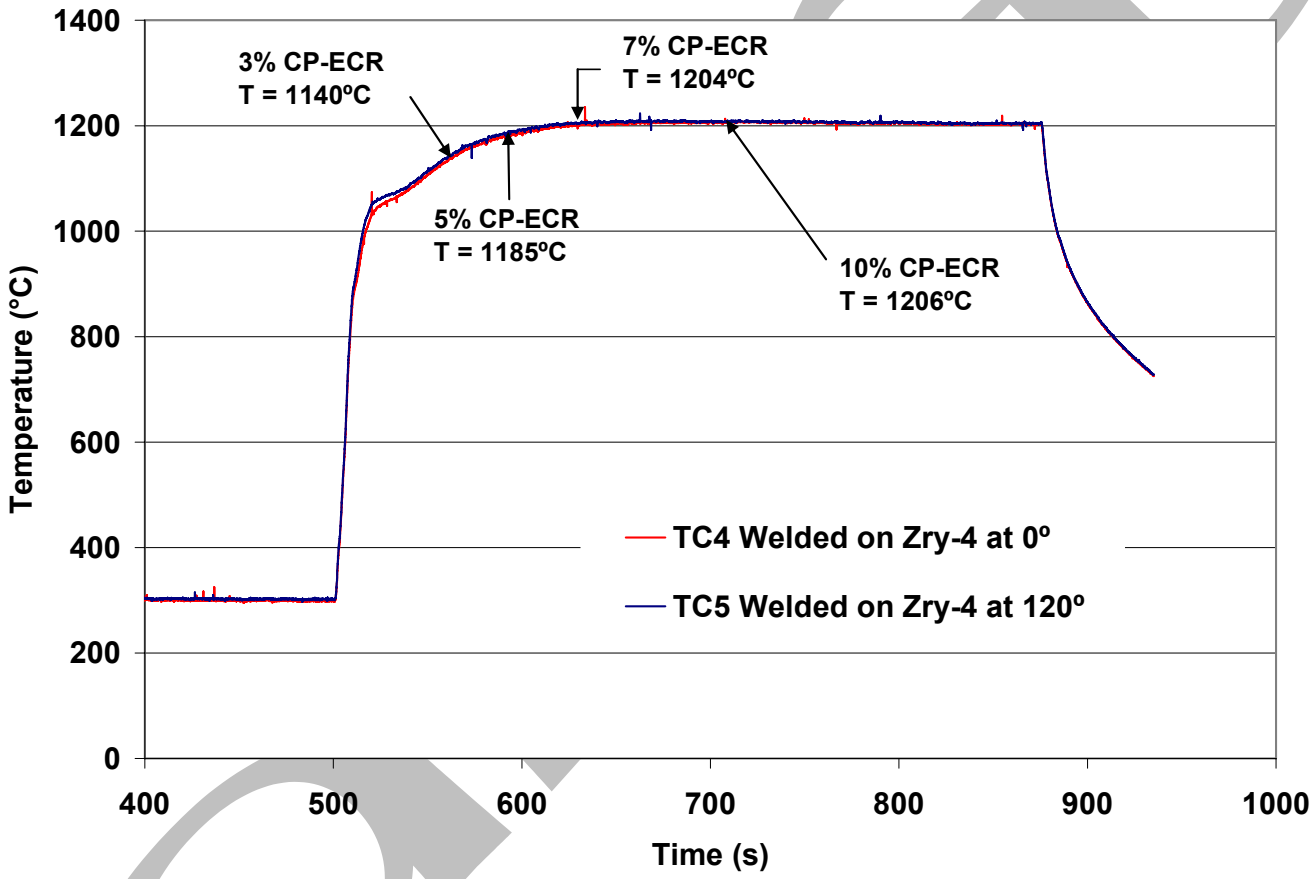

Figure 119. Out-of-cell thermal benchmark results for as-fabricated cladding in the test train used to conduct in-cell two-sided oxidation tests with high-burnup HBR cladding. The results were used to plan oxidation times for two-sided tests with high-burnup HBR cladding samples.

Another test train was constructed after running the in-cell tests, and the thermal benchmark was conducted using the same controller parameters as were used for the in-cell tests. Two tests were conducted in sequence with thermocouples welded to the cladding metal: ramp from 300ºC to 1200ºC and hold long enough to grow a 37-μm oxide on the cladding inner- and outer-surfaces and slow-cool to RT; and repeat the ramp-and-hold test with the oxidized cladding. Figure 120 shows the temperature ramp-and-hold results for initially bare cladding, and Figure 121 shows results for cladding with initial oxide layers of 37-μm on inner and outer surfaces. By comparing the two figures, it can be seen that for pre-oxidized cladding: the temperature at the end of the rapid ramp is lower (1017ºC vs. 1060ºC), the time to reach the hold temperature is about the same (140 s vs. 130 s) and the hold temperature is slightly lower (1193ºC vs. 1201ºC). Temperatures from these two benchmark runs are compared at relevant in-cell-test times in Table 50 under columns for the bare-cladding results (HBRU#73A) and the pre-oxidized cladding results (HBRU#73B). A small correction was then made to the temperature history for

Table 50 Thermal Benchmark Results for Test HBRU#44 with As-fabricated Zry-4 (Figure 119), for Test HBRU#73A with As-fabricated Zry-4 (Figure 120), and for Test HBRU#73B with Pre-oxidized Zry-4 (Figure 121); estimated temperatures for high-burnup test samples (HBRI) are given in column 3

HBRI Test #	Test Time[a] s	Deduced HBRI T, ºC	HBRU#44 (Figure 116) T, ºC	HBRU#73A (Figure 117) T, ºC	HBRU#73B (Figure 118) T, ºC
2	62	1110	1141	1136	1105
1	93	1169	1186	1180	1163
3	132	1196	1204	1196	1188
5	155	1197	1206	1201	1192
6	155	1197	1206	1201	1192
4	206	1198	1206	1201	1193

[a]From beginning of ramp at 300ºC to end of hold time.

pre-oxidized cladding by accounting for differences in test trains used to conduct the in-cell tests and used to conduct the bare vs. pre-oxidized cladding thermal benchmarks. Also shown in Table 50 (under the heading HBRU#44) are the bare-cladding temperatures (see Figure 119) measured at relevant test times for the test train used to conduct the in-cell tests. The difference between the two test-train results for the same controller parameters and bare cladding samples is ≈5ºC. Thus, for interpretation of in-cell tests, the temperatures in Figure 120 were increased in gradual steps during the ramp to give a hold temperature increase of 5ºC. The results are plotted in Figure 122 and summarized, along with other test parameters, in Table 51.

It is relatively straightforward to demonstrate that the temperature history in Figure 122 represents a lower-bound during the temperature ramp for the high-burnup samples tested in-cell. The heat of oxidation is proportional to the oxidation rate, which is proportional to the inverse of the oxide-layer thickness for dense oxide layers grown in steam at high temperature (see Equation 1). Even if the corrosion layer ($\delta_c \approx 70$ μm) and the fuel-cladding-bond oxide layer ($\delta_b \approx 10$ μm) grown at reactor temperatures were as protective as high-temperature-grown oxide layers, the initial heat generation would be proportional to $1/\delta_c + 1/\delta_b = 0.114\ \mu m^{-1}$. For the thermal benchmark test with pre-oxidized cladding, the initial heat generation rate is proportional to 2/37-μm = $0.054\ \mu m^{-1}$. Therefore the initial heating rate

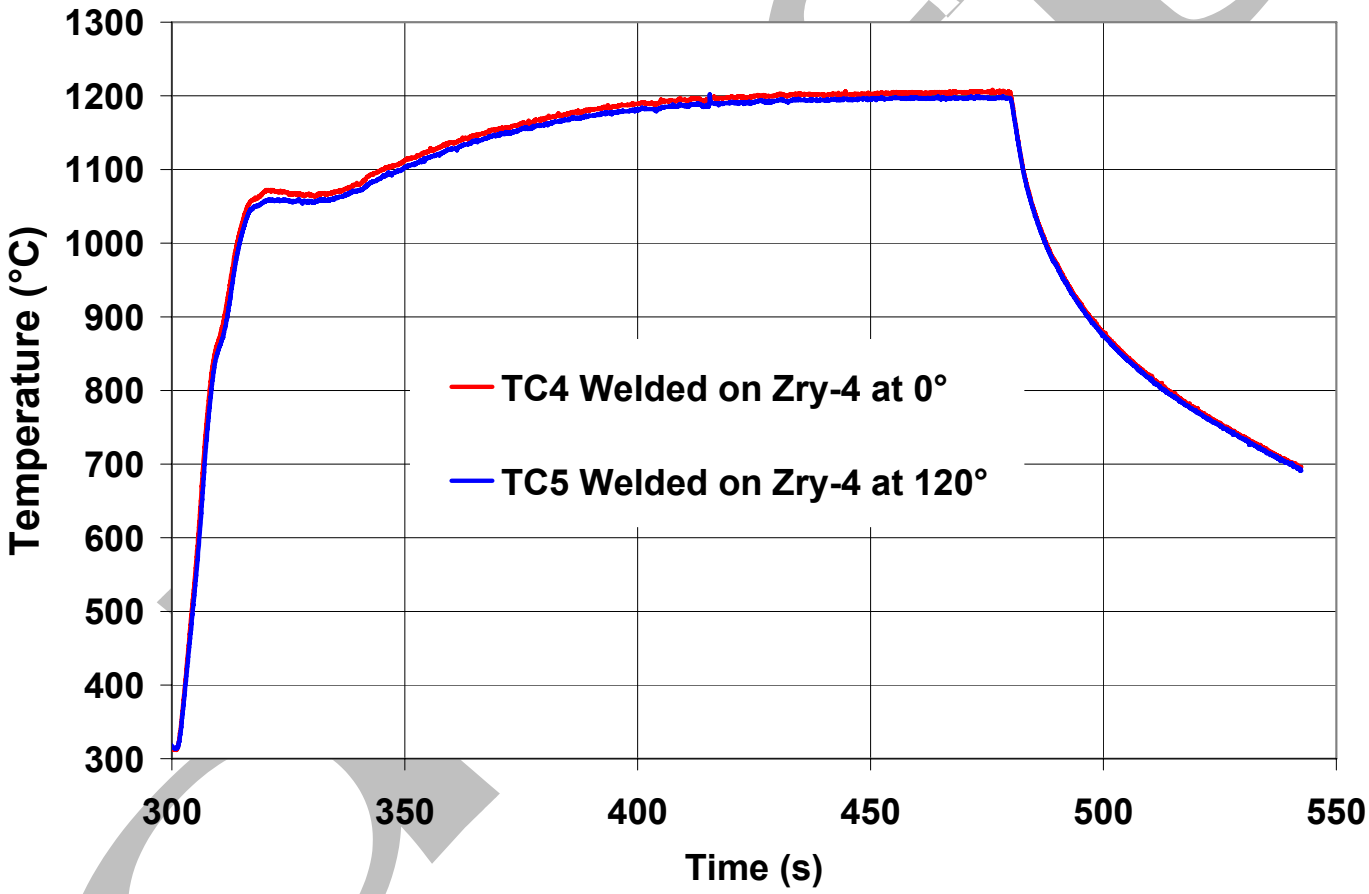

Figure 120. Results of thermal benchmark test conducted after the in-cell oxidation tests with another test train and with TCs welded onto the outer-surface of as-fabricated HBR-type Zry-4 cladding. Controller parameters were the same as those used to generate Figure 119 results.

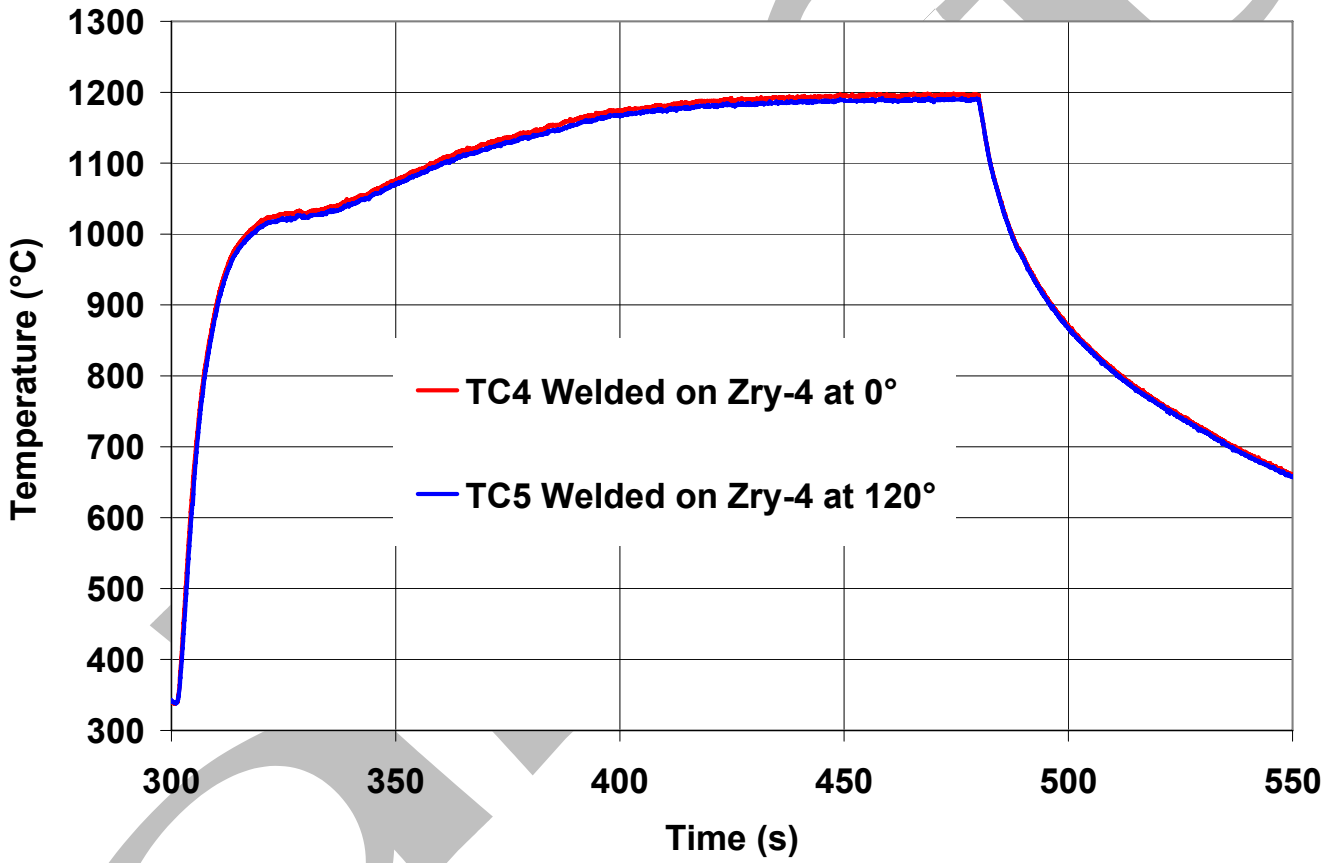

Figure 121. Thermal benchmark results for pre-oxidized HBR-type Zry-4 with TCs welded onto bare-cladding outer surface and with steam-induced oxide layers of 37 μm grown on the inner- and outer-surface of the cladding sample prior to the temperature ramp. Controller parameters were the same as those used to generate results in Figures 119 and 120.

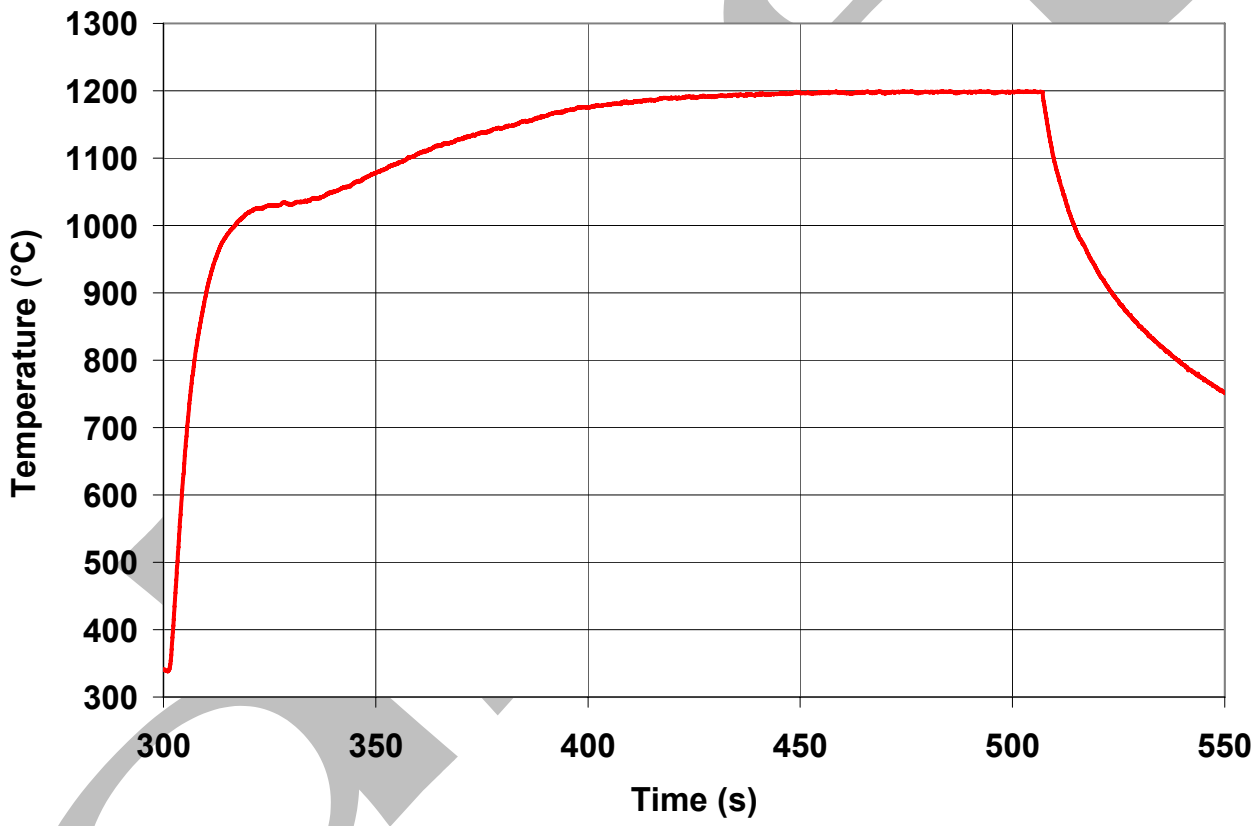

Figure 122. Temperature history used to calculate CP-ECR values and to interpret results for the in-cell two-sided oxidation tests conducted with high-burnup HBR Zry-4 cladding samples.

in the thermal benchmark test is <50% of the initial heat generated by the corroded high-burnup cladding during the in-cell tests. However, the temperature history in Figure 122 should be a reasonable lower-bound because beyond a certain oxide thickness (≈10 μm) heat of oxidation is too small to have a significant affect on cladding temperatures during the heating ramp.

Table 51 Sample Characterization and Test Conditions for Two-sided Oxidation Tests Conducted with High-burnup HBR Zry-4 Cladding; SC is slow cooling and Q is quench at 800ºC

Test ID #	Hydrogen Content wppm	Test Time[a] s	Target CP-ECR %	Corrected CP-ECR %	Maximum T ºC	Time at T ≥ 1180ºC s	Cooling
2	550±100	62	3	2.7	1110	0	SC
1	550±100	93	5	4.3	1169	0	SC
3	550±100	132	7	6.4	1196	27	SC
5	550±100	155	8	7.4	1197	50	SC
6	740±110	155	8	7.5	1197	50	Q
4	550±100	206	10	9.3	1198	101	SC

[a]Includes time for ramp from 300ºC and hold time.

The target CP-ECR values were chosen based on the post-quench ductility results for prehydrided HBR-type Zry-4. From Figures 100 and 101, it was estimated that high-burnup cladding with 550 wppm hydrogen would be brittle at 5%< CP-ECR <7.5%. The effects of slow-cooling on ductility were not known at the time the high-burnup HBR tests were planned and conducted. Tests were planned at lower (3% and 5%) and higher (7% and 10%) CP-ECR levels in order to bracket the expected ductile-to-brittle transition CP-ECR. Additional tests were conducted at 8% target CP-ECR after data for the first set of tests showed that ductility had been retained up to 7% target CP-ECR. Table 51 gives the test conditions for the two-sided oxidation tests, including the target CP-ECR values (based on Figure 119) and the corrected CP-ECR values (based on Figure 122).

Post-test measurements included sample weight, layer (corrosion, steam-oxide, and oxygen-stabilized alpha) thicknesses, hydrogen concentration and post-test ductility at 135ºC. All test samples decreased in weight, indicating that corrosion-layer spallation (probably during cooling) resulted in greater weight loss than the gain due to oxygen pickup. The metallographic results are particularly interesting in that they reveal information regarding fundamental phenomena that influence oxygen pickup, oxygen diffusion and post-test ductility. Based on the results of the oxidation tests with high-burnup Limerick BWR cladding (see 3.2 and Yan et al. [15, 32]), it was concluded that the corrosion layer was non-protective and "transparent" to steam oxidation. However, the Limerick-cladding corrosion layer was only ≈10-μm thick (≈3-to-18 μm variation around the cladding circumference). Also, the one-sided oxidation tests with Limerick cladding were run for relatively long times (300-6000 s), which resulted in very thick outer-surface oxide layers. If the corrosion layer did have any effect on oxidation kinetics, it was not detectable for these sample and test conditions. In particular, the measured oxide layer thickness and the weight gain determined from layer thicknesses agreed quite well with CP-predicted values for as-fabricated cladding.

Table 52 summarizes the results of the steam-oxide-thickness measurements taken from metallographic images. Only the 7.4% and 9.3% CP-ECR oxide thicknesses are given, along with the

corresponding weight gains. Because of problems encountered in mounting the lower CP-ECR samples and the difficulty in distinguishing steam-oxide from corrosion layer, the uncertainty for these samples was too high to yield reliable data. For the higher CP-ECR samples, the measured steam-oxide thickness on the outer-surface of the cladding is clearly less than the inner-surface-oxide thickness and less than the CP-predicted thickness. The results indicate that the thick HBR corrosion layer is partially protective with respect to steam oxidation. The weight gains, determined from metallographic results in Tables 52 and 53, are less than the CP-predicted weight gains. In terms of ECR based on these weight gains, the 7.4% CP-ECR sample had a measured ECR of 5.6% and the 9.3% CP-ECR sample had a measured ECR of 7.8%. The difference in ECR is 1.5-1.8%.

Table 52 Results of Quantitative Metallography for Two-sided-oxidized, High-burnup HBR Zry-4 following Steam Oxidation: Oxide Layer Thickness (δ_{ox}) and Measured ECR; data are from OM images at eight circumferential locations around sample cross section (see Figures 124-126 for images from one-of-eight locations for HBRI#4 and #5 samples)

Test ID #	Test Time[a] s	Maximum T ºC	CP-ECR %	Measured ECR %	CP-δ_{ox} µm	Measured δ_{ox} µm	
						OD	ID
2	62	1110	2.7	---	11	---	---
1	93	1169	4.3	---	18	---	---
3	132	1196	6.6	---	26	---	---
5	155	1197	7.4	5.6±0.2	30	19±2	26
6	155	1197	7.5	---	30	---	---
4	206	1198	9.3	7.8±0.4	38	28±4	38

[a]Includes time for ramp from 300ºC and hold time.

The effect of the fuel-cladding bond on the oxidation growth rate at the inner-surface is less clear. This bond layer is only ≈11±4 µm thick and, like the thin corrosion layer on the Limerick cladding, its effect on oxide growth rate was not detectable. Between 7-to-9% CP-ECR, the measured ID oxide layer equals the CP-predicted value, indicating that the thin fuel cladding bond is much less protective to steam oxidation than the thick corrosion layer.

Although the corrosion layer appears to slow down the growth of the OD high-temperature oxide, it does not appear to slow down the growth of the oxygen-stabilized alpha layer. Table 53 and Figure 123 show the measured OD and ID oxygen-stabilized alpha-layer thickness values, as compared to the CP-predicted values. Unlike the oxide layers, the OD and ID alpha layers are comparable and agree reasonably well with the CP-predicted values. The difference of 1-2 µm between measured and predicted OD alpha-layer thickness is not significant because of the uncertainty in the CP-correlation due to the variable hydrogen pickup in the Cathcart et al. [13] samples. The slightly thicker (2 µm) OD vs. ID alpha layer may or may not be significant. The results indicate that oxygen diffuses directly from the corrosion layer to the cladding metal resulting in growth of the oxygen-stabilized alpha layer. Oxygen from this alpha layer is available for diffusion into the beta layer.

Table 53 Results of Quantitative Metallography for Two-sided-oxidized, High-burnup HBR Zry-4 following Steam Oxidation: Oxygen-stabilized Alpha Layer Thickness (δ_α); data are from images at eight circumferential locations around sample cross section (see Figures 124-125 for OM images from one-of-eight locations for sample HBRI#5)

Test ID #	Test Time[a] s	Maximum T °C	CP-ECR %	Measured ECR %	CP- δ_α µm	Measured δ_α µm	
						OD	ID
2	62	1110	2.7	---	9	8.4	6.2
1	93	1169	4.3	---	16	14	12
3	132	1196	6.4	---	25	23	21
5	155	1197	7.4	5.6±0.2	29	27	25
6	155	1197	7.5	---	29	---	---
4	206	1198	9.3	7.8±0.4	37	35	33

[a]Includes time for ramp from 300ºC and hold time.

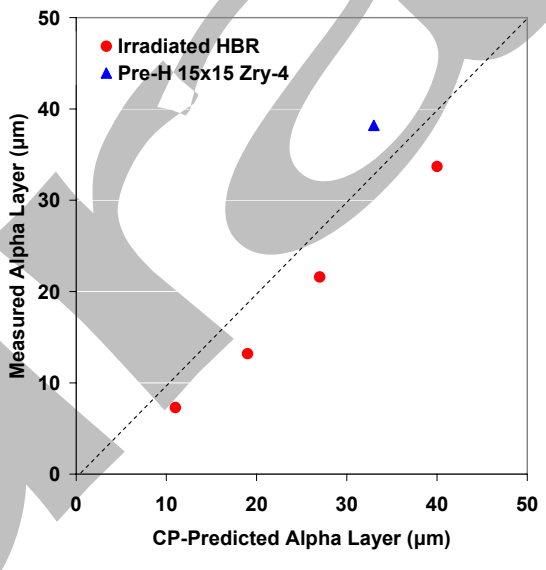

Figure 123. Comparison of measured average ([OD+ID]/2) alpha-layer thickness vs. CP-predicted value for: high-burnup (550±100 wppm) HBR samples oxidized (two-sided) at 1100-1200ºC; and prehydrided (600 wppm) HBR-type Zry-4 sample oxidized at ≈1200ºC to 7.5% CP-ECR.

Metallographic (optical microscopy, OM) images were taken of the oxidized high-burnup HBR Zry-4 samples. Higher quality OM images were obtained for the 7.4% and 9.3% CP-ECR samples. In addition, SEM images were taken of the 7.4% CP-ECR sample. Figure 124a shows a partial cross section emphasizing the outer-surface of the 7.4% CP-ECR sample. The corrosion layer is visible, but its

thickness is much smaller than the 71-μm of the as-irradiated HBR Zry-4. Some of this layer was consumed during the oxidation test, and most of it was lost during cooling (spallation). Also shown in Figure 124a are the oxide layer formed at high temperature, the oxygen-stabilized alpha layer and part of the prior (previous) beta layer. Because the corrosion layer was not fully protective (numerous micro- and macro-cracks), the high-temperature oxide grew underneath the corrosion layer, which remained visible. Figure 124b shows the SEM image from another position along the 7.4% CP-ECR sample. The distinction between the corrosion layer and the high-temperature oxide layer is much clearer in the SEM image, which was then used to draw the boundary lines in the Figure 123a.

Similar OM and SEM images were obtained for the inner-surface area of the 7.4% CP-ECR sample. Figure 125a shows the OM image, in which the oxide layer, the oxygen-stabilized alpha layer, and part of the prior-beta layer are clearly visible. No boundary is observed between the fuel-cladding-bond oxide and the high-temperature oxide. Figure 125b shows the SEM image for the 7.4% CP-ECR sample inner-surface at another axial location.

The outer- and inner-surface oxide layers for the 9.3% CP-ECR high-burnup HBR Zry-4 sample are better viewed by using polished samples for OM imaging. Figure 126a shows the outer-oxide layer. The unevenness of the outer boundary and the morphology of this region suggest the presence of corrosion oxide, although the thickness is small due to partial loss of this layer. Because the epoxy was not vacuum-impregnated, there was a small gap between the outer surface and the epoxy, which allowed room for some of the corrosion layer to spall and drop below the imaged surface during grinding and polishing. Figure 126b shows the inner-surface oxide layer in the as-polished condition. There is no indication of a fuel-cladding bond layer in this image. Based on readings taken from eight circumferential areas, the average high-temperature oxide layer thickness is 28±4 μm for the outer-surface oxide and 38 μm for the inner-surface oxide (see Table 52). The variation in the outer-surface high-temperature oxide thickness is due to uncertainties in determining the interface between the corrosion layer and the high-temperature oxide layer, as well as the circumferential variation in oxide layer thickness.

The oxygen-stabilized alpha layer and the prior-beta layer are better imaged from etched surfaces. Figures 127a and 127b show the outer-surface and inner-surface regions, respectively, of these layers. The contrast between the oxygen-stabilized alpha layer and the prior-beta layer is quite good and allows for an accurate determination of the alpha-layer thickness. Based on readings from eight circumferential areas, the average alpha-layer thickness values (see Table 53) are about the same near the outer surface (35 μm) and the inner surface (33 μm).

Ring-compression tests were conducted at 135ºC and 0.0333 mm/s crosshead displacement rate with ≈8-mm-long samples sectioned from the oxidation and oxidation-quench samples. Offset displacements were determined from load-displacement curves and normalized to the cladding metal outer diameter (10.6 mm) to calculate offset strain. In addition, the outer diameter of the oxidized cladding was measured in the loading direction prior to, and after, compression testing. As is standard protocol for the ANL ring-compression tests, the tests were stopped after the first significant load drop to determine if through-wall failure along the length of the sample had occurred. Table 54 summarizes the results of the ring-compression tests.

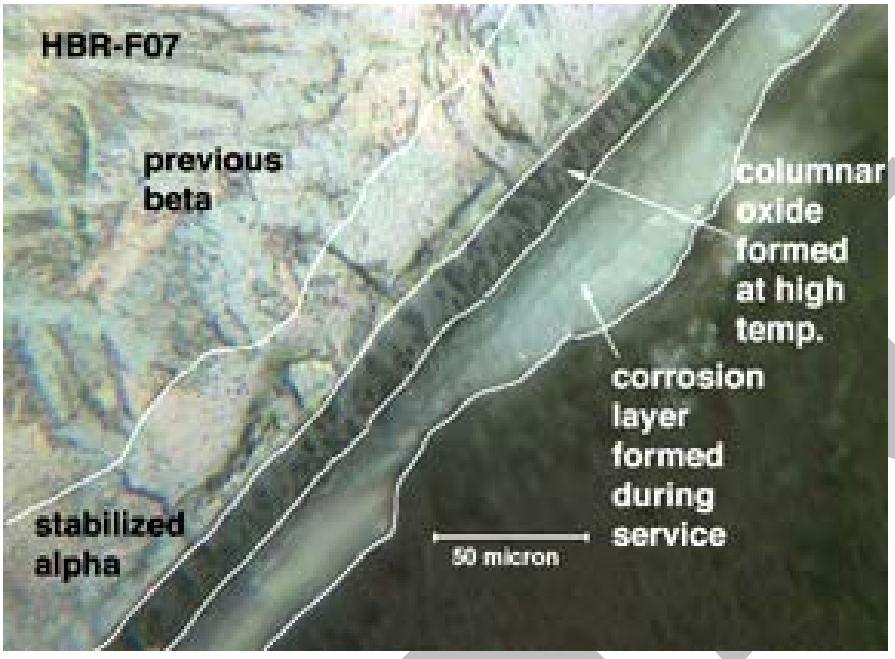

(a)

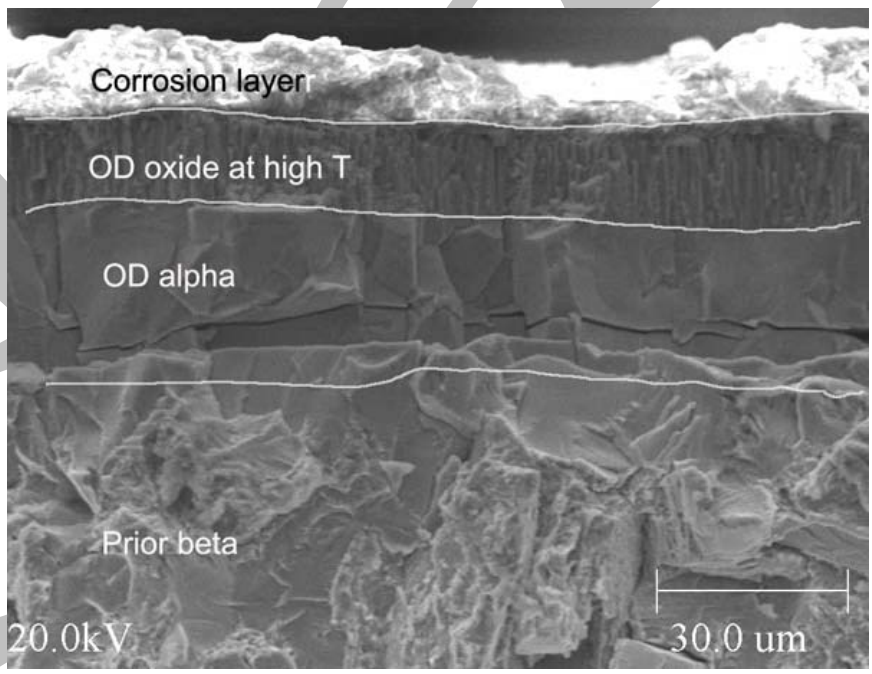

(b)

Figure 124. High-magnification images of the outer surface of high-burnup HBR Zry-4 sample following oxidation (two-sided) at 1200ºC to 7.4% CP-ECR and slow cooling to RT: (a) OM; and (b) SEM.

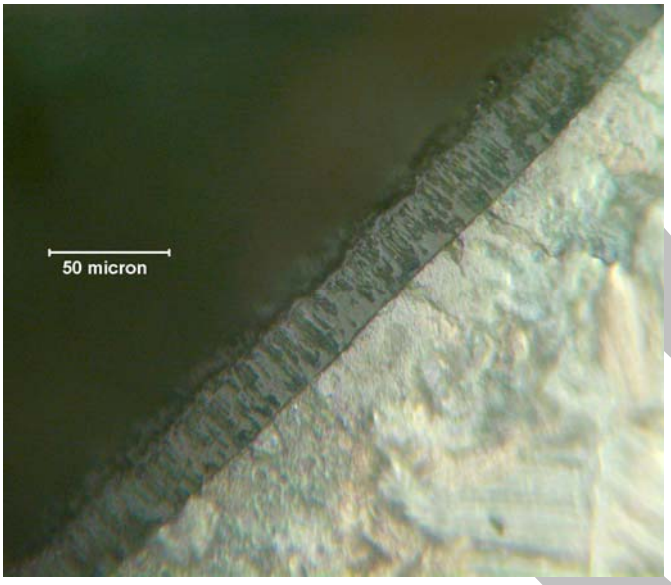

(a)

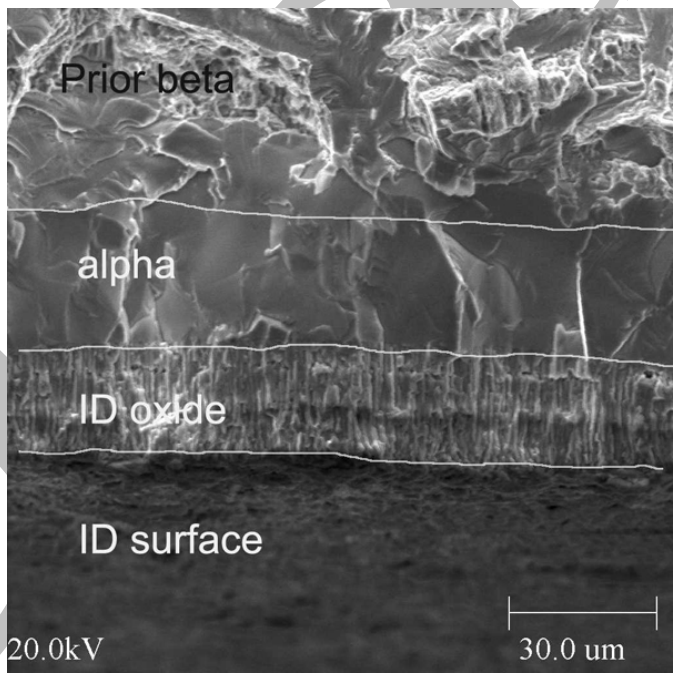

(b)

Figure 125. High-magnification images of the inner surface of high-burnup HBR Zry-4 sample following oxidation (two-sided) at 1200ºC to 7.4% CP-ECR and slow cooling to RT: (a) OM; and (b) SEM.

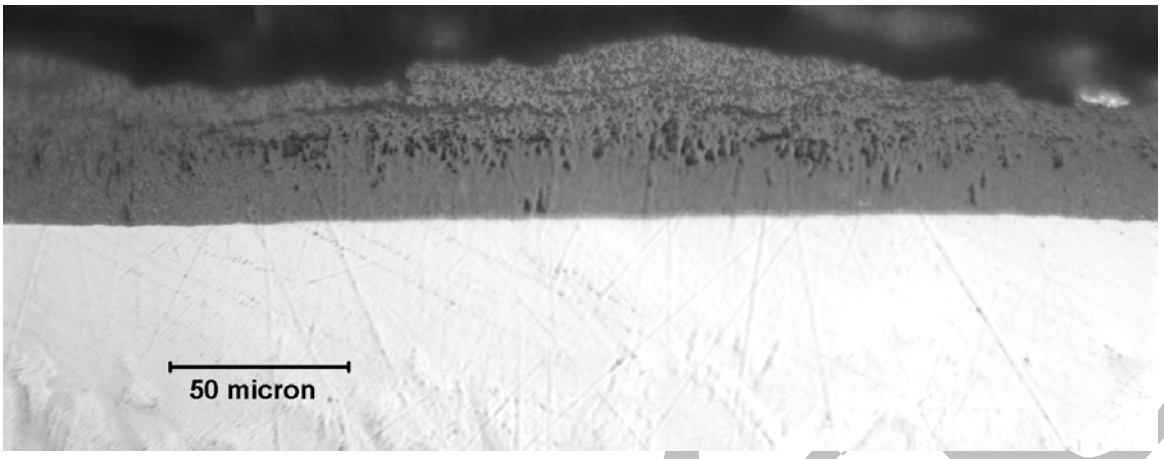

(a)

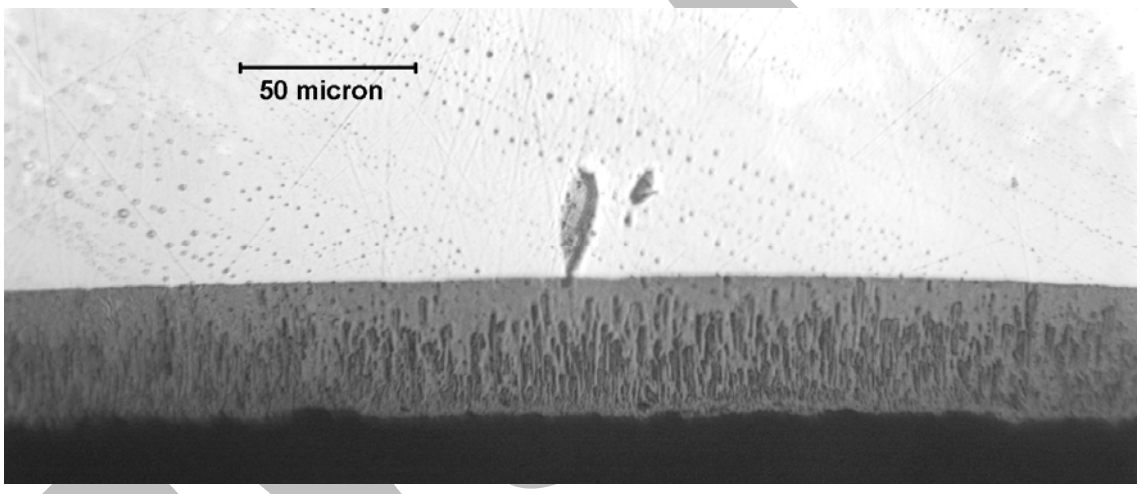

(b)

Figure 126. Optical microscopy images of the outer (a) and inner (b) surfaces of the high-burnup HBR Zry-4 sample oxidized (two-sided) at ≈1200ºC to 9.3% CP-ECR followed by slow cooling to RT. The sample is in the as-polished condition.

The CP-ECR values in Tables 51-54 are calculated for the heating phase of the transient. The total ECR (ECR_t) can be calculated from the relationship $ECR_t = [(ECR_h)^2 + 2.3]^{0.5}$ to give total CP-ECR values of 3.1%, 4.6%, 7.6% and 9.4%, respectively, for heating-phase CP-ECR values of 2.7%, 4.3%, 6.4%, 7.4% and 9.3%.

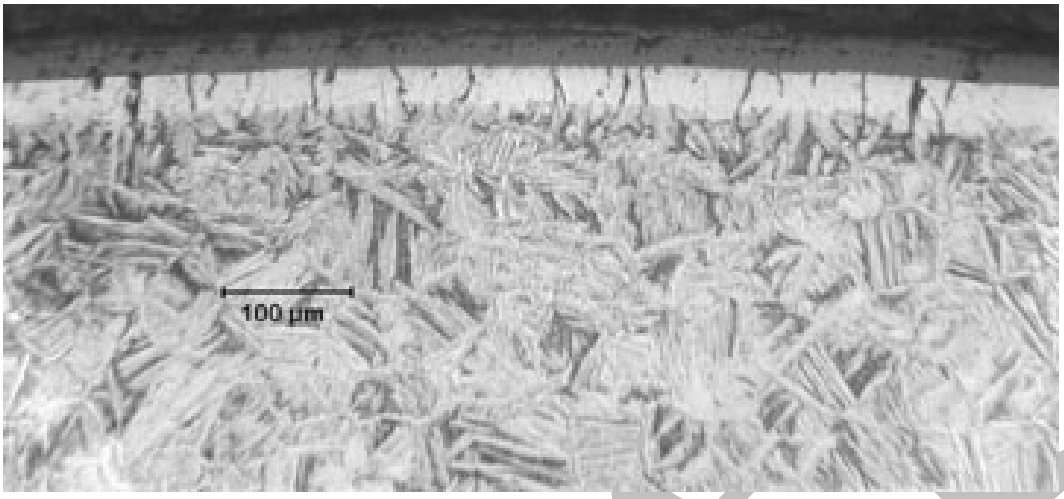

(a)

(b)

Figure 127. Optical microscopy images of the outer (a) and inner (b) surfaces of the high-burnup HBR Zry-4 sample oxidized (two-sided) at 1200ºC to 9.3% CP-ECR followed by slow cooling to RT. The sample is in the etched condition.

Table 54 Results of Ring-Compression Tests for High-burnup HBR Zry-4 Cladding Samples Oxidized (Two-sided) at 1110-1198ºC to 2.7-9.3% CP-ECR and Slow Cooled (SC) to RT or Quenched (Q) at 800ºC; tests were conducted on ≈8-mm-long rings at 135ºC and 0.0333 mm/s displacement rate; offset and permanent displacements were normalized to the cladding metal outer diameter (10.6 mm) to calculate strains

Test ID #	Hydrogen Content wppm	Test Time[a] s	Cooling	CP-ECR %	Maximum Oxidation T ºC	Plastic Stains, %	
						Offset	Permanent
2	550±100	62	SC	2.7	1110	>45	>43
1	550±100	93	SC	4.3	1169	>12 ≈37	--- ---
3	550±100	132	SC	6.4	1196	4.0	2.6
5	550±100	155	SC	7.4	1197	4.0	2.9
6	800±110	155	Q	7.5	1197	0.2	0.8
4	550±100	206	SC	9.3	1198	0.5	0.6

[a]Includes time for ramp from 300ºC and hold time (see Figure 121 for temperature history).

The load-displacement curves are presented because they reveal more information (e.g., maximum load) than just the summary values in Table 54. Figure 128 shows the load-displacement curve for the sample oxidized to 2.7% CP-ECR at a maximum temperature of 1110ºC during the ramp. The test was stopped after an offset displacement of 4.75 mm, which is close to the geometrical limit where the top and bottom ends contact the thermocouple across the sample. The sample was intact and the increasing load with displacement suggests that this sample had as much ductility as the as-fabricated HBR-type Zry-4 cladding. The results are significant because the presence of 550±100 wppm hydrogen had no effect on the ductility of the sample at such a low oxidation level. With a test time of only 62 s from 300ºC to 1110ºC, there was not enough time at high temperature for significant oxygen diffusion into the beta layer to occur.

Based on the post-quench-ductility results for prehydrided samples (see Figure 100), the 4.3% CP-ECR sample was expected to have low ductility. Two 8-mm-long rings were sectioned from the oxidation sample. The first ring tested experienced a sharp 40% load drop after 12% offset strain (see Figure 129a). The load drop was accompanied by a sharp cracking noise. However, the post-test sample had a crack initiating on the inner-surface that did not penetrate through the wall. The second ring was tested under the same conditions (see Figure 129b). The load decrease with displacement was gradual, indicative of a highly ductile ring, and the only sharp load drop observed (and cracking sound heard) was at the end of the test at very low load. After 53% offset strain, the ring was in the shape of a bow tie (infinity symbol) with a single crack through the wall of the cladding across the length of the ring. Although a partial crack may have formed anywhere in the range of 18-53% offset stain and developed into a through-wall crack at 53% offset strain, it is more likely that the slow-growing crack penetrated the wall at an intermediate strain. Based on judgment and experience, 37% offset strain is assumed to represent the ductility of this sample. It is much higher than offset strains measured for prehydrided samples, which were quenched at 800ºC following oxidation to 5% CP-ECR. The lower peak oxidation temperature (1169ºC vs. 1180-1190ºC), the lower CP-ECR (4.3% vs. 5.0%), and the cooling history (slow cooling vs. quench) all contributed to the relatively high ductility of this sample.

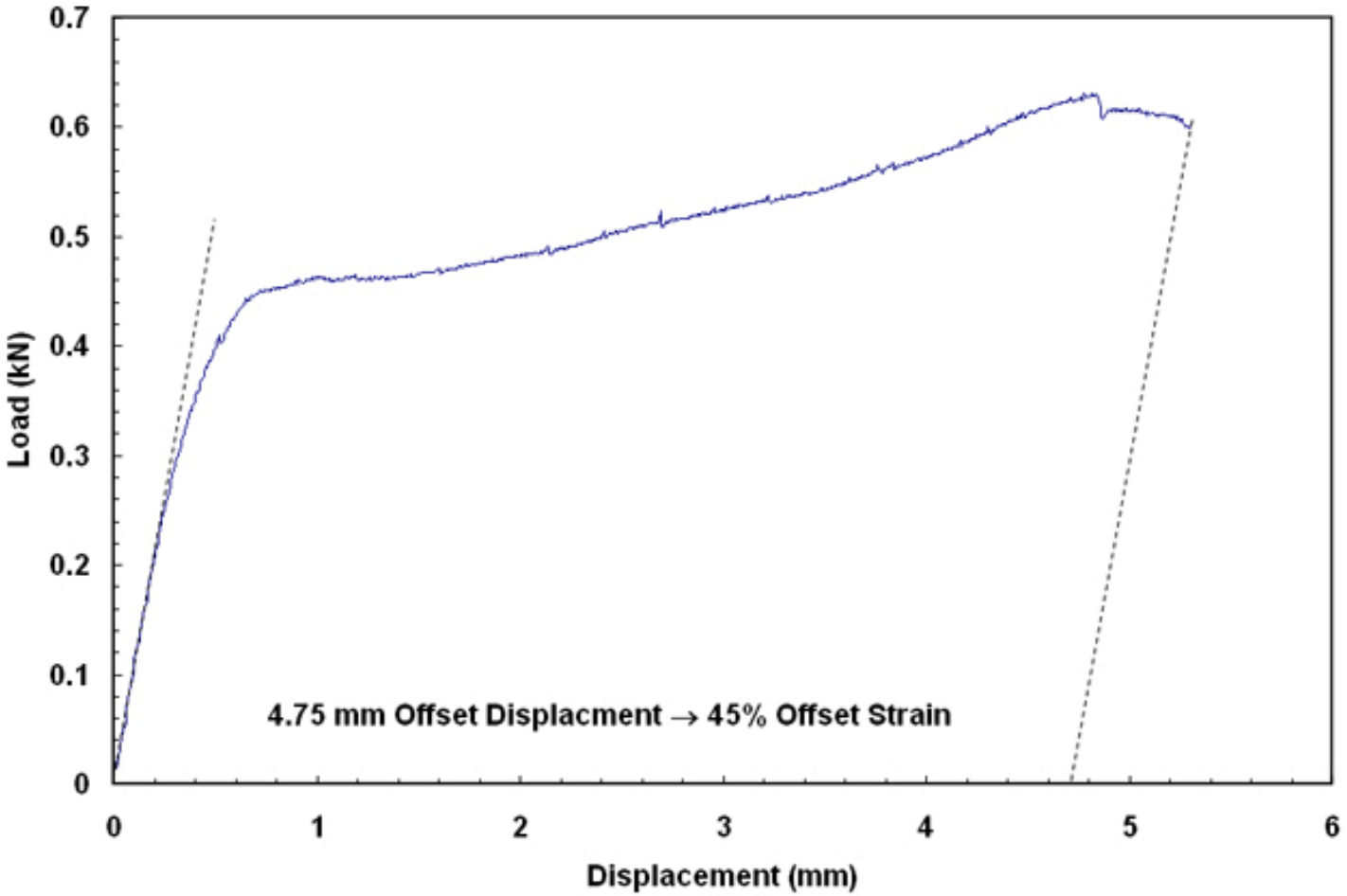

Figure 128. Load-displacement curve for high-burnup HBR Zry-4 sample (550±100 wppm H) oxidized (two-sided) at T ≤ 1110ºC to 2.7% CP-ECR and slow cooled to RT. The ring-compression test was conducted at 135ºC and 0.0333 mm/s displacement rate. The ring was intact after the test, indicating that ductility was > 45%.

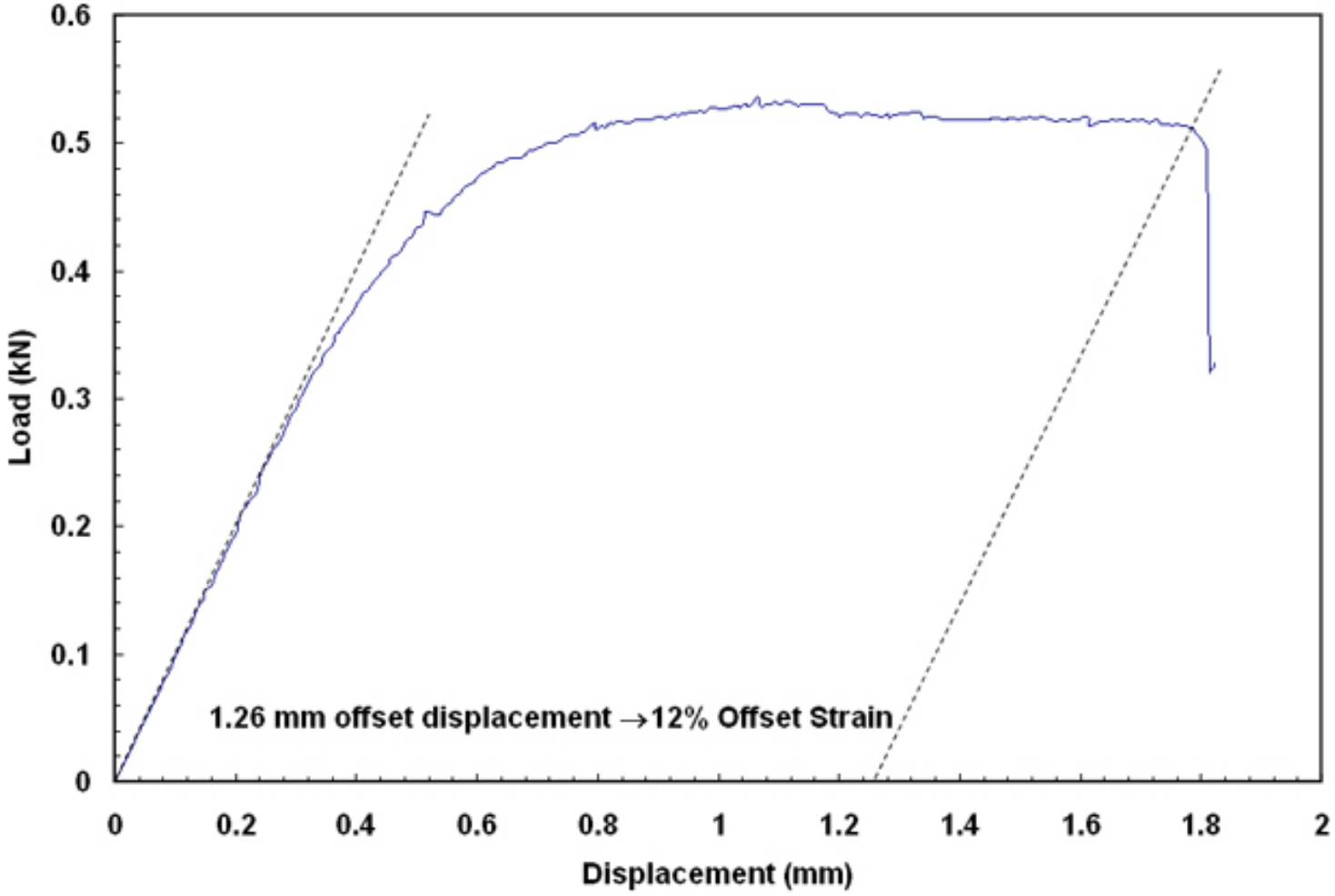

Figure 129a. Load-displacement curve for high-burnup HBR Zry-4 Ring #1 (550±100 wppm H) cut from sample oxidized (two-sided) at T ≤ 1169ºC to 4.3% CP-ECR and slow cooled to RT. The ring-compression test was conducted at 135ºC and 0.0333 mm/s displacement rate. The ring had a partial-wall crack after the first load drop, indicating that ductility was > 12%.

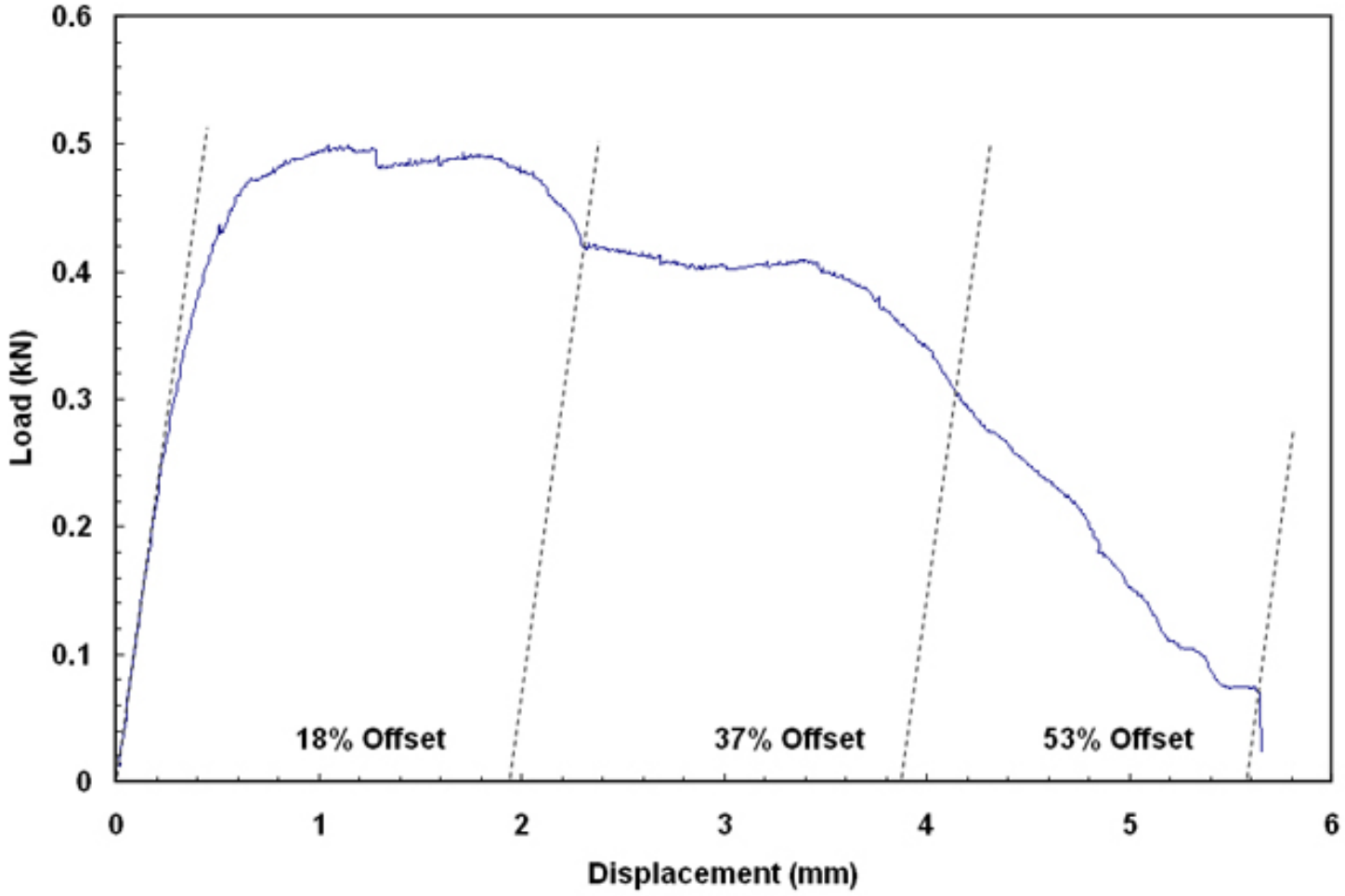

Figure 129b. Load-displacement curve for high-burnup HBR Zry-4 Ring #2 (550±100 wppm H) cut from sample oxidized (two-sided) at T ≤ 1169ºC to 4.3% CP-ECR and slow cooled to RT. The ring-compression test was conducted at 135ºC and 0.0333 mm/s displacement rate. The ring had a single through-wall crack after 53% offset strain. Because it is not clear at what strain this crack occurred, the offset strain (37%) corresponding to a 40% load drop is used to represent the ductility of the sample.

Figure 130 shows the load-displacement curve for the high-burnup HBR Zry-4 sample with 550±100 wppm hydrogen, which was oxidized to 6.4% CP-ECR at a peak oxidation temperature of 1196ºC. The results are easy to interpret because the sharp load drop did correspond to through-wall failure across the length of the ring. The offset and permanent strains for this sample are given in Table 54 as 4.0% and 2.6%, respectively. By the ANL criteria (≥2% offset strain and/or ≥1% permanent strain), the sample is ductile. However, the low ductility indicates a significant decrease in ductility between 4.3% and 6.4% CP-ECR oxidation levels.

The 7.4% CP-ECR test was conducted because it was estimated that embrittlement would occur at this oxidation level for Zry-4 with 550±100 wppm hydrogen. However, as shown in Figure 131, the offset strain (4.0%) for this sample was the same as for the 6.3% CP-ECR sample, and the permanent strain was slightly higher (2.9% vs. 2.6%). The test was repeated with another high-burnup HBR Zry-4 sample with higher hydrogen content (740±110 wppm) and with quench at 800ºC. Because of the higher corrosion level of this sample (95 μm vs. 74 μm), the cladding metal wall was slightly thinner and the CP-ECR was slightly higher (7.5% vs. 7.4%) for the same test time. Consistent with prehydrided samples (>400 wppm H) oxidized at 1200ºC to 7.5% CP-ECR and quenched at 800ºC, this high-burnup sample was highly brittle (see Figure 132). The 9.3% CP-ECR test, which was slow-cooled, was conducted before the 7.4-7.5% CP-ECR tests. As shown in Figure 133, the sample was highly brittle with an offset strain of 0.5% and a permanent strain of 0.6%.

Figure 134 shows the post-oxidation and post-quench ductility data plotted as a function of CP-ECR. A trend curve is also plotted for the slow-cooled samples with 550±100 wppm hydrogen. Using interpolation, it appears that the ductile-to-brittle transition CP-ECR for these high-burnup samples is ≈8% following slow cooling to RT. For high-burnup Zry-4 with 740±100 wppm hydrogen, the transition CP-ECR is clearly <7.5%.

An important motivation for testing high-burnup cladding is to determine if prehydrided cladding is a good surrogate for high-burnup cladding. The post-oxidation and post-quench ductility results presented in Section 4 are compared to the high-burnup results in Table 55 for samples with comparable hydrogen content. The prehydrided samples at 5% CP-ECR have ductility values between the high- and low-ductility values for high-burnup cladding at lower (4.3%) and higher (6.4%) CP-ECR levels. For 7.4% CP-ECR oxidized samples, slow-cooled high-burnup Zry-4 has a higher ductility than the slow-cooled prehydrided Zry-4. Based on this limited comparison, prehydrided Zry-4 appears to embrittle at lower combinations of CP-ECR and hydrogen content than high-burnup Zry-4. However, a more detailed comparison of the data for slow-cooled samples indicates that the difference could be due to data scatter.

Table 55 Comparison of Ductility Data from Two-sided Oxidation Tests at 1200ºC with High-burnup and Prehydrided (Unirradiated) Zry-4; Q = quench and SC= slow cooling

Cladding Condition	H-Content wppm	CP-ECR %	Tmax ºC	Cooling	Offset Strain %	Permanent Strain %
High-burnup	550±100	4.3	1170	SC	37	---
Prehydrided	517-545	5.0	1190	Q-800ºC	9.5±4.0	---
High-burnup	550±100	6.4	1196	SC	4.0	2.6
High-burnup	550±100	7.4	1197	SC	4.0	2.9
Prehydrided	550±20	7.4	1200	SC	1.6±0.2	1.1±0.2
Prehydrided	533	7.5	1200	Q-800ºC	0.5	---

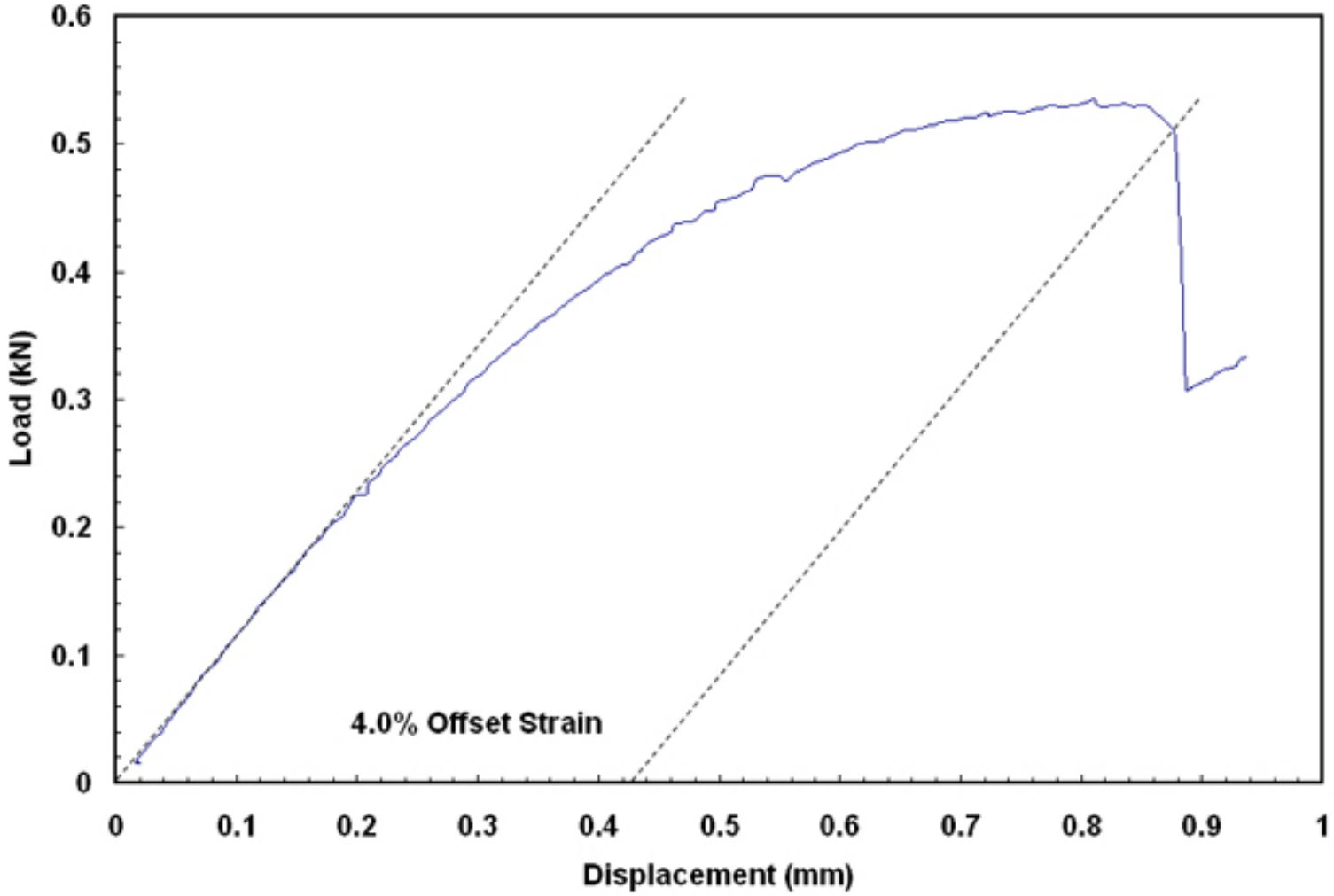

Figure 130. Load-displacement curve for high-burnup HBR Zry-4 (550±100 wppm H) sample oxidized (two-sided) at T ≤ 1196ºC to 6.4% CP-ECR and slow cooled to RT. The ring-compression test was conducted at 135ºC and 0.0333 mm/s displacement rate. The ring had a single through-wall crack along the length of the sample at 4.0% offset strain, corresponding to the sharp load drop.

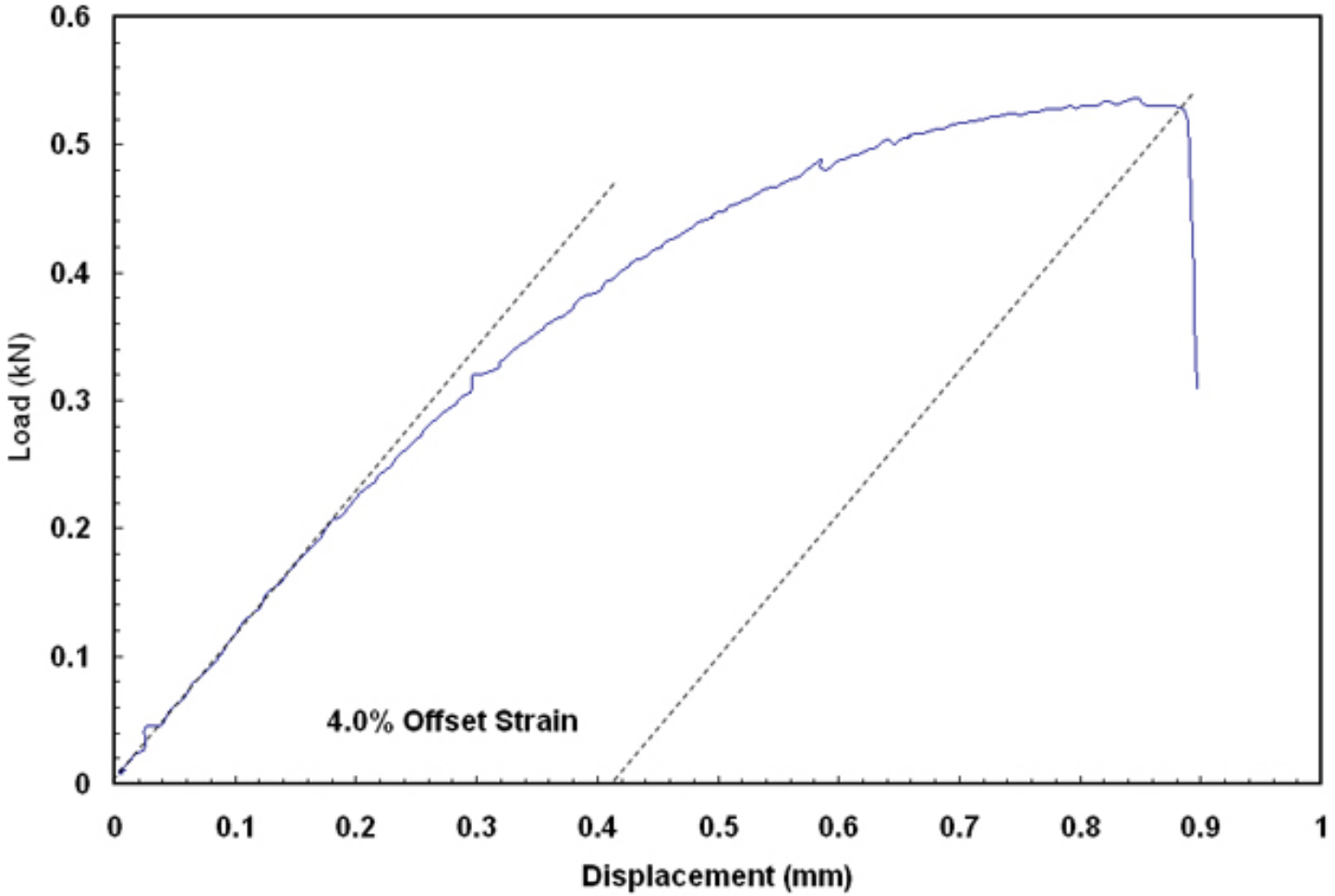

Figure 131. Load-displacement curve for high-burnup HBR Zry-4 (550±100 wppm H) sample oxidized (two-sided) at 1197ºC to 7.4% CP-ECR and slow cooled to RT. The ring-compression test was conducted at 135ºC and 0.0333 mm/s displacement rate. The ring had a single through-wall crack along the length of the sample at 4.0% offset strain, corresponding to the sharp load drop.

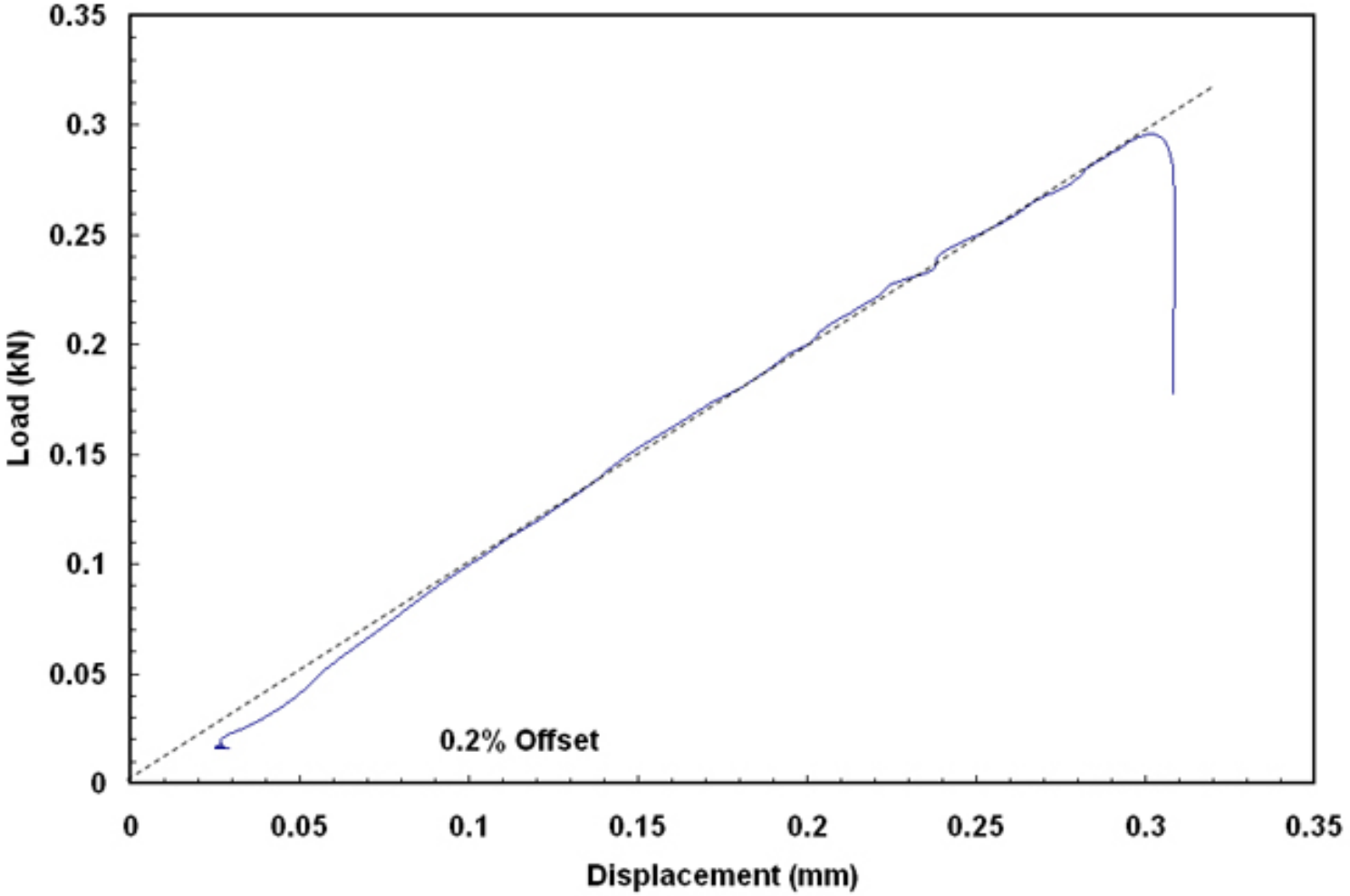

Figure 132. Load-displacement curve for high-burnup HBR Zry-4 (740±110 wppm H) sample oxidized (two-sided) at 1198ºC to 7.5% CP-ECR and quenched at 800ºC. The ring-compression test was conducted at 135ºC and 0.0333 mm/s displacement rate. The sharp load drop occurred essentially in the elastic deformation region and corresponded to a single through-wall crack along the length of the sample and no ductility.

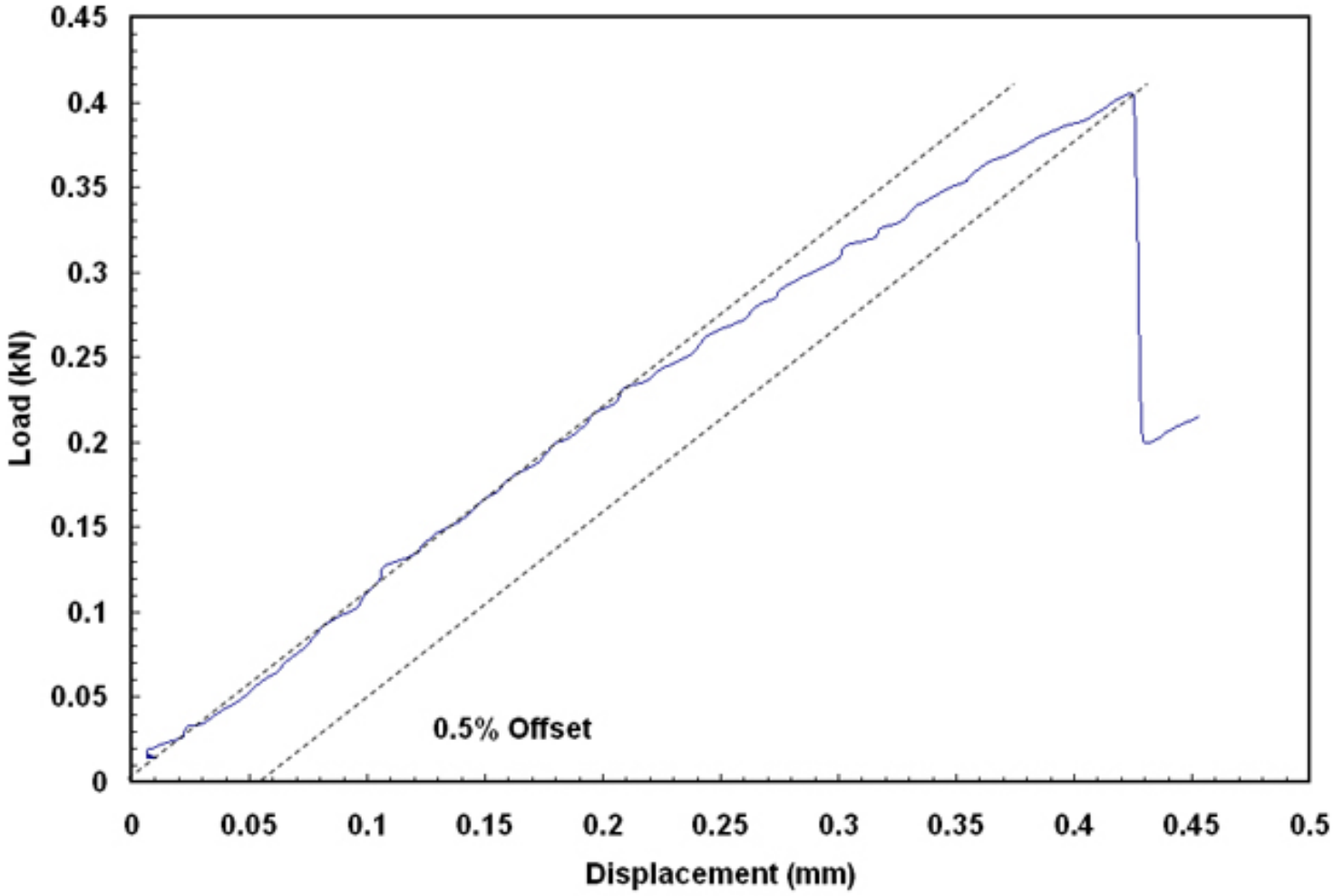

Figure 133. Load-displacement curve for high-burnup HBR Zry-4 (550±100 wppm H) sample oxidized (two-sided) at 1198ºC to 9.3% CP-ECR and slow cooled to RT. The ring-compression test was conducted at 135ºC and 0.0333 mm/s displacement rate. The ring had a single through-wall crack along the length of the sample at very low offset strain (brittle), corresponding to the sharp load drop.

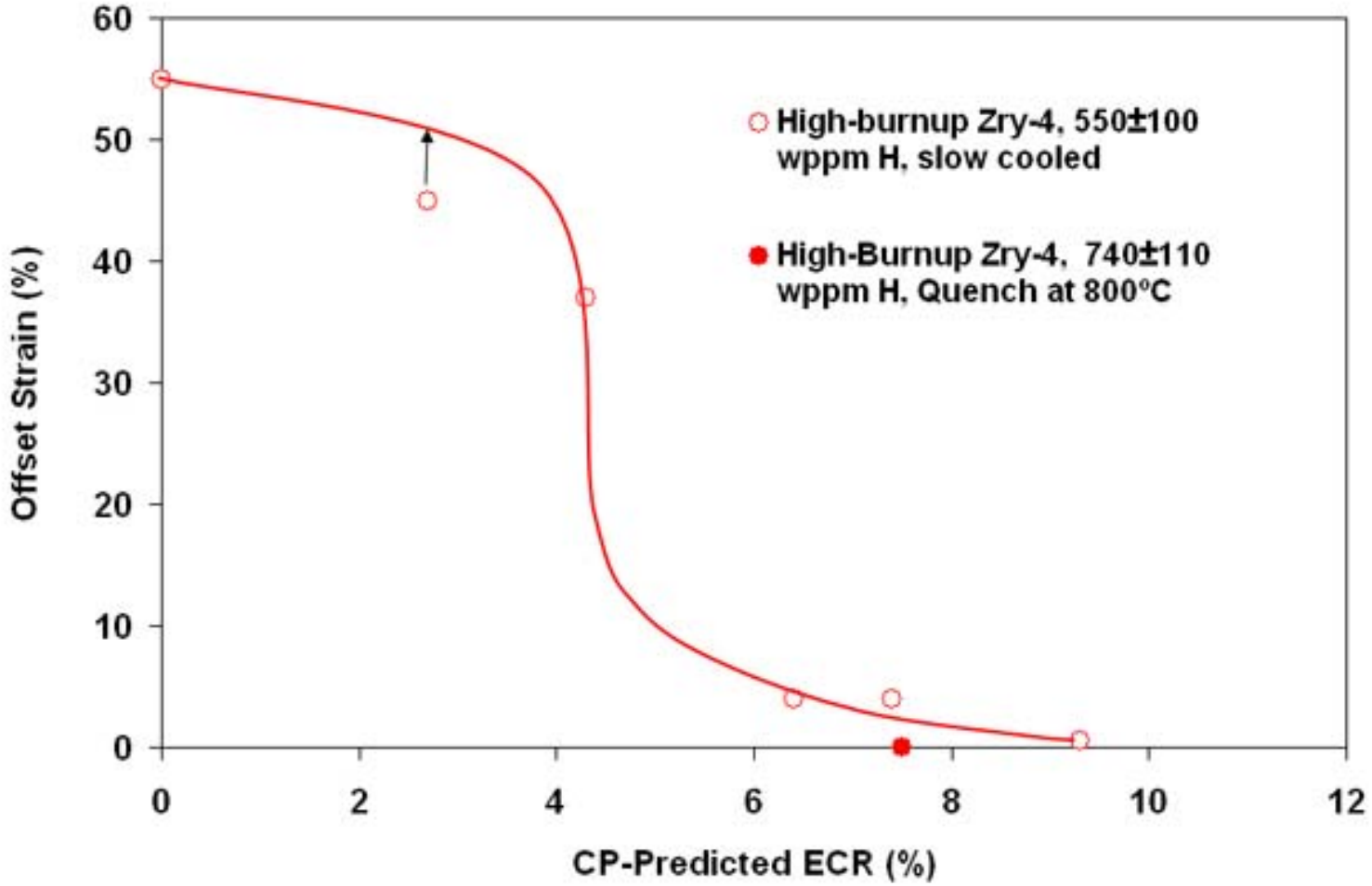

Figure 134. Ductility at 135ºC vs. CP-ECR for high-burnup HBR Zry-4 cladding following oxidation (two-sided) at ≤1200ºC and either slow cooling to room temperature or quench at 800ºC. For the slow-cooled samples, the ductile-to-brittle transition CP-ECR is ≈8%.

As shown in Figures 105 and 106, the embrittlement of prehydrided Zry-4 samples oxidized at 1200ºC and quenched at 800ºC is very sensitive to hydrogen content. The same sensitivity is expected for quench temperatures in the range of 600-800ºC. However, slow-cooled cladding samples oxidized to the same ECR levels (5%, 6%, and 7.5%) appear to maintain a small, but significant, ductility with increasing hydrogen content. This behavior of slow-cooled Zry-4 allows more latitude in comparing the ductility of oxidized prehydrided and high-burnup Zry-4 as a function of CP-ECR for hydrogen contents in the range of 470-720 wppm. The comparison is shown in Table 56 for offset and permanent strains as a function of CP-ECR (5-9.3%). Figure 135 compares the permanent strains, which are a more reliable measure of ductility for measured strains ≥1%. The results suggest that for slow-cooled samples, the ductility of prehydrided Zry-4 is comparable within data scatter to the ductility of high-burnup Zry-4.

Table 56 Ductility Data from Two-sided Oxidation Tests at 1200ºC followed by Slow Cooling for High-burnup and Prehydrided (Unirradiated) Zry-4 Cladding Samples

Cladding Condition	H-Content wppm	CP-ECR %	Offset Strain %	Permanent Strain %
Prehydrided	720	5.0	3.4	2.7
Prehydrided	470	6.0	2.1	1.7
Prehydrided	470	6.0	4.9	3.6
High-burnup	550±100	6.4	4.0	2.6
Prehydrided	490	7.4	3.3	2.4
Prehydrided	530	7.4	1.4	0.9
Prehydrided	570	7.4	1.8	1.3
High-burnup	550±100	7.4	4.0	2.9
High-burnup	550±100	9.3	0.5	0.6

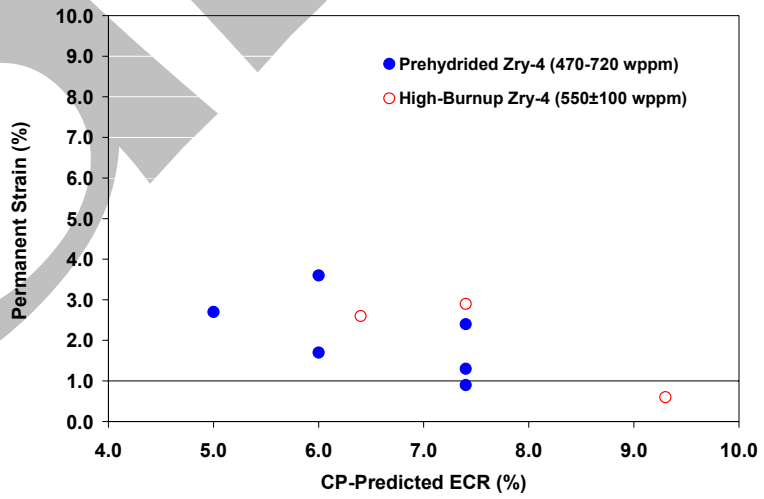

Figure 135. Permanent stain data from two-sided oxidation tests at 1200ºC followed by slow cooling to RT for high-burnup and prehydrided (unirradiated) Zry-4 cladding samples.

5.1.3 Results of one-sided oxidation tests for high-burnup HBR 15×15 Zry-4

The main purpose of conducting the one-sided oxidation tests was to investigate post-oxidation ductility of high-burnup Zry-4 cladding away from the balloon region where there would be no inner-surface steam oxidation. Of particular interest was the influence of the outer-surface corrosion layer on steam-oxidation kinetics at 1200ºC and post-test ductility. Test planning and initial data interpretation were based on the CP-ECR calculated for outer-surface steam oxidation of bare cladding, which is consistent with the manner in which LOCA embrittlement calculations are currently performed for licensing purposes. This calculation does not account for the oxygen source inside fueled-cladding samples from the fuel-cladding bond and the fuel itself. Of these two internal sources of oxygen, only the fuel-cladding bond oxygen source could be investigated in these studies with defueled cladding. Differences in ductility vs. CP-ECR between the one-sided- and two-sided-oxidized high-burnup samples, along with metallographic results, were used to infer the influence of the fuel-cladding bond oxide on embrittlement. The effects on ductility of oxygen in the fuel are discussed in Section 6.

The system used in 2001 to conduct oxidation kinetics studies with high-burnup Limerick Zry-2 was duplicated in 2005 to conduct these one-sided oxidation tests. The test train was essentially the same as the one shown in Figure 9 without the drilled holes. Steam leakage into the inner volume through the sample-gasket and gasket-spacer interfaces was a concern, but it was not a major problem with the tests conducted in 2001. The slow-flowing argon purge through the center of the samples was sufficient to minimize inner-surface oxidation at the ends of the sample to <10% of the sample length. Hydrogen pickup through the inner-surface of the cladding due to hydrogen generation from the small amount of steam leakage did not appear to be a significant issue in 2001 because the hydrogen content of the as-irradiated Zry-2 cladding was ≈70 wppm and the hydrogen content of the post-oxidation samples was <100 wppm. The 1200ºC Zry-2 samples were exposed to steam for 300-1200 s in the 2001 tests. The times for the 2005 tests with high-burnup Zry-4 were considerably shorter (174-534 s).

For the one-sided tests, the same test train was used for the out-of-cell thermal benchmarks and for the in-cell tests. Figure 136 shows the results of the thermal benchmark test using as-fabricated HBR-Type Zry-4 cladding. The controller parameters were chosen to ramp quickly to high temperature without temperature overshoot. Also shown in Figure 136 are the results of thermal benchmark tests with the starting cladding material pre-oxidized in steam at 1200ºC to 42-µm and to 62-µm outer-surface oxide layer thicknesses. Two thermocouples were welded directly to the Zry-4 metal prior to pre-oxidation for these tests. The average of the two thermocouple readings is plotted in Figure 136. The heat-of-oxidation effect on the cladding temperature appears to be negligible for pre-oxidized cladding with a 42-µm oxide layer. The temperature history for the sample with the 62-µm oxide layer is about the same as the one for the 42-µm oxide layer. The 42-µm pre-oxide-layer temperature history was used to plan and interpret test results for the one-sided high-burnup HBR Zry-4 tests. Figure 137 compares the faster-ramp temperature history for the one-sided oxidation tests to the slower-ramp temperature for the two-sided tests (see 5.1.2).

Table 57 summarizes the test conditions for the one-sided-oxidation tests. All samples were slow cooled from 1200ºC. The test chamber inlet port, which had been used to flood the chamber with quench water in two-sided-oxidation tests, was used for the argon purge in these tests. As can be seen in Table 56, all samples reached 1200ºC oxidation temperature and were at 1200ºC for substantial periods of time.

Figure 138 shows the cutting diagram for the oxidized high-burnup Zry-4 samples. Because of concern regarding inner-surface oxidation and hydrogen pickup away from the sample midplane, only one 8-mm-long ring (C2) was sectioned from the midplane region for ring-compression testing.

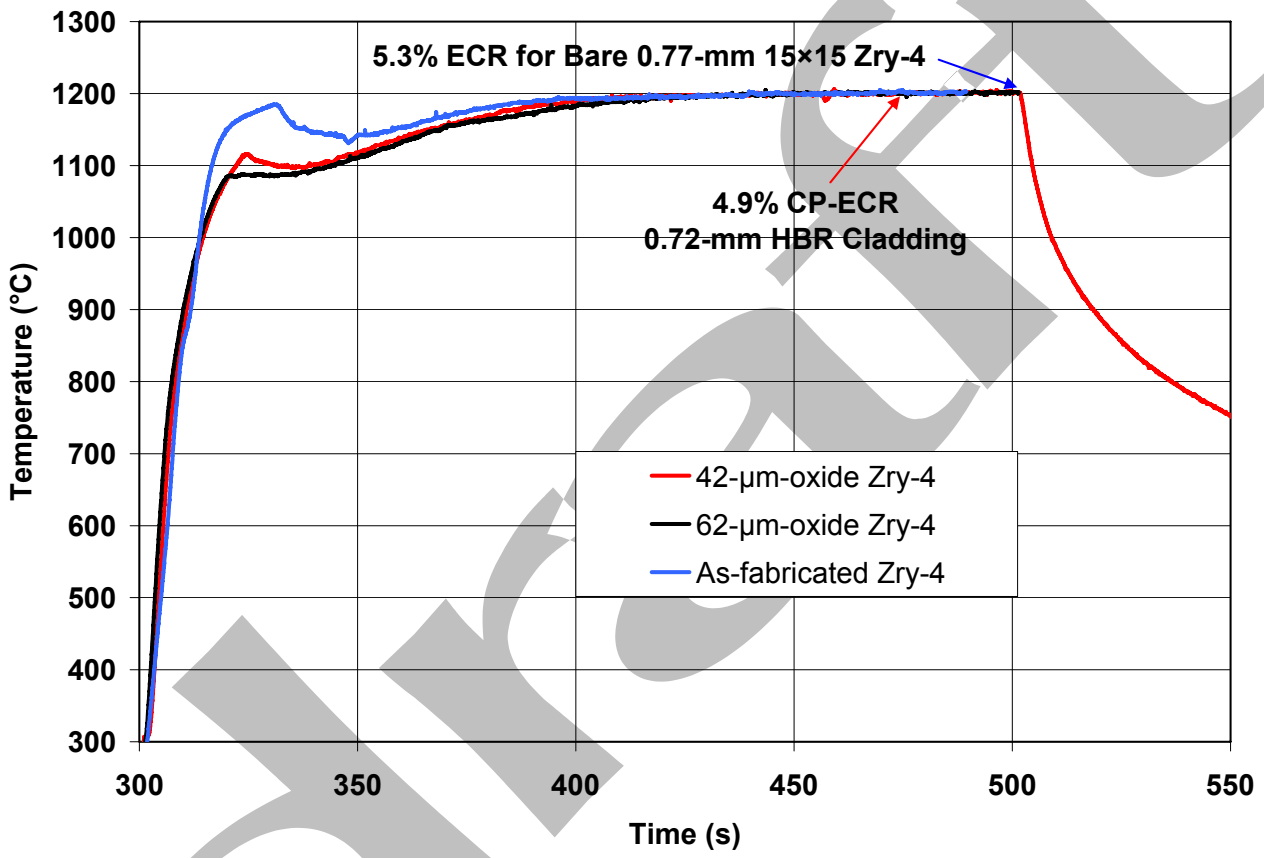

Figure 136. Thermal-benchmark results for unirradiated, HBR-type Zry-4 exposed to one-sided (outer-surface) oxidation: as-fabricated; pre-oxidized to 42-µm outer-surface oxide layer; and pre-oxidized to 62-µm outer-surface oxide layer. The temperature history for the 42-µm oxide layer benchmark was used to plan and interpret the results from the one-sided oxidation tests with corroded (68-µm), high-burnup, HBR Zry-4.

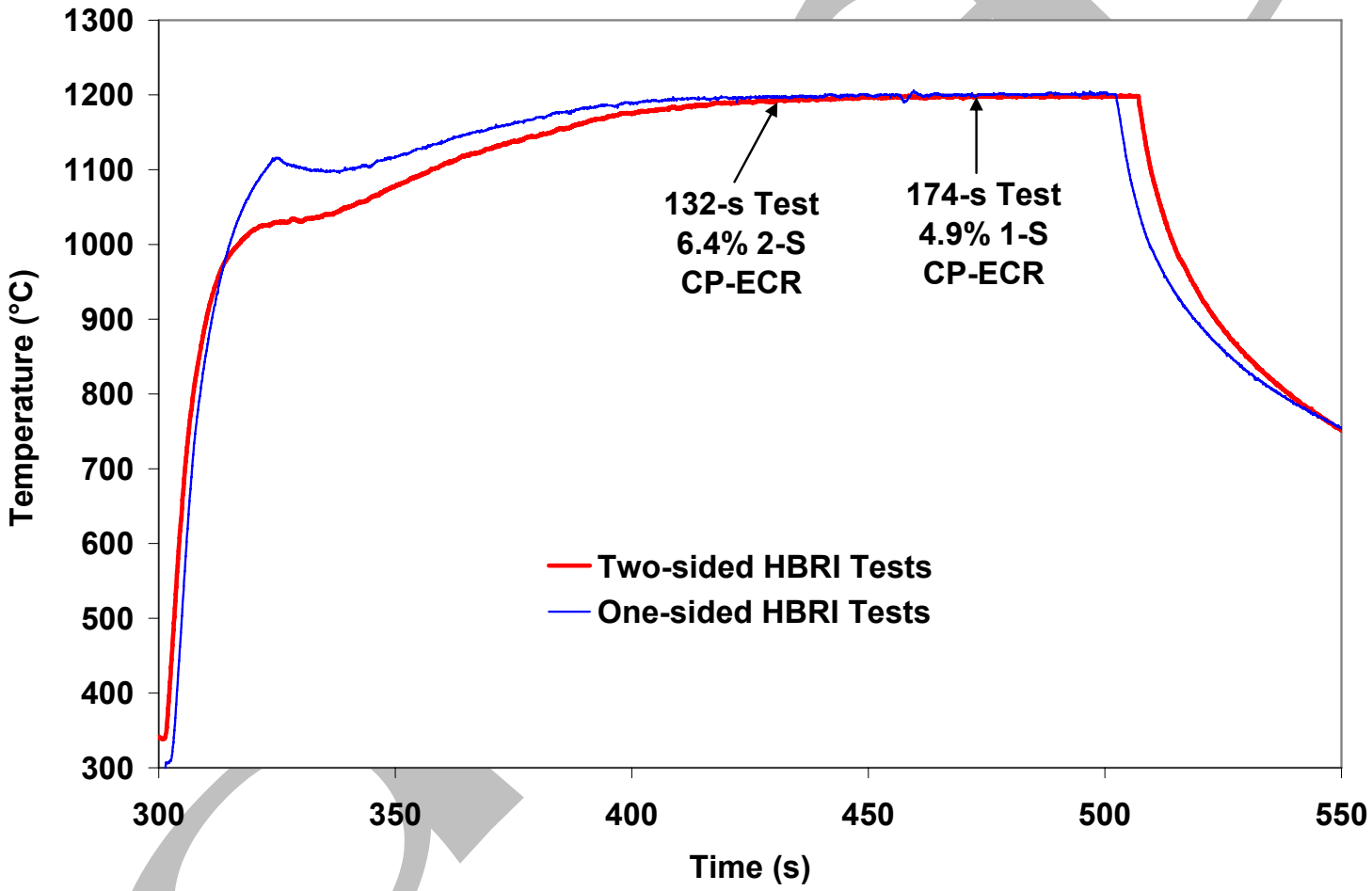

Figure 137. Comparison of temperature histories for the one-sided and two-sided steam oxidation tests using high-burnup HBR Zry-4 cladding samples.

Hydrogen analysis was performed on the ring after ring-compression testing. The samples on either side of the 8-mm-long ring (C1 and C3) were used for metallographic examination.

Table 57 Sample Characterization and Test Conditions for One-sided Steam Oxidation Tests (HBRI) Conducted with High-burnup HBR Zry-4 Cladding; SC is slow cooling

HBRI Test ID #	Corrosion Layer μm	Hydrogen Content wppm	Test Time[a] s	One-sided CP-ECR %	Maximum T ºC	Time at T ≥ 1180ºC s	Cooling
7	68	550±100	174	4.9	1200	85	SC
11	44	≈400	174	4.8	1200	85	SC
8	68	550±100	323	7.3	1200	234	SC
12	≈40	≈360	323	7.1	1200	234	SC
10	68	550±100	419	8.5	1200	330	SC
9	68	550±100	534	9.7	1200	445	SC

[a]Includes time for ramp from 300ºC and hold time.

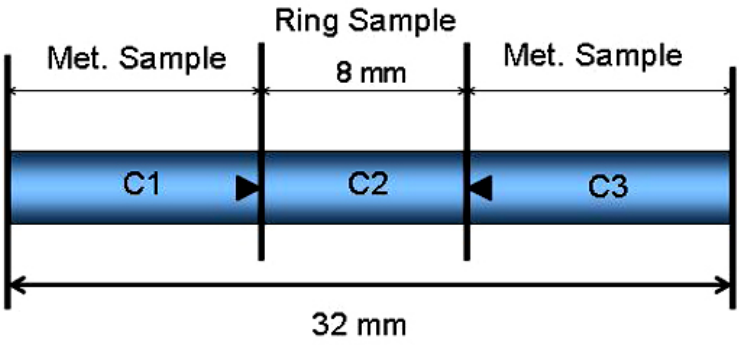

Figure 138. Sectioning diagram for one-sided-oxidized, high-burnup HBR Zry-4 samples. Points of triangles indicate surfaces designated for metallographic characterization.

Table 58 summarizes the post-test results for the high-temperature oxide layer formed on the cladding outer surface and the hydrogen content of the samples. The post-test hydrogen analysis was performed on ring-sectors cut from the oxidized-and-compressed rings. The hydrogen values were not corrected for weight gain due to oxidation. The weight of the post-oxidized samples was only slightly less than the weight of the pre-oxidized samples. Although the main purpose of the post-test hydrogen analysis was to determine if the samples picked up additional hydrogen due to steam leakage and inner-surface oxidation near the ends of the sample, the results indicated that fuel-mid-plane samples oxidized for 174-419 s actually lost hydrogen. The last column in Table 58 indicates whether or not inner-surface oxidation was observed at the ends of the 8-mm-long ring used for ring-compression ductility tests. No inner surface oxide was observed for the HBRI#7 (4.9% 1-S CP-ECR) and the HBRI#8 (7.3% 1-S CP-ECR) test samples. For HBRI#10 (8.5% 1-S CP-ECR) about 15% of the inner-surface exhibited some oxide-layer growth from steam leakage. For HBRI#9 (9.7% 1-S CP-ECR), over 80% of the cross section at 4 mm from the ring midplane had some degree of inner-surface oxide. These observations were made on the OM-sample cross section adjacent to the cross section at the end of the ring. Although the HBRI#11-12 samples were not imaged, both samples appeared to pick up ≈180 wppm H.

Table 58 Post-test Results for High-temperature Oxide Layer Thickness and Hydrogen Content for High-burnup HBR Zry-4 Samples (HBRI) Oxidized in Steam (One-sided) at 1200ºC

HBRI Test ID #	Pre-Test H-Content wppm	Test Time[a] s	One-sided CP-ECR %	OD High-T Oxide, µm		Post-Test H-Content wppm	ID Oxide Layer
				CP	Meas.		
7	550±100	174	4.9	38	31±6	335±31	None
11	≈400	174	4.8	--	--	570±70	{To be Examined}
8	550±100	323	7.3	56	42±7	190±12	None
12	≈360	323	7.1	--	--	550±70	{To be Examined}
10	550±100	419	8.5	65	53±7	318±44	15% of Met. Cross Section
9	550±100	534	9.7	74	63±8	767±59	>80% of Met. Cross Section

[a]Includes time for ramp from 300ºC and hold time.

Figure 139 compares the measured vs. CP-predicted high-temperature oxide-layer thicknesses for the outer surface. The measured values are ≈11-µm less than the predicted values. These results are consistent with the two-sided-oxidation test results, which showed an average difference of 12 µm. They confirm that the corrosion layer slows down the initial growth rate of the steam-oxide layer.

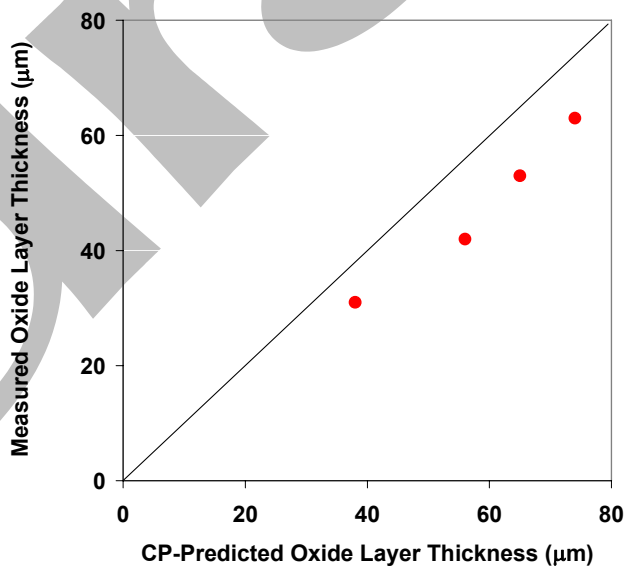

Figure 139. Comparison of measured and CP-predicted steam-induced outer-surface oxide layer thicknesses for high-burnup HBR Zry-4 samples oxidized at 1200ºC to one-sided CP-ECR values of 4.9-9.7%. Samples had a 68-µm pre-test corrosion layer.

Table 59 shows the CP-predicted values for the oxygen-stabilized alpha layer formed under steam oxidation conditions. Also shown in Table 59 are the measured values at the inner- and outer-surfaces for the HBRI#7 sample after a test time of 174 s prior to slow cooling to RT. Although there is no steam flow along the inner-surface, the alpha layer formed from reduction of the fuel-cladding bond layer is comparable to the alpha layer formed at the corroded outer-surface, which was exposed to steam flow.

Table 59 Post-test Results for Outer- and Inner-surface Alpha Layers Stabilized at 1200ºC for High-burnup HBR Zry-4 Samples (HBRI) Oxidized in Steam (One-sided)

HBRI Test ID #	Post-Test H-Content wppm	Test Time[a] s	One-sided CP-ECR %	Alpha Layer Thickness μm			ID Oxide Layer
				CP OD	Meas. OD	Meas. ID	
7	335±31	174	4.9	38	42±4	36±5	None
11	570±70	174	4.8	38	{New data}	{New data}	{To be Examined}
8	190±12	323	7.3	57	58±7	35±8	None
12	550±70	323	7.1	57	{New data}	{New data}	{To be Examined}
10	318±44	419	8.5	66	70±8	--	15% of Met. Cross-section
9	767±59	534	9.7	76	77±7	---	>80% of Met. Cross-section

[a]Includes time for ramp from 300ºC and hold time.

For each test sample, up to eight metallographic images at equally spaced circumferential locations were used to obtain the quantitative data in Tables 58-59. Examples of metallographic images used to measure the high-temperature oxide-layer and alpha-layer thickness are shown in Figures 140-143. The contrast has been adjusted in Figure 140b for the 174-s test sample (HBRI#7) to allow distinction between the oxygen-stabilized alpha layer grown at 1200ºC at the outer-surface as compared to the alpha incursions precipitated during cooling. The outer-surface alpha layer stabilized at 1200ºC is whiter in appearance and relatively uniform in thickness, while the alpha incursions at the outer-surface are gray-white and exhibit a more uneven alpha-beta interface (see Figure 140b for outer surface). Alpha-layer thickness is more difficult to measure at the inner-surface because the alpha-beta boundary is not as smooth and the color contrast is not as sharp between alpha stabilized at 1200ºC and alpha incursions. Also, recall from Figures 113-114 that the fuel-cladding bond layer is not uniform in thickness (11±4 μm). However, the measured alpha-layer thickness is consistent with the complete reduction of the fuel-cladding bond oxide, which is estimated to occur at ≈100 s into the 174-s test. Assuming this estimated time, the inner-surface alpha layer would continue to grow from 100 s to 174 s at a slower rate than the outer-surface alpha layer, which essentially had an infinite source of oxygen to sustain the growth of the outer-surface layer. The observed difference in alpha-layer thicknesses is relatively small. For the two-sided oxidation tests, the inner-surface alpha layer was ≈2-μm thinner than the outer-surface alpha layer. Accounting for this difference, the inner-surface alpha layer grown from reduction of the fuel-cladding bond is only ≈4 μm less than expected under flowing steam conditions. The results for the 323-s test sample (HBRI#8) are also listed in Table 59. While the OD alpha layer continues to grow from 174 s to 323 s, the ID alpha layer shows no increase in thickness within the precision of the measurements. The

results are consistent with what one would expect following the complete reduction of the fuel-cladding bond at ≈100 s during the test.

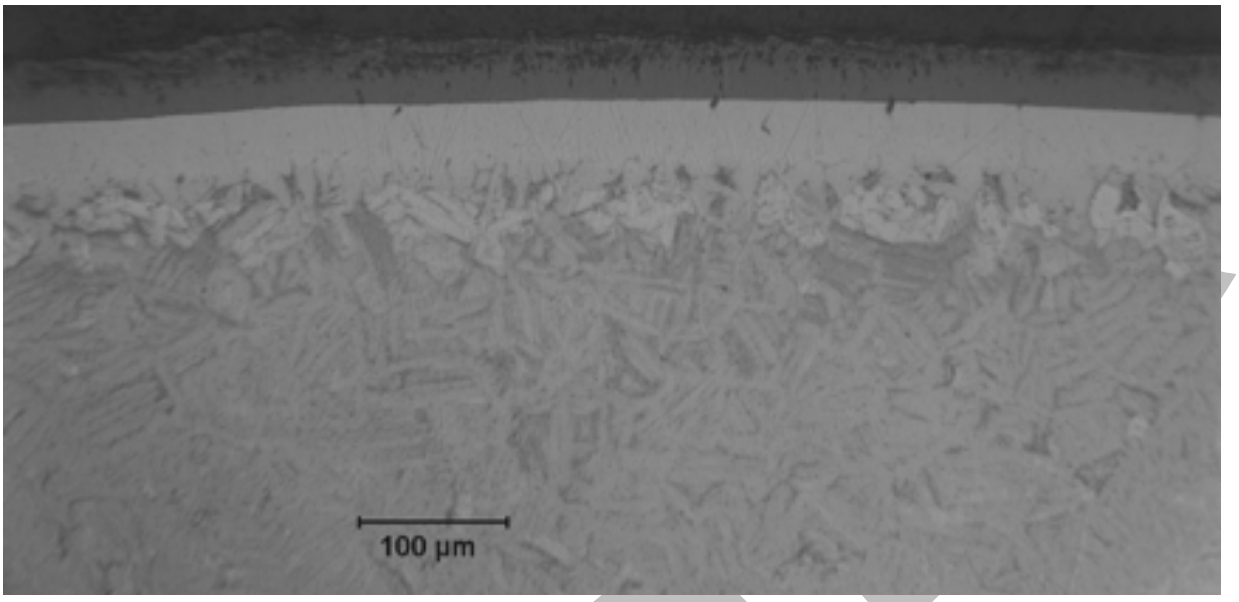

(a)

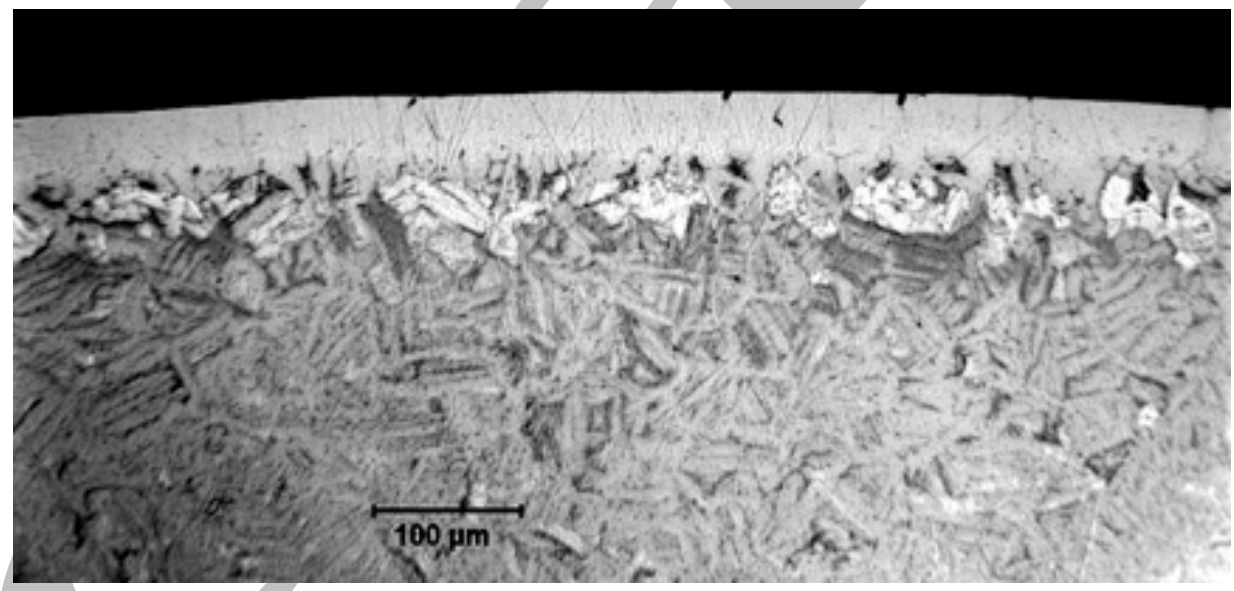

(b)

Figure 140. Outer surface of high-burnup HBR Zry-4 sample one-sided-oxidized at 1200ºC for 174-s test time to 4.9% CP-ECR: (a) contrast for viewing the oxide layer; and (b) contrast for viewing the alpha layer.

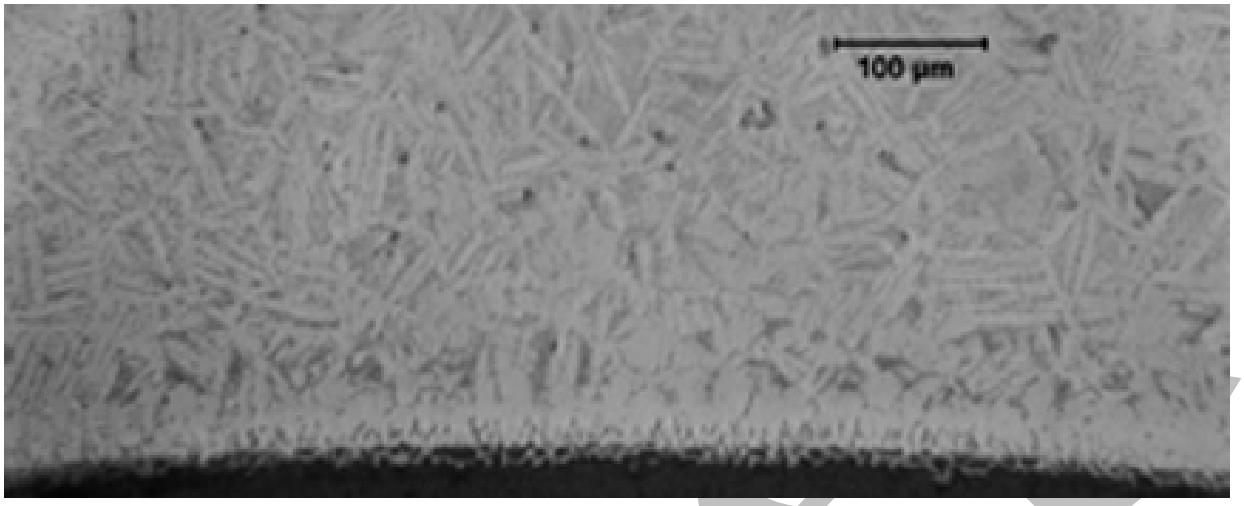

(a)

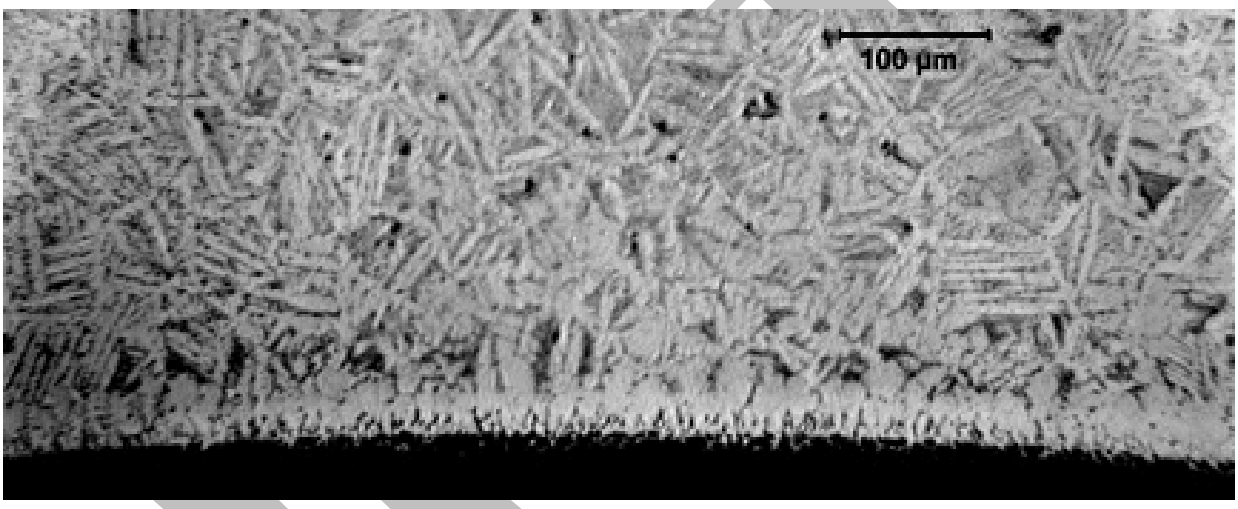

(b)

Figure 141. Inner surface of high-burnup HBR Zry-4 sample one-sided-oxidized at 1200ºC for 174-s test time to 4.9% CP-ECR: (a) normal contrast; and (b) contrast and brightness adjusted for viewing the alpha layer in the central part of the micrograph.

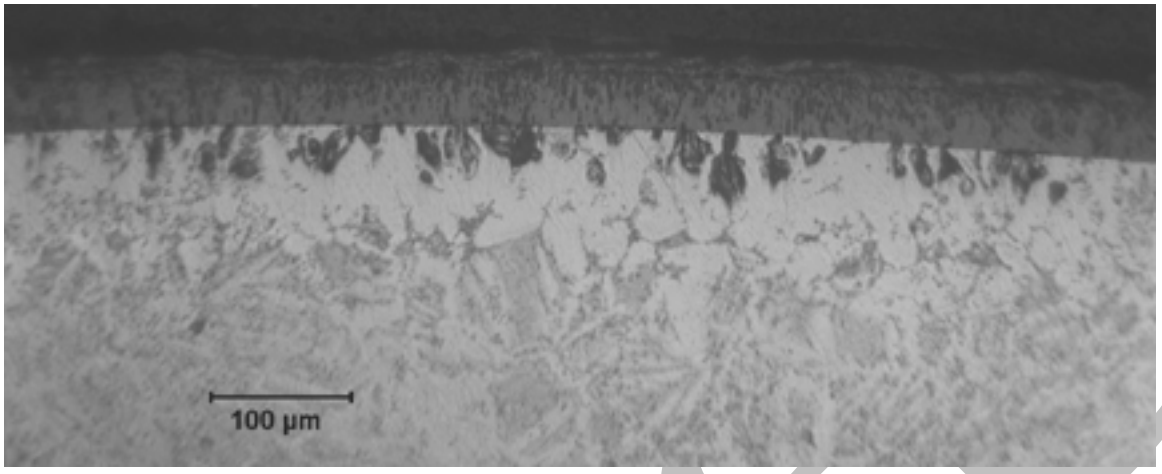

(a)

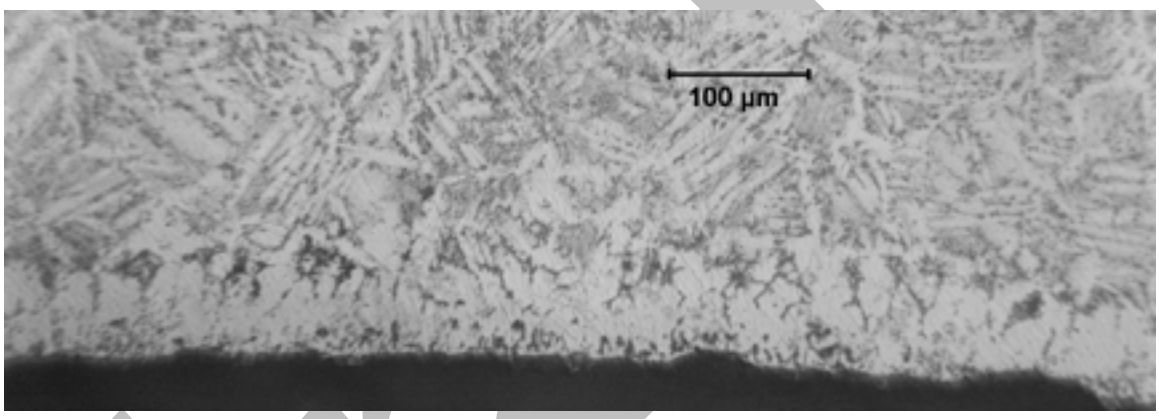

(b)

Figure 142. High-burnup HBR Zry-4 sample one-sided-oxidized at 1200ºC to 7.3% CP-ECR: (a) outer surface; and (b) inner surface.

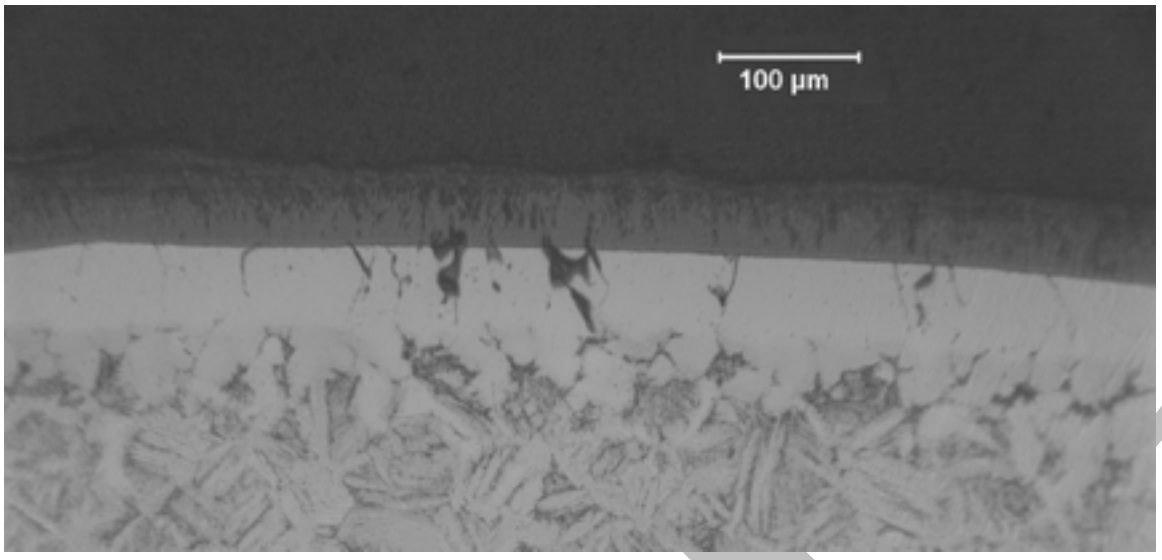

(a)

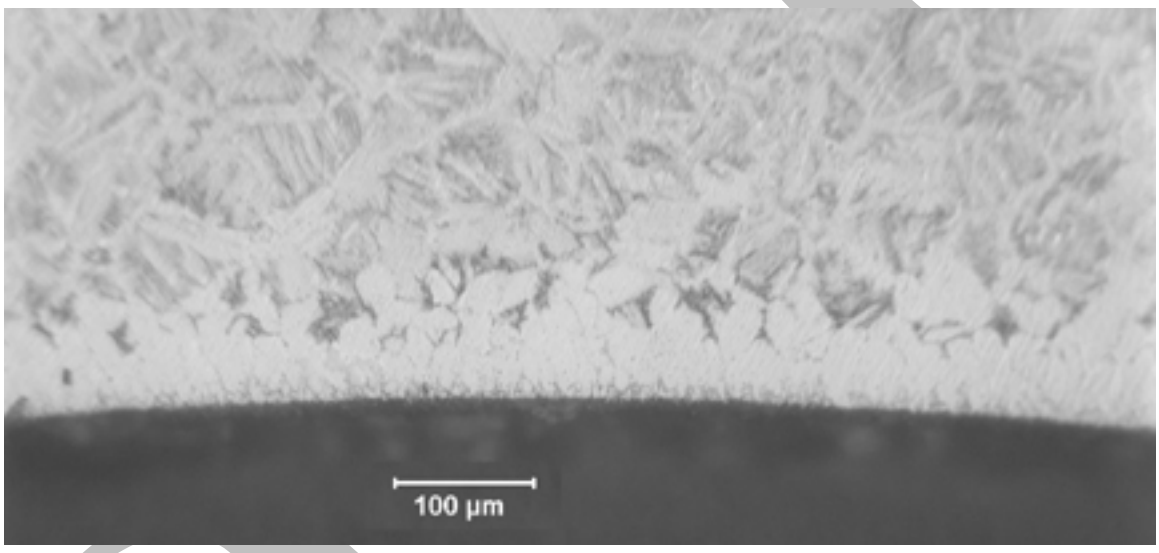

(b)

Figure 143. High-burnup HBR Zry-4 sample one-sided-oxidized at 1200ºC to 8.5% CP-ECR: (a) outer surface; and (b) inner surface.

Post-oxidation ring-compression tests were performed with the six oxidized high-burnup HBR Zry-4 samples. Ductility data are summarized in Table 60. The results are quite interesting even though the hydrogen content was not constant during these one-sided oxidation tests.

Table 60 Ring-Compression Test Results for the Ductility at 135ºC of High-burnup HBR Zry-4 Samples Oxidized (One-sided) in Steam at 1200ºC and Slow Cooled to RT; CP-ECR values are based on outer-surface oxidation

Test ID #	Post-Test H-Content wppm	Test Time[a] s	One-sided CP-ECR %	Plastic Displacement, mm		Plastic Strain, %		ID Oxidation
				Offset	Perm.	Offset	Perm.	
7	335±31	174	4.9	0.89	0.65	8.4	6.1	None
11	570±70	174	4.8	0.39	0.27	3.7	2.5	{To be Examined}
8	190±12	323	7.3	0.47	0.39	4.4	3.7	None
12	550±70	323	7.1	0.10	0.10	0.9	0.9	{To be Examined}
10	318±44	419	8.5	0.40	0.33	3.8	3.1	≈15% at Ends of Ring
9	767±59	534	9.7	0.02	0.01	0.2	0.1	>80% at Ends of Ring

[a]Includes time for ramp from 300ºC and hold time.

The ductility data for the 4.9% (HBRI#7) and 7.3% (HBRI#8) 1-S CP-ECR samples are evaluated because the rings used for these tests exhibited no evidence of inner-surface oxide formation. Nevertheless, both samples had well defined inner-surface alpha layers, which were formed by diffusion of oxygen from the fuel-cladding bond oxide. This can be demonstrated by comparing the OM cross-section images (see Figure 144) from unirradiated and high-burnup Zry-4 samples oxidized to ≈5% 1-S CP-ECR. The unirradiated Zry-4 sample (0.77-mm wall) was one-sided-oxidized for a test time of 190 s. The outer-surface oxide and alpha layers were well developed, and the inner-surface was free of oxide and alpha (see Figure 144a). By contrast, the high-burnup Zry-4 sample in Figure 144b had a well-developed alpha layer at the inner-surface. Similar results were obtained for unirradiated (7.5% CP-ECR) and high-burnup (7.3% CP-ECR) samples one-sided oxidized at 1200ºC.

The one-sided-oxidized high-burnup Zry-4 rings failed due to a crack initiating at the inner-surface and propagating towards the outer surface. The failure location was under the loading platen or above the support platen where the maximum tensile bending stress occurs at the cladding inner surface. Thus, the oxygen-stabilized alpha layer at the cladding inner-surface is brittle enough to initiate the crack. With increasing ring displacement and some plastic deformation, the crack grows through the prior-beta layer and the brittle outer-surface alpha layers. These results suggest that the oxygen in the fuel-cladding bond contributes to the embrittlement of high-burnup cladding exposed to steam at the outer surface.

The test results for lower grid-span samples oxidized to 4.8% and 7.1% 1-S CP-ECR are useful for quantitative comparison purposes because their end-of-test hydrogen contents are comparable to the hydrogen content of the two-sided-oxidized HBR samples. The load-displacement curves for the one-sided-oxidized samples are shown in Figures 145 (4.8% CP-ECR) and 146 (7.1% CP-ECR). The ductility data from Tables 55 (two-sided results) and 60 (one-sided results) are compared in Table 61 and Figure 147 for samples with ≈550 wppm hydrogen, which were slow cooled.

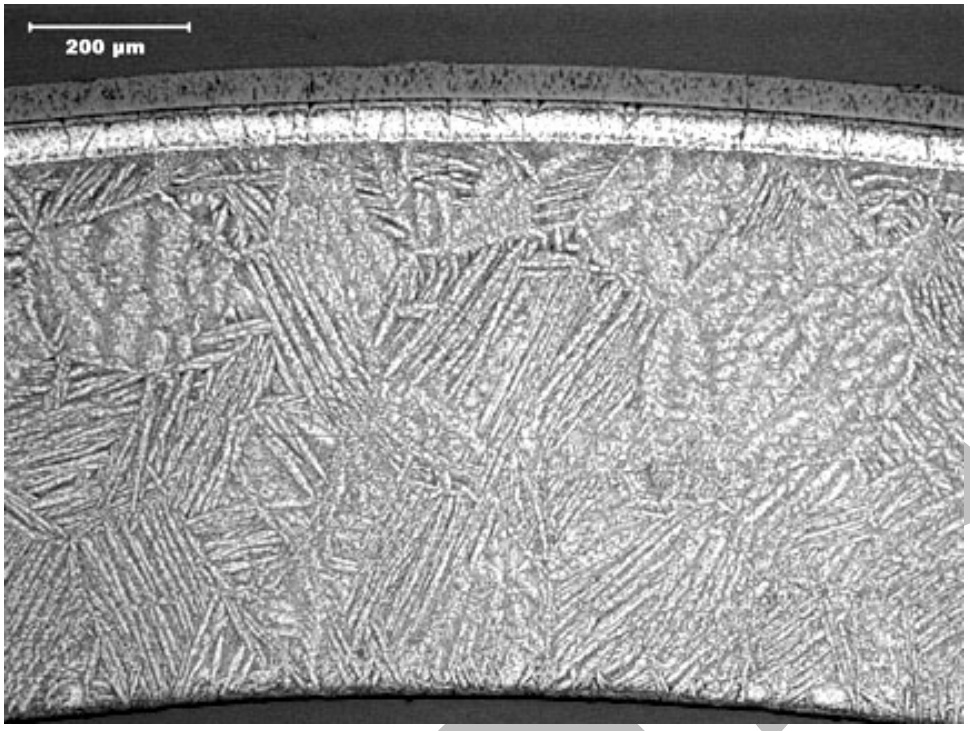

(a)

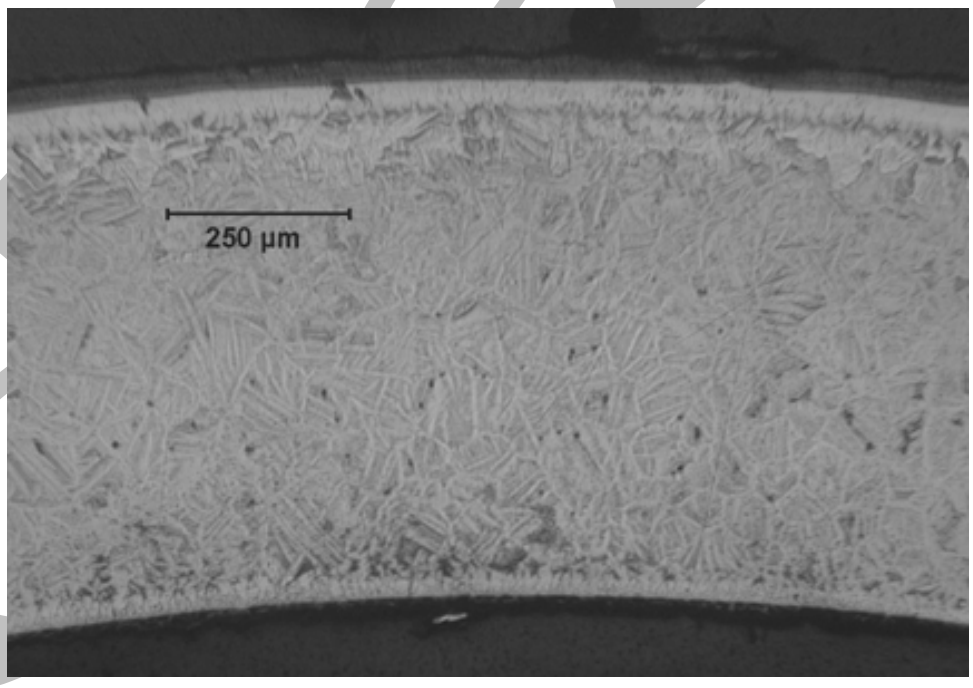

(b)

Figure 144. Comparison of Zry-4 samples oxidized (one-sided) in steam at 1200ºC to 5% CP-ECR: (a) as-fabricated HBR-type Zry-4 at 4 mm from sample midplane; and (b) high-burnup HBR Zry-4 at 4 mm from sample midplane.

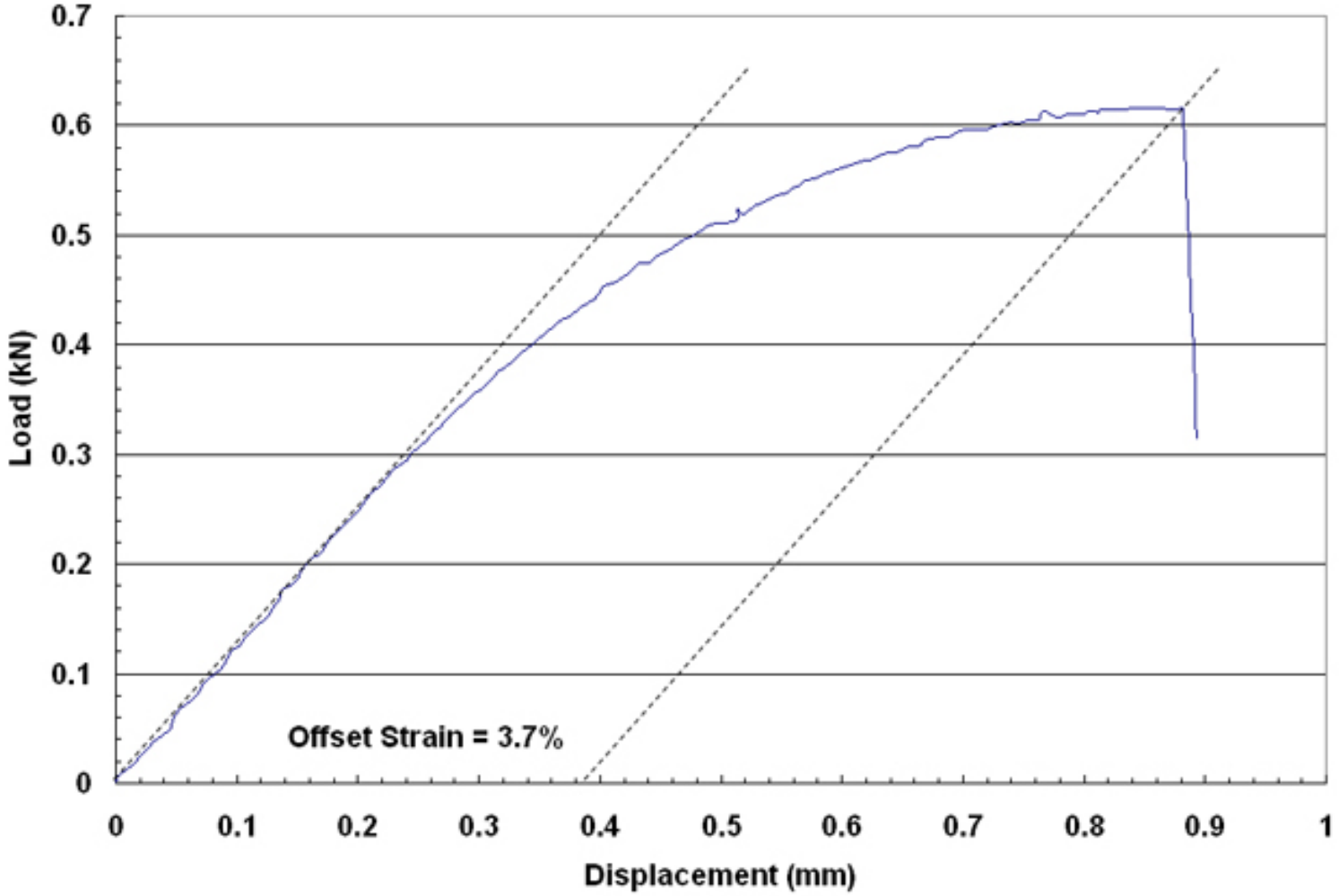

Figure 145. Load-displacement curve for HBRI#11 sample one-sided-oxidized to 4.8% CP-ECR at 1200ºC and ring-compressed at 135ºC and 0.0333 mm/s displacement rate. The sample developed a tight through-wall crack along the 8-mm length at the support position with the crack initiating from the inner surface. Offset displacement was 0.39 mm and permanent displacement in the loading direction was 0.27 mm.

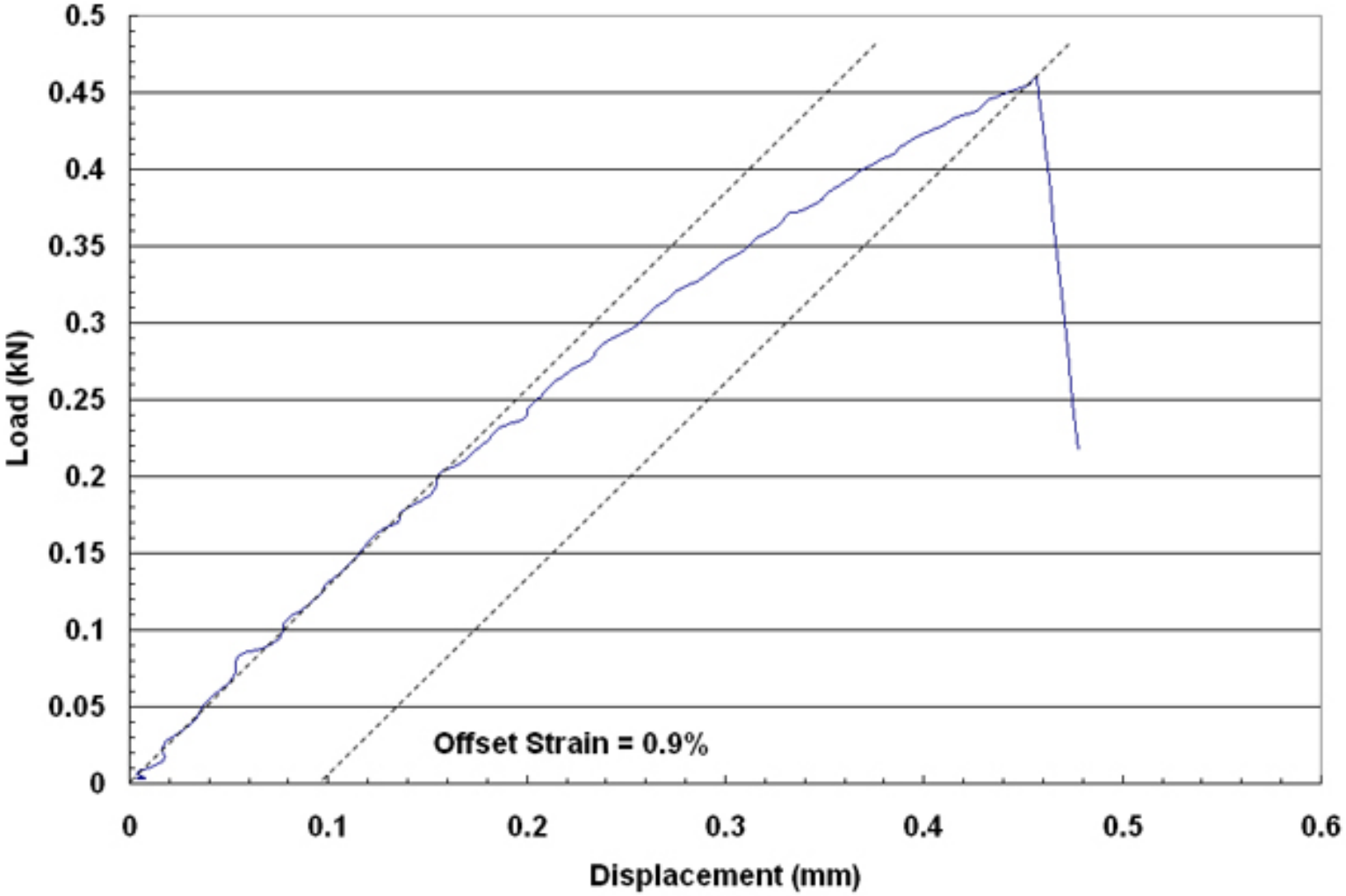

Figure 146. Load-displacement curve for HBRI#12 sample one-sided-oxidized to 7.1% CP-ECR at 1200ºC and ring-compressed at 135ºC and 0.0333 mm/s displacement rate. The sample developed a tight through-wall crack along the 8-mm length at the support position with the crack initiating from the inner surface. Offset displacement was 0.1 mm and permanent displacement in the loading direction was 0.1 mm.

Table 61 Comparison of Post-oxidation Ductility Values for High-burnup HBR Zry-4 Cladding Samples Oxidized at ≤1200ºC and Slow Cooled to RT; test type is indicated by 2-S for two-sided oxidation and 1-S for one-sided oxidation; tests were conducted on ≈8-mm-long rings at 135ºC and 0.0333 mm/s displacement rate; offset and permanent displacements were normalized to the cladding metal outer diameter (10.6 mm) to calculate strains

Test ID #	Hydrogen Content wppm	Test Time[a] s	Test Type	CP-ECR %	Maximum Oxidation T ºC	Plastic Stains, %	
						Offset	Permanent
2	550±100	62	2-S	2.7	1110	>45	>43
1	550±100	93	2-S	4.3	1169	>12 ≈37	--- ---
11	570±70	174	1-S	4.8[b]	1200	3.7	2.5
3	550±100	132	2-S	6.4	1196	4.0	2.6
12	550±70	323	1-S	7.1[b]	1200	0.9	0.9
5	550±100	155	2-S	7.4	1197	4.0	2.9
4	550±100	206	2-S	9.3	1198	0.5	0.6

[a]Includes time for ramp from 300ºC and hold time.
[b]CP-ECR values calculated for one-sided steam oxidation.

The results shown in Figure 147 have been plotted in the usual way vs. CP-ECR; i.e., one-sided values are used for the one-sided tests and two-sided values are used for the two-sided tests. When plotted in this manner, the one-sided-test ductility values fall significantly below the data and trend line for the two-sided-test ductility values. Three factors have been considered to understand differences.

The first factor is the differences in heating rate and test time at 1200ºC (see Figure 137). The relatively high ductility values for two-sided-oxidized HBRI#2 (2.7% CP-ECR) and HBRI#1 (4.3% CP-ECR) can be rationalized based on oxidation temperatures significantly below 1200ºC. However, for remaining three two-sided tests and the two one-sided tests, equivalent times at temperature and CP-ECR levels are more comparable. Differences in heating rate and hold time at 1200ºC would not explain the differences in ductility levels observed in Figure 147.

The second factor considered is the additional oxygen source from slow steam leakage inside the cladding during the one-sided tests. Although no oxide layer was observed at the edges of the rings used for the ring compression tests, low-partial-pressure steam in a hydrogen atmosphere can grow an oxygen-stabilized alpha layer without growing an oxide layer. For the 174-s and 323-s samples examined, no oxide layer was observed at the edges of the 8-mm-rings used to determine ductility and the oxygen content in the fuel-cladding bond was sufficiently high enough to grow the alpha layers observed. For these two test times, steam leakage is not considered to be a significant source of oxygen for embrittlement.

The third factor considered is the effect of the fuel-cladding bond on embrittlement. For the two-sided oxidation tests, the effects of the bond-layer oxygen could not be discerned in the presence of flowing steam. However, for the one-sided steam-oxidation tests, the fuel-cladding bond oxide is considered to be a significant source of oxygen for formation and growth of an alpha layer concurrent

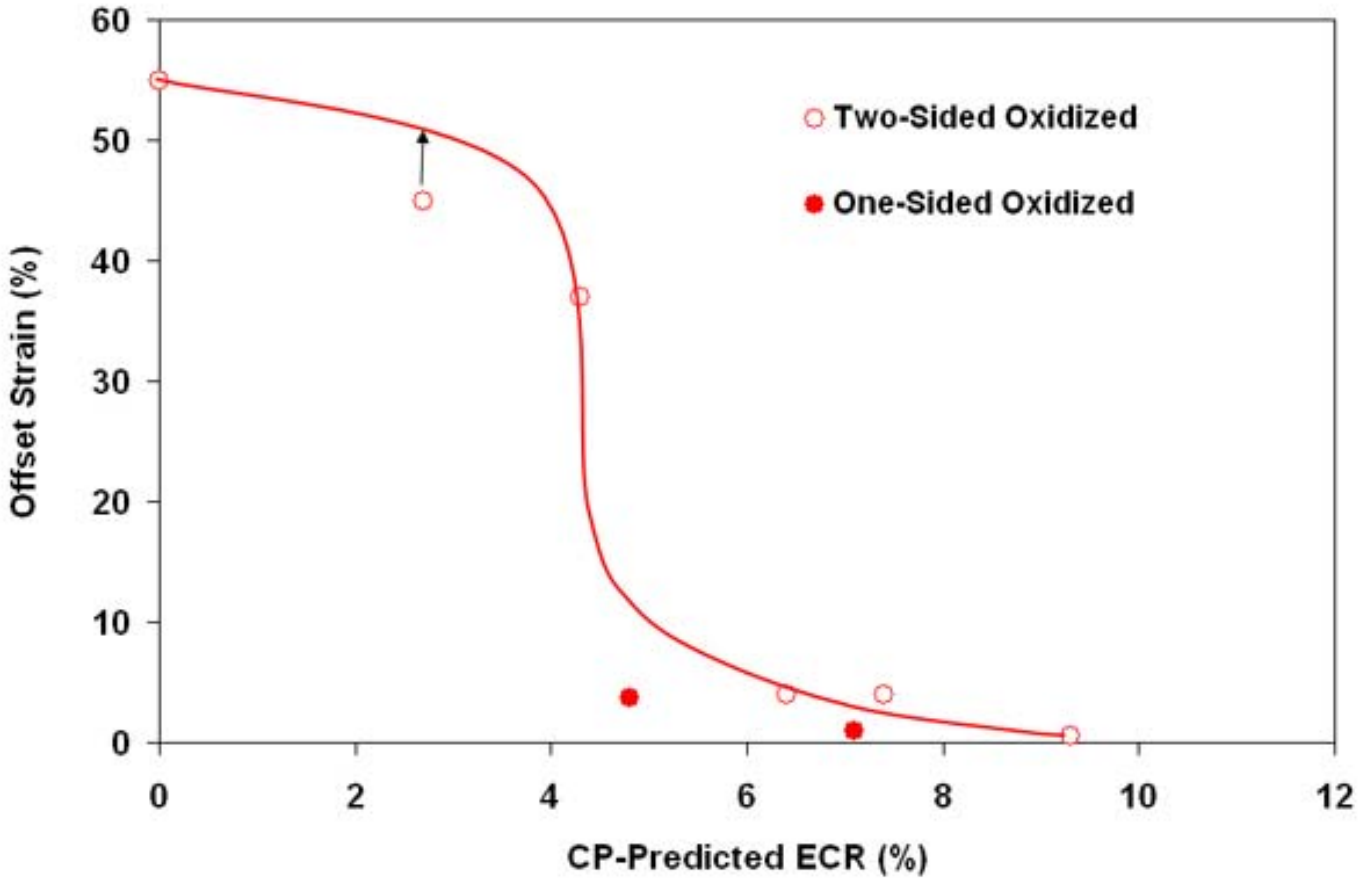

Figure 147. Offset strain data at 135ºC for high-burnup HBR Zry-4 samples with ≈550-wppm hydrogen oxidized to a maximum temperature of 1200ºC and slow cooled. Data are from two-sided and one-sided oxidation tests. Trend curve is based on two-sided-oxidation test results.

with diffusion of oxygen into the beta layer. The samples were brittle enough at the inner surface to initiate and propagate cracks through the wall of the cladding. Of the three factors considered, the fuel-cladding bond oxygen source, which is not accounted for in the one-sided CP-ECR calculation, is considered to be the dominant factor in reducing the ductility of the one-sided-oxidized high-burnup Zry-4 samples. Additional embrittlement related to the presence of fuel bonded to the cladding is discussed in Section 6.

The ductile-to-brittle transition CP-ECR for as-fabricated HBR-type Zry-4 oxidized at 1200ºC is 14% following quench at 800ºC. Based on the behavior of modern 17×17 Zry-4, ZIRLO and M5, this transition CP-ECR is expected to be independent of quench temperature for as-fabricated cladding alloys. For high-burnup HBR-type Zry-4 oxidized under the same conditions (two-sided) at 1200ºC and slow-cooled, this transition CP-ECR is reduced to ≈8%. Based on limited results for high-burnup Zry-4 cladding and extensive results for prehydrided Zry-4 cladding (see Section 4), it appears that this transition CP-ECR would be ≈6% following quench at 600-800ºC. This is a reduction of ≈8% CP-ECR due to high-burnup effects (i.e., hydrogen). The corrosion level ECR is ≈5.5% for the high-burnup samples with 550-wppm hydrogen. If the pre-transient corrosion level were used to compensate for the high-burnup effects, it would have to be multiplied by ≈1.5 to compensate for the difference between 14% CP-ECR (as-fabricated) and ≈6% CP-ECR (high-burnup) ductile-to-brittle transition values. Hydrogen contents higher than ≈600 wppm would cause a lower transition CP-ECR for Zry-4 following oxidation at 1200ºC and quench at 600-800ºC. The high-burnup sample with 740-wppm hydrogen and 7%-ECR corrosion level was brittle following oxidation to 7.5% CP-ECR and quench. Quench temperatures below 600ºC may increase the transition CP-ECR and hydrogen content if the cooling time is long enough at <600ºC. With regard to cooling time, it should be emphasized that the cooling rate increases with time between the maximum LOCA temperature and the wetting temperature, while for the ANL and CEA experiments, the cooling rate decreases exponentially with time during this interval. The experimental results for slow-cooling without quench or cooling to <600ºC with quench at <600ºC may result in ductility enhancement that would not occur during a LOCA.

For one-sided steam oxidation, which is relevant to cladding outside the balloon region, it was found that the fuel-cladding-bond oxide provides an additional source of oxygen for embrittlement beyond what would be calculated for single-sided steam oxidation. The ductile-to-brittle transition CP-ECR decreased from ≈8% to ≈6% for slow-cooled high-burnup Zry-4 samples exposed to outer-surface steam flow. The results suggest that calculated CP-ECR values based on one-sided oxidation alone should use a lower ductile-to-brittle transition value or the calculational method should be revised to account for additional oxygen sources (e.g., fuel-cladding bond and fuel) inside the cladding.

5.2 Results for high-burnup 17×17 ZIRLO Cladding

{Results to be inserted here}

5.3 Results for high-burnup 17×17 M5 Cladding

{Results to be inserted here}

6 LOCA Integral Test Results

During the development and benchmarking of the LOCA integral test apparatus, numerous tests were conducted with as-fabricated 8×8 and 9×9 Zry-2 filled with zirconia pellets to simulate the heat capacity of the fuel. Four tests have been conducted with high-burnup fuel rod samples from Limerick fuel rods: ICL#1 test was conducted in argon up through ballooning and burst to provide data on ballooning strain and minimum wall thickness; ICL#2 was conducted in steam with a 300-s hold time at 1204ºC, cooling at 3ºC/s to 800ºC and slower-cooling to RT; ICL#3 was conducted under the same conditions as ICL#2 through cooling to 800ºC, followed by quench and rapid cooling from 800ºC to 460ºC; and ICL#4 was conducted through the complete LOCA sequence with quench and rapid cooling from 800ºC to 100ºC. The LOCA test apparatus is shown in Figures 6 (photograph) and 7 (schematic). The LOCA integral test sample, test train and quartz tube chamber are shown in Figure 15. The LOCA test apparatus, pre-test sample characterization, post-test nondestructive examination results, and post-test destructive examination results are described in detail by Yan et al. [15, 22, 32, 33]. In this section, test results related to post-oxidation and post-quench ductility are emphasized. Some background information is also provided for the convenience of the reader.

6.1 As-fabricated 9×9 Zry-2 oxidized at 1204ºC

6.1.1 Ballooning and burst

In additional to the numerous tests conducted during the developmental phase of the LOCA integral test apparatus, particular tests were conducted to provide baseline data for the in-cell tests. These out-of-cell (OC) tests with as-fabricated 9×9 Limerick (L)-type cladding parallel the thermal history of the in-cell (IC) tests with high-burnup 9×9 Limerick (L) cladding. The reference temperature histories for test with slow-cooling from 800ºC and rapid cooling (i.e., quench) from 800ºC are shown schematically in Figure 16. Figure 148 shows the reference internal-pressure and temperature histories for tests with quench at 800ºC. The reference hold time at 1204ºC is 300 s. Tests with as-fabricated Zry-2 were also conducted for hold times of 1 s and 120 s and ramp-to-burst tests were conducted in argon.

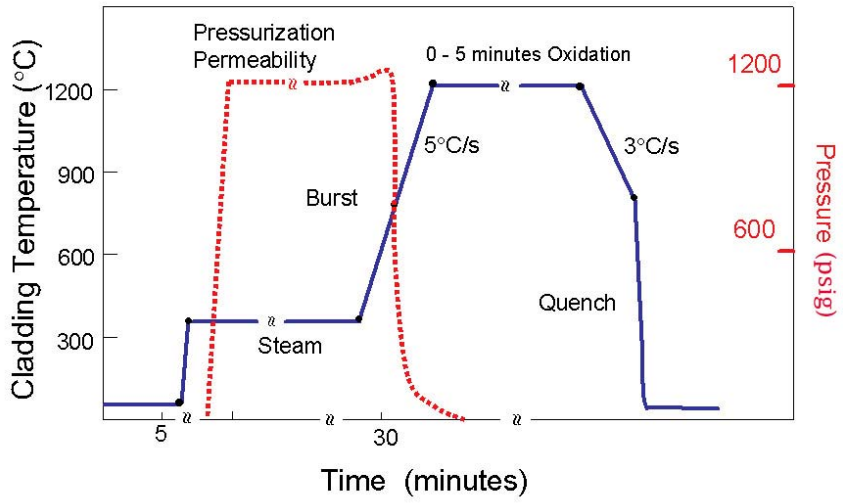

Figure 148. Temperature and pressure histories for full LOCA integral test sequence, including quench from 800˚C to 100˚C.

Table 62 summarizes the out-of-cell tests conducted to parallel the in-cell tests, as well the shorter hold-time tests used to characterize the increase in hydrogen content due to secondary hydriding from inner-surface oxidation. For ballooning and burst characterization, samples from tests such as OCL#8 are the best to use because to capture images of the overall sample geometry, the ballooning diameter and axial extent, the burst length and opening, and the cross section at the midplane burst region where the reference thickness is determined for the ECR calculations. Time at temperature, oxidation, and quench all result in changes in the geometrical details at the time of burst. Figure 149 shows: (a) side view of the overall sample geometry; (b) enlarged side view of the ballooned-and-burst region; and (c) enlarged frontal view of the ballooned-and-burst region. Figure 149a shows the bending of the sample that occurred just prior to ballooning during anisotropic creep and plastic deformation of the alpha-phase cladding under internal pressure. Based on real-time videos, the ballooning follows very shortly after bending, and burst follows very shortly after ballooning begins. For all samples tested in the ANL LOCA integral apparatus, the maximum ballooning strain and burst occurred on the concave side of the bending curve. The local bending in the ballooned-and-burst region is imaged in Figure 149b. Figures such as 149c are used to determine the shape (dog bone), the axial length, and maximum opening of the burst.

Following imaging of the sample, outer-diameter measurements were performed for the reference 0º orientation (burst side to 180º from the burst side) and from a diameter orientation 90º from the reference orientation. These measurements were made using a micrometer at 20-30 axial locations to determine the maximum ballooning diameter and the axial profile for the two orientations. The differences (Δd) between the measured diameters and the as-fabricated diameter (D_o= 11.18 mm, 0.440 inches) were used to determine the ballooning strain ($\Delta d/D_o$). Figure 150 shows the $\Delta d/D_o$ axial profiles for the OCL#8 test sample at the 0º and 90º orientations. The minimum wall thickness (h_{min}) for ECR calculations (averaged over the burst cross section) can de estimated form these data by averaging the strains at the two orientations ([70% + 50%]/2 at the burst midplane), selecting the maximum value (Max $\{(\Delta d/D_o)_{avg}\} = \Delta D/D_o = 60\%$) and using the constant-volume plasticity relationship:

$$h_{min} = h_o/(1 + \Delta D/D_o), \quad (7)$$

where h_o is the as-fabricated wall thickness (0.71 mm) and the plastic strain in the axial direction is assumed to be zero at the burst midplane. These assumptions were tested by sectioning the OCL#8 sample at the burst midplane and obtaining high magnification images from which the circumferential strain ($\Delta C/C_o$) could be measured directly, as well as the wall thickness. As shown in Figure 151, the wall thickness is maximum at ≈180º from the burst opening and minimum at the edges of the burst opening. The area-averaged wall thickness determined from Figure 151 was 0.434 mm, the circumferential strain around the cladding mid-wall was 60%, and the wall thickness determined form Equation 7 was 0.444 mm. The difference between the precise measurement and the Equation-7 calculation is only 2%. Thus, Equation 7 is a practical algorithm for calculating the minimum wall thickness to be used in ECR calculations corresponding to the minimum wall thickness. The methodology has also been validated for oxidized ballooned-and-burst cladding. Figure 151 has also been used to gain a better appreciation for circumferential variation in cladding thickness, for the local effects of two-sided oxidation and for interpretation of the effects of quench on burst opening. The thin cladding at the edges of the burst region experiences a high level of oxidation during a LOCA-type transient as compared to the thicker cladding 180º from the burst region. Locally, this cladding will be highly brittle and the edges will most likely fragment during quench resulting in a larger post-test burst width. Such behavior has no consequence relative to the current LOCA criteria, which apply to average rather than local behavior of the burst cross section. However, the Figure 151 results are useful in order to rationalize observed changes to the burst region due to oxidation and quench.

Table 62 Summary of LOCA Integral Test Results for Out-of-cell Tests with Near-archival As-fabricated (Unirradiated) 9×9 Zry-2 Samples Filled with Zirconia Pellets; outer diameter and wall thickness of as-fabricated cladding are 11.18 mm and 0.71 mm, respectively

Parameter	OCL#5	OCL#8	OCL#22	OCL#17	OCL#11	OCL#13
Environment	Argon	Argon	Steam	Steam	Steam	Steam
Hold Temperature, °C	---	---	1204	1204	1204	1204
Hold Time, s	---	---	1	120	300	300
Quench (Q) at 800ºC or Slow Cooling (SC)	SC	SC	Q-800ºC	Q-800ºC	SC	Q-800ºC
$(P_g)_{max}$, MPa	8.96	8.62	8.87	9.10	8.61	9.09
T at $(P_g)_{max}$, °C	660	687	690	6.83	680	676
Burst Pressure (P_B), MPa	8.26	7.67	6.90	9.07	7.93	6.43
Burst Temperature (T_B), °C	733±5	766±17	747±37	750	753±22	766±25
Burst Center Relative to Specimen Midplane mm	+20	-10	+25	-13	+35	28
Burst Shape	Dog Bone	Dog Bone	Dog Bone	Dog Bone	Dog Bone	Dog Bone
Burst Length, mm	13	17	17	10	11	10
Max. Burst Width, mm	2.5	2.5	1	0.8	1	1
Length of Balloon, mm	100	140	140	145	140	150
$(\Delta D/D_o)_{max}$[a], %	44±10	60±10	54	49±11	43±10	43±8
$(\Delta C/C_m)_{max}$[b], %	---	60	---	---	---	---
Reference Minimum Wall Thickness for ECR mm	≈0.50	0.434	0.46	0.48	0.50	0.50
Maximum CP-ECR, %	0	0	9	15	21	21

[a]From profilometry at 0° and 90° relative to burst orientation

[b]Midwall circumferential strain determined from low-magnification photomicrographs

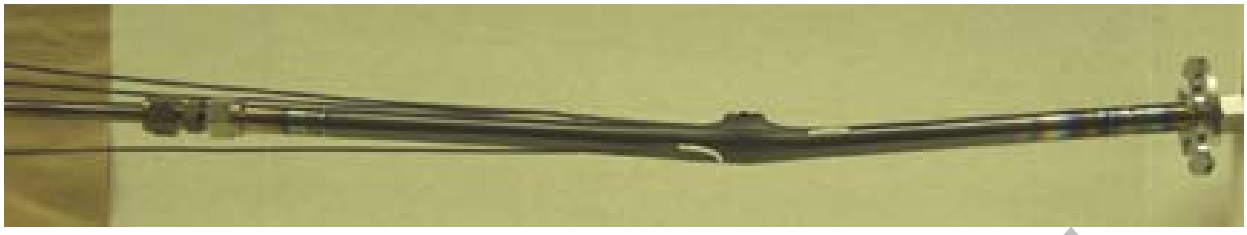

(a)

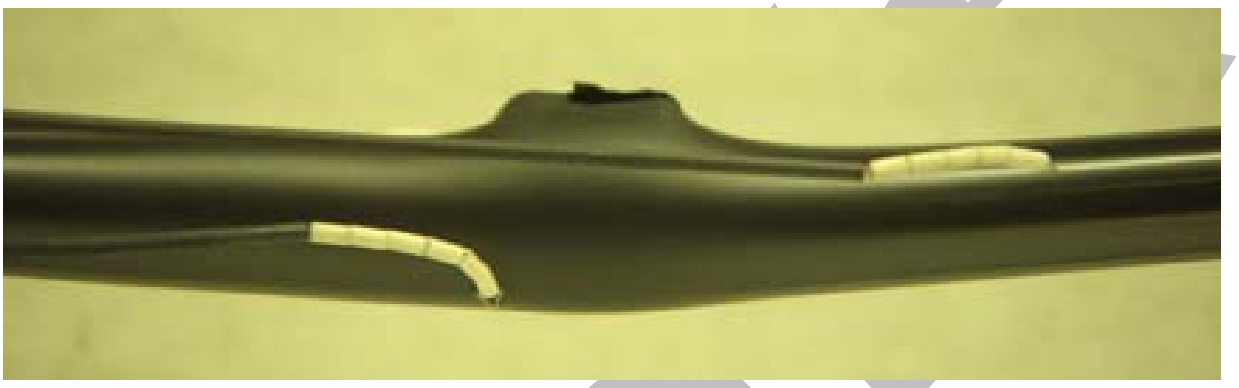

(b)

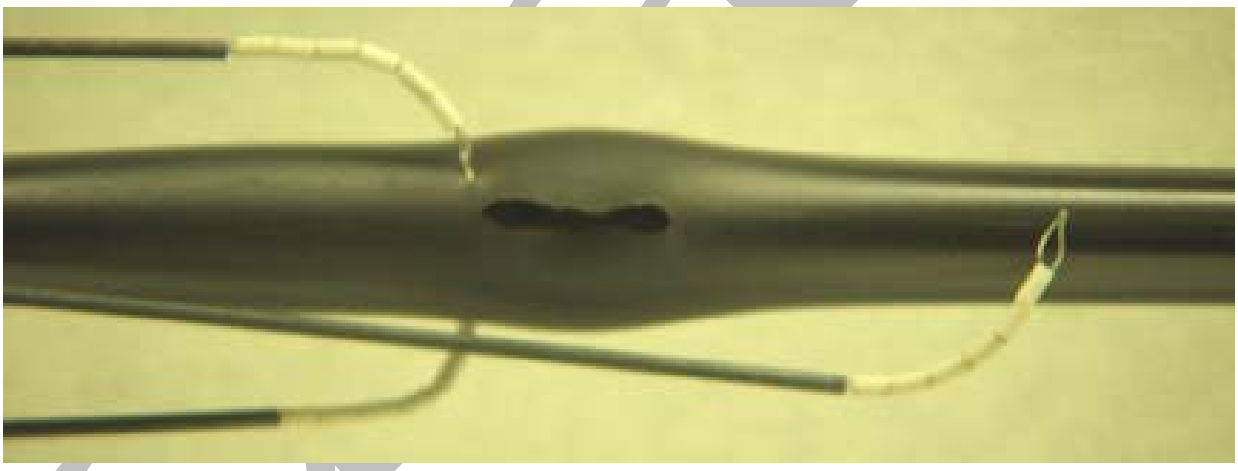

(c)

Figure 149. Images of the OCL#8 test sample after heating in argon to burst at ≈770ºC (due to a maximum internal pressure of 8.62 MPa [gauge] and an estimated pressure of ≈7.7 MPa just prior to burst) and slow cooling: (a) low magnification of side view of sample; (b) higher magnification of side view of ballooned-and-burst region; and (c) higher magnification of frontal view of burst opening. Top of the sample, from which the thermocouples were inserted prior to welding, is to the left in these photographs.

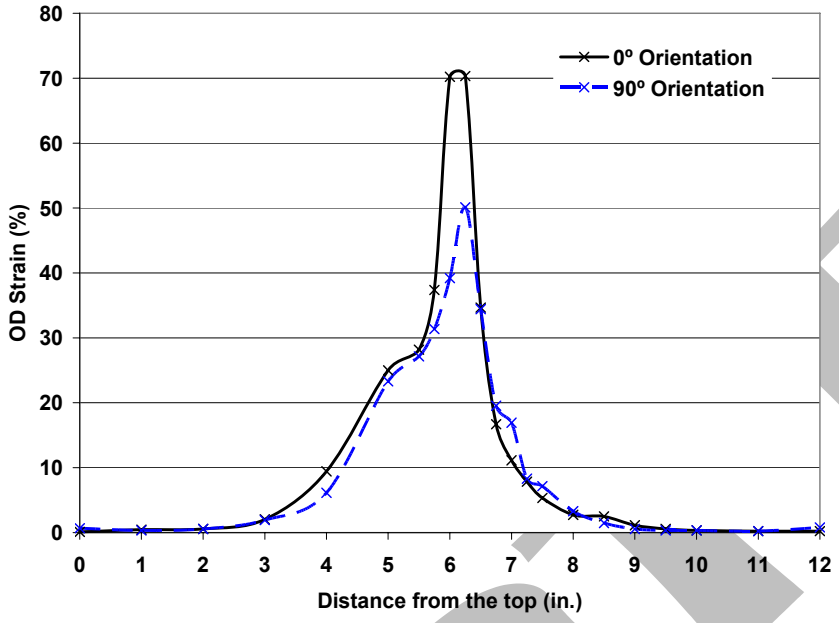

Figure 150. Axial profile of the diametral ballooning strain at two orientations relative to the burst opening (0º) and 90º from the burst opening for test sample OCL#8 heated under internal pressure in argon up to burst at ≈770ºC and slow cooled to RT.

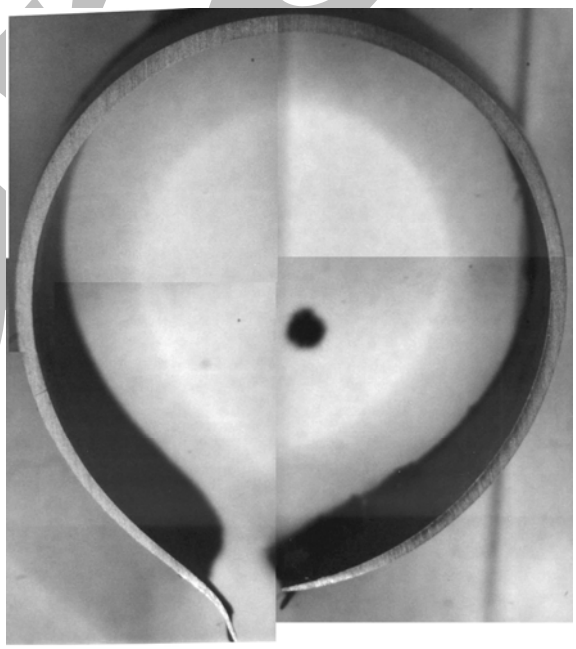

Figure 151. Cladding cross section at burst midplane for OCL#8 sample (see Figure 150).

The axial distribution of cladding strain shown in Figure 150 is typical of samples that developed a single balloon (e.g., OCL#5 and OCL#11). Ballooning and burst are instability phenomena. Differences were observed in maximum ballooning strain (≈40% to 60%), axial extent of ballooning (100-150 mm), burst location relative to the sample midplane (-13 mm to +35 mm), burst length (11-17 mm) and maximum burst opening (0.8-2.5 mm). These test-to-test result differences are to be expected for instabilities of this nature. However, later tests (e.g., OCL#13, OCL#17, and OCL#22) exhibited a secondary balloon region in addition to the larger primary balloon region containing the burst opening. Diametral strain profiles for OCL#5 and OCL#6 are shown in Section 6.2 in comparison plots with results from corresponding high-burnup test-sample results (ICL#1 and ICL#2). Diametral profiles for the three test samples with secondary balloon regions are shown in Figures 152-154. The secondary balloons have a maximum diametral strain of 15-30%. However, the presence of these secondary balloons appears to have very little influence on the axial extent of ballooning. The criterion for determining this axial extent is ≥2% strain, along with some judgment based on the intersection of the steeply decreasing part of the profile and the flat portion of the profile.

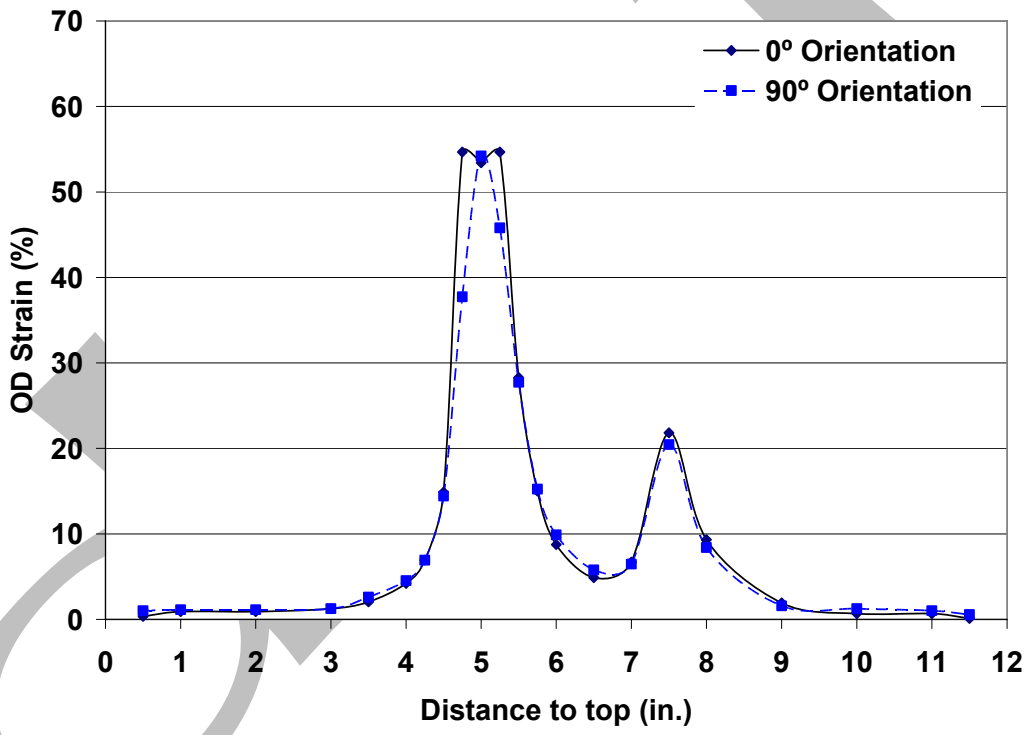

Figure 152. Ballooning strain profile for OCL#22 test sample held for 1 s at 1204ºC, cooled to 800ºC and quenched.

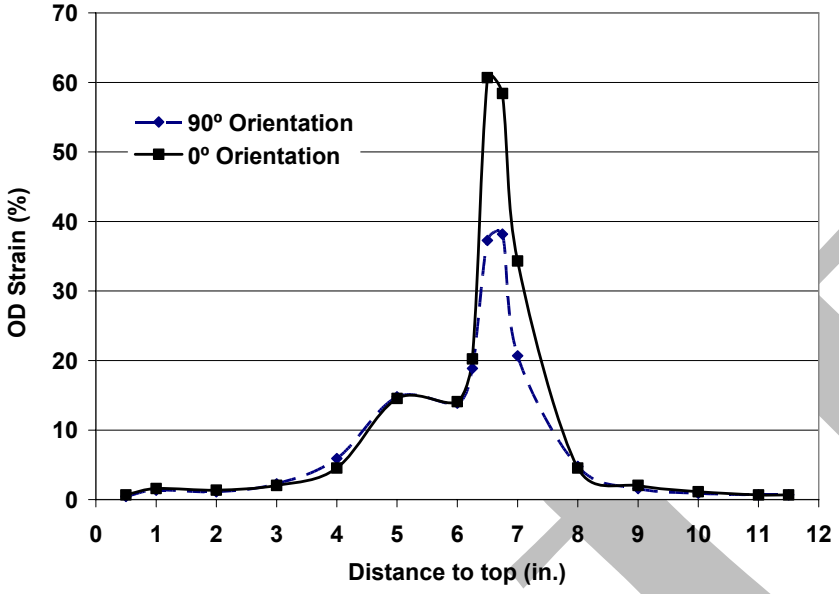

Figure 153. Ballooning strain profile for OCL#17 test sample held for 120 s at 1204ºC, cooled to 800ºC and quenched.

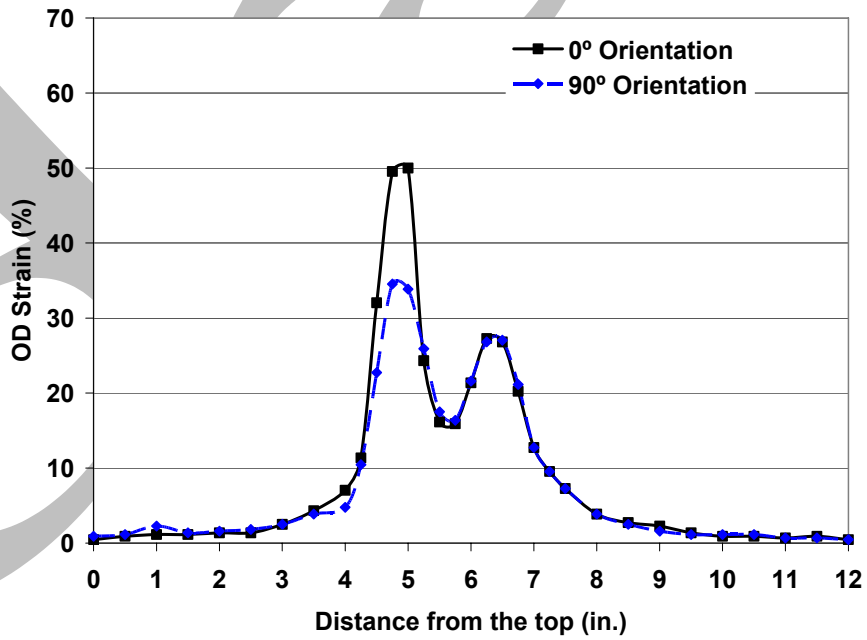

Figure 154. Ballooning strain profile for OCL#13 test sample held for 300 s at 1204ºC, cooled to 800ºC and quenched.

6.1.2 Oxidation and hydrogen pickup due to secondary hydriding

Due to steam leakage through the burst opening, oxidation within the balloon region is expected to be two-sided. Such oxidation results in hydrogen release to the near-stagnant steam within the test sample. Unlike the outer surface exposed to flowing steam, a large fraction of the released hydrogen is trapped inside the sample and available for pickup by the inner-metal surface in and near the balloon region. Data from quantitative metallography and LECO oxygen-content measurements have been used to determine oxygen pickup (ΔC_O in wt.%) and corresponding ECR (in %). In order to determine oxygen pickup from the LECO data, two sets of corrections must be made to the raw data. The first set of corrections involves renormalizing the LECO oxygen content in wt.% to the weight of the metal prior to oxidation and subtracting the oxygen content in the as-fabricated cladding (C_{Oi} = 0.11 wt.% for 9×9 Zry-2). The second correction accounts for loss of brittle oxide during LECO sample preparation. Some oxide is lost during sectioning of 2-mm-long rings. More is lost during the "snipping" of four arc lengths from the ring. This sample subdivision is needed to prevent exceeding the oxygen-level limit of the LECO detector. In previous work, oxygen pickup has been determined by three means: sample weight gain, quantitative metallography, and refined LECO oxygen content-data. The oxygen content determined from the raw LECO data exhibited lower oxygen pickup than determined by means of sample weight gain and metallography. By multiplying the raw LECO data by a factor of 1.1, good agreement was obtained by all three techniques. The 1.1 factor is used to determine measured ECR. However, the correction factor is not needed to determine hydrogen pickup (ΔC_H). The equations used to convert the raw LECO oxygen (L_O in wt.%) and hydrogen (L_H in wppm) data to ECR and hydrogen pickup are:

$$\Delta C_O = (L_O - C_{Oi})/(1 - L_O/100\%), \text{ wt.\%} \quad (8)$$

$$ECR = 2.85\ (1.1 \times L_O - C_{Oi})/(1 - 1.1 \times L_O/100\%), \% \quad (9)$$

$$\Delta C_H = (1 + \Delta C_O/100\%)\ L_H - C_{Hi}, \text{ wppm} \quad (10)$$

where C_{Hi}, is the hydrogen content (5 wppm) of as-fabricated 9×9 Zry-2.

The LECO data for OCL#22 (1-s hold time at 1204ºC) and OCL#17 (120-s hold time at 1204ºC) – both taken after bend-to-failure tests – are shown in Figures 155 and 156, respectively. For the OCL#22 test sample, the maximum oxygen and hydrogen measurements were 3.95 wt.% and 2105 wppm, respectively. At the axial location where the maximum hydrogen reading was found the LECO oxygen-content measurement was 2.33 wt.%. Using Equations 8-10, the maximum ECR is calculated to be 11% and the maximum hydrogen pickup is calculated to be 2150 wppm. The 11% ECR value is higher than the 9% CP-predicted value in Table 62. If the 1.1 factor is not used for such a low-oxidation level sample (i.e., oxide loss during cutting and snipping is smaller than assumed), the measured ECR is reduced to 10%. The maximum hydrogen content measured by LECO was 2700 wppm where the oxygen pickup was 2.36 wt.%. The hydrogen pickup calculated by Equation 10 is 2760 wppm. The magnitude of the

hydrogen pickup is quite large for such a short hold-time at 1204ºC. The results suggest that significant hydrogen pickup occurs early in the LOCA transient. Enough hydrogen is released to the cladding interior due to inner-surface oxidation during the ramp to result in high hydrogen pickup.

The OCL#17 LECO data shown in Figure 156 were taken from half of the sample. The maximum measured oxygen and hydrogen contents were 4.24 wt.% and 2936 wppm, respectively. The ECR determined from Equation 9 is 14%, which agrees with the CP-predicted value. Using 2.39 wt.% oxygen measured by LECO at the peak hydrogen location, gives a hydrogen pickup of 3000 wppm. In terms of peak hydrogen pickup, relatively little is picked up during the 119-s additional hold time at 1204ºC.

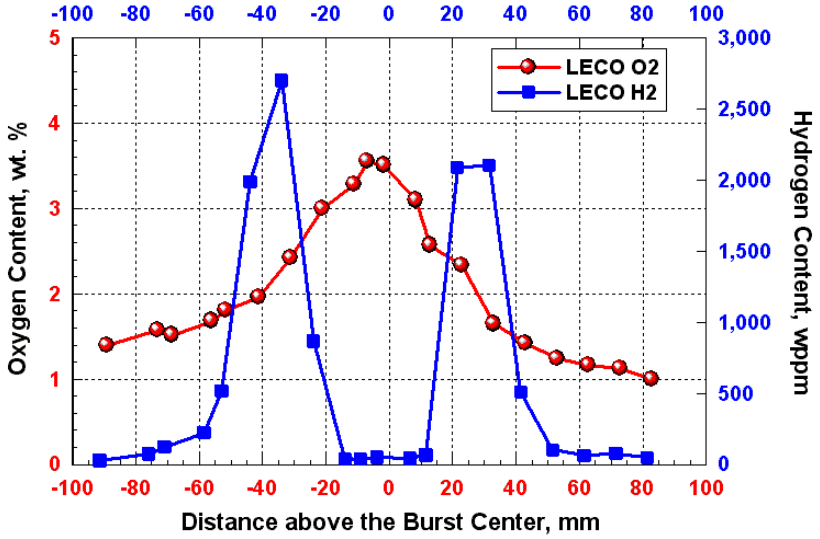

Figure 155. LECO oxygen and hydrogen content data for OCL#22 sample ramped in steam from 300ºC to 1204ºC at 5ºC/s, held at 1204ºC for 1 s, cooled at 3ºC/s to 800ºC and quenched.

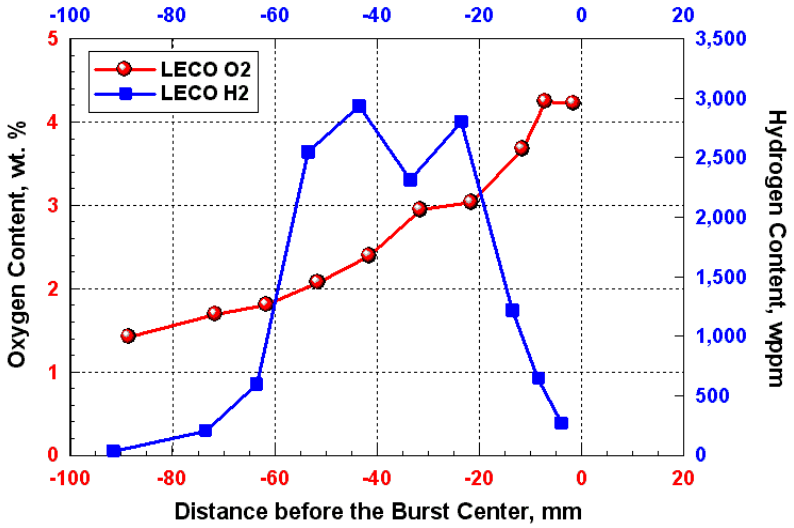

Figure 156. LECO oxygen and hydrogen content data for OCL#17 sample ramped in steam from 300ºC to 1204ºC at 5ºC/s, held at 1204ºC for 120 s, cooled at 3ºC/s to 800ºC and quenched.

LECO data were also obtained for the OCL#11 sample (300-s hold time at 1204ºC). Oxygen pickup from quantitative metallography was also determined. Figure 157 shows: (a) the LECO data; and (b) the converted data for ECR and hydrogen pickup. The quantitative metallography and LECO results are in excellent agreement. The maximum ECR determined from data is 18.5%, as compared to 21% CP-predicted ECR in Table 62. The maximum hydrogen pickup was 3900 wppm. Thus, >70% of the maximum hydrogen pickup occurs during the ramp to 1204ºC.

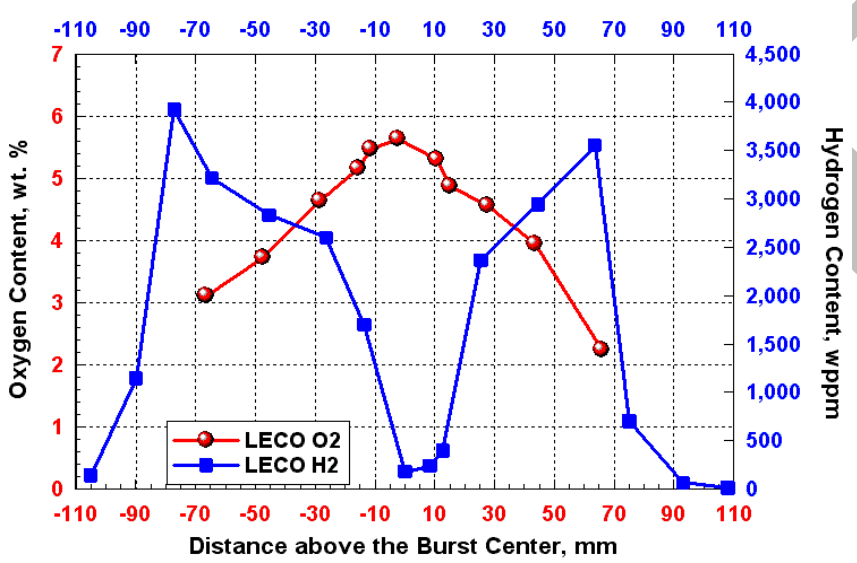

(a)

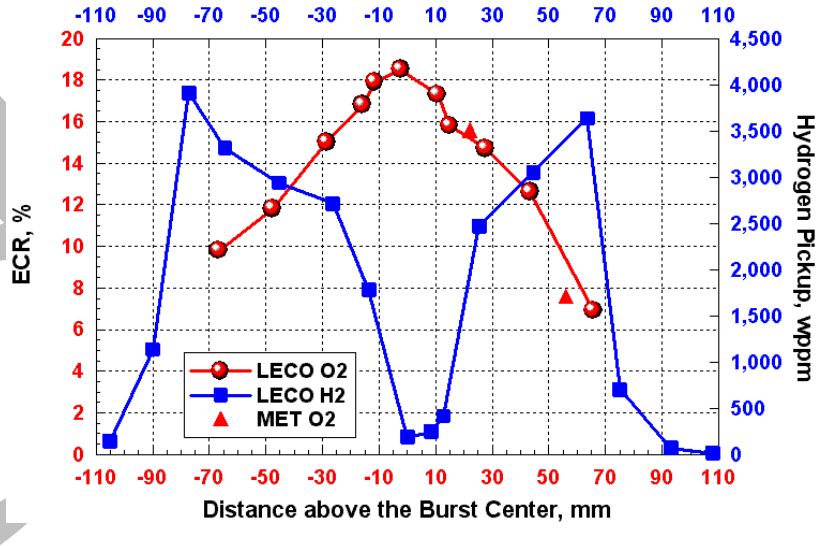

(b)

Figure 157. Data for OCL#11 sample ramped in steam from 300ºC to 1204ºC at 5ºC/s, held at 1204ºC for 300 s, cooled at 3ºC/s to 800ºC and slow cooled from 800ºC to RT: (a) LECO oxygen- and hydrogen-content data; and (b) ECR derived from LECO and metallography data and hydrogen pickup derived from LECO data.

Extensive metallographic characterization was performed for the OCL#11 test sample. The results for the burst midplane are presented in Figure 158 because they lead to insights regarding the post-test strength and ductility corresponding to the maximum ECR. For the LOCA integral test samples, the four-point bend test is used to determine ductility. The four-point-bend fixture (see Section 6.1.3) has a 150-mm span between loading points. Within this span a uniform bending moment is applied to the sample. The span covers the ballooned region, along with some of the region outside the balloon. Figure 158 shows "local" ECR values determined from quantitative metallography. Although for licensing purposes, the maximum ECR in the balloon region is defined in terms of the minimum cross-section-averaged wall thickness, there is considerable variation in percent oxidation and embrittlement around this cross-section. The burst tips are highly oxidized and brittle. The oxidation level decreases from >36% ECR at 0º (relative to the burst opening), where the wall is thinnest, to 13% ECR at 180º where the wall is thickest. In comparing Figure 158 to Figure 151, it is clear that the thin and highly oxidized cladding at the edges around the burst opening was probably lost during handling, cutting and metallographic mount preparation. Based on Figure 158, if the four-point-test is conducted in the traditional way with the flawed region (burst region) under axial tension during the start of the bending test, then the crack will proceed rapidly through that region. Whether or not the sample has any bending ductility will depend on the whether or not the cladding near the back of the burst region (within 150º to 210º relative to the burst) will have sufficient ductility to blunt the crack propagating across the cladding section.

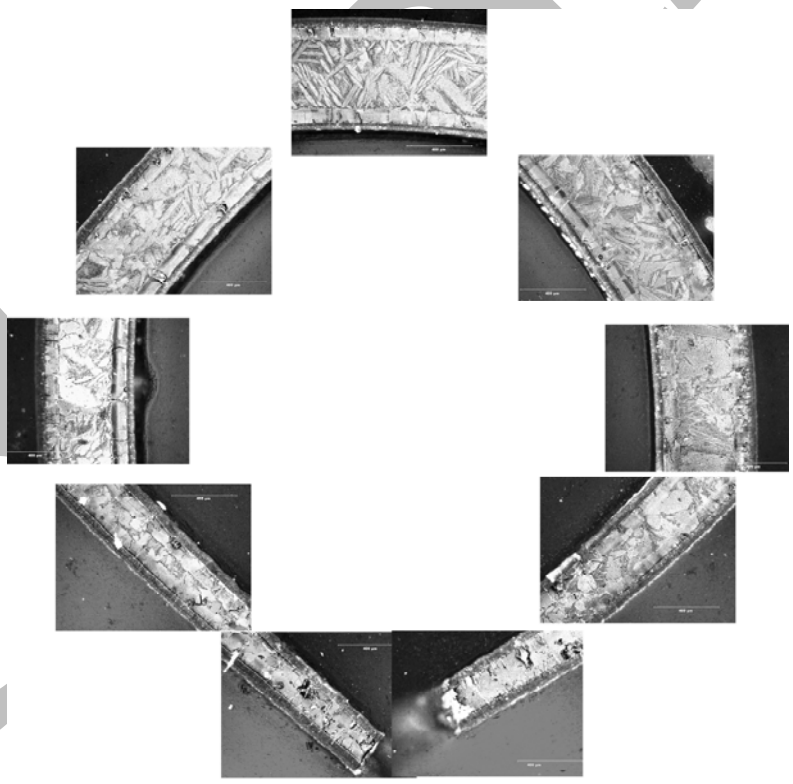

Figure 158. Metallographic images at 9 locations around the cross section of the midplane of the burst region of the OCL#11 test sample (300 s at 1204ºC). The cross-section-averaged ECR is 18.5%. Locally, the oxidation level varies from >36% to 13%.

6.1.3 Post-quench ductility for unirradiated LOCA integral samples

The Instron used to conduct the ring compression tests was also used to conduct four-point bend tests. A special loading platen and fixture was designed to apply a uniform bending moment over 150 mm of the sample with the burst-region midplane located approximately at the center of the 150 mm. The test apparatus was benchmarked by comparing elastic bending results for as-fabricated HBR-type 15×15 cladding to the text book solution for bending stiffness (force divided by displacement). The bending tests were conducted in the displacement-controlled mode. Measured displacement corresponds to the displacement at the loading points, ±75 mm from the center of the as-fabricated cladding or ±75 mm from the burst midplane location.

Several four-point-bend demonstrations were conducted with post-test samples with the same temperature history as the OCL#13 test sample listed in Table 62. These samples were weak enough to be bent and broken by hand. With the burst area under bending tension, clean breaks occurred at the burst midplane under the uniform bending moment. With the burst area under compression, an axial crack formed at the burst tip, propagated into the high oxygen-hydrogen region between the burst midplane and the balloon neck and caused cross-section failure due to bending in this region. Thus, while the burst region is structurally very weak, the thicker cladding region away from the burst is stronger in the unflawed condition, but is brittle enough to fail first in the flawed condition. This illustrates the difficulties that arise from relying on the strength of brittle material. The strength, or resistance to load, decreases dramatically if a flaw is present.

The bending demonstrations were useful in planning purposes. However, the four-point-bend tests were needed for quantitative data. Test samples OCL#22 (1-s hold time at 1204ºC) and OCL#17 (120-s hold time at 1204ºC) were subjected to four-point-bending. Figure 159 shows the pre- and post-test sample, along with the Instron load-displacement curve. Most of the burst midplane cross section fails in a brittle mode, as indicated by the sharp load drop of >70% at a bending moment of 21 N·m. However, the region 180º from the burst opening is highly ductile. Within the deflection limits of the apparatus, this back ligament does not fail.

Figure 160 shows the four-point-bend results for the OCL#17 sample, which was oxidized to a higher level than the OCL#22 sample. This higher oxidation level results in a lower maximum bending moment (12 vs. 21 N·m) and brittle failure across the whole cross section. As predicted, by orienting the sample such that the burst region is in bending tension, failure occurs near the burst midplane cross-section. Because of the bending orientation, the high-hydrogen cross section with the thicker wall and the lower level of oxidation did not fail even though it was probably more brittle than the weaker burst cross section,

Although additional tests were not conducted at higher oxidation levels (i.e., hold times at 1204ºC), the trend is clear: as the oxidation level increases, the bending resistance of the burst region decreases (i.e., failure bending moment decreases) and the rest of the balloon region outside the burst area continues to embrittle as the oxygen and hydrogen content of this region increases.

From an embrittlement point of view, the hydrogen pickup due to oxidation inside the cladding increases so fast that it would be difficult to find an ECR low enough to guarantee ductility in the balloon region, even if ring-compression tests were performed at 135ºC on rings cut away from the burst region. However, the strength or fracture toughness of the balloon region decreases as the oxidation level increases. The results suggest that some ECR limit would be needed in the balloon region to prevent

(a)

(b)

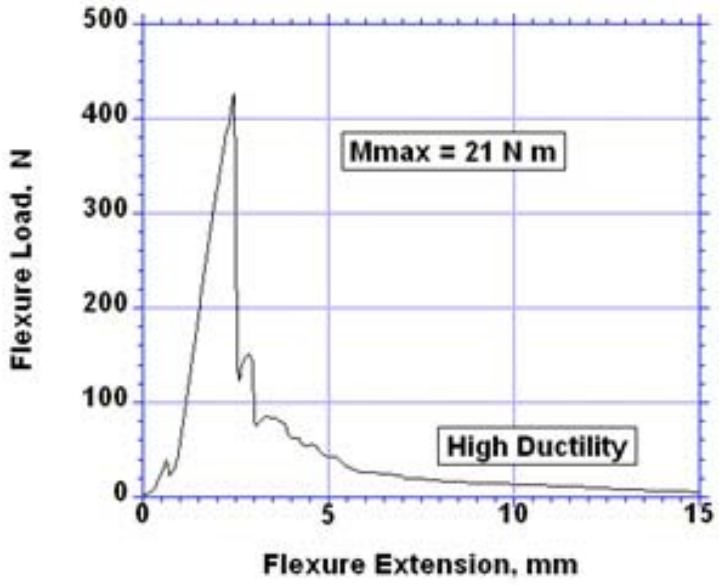

(c)

Figure 159. Bending test results for LOCA integral test sample OCL#22: (a) pretest appearance with burst area on bottom; (b) post-test appearance with burst area on bottom; and (c) bending load vs. displacement (flexure extension) at the loading points.

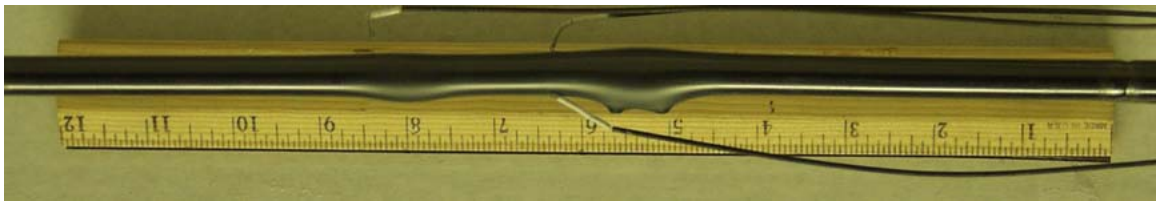

(a)

(b)

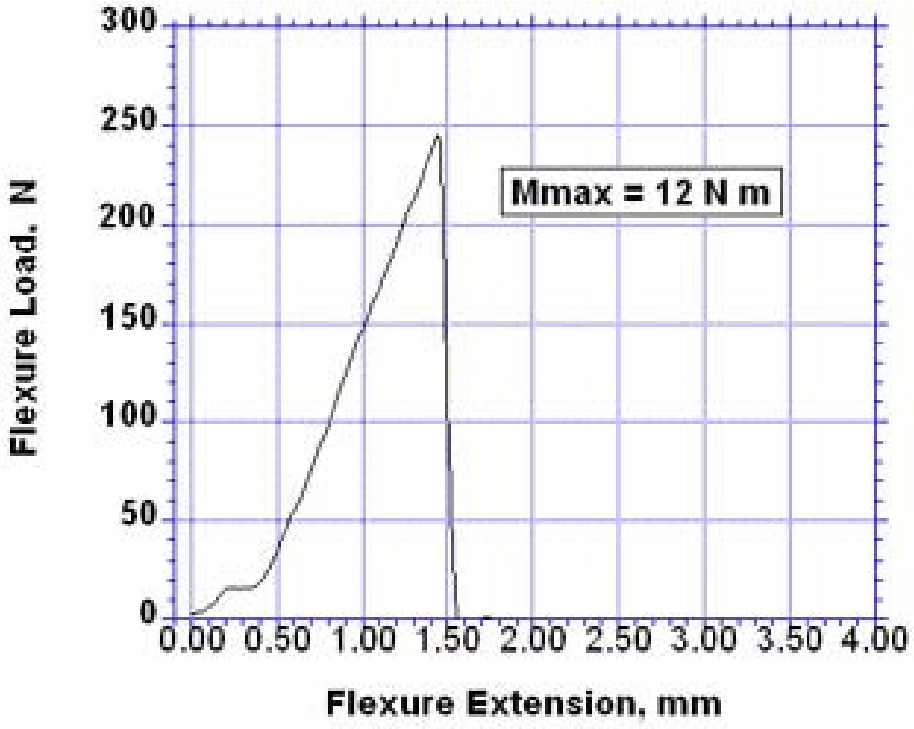

(c)

Figure 160. Bending test results for LOCA integral test sample OCL#17: (a) pretest appearance with burst area on bottom; (b) post-test appearance with burst area on bottom; and (c) bending load vs. displacement (flexure extension) at the loading points.

across-wall failures from occurring due to thermal stresses during quench, side loads due to rod-to-rod impact, and dead-weight loading of the cladding. Based on these studies, that limit would be >14% CP-ECR and <26% CP-ECR. The current 17% limit should be sufficient to guarantee the minimal toughness.

6.2 High-burnup Limerick BWR 9×9 Zircaloy-2 oxidized at 1204ºC

Based on characterization of as-irradiated, high-burnup Limerick cladding (rod F9) at the fuel midplane and at 0.7-m above the midplane, the corrosion layer thickness (≈10 μm), the hydrogen content (≈70 wppm), and the fuel morphology were observed to be relatively constant for these axial locations. These values were assumed for the as-irradiated Limerick sections used for LOCA integral tests. Figures 161-162 show the locations of the ICL#1-2 samples from rod F9 and the ICL#3-4 samples from rod J4. The burnup of these rods was 56-57 GWd/MTU. Additional fuel characterization was performed within the region labeled "Practice Samples" in Figure 161. These samples were used to test the fuel removal device and to verify that removal of 13-25 mm of fuel from the ends of the LOCA sample by means of a hammer drill did not disturb the remaining fuel column.

In-cell LOCA integral tests were conducted with two thermal couples strapped to the outer surface of the cladding 50-mm above the sample centerline. One of these was used to control the furnace power to give a hold temperature of 1204ºC at that location. The other thermocouple, located 180º from the control thermocouple, was used to measure circumferential variation in cladding temperature. Based on benchmark tests (e.g., OCL#14) with unirradiated Zry-2, the difference in output between a strapped and a welded thermocouple (TC) at the same axial elevation is ≈10ºC. Some of this difference may be due to circumferential temperature variation as the two TCs did not have the same circumferential location. Within the expected axial and circumferential variations in high-burnup cladding temperature during and following ballooning and burst, the difference between strapped and welded TC readings is not considered significant.

6.2.1 Ballooning and burst of high-burnup samples

Table 63 summarizes the results of the four in-cell (IC) tests with high-burnup fueled Limerick cladding, along with companion out-of-cell tests OCL#5 and OCL#11. Both ICL#1 and OCL#5 were ramp-to-burst tests in argon. The burst temperatures, pressures and maximum diametral strains are remarkably close for these two tests. In terms of these parameters, high-burnup operation had little effect on cladding burst conditions and strains. Hydrogen pickup during normal reactor operation would be expected to affect both the burst conditions and the burst strain. However, high-burnup Limerick cladding had low-hydrogen content resulting from its thin corrosion layer.

The primary differences observed between the high-burnup cladding and the unirradiated cladding was in the pre-burst bending (less for high-burnup), the axial extent of the balloon region (less for high-burnup), and the shape of the burst region (oval for high burnup). Figure 163 shows a comparison of the ballooned-and-burst regions for the ramp-to-burst samples ICL#1 and OCL#5. Figure 164 shows the comparison in burst openings between the ICL#2 and OCL#11 test samples. The profiles of diametral strain for these companion tests are compared in Figure 165.

In Figure 166, the four in-cell test samples are shown. As expected, the partially quenched sample (ICL#3) and the fully quenched sample (ICL#4) have wider burst openings due to loss of thin, brittle cladding near the edges of the burst opening.

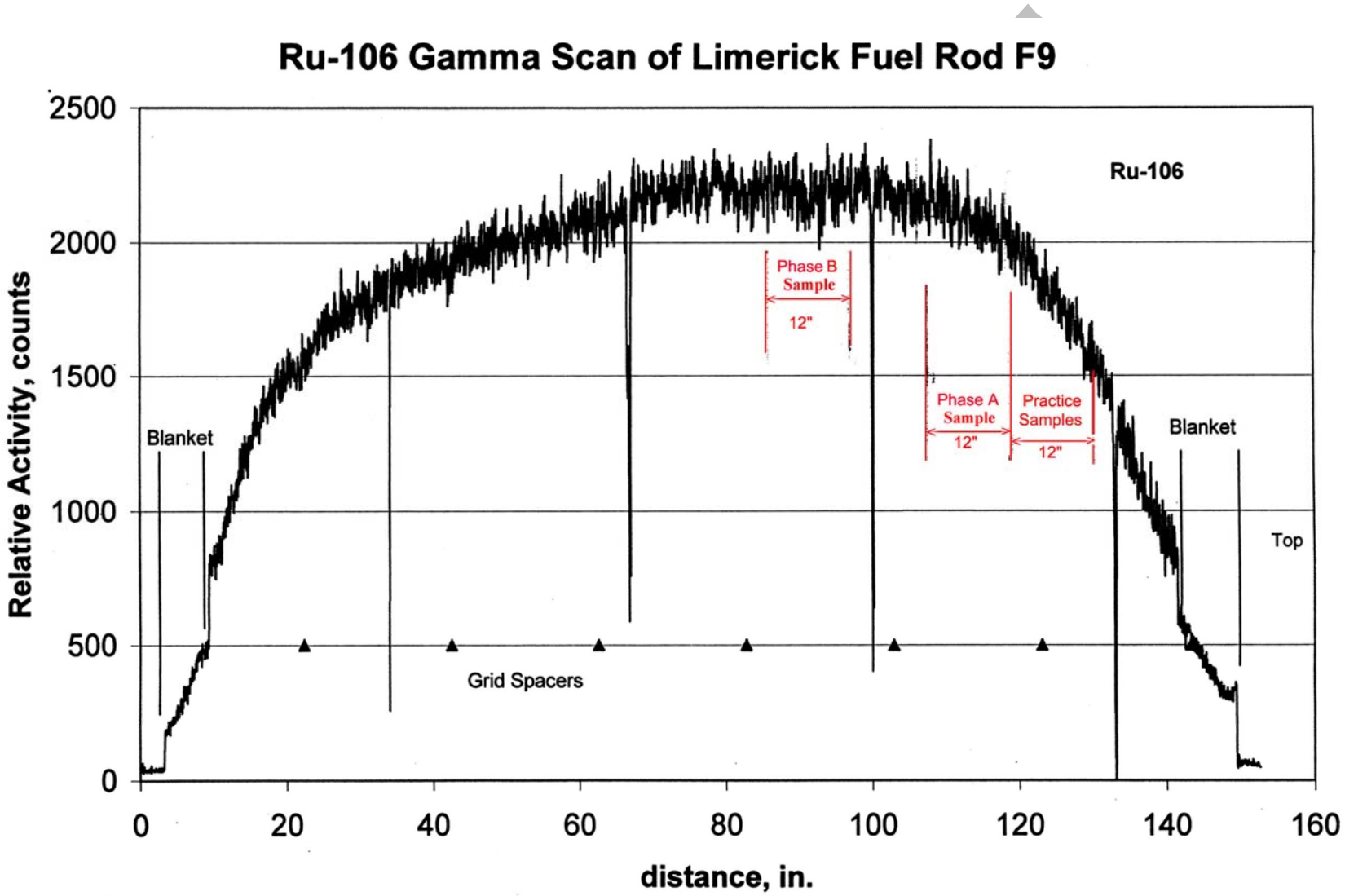

Figure 161. Gamma scan profile for high-burnup Limerick rod F9 showing locations of LOCA integral samples ICL#1 (labeled Phase A) and ICL#2 (labeled Phase B). Fuel and cladding characterization were performed at the fuel midplane, at 0.7 m above the midplane and at ≈1.1 m above fuel midplane.

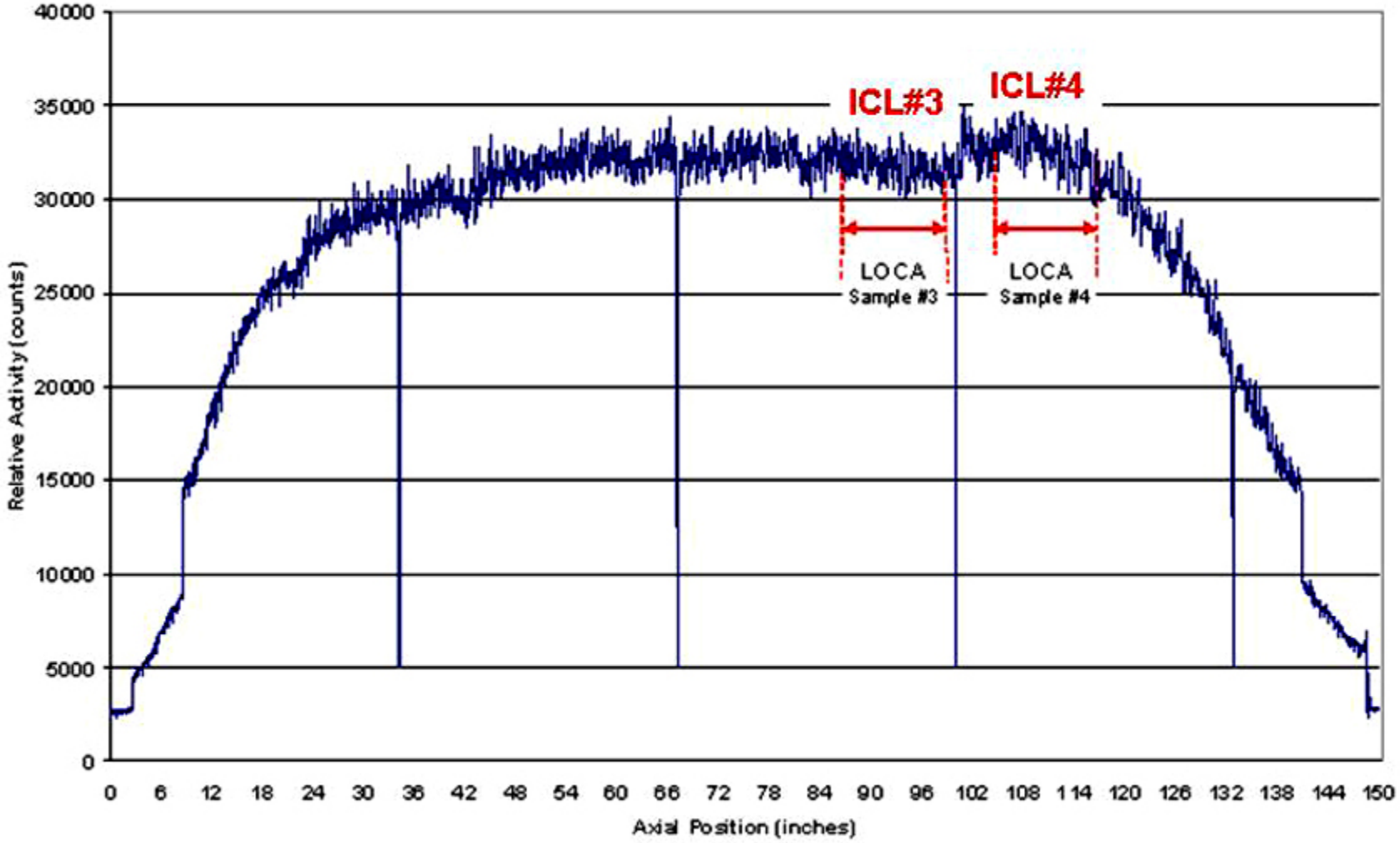

Figure 162. Gamma scan profile for high-burnup Limerick rod J4 showing axial locations of LOCA integral samples ICL#3 and ICL#4.

Table 63 Summary of In-cell LOCA Integral Tests (ICL) with High-burnup Fueled Cladding Specimens from Limerick BWR. Also shown are the results of companion out-of-cell (OC) tests OCL#5 and OCL#11 with non-irradiated Zry-2 cladding.

Parameter	ICL#1	OCL#5	ICL#2	OCL#11	ICL#3	ICL#4
Environment	Argon	Argon	Steam	Steam	Steam	Steam
Hold Temperature, ºC	---	---	1204	1204	1204	1204
Hold Time, s	0	0	300	300	300	300
Quench (Q) at 800ºC or Slow Cooled (SC)	SC	SC	SC	SC	Q-800ºC to 460ºC	Q-800ºC
Max. Pressure, MPa	8.96	8.96	8.87	8.61	9.00	8.86
Burst Pressure, MPa	8.61	8.28	8.01	7.93	8.60	8.00
Burst Temperature, °C	≈755	733	≈750	753	≈730	≈790
Burst Shape	Oval	Dog Bone	Oval	Dog Bone	Oval	Oval
Burst Length, mm	13	13	14	11	11	15
Max. Burst Width, mm	3	2.5	3.5	1	4.6	5.1
Length of Balloon, mm	≈70	100	≈ 90	≈ 140	≈ 100	≈ 80
$(\Delta D/D_o)$max, %	38±9	44±10	39±10	43±10	43±9	36±9
Max. Calculated ECR, %	0	0	≈20	≈21	≈21	≈20

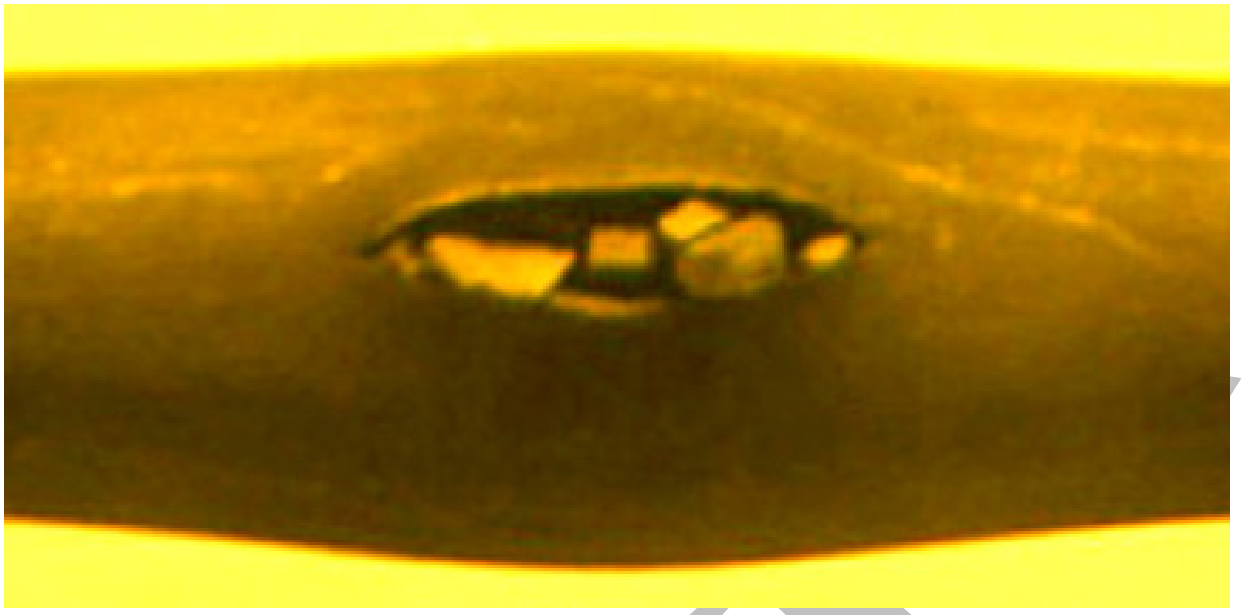

(a)

(b)

Figure 163. Comparison of burst openings for (a) In-cell LOCA integral test ICL#1 specimen from high-burnup Limerick rod F9 and (b) out-of-cell companion test OCL#5 specimen from unirradiated Zry-2 cladding. Burst lengths are both ≈13-mm long for these ramp-to-burst test samples.

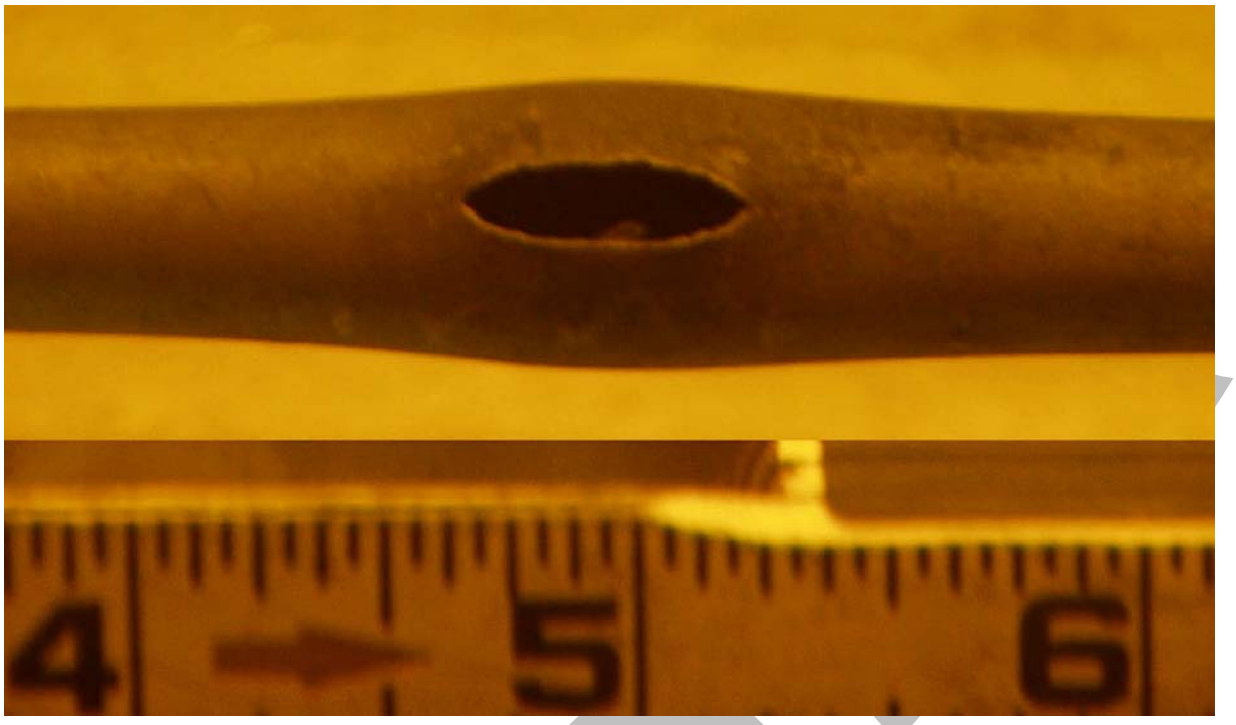

(a)

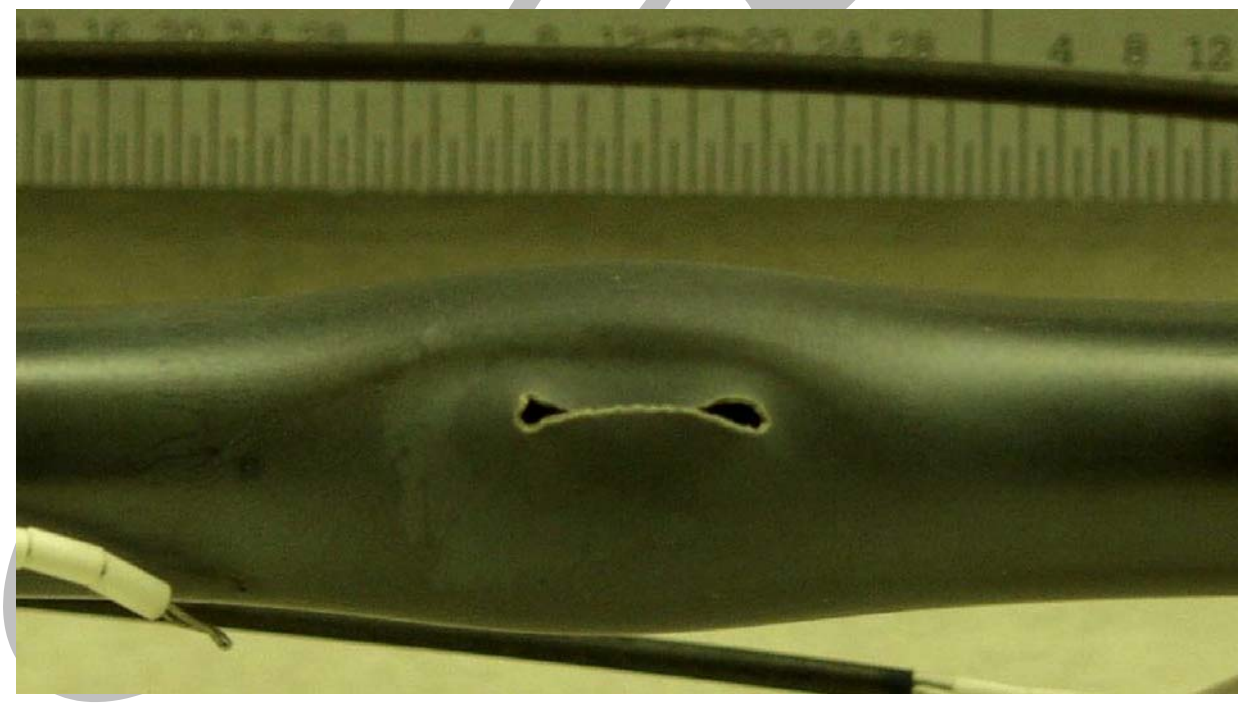

(b)

Figure 164. Comparison of burst openings for (a) high-burnup Limerick ICL#2 specimen; and (b) unirradiated OCL#11 Zry-2 specimen after 300-s exposure to steam at 1204°C, followed by slow cooling to RT.

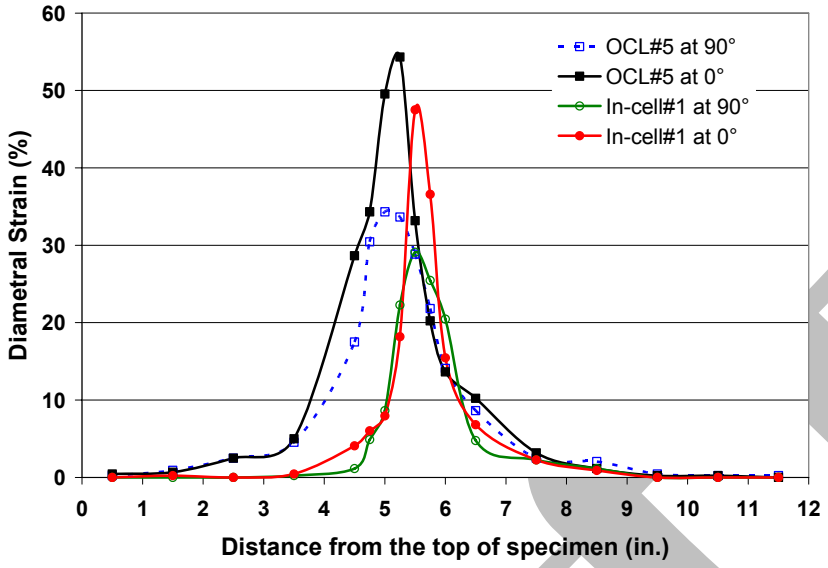

Figure 165a. Outer-diameter strain for in-cell test ICL#1 sample (high-burnup Limerick fueled Zry-2) and companion out-of-cell test OCL#5 sample (unirradiated Zry-2 filled with zirconia pellets). Both tests were ramp-to-burst tests in argon, followed by slow cooling to RT.

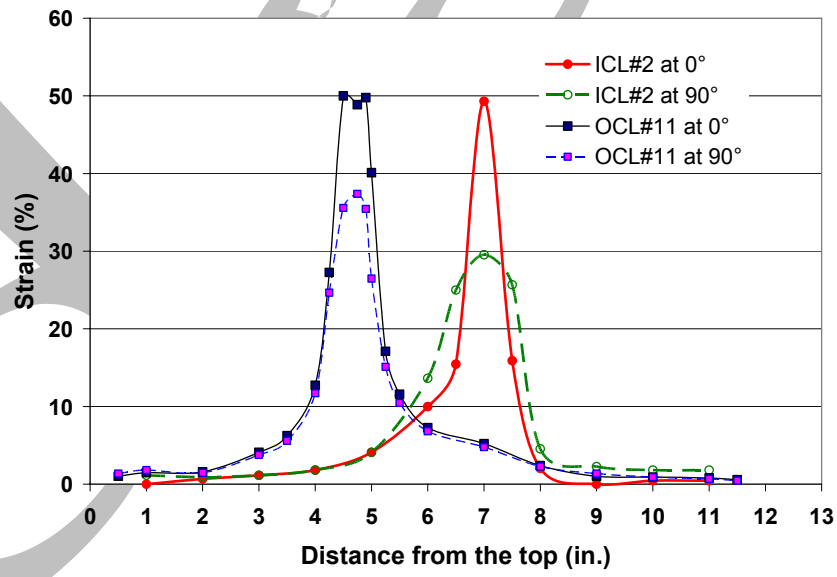

Figure 165b. Outer-diameter strain for in-cell test ICL#2 sample (high-burnup Limerick fueled Zry-2) and companion out-of-cell test OCL#5 sample (unirradiated Zry-2 filled with zirconia pellets). Both samples were ramped to 1204ºC in steam, held at 1204ºC for 300 s, and slow cooled to RT.

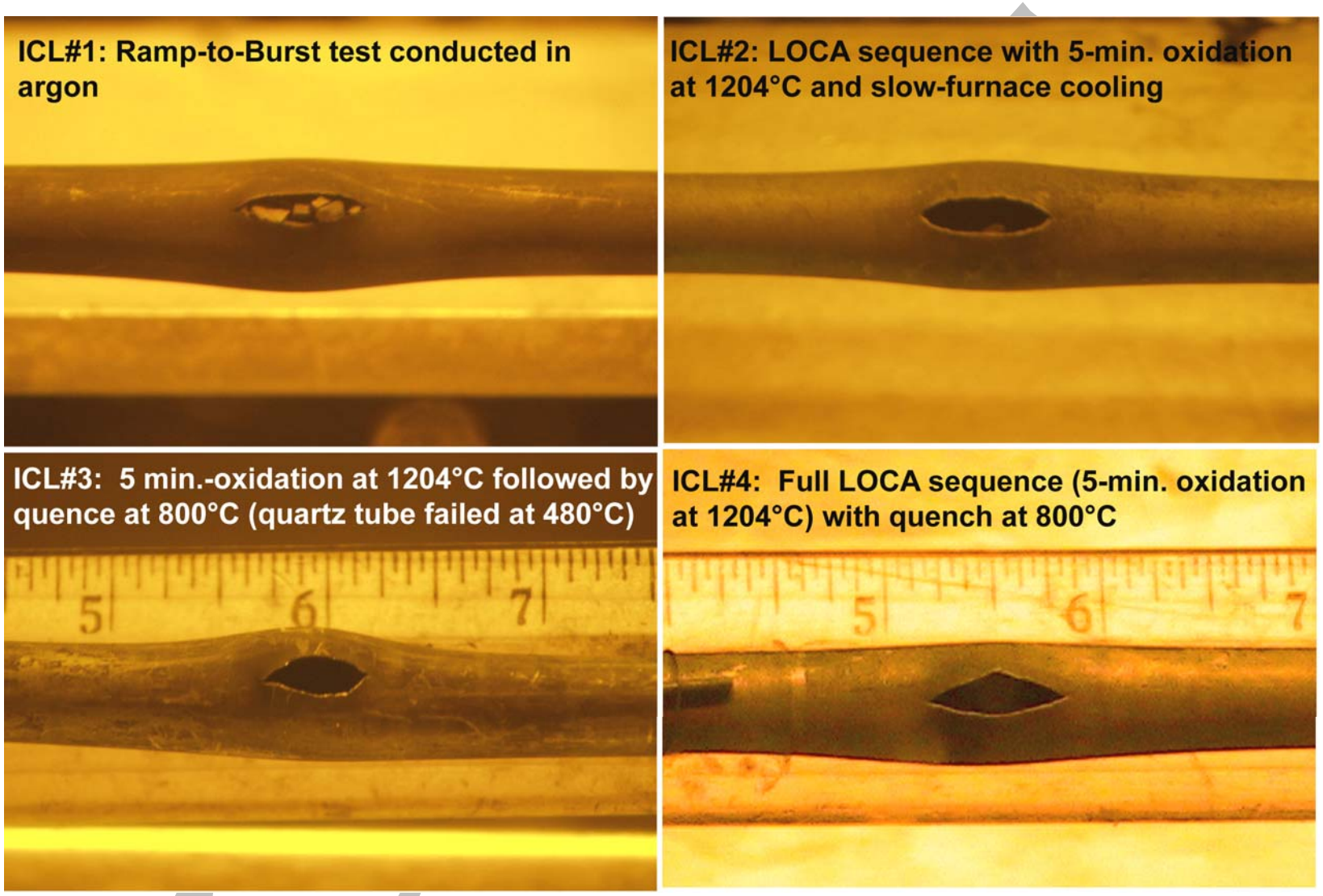

Figure 166. Comparison of ballooned-and-burst regions of the four in-cell LOCA integral test samples.

6.2.2 Oxidation and hydrogen pickup due to secondary hydriding for high-burnup samples

For ICL test samples #2 and 3, extensive metallographic characterization and LECO measurements were performed within ±50 mm of the burst midplane to determine the degree of steam oxidation (two-sided vs. one-sided and OD vs. ID oxide-layer thickness within the balloon region), the axial profile of oxygen pickup by means of LECO and metallography, and the axial profile of hydrogen pickup. Low-magnification images were obtained for the fuel morphology within ±50 mm and outside the balloon region (see Section 6.3).

For the ICL#2 sample, whose burst opening had to be epoxied to prevent fuel fall out during movement of high-dose-rate samples to allow for shield-window maintenance, LECO hydrogen and oxygen samples were limited to those away from epoxied region, which extended away from the burst opening into the balloon. The sectioning diagram for ICL#2 metallography is shown in Figure 167, along with a compressed view of the diametral strain profile to show the location of the burst midplane and the axial extent of the balloon region. LECO hydrogen and oxygen measurements were made at locations H_1 and H_2, both regions that contained no epoxy.

The ICL#3-sample sectioning diagram, along with the diametral strain profile, is shown in Figure 168. As indicated in the figure caption, the sample fractured at three locations during handling: bending failure at A; impact failure at C; and failure due to removal of tape from the burst opening region at B. These locations were designated initially for metallography only. Following the handling failures, two of the surfaces were imaged by SEM for fractographic analysis. Not shown in the figure are the locations for LECO oxygen and hydrogen measurements.

The results from LECO hydrogen and oxygen measurements, the ECR determined form oxygen pickup from LECO and metallographic data, and the hydrogen pickup are emphasized because hydrogen and oxygen pickup have a significant influence on ductility. Figure 169 shows the LECO results for oxygen and hydrogen concentrations for the ICL#2 and ICL#3 test samples with axial locations referenced to the burst midplane. Equations 8-10 were used to convert the LECO data to oxygen pickup, ECR and hydrogen pickup. The pretest hydrogen and oxygen contents for high-burnup Limerick cladding (0.7-wt.% oxygen and 70-wppm hydrogen) were used in these calculations. The results are shown in Figure 170. The ECR determined from LECO and metallographic data are reasonably close. Based on a reasonable extrapolation of these two off-center locations, the maximum ECR for the ICL#3 sample is ≈18%. This is remarkably close to the targeted value of 20% CP-ECR for two-sided steam oxidation. The hydrogen pickup (maximum >3000 wppm) is as high as the values measured for unirradiated cladding. The hydrogen peaks are closer to the center of the burst region, consistent with the shorter axial extent of ballooning for the high-burnup cladding. However, the hydrogen pickup near the burst midplane is significantly larger for high-burnup cladding than for unirradiated cladding. The combination of high hydrogen and high oxygen pickup in most of the balloon region (±40 mm) suggests that the cladding should be quite brittle within this region. Recall that the unirradiated LOCA test samples had very low hydrogen pickup in the burst region.

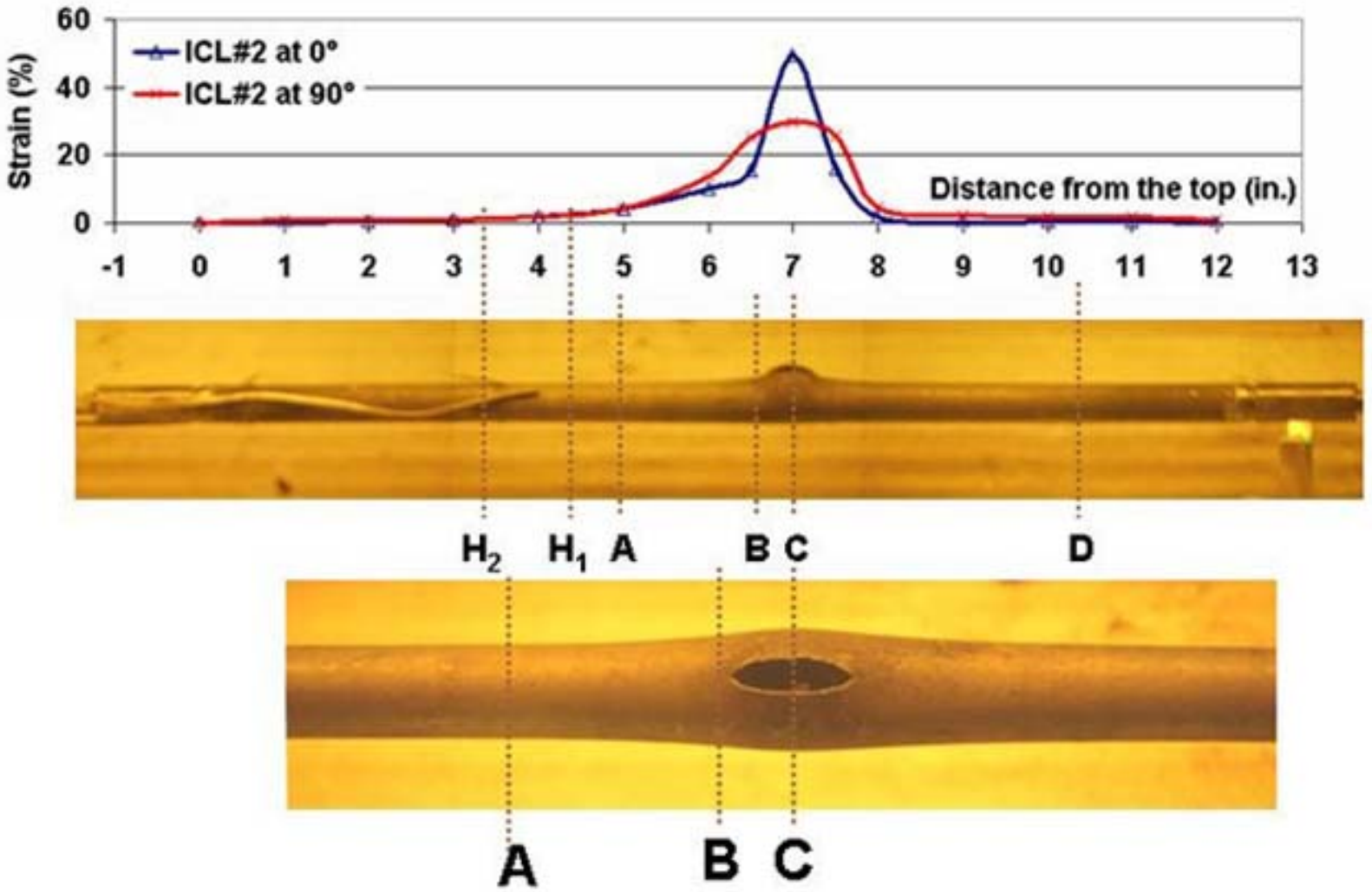

Figure 167. Sectioning diagram for ICL#2 (300 s at 1204ºC, slow cooling to RT) sample. Locations A, B and C are metallography locations. H_1 and H_2 are locations for LECO hydrogen and oxygen measurements.

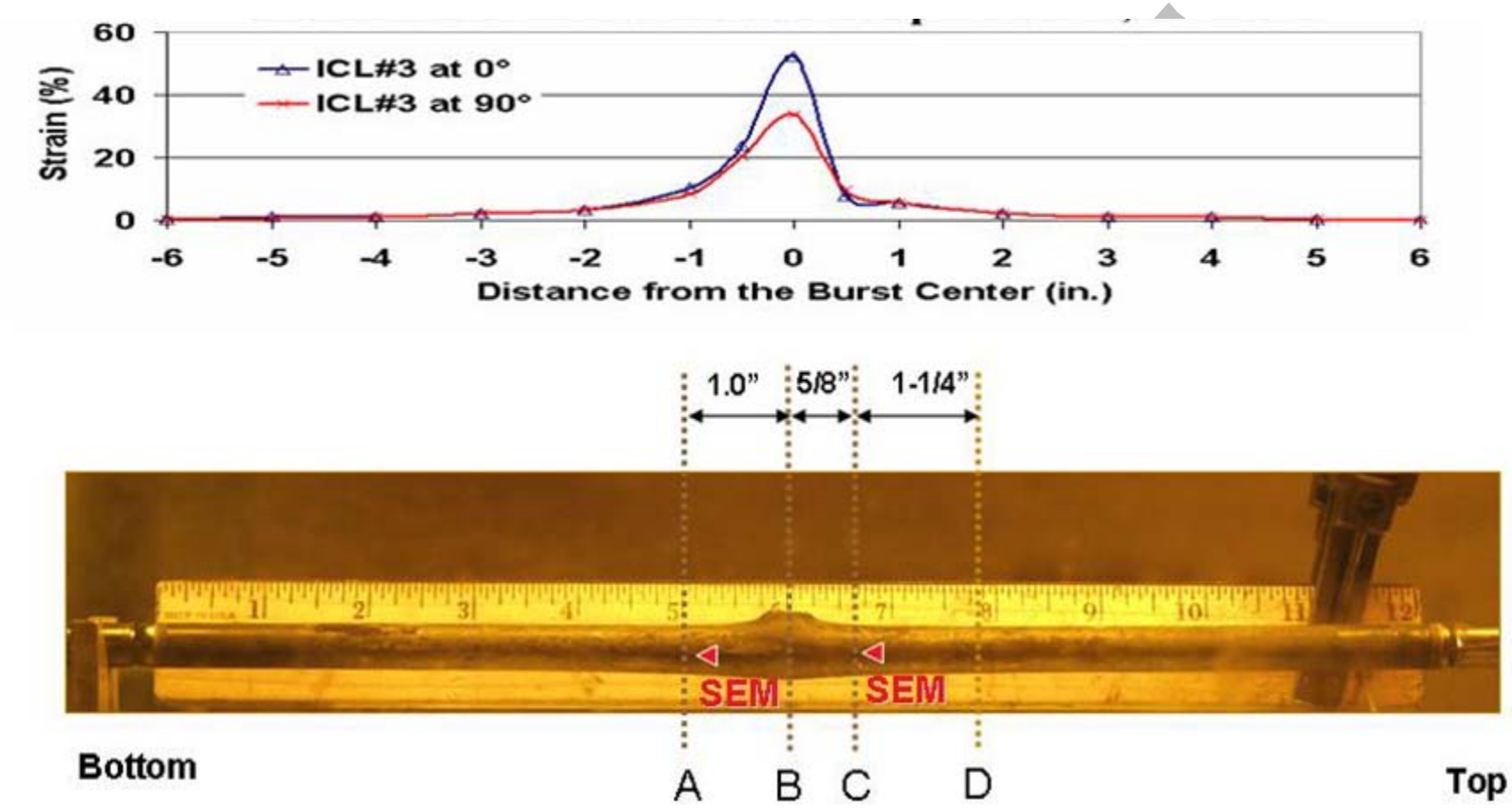

Figure 168. Sectioning diagram for ICL#3 (300 s at 1204ºC, quench from 800ºC to 460ºC, slow cooling to RT) sample. The sample fractured at locations A, B and C during handling prior to the sectioning at D. LECO hydrogen and oxygen samples not shown.

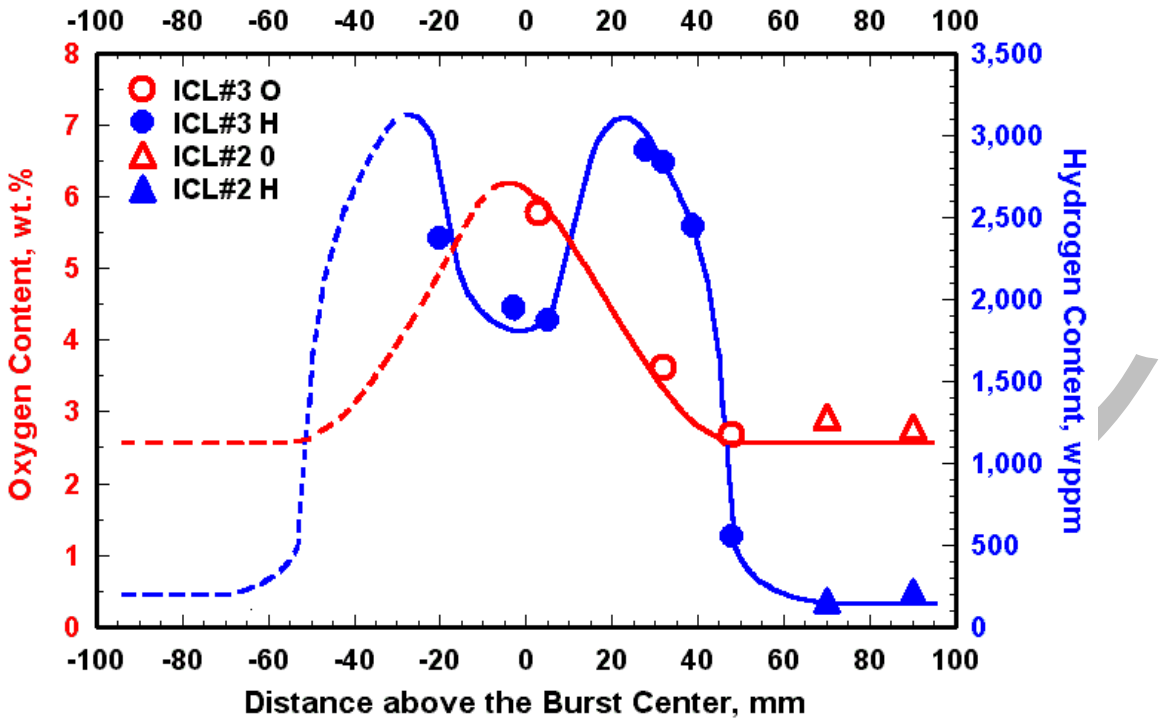

Figure 169. LECO oxygen- and hydrogen-content data for ICL#2 and ICL#3 test samples, both oxidized for 300 s at 1204°C. Concentrations are referenced to the weight of the oxidized samples.

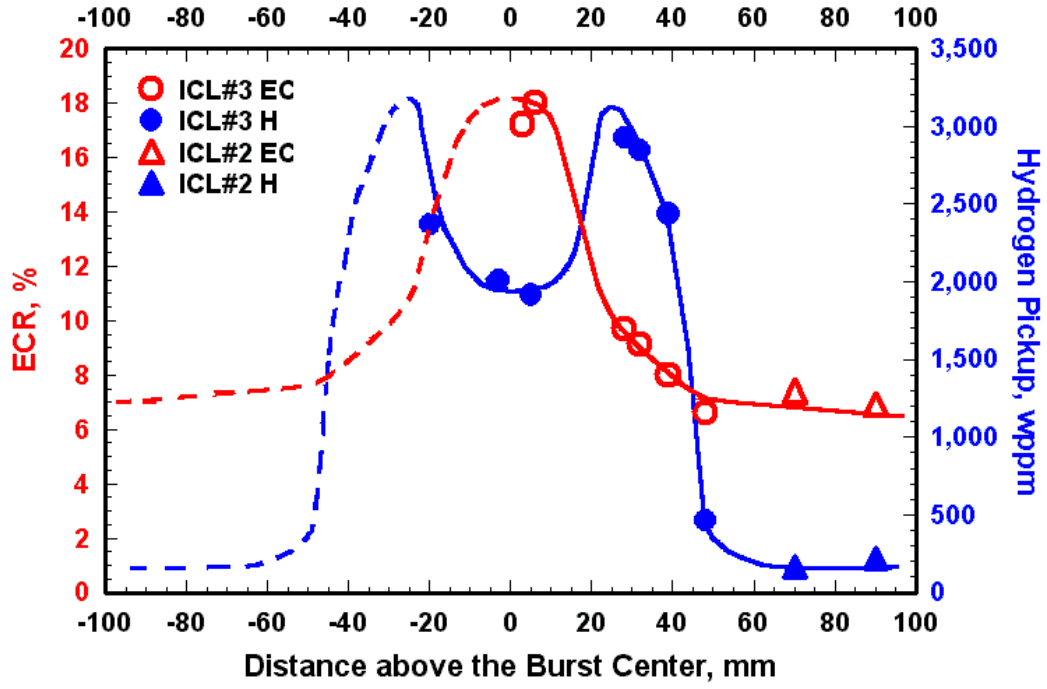

Figure 170. Axial distribution of ECR (based on LECO-oxygen and metallographic data) and hydrogen pickup (based on LECO data in Figure 169) for ICL#2 and ICL#3 test samples.

6.2.3 Post-quench ductility of high-burnup samples

LOCA test samples were not subjected to four-point-bend tests. However, based on optical microscopy and SEM imaging, along with hydrogen and oxygen pickup, embrittlement of these samples can be inferred. SEM fractography was performed at two locations (A and C) of the ICL#3 test sample that failed during handling. The results for location C (≈20 mm above the burst midplane) are shown in Figure 171. The morphology of the fracture surface supports the contention that the RT failure was brittle. Similar results were obtained at location A. Given the high combinations of ECR and hydrogen pickup at these locations (≈25 mm below the burst midplane for A), it is highly probable that these locations would have failed in a brittle mode even if they were tested at 135º.

It is encouraging that all four LOCA integral samples remained intact during and following quench. However, thermal stresses due to quench are relatively low. The samples are fixed at the top and free to expand and contract in the axial direction. If contraction during quench were partially constrained and/or if impact loads due to rod-to-rod contact during quench vibration were high enough to cause failure, then it is predicted that the failure mode would be brittle. It is also predicted, based on ANL bend test results and JAEA axial constraint tests that such loading would result in a clean beak across the cladding wall, rather than fragmentation. Except for the highly oxidized cladding at the edges of the burst region, the brittle cladding within the balloon region does not appear to be susceptible to fragmentation for maximum CP-ECR values < 20%.

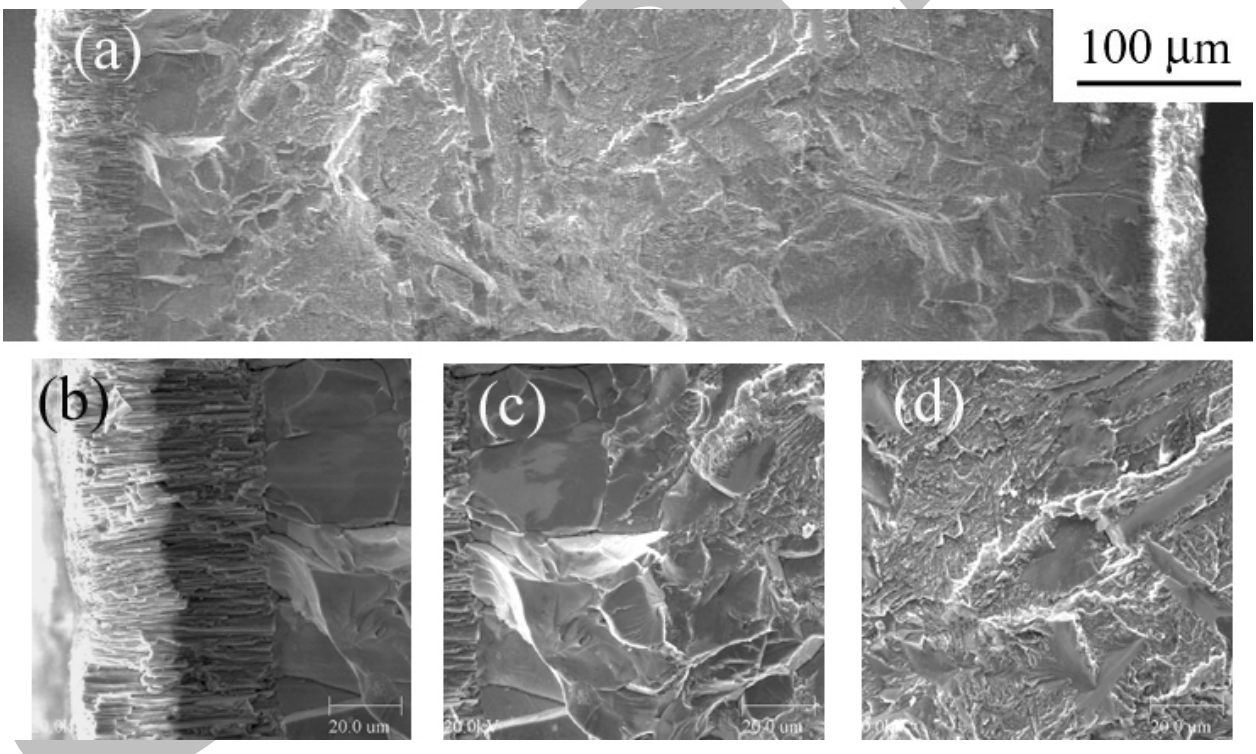

Figure 171. SEM fractography for ICL#3 samples at axial location C in Figure 168 (≈20 mm above the burst midplane): (a) cladding cross section, (b) oxide layer, (c) oxygen-stabilized alpha layer, and (d) prior-beta layer. Interpolating from the results in Figure 170, the estimated hydrogen pickup is ≈3000 wppm and the estimated measured ECR is ≈10%.

6.3 Cladding inner-surface oxygen pickup from fuel-cladding bond and fuel

As shown in Figure 115, high-burnup Limerick cladding has a fuel-cladding bond thickness of 10±5 μm. For this BWR fuel, the bond thickness is not uniform around the inner surface of the cladding. For the one-sided oxidation tests with defueled Limerick cladding, Figure 115b shows that the bond layer remains after defueling in nitric acid. The minimum hold time at 1200ºC for the Limerick one-sided-oxidized samples was 300 s. Figure 172 shows one of eight micrographs taken at the midplane of the high-burnup Limerick sample oxidized for 300 s at 1200ºC. For the post-test sample, there is no indication of an inner-surface bond-oxide layer or of the oxygen-stabilized alpha layer that would have formed during reduction of the bond layer. Based on the estimate in Section 5 that such a bond layer would be reduced after ≈100 s during the ramp from 300ºC to 1200C, oxygen from the alpha layer would have continued to diffuse into the beta layer until its oxygen content were too low to stabilize the alpha phase at 1200ºC. This observation is consistent with the results of the shorter-time HBRI one-sided oxidation tests.

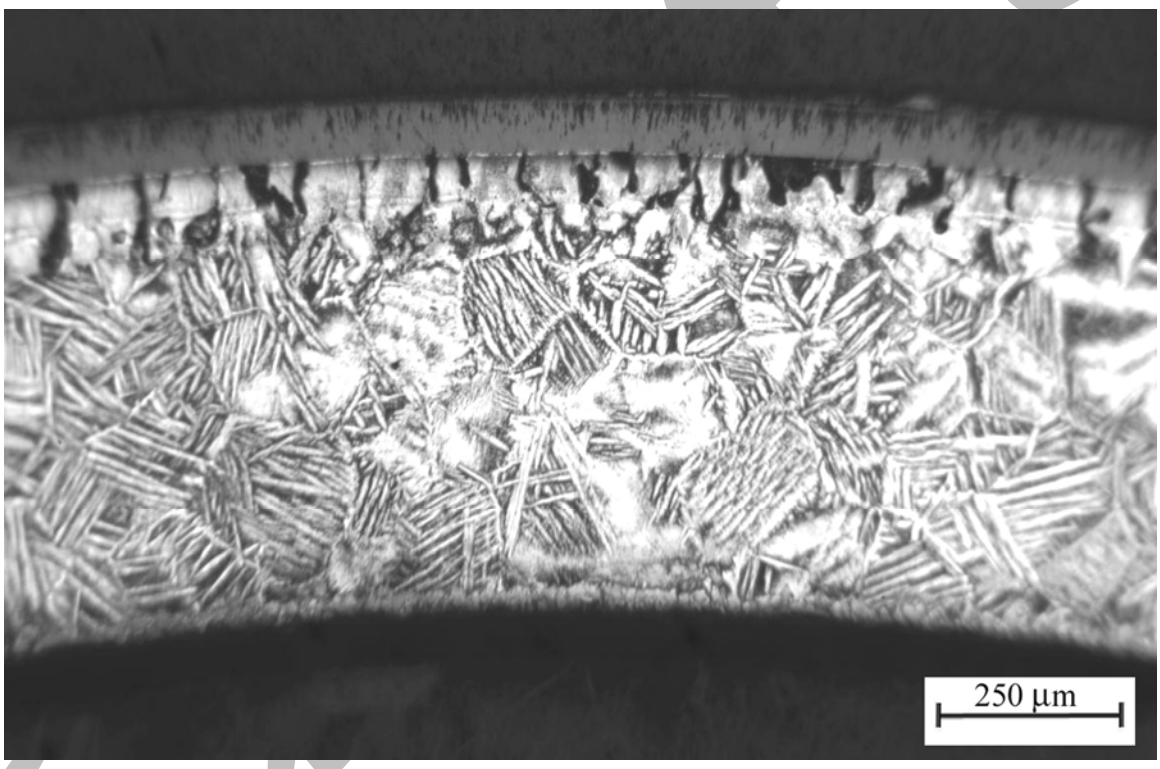

Figure 172. High-burnup Limerick oxidation sample following one-sided oxidation in steam at 1200ºC for a 300-s hold time.

The degree to which the Zircaloy metal will pickup oxygen from the fuel depends on how much fuel remains attached to the bond during the outward expansion of the cladding. The fuel-to-bond strength is greater than the fuel strength; thus, some fuel will remain bonded as the cladding deforms outward. Figure 173 shows one circumferential location at the burst midplane for the ICL#3 sample where there are chunks of fuel still bonded to the cladding. However, there is ample steam at this location to oxidize the cladding inner-surface. The presence of this fuel does not appear to influence the high-temperature steam-oxide layer growth; the outer-surface oxide is about as thick as the inner-surface oxide.

The fuel morphology for the ICL#2 sample at locations 180 mm below (b) and 50 mm above (c) the burst midplane are shown in Figure 174 and compared to the fuel morphology of the as-irradiated rod (a). The cladding strain at 180 mm below the burst is <2%, while the cladding strain at 50 mm above is ≈5%. Most of the fuel appears to have pulled away from the cladding at 50 mm above the burst, while there is little change in fuel morphology at 180 mm below the burst region, which is outside the uniformly heated zone.

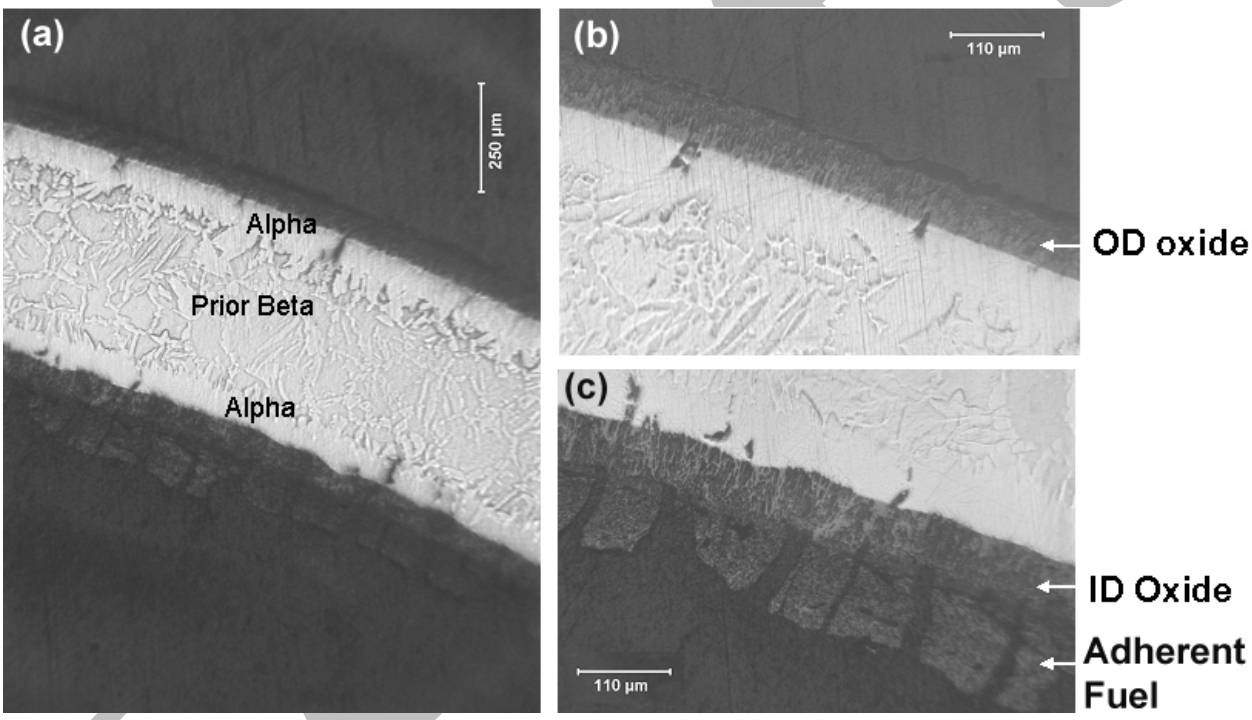

Figure 173. Metallographic results for a circumferential location at the burst midplane of the ICL#3 sample, oxidized for 300 s at 1204ºC. Fuel particles adherent to the cladding inner surface are shown in (c).

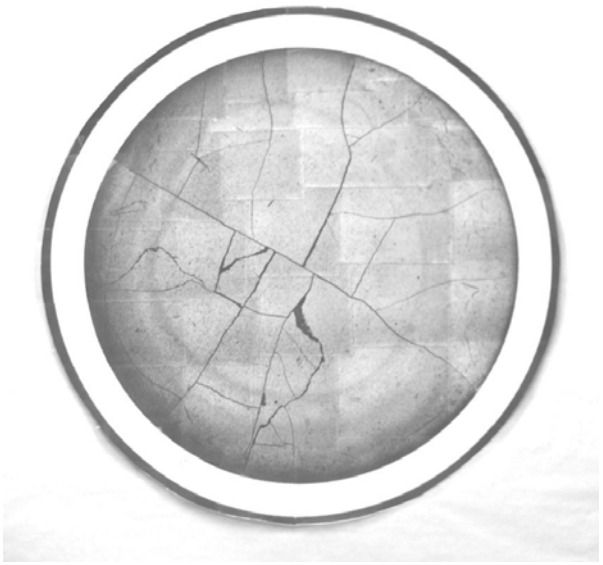

(a)

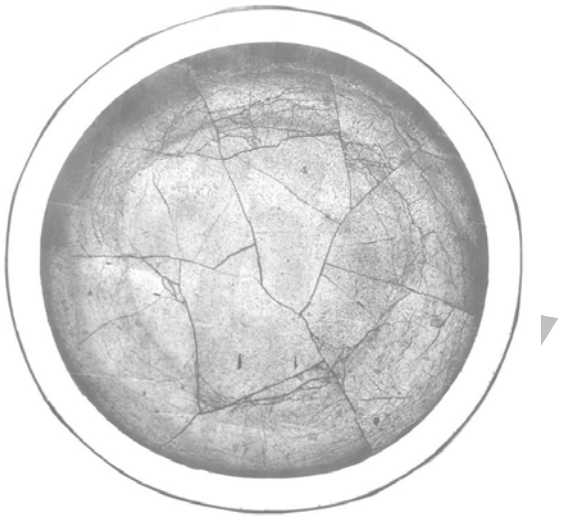

(b)

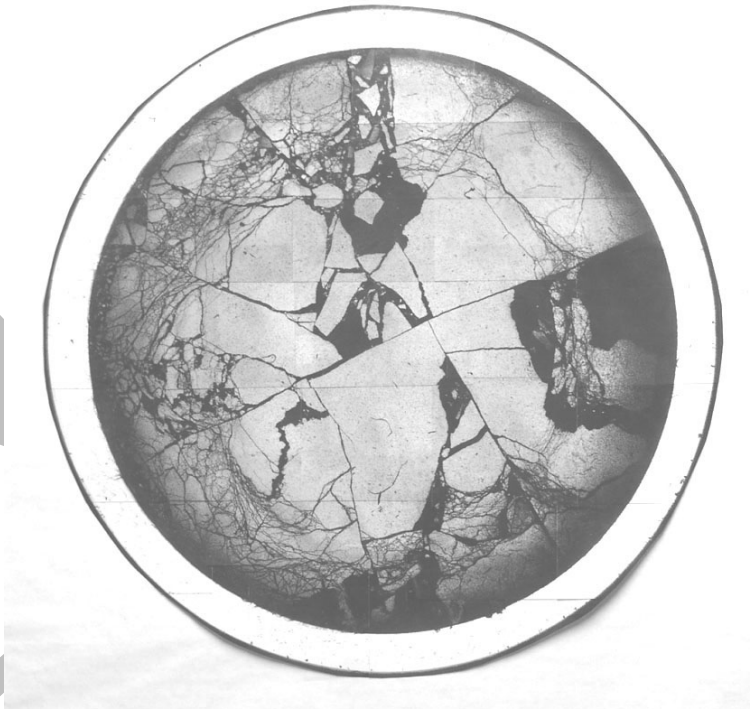

(c)

Figure 174. Fuel morphology for ICL#2 LOCA sample: (a) as-irradiated, pre-test condition; (b) post-test condition 180 mm below burst midplane; and (c) post-test condition at 50 mm above the burst midplane.

Except for local regions on the inner-surface of the ICL#2 cladding, no oxygen-stabilized alpha layer is observed. This suggests that whatever oxygen has been picked up from the fuel-cladding bond layer and fuel particles or chunks adherent to the bond layer has been reduced after 300 s at 1200ºC near the edges of the balloon. One local area of oxygen-stabilized alpha found at 50 mm above the burst midplane for the ICL#2 sample (see Figure 174c for fuel morphology) is shown in Figure 175. Although this alpha layer could have been caused by local steam leakage, it is likely that it formed through oxygen pickup from the fuel.

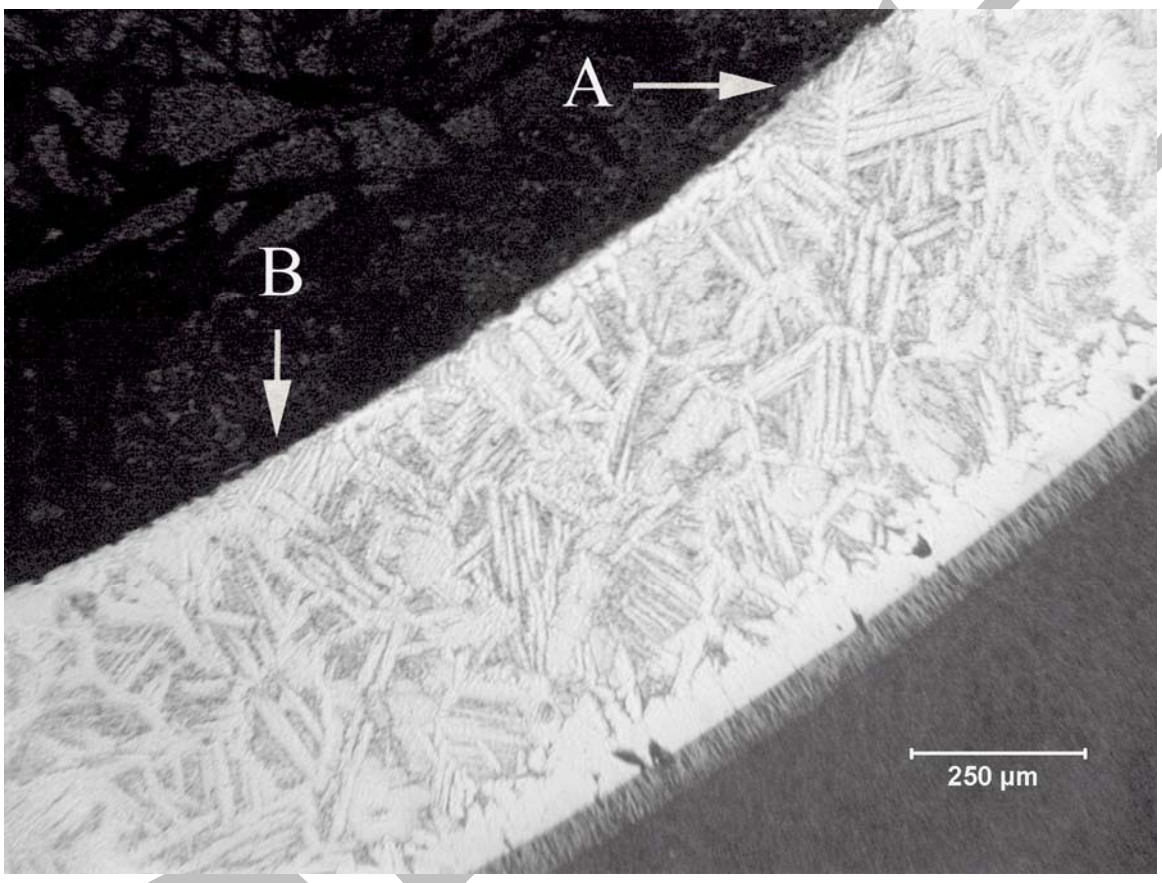

Figure 175. Evidence of local area on cladding inner surface of oxygen-stabilized alpha (B) for ICL#2 sample at 50 mm above the burst midplane. The inner-surface region indicated by "A" does not have such an alpha layer and is more typical of what is observed for most of the inner surface at this axial location.

Although the observations from the LOCA integral test samples are not substantial, it is well known that UO_2 fuel can be the source of oxygen for diffusion into the cladding metal. Hobbins and coworkers made such an observation in one of the Power-Coolant Mismatch tests in the Power Burst Facility [34]. In that test, in which the cladding collapsed onto the fuel, an ID alpha layer was observed. Hobbins concluded that the thickness of the ID alpha layer was of comparable magnitude to the OD alpha layer that came from the reaction with steam. Hobbins also gave some evidence that this would only happen when there is hard contact between the cladding and the pellet.

Two years later, Hofmann and Politis [14] confirmed Hobbins's observations. Hofmann put fresh UO_2 pellets inside sealed unirradiated Zircaloy tubes and heated them in argon under various pressures. Hofmann found an ID alpha layer and also concluded that the uptake of oxygen due to the interaction with UO_2 was approximately as high as that by the reaction with steam. Hofmann's tests confirmed that solid contact was necessary and that the rate of oxygen transport via the gas phase is too slow.

Taken together, these observations support the picture illustrated in Figure 5. The fact that the alpha layers near the ID are always about the same thickness as those observed near the OD when an ID oxygen source is present suggests that oxygen diffusion in the cladding metal is the rate-limiting step – provided the oxygen source is in intimate contact with the surface of the metal.

Typical analyses show that there would be no hard contact between fuel pellets and cladding during a LOCA transient at very low burnups, so ID oxygen pickup would not be expected in low-burnup fuel. However, fuel bonding occurs at high burnups after the fuel-to-cladding gap has been closed for a long time, and bonding appears to provide the intimate contact that is needed.

Bonding occurs earlier in PWR fuel than in BWR fuel because the higher system pressure in PWRs results in more cladding creepdown. Bonding between the fuel and the cladding eventually occurs in BWRs as well. From ANL characterization work performed for Limerick BWR high-burnup (57 GWd/MTU) fuel, Surry low-burnup (36 GWd/MTU) fuel, TMI-1 PWR intermediate-burnup (48 GWd/MTU), and H. B. Robinson PWR high-burnup (63-67 GWd/MTU) fuel, it appears that bonding (and hence ID oxygen ingress during a LOCA) would begin at ≈30 GWd/t in PWR fuel and be complete around ≈50 GWd/t, whereas it would not begin in BWRs until ≈40-50 GWd/t.

7 Empirical Criteria for Embrittlement

Although progress has been made in developing a mechanistic understanding of the embrittlement process, several mechanisms are active and each involves multiple parameters. For this complex situation, it was not possible within the scope of the present work to develop a full set of mechanistic equations and model parameters for practical applications. It was possible, however, to identify empirical criteria that adequately predict the onset of embrittlement. In identifying these criteria, an effort was made to stay close to current industry practice and to utilize parameters that can be readily quantified.

In evaluating the empirical criteria proposed in this section, it is useful to review the effects of oxygen and hydrogen on embrittlement, as well the effects of heating and cooling rates on the ductile-to-brittle transition. For as-fabricated cladding oxidized (two-sided) at 1200ºC, oxygen-induced hardening of the prior-beta layer resulted in high ductile-to-brittle transition CP-ECR values for modern alloys. Ductility (≥1% permanent strain or ≥2% offset strain) was maintained for CP-ECR values in the range of 17-20%. The oxygen diffusion coefficient in the beta layer increases exponentially with temperature, and the solubility limit also increases with temperature. The increase in solubility with temperature is very important as Zr-alloy cladding embrittles at higher CP-ECR values when oxidized at 1025ºC (solubility limit of 0.27 wt.%) and 1100ºC (solubility limit of 0.38 wt.%), as compared to 1200ºC (solubility limit of 0.57 wt.%). For Zry-4, the increase in oxygen concentration is essentially proportional to CP-ECR up to about 17% at which point 92% of the equilibrium concentration is reached for an initial oxygen concentration of 0.12 wt.%. Thus, expressing embrittlement threshold in terms of CP-ECR appears to work well for as-fabricated Zry-4. Although less is know about the solubility limits for ZIRLO and M5, the same approach works for these alloys.

The effects of hydrogen on the embrittlement of Zry-4 oxidized at 1200ºC are well documented in this report. For unirradiated 17×17 Zr-4, the embrittlement CP-ECR threshold is reduced from 17% to 10% for ≈300-wppm H and to 7.5% for ≈375 wppm H. For unirradiated HBR-type 15×15 Zry-4, the embrittlement CP-ECR threshold is reduced from 14% to 7.5% for ≈375-wppm H, to ≈5.5% for 450-wppm H and to 5% for ≈600-wppm hydrogen. These results are based on ductility data for samples that were quenched at 800ºC. The results for prehydrided and high-burnup Zry-4 oxidized at 1200ºC are reasonably well understood. Hydrogen contents >350 wppm increase the solubility of oxygen in the beta layer from ≈0.6 to ≈1. For early oxidation times, the rate of beta-layer oxygen uptake is increased due to the increase in oxygen content at the alpha-beta boundary, which increases the concentration gradient. If the oxygen content for embrittlement is about 0.6 wt.%, this critical level is reached at much shorter times and corresponding CP-ECR values for Zry-4 cladding with hydrogen concentrations typical of high-burnup cladding. In addition to the increase in concentration-driven diffusion rate and solubility, prehydrided cladding appears to embrittle faster than would be predicted based simply on the increase in beta-layer oxygen content. Based on data comparisons for prehydrided Zry-4 cladding with and without quench at 800ºC, there appears to be some intrinsic hydrogen embrittlement in addition to the indirect embrittlement effect of increasing the oxygen solubility.

The ductile-to-brittle-transition CP-ECR was found to be relatively insensitive to heating and cooling rates, as well as quench temperature, for as-fabricated alloys. For the transition CP-ECR values in the range of 17-20%, the range of experimental heating rates resulted in sufficient hold time at 1200ºC to allow oxygen saturation in the beta layer at the end of the hold time. Oxygen pickup in the beta layer and increase in CP-ECR were calculated to be insignificant during the rapid experimental cooling rate. The ductile-to-brittle transition CP-ECR values were also insensitive to quenching at 800ºC vs. slow cooling from 800ºC to RT.

However, for prehydrided and high-burnup Zry-4, the transition CP-ECR values were low, and these values were highly dependent on heating rates, temperature overshoot, cooling rates to 600-800ºC, and quench at 600-800ºC vs. slow cooling from these temperatures to RT. With regard to heating rate and hold time, a faster heating rate and longer hold time would result in more oxygen diffusion into the beta layer, more hardening and greater loss of ductility. For slower cooling rates and lower quench temperatures, more extensive oxygen and hydrogen redistribution would occur in the prior-beta layer resulting in ductility enhancement and higher transition CP-ECR values. Figure 176 shows the experimental heating and cooling rates for the high-burnup Zry-4 samples (HBRI) oxidized two-sided to a maximum oxidation temperature of ≈1185ºC. The CP-ECR for the experimental heating rate given by the solid-line curve in Figure 176 corresponds to a total CP-ECR of 5.7%: 5.5% accumulated at the end of the heating phase and an additional 0.2% for the cooling phase. The experimental heating rate is a reasonable representation of calculated large-break LOCA heating rates and is much faster than heating rates for small-break LOCAs [35,36]. However, the experimental cooling rate from high temperature to 800ºC is much faster than calculated cooling rates (3-5ºC/s) for large-break PWR LOCAs [35,36]. Also shown in Figure 176 are the idealized LOCA cooling rates of 3ºC/s and 5ºC/s. The heating-phase CP-ECR is 5.5% for all three temperature transients and the beta-layer oxygen-embrittlement is expected to be the same for all three temperature transients. However, the calculated CP-ECR increases as the cooling rate decreases: 5.7% (experimental cooling), 6.4% (5ºC/s cooling) and 6.9% (3ºC/s). Thus, the experimental results give a lower-bound ductile-to-brittle transition CP-ECR. This is important in using the data for prehydrided and high-burnup Zry-4 cladding to develop and test empirical embrittlement criteria based on a reasonable bound for LOCA transients.

For measured corrosion layer thicknesses of 71-74 μm and hydrogen pickup of 550 wppm, the high-burnup 15×15 Zry-4 samples are estimated to be brittle following oxidation to 5.5% heating-phase CP-ECR and 5.7% total-transient CP-ECR following quench at 800ºC. In addition to the fast experimental cooling rate, the experimental quench temperature of 800ºC appears to be an upper-bound for large-break PWR LOCA transients [35,36]. Because of intrinsic hydrogen embrittlement, slow-cooling rates and quench temperatures below 600ºC result in a small, but significant, enhancement in ductility. During cooling to 600-800ºC, oxygen segregates within the prior-beta layer to form oxygen-rich regions (i.e., oxygen-stabilized alpha) and low-oxygen regions (i.e., beta). Most of the hydrogen is in low-oxygen beta which then transforms with further cooling into low-oxygen alpha. Quench at 600-800ºC essentially freezes the dissolved hydrogen in the low-oxygen material. Slow cooling below 600-800ºC allows some of the hydrogen to come out of solution and precipitate outside the low-oxygen regions. Thus, although oxygen diffusion is too slow below 600-800ºC to allow further redistribution of oxygen within the prior-beta layer, hydrogen is mobile enough to diffuse short distances during slow cooling from 600-800ºC to 135ºC. The small enhancement in ductility with slow cooling to RT appears to be due to the precipitation of small hydrides outside the low-oxygen part of the prior-beta layer. Thus, experimental results presented for samples quenched at 600-800ºC would give lower-bound transition CP-ECR values for LOCA transients with slow cooling rates to quench and quench at <600ºC. Conversely, experimental results for samples slow cooled to RT without quench would give an upper-bound transition CP-ECR for a given hydrogen content.

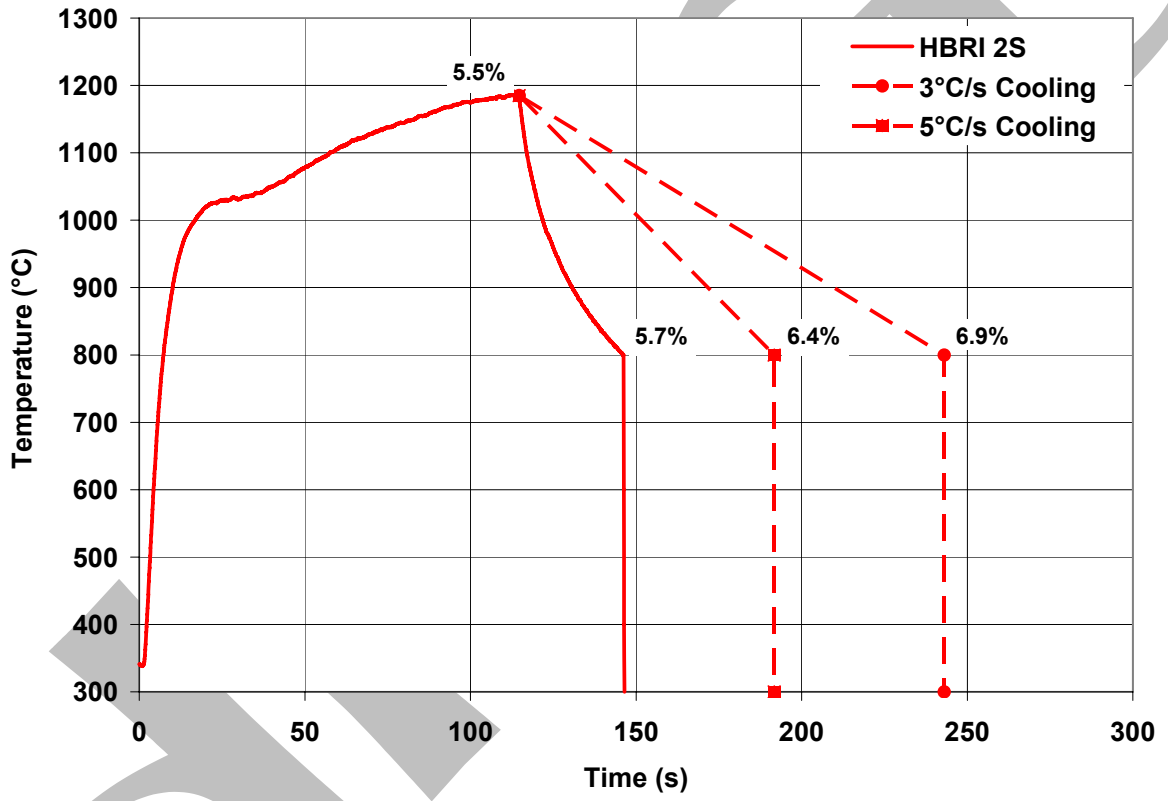

Figure 176. Comparison of the effects of cooling rates on CP-ECR for the experimental cooling rate used for two-sided oxidation tests (HBRI) with high-burnup Zry-4 cladding and large-break LOCA transient cooling rates of 3ºC/s and 5ºC/s. The heating-phase CP-ECR value (5.5%) is the same for all three cooling rates, but the total transient CP-ECR increases as the cooling rate decreases.

7.1 Criteria for beta-layer embrittlement of unirradiated cladding

Early work showed that the time needed to embrittle unirradiated cladding material decreases smoothly as temperature increases up to 1200-1300ºC [Fig. 9, Ref. 1]. Above that temperature range, the time needed to embrittle unirradiated cladding material begins to decrease rapidly. The early stages of this rate change have been seen in some of the temperature excursions in this work, but not enough data were obtained to show it explicitly. Nevertheless, the origin of this change is understood and is a consequence of the increased rate of beta-layer embrittlement due to enhanced oxygen diffusivity and solubility at higher temperatures.

In most (or all) countries, safety analyses are done with a mandated limit of about 1200ºC (2200ºF = 1204ºC). That limit avoids oxygen embrittlement of the beta layer in unirradiated material up to high oxidation levels (17-20% CP-ECR). Because of this character and its common usage, 1200ºC has been adopted in the present work and has been used in arriving at other indicators of embrittlement.

Because diffusion of oxygen into metal is much faster at high temperatures than at low temperatures, oxygen-induced embrittlement in the beta layer occurs in much shorter times at high temperatures than at low temperatures. Following the current industry practice, embrittlement has been correlated with surface oxidation, which also proceeds much faster at high temperatures than at low temperatures. All of the empirical fitting has been done with the Cathcart-Pawel (CP) weight gain (oxidation) equation, Equation 4, with the assumption that weight gain is zero at time zero. This weight gain has been converted to equivalent cladding reacted (ECR) in percent using Equations 5 or 6, and the result is noted as CP-ECR.

It is clear from Section 3 that embrittlement begins at a lower CP-ECR value at 1200ºC than at lower temperatures. Therefore, a CP-ECR limit based on 1200ºC data gives a conservative indication of the onset of embrittlement. For belt-polished 17×17 Zry-4, ZIRLO, and M5, ductility would be maintained in unirradiated cladding oxidized at 1200ºC up to 17%, 19%, and 20% CP-ECR, respectively, as can be seen in Figures 51 and 67 (see Tables 11, 24 and 30 for permanent strains). For 15×15 Zry-4 with a rough surface, ductility would be maintained up to 14% CP-ECR at 1200ºC, as can be seen in Figure 28 (see Table 15 for permanent strain). Belt-polished 15×15 Zry-4 maintains ductility up to 19% CP-ECR, as shown in Figure 28 (see Table 16 for permanent strains).

Therefore, a CP-ECR value can be determined from ring-compression tests at 135ºC for any of these cladding materials that have been oxidized at 1200ºC, and that value will give a reliable indication of the onset of embrittlement for unirradiated cladding under LOCA conditions, provided that breakaway oxidation does not occur (see Section 7.5). The CP-ECR determined for as-fabricated alloys oxidized at 1200ºC will give a lower-bound limit for LOCA transients with a peak temperature ≤1200ºC. Because the experimental samples in this study had an average temperature of 1200ºC and a local oxidation temperature of ≈1205ºC, uniform-temperature tests could also be performed at the current temperature limit of 1204ºC, which would give results comparable to those for samples oxidized at 1200ºC. The difference in beta-phase oxygen solubility between these two temperatures is small for Zry-4: 0.571 wt.% at 1200ºC and 0.580 wt.%.

7.2 Criteria for beta-layer thinning of unirradiated cladding

Embrittlement due to beta-layer thinning will not occur if the time at temperature is sufficiently limited. Within the test times used in this experimental work, beta-layer thinning was not a limiting phenomenon. At 1200ºC, the beta-layer thickness at the ductile-to-brittle-transition CP-ECR ranged from 0.2 to 0.4 mm. Limiting the CP-ECR based on beta-layer embrittlement for oxidation at 1200ºC is sufficient to preclude embrittlement due to beta-layer thinning. For test temperatures of 1000ºC and 1100ºC, modern, belt-polished 17×17 alloys remained ductile at RT up to 20% CP-ECR with beta-layer thicknesses of 0.2-0.3 mm. For 1000ºC, limiting the time based on breakaway oxidation is sufficient to preclude embrittlement due to beta-layer thinning. For 1100ºC, neither oxygen-induced embrittlement nor breakaway oxidation appears to be limiting. Beta-layer thinning is the most likely embrittlement mechanism at 1100ºC. However, for all alloys tested, this limit would occur at CP-ECR values > 20%. Therefore, by limiting the CP-ECR based on ductility loss for 1200ºC oxidation, beta-layer thinning would not be a factor in cladding embrittlement. As pointed out in Ref. 1, beta-layer thinning does result in a decrease in strength and fracture-toughness (as determined by impact tests). However, based on the results in the current study, post-quench ductility appears to be relatively insensitive to beta-layer thickness for ≥0.2-mm-thick prior-beta layers.

7.3 Criteria for localized embrittlement in a balloon

Current industry practice uses the average of an enlarged cladding diameter and a corresponding reduced wall thickness in a balloon to calculate two-sided oxidation of the cladding (and two-sided oxygen pickup). The calculated CP-ECR is then compared with a limiting value. It is clear from Section 6.2.1 that this procedure does not guarantee ductility in a balloon. Hydrogen absorption at the cladding ID is so pronounced that we have not found a practical limit that could be used to ensure ductility.

Nevertheless, the current practice does limit oxygen concentrations in the balloon wall and maintains some material toughness. When this practice is used, as was seen in Sections 6.2 and 6.3, the cladding survived quenching without fracture. Although this is a less conservative condition than retaining ductility, quench survival is an important step in maintaining a coolable geometry following a LOCA and is considered sufficient in licensing in some countries (e.g., Japan [37]).

7.4 Criteria for hydrogen-enhanced beta-layer embrittlement

Hydrogen, which enters the outer cladding surface during normal lifetime operation, increases oxygen solubility in the beta layer even at temperatures below 1200ºC. This reduces ductility compared with unirradiated cladding, as seen in Figure 134. The more hydrogen that is absorbed, the bigger the effect will be. Since hydrogen absorption is a by-product of the corrosion process, the effect will increase with increasing corrosion. Based on NRC Information Notice (IN) 98-29 [38], it was recommended that high-burnup effects be accounted for by including the corrosion layer in the calculation of total ECR. This recommended approach is tested by using the data generated in this program for high-burnup HBR 15×15 Zry-4, as well as for unirradiated prehydrided HBR-type 15×15 Zry-4. However, the IN 98-29 recommendation is generalized by including a factor times the corrosion ECR (ECR_{cor}). Thus, the empirical approach proposed and tested can be expressed as:

$$\text{CP-ECR}_t \leq (\text{CP-ECR}_{\text{unirad}})_{\text{limit}} - F \times \text{ECR}_{\text{cor}} \quad (11)$$

where CP-ECR_t is the ECR accumulated during the LOCA transient, $(\text{CP-ECR}_{\text{unirad}})_{\text{limit}}$ is the ductile-to-brittle transition CP-ECR for as-fabricated cladding, and F is the multiplicative factor. The database used to test this empirical criterion and to determine the F-factor for high-burnup Zry-4 is summarized in Table 64.

For HBR-type 15×15 Zry-4 oxidized at 1204ºC and quenched at 800º, $(\text{CP-ECR}_{\text{unirad}})_{\text{limit}}$ is estimated (by interpolation) to be ≈14%, which means that ductility is preserved in the as-fabricated cladding for ≤14% CP-ECR. ECR_{cor} is 5.3-5.6% for high-burnup samples with 71-74 μm thick corrosion layer and 550-wppm hydrogen, and 7.1% for the one sample with a 95-μm-thick corrosion layer and 740-wppm hydrogen. Figure 177 shows the post-quench ductility vs. CP-ECR results for the as-fabricated HBR-type cladding oxidized at 1204ºC and quenched at 800ºC, along with the ductility results for high-burnup HBR Zry-4 oxidized at ≈1200ºC and slow cooled from 800ºC to RT. For slow-cooled high-burnup Zry-4, the ductile to brittle CP-ECR is ≈8.5%, based on interpolation. Thus for the slow-cooled high-burnup samples, F in Equation 11 would be (14% - 8.5%)/(5.3%) = 1.0.

If the high-burnup samples had been quenched at 800ºC, the ductile-to-brittle CP-ECR would decrease to ≈5.7%. For 800ºC-quench, the F factor would be (14% – 5.7%)/5.3% = 1.6. For the one high-burnup sample that was quenched, we can use the result to test Equation 11 for consistency. This sample had a corrosion ECR of 7.1%, a hydrogen content of 740 wppm and no post-quench ductility following oxidation to 7.7% CP-ECR. Based on Equation 7, embrittlement would be expected to occur at ≈2.6% CP-ECR. The experimental result is consistent with the predicted result.

The results in Figure 176 can be used to remove some of the conservatism in the F factor for cladding quenched at 800ºC. Based on more LOCA-relevant cooling rates for large-break PWR LOCAs, the 5.5% CP-ECR at the end of the heating phase would result in 6.4% CP-ECR for 5ºC/s cooling rate and 6.9% CP-ECR for 3ºC/s cooling rate. These cooling rates lead to F factors of 1.4 (5ºC/s cooling rate) and 1.3 (3ºC/s cooling rate). Further conservatism could be removed if the calculated LOCA quench temperature (i.e., wetting temperature leading to very rapid cooling) were <600ºC. Although such quench temperatures were not investigated in this study, they would likely lead to F factors in the range of 1.2±0.2. If quench temperatures at <600ºC can be justified, then it would be relatively straightforward to investigate the effects of such quench temperatures with prehydrided Zry-4.

The empirical correlation represented by Equation 11 requires one set of performance tests to determine the ductile-to-brittle transition CP-ECR for each as-fabricated cladding alloy oxidized at 1200ºC. Based on ANL experience, two-sided-oxidation tests should be conducted with relatively fast heating and cooling rates for temperatures in the range of 800-1200ºC. Heating and cooling rates ≥ 3ºCs should be sufficient in this temperature range. The samples should be quenched at ≥800ºC although ANL results indicate that transition CP-ECR values were insensitive to quench at 800ºC vs. no quench and slow cooling to RT. One-sided-oxidation tests are also acceptable performance tests. As the one-sided tests require long time at 1200ºC to reach the transition CP-ECR limit, slower heating and cooling rates (e.g., 1-3ºCs) would be acceptable.

Table 64 Post-quench and Post-oxidation Ductility Data at 135ºC used to Determine the Ductile-to-Brittle Transition CP-ECR for As-fabricated, Prehydrided and High-burnup Zry-4 Oxidized at ≈1200ºC; ECR_{cor} is corrosion ECR; CP-ECR_h is calculated through the end of the heating phase; and CP-ECR_t is total transient value, including cooling to 800ºC

Material Condition	**Quench (Q) or Slow Cooling (SC)**	**T_{max} ºC**	**ECR_{cor} %**	**CP-ECR_h %**	**CP-ECR_t %**	**Ductility, %**	
						Offset	**Permanent**
As-fabricated	Q-800ºC	1204 ±10	0 0	13.0 12.8	13.1 12.9	3.4 3.1	1.5 1.2
As-fabricated (Interpolation)	**Q-800ºC**	**1204** ±10	**0**	**14.2±0.5**	**14.3±0.5**	**2.2**	**1.0**
As-fabricated	Q-800ºC	1204 ±10	0	15.0	15.1	1.6	0.8
Prehydrided 514±33 wppm	Q-800ºC	1190 ±10	0	5.0	5.3	8.4±4.4	---
Prehydrided 600 wppm (Interpolated)	**Q-800ºC**	**1190** ±10	**0**	**5.0**	**5.3**	**2**	**---**
Prehydrided 636 wppm	Q-800ºC	1190 ±10	0	5.0	5.3	0.5	0.6
Prehydrided ≈550 wppm (Interpolated)	**Q 600-800ºC**	**1190** ±10	**0**	**≈5.5±0.3**	**≈5.7±0.3**	**≈2**	**---**
Prehydrided 450 wppm	Q-800ºC Q-700ºC Q-600ºC	1201 ±3	0	6.0	6.2	0.9±0.2	0.6±0.1
High Burnup 550±100 wppm	SC	1110	5.3	2.7	3.1	>45	>43
High Burnup 550±100 wppm	SC	1170	5.3	4.3	4.6	37	---
High Burnup 550±100 wppm	SC	1195	5.3	6.4	6.6	4.0	2.6
High Burnup 550±100 wppm	SC	1195	5.6	7.4	7.6	4.0	2.9
High Burnup 550±100 wppm (Interpolated)	**SC**	**1195**	**5.3**	**8.3±0.5**	**8.5±0.5**	**2**	**1**
High Burnup 550±100 wppm	SC	1195	5.3	9.3	9.4	0.5	0.6

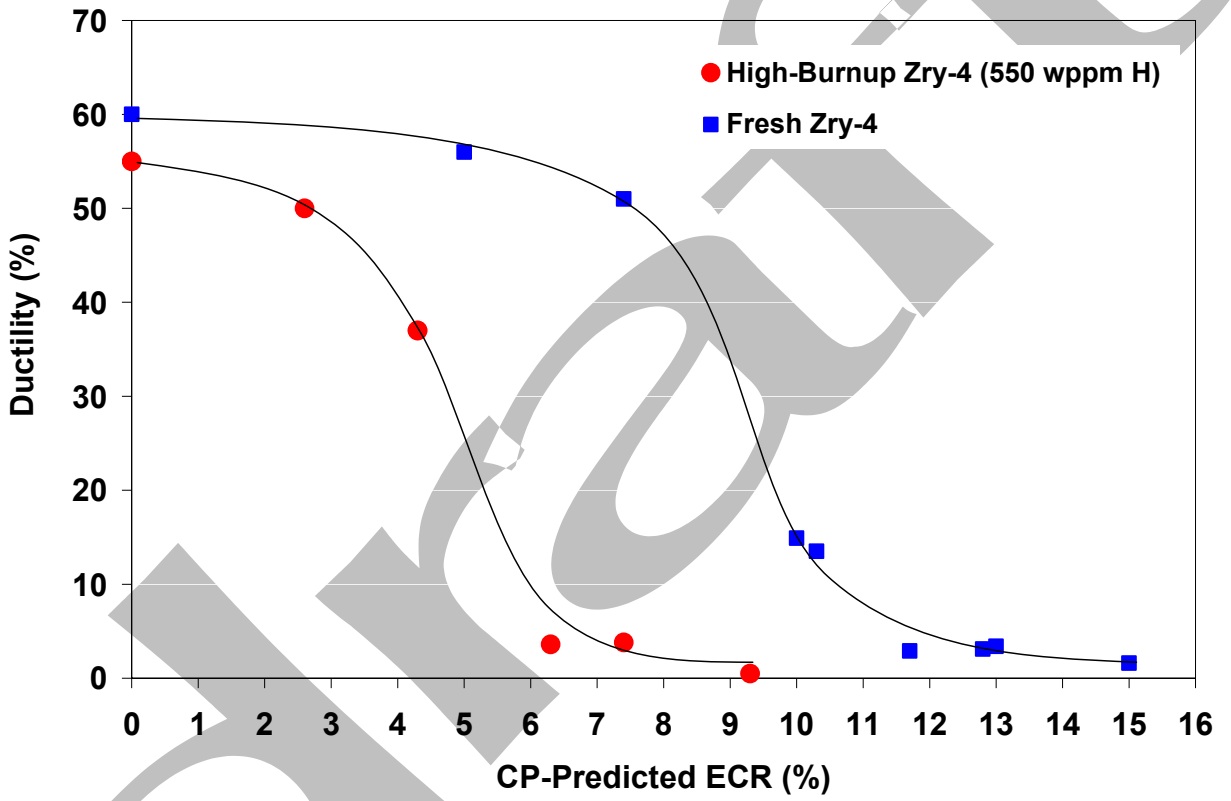

Figure 177. Comparison between offset strains for high-burnup Zry-4 (71-74 μm corrosion-layer thickness, 550-wppm hydrogen) and as-fabricated (fresh) HBR-type 15×15 Zry-4. Cladding samples were two-sided-oxidized at ≈1200ºC and cooled at ≈13ºC/s to 800ºC. As-fabricated samples were quenched at 800ºC, while the high-burnup samples were slow cooled from 800ºC to RT.

The F factor in Equation 7 has been derived for Zry-4 based on a combination of test results for as-fabricated cladding, prehydrided cladding, and high-burnup cladding. The agreement was quite good (see Figure 135) between post-oxidation ductility for prehydrided and high-burnup Zry-4 cladding samples following cooling without quench. The one high-burnup Zry-4 sample (740-wppm-H) that was quenched at 800ºC was brittle following oxidation to 7.5% CP-ECR. This result is consistent with the data set for prehydrided cladding oxidized to 7.5% CP-ECR and quenched at 800ºC. For the M5 and ZIRLO cladding alloys tested in this program and for newer alloys, the sensitivity of these alloys to hydrogen may be different than the sensitivity of Zry-4 post-quench ductility to hydrogen content. This can be investigated by means of a series of tests conducted with prehydrided alloys. However, such tests require more extensive planning to ensure that they give a reasonable lower bound on the ductile-to-brittle transition CP-ECR for prehydrided alloys oxidized at high temperature. Relevant hydrogen levels, heating rates, cooling rates, and quench temperatures need to de determined and justified.

7.5 Criteria for breakaway oxidation

In Figure 29, it is seen that the minimum time for breakaway oxidation in Zircaloy-4 occurs around 1000ºC. The picture is about the same for other cladding alloys, but the minimum does not always occur exactly at 1000ºC. Nevertheless, the minimum can be found by searching in the neighborhood of 1000ºC, and the minimum time can be determined using a hydrogen pickup concentration of 200 wppm as the threshold for breakaway. There is another temperature range (around 775ºC) with relatively low breakaway times. However, the oxidation rate is very slow at the lower temperatures, the hydrogen generation rate is very slow, and it takes a much longer time after breakaway oxidation to pick up 200 wppm of hydrogen. Although this lower temperature region should be characterized, it is unlikely that the time for embrittlement at ≈775ºC would be higher than the time to embrittle at ≈1000ºC.

Diffusion of oxygen in the metal is of course very slow at lower temperatures. Further, there will be no beta material in any of these zirconium-tin-niobium alloys at temperatures below about 650ºC because that is the lowest phase transition temperature of the alloys. Hence a relatively low concentration of oxygen will remain in solution in the alpha-phase metal below 650ºC, and the cladding will remain ductile. It should not be necessary to consider temperatures below the phase transition. Therefore, if the total time spent above 650ºC is less than the measured breakaway time described above, breakaway will not occur.

From Tables 19, 26, and 32 it is seen that the breakaway times for modern belt-polished Zry-4, ZIRLO, and M5 are about 5000, 3000, and 6000 seconds, respectively. It is also seen from Table 18 that older rough-surface Zry-4 has a breakaway time of about 3500 seconds. These limits are particularly important for some small-break LOCAs with lower oxidation temperatures and much longer oxidation times above 650ºC. On the other hand, the breakaway time for E110 can be seen in Figure 89 to be only about 500 seconds, which is a much shorter time than the duration of small-break LOCAs.

7.6 Criteria for oxygen pickup from the cladding inside diameter (ID)

Accounting for ID oxygen pickup can be done in an analysis rather than with criteria *per se*. Because ID oxygen pickup is already accounted for within the ballooned region using the current industry practice, it is only necessary to modify the analysis for cladding locations away from a balloon to account for the more general ID oxygen pickup in high-burnup fuel.

For fresh cladding that experiences LOCA conditions, there is no oxygen pickup from the cladding ID away from the balloon and Equation 5 for one-sided oxidation will give the appropriate CP-ECR. For

moderate-to-high burnup fuel, however, oxygen pickup at the inner cladding surface will be bounded by the oxygen pickup due to steam oxidation. Thus, two-sided oxidation will give a reasonable upper-bound on the transient CP-ECR to be compared to the transient CP-ECR limit.

The exact burnup for a transition from Equation 5 to Equation 6 is not well defined. For burnups above 30 GWd/MT in PWRs and 40 GWd/MT in BWRs, there will be some fuel-to-cladding bonding and this is an indication that there will be some ID oxygen pickup during a LOCA. By 50 GWd/MT for PWRs (60 GWd/MT for BWRs), fuel bonding is likely to be well developed and ID oxygen pickup from the bond and fuel may be as high as the OD oxygen pickup from flowing steam.

7.7 Summary

Two tests can be used to make a practical prediction of the onset of embrittlement. The first is a determination of the time that would produce breakaway oxidation, as described in Section 7.5. If the LOCA transient of interest persists for less than this time, then the second test is needed. The second test involves the determination of the ductile-to-brittle transition CP-ECR for the as-fabricated alloy oxidized at 1200ºC, quenched at 800ºC and ring-compressed at 135ºC.

If $(\text{CP-ECR}_{\text{unirrad}})_{\text{limit}}$ is the threshold value as described in Section 7.1 and ECR_{cor} is the percent of the wall-thickness consumed by corrosion of irradiated cladding, then $\text{CP-ECR}_{\text{unirrad}} - F \times \text{ECR}_{\text{cor}}$ will give a good indication of the embrittlement threshold of high-burnup Zry-4. Based on the experimental results for high-burnup Zry-4 and extrapolation to upper-bound LOCA cooling rates, F = 1.4 for samples rapidly cooled (≤5ºC/s) to 800ºC and quenched at 800ºC; and F = 1.0 for samples cooled to RT without quench. Based on two sets of tests, F = 1.4 would apply to quench temperatures in the range of 600-800ºC. The F factor of 1.4 might be overly conservative for quench temperatures <600ºC. Lower quench temperatures result in higher transient CP-ECR values leading to embrittlement. For this range of LOCA transients, the estimated value for F is 1.2±0.2.

If no fuel-to-cladding bonding is present, Equation 5 for one-sided oxidation will give the appropriate CP-ECR. If there is complete bonding, Equation 6 for two-sided oxidation will give a bounding CP-ECR to account for oxygen pickup from the inner surface of the cladding.

Although these tests will give a good prediction of the onset of embrittlement for most of the fuel rod, that prediction will not apply within the burst region, which will almost always be brittle due to high hydrogen pickup from the inner surface of the cladding.

References

1. G. Hache and H. M. Chung, "The History of LOCA Embrittlement Criteria," NUREG/CP-0172 (2001) pp 205-237

2. L. Yegorova, K. Lioutov, N. Jouravkova, A. Konobeev, V. Smirnov, V. Chesanov, and A. Goryachev, "Experimental Study of Embrittlement of Zr-1%Nb VVER Cladding under LOCA-Relevant Conditions," NUREG/IA-0211 (2005).

3. Annual Book of ASTM Standards, "Standard Specification for Wrought Zirconium Alloy Seamless Tubes for Nuclear Reactor Fuel Cladding," Vol. 02.04 (1997).

4. R. J. Comstock, G. Schoenberger, and G. P. Sabol, "Influence of Processing Variables and Alloy Chemistry on the Corrosion Behavior of ZIRLO Nuclear Fuel Cladding," *Zirconium in the Nuclear Industry: Eleventh International Symposium, ASTM STP 1295,* E. R. Bradley and G. P. Sabol, Eds., American Society for Testing and Materials, 1996, pp. 710-725.

5. W. J. Leech, "Ductility Testing of Zircaloy-4 and ZIRLO™ Cladding After High Temperature Oxidation in Steam," NEA/CSNI/R(2001)18, pp. 135-143.

6. J.-P. Mardon, D. Charquet, and J. Senevat, "Influence of Composition and Fabrication Process on Out-of-Pile and In-Pile Properties of M5 Alloy," *Zirconium in the Nuclear Industry: Twelfth International Symposium, ASTM STP 1354,* G. P. Sabol and G. D. Moan, Eds., American Society for Testing and Materials, West Conshohocken, PA, 2000, pp. 505-524.

7. P. V. Shebaldov, M. M. Peregud, A. V. Nikulina, Y. K. Bibilashvilli, A. F. Lositski, N. V. Kuz'menko, V. I. Belov, and A. E. Novoselov, "E1110 Alloy Cladding Tube Properties and Their Interrelation with Alloy Structure-Phase Condition and Impurity Content," *Zirconium in the Nuclear Industry: Twelfth International Symposium, ASTM STP 1354,* G. P. Sabol and G. D. Moan, Eds., American Society for Testing and Materials, West Conshohocken, PA, 2000, pp. 545-559.

8. O. Kubaschewski, Metallurgical Thermochemistry, Pergamon Press, 1967.

9. James P. Coughlin, "Contributions to the Data on Theoretical Metallurgy," XII, Heats and Free Energies of Formation of Inorganic Oxides, U.S. G.P.O., 1954.

10. G. M. O'Donnell, H. H. Schott, and R. O. Meyer, "A New Comparative Analysis of LWR Fuel Designs," NUREG-1754 (2001) pp. .

11. L. Yegorova, K. Lioutov, N. Jouravkova, O. Nechaeva, A. Salatov, V. Smirnov, A. Goryachev, V. Ustinenko, and I. Smirnov, "Experimental Study of Narrow Pulse Effects on the Behavior of High Burnup Fuel Rods with Zr-1%Nb Cladding and UO_2 Fuel (VVER type) under Reactivity-Initiated Accident Conditions: Program Approach and Analysis of Results," NUREG/IA-0213, Vol. 1 (2006).

12. L. Baker and L. C. Just, "Studies of Metal-Water Reactions at High Temperatures; III. Experimental and Theoretical Studies of the Zirconium-Water Reaction," ANL-6548, May 1962.

13. J. V. Cathcart, R. E. Pawel, R. A. McKee, R. E. Druscel, G. J. Yurek, J. J. Cambell, and S. H. Jury, "Zirconium Metal-Water Oxidation Kinetics IV. Reaction Rate Studies," ORNL/NUREG-17, Aug. 1977.

14. P. Hofmann and C. Politis, "Chemical Interaction Between Uranium Oxide and Zircaloy-4 in the Temperature Range Between 900 and 1500˚C," *Zirconium in the Nuclear Industry (Fourth Conference),* ASTM STP 681, American Society for Testing and Materials, 1979, pp. 537-560.

15. Y. Yan, R. V. Strain, T. S. Bray, and M. C. Billone, "High Temperature Oxidation of Irradiated Limerick BWR Cladding," NUREG/CP-0176, (2002) pp. 353-372.

16. D. O. Hobson, "Ductile-Brittle Behavior of Zircaloy Fuel Cladding," pp. 274-288.

17. D. O. Hobson and P. L. Rittenhouse, "Embrittlement of Zircaloy-Clad Fuel Rods by Steam during LOCA Transients," ORNL-4758 (1972).

18. H. M. Chung and T. F. Kassner, "Pseudobinary Zircaloy-Oxygen Phase Diagram," J. Nucl. Matls. 84 (1979) 327-339.

19. S. Leistikow and G. Schantz, "The Oxidation Behavior of Zircaloy-4 in Steam between 600 and 1600˚C", Werkstoffe und Korrosion 36, (1985) 105-116.

20. S. Leistikow and G. Schanz, "Oxidation Kinetics and Related Phenomena of Zircaloy-4 Fuel Cladding Exposed to High Temperature Steam and Hydrogen-Steam Mixtures under PWR Accident Conditions," Nucl. Eng. And Des. 103 (1987) 65-84.

21. J. P. Mardon, J. C. Brachet, L. Portier, V. Maillot, T. Forgeron, A. Lesbros, and N. Waeckel, "Influence of Hydrogen Simulating Burn-Up Effects on the Metallurgical and Thermal-Mechanical Behavior of M5™ and Zircaloy-4 Alloys under LOCA Conditions," ICONE13-50457, 13th Intl. Conf. on Nucl. Eng., Beijing, China, May 16-20, 2005, pp. 1-9.

22. Y. Yan, R. V. Strain, and M. C. Billone, "LOCA Research Results for High-Burnup BWR Fuel," NUREG/CP-0180 (2003) pp. 127-155.

23. B. Cheng and R. B. Adamson, "Mechanistic Studies of Zircaloy Nodular Corrosion," *Zirconium in the Nuclear Industry: Seventh International Symposium, ASTM STP 939,* R. B. Adamson and L. F. P. Van Swam, Eds., American Society for Testing and Materials, Philadelphia, 1987, pp. 387-416.

24. B. Cheng, H. A. Levin, R. B. Adamson, M. O. Marlowe, and V. L. Monroe, "Development of a Sensitive and Reproducible Steam Test for Zircaloy Nodular Corrosion," *Zirconium in the Nuclear Industry: Seventh International Symposium*, *ASTM STP 939,* R. B. Adamson and L. F. P. Van Swam, Eds., American Society for Testing and Materials, Philadelphia, 1987, pp. 257-283.

25. A. V. Nikulina, L. N. Andreeva-Andrievskaya, V. N. Shishov, Yu. V. Pimenov, "Influence of Chemical Composition of Nb Containing Zr Alloy Cladding Tubes on Embrittlement under Conditions Simulating Design Basis LOCA," presentation at the 14th Intl. Symp. on Zirconium in the Nuclear Industry, Stockholm, Sweden, June 13-17, 2004.

26. R. E. Pawel, R. A. Perkins, R. A. McKee, J. V. Cathcart, G. J. Yurek, and R. E. Druschel, "Diffusion of Oxygen in Beta-Zircaloy and the High Temperature Zircaloy-Steam Reaction," *Zirconium in the Nuclear Industry, ASTM STP 633,* A. L. Lowe, Jr. and G. W. parry, Eds., American Society for Testing and Materials, 1977, pp. 119-133.

27. E. J. Ruzauskas and K. N. Fardell, "Design, Operation, and Performance Data for High Burnup PWR Fuel from the H. B. Robinson Plant for Use in the NRC Experimental Program at Argonne National Laboratory," 1001558, EPRI, Palo Alto, CA (2001).

28. L. F. Van Swam, G. M. Bain, W. C. Dey, D. D. Davis, and H. Heckermann, "BWR and PWR fuel Performance at High Burnup," *Proceedings of the 1997 Intl. Topical Meeting on LWR Fuel Performance,* Porland, Oregon, March 2-6, 1997.

29. H. Tsai and M. C. Billone, "Characterization of High-Burnup PWR and BWR Rods, and PWR Rods after Extended Dry-Cask Storage," NUREG/CP-0180 (2003) pp. 157-168.

30. L. F. Van Swam, A. A. Strasser, J. D. Cook, and J. M. Burger, "Behavior of Zircaloy-4 and Zirconium Liner Zircaloy-4 Cladding at High Burnup," *Proceedings of the 1997 Intl. Topical Meeting on LWR Fuel Performance,* Portland, OR, March 2-6, 1997.

31. K. Une, K. Nogita, S. Kashibe, T. Toyonaga, and M. Amaya, « Effect of Irradiation-Induced Microstructural Evolution on High Burnup Fuel Behavior, » *Proceedings of the 1997 International Topical Meeting on LWR Fuel Performance*, Portland, OR, March 2-6, 1997.

32. Y. Yan, R. V. Strain, and M. C. Billone, "LOCA Research Results for High-Burnup BWR fuel," NUREG/CP-0180 (2003) 127-155.

33. Yong Yan, Michael C. Billone, Tatiana A. Burtseva, and Hee M. Chung, "LOCA Integral Test Results for High-Burnup BWR Fuel," NUREG/CP-0192 (2005) pp. 138-158.

34. R. R. Hobbins, G. R. Smolik, and G. W. Gibson, "Zircaloy Cladding Behavior During Irradiation Tests Under Power-Cooling-Mismatch Conditions," *Zirconium in the Nuclear Industry,* ASTM STP 633, A. L. Lowe and G. W. Parry, Eds., American Society for Testing and Materials, 1977, pp. 182-208.

35. B. E. Boyack, A. T. Motta, K. L. Peddicord, C. A. Alexander, J. G. M. Andersen, J. A. Blaisdell, B. M. Dunn, D. Ebeling-Koning, T. Fuketa, G. Hache, L. E. Hochreiter, S. E. Jensen, S. Langenbuch, F. J. Moody, M. E. Nissley, K. Ohkawa, G. Potts, J. Rashid, R. J. Rohrer, J. S. Tulenko, K. Valtonen, N. Waeckel, and W. Wiesenack, "Phenomenon Identification and Ranking Tables (PIRTs) for Loss-of-Coolant Accidents in Pressurized and Boiling Water Reactors Containing High Burnup Fuel," NUREG/CR-6744 (2001).

36. M. E. Nissley, C. Frepoli, and K. Ohkawa, "Realistic Assessment of Fuel Rod Behavior Under Large-Break LOCA Conditions," NUREG/CP-0192 (2005) pp. 231-273.

37. Fumihisa Nagase and Toyoshi Fuketa, "Results from Studies on High Burn-up Fuel Behavior under LOCA Conditions," NUREG/CP-0192 (2005) pp. 197-230.

38. NRC Information Notice 98-29: Predicted Increase in Fuel Rod Cladding Oxidation, August 3, 1998.